PERSPECTIVES FOR THE NEXT GENERATION OF VIRUS RESEARCH: SPEARHEADING THE USE OF INNOVATIVE TECHNOLOGIES AND METHODOLOGIES

EDITED BY: Takatoki Yamamoto, Ayae Honda, Toshinori Sato and Akihide Ryo
PUBLISHED IN: Frontiers in Microbiology

frontiers Research Topics

Frontiers Copyright Statement

© Copyright 2007-2017 Frontiers Media SA. All rights reserved.

All content included on this site, such as text, graphics, logos, button icons, images, video/audio clips, downloads, data compilations and software, is the property of or is licensed to Frontiers Media SA ("Frontiers") or its licensees and/or subcontractors. The copyright in the text of individual articles is the property of their respective authors, subject to a license granted to Frontiers.

The compilation of articles constituting this e-book, wherever published, as well as the compilation of all other content on this site, is the exclusive property of Frontiers. For the conditions for downloading and copying of e-books from Frontiers' website, please see the Terms for Website Use. If purchasing Frontiers e-books from other websites or sources, the conditions of the website concerned apply.

Images and graphics not forming part of user-contributed materials may not be downloaded or copied without permission.

Individual articles may be downloaded and reproduced in accordance with the principles of the CC-BY licence subject to any copyright or other notices. They may not be re-sold as an e-book.

As author or other contributor you grant a CC-BY licence to others to reproduce your articles, including any graphics and third-party materials supplied by you, in accordance with the Conditions for Website Use and subject to any copyright notices which you include in connection with your articles and materials.

All copyright, and all rights therein, are protected by national and international copyright laws.

The above represents a summary only. For the full conditions see the Conditions for Authors and the Conditions for Website Use.

ISSN 1664-8714
ISBN 978-2-88945-215-6
DOI 10.3389/978-2-88945-215-6

About Frontiers

Frontiers is more than just an open-access publisher of scholarly articles: it is a pioneering approach to the world of academia, radically improving the way scholarly research is managed. The grand vision of Frontiers is a world where all people have an equal opportunity to seek, share and generate knowledge. Frontiers provides immediate and permanent online open access to all its publications, but this alone is not enough to realize our grand goals.

Frontiers Journal Series

The Frontiers Journal Series is a multi-tier and interdisciplinary set of open-access, online journals, promising a paradigm shift from the current review, selection and dissemination processes in academic publishing. All Frontiers journals are driven by researchers for researchers; therefore, they constitute a service to the scholarly community. At the same time, the Frontiers Journal Series operates on a revolutionary invention, the tiered publishing system, initially addressing specific communities of scholars, and gradually climbing up to broader public understanding, thus serving the interests of the lay society, too.

Dedication to Quality

Each Frontiers article is a landmark of the highest quality, thanks to genuinely collaborative interactions between authors and review editors, who include some of the world's best academicians. Research must be certified by peers before entering a stream of knowledge that may eventually reach the public - and shape society; therefore, Frontiers only applies the most rigorous and unbiased reviews.
Frontiers revolutionizes research publishing by freely delivering the most outstanding research, evaluated with no bias from both the academic and social point of view.
By applying the most advanced information technologies, Frontiers is catapulting scholarly publishing into a new generation.

What are Frontiers Research Topics?

Frontiers Research Topics are very popular trademarks of the Frontiers Journals Series: they are collections of at least ten articles, all centered on a particular subject. With their unique mix of varied contributions from Original Research to Review Articles, Frontiers Research Topics unify the most influential researchers, the latest key findings and historical advances in a hot research area! Find out more on how to host your own Frontiers Research Topic or contribute to one as an author by contacting the Frontiers Editorial Office: **researchtopics@frontiersin.org**

PERSPECTIVES FOR THE NEXT GENERATION OF VIRUS RESEARCH: SPEARHEADING THE USE OF INNOVATIVE TECHNOLOGIES AND METHODOLOGIES

Topic Editors:
Takatoki Yamamoto, Tokyo Institute of Technology, Japan
Ayae Honda, Hosei University, Japan
Toshinori Sato, Keio University, Japan
Akihide Ryo, Yokohama City University School of Medicine, Japan

Infectious diseases are associated with approximately 20% of global mortality, with viral diseases causing about one third of these deaths. Besides newly emerging and re-emerging viral infections will continue to pose a threat to human survival globally. In this case scientific advances have greatly been increased to defend against those pathogens. For example, rapid genomic sequencing, proteomics, epigenomics, nanotechnology, and other advanced tools are being applied to detect viruses at the point of care and to track their spread within human populations as well as to understand virus-host interaction and virus induced pathogenesis. From rapid identification of new viruses to prevention with vaccination and treatment with effective therapeutics, biomedical research has continuously provided tools to meet the constant threat of emerging viral pathogens. Despite these advances, each new disease brings unique challenges to scientists every year. So we must stay at the cutting edge of scientific discovery, working energetically to develop new tools to combat the ever-changing threats they pose. Our research topic highlights such advanced and new technology based virus research which definitely bolsters the researcher's ability to tackle emerging, re-emerging and stable viral pathogens. We are credulous that the papers including in the e-books will be beneficial to the experts in the field to understand the molecular, immunological, ecological and clinical aspects of the next generation researches for the prevention and control of infectious diseases caused by viruses.

Citation: Yamamoto, T., Honda, A., Sato, T., Ryo, A., eds. (2017). Perspectives for the Next Generation of Virus Research: Spearheading the Use of Innovative Technologies and Methodologies. Lausanne: Frontiers Media. doi: 10.3389/978-2-88945-215-6

Table of Contents

05 ***Editorial: Perspectives for the Next Generation of Virus Research: Spearheading the Use of Innovative Technologies and Methodologies***
Takatoki Yamamoto, Ayae Honda, Toshinori Sato and Akihide Ryo

Chapter 1: Research Article

1.1. Virus-Host Interactions

07 ***Influenza Virus Infection Induces Host Pyruvate Kinase M Which Interacts with Viral RNA-Dependent RNA Polymerase***
Yukari Miyake, Kosuke Ishii and Ayae Honda

14 ***The Influence of Virus Infection on the Extracellular pH of the Host Cell Detected on Cell Membrane***
Hengjun Liu, Hisataka Maruyama, Taisuke Masuda, Ayae Honda and Fumihito Arai

22 ***Liposome-Mediated Herpes Simplex Virus Uptake Is Glycoprotein-D Receptor-Independent but Requires Heparan Sulfate***
Lorrie A. Burnham, Dinesh Jaishankar, Jeffrey M. Thompson, Kevin S. Jones, Deepak Shukla and Vaibhav Tiwari

32 ***H11/HSPB8 Restricts HIV-2 Vpx to Restore the Anti-Viral Activity of SAMHD1***
Ayumi Kudoh, Kei Miyakawa, Satoko Matsunaga, Yuki Matsushima, Isao Kosugi, Hirokazu Kimura, Satoshi Hayakawa, Tatsuya Sawasaki and Akihide Ryo

46 ***Binding of Hemagglutinin and Influenza Virus to a Peptide-Conjugated Lipid Membrane***
Teruhiko Matsubara, Rabi Shibata and Toshinori Sato

1.2. Novel Methodology and Technology Based Virus Research

55 ***Analysis of the Changes in Expression Levels of Sialic Acid on Influenza-Virus-Infected Cells Using Lectin-Tagged Polymeric Nanoparticles***
Jaebum Cho, Yukari Miyake, Ayae Honda, Keiichiro Kushiro and Madoka Takai

64 ***Specific Destruction of HIV Proviral p17 Gene in T Lymphoid Cells Achieved by the Genome Editing Technology***
Tsunao Kishida, Akika Ejima and Osam Mazda

69 ***Proteomic Analysis of a Novel* Bacillus *Jumbo Phage Revealing Glycoside Hydrolase As Structural Component***
Yihui Yuan and Meiying Gao

80 ***Characterization of the Deamination Coupled with Sliding along DNA of Anti-HIV Factor APOBEC3G on the Basis of the pH-Dependence of Deamination Revealed by Real-Time NMR Monitoring***
Keisuke Kamba, Takashi Nagata and Masato Katahira

91 ***A cell-free enzymatic activity assay for the evaluation of HIV-1 drug resistance to protease inhibitors***
Satoko Matsunaga, Takashi Masaoka, Tatsuya Sawasaki, Ryo Morishita, Yasumasa Iwatani, Masashi Tatsumi, Yaeta Endo, Naoki Yamamoto, Wataru Sugiura and Akihide Ryo

101 ***Nonlinear electrical impedance spectroscopy of viruses using very high electric fields created by nanogap electrodes***
Ryuji Hatsuki, Ayae Honda, Masayuki Kajitani and Takatoki Yamamoto

1.3. Detection and Quantification

108 ***Development of Monoclonal Antibody and Diagnostic Test for Middle East Respiratory Syndrome Coronavirus Using Cell-Free Synthesized Nucleocapsid Antigen***
Yutaro Yamaoka, Shutoku Matsuyama, Shuetsu Fukushi, Satoko Matsunaga, Yuki Matsushima, Hiroyuki Kuroyama, Hirokazu Kimura, Makoto Takeda, Tomoyuki Chimuro and Akihide Ryo

123 ***Visual Detection of West Nile Virus Using Reverse Transcription Loop-Mediated Isothermal Amplification Combined with a Vertical Flow Visualization Strip***
Zengguo Cao, Hualei Wang, Lina Wang, Ling Li, Hongli Jin, Changping Xu, Na Feng, Jianzhong Wang, Qian Li, Yongkun Zhao, Tiecheng Wang, Yuwei Gao, Yiyu Lu, Songtao Yang and Xianzhu Xia

132 ***Finite Element Analysis on Nanomechanical Detection of Small Particles: Toward Virus Detection***
Gaku Imamura, Kota Shiba and Genki Yoshikawa

139 ***Quantification of Virus Particles Using Nanopore-Based Resistive-Pulse Sensing Techniques***
Lu Yang and Takatoki Yamamoto

Chapter 2: Review Article

146 ***DGV: Dengue Genographic Viewer***
Akifumi Yamashita, Tetsuya Sakamoto, Tsuyoshi Sekizuka, Kengo Kato, Tomohiko Takasaki and Makoto Kuroda

154 ***Strategies for Human Tumor Virus Discoveries: From Microscopic Observation to Digital Transcriptome Subtraction***
Ezra D. Mirvish and Masahiro Shuda

162 ***Filopodia and Viruses: An Analysis of Membrane Processes in Entry Mechanisms***
Kenneth Chang, John Baginski, Samer F. Hassan, Michael Volin, Deepak Shukla and Vaibhav Tiwari

175 ***Biogenesis, Function, and Applications of Virus-Derived Small RNAs in Plants***
Chao Zhang, Zujian Wu, Yi Li and Jianguo Wu

Chapter 3: Data Report

187 ***Genome Sequence of* Dengue virus 3 *from the* Pythium insidiosum *Transcriptomes***
Yeonhwa Jo, Hoseong Choi and Won K. Cho

frontiers in Microbiology

EDITORIAL
published: 11 May 2017
doi: 10.3389/fmicb.2017.00758

Editorial: Perspectives for the Next Generation of Virus Research: Spearheading the Use of Innovative Technologies and Methodologies

Takatoki Yamamoto[1], *Ayae Honda*[2], *Toshinori Sato*[3] *and Akihide Ryo*[4]*

[1] *Department of Mechanical Engineering, School of Engineering, Tokyo Institute of Technology, Tokyo, Japan,* [2] *Department of Frontier Bioscience, Hosei University, Tokyo, Japan,* [3] *Department of Biosciences and Informatics, Faculty of Science and Technology, Keio University, Yokohama, Japan,* [4] *Department of Microbiology, Yokohama City University School of Medicine, Yokohama, Japan*

Keywords: technology, nano-sensor, optical tweezer, proteomics, glycomics, bio-informatics, peptide, DNA editing technology

Editorial on the Research Topic

Perspectives for the Next Generation of Virus Research: Spearheading the Use of Innovative Technologies and Methodologies

OPEN ACCESS

Edited by:
Akio Adachi,
Tokushima University, Japan

Reviewed by:
Akio Adachi,
Tokushima University, Japan
Mikako Fujita,
Kumamoto University, Japan

***Correspondence:**
Akihide Ryo
aryo@yokohama-cu.ac.jp

Specialty section:
This article was submitted to Virology, a section of the journal Frontiers in Microbiology

Received: *14 March 2017*
Accepted: *12 April 2017*
Published: *11 May 2017*

Citation:
Yamamoto T, Honda A, Sato T and Ryo A (2017) Editorial: Perspectives for the Next Generation of Virus Research: Spearheading the Use of Innovative Technologies and Methodologies. Front. Microbiol. 8:758. doi: 10.3389/fmicb.2017.00758

Science and technology are fundamental to overcome future challenges and threats to humankind. For instance, infectious diseases have emerged and re-emerged as a major global hazard in the early twenty-first century. This threat has become accepted as one of the most important issues to be tackled by science. Technological innovations have led to a better understanding of ongoing scientific challenges such as those posed by viruses. Our research topic aims to advance the field of virology by promoting cutting-edge technologies and technology convergence that have not been commonly used before. The technologies that could be cataloged in this novel collection include nanobiosensors, nanopore/nanochannel detectors, optical tweezers, functional proteomics, functional glycomics, trans-omics informatics, peptide-based drug discovery, next-generation sequencing and DNA editing technology.

This Research Topic contains 3 review articles, 1 mini-review article, 1 data report and 15 original research articles.

Miyake et al. at first research article identifies the host factor pyruvate kinase M2 that interacts with the PA subunit of RNA-dependent RNA polymerase (RdRp), which is vital for transcription and replication of influenza virus. This article integuments molecular mechanism of host-virus interaction and offers the exciting insight into the development of new therapeutic approaches. The review article by Yang and Yamamoto provides the overview of the sophisticated nanopore based electrical sensing techniques for quantitative detection of virus particles. Here the authors show that nanostructure-based electrical sensors may use for real-time, sensitive detection of new and unknown virus particles in the absence of biochemical information. In the third issue the authors (Liu et al.) depict that extracellular pH reduces near cell membrane followed by influenza virus infection. In this study they develop a sensor based on Rhodamine B and FITC fluorescence for measurement of pH changes. Cho et al. uses the fluorescent polymeric nanoprobes for observing the levels of sialic acid receptors expressed on cell membrane to examine the progression of influenza viral infection. Human Immunodeficiency Virus (HIV) infection causes integration of proviral DNA into the chromosomes that potentially leads to reemergence of virus. In the fifth research article Kishida et al. manifests that this proviral DNA can be destructed by genome

editing technology. In the sixth subject the authors explore a novel fact for entry of HSV-1 into the Chinese hamster ovary (CHO-K1) cell using lipofectamine transfection reagent (Burnham et al.). Glycoprotein-D receptor is mainly responsible for HSV-1 entry into the cell but here they delineate that HSV-1 is entered into CHO-K1 cell independent of gD receptor.

Jo et al. publishes a data report for complete genome sequencing of Dengue Virus (DENV) 3 from the *Pythium insidiosum* transcriptomes. In this data report the authors use several modern and new techniques such as NGS, MEGA BLAST, FASTA which give incredible acquaintance to the readers for future virus research. The research article by Kudoh et al. develops a new proteomic approach to study virus host interaction. They show how host regulatory factor HSPB8 negatively affects the replication of HIV-2 that may be decisive for preventing placental infection of HIV-2 during pregnancy. In the ninth case Yamashita et al. designs a database Dengue Genographic Viewer (DGV) which is freely available at online. DGV covers the geographical distribution of DENV genotype and serotype in a user specified time span. DGV may aid in planning to scientists for the control of DENV infections. Yuan and Gao identifies several phage structural proteins by structural proteome analysis. The review article by Mirvish and Shuda aims at deciphering the discovery of the human tumor viruses using Digital Transcriptome Subtraction (DTS) than other conventional microscopic observation. The focus is how DTS developed and used for the discovery of merkel cell polyomavirus (MCV). In the 12th research article Kamba et al. represents the methodology for the real time NMR spectroscopy and the ease of its usage and legibility to systems having different temporal and spatial resolution. In the 13th case as original research article Yamaoka et al. develop a novel, rapid and reliable antigen detection assay for MERS coronavirus using the monoclonal antibodies. They produce the monoclonal antibodies by wheat germ cell free system using NP antigen of MERS-CoV. This study serves the necessary cue that the wheat germ cell-free system is useful for the development of diagnostic mAbs against new emerging pathogens. Cao et al. at 14th research article establishes a method to diagnose WNV using isothermal amplification combined with a vertical flow visualization strip. This assay is rapid, simple and suitable for clinical application in the field. In the next article Imamura et al. focuses an approach to detect viruses with nanomechanical sensors. The research article by Matsubara et al. depicts a penta peptide of lipid membrane that binds to hemagglutinin (HA) during influenza virus infection by mimicking sialic acid. Chang et al. review the significance of filopodia in viral diseases. Here the authors overview the key determinants of filopodial induction and their influence on cell topography including receptor expression for viral entry. In the 18th review article Zhang et al. provides an overview of virus derived small interfering RNAs (vsiRNAs) pathways focusing the advances in vsiRNAs biogenesis and function in the field of plant virus research. In the 19th research article Matsunaga et al. develops a novel *in vitro* method, the cell-free drug susceptibility assay (CFDSA), for monitoring phenotypic information regarding the drug resistance of HIV-1 protease (PR). The CFDSA utilizes a wheat germ cell-free protein production system to synthesize enzymatically active HIV-1 PRs. Finally in the last issue Hatsuki et al. in the original research article proposes a virus detection method by nonlinear impedance spectroscopy under a strong electric field between two nanogap electrodes.

In summary, it is concluded that these works are well outlined to flourish the new and innovative approaches understanding the basic and clinical aspects of the technology-based virus research. We are optimistic that this collection of papers will eventually boost the knowledge of readers and serve as fundamental frameworks for future virus research.

AUTHOR CONTRIBUTIONS

All authors listed, have made direct and intellectual contribution to the work, and approved it for publication.

FUNDING

This work was supported in part by a Creation of Innovation Centers for Advanced Interdisciplinary Research Areas Program and JSPS Grants-in-Aid for Scientific Research (16H05198) to AR.

ACKNOWLEDGMENTS

We thank the all contributors who made the Research Topic successful. We also thank Hajera Khatun for editing the manuscript.

Conflict of Interest Statement: The authors declare that the research was conducted in the absence of any commercial or financial relationships that could be construed as a potential conflict of interest.

Copyright © 2017 Yamamoto, Honda, Sato and Ryo. This is an open-access article distributed under the terms of the Creative Commons Attribution License (CC BY). The use, distribution or reproduction in other forums is permitted, provided the original author(s) or licensor are credited and that the original publication in this journal is cited, in accordance with accepted academic practice. No use, distribution or reproduction is permitted which does not comply with these terms.

frontiers in Microbiology

ORIGINAL RESEARCH
published: 09 February 2017
doi: 10.3389/fmicb.2017.00162

Influenza Virus Infection Induces Host Pyruvate Kinase M Which Interacts with Viral RNA-Dependent RNA Polymerase

Yukari Miyake, Kosuke Ishii and Ayae Honda†*

Department of Frontier Bioscience, Hosei University, Tokyo, Japan

Influenza virus RNA-dependent RNA polymerase (RdRp) is a heterotrimer of three viral proteins, PB1, PB2, and PA and is involved in both transcription and replication of the negative strand of the viral RNA (vRNA) genome. RdRp is multifunctional, possessing RNA polymerase, cap binding, and endonuclease activities. The enzyme synthesizes three different RNAs, complementary RNA (cRNA) and messenger RNA (mRNA) from vRNA, and vRNA from cRNA. To synthesize these three RNAs, RdRp requires conversion of its function by host factor. Here, we performed yeast two-hybrid screening to identify the relevant host factor, revealing that pyruvate kinase M2 (PKM2) interacted with the PA subunit of influenza virus RdRp. PKM2 is one of two enzymes (PKM1 and PKM2) produced by alternative splicing of the pyruvate kinase M (*PKM*) pre-mRNA. We determined the interacting regions in both PKM2 and PA, the expression level of PKM by western blotting at different time points after viral infection, and the effects of transfection of siRNA targeting PKM on influenza virus replication. The results demonstrated that the C-terminal region of PKM2 interacted with the C-terminus of the PA subunit, that the expression level of PKM2 increased with influenza virus infection time, and that this enzyme is essential for influenza virus multiplication. Moreover, isoelectric focusing of uninfected and influenza virus infected cell extracts, followed by gradient gel electrophoresis to separate the PKM1 and PKM2 isoforms and western blotting indicated that PKM2 became more acidic after influenza infection. The decreased pH of PKM2 may have been due to phosphorylation, and phosphorylated PKM2 is active as a pyruvate kinase and protein kinase; therefore, it is possible that PKM2 may transfer a phosphate group to PA and consequently transform the function of RdRp from transcriptase to replicase.

Keywords: influenza virus, RdRp, pyruvate kinase M, RNA synthesis, PA subunit, yeast two-hybrid screening, PKM2, PKM1

OPEN ACCESS

Edited by:
Francois Villinger, University of Louisiana at Lafayette, USA

Reviewed by:
Peirong Jiao, South China Agricultural University, China
Sanjeev Gumber, Emory University, USA

****Correspondence:***
Ayae Honda
ayhonda85@gmail.com

†Present address:
Ayae Honda, School of Pharmacology, Nihon University, Narashinodai, Japan

Specialty section:
This article was submitted to Virology, a section of the journal Frontiers in Microbiology

Received: *21 April 2016*
Accepted: *20 January 2017*
Published: *09 February 2017*

Citation:
Miyake Y, Ishii K and Honda A (2017) Influenza Virus Infection Induces Host Pyruvate Kinase M Which Interacts with Viral RNA-Dependent RNA Polymerase. Front. Microbiol. 8:162. doi: 10.3389/fmicb.2017.00162

INTRODUCTION

The genome of influenza virus is composed of eight negative RNA molecule segments (Palese and Shaw, 2007). RNA-dependent RNA polymerase (RdRp) binds to the promoter region of each segment of genome RNA and nucleoprotein (NP) binds along the genomic RNA (Honda and Ishihama, 1987/1997). The influenza virus invades the cytoplasm of host cells in endosomes by

binding to sialic acid on cellular membranes via hemagglutinin (HA), a viral glycoprotein on the envelope of the influenza viral particle (Lakadamyali et al., 2004), and is transported to the vicinity of the nucleus, where decapsidation of the virus occurs and a vRNP complex, consisting of viral RNA (vRNA), RdRp, and NP is released from the endosome (Lakadamyali et al., 2004). Replication and transcription of vRNA occur in the nucleus. RdRp catalyzes the synthesis of three species of RNA (Krug et al., 1989): complementary RNA (cRNA), messenger RNA (mRNA), and vRNA. Initiation of mRNA synthesis requires host capped RNA as a primer, while neither vRNA nor cRNA synthesis rely on a primer for initiation. In viral particles, RdRp synthesizes mRNA but not cRNA or vRNA (Honda et al., 1990); while in virus-infected cells, the same enzyme synthesizes not only mRNA, but also cRNA and vRNA.

RNA-dependent RNA polymerase is a heterotrimer composed of the viral proteins PB1, PB2, and PA. PB1 plays a key role in both RdRp assembly and the catalytic function of RNA synthesis, PB2 interacts with the cap structure of host cell mRNA (Krug et al., 1989; Honda et al., 1999), and PA has both endonuclease activity when bound with PB2, and genomic RNA promoter binding activity when bound with PB1 (Dias et al., 2009). Purified RdRp from *Trichoplusia ni* Tn5 cells coinfected with recombinant baculoviruses expressing the three RdRp subunits (PB1, PB2, and PA) could synthesize only mRNA, but not the two other RNA species (Honda et al., 2002). RdRp generated from its three subunits encoded by an expression vector transfected into cells can synthesis all of the three different RNA species (Nakagawa et al., 1996). These results indicate that RdRp must be converted by some host factor(s) to enable catalysis of the synthesis of the three types of RNA. Therefore, we performed yeast two-hybrid screening to identify the host factor involved in the conversion of RdRp. Our results identified several candidate proteins, among which the host protein, PKM2, was found to interact with the C-terminus of the PA subunit, which interacts with the PB1 subunit (Toyoda et al., 1996).

Pyruvate kinase (EC 2.7.1.40) catalyzes the formation of pyruvate and ATP from phosphoenolpyruvate (PEP) and ADP, and is an important enzyme in the regulation of glycolysis (Llorente et al., 1970). The pyruvate kinase M (*PKM*) gene consists of 12 exons. The pyruvate kinase M1 (*PKM1*) and pyruvate kinase M2 (*PKM2*) isoforms are produced by exclusive alternative splicing of PKM pre-mRNA (Noguchi et al., 1986) and they are both composed of 11 exons, lacking exons 10 and 9, respectively, with a molecular size difference between the encoded proteins of approximately 1.0 kDa. In the nucleus, PKM2 regulates cell proliferation (Hoshino et al., 2007) and binds directly to phosphorylated histone H3, thus promoting gene transcription (Yang et al., 2012).

The present study was performed to identify the host factor that interacts with the PA subunit of RdRp, and to determine its expression level and modification during influenza virus infection. Our results indicated that PKM protein expression was induced by influenza virus multiplication, and that PKM was required for virus multiplication. We also determined that the C-terminal region of PKM2 interacted with the C-terminal region of the PA subunit. Following influenza virus infection, the pH of PKM1 became basic, while that of PKM2 became more acidic, indicating that the interaction between PKM2 and PA may result in transfer of a phosphate group from PKM2 to the PA subunit of RdRp and the consequent conversion of the function of RdRp from transcriptase to replicase.

MATERIALS AND METHODS

Yeast Two-Hybrid Screening

As an initial screen for host proteins that interact with RdRp, the full-length cDNAs of each influenza virus RNA polymerase subunit were inserted into the bait vector, pHybLex/Zeo, for expression as fusion proteins with the LexA DNA-binding domain, while a HeLa cell cDNA library (Invitrogen, USA) was inserted into the prey vector, pYes/Trp2, to construct an expression plasmid library encoding proteins fused with a transcription activation domain. After co-transfection of the two types of plasmid into *Saccharomyces cerevisiae* L40, transformants were subjected to first screening on selection medium containing 300 mg/mL Zeocin and without tryptophan, histidine, or lysine. Viable colonies were picked and subjected to second round of screening for detection of β-galactosidase activity. Zeocin-resistant and β-galactosidase-positive cDNA clones were isolated. For confirmation, two-hybrid screening was performed using the opposite combinations (i.e., positive clones fused to the DNA binding domain and RdRp domains fused to the activation domain). Finally, cDNAs of positive clones were sequenced.

Yeast two-hybrid screening was also performed to confirm the interactions between the identified HeLa cell proteins and influenza virus RNA polymerase, and to map the sites of contact sites between the two proteins. For these experiments, cDNAs encoding the influenza virus RNA polymerase PA subunit and segments thereof were inserted into the pHybLex/Zeo vector for expression as respective DNA-binding domain fusion proteins, while full length and partial *PKM2* cDNAs were expressed as fusion proteins with the activation domain.

Cells and Virus

H292 cells (human lung epithelial cell, purchased from ATCC) were maintained in Eagle's Minimum Essential Medium (EMEM; Nissui, Japan) with 10% Fetal Bovine Serum (FBS, Gibco, USA) in a humid incubator at 37°C and 5% CO_2 (Thermo, USA). Influenza virus A/PR/8/34 was used throughout the study.

Virus Infection

Semi-confluent H292 cells were infected with influenza virus at multiplicity of infection (MOI) of 1, followed by washing with EMEM (pH 7) without FBS. Virus adhesion was carried out in a humid incubator at 34°C and 5% CO_2 for 1 h, corresponding to 0 h post-infection (hpi). After incubation for 1 h, the viral solution was removed and replaced with EMEM containing 10% FBS and incubation continued for the required time.

Western Blotting Assay

Uninfected and virus infected cells were removed from culture vessels using 0.05% trypsin/0.04% EDTA/PBS and washed with PBS three times by centrifugation at 100 g (Tomy MX301, Japan) at 4°C for 5 min. The cell pellet was disrupted in 100 μL hypotonic buffer containing 20 mM HEPES (pH 7.5), 1.5 mM $MgCl_2$, 0.1% Triton X-100, and 10 mM KCl with glass milk in Precelly 24 (Bertin, France) at 6500 rpm for 20 s, and then placed on ice for 5 s; this combined step was repeated seven times. The disrupted cell pellet was centrifuged at 21130 g for 30 min at 4°C. The resultant supernatant was transferred into new 1.5 mL tubes.

To investigate PKM expression in uninfected and influenza infected cells, and in siRNA experiments, aliquots of supernatant corresponding to 10^5 cells were separated by 8% sodium dodecyl sulfate-polyacrylamide gel electrophoresis (SDS-PAGE) followed by blotting on to polyvinylidene fluoride (PVDF) membrane (Nippon Genetics, Japan) with 5 mM N-cyclohexyl-3-aminopropanesulfonic acid (CAPS; Dojindo, Japan) buffer at 4°C and 0.25 A for 1 h. The blotted membranes were blocked with 5% skim milk/PBS for 1 h, washed, and then incubated in 1000x diluted rabbit anti-PKM antibody (Abcam, USA) for 1 h at 37°C. The membranes were then incubated with horseradish peroxidase-conjugated anti-rabbit IgG for 1 h at 37°C, followed by detection with chemiluminescence using an LAS 3000 mini imaging system (Fuji Film, Japan). The relative amount of PKM was calculated by the intensity of each band measured using the LAS 3000 mini software.

For separation of the PKM1 and PKM2 isoforms following isoelectric, proteins were separated by SDS-PAGE, using 6–15% gradient gels at 30 mA for 90 min. After SDS-PAGE, the proteins in the gel were blotted onto PVDF membranes at 0.2 A, 10°C for 1 h, and reacted with anti-PKM antibody (Abcam, USA) and then horseradish peroxidase-conjugated anti-mouse IgG followed by chemiluminescence detection using an LAS 3000 mini imaging system.

Separation of Cytoplasmic Proteins by Isoelectric Focusing

Prior to separation of cytoplasmic proteins by isoelectric focusing, influenza virus-infected and uninfected cells were harvested by trypsinization and centrifugation at 100 g, and the pellets disrupted in 5 M urea solution with glass milk in Precelly 24, as described in section 2.4. The resultant supernatant was further centrifuged at 186000 g (Beckman, Optima ultracentrifuge, USA) for 1 h at 4°C. Aliquots of 1 mg of supernatant protein were applied to equilibrated Bio-Lyte (pH 3–10; Bio-Rad, USA). Protein separation was performed in a Rotofor (Bio-Rad, USA). A pre-run was performed at 3 W using 20 mL of MilliQ water and isoelectric focusing was performed at 8 W for 4–6 h/15 W, 4°C, 60 min/8 W and then 10°C for 30 min. After separation, 20 samples were fractionated into 5 mL tubes. The pH of each sample was measured using a pH meter (Horiba, Japan) and fractions were assayed by western blotting (see Western Blotting Assay). We performed this experiment three times to confirm the results.

siRNA Transfection

H292 cells in exponential growth phase were treated with 0.05% trypsin for 30 s followed by removal of excess trypsin and further incubation for 15 min at 37°C, harvesting by centrifugation at 100 g, and resuspension in buffer R, which was supplied with a commercial kit (Neon® Transfection System, Thermo Fisher, USA). Aliquots of 5×10^5 cells were mixed with 5 nmol of siRNA targeting *PKM2* and transfected using a Microporator (Digital Bio, Korea) at 1600 V, 20 ms, once. After siRNA transfection, the electroporated cells were resuspended in EMEM supplemented with 10% serum and cultured for 24 h. Cells were then infected with influenza virus at an MOI of 1. The assay was repeated three times. Cell lysates were subject to SDS-PAGE and western blotting to detect PKM (see Western Blotting Assay).

RESULTS

The Influenza Virus RdRp PA Subunit Interacts with Pyruvate Kinase M

To understand the mechanism underlying the conversion of influenza virus RdRp function in host cells, we carried out yeast two-hybrid screening to identify host factor(s) interacting with RdRp and which RdRp subunit(s) were involved in the interaction using recombinant plasmids (Honda et al., 2007), as described in Section "Yeast Two-Hybrid Screening." Screening of positive (interacting) yeast colonies demonstrated that the full-length PA expression vector interacted non-specifically with all vectors. Therefore, as shown in previous paper (Honda et al., 2007) we prepared cDNA clones encoding four fragments of PA (**Table 1**) in pHybLex/Zeo, and used these to screen for interacting host factor(s). Nine positive clones were obtained after screening, one of which contained the cDNA, *PKM2*. We tested whether PB1 or PB2 interacted with PKM. As shown in **Table 1**, both PB1 and PB2 did not interact with PKM.

The region of PKM2 that interacted with the PA subunit was then identified by a further yeast two-hybrid screening experiment. As shown in **Table 2**, the C-terminal region of PA interacted with the C-terminal region of PKM2. In addition, we also constructed two pHybLex/Zeo vectors carrying inserts corresponding to N- and C-terminal regions of PKM2 (**Figure 1A**), and examined the interaction of these domains with the C-terminal region of PA. The results indicated that

TABLE 1 | Identification of RNA-dependent RNA polymerase (RdRp) subunits that interact with pyruvate kinase M (PKM).

Influenza virus RdRp subunits (bait)	PKM (prey)
PB1	–
PB2	–
PA (1–346)	–
PA (347–452)	–
PA (453–638)	–
PA (639–716)	+

Numbers indicate amino acid number from the N-terminus. –, no β-Gal activity detected; +, β-Gal activity detected.

TABLE 2 | Identification of interaction sites between PA and PKM.

PA fragment (bait)	PKM (1–413; prey)	PKM (414–531; prey)
PA (1–346)	–	–
PA (347–452)	–	–
PA (453–638)	–	–
PA (639–716)	–	+

Numbers indicate amino acid number from the N-terminus. –, no β-Gal activity detected; +, β-Gal activity detected.

C-terminal region of PA interacted with the C-terminus of PKM2 (**Figure 1B**).

Multiplication of Influenza Virus Is Induced by PKM

Next, we performed western blotting to investigate whether influenza virus multiplication induced PKM2 expression. H292 cells were infected with influenza virus at an MOI of 1 and harvested at different time points (0, 2, 4, 6, and 8 hpi). Western blotting of cell lysates with anti-PKM antibody indicated that the PKM expression level in influenza virus-infected cells was increased by more than fivefold compared to uninfected cells at 4 hpi; however, expression of the viral PB1 subunit was detected later than that of PKM (at 6 hpi) (**Figure 2**). These observations indicate that PKM expression was induced at an early stage of viral multiplication. The timing of PKM expression time after virus infection was similar to that of Ebp1, ErbB3 (an epidermal receptor tyrosine kinase)-binding protein and also interacted with PB1 subunit of RdRp (Ejima et al., 2011), and the elevated levels of PKM lasted until 8 hpi.

PKM was Modified by Influenza Virus Multiplication

To examine modification of PKM during influenza virus multiplication, the cytoplasmic proteins isolated at various times after infection were separated in isoelectric focusing solution using a Rotofor. The molecular masses of the PKM1 and PKM2 isoforms are approximately 58 and 57 kDa, respectively. To visualize the size difference, the proteins were separated by SDS-PAGE on 6–15% gradient gels. Western blots of the separated protein fractions probed with anti-PKM indicated that the pH values of both PKM1 and PKM2 obtained from uninfected cells were close to 8.1 (**Figure 3**). However, during adhesion of influenza virus particles for 1 h at 34°C (at the 0 hpi timepoint), PKM1 became more basic, while PKM2 remained at pH 8. Interestingly, PKM2 shifted to the acidic region at 2 hpi, while PKM1 shifted further into the basic region (pH 9) (**Figure 3**).

Influence of PKM on Influenza Virus Replication

Influenza virus replication consumes large amounts of nucleic acids for synthesis of vRNA, cRNA, and mRNA to produce progeny virus. The process of synthesizing large quantities of RNA also requires huge amounts of energy, for which ATP production is necessary, which requires either high levels

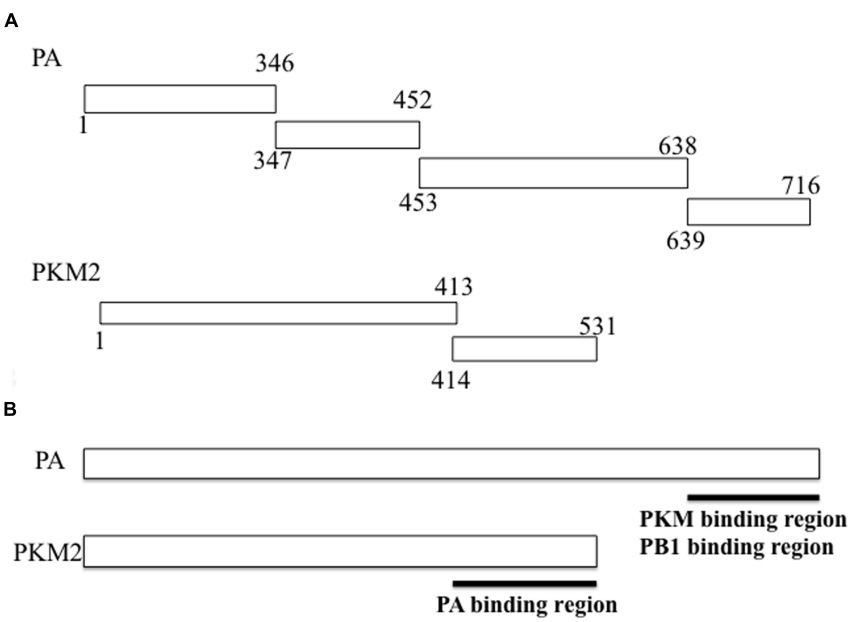

FIGURE 1 | Fragments of RNA-dependent RNA polymerase (RdRp) PA subunit and pyruvate kinase M (PKM) cloned into vectors for use in yeast two-hybrid screening assays. (A) For confirmation of the PA-PKM2 interaction and mapping of the contact site on each protein, cDNA sequences encoding each of the indicated PA regions were inserted into the pHybLex/Zeo "bait" plasmid for expression as fusion proteins with the DNA-binding domain, while cDNA sequences encoding each PKM2 fragment were inserted into the pYESTrp2 "prey" plasmid for expression of fusion proteins with the activation domain. After co-transfection of bait and prey plasmids into *Saccharomyces cerevisiae* L40, a β-galactosidase assay was carried out. Results are summarized in **Tables 1** and **2**. **(B)** The interacting regions between PA and PKM2 were mapped.

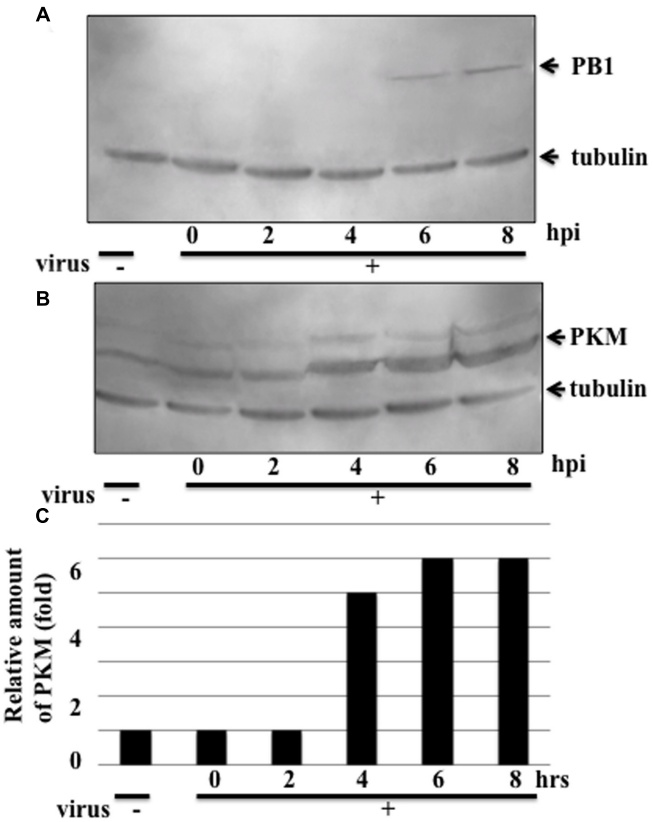

FIGURE 2 | Expression levels of the influenza virus RdRp PB1 subunit and PKM. Influenza virus-infected cells were harvested at various time points and proteins separated by 8% SDS-PAGE, blotted onto PVDF membranes, and then reacted with anti-PB1 and anti-PKM antibodies, followed by chemiluminescence detection. 0, 2, 4, 6, and 8 hpi indicate time after influenza virus infection. Tubulin was detected as an internal marker. **(A)** PB1 expression **(B)** PKM expression **(C)** Relative amount of PKM, calculated from band intensities, standardized by the intensity of tubulin.

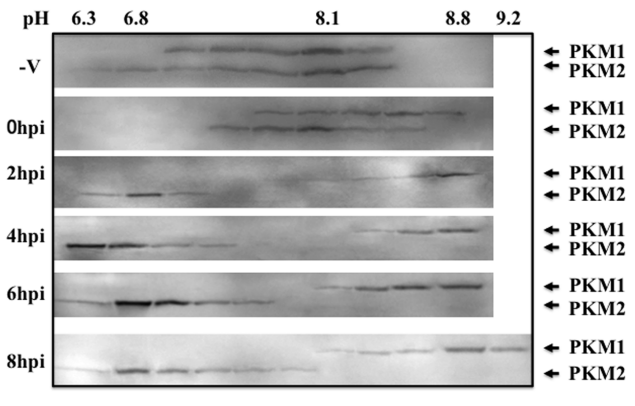

FIGURE 3 | Isoelectric focusing analysis of PKM. Cells were disrupted at various time points following influenza virus infection (0–8 hpi) and the proteins separated in a Rotofor by isoelectric focusing, using an ampholyte (pH 3–10). After separation by isoelectric focusing, solutions were fractionated into 20 tubes. The pH of each tube was measured using a pH meter (Horiba). Next, 40 μL of each fraction was separated by SDS-PAGE on 6–15% gradient gels to separate the two PKM isoforms (PKM1 and PKM2), followed by blotting and immunostaining using anti-PKM antibody with chemiluminescence detection.

or activation of PKM. To assess the pyruvate kinase level required for influenza virus multiplication, we designed an siRNA targeting PKM (**Figure 4A**). To reduce the levels of PKM in host cells, 5 nmol of siRNA was transfected into H292 cells as described in Section "siRNA Transfection." The PKM levels in siRNA-transfected cells were decreased by more than fourfold compared to untransfected cells (**Figures 4B,D**, lanes 1 and 2, respectively). siRNA-transfected H292 cells were infected with influenza virus at an MOI of 1, and at 6 hpi, the influenza virus-infected cells were harvested, and PB1 expression examined by western blotting. As shown in **Figures 4C,D**, lanes 3 and 4, the expression levels of PB1 were lower in siRNA-transfected, compared with untransfected, cells. These results indicate that PKM is important for influenza virus replication.

DISCUSSION

The RdRp enzyme can catalyze the synthesis of three species of RNA (Krug et al., 1989); however, purified RdRp from recombinant baculovirus coinfected with Tn5 requires a primer for RNA synthesis, and cannot synthesize all three different RNAs. In contrast, purified heterotrimer from recombinant

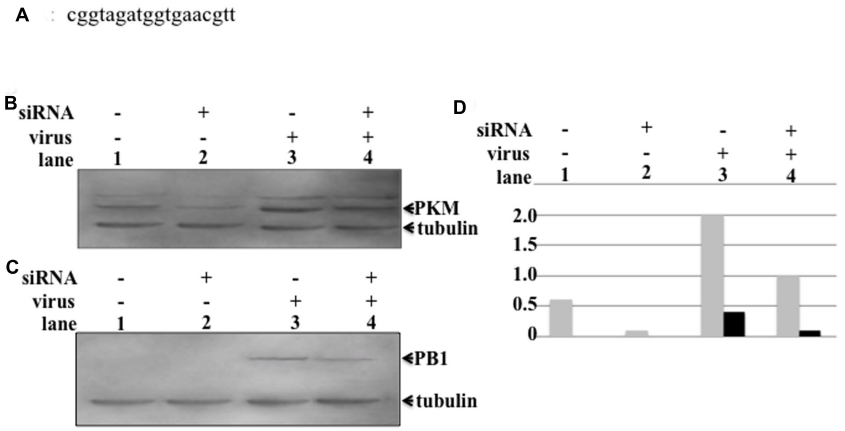

FIGURE 4 | Influence of PKM on influenza virus multiplication. PKM siRNA was transfected into semi-confluent cells by electroporation, followed by incubation overnight in a humid, 5% CO_2 incubator at 37°C. After overnight incubation, influenza virus-infected cells were transfected with siRNA at an MOI of 1. At various time points after infection, cells were harvested and disrupted, and proteins separated by 8% SDS-PAGE, followed by blotting onto PVDF membranes. The membranes were then reacted with anti-PB1 and anti-PKM antibodies, followed by chemiluminescence detection. **(A)** The sequence of the siRNA targeting PKM2. **(B)** Lanes 1 and 2, PKM expression level in uninfected cells (lane 1, siRNA-untransfected cells and lane 2, siRNA-transfected cells). Lanes 3 and 4, PKM expression level of virus-infected cells (lane 3, siRNA-untransfected cells; lane 4, siRNA-transfected cells). **(C)** PB1 expression levels of uninfected and virus-infected cells. Lanes 1 and 2, PB1 expression level in virus uninfected cells (lane 1, siRNA-untransfected cells; lane 2, siRNA-transfected cells). Lanes 3 and 4, PB1 expression levels of virus-infected cells (lane 3, siRNA-untransfected cells; lane 4, siRNA-transfected cells). **(D)** Relative amount of PKM and PB1, calculated from band intensities, standardized by the intensity of tubulin; gray bar represents PKM, black bar represents PB1.

baculovirus coinfected with Tn5 exhibited both primer-dependent and independent RNA synthesis (Honda et al., 2002), indicating that influenza virus RdRp requires some host factor(s) to synthesize the three species of RNA.

From yeast two-hybrid screening, the host protein, PKM2, was shown to interact with the PA subunit of RdRp. PKM2 catalyzes transfer of a phosphate group from PEP to ADP, yielding one molecule of pyruvate and one molecule of ATP (Altenberg and Greulich, 2004). Investigation of PKM protein levels indicated that its expression was induced by influenza virus infection at 4 hpi before viral protein detection by western blotting (**Figures 2A,B**). PKM is an important enzyme for generation of ATP, and influenza virus replication involves the synthesis of large amounts of vRNA, cRNA, and mRNA, which requires copious quantities of ATP; therefore, the induction of PKM expression by influenza virus infection is logical. At 4 hpi, the expression of PKM was increased and influenza virus transcription and replication also increased at this time point, hence these two phenomena were correlated. This result indicates the possibility of phosphorylation of the PA subunit by PKM; however, our results do not determine whether PKM2 interacts with the PA subunit as a monomer or as part of the RdRp complex, to alter the function of RdRp. To answer this question our future experiments will include phosphorylation assays of the PA subunit along with assays to determine whether the function of RdRp can be altered by interaction with PKM2.

York et al. (2014) reported that serine/threonine protein phosphatase 6 (PP6) interacts with PB1 and PB2 subunits directly and demonstrated that cells in which PP6 was knocked-down using siRNA exhibited reduced vRNA accumulation and attenuated viral growth. Their results indicate that phosphate has an important role in influenza virus replication. Our result is the first report of the interaction between PKM2 and the PA subunit, and of reduction of PKM2 expression resulting in decreased influenza virus protein expression.

Pyruvate kinase M2 phosphorylates histone H3 and promotes gene transcription and tumorigenesis (Yang et al., 2012). The PKM2 dimer functions as a protein kinase and promotes cell proliferation (Gao et al., 2012). As shown in **Figure 3**, following influenza virus infection, PKM1 became more basic, while PKM2 became more acidic. The decreased pH of PKM2 may have been due to phosphorylation, and phosphorylated PKM2 is active as a pyruvate kinase and protein kinase. The protein kinase function of PKM2 may be important for influenza virus replication. Knock-down of the *PKM2* gene decreased EGFR phosphorylation (Hsu et al., 2016) and PKM2 can translocate into the nucleus and interact with the HIF-1α subunit to transactivate target genes (Dong et al., 2014). These functions of PKM2 suggest a very attractive hypothesis that PA in RdRp may be phosphorylated by PKM2, leading to the conversion of the function of RdRp from transcriptase to replicase, as phosphorylated PKM2 may transfer a phosphate group to PA.

In our previous report, we determined that the PA-PB1 heterodimer functions as a replicase. Based on this result, we speculated that the PA subunit may have an important role in the replicase function of RdRp. In this study, we did not directly demonstrate PA subunit modification by interaction with PKM2; however, the PA subunit of RdRp may be phosphorylated and function as a converter of RdRp from a transcriptase to a replicase. We are currently engaged in experiments to clarify whether the function RdRp can be converted by phosphorylation of PA by PKM2. In support of this hypothesis, depletion of

pyruvate kinase using siRNA targeting PKM2 inhibited influenza virus replication (**Figures 4B,C**). It will be necessary to assess the mechanism underlying the inhibition of virus replication by depletion of PKM. Further studies are required to determine whether phosphorylated PKM2 transfers a phosphate group to PA and induces an alteration in RdRp function.

AUTHOR CONTRIBUTIONS

YM carried out western blotting. KI performed protein extraction from cells and 2D assay. AH designed this experiment and wrote the manuscript.

FUNDING

This work was supported by CREST (Japan Science and Technology Agency) and Ministry of Education, Culture, Sports, Science, and Technology of Japan.

ACKNOWLEDGMENTS

We thank T. Okamoto (National Institute of Genetics) for preparation of model RNA templates and A. Iwata (Nippon Institute of Biological Science) for preparation of anti-P protein antibodies.

REFERENCES

Altenberg, B., and Greulich, K. D. (2004). Genes of glycolysis are ubiquitously overexpressed in 24 cancer classes. *Genomics* 84, 1014–1020. doi: 10.1016/j.ygeno.2004.08.010

Dias, A., Bouvier, D., Crépin, T., McCarthy, A. A., Hart, D. J., Baudin, F., et al. (2009). The cap-snatching endonuclease of influenza virus polymerase resides in the PA subunit. *Nature* 458, 914–918. doi: 10.1038/nature07745

Dong, T., Yan, Y., Chai, H., Chen, S., Xiong, X., Sun, D., et al. (2014). Pyruvate kinase M2 affects liver cancer cell behavior through up-regulation of HIF-1a and Bcl-xL in culture. *Biomed. Pharmacother.* 69, 277–284. doi: 10.1016/j.biopha.2014.12.010

Ejima, M., Kadoi, K., and Honda, A. (2011). Influenza virus infection induces cellular Ebp1 gene expression. *Genes Cells* 16, 927–937. doi: 10.1111/j.1365-2443.2011.01541.x

Gao, X., Wang, H., Yang, J. J., Liu, X., and Liu, Z. R. (2012). Pyruvate kinase M2 regulates gene transcription by acting as a protein kinase. *Mol. Cell* 45, 598–609. doi: 10.1016/j.molcel.2012.01.001

Honda, A., and Ishihama, A. (1987/1997). The molecular anatomy of influenza virus RNA polymerase. *J. Biol. Chem.* 378, 483–488.

Honda, A., Mizumoto, K., and Ishihama, A. (1999). Two separate sequences of PB2 subunit constitute the RNA cap-binding site of influenza virus RNA polymerase. *Genes Cells* 4, 475–485. doi: 10.1046/j.1365-2443.1999.00275.x

Honda, A., Mizumoto, K., and Ishihama, A. (2002). Minimum molecular architectures for transcription and replication of the influenza virus. *Proc. Natl. Acad. Sci. U.S.A.* 99, 13166–13171. doi: 10.1073/pnas.152456799

Honda, A., Mukaigawa, J., Yokoiyama, A., Kato, A., Ueda, S., Nagata, K., et al. (1990). Purification and molecular structure of RNA polymerase from influenza virus A/PR8. *J. Biochem.* 107, 624–628.

Honda, A., Okamoto, T., and Ishihama, A. (2007). Host factor Ebp1: selective inhibitor of influenza virus transcriptase. *Genes Cells* 12, 133–142. doi: 10.1111/j.1365-2443.2007.01047.x

Hoshino, A., Hirst, J. A., and Fujii, H. (2007). Regulation of cell proliferation by interleukin-3-induced nuclear translocation of pyruvate kinase. *J. Biol. Chem.* 282, 17706–17711. doi: 10.1074/jbc.M700094200

Hsu, M.-C., Hung, W. C., Yamaguchi, H., Lim, S. O., Liao, H. W., Tsai, C. H., et al. (2016). Extracellular PKM2 induces cancer proliferation by activating the EGFR signaling pathway. *Am. J. Cancer Res.* 6, 628–638.

Krug, R. M., Alonso-Caplen, F. V., Julkenun, I., and Katze, M. G. (1989). "Expression and replication of the influenza virus genome," in *The Influenza Viruses*, ed. R. M. Krug (New York, NY: Plenum Press), 89–152.

Lakadamyali, M., Rust, M. J., and Zhuang, X. (2004). Endocytosis of influenza viruses. *Microbes Infect.* 6, 926–936. doi: 10.1016/j.micinf.2004.05.002

Llorente, P., Marco, R., and Sols, A. (1970). Regulation of liver pyruvate kinase and the phosphoenolpyruvate crossroads. *Eur. J. Biochem.* 13, 45–54. doi: 10.1111/j.1432-1033.1970.tb00897.x

Nakagawa, Y., Oda, K., and Nakada, S. (1996). The PB1 subunit alone can catalyze cRNA synthesis, and the PA subunit in addition to the PB1 subunit is required for viral RNA synthesis in replication of the influenza genome. *J. Virol.* 70, 6390–6394.

Noguchi, T., Inoue, H., and Tanaka, T. (1986). The M1- and M2-type isozymes of rat pyruvate kinase are produced from the same gene by alternative RNA splicing. *J. Biol. Chem.* 261, 13807–13812.

Palese, P., and Shaw, M. (2007). "Orthomyxoviridae: the viruses and their replication," in *Fields Virology*, 5th Edn, eds D. M. Knipe and P. M. Howley (Philadelphia: Lippincott Williams & Wilkins), 1647–1689.

Toyoda, T., Adyshev, D. M., Kobayashi, M., Iwata, A., and Ishihama, A. (1996). Molecular assembly of the influenza virus RNA polymerase: determination of the subunit-subunit contact sites. *J. Gen. Virol.* 77, 2149–2157. doi: 10.1099/0022-1317-77-9-2149

Yang, W., Xia, Y., Hawke, D., Li, X., Liang, J., Xing, D., et al. (2012). PKM2 phosphorylates histone H3 and promotes gene transcription and tumorigenesis. *Cell* 150, 685–696. doi: 10.1016/j.cell.2012.07.018

York, A., Hutchinson, E. C., and Fodor, E. (2014). Interactome analysis of the Influenza A virus transcription/ replication machinery identifies protein phosphatase 6 as a cellular factor required for efficient viral replication. *J. Virol.* 88, 13284–13299. doi: 10.1128/JVI.01813-14

Conflict of Interest Statement: The authors declare that the research was conducted in the absence of any commercial or financial relationships that could be construed as a potential conflict of interest.

Copyright © 2017 Miyake, Ishii and Honda. This is an open-access article distributed under the terms of the Creative Commons Attribution License (CC BY). The use, distribution or reproduction in other forums is permitted, provided the original author(s) or licensor are credited and that the original publication in this journal is cited, in accordance with accepted academic practice. No use, distribution or reproduction is permitted which does not comply with these terms.

frontiers in Microbiology

ORIGINAL RESEARCH
published: 17 August 2016
doi: 10.3389/fmicb.2016.01127

The Influence of Virus Infection on the Extracellular pH of the Host Cell Detected on Cell Membrane

Hengjun Liu[1], Hisataka Maruyama[1], Taisuke Masuda[1], Ayae Honda[2] and Fumihito Arai[1]*

[1] Department of Micro-Nano Systems Engineering, Nagoya University, Nagoya, Japan, [2] Department of Frontier Bioscience, Hosei University, Tokyo, Japan

Influenza virus infection can result in changes in the cellular ion levels at 2–3 h post-infection. More H^+ is produced by glycolysis, and the viral M2 proton channel also plays a role in the capture and release of H^+ during both viral entry and egress. Then the cells might regulate the intracellular pH by increasing the export of H^+ from the intracellular compartment. Increased H^+ export could lead indirectly to increased extracellular acidity. To detect changes in extracellular pH of both virus-infected and uninfected cells, pH sensors were synthesized using polystyrene beads (ϕ1 μm) containing Rhodamine B and Fluorescein isothiocyanate (FITC). The fluorescence intensity of FITC can respond to both pH and temperature. So Rhodamine B was also introduced in the sensor for temperature compensation. Then the pH can be measured after temperature compensation. The sensor was adhered to cell membrane for extracellular pH measurement. The results showed that the multiplication of influenza virus in host cell decreased extracellular pH of the host cell by 0.5–0.6 in 4 h after the virus bound to the cell membrane, compared to that in uninfected cells. Immunostaining revealed the presence of viral PB1 protein in the nucleus of virus-bound cells that exhibited extracellular pH changes, but no PB1 protein are detected in virus-unbound cells where the extracellular pH remained constant.

Keywords: influenza virus, FITC, pH sensor, extracellular pH, immunostaining

OPEN ACCESS

Edited by:
Akio Adachi,
University of Tokushima, Japan

Reviewed by:
Kiyoko Iwatsuki-Horimoto,
University of Tokyo, Japan
Peirong Jiao,
South China Agricultural University, China
Julie McAuley,
University of Melbourne at the Peter Doherty Institute for Infection and Immunity, Australia

****Correspondence:***
Hengjun Liu
liuhj@biorobotics.mech.nagoya-u.ac.jp

Specialty section:
This article was submitted to Virology, a section of the journal Frontiers in Microbiology

Received: *27 February 2016*
Accepted: *06 July 2016*
Published: *17 August 2016*

Citation:
Liu H, Maruyama H, Masuda T, Honda A and Arai F (2016) The Influence of Virus Infection on the Extracellular pH of the Host Cell Detected on Cell Membrane. Front. Microbiol. 7:1127. doi: 10.3389/fmicb.2016.01127

INTRODUCTION

The influenza virus can infect a wide range of vertebrate species, resulting in changes in the activity of host ATPase (Guinea and Carrasco, 1995) as well as in the cellular ion levels (Pinto et al., 1992). Several studies have reported that large amounts of RNA are synthesized within a short period after the influenza virus enters the cell, thereby suggesting that the rate of ATP consumption would be higher in influenza virus-infected cells than in uninfected cells (Guinea and Carrasco, 1995; Hui and Nayak, 2001). The virus-infected cells synthesize some ATP by oxidative metabolism, and some by glycolysis. Glycolysis is the metabolic pathway that converts glucose ($C_6H_{12}O_6$) into pyruvate ($CH_3COCOO^- + H^+$). Pyruvate can be converted into lactate reversibly. High rates of glycolysis and lactate are reported as a common feature of virus-infected cells (Allison, 1963; Singh et al., 1974). This follows from the intimate association between lactate and H^+ gradient across the cell plasma membrane (Allison, 1963). One obvious hypothesis is that the export of metabolic acids (lactate and CO_2) and H^+ from the cell into the near-surroundings will acidify the extracellular compartment. Some researchers have reported a reduction in intracellular pH

(pH_i) of virus-infected cells (Steinhauer et al., 1991; Ciampor et al., 1992). But no researches have reported the extracellular pH (pH_e) change induced by virus infection. The investigation on pH_e can improve our understanding of the metabolic pathway of the cell and also the pH gradients inside and outside the cell membrane.

Measurements of pH in cells and other micro-environments have largely been carried out using responsive fluorescence dyes. Recently, pH responsive sensors based on fluorescence dyes have been developed and are used in imaging and measurements in living cells and small environments (Oyama et al., 2012; Yin et al., 2012). They have the advantage of stable fluorescence, require low stimulus levels for activation, and enable single cell measurement. Thus, these fluorescence pH sensors have the potential to be used in the pH measurements of virus-infected cells. In our previous work (Liu et al., 2014), pH sensors were synthesized using polystyrene beads (ϕ1 μm) containing Rhodamine B and Fluorescein isothiocyanate (FITC). The fluorescence intensity of FITC can respond to both pH and temperature. So Rhodamine B was also introduced in the sensor for temperature compensation. After temperature compensation, the pH can be measured by fluorescence changes of FITC. In this paper, the pH_e changes of the cell after influenza virus infection were investigated using the synthesized pH sensor by adhering the sensor to the cell membrane. The reasons for pH_e changes and the role of different ion channels will be also discussed in this paper.

MATERIALS AND METHODS

Cell Culture

Madin-Darby canine kidney (MDCK) cells were used for experiments. Prior to injection, the cells were cultured in a glass-based dish (ϕ 3 cm, Asahi Glass Co. Ltd., Japan) and incubated at 37°C, bubbled with 95% air, and 5% CO_2 gas. Eagle Minimum Essential Medium (EMEM) containing 10% fetal bovine serum (FBS) was used as the cell medium.

Fluorescence Labeling of Virus

Influenza virus A/Puerto Rico/8/34 (H1N1) (wild type) was propagated in 10-day-old embryonated chicken eggs. The influenza virus (in allantoic fluid) was incubated with Syto21 (2 μg/mL in PBS) for 30 min at room temperature. The virus solution was centrifuged for 2 min at 700 × g using a spin column containing Sephadex G50 beads (Pharmacia, USA) to remove the excess dye. The flow-through virus solution was then used in further experiments.

Preparation of the pH Sensor

As described in our previous work (Liu et al., 2014), polystyrene microbeads (ϕ1 μm) with amino-group modified surfaces were used as the sensor carriers. FITC has been used in pH sensor (Liu et al., 2000), but our previous study showed that temperature could affect the pH sensitivity of FITC. In order to fabricate the pH sensor, FITC was modified on the bead surface for pH sensing, while Rhodamine B was introduced inside the bead for temperature compensation. First, a solution of amino-polystyrene beads and 1 g/L Rhodamine B (in alcohol) (1:1 v/v) was stirred for 5 min and then washed with deionized (DI) water. The beads were then added to an FITC saturated aqueous solution for 1 h, followed by three washes with DI water.

Virus Infection

MDCK cells were cultured with influenza viruses labeled with Syto 21 for 15 min at 34°C in serum-free medium (1000 copies/ml). After 15 min, some of the viruses were bound to the cell membranes, following which the serum-free medium containing unbound virus was replaced with a new serum-containing medium.

pH_e Measurement of Influenza Virus-Bound and Unbound Cells

After removing the unbound virus particles, the complete medium and pH sensors were added to the dish. The pH sensor was then transferred and attached to the surface of virus-bound and virus-unbound cells by using optical tweezers. A near-infrared laser, considered to be safe for cells, was employed for the optical tweezers (Maruyama et al., 2009). The maximum power of the laser was over 5 W and its wavelength was 1064 nm. The optical tweezers have been used widely in the transfer of small objects (nm-μm), such as micro-sensor (Maruyama et al., 2013) and a single virus (Masuda et al., 2014). **Figure 1** shows a schematic of the pH_e measurement of virus-infected cell by pH sensor adhered on cell membrane. The sensor is adhered on cell membrane and it is also placed in the extracellular environment. So the pH sensor which adhered to cell membrane can detect the pH_e changes close to the cell membrane. pH_e changes are closely related with the ions and solutions exchanges between the both sides of cell membrane. The other micro-sensor is adhered on the substrate as the contrast sensor. By detecting the fluorescence changes of the sensor adhered on substrate, the fluorescence changes of FITC induced by the excitation light can be investigated. Then fluorescence changes of the sensor (on cell membrane) induced by virus infection can be investigated with the compensation of fluorescence fading resulted from excitation light. The fluorescence intensity of FITC of the sensors was measured for about 6 h after the sensor was adhered to the cell surface using a Nikon TiE microscope fitted with a 100 × objective lens. All experiments were carried out in the culture chamber (5% CO_2, 34°C).

Experimental System Setup

The fluorescence image of the target was obtained from an inverted confocal microscope (Ti-E Nikon) equipped with a high magnification lens (Plan Fluor 100×, Nikon) and CCD camera (iXon, Andoe). Wavelengths of 470 and 532 nm were selected as the excitation wavelengths for FITC and Rhodamine B, respectively. Rhodamine B is excited by green light (532 nm) and emits red fluorescence (peak wavelength 585 nm). FITC is excited by blue light (470 nm) and emits green fluorescence (peak wavelength 520 nm). The fluorescent images can be

Abbreviations: pH_i, intracellular pH; pH_e, extracellular pH.

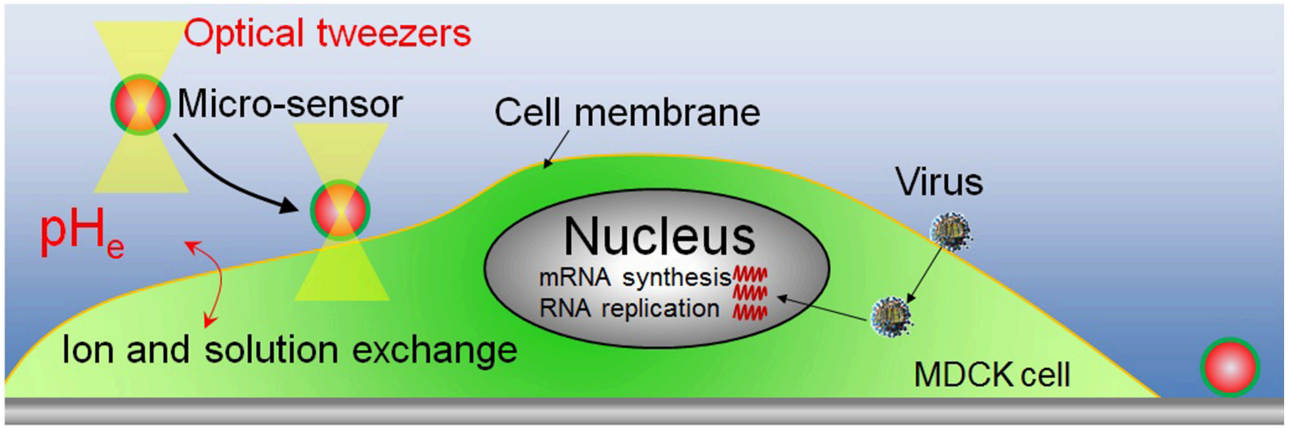

FIGURE 1 | Schematic of the pH_e measurement of virus-infected cell by pH sensor adhered on cell membrane.

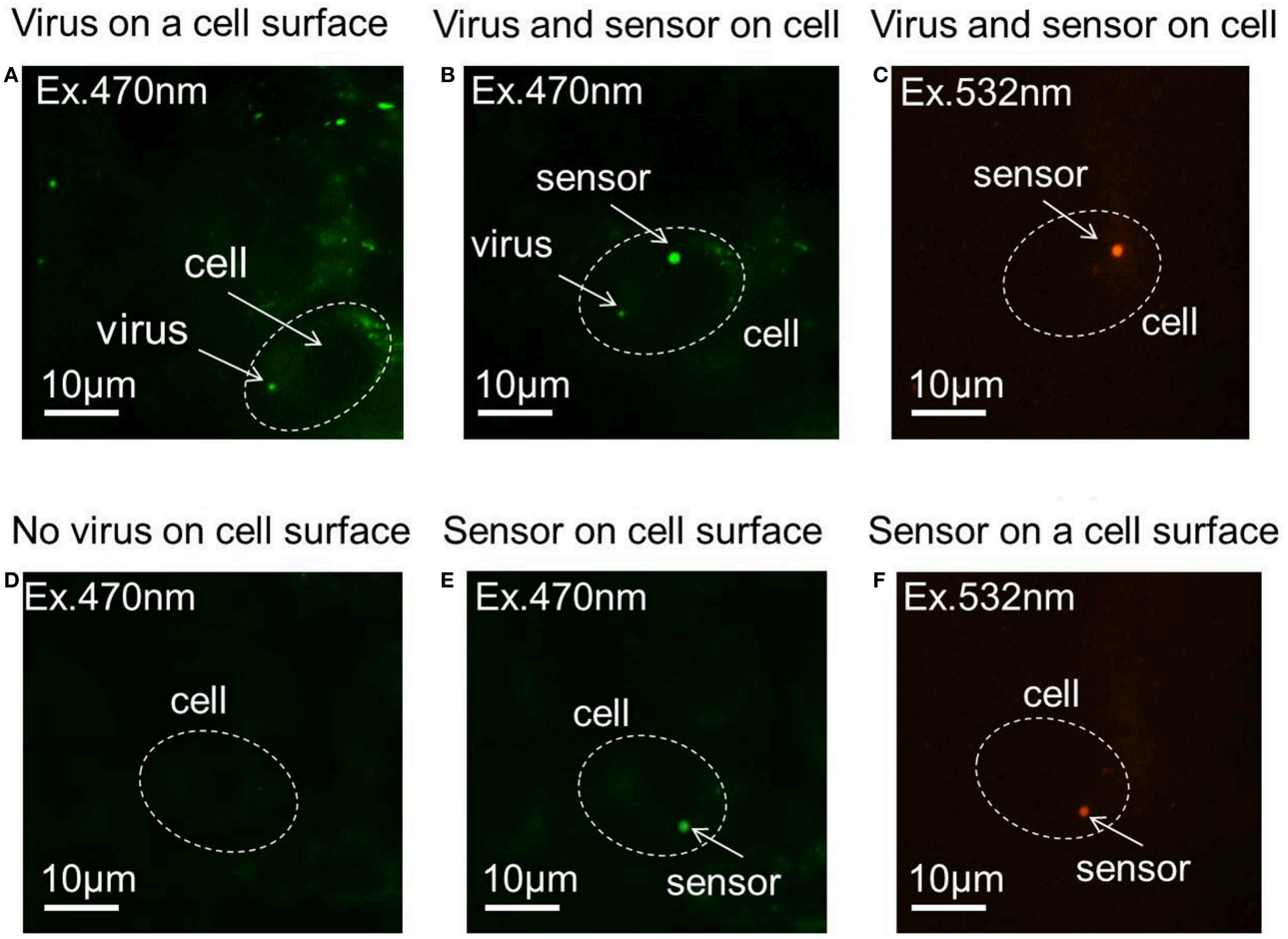

FIGURE 2 | Fluorescence images of the pH sensor and virus on the cell membrane. (A) Virus adhered to the cell surface. **(B)** A pH sensor adhered to the same cell with a virus on its surface, with an excitation of 470 nm laser. **(C)** A pH sensor adhered to the same cell with a virus on its surface, with an excitation of 532 nm laser. **(D)** Virus-unbound cell. **(E)** A pH sensor adhered to a virus-unbound cell, with an excitation of 470 nm laser. **(F)** A pH sensor adhered to a virus-unbound cell, with an excitation of 532 nm laser.

taken automatically in a certain time interval (30 min in our experiment).

Immunostaining of the Cells

After the measurement experiments, all cell in the glass-based dish was immunostained with anti-PB1 (after 6 h post-infection). Actually, we marked the cells which have been observed for pH sensing in Section pH_e Measurement of Influenza Virus-bound and Unbound Cells and then found the same cells in the glass-based dish after immunostaining. The cells were washed three times with phosphate-buffered saline (PBS) and fixed with 4% paraformaldehyde solution at room temperature for 10 min. They were re-washed three times with PBS, treated with 0.5% Triton X-100 for 5 min, and blocked with 1% bovine serum albumin (BSA) in PBS at room temperature. Lastly, the cells were incubated with anti-PB1 antiserum for 1 h at 37°C and washed by 1% BSA/PBS solution, following which the cells were incubated with anti-rabbit IgG conjugated with Alexa 488 for 1 h at 37°C. The cells were observed under a microscope fitted with a 100 × objective lens (Zeiss LSM 510 META).

RESULTS

Virus Infection and pH Sensor Adhesion

Figures 2A,D show virus-bound and virus- unbound cells, respectively. The virus is detected by the fluorescence of Syto 21. The pH sensor was then attached to virus-bound and virus–unbound cells using optical tweezers (**Figures 2B,E**), and the fluorescence of Rhodamine B and FITC can be observed under excitation sources of 532 and 470 nm, respectively. The sensor and virus that adhered to the surface of the same cell can be distinguished not only by their different sizes but also by the presence of fluorescence at 532 nm, as Syto 21 of the virus cannot be excited at that wavelength, but Rhodamine B of the sensor will fluoresce. **Figures 2C,F** show the fluorescence of Rhodamine B of the sensor, with no fluorescence observed from Syto 21 of the virus.

pH Changes in Virus-Bound and –Unbound Cells

The relative fluorescence intensity changes of FITC of the sensor adhered to substrate induced by the excitation light are shown in **Figure 3**. The fluorescence intensity is decreased by the excitation light and decreasing with the excitation time. The relative fluorescence changes of the sensor (on cell membrane) induced by virus infection can be investigated with the compensation of fluorescence fading as shown in **Figure 3**. **Figure 4** shows the relative fluorescence intensity changes of the sensors adhered to different cells in 6 h. **Figure 4A** shows the fluorescence intensity of the sensor which was adhered to the virus-bound cell decreased from 2 h after the virus adhesion. However, there was no obvious change in the fluorescence intensity of the sensor adhered to the virus-unbound cell as shown in **Figure 4B**.

Based on the sensitivity of FITC to pH changes as reported in our previous study (Liu et al., 2014), the pH_e changes can be calculated directly from the fluorescence intensity changes of FITC in **Figure 4**. It is important to note that there will be changes

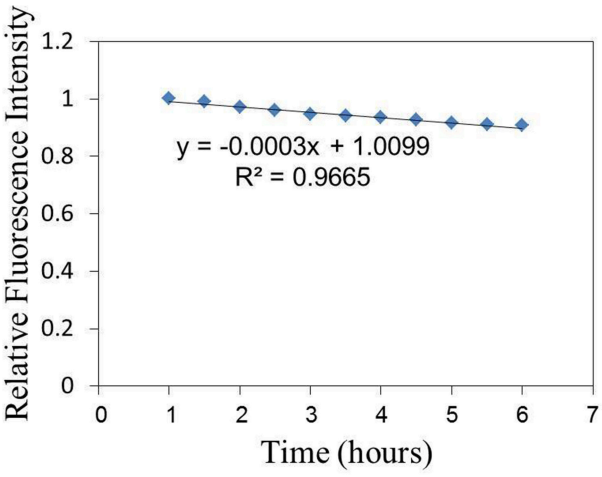

FIGURE 3 | The relative fluorescence intensity changes of FITC of the sensor adhered to substrate induced by the excitation light.

in cellular temperature after infection with the virus. Several studies have reported that large amounts of RNA are synthesized within a short period after the influenza virus enters the cell, thereby suggesting that the rate of ATP consumption would be higher in influenza virus-infected cells than in uninfected cells (Guinea and Carrasco, 1995; Hui and Nayak, 2001). A higher rate of ATP consumption compared to its metabolism in the cell will likely increase the temperature of the virus-bound cell. This temperature change can also be responsible for changing the FITC fluorescence, and thus the fluorescence intensity changes of FITC in **Figure 4** could include two parts: those induced by pH changes and those by temperature changes. Then temperature compensation is necessary for pH calculation. In our previous work (Liu et al., 2014), the calibration and compensation of the pH sensor has been discussed. The fluorescence responses of FITC to pH at different temperatures have been detected. So the pH sensitivity of the sensor which is related to temperature has been summarized. If we can get the temperature information, the pH sensitivity of the sensor can be calculated. Then the pH change can be calculated basing on the pH sensitivity of the sensor and also the fluorescence intensity changes of the sensor. This is the method of temperature compensation which is aimed at removing the effect of temperature on pH measurement.

The results of pH_e changes of the virus-bound cell after temperature compensation are shown in **Figures 4C,D**. pH_e of influenza virus-bound cell decreased by approximately 0.55 in 4 h after virus binding. There was no obvious decrease in pH_e of uninfected cell (**Figure 4D**). The average pH_e changes of 8 virus-bound and 8 -unbound cells (from 3 different dish samples) are shown in **Figure 5**. The results show that pH_e of virus-bound cells decreases by 0.5–0.6 in 4 h after virus binding (**Figure 5A**). No obvious changes in pH_e were detected on virus-unbound cells (**Figure 5B**).

Immunostaining of the Cells

To confirm the viral infection after binding on the cell surface as well as viral replication in the cells, the cells (utilized in pH

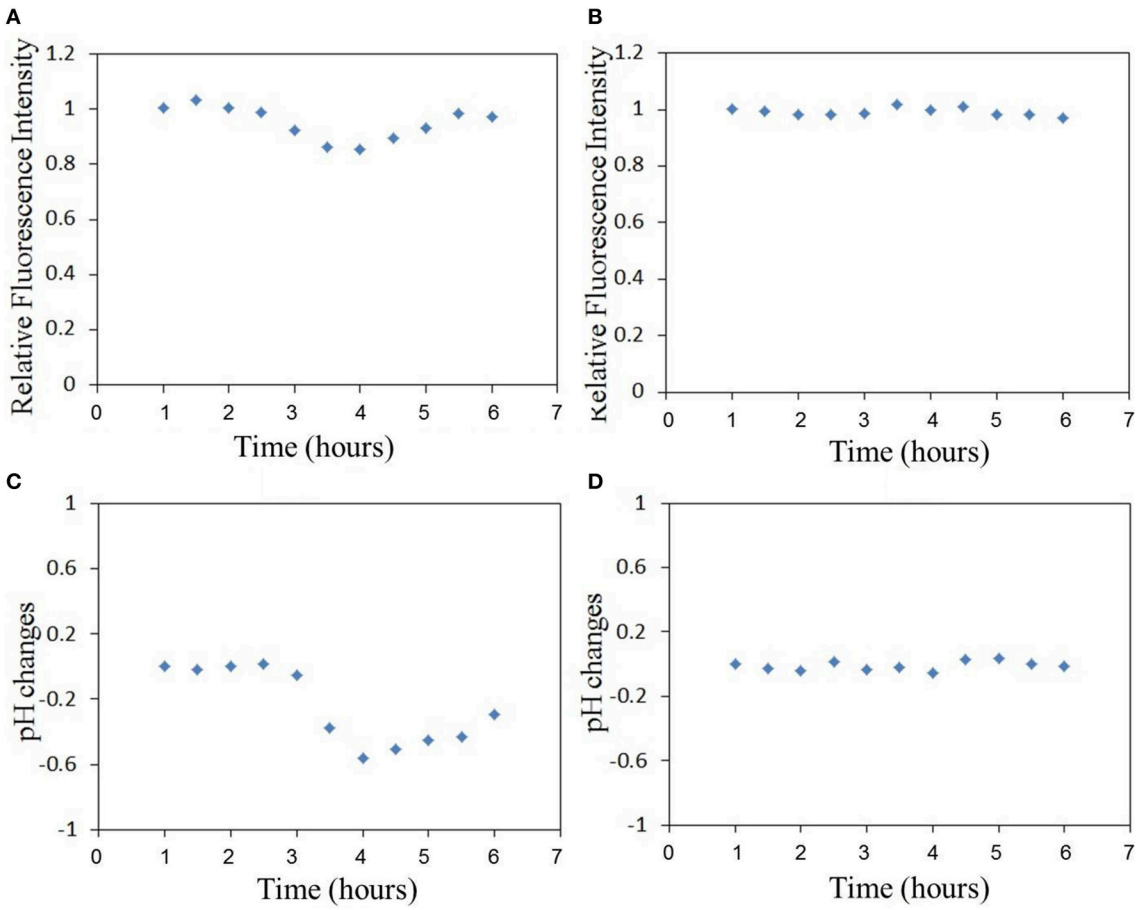

FIGURE 4 | The relative fluorescence intensity changes of FITC of the sensor adhered to (A) virus-bound cell and (B) virus-unbound cell, and the pH_e changes of (C) virus-bound cell and (D) virus-unbound cell calculated basing on the fluorescence changes in (A,B), (Time-course measurements are initiated post-virus binding to the cell membrane).

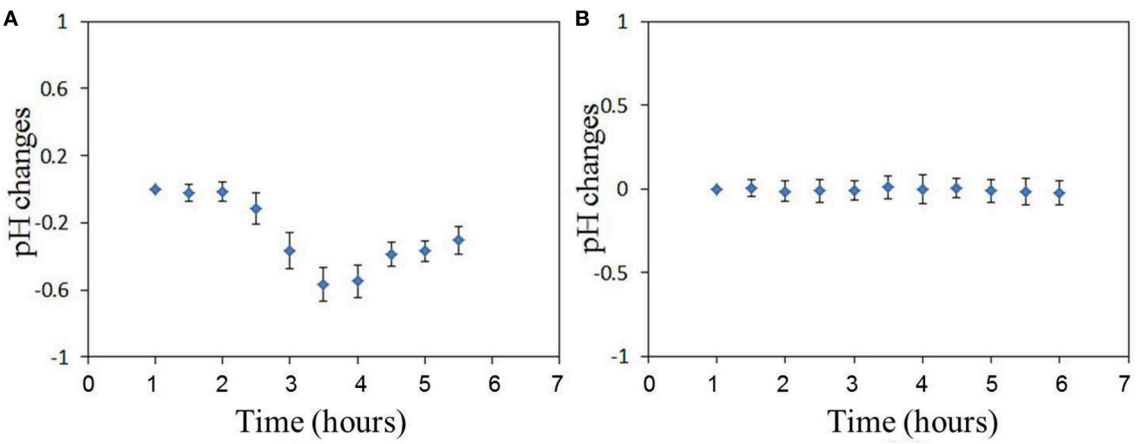

FIGURE 5 | The average pH_e changes of (A) virus-bound cells and (B) virus–unbound cells ($n = 8$).

sensing in Section pH changes in virus-bound and –unbound cells) were immunostained with anti-PB1 antiserum after pH measurement. Since PB1 protein is known to be a part of the RNP complex involved with aiding viral genome replication, detection of PB1 protein within the nucleus of an infected cell is expected. We marked the cells which have been utilized in pH

sensing and then found the same cells in the glass-based dish after immunostaining. Using this method, we can confirm the observed cells utilized in **Figure 5A** are infected successfully and the cells utilized in **Figure 5B** are not infected by virus. **Figure 6** shows viral PB1 protein are detected in the nucleus of virus-bound cells (in one dish sample) that exhibited pH_e changes, but no PB1 protein are detected in virus-unbound cells where the pH_e remained constant. The virus-bound cells from other dish samples which are utilized in pH sensing have showed the same results. These results suggest that the virus replicates in the nucleus of the host cell induces pH_e changes. Our data clearly demonstrates a difference in pH_e near cell membrane between the influenza virus-infected and uninfected cells.

DISCUSSION

Primary Highlights of the Study

In this study, we prepared a sensor based on Rhodamine B and FITC fluorescence, and successfully implemented it in the measurement of pH_e changes close to the cell membrane of influenza virus-infected and uninfected cells. We found that influenza virus multiplication decreased pH_e close to the cell membrane by approximately 0.5–0.6 units. Immunostaining revealed the presence of PB1 protein in the nucleus of virus-bound cells that exhibited pH_e changes, but not in virus-unbound cells where the pH_e remained constant. These results suggest that the influenza virus infection and proliferation in the host cell could induce a pH_e decrease near cell membrane.

Proposed Mechanisms of Decrease in pH_e after Virus Infection

The decrease in pH_e near the cell membrane after virus infection should be related with two factors: the H^+ produced in the cytoplasm and its release into the extracellular environment. First, high rates of glycolysis are required to produce more ATP which is necessary for large amounts of virus replications in host cell. The glycolysis will produce more metabolic acids and H^+ in cytoplasm. Actually, many researches have reported that there was 0.3–0.4 unit reduction in pH_i of virus-infected cells (Steinhauer et al., 1991; Ciampor et al., 1992). The decrease in pH_i of virus-infected cell is not only related with glycolysis but also the functions of M2 protein embedded in the viral lipid membrane. As shown in **Figure 7**, the well characterized M2 viroporin of influenza virus plays roles both during viral entry and egress. During entry, the M2 proton channel shunts H^+ from the acidic endosome to the virion interior, leading to membrane fusion and then release of the genome as well as H^+ initiation. The release of H^+ to the cytoplasm results in a decrease in cytoplasmic pH. In certain subtypes, M2 also equilibrates the intraluminal pH of the trans-Golgi network with the cytoplasm, preventing premature conformational changes in the viral hemagglutinin (HA) during exit (Takeda et al., 2002; Pinto and Lamb, 2006; Betakova, 2007). This results in pH increase inside the trans-Golgi network and a pH decrease in cytoplasm.

Then the cells might regulate the pH_i by increasing the export of H^+ from the intracellular compartment (Gillies et al., 1992). Export of increased H^+ could lead indirectly to increased extracellular acidity. As we know that there are many ion channels on cell membrane as shown in **Figure 7**. Cl^- channels are known to take part in the transfer of water and ions, and volume regulating of cells by modulating a volume regulated anion current (Sardini et al., 2003). Na^+/ H^+ exchange and H^+–pump in the plasma membrane are reported to be related with the control and regulation of pH_i (Harvey, 1988). So the pH_i can be regulated by H^+ export from cell to maintain its normal pH, and the pH_e will decrease as a result of H^+ export.

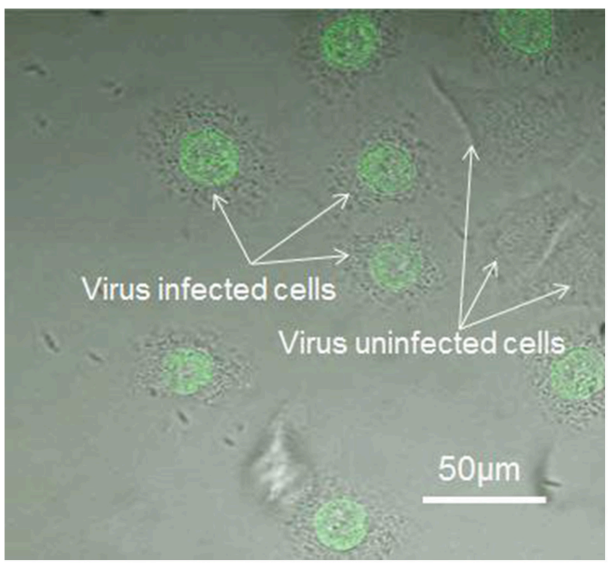

FIGURE 6 | Immunostaining of the virus-bound and -unbound cells (detected using anti-PB1 serum and an anti-rabbit IgG labeled with Alexa 488).

Potentials in Local pH_e Measurement of a Single Cell

Many researches were focused on the investigation of pH_i after virus infection. For example, Moore et al. (1988) reported that sindbis virus infection decreased the intracellular pH by approximately 0.5 as measured using a pH-sensitive fluorescence probe. But the measurement of pH_e as well as the pH gradients on both sides of cell membrane has not been investigated very well. Since individual cells can differ dramatically in size, protein levels, and expressed RNA transcripts. Single cell analyses are needed to better understand cellular responses in tissues and complex environments, and would give an accurate assessment of the behavior of the cell as one cell is studied at a time. Our proposed pH sensor which is fabricated from polystyrene microbeads can be used on the investigation of pH_e for a single cell near the cell membrane. It can be adhered to a special part of the cell, allowing local pH_e measurements of a single cell.

Future Research

The data from the surface virus-bound cells clearly demonstrated that there was a difference in pH_e between the influenza

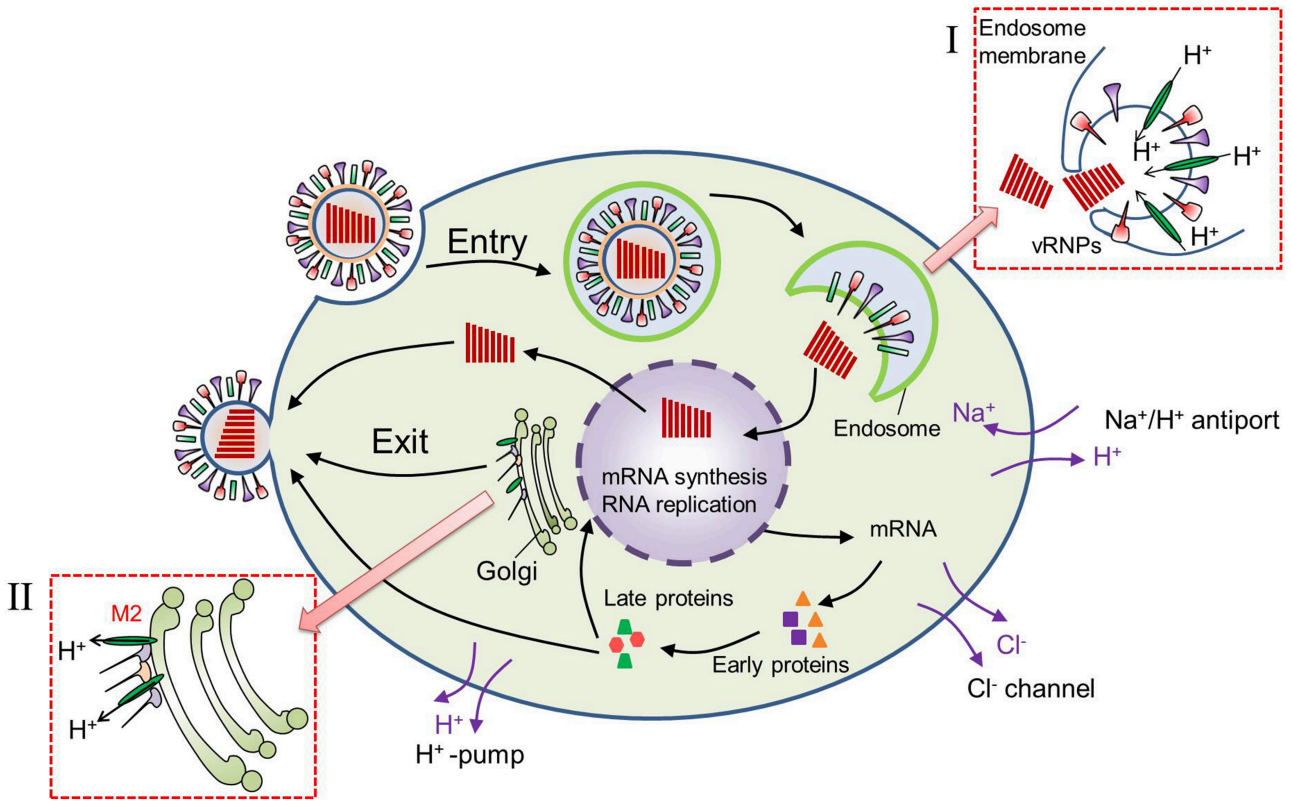

FIGURE 7 | Virus replication cycle after virus infection into a cell. (I) During virus entry, M2 proton channel shunts H+ from the acidic endosome to the virion interior, leading to membrane fusion and release of the genome. (II) During virus exit, M2 shunts H+ from trans-Golgi network to the cytoplasm, preventing premature conformational changes in the viral hemagglutinin (HA).

virus-infected and uninfected cells. On the basis of our discovery, we can also examine the pH of other virus-infected cells. We consider that pH changes in virus-infected cells may differ among viruses. Thus, further studies will be required to understand the virus specificity amounting to different pH changes. Secondly, the pH_i is not consistent in cytoplasm and pH_i distribution in the cell has been investigated (Shi et al., 2012; Chen et al., 2013). So the pH_e is considered to be inconsistent since pH_e change is related with the ions and solution exchanges on both sides of cell membrane. The pH_e difference and gradient in different position is really anticipated in the future. Thirdly, in our experiments, the pH sensor was placed on the cell membrane, and hence the results cannot accurately describe the activities inside the cell. At present, we are constructing rapid and low invasive injection method of the nanobead sensor into the cytoplasm (Zhong et al., 2016). In the future work, pH_i will be investigated after the pH sensor is injected in cytoplasm. Then the comparison between pH_i and pH_e can improve our understanding of the metabolic pathway of the cell and also the pH gradients on both sides of cell membrane.

AUTHOR CONTRIBUTIONS

Most of the experimental datas and images have been taken by HL. The experiments of sensor fabrication and sensitivity calibration have been done in Arai Laboratory (in Nagoya) and the virus infection experiment and measurements have been done in Honda Laboratory (in Tokyo) with the assistance of AH, TM, and HM. The paper has been written by HL and revised by FA and HM. All of the authors have contributed to the discussions of the paper writing.

ACKNOWLEDGMENTS

This work was supported by CREST (Japan Science and Technology Agency).

REFERENCES

Allison, A. C. (1963). Activation of lysosomal enzymes in virus-infected cells and its possible relationship to cytopathic effects. *J. Exp. Med.* 117, 879–887. doi: 10.1084/jem.117.6.879

Betakova, T. (2007). M2 protein-A proton channel of influenza A virus. *Curr. Pharm. Des.* 13, 3231–3235. doi: 10.2174/138161207782341295

Chen, S., Hong, Y., Liu, Y., Liu, J., Leung, C. W. T., Li, M., et al. (2013). Full-range intracellular pH sensing by an aggregation-induced emission-active

two-channel ratiometric fluorogen. *J. Am. Chem. Soc.* 135, 4926–4929. doi: 10.1021/ja400337p

Ciampor, F., Thompson, C. A., Grambas, S., and Hay, A. J. (1992). Regulation of pH by the M2 protein of influenza A viruses. *Virus Res.* 22, 247–258. doi: 10.1016/0168-1702(92)90056-F

Gillies, R. J., Zaguilan, R. M., Peterson, E. P., and Perona, R. (1992). Role of intracellular pH in mammalian cell proliferation. *Cell. Physiol. Biochem.* 2, 159–179. doi: 10.1159/000154638

Guinea, R., and Carrasco, L. (1995). Requirement for vacuolar proton-ATPase activity during entry of influenza virus into cells. *J. Virol.* 69, 2306–2312.

Harvey, B. J. (1988). Role of Na^+/H^+ exchange in the control of intracellular pH and cell membrane conductances in frog skin epithelium. *J. Gen. Physiol.* 92, 793–810. doi: 10.1085/jgp.92.6.793

Hui, E. K., and Nayak, D. P. (2001). Role of ATP in influenza virus budding. *Virol* 29, 329–341. doi: 10.1006/viro.2001.1181

Liu, H., Maruyama, H., Masuda, T., Honda, A., and Arai, F. (2014). Multi-fluorescent micro-sensor for accurate measurement of pH and temperature variations in micro-environments. *Sens. Actuators B. Chem.* 203, 54–62. doi: 10.1016/j.snb.2014.06.079

Liu, Y. H., Dam, T. H., and Pantano, P. (2000). A pH-sensitive nanotip array imaging sensor. *Anal. Chim. Acta* 419, 215–225. doi: 10.1016/S0003-2670(00)00988-0

Maruyama, H., Fukuda, T., and Arai, F. (2009). Functional gel-microbead manipulated by optical tweezers for local environment measurement in microchip. *Microfluid. Nanofluidics.* 6, 383–390. doi: 10.1007/s10404-008-0401-6

Maruyama, H., Masuda, T., and Arai, F. (2013). "Selective injection of fluorescence sensor encapsulated in the functional lipid capsule for intracellular measurement," in *26th 2015 International Symposium on Micro-NanoMechatronics and Human Science* (Nagoya), 1–2.

Masuda, T., Maruyama, H., Honda, A., and Arai, F. (2014). Virus enrichment for single virus infection by using 3D insulator based dielectrophoresis. *PLoS ONE* 9:e94083. doi: 10.1371/journal.pone.0094083

Moore, L. L., Bostick, D. A., and Garry, R. F. (1988). Sindbis virus infection decreases intracellular pH: alkaline medium inhibits processing of sindbis virus polyproteins. *Virology* 166, 1–9. doi: 10.1016/0042-6822(88)90139-0

Oyama, K., Takabayashi, M., Takei, Y., Arai, S., Takeoka, S., Ishiwata, S., et al. (2012). Walking nanothermometers: spatiotemporal temperature measurement of transported acidic organelles in single living cells. *Lab Chip.* 12, 1591–1593. doi: 10.1039/c2lc00014h

Pinto, L. H., Holsinger, L. J., and Lamb, R. A. (1992). Influenza virus M2 protein has ion channel activity. *Cell* 69, 517–528. doi: 10.1016/0092-8674(92)90452-I

Pinto, L. H., and Lamb, R. A. (2006). The M2 proton channels of influenza A and B viruses. *J. Biol. Chem.* 281, 8997–9000. doi: 10.1074/jbc.R500020200

Sardini, A., Amey, J. S., Weylandt, K. H., Nobles, M., Valverde, M. A., and Higgins, C. F. (2003). Cell volume regulation and swelling-activated chloride channels. *Biochim. Biophys. Acta* 1618, 153–162. doi: 10.1016/j.bbamem.2003.10.008

Shi, W., Li, X., and Ma, H. (2012). A tunable ratiometric pH sensor based on carbon nanodots for the quantitative measurement of the intracellular pH of whole cells. *Angew. Chem. Int. Ed. Engl.* 124, 6538–6541. doi: 10.1002/ange.201202533

Singh, V. N., Singh, M., August, J. T., and Horecker, B. L. (1974). Alterations in glucose metabolism in chick-Embryo cells transformed by rous sarcoma virus: intracellular levels of glycolytic intermediates. *Proc. Natl. Acad. Sci. U.S.A.* 71, 4129–4132. doi: 10.1073/pnas.71.10.4129

Steinhauer, D. A., Wharton, S. A., Skehel, J. J., Wiley, D. C., and Hay, A. J. (1991). Amantadine selection of a mutant influenza virus containing an acid-stable hemagglutinin glycoprotein: evidence for virus-specific regulation of the pH of glycoprotein transport vesicles. *Proc. Natl. Acad. Sci. U.S.A.* 88, 11525–11529. doi: 10.1073/pnas.88.24.11525

Takeda, M., Pekosz, A., Shuck, K., Pinto, L. H., and Lamb, R. A. (2002). Influenza A virus M2 ion channel activity is essential for efficient replication in tissue culture. *J. Virol.* 76, 1391–1399. doi: 10.1128/JVI.76.3.1391-1399.2002

Yin, L., He, C., Huang, C., Zhu, W., Wang, X., Xu, Y., et al. (2012). A dual pH and temperature responsive polymeric fluorescent sensor and its imaging application in living cells. *Chem. Commun. (Camb).* 48, 4486–4488. doi: 10.1039/c2cc30404j

Zhong, J., Liu, H. J., Maruyama, H., Masuda, T., and Arai, F. (2016). Continuous-wave laser-assisted injection of single magnetic nanobeads into living cells. *Sens. Actuators B. Chem.* 230, 298–305. doi: 10.1016/j.snb.2016.01.149

Conflict of Interest Statement: The authors declare that the research was conducted in the absence of any commercial or financial relationships that could be construed as a potential conflict of interest.

Copyright © 2016 Liu, Maruyama, Masuda, Honda and Arai. This is an open-access article distributed under the terms of the Creative Commons Attribution License (CC BY). The use, distribution or reproduction in other forums is permitted, provided the original author(s) or licensor are credited and that the original publication in this journal is cited, in accordance with accepted academic practice. No use, distribution or reproduction is permitted which does not comply with these terms.

frontiers in Microbiology

ORIGINAL RESEARCH
published: 22 June 2016
doi: 10.3389/fmicb.2016.00973

Liposome-Mediated Herpes Simplex Virus Uptake Is Glycoprotein-D Receptor-Independent but Requires Heparan Sulfate

Lorrie A. Burnham[1†], Dinesh Jaishankar[2†], Jeffrey M. Thompson[1], Kevin S. Jones[3], Deepak Shukla[2] and Vaibhav Tiwari[4]*

[1] Department of Biology, California State University, San Bernardino, CA, USA, [2] Departments of Ophthalmology and Visual Sciences, Bioengineering and Microbiology/Immunology, University of Illinois, Chicago, IL, USA, [3] Department of Biology, Howard University, Washington, DC, USA, [4] Department of Microbiology and Immunology, Midwestern University, Downers Grove, IL, USA

Cationic liposomes are widely used to facilitate introduction of genetic material into target cells during transfection. This study describes a non-receptor mediated herpes simplex virus type-1 (HSV-1) entry into the Chinese hamster ovary (CHO-K1) cells that naturally lack glycoprotein D (gD)-receptors using a commercially available cationic liposome: lipofectamine. Presence of cell surface heparan sulfate (HS) increased the levels of viral entry indicating a potential role of HS in this mode of entry. Loss of viral entry in the presence of actin de-polymerizing or lysosomotropic agents suggests that this mode of entry results in the endocytosis of the lipofectamine-virus mixture. Enhancement of HSV-1 entry by liposomes was also demonstrated *in vivo* using a zebrafish embryo model that showed stronger infection in the eyes and other tissues. Our study provides novel insights into gD receptor independent viral entry pathways and can guide new strategies to enhance the delivery of viral gene therapy vectors or oncolytic viruses.

Keywords: heparan sulfate, virus-cell interactions, viral entry

OPEN ACCESS

Edited by:
Ayae Honda,
Hosei University, Japan

Reviewed by:
Aaron T. Irving,
National University of Singapore, Singapore
Homayon Ghiasi,
Cedars-Sinai Medical Center, USA

****Correspondence:***
Vaibhav Tiwari
vtiwar@midwestern.edu

[†] These authors have contributed equally to this work.

Specialty section:
This article was submitted to Virology, a section of the journal Frontiers in Microbiology

Received: *22 March 2016*
Accepted: *06 June 2016*
Published: *22 June 2016*

Citation:
Burnham LA, Jaishankar D, Thompson JM, Jones KS, Shukla D and Tiwari V (2016) Liposome-Mediated Herpes Simplex Virus Uptake Is Glycoprotein-D Receptor-Independent but Requires Heparan Sulfate. Front. Microbiol. 7:973. doi: 10.3389/fmicb.2016.00973

INTRODUCTION

HSV-1 is prevalent pathogen in various clinical manifestations ranging from common cold sore, gingivostomatitis, herpetic whitlow, corneal herpetic stromal keratitis, genital ulcers, and sometimes more serious complications such as encephalitis and meningitis (Nahmias and Roizman, 1973; Whitley et al., 1998; Whitley and Roizman, 2001). The current model of HSV entry suggests that the virus uses multiple pathways during entry depending on cell types and entry receptors (Spear and Longnecker, 2003; Karasneh and Shukla, 2011; Salameh et al., 2012). HSV-1 entry generally begins with viral attachment to host cells in which HSV glycoproteins B (gB) and C (gC) on the envelope of the virus typically bind to heparan sulfate (HS) on the surface of the host cell (WuDunn and Spear, 1989; Herold et al., 1991; Shieh et al., 1992). This is followed by gD binding to one of its cognate receptors including an intercellular adhesion molecule: nectin −1 or −2 (Geraghty et al., 1998) and a member of the tumor necrosis factor receptor family: herpesvirus entry mediator (HVEM; Montgomery et al., 1996). The virus also uses a modified version of HS known as 3-*O* sulfated heparan sulfate (3-*OS* HS) to bind gD and induce virus cell fusion independent of the known protein receptors (Shukla et al., 1999; Shukla and Spear, 2001). Viral interactions with

these receptors initiate fusion between the viral envelope and the membrane of the cell, which also requires participation of two additional HSV glycoproteins gH and gL (Pertel et al., 2001; Spear and Longnecker, 2003). Upon fusion, the nucleocapsid and tegument are released into the cytoplasm where they are transported to the nucleus via microtubules. Our previous studies have shown that HSV entry exploits host cell cytoskeleton via a novel phagocytic uptake in human corneal fibroblasts (CF) cells and that modified 3-*OS* HS plays a significant role in promoting viral entry and spread via F-actin membrane extensions such as filopodia (Clement et al., 2006; Oh et al., 2010; Choudhary et al., 2013).

Because HSV depends on a receptor-mediated entry, CHO cells that naturally lack gD receptors and hence resistant to HSV infections (Montgomery et al., 1996), are a well-known model to study receptor-independent entry of HSV. To make them susceptible, these cells need to be transfected with one of the gD receptors. During one of our transfection experiments, we accidently infected CHO-K1 cells lacking gD receptors with HSV-1 in the presence of cell transfection reagent, Lipofectamine 2000. To our surprise we observed robust viral entry. This was interesting as virus entry was observed in the absence of any gD receptors. Based on this finding, our study investigates a non-receptor mediated HSV entry. It demonstrates a role for HS and the cytoskeleton filaments in gD receptor-independent endocytosis of HSV into naturally resistant CHO-K1 cells. Overall, we provide a new understanding of gD receptor-independent viral entry mechanisms and help generate a new strategy to enhance the delivery of viral gene therapy vectors.

MATERIALS AND METHODS

Western University of Health Sciences (WUHS) Institutional Animal Care and Use Committee specifically approved this study (IACUC protocol number 026).

Cell Culture and Viruses

Wild-type Chinese hamster ovarian-K1 (CHO-K1), reporter CHO-Ig8 cells that expresses β-galactosidase upon viral entry (Montgomery et al., 1996), CHO-745 that lack glycosaminoglycans including HS (WuDunn and Spear, 1989), Vero, HeLa, and primary cultures of human corneal fibroblasts (CF) cells (Clement et al., 2006) were used in this study. The CF was procured from corneal tissue purchased from Illinois eye bank. www.eversightvision.org/illinois/. All CHO cells were grown in Ham's F-12 medium (Gibco/BRL, Carlsbad, CA, USA) supplemented with 10% fetal bovine serum (FBS) and 1% penicillin and streptomycin (P/S, Gibco/BRL). Vero and HeLa cells were grown in Dulbecco's modified Eagle's medium (DMEM) supplemented with 10% FBS and P/S. Primary cultures of human CF were maintained as previously described. The β-galactosidase expressing recombinant HSV-1 (KOS) gL86 and GFP-expressing HSV-1 (K26GFP) were provided by P.G. Spear (Northwestern University, Chicago) and P. Desai (Johns Hopkins University; Desai and Person, 1998). The HSV-1 gL86 is a recombinant virus in which a portion of the "gL" gene was replaced with the *lac Z* gene encoding for the β-galactosidase enzyme (Montgomery et al., 1996). Only upon entry and successful infection, the β-galactosidase enzyme is synthesized and activated. Thus, the activity of this enzyme, using a substrate like ONPG, is measured as an indicator of viral entry. In our experiments the enzymatic activity was measured as optical density (OD) at 410 nm by a spectrophotometer.

HSV-1 Viral Entry Assay

CHO-K1, cells were grown in 96 or 6 well-plates to subconfluence and infected with β-galactosidase expressing recombinant gL86 100 pfu/cell using Lipofectamine 2000 (Invitrogen). Uninfected cells in the presence and absence of lipofectamine were used as negative controls. Six hours post-infection (hpi), β-galactosidase assays were performed using *o*-nitrophenyl-D-galactopyranoside (ImmunoPure ONPG; Pierce) or 5-bromo-4-chloro-3-indolyl-_-D-galactopyranoside (X-gal; Sigma). For the soluble substrate, the enzymatic activity was measured at 410 nm using a microplate reader (Molecular Devices spectra MAX 190, Sunnyvale, CA). For X-gal assay, the cells were fixed (2% formaldehyde and 0.2% glutaraldehyde) and permeabilized (2 mM MgCl2, 0.01% deoxycholate, and 0.02% nonidet NP-40 Sigma). Finally, 1mL of β-galactosidase reagent (1.0 mg/mL X-gal in ferricyanide buffer) was added to each well and incubated at 37°C for 90 min before the cells were examined using brightfield microscopy under the 20 × objectives (Nikon D-Eclipse-C1). Similar experiments were performed using β-galactosidase expressing CHO-Ig8 cells.

Immunofluorescence Imaging

Cultured monolayers of human corneal fibroblasts (CF) were infected with HSV-1 K26GFP at 50 PFU in serum free media Opti-MEM, and this was followed by fixation of cells at 1 h post-infection using fixative buffer (2% formaldehyde and 0.2% glutaradehyde). The cells were then washed with NaCl/Pi and permeabilized with 2 mM $MgCl_2$, 0.01% deoxycholate, and 0.02% Nonidet NP-40 for 20 min. After rinsing with NaCl/Pi, 10 nM rhodamine-conjugated phalloidin (Invitrogen) was added for F-actin staining at room temperature for 45 min. Finally, the cells were washed three times with one NaCl/Pi. Images of immunofluorescent labeled cells were acquired by using a confocal microscope (Nikon D-Eclipse-C1) using the software EZ-C1.

Scanning Electron Microscopy (SEM)

Wild-type CHO-K1 and CHO-745 cells were grown in 60 mm plates and infected with HSV-1 (KOS) at 50 pfu/cell for 0, 30, and 60 min at 37°C. Uninfected cells in the presence and absence of lipofectamine were used as negative controls. The cells were then fixed with 2% formaldehyde/ 4% glutaraldehyde in 1 × Dulbecco's phosphate buffer saline (PBS) prior to SEM study. This was followed by fixing cells with 1% osmium tetroxide for 40 min. Dehydration was done in an increasing order (25–100%) of ethanol treatment at 5 min each, respectively. Hundred percentage ethanol was repeated to ensure dehydration. Cover slips were removed from dishes and mounted on aluminum studs previously cleaned with 100% ethanol. Cover slip edges were painted with colloidal silver for conduction and dried in a Critical Point Dryer (Samdri-780A). Samples were then coated

with gold using a Sputter Coater (Hummer VI-A) for 2 min. Samples were viewed using a Hitachi S-2700 Scanning Electron Microscope (SEM). Images were captured at 1000–5000x using 4Pi Revolution image capture system.

Western Blots

Heparan sulfate (HS) positive CHO-K1 and HS negative CHO-745 cells were infected for 3 h at 37°C with HSV-1 gL86 virus at 10 PFU/cell in presence and absence of lipofectamine (8 μg/mL). Cells were lysed in radioimmunoprecipitation buffer (RIPA, Sigma) with Proteinase and Phosphatase (Halt, Pierce Biotechnology) and electrophoresed on a 4–12% Bis-Tris Gel (NuPage). A PVDF membrane (Novex) was used for transfer. After initial non-specific blocking in 5% non-fat milk, the membrane was then incubated with primary (VP16 mouse monoclonal, Santa Cruz; GAPDH rabbit polyclonal, Santa Cruz) and secondary HRP-conjugated antibodies (Jackson). The membrane was then developed (ECL, Pierce) and visualized (ImageQuant LAS 4000, GE Healthcare).

Zebrafish Experiments

Usage of Zebrafish (ZF) embryo experiment was conducted under approved protocol (IACUC/026) by WUHS, Pomona, California. WIK strain of 1 day old Zebrafish embryos were obtained from ZFIN. On day 3 the zebrafish embryos were infected with a mixture containing 10^8 HSV in 10 μg/mL lipofectamine (10 μg/mL) in 96 well-dishes. In parallel experiments, zebrafish embryos were pre-treated with heparinase I and II (1U/ml for 5 h) or mock treated before HSV-1 infection. Addition of the soluble substrate [o-nitrophenyl-β-D-galactopyranoside (ONPG, ImmunoPure, Pierce; 3 mg/ml)] in the culture medium followed by fluorescence measurement led to the generation of dose–response curves for HSV-1 infected zebrafish embryos. The enzymatic activity was measured at 410 nm using a micro-plate reader. For X-gal assay, after 24 h post-infection, the embryos were fixed (2% formaldehyde and 0.2% glutaraldehyde) overnight at 4°C, permeabilized (2 mM MgCl2, 0.01% deoxycholate, and 0.02% nonidet NP-40 (Sigma) for 8 h at 4°C and then 1 mg/mL X-gal in ferricyanide buffer was added to the embryos and left overnight at 37°C. The embryos were then imaged the next day.

Statistics

The data presented in each experiment are the means of triplicate measures and are representative of three independent experiments. Significant differences were calculated using *t*-test (Analysis of Variance). $P < 0.05$ was considered statistically significant.

RESULTS

HSV-1 Entry Is Enhanced by Lipofectamine in the Absence of Glycoprotein D (gD) Receptors and Is Viral Strain Independent

In order to confirm that lipofectamine helps facilitate HSV-1 infection, an entry assay was performed using the resistant CHO-K1 cell line (Montgomery et al., 1996). We used commercially available cationic liposome (Lipofectamine 2000) in our experiments. HSV-1 entry into the cells was determined by using β-galactosidase expressing HSV-1 reporter virus (gL86). Expression levels of β-galactosidase are induced by HSV infection and therefore it can be used as a measureable indicator of viral entry (Montgomery et al., 1996). Quantification and visualization of β-galactosidase levels by using two different substrates: ONPG and X-gal, show that HSV-1 gL86 pre-incubation with lipofectamine (L) resulted in higher levels of HSV-1 entry in receptor (R) negative CHO-K1 cells (**Figures 1A,B**). Similarly, enhanced viral entry was also noted in wild-type CHO-K1 cells when Green fluorescent protein (GFP)-tagged HSV-1 virions (K26GFP; Desai and Person, 1998) was in a mixture with lipofectamine (**Figure 1C**). To check if non-receptor mediated viral entry is HSV strain dependent, we tested the ability of lipofectamine to enhance viral entry of different strains of HSV-1/-2 (F, G, MP, and 17 strains). Here we used CHO Ig8 cells that express β-galactosidase upon viral entry (Montgomery et al., 1996). The HSV strains were pre-incubated with lipofectamine and subsequently infection was performed. The results from this experiment showed that lipofectamine enhanced entry of different HSV strains in a dosage dependent manner as evident by ONPG assay (**Figure 1D**). It has been previously shown that liposome encapsulation of retrovirus and hepatitis D virus allows efficient infection in resistant cell lines (Innes et al., 1990; Bichko et al., 1994). A similar effect is likely seen with lipofectamine/HSV mixture.

Presence of Lipofectamine-HSV-1 Mixture Further Enhances Entry in Natural Target Cells

We next evaluated the ability of lipofectamine to enhance HSV-1 entry into naturally permissive or target cell lines. Confluent monolayers of HeLa, Vero, and primary cultures of human CF were plated and infected with HSV-1(gL86) in the presence and absence of lipofectamine and the entry of HSV-1 were measured using the assay mentioned above. β-galactosidase expression levels were higher in the cells that were treated with lipofectamine (black bar) than the parallel untreated control (white bar). The entry was not significantly higher as HeLa, Vero, and CF are known to express gD receptors and are already highly susceptible to HSV-1 infection (Tiwari et al., 2006; **Figure 2A**). In order to obtain more direct and visual evidence of lipofectamine-mediated HSV-1 entry in CF cells, K26GFP was pre-incubated with lipofectamine to infect cultured CF, and fluorescence microscopy was used to visualize the virions (**Figure 2B**). The GFP-punctate dots with high intensity were noticed when HSV-1 was allowed to infect in the presence of lipofectamine (**Figure 2Bc**), compared to GFP-HSV-1 in the absence of lipofectamine (**Figure 2Bb**). This suggests that lipofectamine-virus mixture were equally effective in delivering HSV-1 into susceptible cells expressing gD receptors and the system of introducing lipofectamine-virus mixture into susceptible cells were not interfered by the presence of gD receptors.

Lipofectamine-HSV-1 Mixture Mediated Entry is Concentration Dependent

To quantitatively demonstrate the effectiveness of lipofectamine in allowing HSV-1 entry into resistant CHO-K1 cells, we incubated different concentrations (from 1.0–8.0 μg/mL) of lipofectamine with gL86 for 15 min at room temperature. The PBS treated gL86 was considered as a control for comparison. Maximum viral entry, via ONPG and X-gal assays, was detected at a higher concentration (8.0 μg/mL) of lipofectamine (**Figures 2C,Dd**). Again, HSV-1 without lipofectamine failed to infect CHO-K1 cells (**Figure 2Da**). Similar concentration (8.0–10 μg/mL) of lipofectamine has been reported to mediate ecotropic murine leukemia virus and hepatitis D virus infections (Innes et al., 1990; Bichko et al., 1994).

Cell Surface Heparan Sulfate Plays a Critical Role during Lipofectamine-Mediated gD-Receptor-Independent HSV-1 Entry

We further probed the mechanism non-receptor mediated entry by investigating the role of cell surface HS which are highly expressed on CHO-K1 cells. It is well-documented that HS is a negatively charged cell surface attachment receptor that virtually

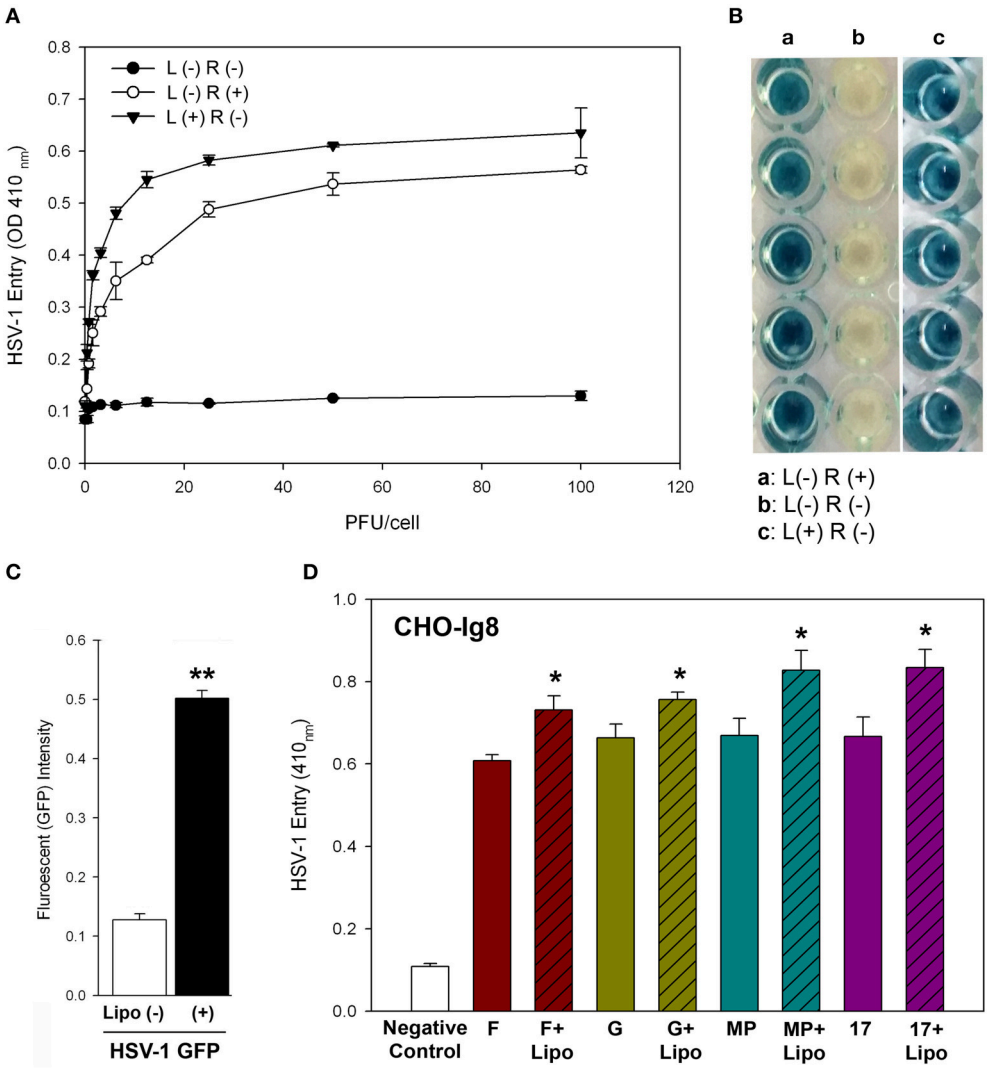

FIGURE 1 | Lipofectamine-HSV-1 entry into receptor negative CHO-K1 cells. (A) ONPG virus entry in CHO-K1 cells infected with gL86 in the presence (+) and absence (–) of lipofectamine (4 μg/mL) quantified at 6hpi. **(B)** Stained images of X-gal in CHO-K1 cells infected with gL86 in the presence (+, panel c) and absence (–, panel b) of lipofectamine (4 μg/mL). **(C)** Wild type CHO-K1 cells were infected with K26-GFP with and without lipofectamine (4 μg/mL) and fluorescence intensity was quantified 3hpi. Asterisks indicate significant difference from the uninfected control ($P < 0.05$, *t*-test); error bars represent *SD* ($n = 4$). **(D)** 3-*OST*-3 isoform expressing CHO Ig8 cells were infected with the indicated strains in the presence (bars with cross line) and absence (plain bars) of lipofectamine and virus entry was measured by ONPG. The data shown are the means of triplicate measures and are representative of three independent experiments. Asterisks indicate significant difference from the uninfected control ($P < 0.05$, *t*-test); error bars represent *SD* ($n = 3$). L, Lipofectamine; R, Receptor.

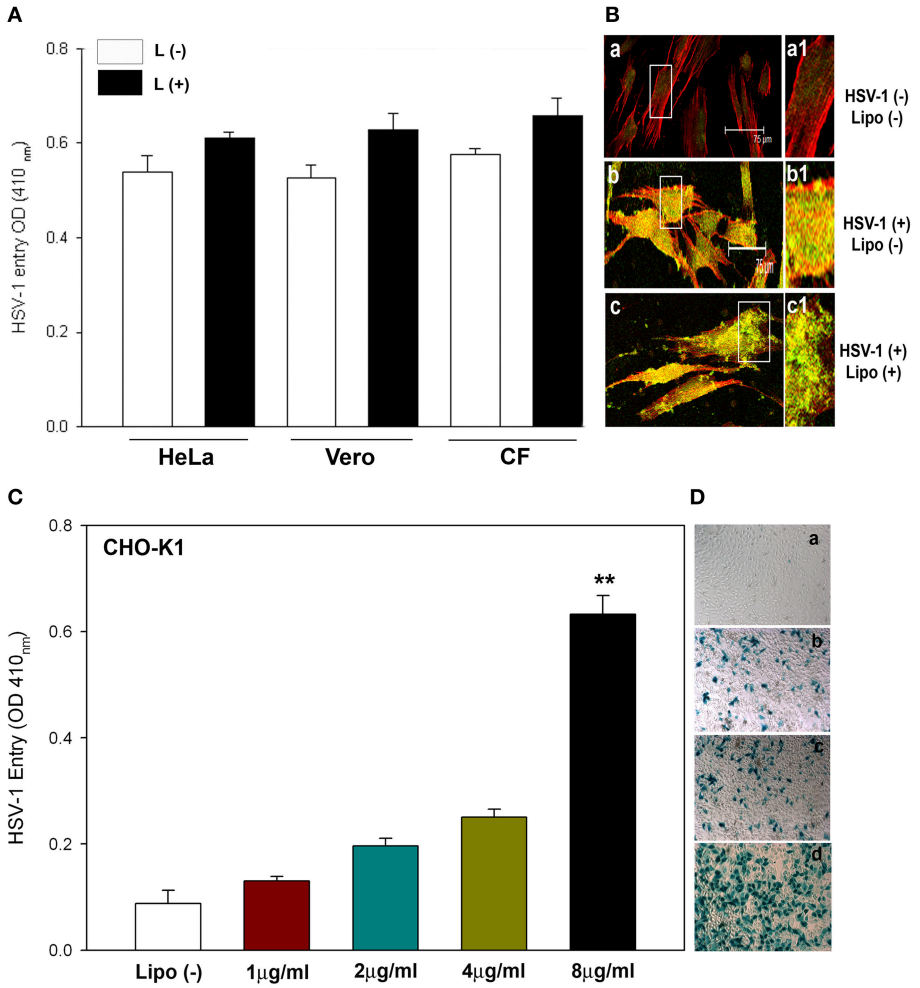

FIGURE 2 | Enhanced effect on HSV-1 entry in naturally susceptible cells in the presence of lipofectamine. (A) The indicated cells were plated in 96 well-plates and infected with gL86 virus in the presence (black bars) and absence of (white bars) lipofectamine. The viral entry was measured by ONPG assay 6hpi. L, Lipofectamine **(B)** Human CF, stained with actin (shown as red), was infected with K26-GFP in the presence (panel c) and absence (panel b) of lipofectamine. Uninfected and lipofectamine untreated CF served as negative control (panel a). The boxed regions in panel a–c are highlighted as a1–c1. The data shown are the means of triplicate measures and are representative of three independent experiments. **(C)** Lipofectamine concentration dictates HSV-1 entry. CHO-K1 cells in 96 well-plates were infected with gL86 along with the indicated concentrations of lipofectamine. Entry was quantified 6hpi by ONPG assay. Asterisks indicate significant difference from the uninfected control ($P < 0.05$, *t*-test); error bars represent SD ($n = 3$). **(D)** Virus entry by X-gal assay in CHO-K1 cells infected with gL86 with 2 μg/mL (panel b), 4 μg/mL (panel c), and 8 μg/mL (panel d) of lipofectamine and without lipofectamine (panel a). The data shown are the means of triplicate measures and are representative of three independent experiments.

all human herpesviruses recognize during initial attachment to cells (Shukla and Spear, 2001) and has a role in disease manifestations (Ferro, 2013). The significance of HS in absence of gD receptor is well-recognized as CHO-K1 cells allow sufficient viral binding/attachment but not entry because of lack of gD-receptor, while CHO mutant cells defective in HS biosynthesis (CHO-745) do not allow viral binding or attachment (Shukla et al., 1999). To determine whether presence of anionic HS assists the delivery of cationic lipofectamine-virus mixture into cells, we infected both CHO-K1 and CHO-745 cells with HSV-1 in the presence and absence of lipofectamine. The untreated HSV-1 was kept as negative control for both types of cells. Entry was quantified by ONPG assay and the levels of viral tegument protein: VP16 (Heine et al., 1974; Weinheimer et al., 1992) was assessed by western blot. Lipofectamine mediated HSV entry was prominent in wild-type CHO-K1 cell but not in CHO-745 cells (**Figures 3A,B**) suggesting the role of HS involved in viral entry mediated by lipofectamine.

To further verify whether lipofectamine mediated entry was HS-dependent, high resolution scanning electron microscopy (SEM) was performed. HS expressing wild-type CHO-K1 cells and HS deficient CHO-745 cells were infected with HSV-1 in the presence of lipofectamine and processed for SEM. The SEM images demonstrated the presence of large numbers of virus particles attached to F-actin membrane structures including filopodia, which are induced upon infection and

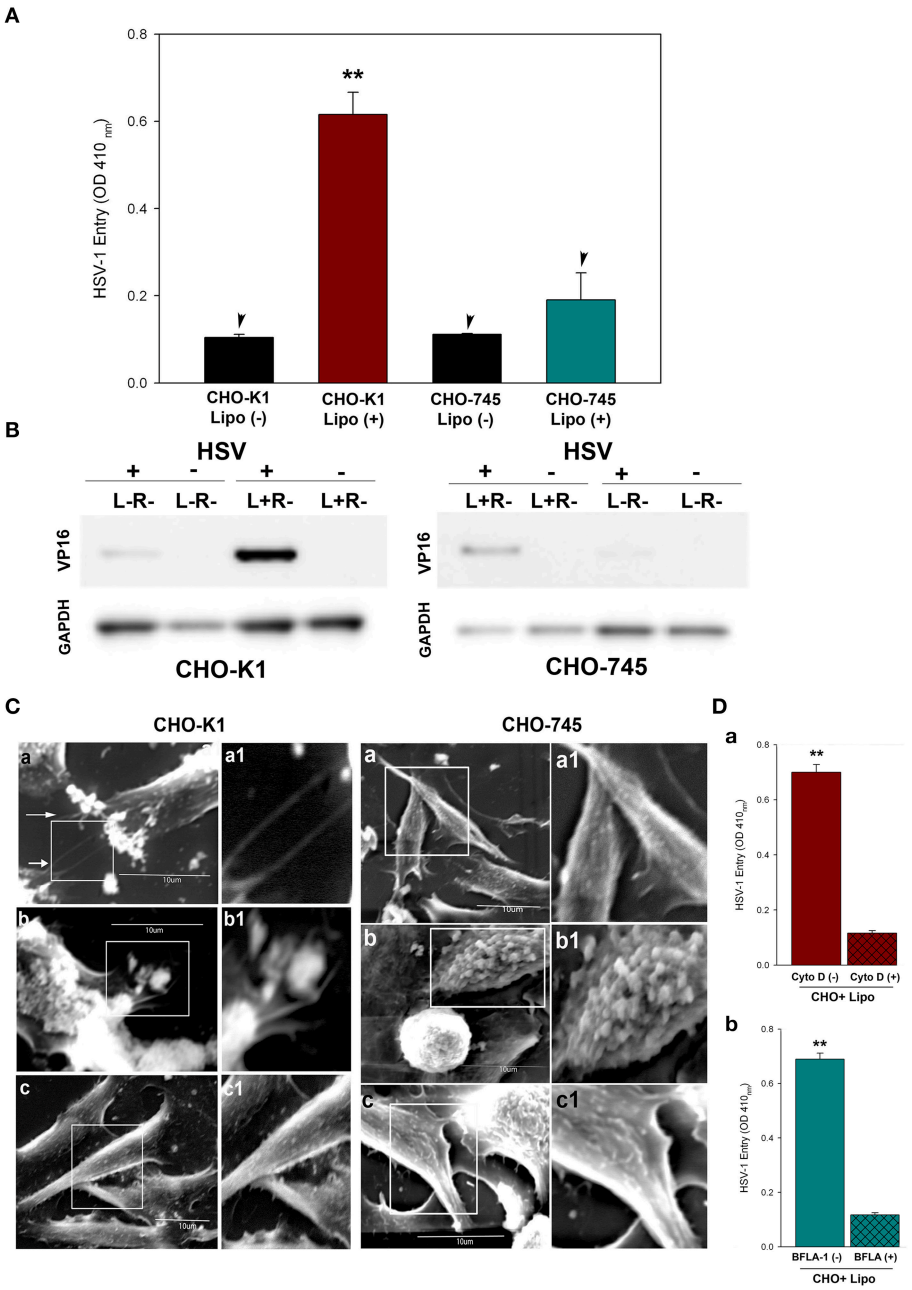

FIGURE 3 | Significance of heparan sulfate (HS) in lipofectamine mediated HSV-1 uptake. (A) Virus entry in CHO-K1 and HS deficient CHO-745 cells infected with gL86 in the presence and absence of lipofectamine (4 μg/mL) was determined by ONPG. Asterisks indicate significant difference from the CHO-K1 cells infected in absence of lipofectamine ($P < 0.05$, *t*-test); error bars represent *SD* ($n = 3$). While CHO-745 cells infected with HSV-1 in presence and absence of lipofecatine had no significant differences. **(B)** VP-16 levels compared between CHO-K1 and HS negative (CHO-745) cells via western blot (L, Lipofectamine; R, Receptor). **(C)**. Scanning electron microscopy (SEM) performed on CHO-K1 cells infected with HSV-1 along with lipofectamine shows filiopodia (panel a) and HSV-1 uptake (panel b), while HSV-1 without lipofectamine infected cells show smooth surface (panel c). The boxed regions in panel a–c are highlighted as a1–c1. In parallel lipofectamine mixture with HSV-1 had little or no actin cytoskeleton activity in CHO-745 cells (panel a,b). Similarly no filopodia were noticed in HSV-1 infected CHO-745 cells in absence of lipofectamine (panel c). The boxed regions in panel a–c are highlighted as a1–c1. The data shown are the means of triplicate measures and are representative of three independent experiments. **(D)** Host cell cytoskeleton is critical during uptake of lipofectamine-HSV-1 mixture in absence of gD receptors. **(D)** Panel a: Cultured monolayers of CHO-K1 cells were pre-treated with the 0.5 μg/mL actin depolymerizing agent Cytochalisin D (Cyto D; panel a) before infecting with gL86 along with lipofectamine. Cells treated with 1 × PBS treated cells were used as a control. Viral entry was measure by ONPG assay. Panel b: Cells were pre-treated with 0.02 μM Bafilomycin A1 (BFLA-1) and then infected with gL86. Viral entry was measured using ONPG assay. The data shown are the means of triplicate measures and are representative of three independent experiments. Asterisks indicate significant difference from the Cyto-D/BFLA-1 treated control ($P < 0.05$, *t*-test); error bars represent SD ($n = 3$).

express higher amounts of HS (Oh et al., 2010; **Figures 3Ca,Cb**), while uninfected CHO-K1 cells had a relatively smooth surface (**Figure 3Cc**). In contrast, virus-lipofectamine mixture were adhered and clumped on the cell membrane of CHO-745 cells (**Figures 3Cb,Cc**) as no or very little outgrowth of filopodia was noticed in both infected and uninfected CHO-745 cells (**Figure 3Ca**). These results show that HS may play a significant role in HSV-1 entry in the absence of gD-receptor.

Endocytosis of Lipofectamine-Virus Mixture during Entry Exploits Actin-Cytoskeleton Including Filopodia

As lipofectamine and HSV mainly enter cells by endocytosis (Nicola et al., 2003; Cui et al., 2012), we speculated that the lipofectamine-HSV mixture is also being endocytosed. It has been reported that HSV entry through endocytosis leads to a change in arrangement of cytoskeleton elements (Lyman and Enquist, 2009). As discussed above, we found enhancement of filopodia formation and the presence of virions on the filopodia from SEM imaging in CHO-K1 cells. Based on this observation, we predicted that actin filaments can be beneficial to non-receptor mediated entry. To demonstrate this, viral entry assay was performed in the presence of an F-actin depolymerizer. CHO-K1 cells were pre-treated with Cytochalasin D (Cyto D) prior to infection. It was postulated that pre-treatment of Cyto-D would have more negative effect provided the actin-based membrane protrusions (such as filopodia) played a role in the attachment and entry of lipofectamine-virus mixture. As predicted, actin depolymerizing agent Cyto-D negatively affected virus entry (**Figure 3D**, Top panel). The expected loss of filopodia due to Cyto-D treatment in these experiments correlates well to our prior knowledge that filopodia plays a significant role during HSV-1 entry (Oh et al., 2010). Next, we examined the role of pH dependence in non-receptor mediated entry. The rationale was based on the fact that lipofectamine-virus mixture might be taken in an endosomal vesicle which has an acidic pH (Geisow and Evans, 1984). Thus, effects of lysosomotropic agent (bafilomycin A1; BFLA-1) that are capable of interfering with vesicular acidification (Lukacs et al., 1990) were tested for their effects on virus entry. Lipofectamine-virus mixture showed significantly low viral entry in the presence of BFLA-1 reinforcing the point that pH plays an important role in non-receptor mediated virus entry (**Figure 3Db**). Taken together, it can be implied that lipofectamine-virus mixture enters through endocytosis and depends on actin filaments for the uptake and low pH for a successful entry.

Lipofectamine-Virus Mixture Promotes HSV Infection in Zebrafish Embryo Model

Finally, we tested the *in vivo* significance of lipofectamine-virus mixture in a Zebrafish (ZF) infection model (Burgos et al., 2008). Using 3 day old ZF embryos, HSV-1 infection with and without lipofectamine was performed. HSV entry in ZF embryos were assessed by ONPG and X-gal assays after 18 h post-infection. A high intensity blue staining of ZF embryos were observed in virus-lipofectamine treated group compared to virus alone infected embryos (**Figures 4Ab,Ac**) indicating that more virus has entered. The mock infected ZF embryo remained colorless following X gal staining (**Figure 4Aa**). A similar pattern of HSV entry was observed and quantified in zebrafish embryos by ONPG assay (**Figure 4B**). Interestingly, pre-treatment of ZF-embryos with heparinase I and II (1 U/mL) reduces lipofectamine mediated virus HSV-1 entry (**Figure 4C**). Thus, it was clear that lipofectamine-mediated virus infection can be achieved in live animal models.

DISCUSSION

To summarize, our study, for the first time, describes how HSV-1 gets into cells by a non-receptor mediated endocytosis, meaning that virus entry and infection can occur without the presence of gD receptors. Receptor mediated endocytosis requires the presence of at least one of the gD receptors (Shukla and Spear, 2001) for viral entry and infection to occur. However, using a lipofectamine-virus mixture, we show that in gD receptor lacking CHO-K1 cells, the virus can successfully enter and infect without the need of gD receptors (**Figure 1**). We compared this mode of entry in natural target cells such as HeLa and primary corneal fibroblasts. Though entry levels were not significant (as these cells naturally express gD receptors), higher entry levels in the presence of lipofectamine were observed consistently in all natural target cells (**Figure 2**). Also, the presence of natural gD receptors in these cells did not interfere with the entry of lipofectamine-virus mixture suggesting that HSV-1 entry in the presence of lipofectamine can still use gD receptors. We also found that lipofectamine-virus mixture is not virus strain dependent (**Figure 1D**), and can be used to enhance entry in live animal models, suggesting the universal nature of lipofectamine-mediated entry.

Previous studies show the importance of the rearrangement of cytoskeleton elements and pH dependence for endocytosis (Nicola et al., 2003; Lyman and Enquist, 2009; Cui et al., 2012). Keeping this into consideration, we show that non-receptor mediated entry requires actin filaments and low pH for a successful HSV-1 entry and blocking either one of these factors results in loss of viral entry indicating that lipofectamine-HSV mixture uses endocytosis as a mode of entry. However, an intriguing question arises at this point: if the virus does not use gD receptor, how does it lose its coat proteins, get endocytosed and become infectious? One of the plausible assumptions could be that low pH of endosomes may play a role in the virus becoming infectious. Low pH is known to bring about conformational changes in glycoprotein B (gB), which are much favorable for fusion with a vesicular membrane and may not require a gD receptor (Dollery et al., 2010). More specifically, some gB receptors such as non-muscle myosin IIA could facilitate the process (Arii et al., 2010). It is also possible that lipofectamine by its membrane permeability property may itself expose the fusogenic domain of gB without requiring the gD/receptor mixture to trigger the process. This mixture could thus be potentially used for delivering a gD null virus for vaccine development and functional studies. Future studies will

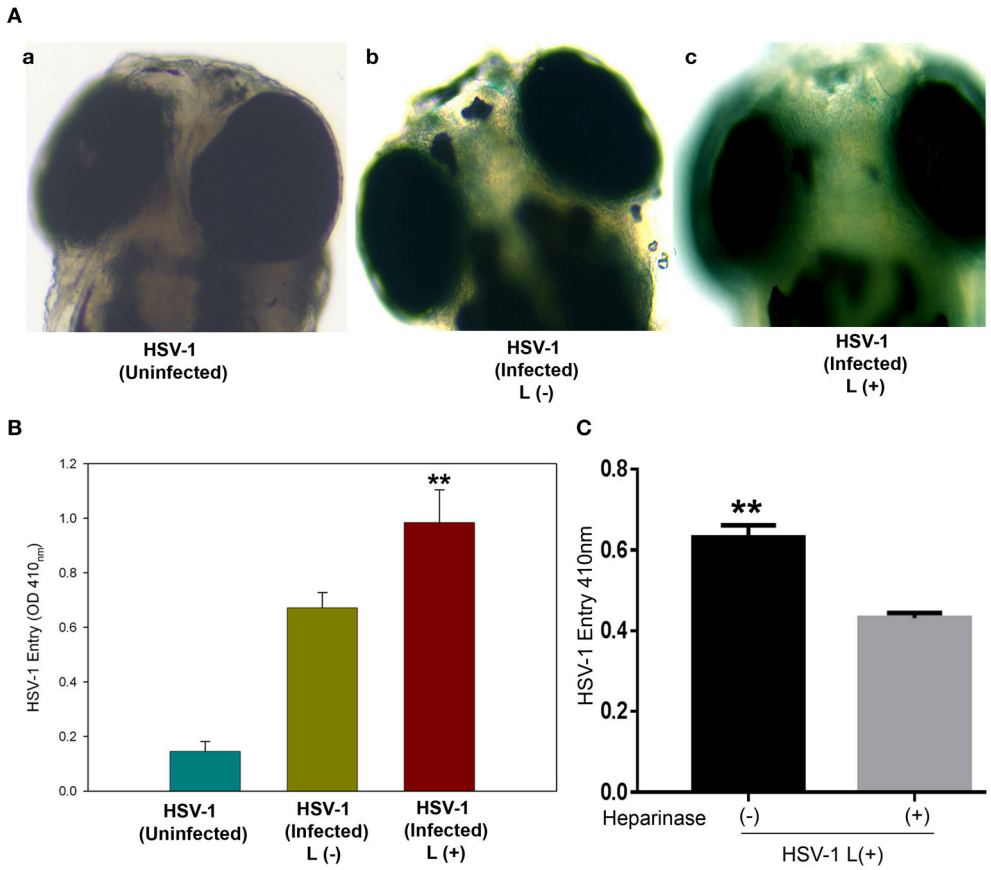

FIGURE 4 | Significance of lipofectamine HSV-1 mixture uptake in Zebrafish embryo model. WIK strain of 3 day old Zebrafish embryo was infected with 10^8 HSV in presence (panel c) and absence (panel b) of lipofectamine (10 μg/mL). **(A)** shows 24hpi X gal staining in Zebrafish embryos, while **(B)** indicates ONPG assay conducted with Zebrafish embryos in the presence and absence of lipofectamine. Asterisks indicate significant difference from the uninfected control ($P < 0.05$, *t*-test); error bars represent *SD* ($n = 3$). L: Lipofectamine. **(C)**: pre-treatment of Zebrafish embryos with heparinase I and II (1U/ml) reduce lipofectamine (L) mediated HSV-1 entry compare to heparinase untreated embryos. Reporter virus based HSV-1 entry assay was conducted by using ONPG assay. The data shown are the means of triplicate measures and are representative of three independent experiments. Asterisks indicate significant difference from the heparinase untreated control ($P < 0.05$, *t*-test); error bars represent *SD* ($n = 3$).

determine the exact mechanism by which the capsid is released into the cytosol.

There is enough evidence to suggest that HS plays an important role in HSV pathogenesis (Shukla and Spear, 2001). In this study we demonstrated a novel role that HS plays in non-receptor mediated entry. The presence of HS on cell surface clearly enhances entry (**Figure 3**). The need for HS could be crucial for Lipofectamine-virus delivery due to fact that HS is negatively charged and may directly interact with cationic liposomes. Entry into animal models such as ZF also requires HS (Antoine et al., 2014) and therefore, the fact that Lipofectamine enhances entry *in vivo* could be used to identify the tissues which may be more susceptible due to the presence of HS. While zebrafish has been shown to support entry of HSV and other viruses, more tedious ways such as microinjection is normally required to initiate viral entry in this model (Burgos et al., 2008; Antoine et al., 2014). Our study also demonstrates a much easier way to facilitate HSV-1 entry in zebrafish (**Figure 4**) and does not require sophisticated microinjection equipment. Interestingly, we observed a higher X-gal staining in the eye and other tissues in the virus-lipofectamine treated group compared to virus alone infected embryos (data not shown). Although more studies are needed to outline the actual mechanism by which lipofectamine-virus mixture is entering and infecting cells and how the diversity of HS proteoglycans can affect this, our demonstration of the HSV uptake in the absence of gD receptors has given a platform to look beyond the role of gD receptors and discover new receptors or components and learn about their role in viral entry and transport. In addition, because the roles of gD in nuclear viral egress (Johnson and Baines, 2011; Johnson et al., 2011) and cell-to-cell spread (Pertel et al., 2001; Akhtar and Shukla, 2009; Karasneh and Shukla, 2011) are well-established, the lipofectamine-virus mixture may be utilized to shed light on the possible roles of gD receptors in the above mentioned events. Further, role of other HSV-1 glycoproteins such as gK which is known to be involved

in virus spread and alterations in viral receptor expression in the eye (Allen et al., 2014), needs to be investigated during HSV-1-liposome mixture mediated infection in zebrafish ocular model.

AUTHOR CONTRIBUTIONS

LB and DJ equally contributed to the work. KJ and VT did the zebrafish experiments. LB and JT did the Electron Microscopy studies. VT designed the study and analyzed the data. DJ, DS, and VT wrote the manuscript. LB, JT, DJ, DS, KJ, and VT read, corrected and approved the final manuscript.

FUNDING

This investigation was supported by internal Instructional grant support (grant number N12587) to VT from WUHS, Pomona, CA, and grants from National Institutes of Health 1R15 AI088429-01A1 and R21 AI105573.

ACKNOWLEDGMENTS

We sincerely acknowledge the facility at California State University, San Bernardino for EM imaging. Usage of Zebrafish embryo experiment was conducted under Western University of Health Sciences (WUHS) protocol IACUC/026.

REFERENCES

Akhtar, J., and Shukla, D. (2009). Viral entry mechanisms: cellular and viral mediators of herpes simplex virus entry. *FEBS J.* 276, 7228–7236. doi: 10.1111/j.1742-4658.2009.07402.x

Allen, S. J., Mott, K. R., and Ghiasi, H. (2014). Overexpression of herpes simplex virus glycoprotein K (gK) alters expression of HSV receptors in ocularly-infected mice. *Invest. Ophthalmol. Vis. Sci.* 55, 2442–2451. doi: 10.1167/iovs.14-14013

Antoine, T. E., Jones, K. S., Dale, M. R., Shukla, D., and Tiwari, V. (2014). Zebrafish: modeling for herpes simplex virus infections. *Zebrafish* 11, 17–25. doi: 10.1089/zeb.2013.0920

Arii, J., Goto, H., Suenaga, T., Oyama, M., Kozuka-Hata, H., Imai, T., et al. (2010). Non-muscle myosin IIA is a functional entry receptor for herpes simplex virus-1. *Nature* 467, 859–864. doi: 10.1038/nature09420

Bichko, V., Netter, H. J., and Taylor, J. (1994). Introduction of hepatitis delta virus into animal cell lines via cationic liposomes. *J. Virol.* 68, 5247–5252.

Burgos, J. S., Ripoll-Gomez, J., Alfaro, J. M., Sastre, I., and Valdivieso, F. (2008). Zebrafish as a new model for herpes simplex virus type 1 infection. *Zebrafish* 5, 323–333. doi: 10.1089/zeb.2008.0552

Choudhary, S., Burnham, L., Thompson, J. M., Shukla, D., and Tiwari, V. (2013). Role of filopodia in HSV-1 entry into zebrafish 3-O-sulfotransferase-3-expressing cells. *Open Virol. J.* 7, 41–48. doi: 10.2174/18743579013070010041

Clement, C., Tiwari, V., Scanlan, P. M., Valyi-Nagy, T., Yue, B. Y., and Shukla, D. A. (2006). novel role for phagocytosis-like uptake in herpes simplex virus entry. *J. Cell Biol.* 174, 1009–1021. doi: 10.1083/jcb.200509155

Cui, S., Wang, B., Zhao, Y., Chen, H., Ding, H., Zhi, D., et al. (2012). The mechanism of lipofectamine 2000 mediated transmembrane gene delivery. *Engineering* 5, 172–175. doi: 10.4236/eng.2012.410B045

Desai, P., and Person, S. (1998). Incorporation of the green fluorescent protein into the herpes simplex virus type 1 capsid. *J. Virol.* 72, 7563–7568.

Dollery, S. J., Delboy, M. G., and Nicola, A. V. (2010). Low pH-induced conformational change in herpes simplex virus glycoprotein B. *J. Virol.* 84, 3759–3766. doi: 10.1128/JVI.02573-09

Ferro, V. (2013). Heparan sulfate inhibitors and their therapeutic implications in inflammatory illnesses. *Expert Opin. Ther. Targets.* 17, 965–975. doi: 10.1517/14728222.2013.811491

Geisow, M. J., and Evans, W. H. (1984). pH in the endosome. Measurements during pinocytosis and receptor-mediated endocytosis. *Exp. Cell Res.* 150, 36–46. doi: 10.1016/0014-4827(84)90699-2

Geraghty, R. J., Krummenacher, C., Cohen, G. H., Eisenberg, R. J., and Spear, P. G. (1998). Entry of alphaherpesviruses mediated by poliovirus receptor-related protein 1 and poliovirus receptor. *Science* 280, 1618–1620. doi: 10.1126/science.280.5369.1618

Heine, J. W., Honess, R. W., Cassai, E., and Roizman, B. (1974). Proteins specified by herpes simplex virus. XII. The virion polypeptides of type 1 strains. *J. Virol.* 14, 640–651.

Herold, B. C., WuDunn, D., Soltys, N., and Spear, P. G. (1991). Glycoprotein C of herpes simplex virus type 1 plays a principal role in the adsorption of virus to cells and in infectivity. *J. Virol.* 65, 1090–1098.

Innes, C. L., Smith, P. B., Langenbach, R., Tindall, K. R., and Boone, L. R. (1990). Cationic liposomes (Lipofectin) mediate retroviral infection in the absence of specific receptors. *J. Virol.* 64, 957–961.

Johnson, D. C., Wisner, T. W., and Wright, C. C. (2011). Herpes simplex virus glycoproteins gB and gD function in a redundant fashion to promote secondary envelopment. *J. Virol.* 85, 4910–4926. doi: 10.1128/JVI.00011-11

Johnson, D. C., and Baines, J. D. (2011). Herpesviruses remodel host membranes for virus egress. *Nat. Rev. Micro.* 9, 382–394. doi: 10.1038/nrmicro2559

Karasneh, G. A., and Shukla, D. (2011). Herpes simplex virus infects most cell types *in vitro*: clues to its success. *Virol. J.* 8:481. doi: 10.1186/1743-422X-8-481

Lukacs, G. L., Rotstein, O. D., and Grinstein, S. (1990). Phagosomal acidification is mediated by a vacuolar-type H(+)-ATPase in murine macrophages. *J. Biol. Chem.* 265, 21099–21107.

Lyman, M. G., and Enquist, L. W. (2009). Herpesvirus interaction with the host cytoskeleton. *J. Virol.* 83, 2058–2066. doi: 10.1128/JVI.01718-08

Montgomery, R. I., Warner, M. S., Lum, B. J., and Spear, P. G. (1996). Herpes simplex virus-1 entry into cells mediated by a novel member of the TNF/NGF receptor family. *Cell* 87, 427–436. doi: 10.1016/S0092-8674(00)81363-X

Nahmias, A. J., and Roizman, B. (1973). Infection with herpes-simplex viruses 1 and 2. II. *N. Engl. J. Med.* 289, 719–725. doi: 10.1056/NEJM197310042891404

Nicola, A. V., McEvoy, A. M., and Straus, S. E. (2003). Roles for endocytosis and low pH in herpes simplex virus entry into HeLa and Chinese hamster ovary cells. *J. Virol.* 77, 5324–5332. doi: 10.1128/JVI.77.9.5324-5332.2003

Oh, M. J., Akhtar, J., Desai, P., and Shukla, D. A. (2010). Role for heparan sulfate in viral surfing. *Biochem. Biophys. Res. Commun.* 391, 176–181. doi: 10.1016/j.bbrc.2009.11.027

Pertel, P. E., Fridberg, A., Parish, M. L., and Spear, P. G. (2001). Cell fusion induced by herpes simplex virus glycoproteins gB, gD, and gH-gL requires a gD receptor but not necessarily heparan sulfate. *Virology* 279, 313–324. doi: 10.1006/viro.2000.0713

Salameh, S., Sheth, U., and Shukla, D. (2012). Early events in herpes simplex virus lifecycle with implications for an infection of lifetime. *Open Virol. J.* 6, 1–6. doi: 10.2174/1874357901206010001

Shieh, M. T., WuDunn, D., Montgomery, R. I., Esko, J. D., and Spear, P. G. (1992). Cell surface receptors for herpes simplex virus are heparan sulfate proteoglycans. *J. Cell Biol.* 116, 1273–1281. doi: 10.1083/jcb.116.5.1273

Shukla, D., Liu, J., Blaiklock, P., Shworak, N. W., Bai, X., Esko, J. D., et al. (1999). A novel role for 3-O-sulfated heparan sulfate in herpes simplex virus 1 entry. *Cell* 99, 13–22. doi: 10.1016/S0092-8674(00)80058-6

Shukla, D., and Spear, P. G. (2001). Herpesviruses and heparan sulfate: an intimate relationship in aid of viral entry. *J. Clin. Invest.* 108, 503–510. doi: 10.1172/JCI200113799

Spear, P. G., and Longnecker, R. (2003). Herpesvirus entry: an update. *Virol* 77, 10179–10185. doi: 10.1128/JVI.77.19.10179-10185.2003

Tiwari, V., Clement, C., Xu, D., Valyi-Nagy, T., Yue, B. Y., Liu, J., et al. (2006). Role for 3-O-sulfated heparan sulfate as the receptor for herpes simplex virus type

1 entry into primary human corneal fibroblasts. *J. Virol.* 80, 8970–8980. doi: 10.1128/JVI.00296-06

Weinheimer, S. P., Boyd, B. A., Durham, S. K., Resnick, J. L., and O'Boyle, D. R. (1992). Deletion of the VP16 open reading frame of herpes simplex virus type 1. *J. Virol.* 66, 258–269.

Whitley, R. J., Kimberlin, D. W., and Roizman, B. (1998). Herpes simplex viruses. *Clin. Infect. Dis.* 26, 541–553. doi: 10.1086/514600

Whitley, R. J., and Roizman, B. (2001). Herpes simplex virus infections. *Lancet* 357, 1513–1518. doi: 10.1016/S0140-6736(00)04638-9

WuDunn, D., and Spear, P. G. (1989). Initial interaction of herpes simplex virus with cells is binding to heparan sulfate. *J. Virol.* 63, 52–58.

Conflict of Interest Statement: The authors declare that the research was conducted in the absence of any commercial or financial relationships that could be construed as a potential conflict of interest.

Copyright © 2016 Burnham, Jaishankar, Thompson, Jones, Shukla and Tiwari. This is an open-access article distributed under the terms of the Creative Commons Attribution License (CC BY). The use, distribution or reproduction in other forums is permitted, provided the original author(s) or licensor are credited and that the original publication in this journal is cited, in accordance with accepted academic practice. No use, distribution or reproduction is permitted which does not comply with these terms.

frontiers in Microbiology

ORIGINAL RESEARCH
published: 13 June 2016
doi: 10.3389/fmicb.2016.00883

H11/HSPB8 Restricts HIV-2 Vpx to Restore the Anti-Viral Activity of SAMHD1

*Ayumi Kudoh[1], Kei Miyakawa[1], Satoko Matsunaga[1], Yuki Matsushima[2], Isao Kosugi[3], Hirokazu Kimura[4], Satoshi Hayakawa[5], Tatsuya Sawasaki[6] and Akihide Ryo[1]**

[1] Department of Microbiology, School of Medicine, Yokohama City University, Yokohama, Japan, [2] Kawasaki City Health and Safety Research Center, Kanagawa, Japan, [3] Department of Regenerative and Infectious Pathology, Hamamatsu University School of Medicine, Hamamatsu, Japan, [4] Infectious Disease Surveillance Center, National Institute of Infectious Diseases, Tokyo, Japan, [5] Division of Microbiology, Department of Pathology and Microbiology, Nihon University School of Medicine, Tokyo, Japan, [6] Proteo-Science Center, Ehime University, Matsuyama, Japan

OPEN ACCESS

Edited by:
Francois Villinger, University of Louisiana at Lafayette, USA

Reviewed by:
Mikako Fujita, Kumamoto University, Japan
Nadine Laguette, Centre National de la Recherche Scientifique, France

***Correspondence:**
Akihide Ryo
aryo@yokohama-cu.ac.jp

Specialty section:
This article was submitted to Virology, a section of the journal Frontiers in Microbiology

Received: *11 March 2016*
Accepted: *25 May 2016*
Published: *13 June 2016*

Citation:
Kudoh A, Miyakawa K, Matsunaga S, Matsushima Y, Kosugi I, Kimura H, Hayakawa S, Sawasaki T and Ryo A (2016) H11/HSPB8 Restricts HIV-2 Vpx to Restore the Anti-Viral Activity of SAMHD1. Front. Microbiol. 7:883. doi: 10.3389/fmicb.2016.00883

Virus–host interactions play vital roles in viral replication and virus-induced pathogenesis. Viruses rely entirely upon host cells to reproduce progeny viruses; however, host factors positively or negatively regulate virus replication by interacting with viral proteins. The elucidation of virus–host protein interaction not only provides a better understanding of the molecular mechanisms by which host cells combat viral infections, but also facilitates the development of new anti-viral therapeutics. Identification of relevant host factors requires techniques that enable comprehensive characterization of virus–host protein interactions. In this study, we developed a proteomic approach to systematically identify human protein kinases that interact potently with viral proteins. For this purpose, we synthesized 412 full-length human protein kinases using the wheat germ cell-free protein synthesis system, and screened them for their association with a virus protein using the amplified luminescent proximity homogenous assay (AlphaScreen). Using this system, we attempted to discover a robust anti-viral host restriction mechanism targeting virus protein X (Vpx) of HIV-2. The screen identified H11/HSPB8 as a Vpx-binding protein that negatively regulates the stability and function of Vpx. Indeed, overexpression of H11/HSPB8 promoted the degradation of Vpx via the ubiquitin–proteasome pathway and inhibited its interaction with SAMHD1, a host restriction factor responsible for blocking replication of HIV. Conversely, targeted knockdown of H11/HSPB8 in human trophoblast cells, which ordinarily express high levels of this protein, restored the expression and function of Vpx, making the cells highly susceptible to viral replication. These results demonstrate that our proteomic approach represents a powerful tool for revealing virus–host interaction not yet identified by conventional methods. Furthermore, we showed that H11/HSPB8 could be a potential host regulatory factor that may prevent placental infection of HIV-2 during pregnancy.

Keywords: virus–host interaction, wheat germ cell-free protein synthesis, AlphaScreen, Vpx, H11, HIV-2

INTRODUCTION

To replicate and propagate, viruses utilize sophisticated mechanisms to hijack the machinery and materials of their host cells. In a virally infected cell, host proteins play crucial roles in multiple biological processes that promote viral replication by providing molecular architecture or functional assistance. To this end, viral proteins need to interact directly or indirectly with host cell proteins that are relevant to the viral life cycle. On the other hand, some host proteins operate as anti-viral factors to counteract or restrict viral replication within infected cells. In turn, certain viral proteins counteract these anti-viral proteins, resulting in sustained viral propagation. Therefore, a comprehensive understanding of dynamic host–virus protein interaction would greatly improve our understanding of the viral life cycle and pathogenesis.

Recent technological advances in high-throughput and quantitative proteomics have enabled us to comprehensively analyze biologically relevant protein–protein interactions. In particular, the development of cell-free protein synthesis (CFPS) systems has enabled high-yield production of active and functional proteins that can be used for biological analysis (Sawasaki et al., 2002; Endo and Sawasaki, 2006; Zawada et al., 2011). Moreover, advances in label-free protein detection techniques enable reliable, high-throughput analysis of protein–protein interactions (Sawasaki et al., 2007). Protein–protein interactions can be also predicted by approaches that combine bioinformatics and structural biology (Roy et al., 2010; Roche et al., 2015). Together, these techniques have contributed to the establishment of comprehensive protein interaction networks, which facilitate understanding of biological mechanisms, both in cells and in the context of viral infection.

Recombinant protein production and purification are essential steps for biochemical and functional characterization of virus and host proteins. In general, however, viral protein expression is limited due to the toxicity and insolubility of viral proteins in living cells (Harbers, 2014; Gagoski et al., 2016). Compared with conventional cell-mediated protein expression methods, the wheat germ CFPS system is more likely to produce properly folded, soluble, and functional virus-encoded proteins. Previous reports showed that the wheat germ system has several advantages over protein expression in other CFPS system such as *E. coli* or HeLa cells, including improved protein solubility and expression of toxic proteins such as viral antigens (Gagoski et al., 2016). Thus, the wheat germ CFPS system represents a rapid and high-throughput methodology for translation of genetic information into protein-mediated biochemical activities for use in virological research (Sawasaki et al., 2007).

Methods for detecting protein–protein interactions can be categorized into several types: most broadly, *in vitro*, *in vivo*, and *in silico* methods. Among *in vitro* methods, the AlphaScreen (derived from "Amplified Luminescent Proximity Homogeneous Assay") technology offers a rapid and simple means for quantifying target protein–protein interactions using a non-radioactive bead-based detection method. Upon excitation at 680 nm, the donor beads, which contain the photosensitizer phthalocyanin, convert molecular oxygen to excited singlet oxygen with a 4 μs half-life. The singlet oxygen can diffuse up to 200 nm to make contact with a thioxene derivative on the AlphaScreen acceptor beads, resulting in amplified chemiluminescent emission between 520 and 620 nm. One donor bead can generate 60,000 singlet oxygens, resulting in exceptionally high signal amplification and permitting adaptation of the AlphaScreen assay to multi-well plate formats (Taouji et al., 2009). Thus, the AlphaScreen technology is suitable for high-throughput analysis of protein–protein interactions.

Viral proteins are controlled by post-translational modifications such as phosphorylation during infection (Nandi and Banerjee, 1995; Rajendra Kumar et al., 2005; Hemonnot et al., 2006; Kudoh et al., 2014). Phosphorylation acts as a molecular switch of target protein, thereby modulating their functions. We previously showed that HIV-1 Gag was regulated by the aPKC-mediated phosphorylation by using a human protein kinase library (Kudoh et al., 2014). Identification of human protein kinases that interact with viral protein could be effective approach to reveal a novel viral–host interaction. HIV-2 encodes an accessory protein Vpx that degrades SAMHD1, a host restriction factor. Although previous reports suggested that HIV-2 Vpx is phosphorylated during infection (Nandi and Banerjee, 1995; Rajendra Kumar et al., 2005), it still remains uncertain if Vpx phosphorylation indeed affects to functions of Vpx toward SAMHD1 degradation. Thus, we decided to investigate molecular interaction between human protein kinases with HIV-2 Vpx protein.

In this study, we performed a high-throughput screen of interactions between viral and host proteins using the wheat germ CFPS system and AlphaScreen. As an illustrative example, we analyzed the functional interaction between HIV-2 Vpx and host protein kinases in order to elucidate the function of Vpx protein. Furthermore, we describe the results of a pilot study designed to test the experimental feasibility of our *in vitro* assay system, and discuss the optimal strategy for characterizing virus–host interactions.

MATERIALS AND METHODS

Viral DNA Constructs and Plasmids

HIV-2 reporter virus vectors pGL-ANΔ*Env*-Luc and pGL-StΔ*Env*Δ*Vpx*-Luc were kindly provided by Dr. Akio Adachi (Tokushima University, Tokushima, Japan). Plasmids expressing FLAG-tagged Vpx were kindly provided by Dr. Akio Adachi (Tokushima University, Tokushima, Japan; Khamsri et al., 2006). Vpx deletion mutants and H11 substitution mutants were generated by PCR-based molecular cloning procedures using PrimeSTAR Max (Takara Bio Inc, Shiga, Japan).

Antibodies

Anti-FLAG (M2), anti-SAMHD1, and anti-vinculin mouse monoclonal antibodies were obtained from Sigma (St. Louis, MO, USA). Anti-HA (3F10) rat monoclonal antibody was obtained

from Roche (Mannheim, Germany). Anti-Hsp22 (H11) rabbit polyclonal antibody was from Abcam (Tokyo, Japan).

Cells and Viruses

HEK293 and HEK293T cells were cultured in DMEM (Gibco-BRL, Rockville, MD, USA) supplemented with 10% (V/V) fetal bovine serum (FBS; Gibco-BRL). Human villous trophoblasts (HVT; ScienCell Research Laboratories, USA, HVT were isolated from human placental villi and cryopreserved at passage primary culture). Pavlov et al. (2003) were cultured in Trophoblast Medium (ScienCell Research Laboratories, Carlsbad, CA, USA). THP-1 cells were cultured in RPMI containing 10% FBS. THP-1 cells were differentiated overnight with 50 ng/ml of phorbol 12-myristate 13-acetate (PMA; Sigma–Aldrich). Vesicular stomatitis virus G glycoprotein (VSV-G)-pseudotyped viruses were produced in HEK293T cells co-transfected with reporter virus and VSV-G plasmids using the calcium-phosphate method. Culture supernatants were collected, and HIV-2 particle yields were quantitated by p27 antigen capture enzyme-linked immunosorbent assay (ELISA; ZeptoMetrix, Buffalo, NY, USA).

In vitro Protein Production

A total of 412 cDNAs encoding human protein kinases were generated as described previously (Tadokoro et al., 2010). The protein production method was also described previously (Sawasaki et al., 2002, 2007; Takai et al., 2010). Briefly, DNA templates containing a biotin-ligating sequence (bls) were amplified by split-PCR using cDNAs and corresponding primers, and then used in a GenDecoder protein production system (Cell Free Science, Ehime, Japan). For synthesis of HIV-2 Vpx protein, Vpx genes derived from the pGL-AN proviral plasmid were generated by split-PCR and used as templates in the Wheat Germ Expression kit (Cell Free Science).

AlphaScreen-Based Protein–Protein Interaction Assays

AlphaScreen assays were performed as described previously (Tadokoro et al., 2010). All recombinant proteins were synthesized using the wheat germ CFPS system, as described above. For each protein kinase, 1 μl of crude recombinant biotinylated construct from the human kinase library was incubated with 1 μl of crude FLAG-Vpx or FLAG-DHFR in 10 μl of kinase assay buffer (100 mM Tris-HCl [pH 8.0], 10 mM MgCl2, 0.1% Tween-20, 0.1% BSA) at 37°C for 1 h in one well of a 384-well OptiPlate (PerkinElmer, Foster City, CA, USA). Using the AlphaScreen IgG (protein A) detection kit (PerkinElmer), 15 μl of detection mixture containing 100 mM Tris-HCl [pH 8.0], 0.01% Tween-20, 1 mg/ml BSA, 5 μg/ml anti-FLAG antibody (GE Healthcare, Buckinghamshire, UK), 5 ng streptavidin-coated donor beads, and 5 ng anti-IgG (protein A) acceptor beads were added to each well, followed by incubation at 26°C for 1 h. AlphaScreen signals were detected on an EnVision device (PerkinElmer) using the AlphaScreen signal detection program.

In vitro Kinase Assays

Biotinylated-DHFR, H11, SAMHD1, and FLAG-Vpx proteins were synthesized in the wheat germ CFPS system, as described above. The synthesized proteins were purified using streptavidin-conjugated magnet beads (Promega, Madison, WI, USA) or Flag M2 beads (Sigma–Aldrich). Purified FLAG-Vpx proteins were then incubated with each biotinylated protein in a 50 μl reaction mixture containing 20 mM Tris-HCl (pH 7.5), 1 mM EDTA, 1 mM dithiothreitol, 150 mM NaCl, 5 mM $MgCl_2$, 0.05% Tween-20, 100 μM ATP, and 2 μCi [γ-32P]ATP. The reaction mixture was incubated for 1 h at 37°C, and the products were subjected to electrophoresis on 10% SDS polyacrylamide gels and detected on a BAS2500 scanner (Fujifilm, Tokyo, Japan).

Western Blotting

Cells were harvested at the indicated time points, washed with phosphate-buffer saline (PBS), and treated with lysis buffer (0.02% sodium dodecyl sulfate [SDS], 0.5% Triton X-100, 300 mM NaCl, 20 mM Tris-HCl [pH 7.6], 1 mM EDTA, 1 mM dithiothreitol) for 20 min on ice. Multiple protease inhibitors, 200 μM sodium vanadate, and 20 mM sodium fluoride were then added to the buffer. The samples were centrifuged at 18,000 *g* for 10 min at 4°C, and the clarified cell extracts were assayed for protein concentration using DC™ protein assay kit (Bio-Rad, Hercules, CA, USA). Equal amounts of proteins (20–50 μg) were resolved by SDS-PAGE on 10% gels (acrylamide, 29.2; bisacrylamide, 0.8) in running buffer (250 mM glycine, 25 mM Tris, 0.1% SDS). The separated proteins were transferred to polyvinylidene difluoride membrane. The membranes were washed with blotting buffer (TBS containing 0.1%-Tween 20), and then blocked for 1 h at room temperature in 10% non-fat powdered milk in blotting buffer. Primary antibodies were added at appropriate dilutions in 3% bovine serum albumin in blotting buffer and rocked overnight at 4°C. The membranes were then washed in blotting buffer and incubated for 1 h at room temperature with a horseradish peroxidase–conjugated secondary antibody. Target proteins were detected using an enhanced chemiluminescence detection system (GE Healthcare). Images were processed with FluorChem FC2 (Alpha Innotech Corp. Tokyo, Japan), acquired using a cooled charge-coupled device (CCD) camera, and assembled using Adobe Photoshop CS5 Extended.

Immunoprecipitation

HEK293 cells were co-transfected with HA-H11 and FLAG-Vpx, and treated with 20 μM of MG132 for 4 h before harvest. Harvested cells were lysed in lysis buffer (50 mM Tris-HCl [pH 8.0], 150 mM NaCl, 1 mM EDTA, 1 mM DTT) containing complete protease inhibitor cocktail (Roche Molecular Biochemicals, Indianapolis, IN, USA) and PhosSTOP phosphatase inhibitor cocktail (Roche Molecular Biochemicals). Lysates were cleared by centrifugation at 12,000 × *g* for 15 min, followed by pull-down with anti-FLAG M2 affinity Gel (Sigma) or anti-HA affinity Gel (Sigma). Samples were separated by SDS-PAGE and analyzed by Western blotting.

Phosphatase Treatment

HEK293 cells were co-transfected with plasmids encoding HA-H11 and harvested at 24 h after transfection. Harvested cells were suspended with lysis buffer (0.02% sodium dodecyl sulfate [SDS], 0.5% Triton X-100, 300 mM NaCl, 20 mM Tris-HCl [pH 7.6], 1 mM EDTA, 1 mM dithiothreitol and Complete [Roche, Basel, Switzerland]) for 20 min on ice. The lysate was then incubated in reaction buffer and calf intestinal alkaline phosphatase (CIAP; Takara Bio Inc., Shiga, Japan) for 2 h at 37°C. The reaction was stopped by the addition of 2 x sample buffer.

Single-Cycle Virus Release Assays

For HA-H11 overexpression assays, PMA differentiated THP-1 cells were transfected with HA-H11 plasmids with Lipofectamin 3000 (Thermo Fisher Scientific, Waltham, MA USA), and 24 h after transfection cells were infected with VSV-G-pseudotyped HIV-2 at a multiplicity of infection (MOI) of 2, and cultured for 2 days. For small interfering RNA (siRNA) targeting *H11* transfected assays, HVT cells were transfected with H11 specific siRNA, GGAGUUGAUGGUGAAGACCAAAGAU, purchased from invivogen (invivogen, San Diego, CA, USA) with using RNAiMAX (Thermo Fisher Scientific, Waltham, MA, USA), and 24 h after transfection cells were infected with VSV-G-pseudotyped HIV-2 at a MOI of 2, and cultured for 2 days. Cell lysates were prepared using HBST buffer (10 mM HEPES [pH 7.4] 150 mM NaCl, 0.5% Triton X-100) containing protease inhibitor cocktail (Roche, Basel, Switzerland).

Tissue Collection

A fallopian tube resected from a patient with ectopic tubal pregnancy was retrieved from the archives of Seirei Hamamatsu General Hospital, Shizuoka, Japan.

Immunohistochemistry

Unstained sections were deparaffinized and rehydrated prior to antigen retrieval. Antigen retrieval was performed in 10 mmol/L citrate buffer (pH 6.0) in a microwave oven. Sections were incubated with anti-Hsp22 antibody for 30 min at room temperature. After washing in PBS, the sections were incubated with peroxidase-conjugated universal immune-enzyme polymer, anti-rabbit solution (Histofine Simple Stain MAX PO-R Nichirei Biosciences, Tokyo, Japan), and then visualized with 3,3-diaminobenzidine (Sigma–Aldrich) and counterstained with hematoxylin.

Ethical Statement

Ethical approval was obtained from the Ethical Committee of Seirei Hamamatsu General Hospital, Shizuoka, Japan (September 22, 2010, #917). A patient provided written informed consent for the collection of samples and subsequent analysis.

Statistical Analysis

Statistical analysis was performed using the Excel Tokei software series (Esumi, Tokyo, Japan). Data are presented as means ± SD. One-way analysis of variance (ANOVA) and Student's *t*-test were used for comparisons of continuous variables. $P < 0.05$ was considered significantly different.

RESULTS

Design and Development of a High-Throughput Protein–Protein Interaction Screen

To build a system for high-throughput protein–protein interaction screening, we utilized a wheat germ CFPS system to synthesize a set of proteins from a host cDNA library (**Figure 1A**). Linear DNAs used as translation templates for CFPS were PCR amplified from a plasmid library of human protein kinase cDNAs. In this step, the template DNAs were fused at the 5′ end to a specific sequence from the SP6 promoter, the E02 enhancer region, and a bls by split-primer PCR using appropriate primers (Sawasaki et al., 2008; Matsuoka et al., 2010). The templates were then transcribed by SP6 RNA polymerase, and the resultant mRNAs were translated in wheat germ extracts. The biotin ligation method yields a biotin label on the bls, allowing specific recognition of the target protein by Amplified Luminescent Proximity Homogenous Assay (AlphaScreen).

Identification of Host Protein Kinases that Interact with HIV-2 Vpx

Protein kinases are enzymes that modify substrate proteins by chemical addition of phosphate groups. Phosphorylation usually results in structural and functional changes in the target protein. Therefore, we investigated functional modification of virus protein by host protein kinases. As an illustration, we sought to identify host protein kinases that functionally associate with the HIV-2 accessary protein Vpx. To this end, we quantitatively monitored protein–protein interactions using AlphaScreen (**Figure 1B**). The binding efficiency of HIV-2 Vpx with each kinase was normalized relative to the luminescent activity of DHFR protein, used as a negative control (**Figure 1C**). When a relative light unit per cutoff (RLU/Co) ratio of $\geq$2.25 was used as the threshold, we found 15 host kinases that could selectively interact with HIV-2 Vpx. Among them, the luminescence signal of H11 (also known as HSPB8) was significantly higher than that of other kinases. Our assay detected Fyn and Erk2 as Vpx interactor (S/N = 2.85 and 1.36, respectively), both of which have been already reported to phosphorylate Vpx (Rajendra Kumar et al., 2005; Singhal et al., 2006). Therefore, we focused on functional analysis of H11 as a previously uncharacterized Vpx-interacting factor.

To confirm the Vpx–H11 interaction, we performed pull-down assays. For this purpose, biotin-labeled H11, DHFR (negative control), SAMHD1 (positive control), and FLAG-tagged Vpx proteins were synthesized individually by wheat germ CFPS. Each biotin-labeled protein was mixed with FLAG-Vpx, and then immunoprecipitated with sepharose

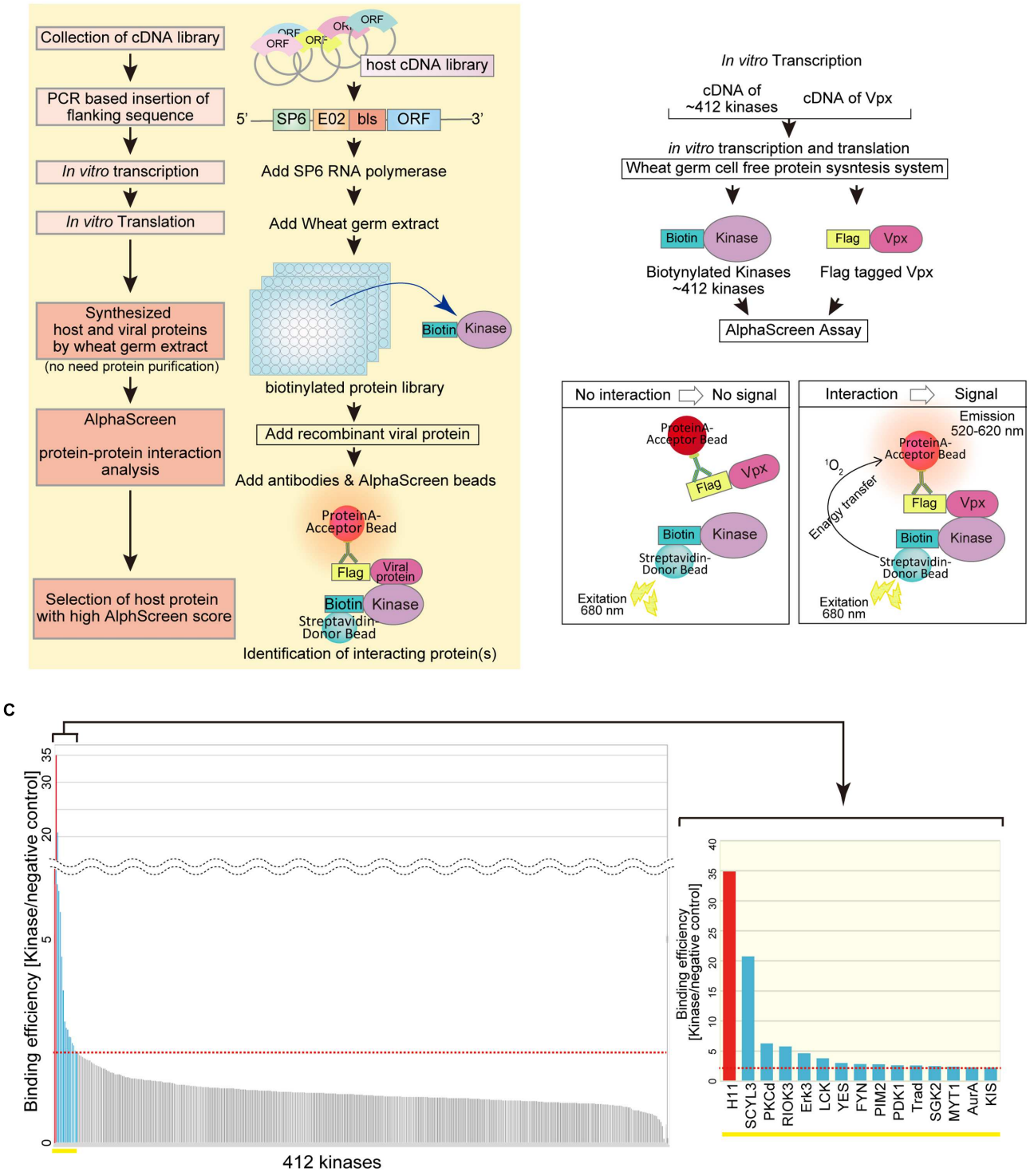

FIGURE 1 | AlphaScreen-based screening of virus–host proteins interactions. (A) Schematic representation of the overall screening procedure. **(B)** Schematic representation of the AlphaScreen-based luminescent system used to screen for human protein kinases that interact with HIV-2 Vpx. All recombinant proteins were produced in the wheat germ CFPS system. Briefly, recombinant FLAG-tagged HIV-2 Vpx or dihydrofolate reductase (DHFR) was incubated with each protein kinase. Protein A–conjugated acceptor beads with anti-FLAG antibody and streptavidin-coated donor beads were added and bound to the tagged substrate. Upon laser excitation, the donor beads convert ambient oxygen to singlet oxygen. When a molecular interaction occurs between HIV-2 Vpx and a particular kinase, singlet oxygen transfers to the acceptor beads, activating emission of light at 520–620 nm. **(C)** HIV-2 Vpx–interacting kinases identified from a human protein kinase library by AlphaScreen. The binding efficiency of HIV-2 Vpx with each kinase was normalized relative to the luminescence of control DHFR.

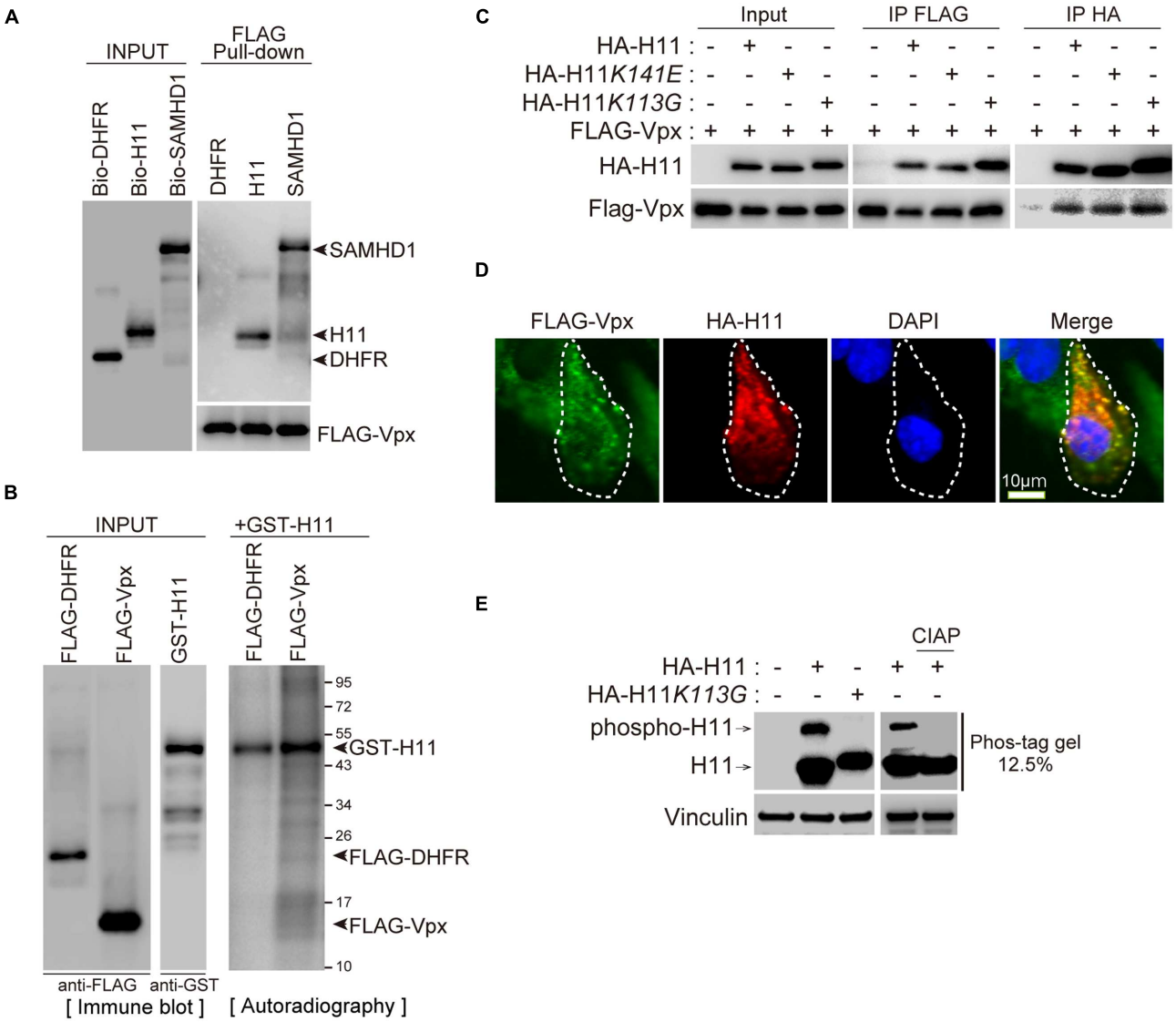

FIGURE 2 | H11 interacts with HIV-2 Vpx. (A) Direct interaction between H11 and HIV-2 Vpx revealed by FLAG pull-down assays. Biotinylated H11, SAMHD1, DHFR, and FLAG-tagged HIV-2 Vpx were produced in the wheat germ CFPS system and affinity-purified. Both input and pull-down samples were subjected to western blotting with HRP-streptavidin and anti-FLAG antibody. **(B)** Immunoprecipitation of HIV-2 Vpx with H11. HEK293T cells were co-transfected with HA-tagged H11, H11*K141E*, or H11*K113G* and FLAG-tagged HIV-2 Vpx in the presence of MG132, and cell lysates were immunoprecipitated with anti-FLAG or anti-HA antibody 24 h later. Input and immunoprecipitation samples were then probed with anti-HA and anti-FLAG antibodies. **(C)** Confocal microscopy analysis of HA-tagged H11 and FLAG-tagged HIV-2 Vpx in HEK293T cells. Scale bar, 10 μm. **(D)** *In vitro* phosphorylation assay of H11. FLAG-tagged DHFR, Vpx, and GST-tagged H11 were produced in the wheat germ CFPS system and affinity-purified. H11-mediated phosphorylation was assessed by incubating recombinant FLAG-DHFR or FLAG-Vpx with recombinant active GST-H11 in the presence of [γ-^{32}P] ATP. The reaction products were analyzed by autoradiography. Left panel shows a western blot of the input recombinant proteins. **(E)** H11 proteins mobility shifts in Phos-tag Gel. HEK293 cells were transfected with plasmids encoding HA-H11 or HA-H11*K113G* (100 ng). Right panel shows separation of HA-H11 with or without CIAP, phosphatase, treatment by Phos-tag affinity approach. The transfected cells were harvested at 24 h post-transfection, and then treated with CIAP. Equal amounts of cell lysates were subjected to a 50 μM phos-tag containing gel or a normal SDS-PAGE and then analyzed by Western blot analysis with HA or Vinculin antibodies. The arrow indicate the position of wild type H11. Phospho-H11 indicates phosphorylated form of H11.

beads conjugated to anti-FLAG antibody (FLAG-beads). H11 was co-precipitated with FLAG-Vpx protein (**Figure 2A**). As reported previously (Hrecka et al., 2011; Laguette et al., 2011), SAMHD1 protein associated with FLAG-Vpx protein (**Figure 2A**). To further validate the interaction, we performed cell-based immunoprecipitation analysis using site-directed H11 mutants, a chaperon-like activity–deficient mutant K141E (Irobi et al., 2004; Shemetov et al., 2008; Shemetov and Gusev, 2011) and a kinase-activity–deficient mutant K113G (Smith et al., 2000). FLAG-Vpx was co-transfected with either HA-

tagged wild type H11 or mutants in HEK293T, and cell lysates were immunoprecipitated using anti-FLAG or anti-HA affinity beads. The wild type and mutant forms of H11 were co-immunoprecipitated with Vpx, and Vpx protein was also co-precipitated with all three forms of H11 (**Figure 2B**), indicating that H11 interacts with HIV-2 Vpx *in vitro* and in cells, irrespective of its kinase or chaperon activity. Moreover, we found that HA- H11 was co-localized with FLAG-Vpx protein in the cytoplasm (**Figure 2C**).

We next investigated whether H11 could directly phosphorylate Vpx protein *in vitro*. Recombinant FLAG-DHFR or FLAG-Vpx proteins were synthesized and purified from wheat germ extract with FLAG beads and used as substrates for *in vitro* kinase assays. H11 did not phosphorylate Vpx, as was also the case for the negative control DHFR, although prominent auto-phosphorylation of H11 was observed (**Figure 2D**). We next analyzed the kinase activity of wild type and H11*K113G*, kinase activity deficient mutant, using Phos-tag affinity approach and western blot (Kinoshita et al., 2006). The phosphorylation of wild type H11 was detected as a distinct band shift. This was not a case with H11*K113G* mutants. The pre-treatment of cell lysates with calf intestine alkaline phosphatase (CIAP) resulted in the loss of band shift, indicating that shifted band represented phosphorylated H11 (**Figure 2E**).

Next, we attempted to identify the binding domain of Vpx with H11. To this end, we used the full-length form of Vpx (residues 1–112) and three deletion mutants (Vpx 1–90, 23–90, and 40–112) (**Figure 3A**). As shown in **Figure 3A**, full-length Vpx, C-terminally deleted Vpx (Vpx 1–90), and N-terminally deleted Vpx (Vpx 40–112) could precipitate with HA-H11 protein, but Vpx lacking both the N-terminal and C-terminal regions (Vpx 23–90) could not. These results demonstrated that either the N-terminus or C-terminus of Vpx is sufficient for the physical association with H11.

To better understand the functional relevance of the Vpx–H11 interaction, we investigated whether H11 could affect Vpx protein expression. Overexpression of HA-H11 repressed the expression of full-length Vpx but not the truncated mutant Vpx 23–90 (**Figure 3B**). Vpx can degrade SAMHD1 in a proteasome-dependent manner (Hrecka et al., 2011; Laguette et al., 2011). Consistent with this, the level of endogenous SAMHD1 decreased upon expression of wild-type (WT) FLAG-Vpx. The reduction in Vpx level resulting from HA-H11 overexpression restored endogenous SAMHD1 expression.

Previous reports showed that N-terminal regions of Vpx includes responsible domain for the interaction with SAMHD1 (Schwefel et al., 2014), and our results above indicate that H11 binds both the N- and C- termini of Vpx. Based on the crystal structure of the Vpx–SAMHD1 complex (Schwefel et al., 2014), the N-terminal SAMHD1-binding region within Vpx may overlap with the H11-binding region (**Figure 3C**), so that H11 may interfere with the SAMHD1-Vpx interaction. To test this hypothesis, we performed *in vitro* binding assays for the Vpx-SAMHD1 interaction in the presence of various amounts of H11. The results revealed that H11 inhibited the interaction between SAMHD1 and Vpx (**Figure 3D**). Collectively, our results suggest that H11 can not only enhance degradation of Vpx, but also directly inhibit its interaction with SAMHD1 for proteasomal degradation.

H11 Degrades Vpx in a Proteasome-Dependent Manner

Next, we asked whether H11 affects the stability of Vpx in cells. Transient transfection of FLAG-Vpx significantly decreased the level of endogenous SAMHD1 in HEK293 cells, as previously reported (**Figure 4A**, lanes 1 and 2) (Hrecka et al., 2011). Moreover, levels of FLAG-Vpx protein were reduced by co-transfection of HA-H11 protein in a dose dependent manner, resulting in restoration of SAMHD1 expression (**Figure 4A**). Overexpression of HA-H11 itself was no effect on endogenous SAMHD1 expression (**Figure 4B**). Degradation of Vpx protein by H11 was completely prevented by the proteasome inhibitor MG132 (**Figure 4C**). Next, we co-transfected HEK293 cells with FLAG-Vpx and WT H11, the kinase activity–deficient mutant K113G (Smith et al., 2000), or the chaperon-like activity–deficient mutant K141E (Shemetov and Gusev, 2011). Relative to vector control, WT H11 and the K113G mutant prominently reduced the level of Vpx, whereas the K141E mutant did not (**Figure 4D**). We then performed a cycloheximide (CHX) assay to determine the effect of H11 on the half-life of Vpx. In these experiments, HEK293 cells were co-transfected with FLAG-Vpx and HA-H11 WT or mutants, and then treated with CHX to inhibit translation. As shown in **Figure 4E**, the stability of FLAG-Vpx was significantly reduced by WT H11 and the K113G mutant, whereas expression of the K141E mutant had no effect. These results demonstrated that H11 promotes proteasome-dependent degradation of Vpx via its chaperone-like activity.

H11 Suppresses HIV-2 Infection in Monocyte-Derived Macrophages

Vpx degrades SAMHD1 in order to evade host intrinsic intracellular immunity and allow sustained HIV replication in myeloid cells (Goldstone et al., 2011; Hrecka et al., 2011; Laguette et al., 2011; Baldauf et al., 2012; Descours et al., 2012; Lahouassa et al., 2012). Therefore, we investigated whether H11-mediated Vpx degradation affects HIV-2 replication in monocyte-derived macrophages (MDMs). For this purpose, we used an HIV-2 clone harboring the luciferase gene (HIV-2-Δ*env*-LUC) and its *vpx*-deficient mutant (HIV-2Δ*env*Δ*vpx*-LUC) to produce chimeric viruses with the fusogenic envelope G glycoprotein of the VSV-G (**Figure 5A**). The infectivity of the generated viruses was tested using MDMs transfected with HA-H11 or vector alone. H11 overexpression suppressed infection of MDMs by WT HIV-2, but not Vpx-deficient HIV-2 (**Figure 5B**). SAMHD1 expression was significantly reduced in cells infected by WT HIV-2 (**Figure 5C**, lane 3), as reported in previous studies (Hrecka et al., 2011; Laguette et al., 2011). On the other hand, the level of SAMHD1 was restored in H11-transfected cells (**Figure 5C**, lane 4). These results suggested that H11 suppresses HIV-2 infection in MDMs via the up-regulation of SAMHD1-mediated virus restriction.

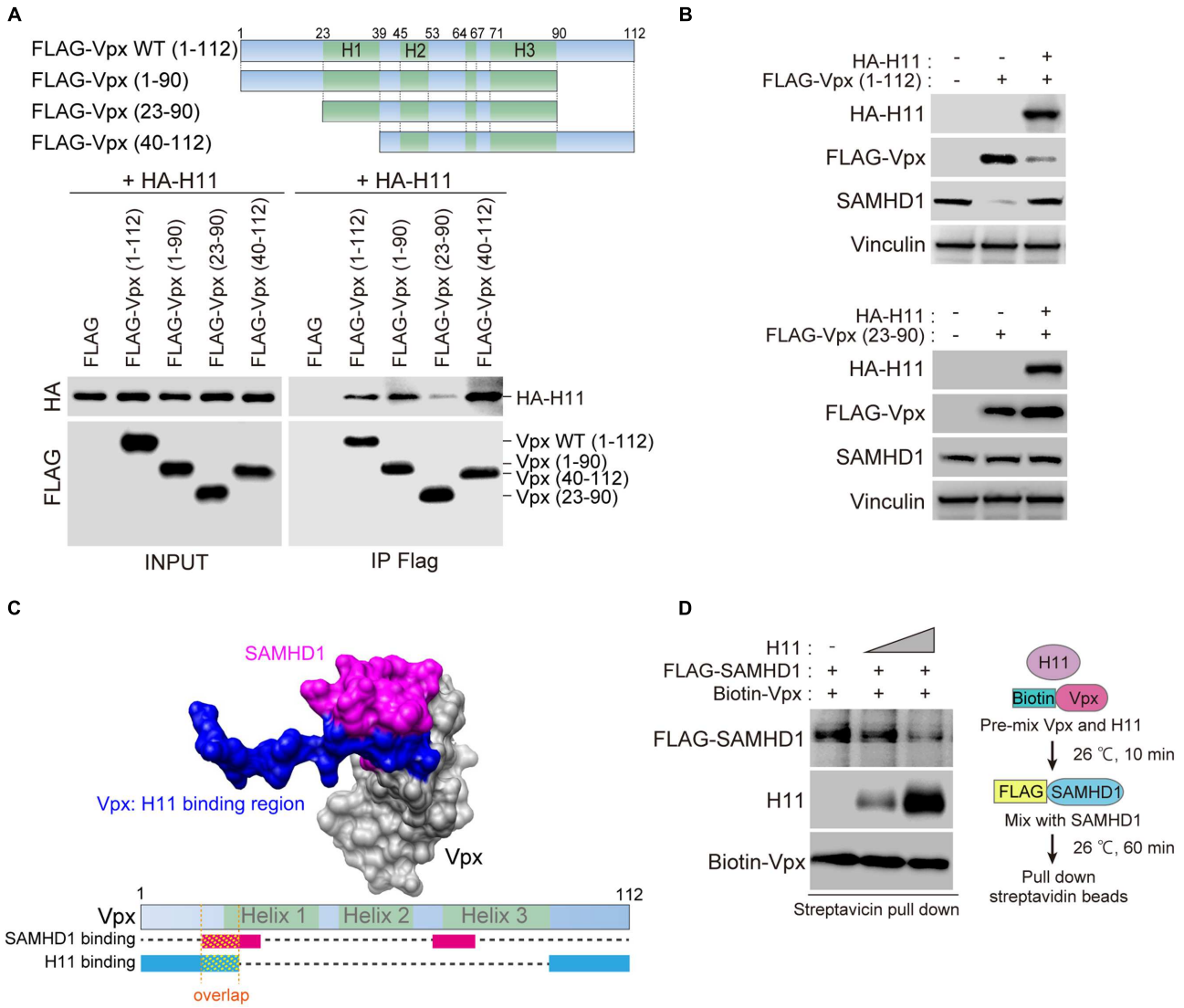

FIGURE 3 | Domains in HIV-2 Vpx that mediate physical interactions with H11. (A) Top panel shows a schematic representation of the wild-type (WT; residues 1–112) and mutant Vpx proteins utilized in the FLAG-pull-down analysis. The name of each Vpx mutant is shown on the left. WT Vpx or the indicated mutants were co-transfected with HA-tagged H11 into HEK293T cells. The transfected cells were treated with 20 μM of MG132 for 4 h before harvest, and harvested at 48 h after transfection. Cell lysates were immunoprecipitated with anti-FLAG antibody. The immunoprecipitated proteins, as well as the starting material (INPUT), were subjected to SDS-PAGE and analyzed by western blot using anti-FLAG and anti-HA antibodies. **(B)** HEK293 cells were transfected with WT (top panel) or truncated mutant (bottom panel) FLAG-Vpx and HA-H11, as indicated. Whole cell extracts were prepared, and equal amounts of proteins from each sample were separated by SDS-PAGE and subjected to western blot analysis using the indicated antibodies. **(C)** Binding structure model of SAMHD1 C-terminal domain (magenta) and Vpx (gray) illustrated by Chimera (http://www.cgl.ucsf.edu/chimera/), based on the X-ray structure (PDB code: 4CC9). The H11-binding domain (blue) was overlaid on Vpx. Bottom panel shows schematic image of Vpx protein. The SAMHD1-binding region is indicated in magenta, and the H11-binding region is indicated in blue. **(D)** Recombinant biotinylated Vpx was pre-mixed with various amounts of H11 for 10 min before the addition of FLAG-tagged SAMHD1. After 60 min, the mixture was processed for pull-down with streptavidin-coated magnetic beads, as shown on the right. Bound proteins were detected by western blot (left panel).

H11 is Highly Expressed in Syncytiotrophoblast Cells

According to the Human Protein Atlas database, *H11* mRNA is significantly highly expressed in placenta (**Figure 6A**)[1] (Uhlen et al., 2005, 2010, 2015; Berglund et al., 2008; Ponten et al., 2008). We analyzed H11 protein levels of in various cell lines. There was no obvious expression of H11 in the human monocyte/macrophage cell lines THP-1 and MonoMac6. By contrast, H11 was highly expressed in HVTs, a cell line derived from primary trophoblasts (**Figure 6B**). To test whether H11 can interact with Vpx in trophoblast cells, we performed an immunoprecipitation analysis using FLAG-Vpx transfected HVT cell extract. Endogenous H11 protein was co-precipitated with FLAG-Vpx (**Figure 6C**). These data prompted us to assess H11

[1]www.proteinatlas.org

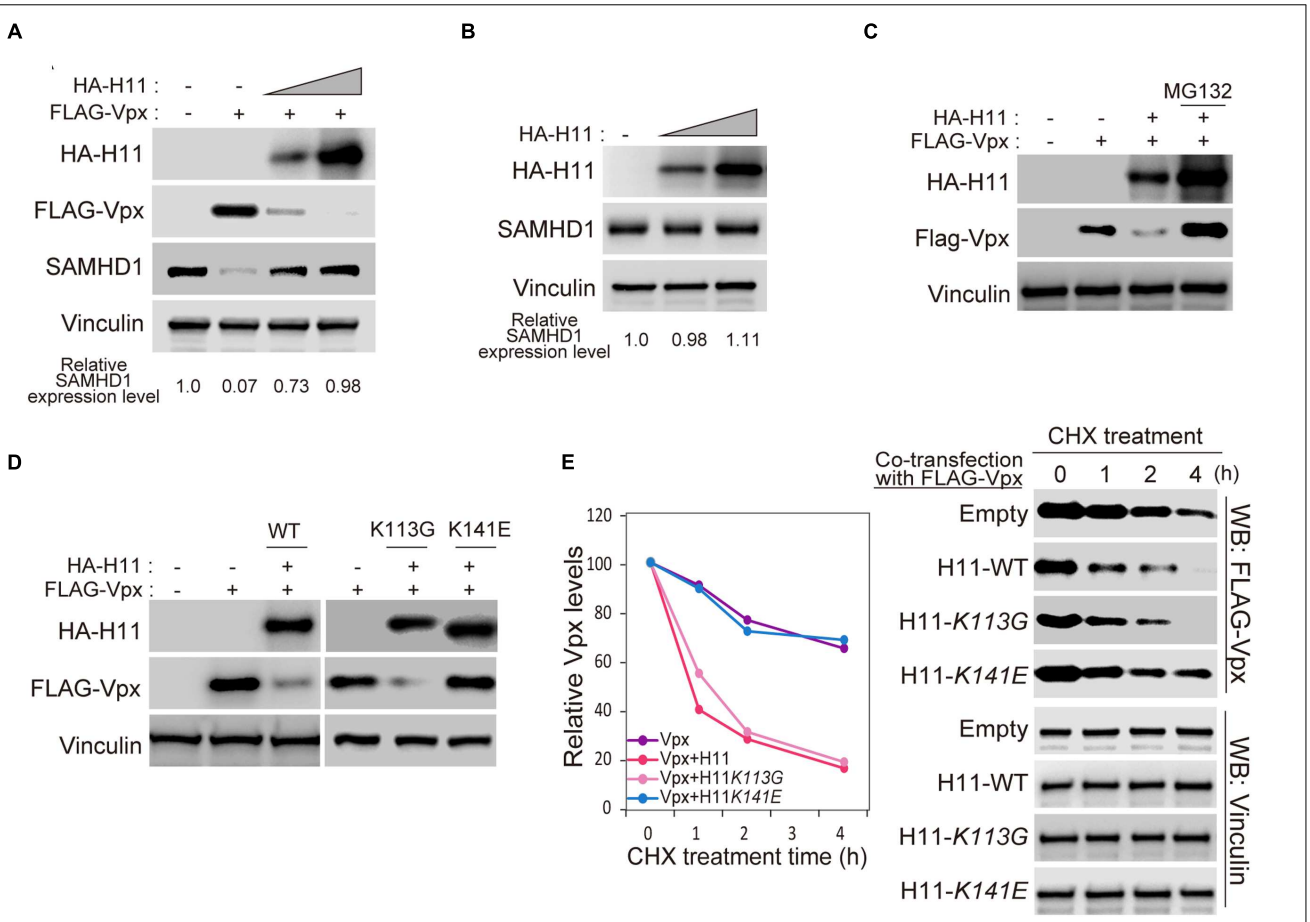

FIGURE 4 | Aberrant expressed H11 degrades HIV-2 Vpx in mammalian cells. (A) HA-H11 degrades FLAG-Vpx. HEK293 cells were co-transfected with plasmids encoding FLAG-Vpx (50 ng) and HA-H11 (100 or 300 ng). Equal amounts of proteins for each sample were separated by SDS-PAGE and subjected western blot analysis using the indicated antibodies. The relative SAMHD1 expression level are shown as indicated. **(B)** HA-H11 expression does not effect on SAMHD1 expression. HEK293 cells were transfected with plasmid encoding HA-H11 (100 or 200 ng). Equal amounts of proteins for each sample were separated by SDS-PAGE and subjected western blot analysis using the indicated antibodies. The relative SAMHD1 expression levels are shown as indicated. **(C)** H11-dependent Vpx degradation is inhibited by MG132 treatment. HEK293 cells were co-transfected with plasmids encoding FLAG-Vpx (50 ng) and HA-H11 (200 ng), and then treated with or without 20 μM of MG132 treatment for 4 h. Equal amounts of proteins for each sample were separated by SDS-PAGE and subjected to western blot analysis using the indicated antibodies. **(D)** H11 degrades Vpx via its chaperone activity. HEK293 cells were co-transfected with plasmids encoding FLAG-Vpx and the indicated HA-H11 variants (WT, K113G, or K141E). Cell lysates were subjected to western blotting using the indicated antibodies. **(E)** FLAG-Vpx cycloheximide chase analysis in cells expressing HA-H11. HEK293 cells were co-transfected with plasmids encoding FLAG-Vpx and the indicated HA-H11 variant (WT, K113G, or K141E), and then treated with or without cycloheximide. Equal amounts of proteins for each sample were separated by SDS-PAGE and subjected to western blot analysis using theanti-FLAG or anti-Vinculin antibodies. Left panel shows quantitation of signal intensity.

expression in human placenta tissues. Immunohistochemistry (IHC) revealed that H11 was specifically expressed both in syncytiotrophoblast and cytotrophoblast cells, this was more prominently in syncytiotrophoblast, which form the border surface of placenta with the maternal circulation (**Figure 6D**).

Targeted Depletion of H11 Restores Vpx Expression and HIV-2 Replication in a Primary Trophoblast Cell Line

Previous studies showed that the frequency of mother-to-infant HIV-2 transmission is very low (<2.5%) even in the absence of antiretroviral therapy during pregnancy (Padua et al., 2009; Burgard et al., 2010). Although the placenta acts as an effective barrier against HIV infection, according to the literature, the underlying molecular mechanisms have not been well characterized. We hypothesized that H11 is functionally involved in the defense against HIV infection at the placenta. To test this idea, we used siRNA targeting *H11* to inhibit endogenous H11 expression in HVT cells. In transduced HVTs, exogenous expression of FLAG-Vpx was relatively low, but increased dramatically following *H11* siRNA transfection (**Figure 6E**). Moreover the level of endogenous SAMHD1 was reduced in concert with an increase of Vpx expression (**Figure 6E**). To further explore the relevance of this phenomena, we asked whether knockdown of *H11* would affect HIV-2 replication. As a replication marker, we measured luciferase activity in cells infected with HIV-2 reporter virus. The

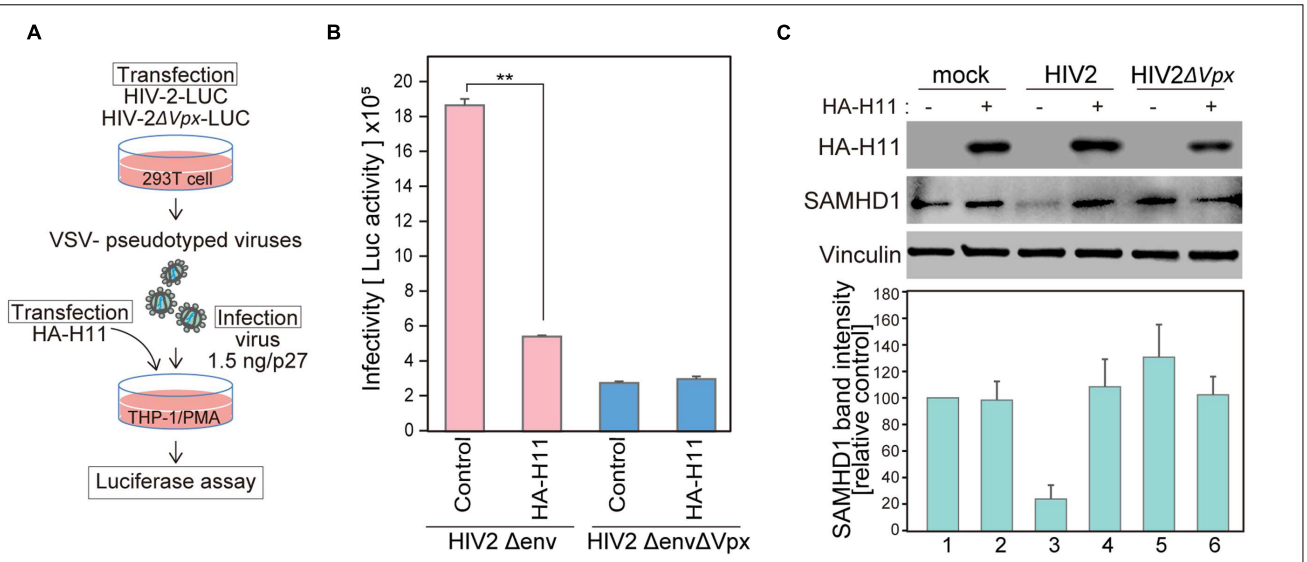

FIGURE 5 | H11 expression decreases single-round HIV-2 infection in MDMs. (A) Schematic representation of the experimental system. **(B, C)** HEK 293T cells were co-transfected with pHIV-2Δenv-luc or pHIV-2ΔenvΔVpx–luc and with pVSV-G. Viral release was measured by quantitation of p27 antigen concentration in culture supernatants at 48 h post-transfection. THP-1 cells were differentiated with PMA for 24 h, and then transfected with plasmids encoding HA-H11 or empty vector (negative control). Twenty-four hours post-transfection, cells were infected with VSV- pseudotyped WT or ΔVpx viruses for 48 h. **(B)** Viral infectivity was detected by measuring luciferase activity in cell lysates. Data are means ± S.E.M. of three independent experiments. $^{**}p < 0.05$, Student *t*-test. **(C)** Forty-eight hours after infection, cells were harvested and analyzed by western blotting using the indicated antibodies. Represent results from one of three independent experiments. Bar charts indicate amounts of SAMHD1, as determined by densitometric analysis of western blots. Data are means ± S.E.M. of three independent experiments.

luciferase activity of HIV-2 Luc was elevated in *H11*-suppressed HVT cells, whereas that of the Vpx-null (HIV-2ΔVpx) virus was not significantly affected (**Figure 6F**). These results further support the idea that HIV-2 replication in human trophoblast cells is negatively regulated by H11-mediated degradation and functional disruption of Vpx.

DISCUSSION

Identification of new virus–host cell interactions is a key challenge in clarifying the nature of viral infection and pathogenesis. An understanding of the molecular mechanisms underlying the virus–host interaction will facilitate the development of new therapeutic strategies against viral infections. Thus, establishment of assay system for comprehensive analysis of virus–host protein interaction may lead to new advances in virus research.

In this study, we developed a new assay system that combines wheat germ CFPS and the AlphaScreen system. This method enabled us to comprehensively screen for any kind of robust virus–host protein interaction. As an illustration, we utilized our system to identify a host factor that interacts with HIV-2 Vpx. We found that H11 interacts with HIV-2 Vpx and promotes its degradation via a proteasome-dependent pathway. In addition, we demonstrated that H11 is highly expressed in human trophoblasts and may prevent maternal-to-fetal transmission of HIV-2 during pregnancy. Thus, our proteomic approach is an efficient and powerful tool for revealing biologically or pathologically relevant molecular events in virus infection.

We exploited the AlphaScreen system to systematically measure virus–host protein interactions. One major advantage of the AlphaScreen technology is that it is a homogeneous (no-wash) assay and can be applied to crude samples such as tissue homogenates, cell lysates, cell culture supernatants, and cell extracts. AlphaScreen beads can only recognize the objective proteins with a specific epitope tag, permitting us to use non-purified proteins synthesized in a wheat cell-free system. This advantage saves considerable time and labor on protein extraction and purification.

For reliable and efficient screening of protein–protein interactions, it is necessary to use proteins with proper tertiary structures and biological functions. Wheat germ CFPS is a eukaryotic translation system that synthesizes proteins that are properly folded and biologically active, as in living mammalian cells. Another desirable property of wheat germ CFPS is its suitability for viral protein production. Viral proteins are usually insoluble and form aggregates in inclusion bodies in living cells. Moreover, viral proteins are generally cytotoxic and induce cell death upon expression. The wheat germ cell-free system is able to produce proteins that are relatively insoluble in other systems because it can tolerate alterations in buffer components, including adjustments to salt concentration and/or addition of various detergents. These advantages underscore the suitability and availability of the wheat germ CFPS for the generation of viral proteins that can be used for comprehensive protein–protein interaction assays.

We introduced the wheat germ CFPS to provide a set of recombinant proteins from a cDNA library of human protein

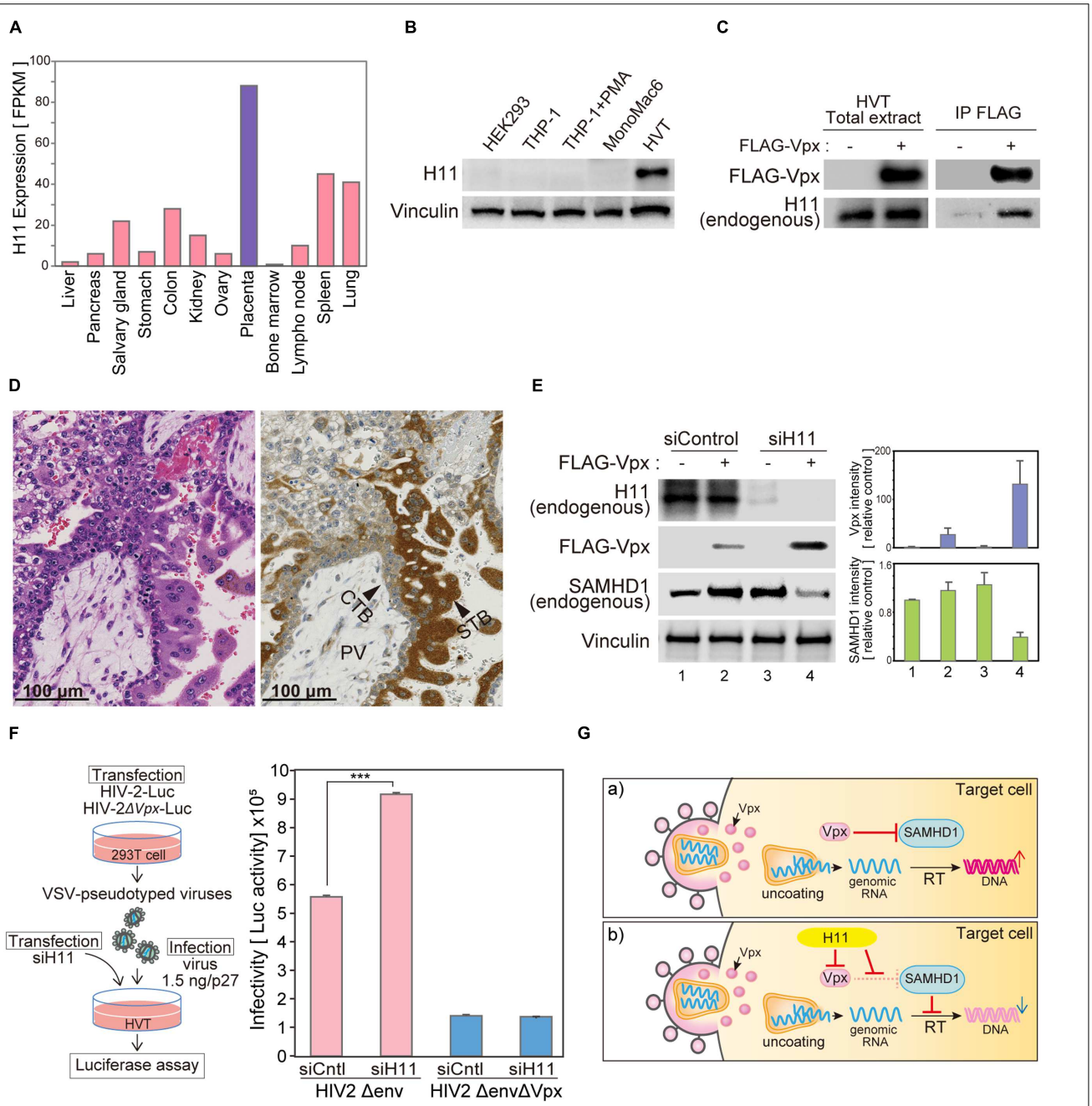

FIGURE 6 | H11 regulates HIV-2 infection in primary trophoblast cells. (A) H11 mRNA levels in human organs and tissues. FPKM values for human H11 were obtained from the Human Protein Atlas Database (www.proteinatlas.org). **(B)** H11 protein expression in six cell lines (HEK293, THP-1 THP-1–derived macrophage, MonoMac 6, and HVT) were examined by western blot; vinculin was used as an internal control. **(C)** Immunoprecipitation of HIV-2 Vpx with H11 in HVT cells. HVT cells were transfected with FLAG-tagged HIV-2 Vpx, and cells were treated with 20 μM of MG132 from 6 h before harvest. Cells were harvested at 24 h after transfection, and lysates were immunoprecipitated with anti-FLAG. Input and immunoprecipitation samples were then probed with anti-H11 and anti-FLAG antibodies. **(D)** Immunohistochemistry (IHC) for detection of H11 in fourth week of human placental tissue. Brown color, IHC staining; blue color, hematoxylin counterstain. PV, placental villi; CTB, cytotrophoblast; STB, syncytiotrophoblast. Scale bars, 100 μm. **(E)** HVT cells were transfected with control or *H11*-targeted siRNA for 24 h, and then transfected with FLAG-Vpx. Twenty-four hours after transfection, cells were harvested and analyzed by western blotting using the indicated antibodies. Represent results from one of three independent experiments. Bar charts indicate the amounts of Vpx or SAMHD1, as determined by densitometric analysis of western blots. Data are means ± S.E.M. of three independent experiments. **(F)** HVT cells were transfected with control or *H11*-targeted siRNA for 24 h before infection with HIV-2. Twenty-four hours after infection, cells were harvested. Viral infectivity was detected by measuring luciferase activity in cell lysates. Data are means ± S.E.M. of three independent experiments. $^{***}p < 0.01$, Student's *t*-test. Left panel shows schematic representation of the experimental system. **(G)** Proposed model for H11-mediated regulation of HIV-2 in trophoblast cells. In the absence of H11, Vpx proteins are delivered into target cells by HIV-2 infection and degrade the host restriction factor SAMHD1, leading to productive infection. On the other hand, when H11 is present, it directly interacts with Vpx, leading to its degradation; consequently, SAMHD1 is liberated from Vpx and able to inhibit HIV-2 replication.

kinases. Our system can produce proteins from linear cDNA templates generated by PCR (Sawasaki et al., 2007; Matsuoka et al., 2010; Matsunaga et al., 2015). Moreover, when a biotin ligation sequence is inserted into cDNAs by PCR, biotinylated proteins can be readily synthesized in the presence of biotin and biotin ligase. The biotinylated proteins are readily discernible by streptavidin, which has high affinity for biotin, and clearly recognized in a homogenous condition such as AlphaScreen assay system (Sawasaki et al., 2008; Matsuoka et al., 2010). Based on these features and the aforementioned advantages, we can perform high-throughput assays under optimal experimental conditions using selective cDNA libraries, e.g., the human protein kinase library used in this study.

HIV-2 infection occurs mainly in West Africa, but its prevalence is increasing in Europe, India, and the United States. Compared with HIV-1, HIV-2 exhibits a longer asymptomatic phase, slower progression to terminal immunosuppression, and lower efficiency of both transmission and replication (∼30-fold lower than HIV-1; Popper et al., 1999; MacNeil et al., 2007; Gottlieb et al., 2008; Gueudin et al., 2008; Nyamweya et al., 2013; Menendez-Arias and Alvarez, 2014). These observations suggest the existence of different modes of host–virus interaction in HIV-2 infection. HIV-2 encodes an accessory protein, Vpx, degrades the cellular restriction factor SAMHD1, which strongly inhibit viral replication in non-dividing cells (Berger et al., 2011; Hrecka et al., 2011; Laguette et al., 2011). Moreover, Vpx enhances nuclear import of the pre-integration complex following infection (Shingai et al., 2015). Vpx is thus essential to maintenance of productive HIV-2 infection in non-dividing cells. However, it remains unclear how Vpx function is regulated in terms of virus–host interaction. Therefore, we focused on Vpx as a target of our proteomic analysis to elucidate host molecular mechanisms involved in the functions and regulation of Vpx in HIV-infected cells.

Viruses can pass through the placental barrier from maternal to fetal blood. A pregnant woman infected with HIV can transmit the virus to her fetus at any time during pregnancy. Previous reports showed that trophoblastic cells of human placenta tissue express CD4 and/or chemokine receptors, such as CCR-5 and CXCR-4, and susceptible to HIV infection (Amirhessami-Aghili and Spector, 1991; Ishii et al., 2000), and both HIV-1 and -2 have been detected *in situ* in placental syncytiotrophoblasts of HIV-positive pregnant women (Lewis et al., 1990; Backe et al., 1992). However, placental HIV-1 and -2 infection during the neonatal period seems to be rare, although the risk of infection becomes much higher during labor and vaginal delivery (Leroy et al., 2002; Padua et al., 2009; Burgard et al., 2010). These results suggest the presence of novel restriction factor(s) in trophoblasts that are capable of suppressing maternal-to-fetal transmission of HIV. In this study, we identified H11 as a putative restriction factor that may suppress HIV-2 replication in THP-1 and trophoblastic cells (**Figure 6G**). Our proteomic analysis revealed that H11 can bind directly to Vpx and promote its proteasomal degradation. Consequently, the host restriction factor SAMHD1 is liberated from Vpx and can suppress HIV-2 replication. H11 is not expressed in immune cells such as MDMs and T cells, but is highly expressed in human placental trophoblastic cells, to a greater extent in the outer syncytiotrophoblast rather than in the inner cytotrophoblast. Previous reports suggested that the antiviral activity of SAMHD1 is limited to non-dividing cells such as terminally differentiated myeloid cells and quiescent CD4+ T lymphocytes. Because syncytiotrophoblasts are generally fully differentiated and non-dividing cells, H11 may give these cells the ability to suppress HIV-2 transmission. Further careful analysis with human samples is necessary to delineate the biological function of H11 in HIV infection.

In summary, we developed a novel protein–protein interaction assay system that combines the wheat germ CFPS system with AlphaScreen technology. Our assay system provides rapid and reliable experimental format for uncovering novel virus–host protein interactions. Further evaluation using different viral species and different sets of human cDNA libraries could validate the utility and benefit of this system for future virological research.

AUTHOR CONTRIBUTIONS

AK designed and performed the experiments and wrote the manuscript. KM accumulated data and performed analysis. SM performed *in vitro* assays and analyzed data. YM analyzed the computational binding model. IK performed and analyzed immunohistochemistry. HK provided reagents and advice on the project. SH provided key materials. KM and TS generated initial observations of this project. AR designed and supervised the research, analyzed the data, and wrote the manuscript. All authors participated in drafting, revising and final approval of the manuscript, and agree to be accountable for all aspects of the work.

FUNDING

This work was supported by JSPS Grant-in-Aid for Young Scientists 26860305 to AK, 24790447 to KM, and by Creation of Innovation Centers for Advanced Interdisciplinary Research Areas Program and grant-in-aid from Japan Agency for Medical Research and Development (AMED) to AR.

ACKNOWLEDGMENTS

The authors thank Drs Akio Adachi and Masako Nomaguchi for materials, and Mayu Miyamoto and Noriko Ikawa for technical supports.

REFERENCES

Amirhessami-Aghili, N., and Spector, S. A. (1991). Human immunodeficiency virus type 1 infection of human placenta: potential route for fetal infection. *J. Virol.* 65, 2231–2236.

Backe, E., Jimenez, E., Unger, M., Schafer, A., Jauniaux, E., and Vogel, M. (1992). Demonstration of HIV-1 infected cells in human placenta by in situ hybridisation and immunostaining. *J. Clin. Pathol.* 45, 871–874. doi: 10.1136/jcp.45.10.871

Baldauf, H. M., Pan, X., Erikson, E., Schmidt, S., Daddacha, W., Burggraf, M., et al. (2012). SAMHD1 restricts HIV-1 infection in resting CD4(+) T cells. *Nat. Med.* 18, 1682–1687. doi: 10.1038/nm.2964

Berger, A., Sommer, A. F., Zwarg, J., Hamdorf, M., Welzel, K., Esly, N., et al. (2011). SAMHD1-deficient CD14+ cells from individuals with Aicardi-Goutieres syndrome are highly susceptible to HIV-1 infection. *PLoS Pathog.* 7:e1002425. doi: 10.1371/journal.ppat.1002425

Berglund, L., Bjorling, E., Oksvold, P., Fagerberg, L., Asplund, A., Szigyarto, C. A., et al. (2008). A genecentric Human Protein Atlas for expression profiles based on antibodies. *Mol. Cell. Proteomics* 7, 2019–2027. doi: 10.1074/mcp.R800013-MCP200

Burgard, M., Jasseron, C., Matheron, S., Damond, F., Hamrene, K., Blanche, S., et al. (2010). Mother-to-child transmission of HIV-2 infection from 1986 to 2007 in the ANRS French Perinatal Cohort EPF-CO1. *Clin. Infect. Dis.* 51, 833–843. doi: 10.1086/656284

Descours, B., Cribier, A., Chable-Bessia, C., Ayinde, D., Rice, G., Crow, Y., et al. (2012). SAMHD1 restricts HIV-1 reverse transcription in quiescent CD4(+) T-cells. *Retrovirology* 9, 87. doi: 10.1186/1742-4690-9-87

Endo, Y., and Sawasaki, T. (2006). Cell-free expression systems for eukaryotic protein production. *Curr. Opin. Biotechnol.* 17, 373–380. doi: 10.1016/j.copbio.2006.06.009

Gagoski, D., Polinkovsky, M. E., Mureev, S., Kunert, A., Johnston, W., Gambin, Y., et al. (2016). Performance benchmarking of four cell-free protein expression systems. *Biotechnol. Bioeng.* 113, 292–300. doi: 10.1002/bit.25814

Goldstone, D. C., Ennis-Adeniran, V., Hedden, J. J., Groom, H. C., Rice, G. I., Christodoulou, E., et al. (2011). HIV-1 restriction factor SAMHD1 is a deoxynucleoside triphosphate triphosphohydrolase. *Nature* 480, 379–382. doi: 10.1038/nature10623

Gottlieb, G. S., Hawes, S. E., Kiviat, N. B., and Sow, P. S. (2008). Differences in proviral DNA load between HIV-1-infected and HIV-2-infected patients. *AIDS* 22, 1379–1380. doi: 10.1097/QAD.0b013e328303496d

Gueudin, M., Damond, F., Braun, J., Taieb, A., Lemee, V., Plantier, J. C., et al. (2008). Differences in proviral DNA load between HIV-1- and HIV-2-infected patients. *AIDS* 22, 211–215. doi: 10.1097/QAD.0b013e3282f42429

Harbers, M. (2014). Wheat germ systems for cell-free protein expression. *FEBS Lett.* 588, 2762–2773. doi: 10.1016/j.febslet.2014.05.061

Hemonnot, B., Molle, D., Bardy, M., Gay, B., Laune, D., Devaux, C., et al. (2006). Phosphorylation of the HTLV-1 matrix L-domain-containing protein by virus-associated ERK-2 kinase. *Virology* 349, 430–439. doi: 10.1016/j.virol.2006.02.043

Hrecka, K., Hao, C., Gierszewska, M., Swanson, S. K., Kesik-Brodacka, M., Srivastava, S., et al. (2011). Vpx relieves inhibition of HIV-1 infection of macrophages mediated by the SAMHD1 protein. *Nature* 474, 658–661. doi: 10.1038/nature10195

Irobi, J., Van Impe, K., Seeman, P., Jordanova, A., Dierick, I., Verpoorten, N., et al. (2004). Hot-spot residue in small heat-shock protein 22 causes distal motor neuropathy. *Nat. Genet.* 36, 597–601. doi: 10.1038/ng1328

Ishii, M., Hayakawa, S., Suzuki, M. K., Yoshino, N., Honda, M., Nishinarita, S., et al. (2000). Expression of functional chemokine receptors of human placental cells. *Am. J. Reprod. Immunol.* 44, 365–373. doi: 10.1111/j.8755-8920.2000.440608.x

Khamsri, B., Murao, F., Yoshida, A., Sakurai, A., Uchiyama, T., Shirai, H., et al. (2006). Comparative study on the structure and cytopathogenic activity of HIV Vpr/Vpx proteins. *Microbes Infect.* 8, 10–15. doi: 10.1016/j.micinf.2005.05.020

Kinoshita, E., Kinoshita-Kikuta, E., Takiyama, K., and Koike, T. (2006). Phosphate-binding tag, a new tool to visualize phosphorylated proteins. *Mol. Cell. Proteomics* 5, 749–757. doi: 10.1074/mcp.T500024-MCP200

Kudoh, A., Takahama, S., Sawasaki, T., Ode, H., Yokoyama, M., Okayama, A., et al. (2014). The phosphorylation of HIV-1 Gag by atypical protein kinase C facilitates viral infectivity by promoting Vpr incorporation into virions. *Retrovirology* 11, 9. doi: 10.1186/1742-4690-11-9

Laguette, N., Sobhian, B., Casartelli, N., Ringeard, M., Chable-Bessia, C., Segeral, E., et al. (2011). SAMHD1 is the dendritic- and myeloid-cell-specific HIV-1 restriction factor counteracted by Vpx. *Nature* 474, 654–657. doi: 10.1038/nature10117

Lahouassa, H., Daddacha, W., Hofmann, H., Ayinde, D., Logue, E. C., Dragin, L., et al. (2012). SAMHD1 restricts the replication of human immunodeficiency virus type 1 by depleting the intracellular pool of deoxynucleoside triphosphates. *Nat. Immunol.* 13, 223–228. doi: 10.1038/ni.2236

Leroy, V., Karon, J. M., Alioum, A., Ekpini, E. R., Meda, N., Greenberg, A. E., et al. (2002). Twenty-four month efficacy of a maternal short-course zidovudine regimen to prevent mother-to-child transmission of HIV-1 in West Africa. *AIDS* 16, 631–641. doi: 10.1097/00002030-200203080-00016

Lewis, S. H., Reynolds-Kohler, C., Fox, H. E., and Nelson, J. A. (1990). HIV-1 in trophoblastic and villous Hofbauer cells, and haematological precursors in eight-week fetuses. *Lancet* 335, 565–568. doi: 10.1016/0140-6736(90)90349-A

MacNeil, A., Sarr, A. D., Sankale, J. L., Meloni, S. T., Mboup, S., and Kanki, P. (2007). Direct evidence of lower viral replication rates in vivo in human immunodeficiency virus type 2 (HIV-2) infection than in HIV-1 infection. *J. Virol.* 81, 5325–5330. doi: 10.1128/JVI.02625-06

Matsunaga, S., Masaoka, T., Sawasaki, T., Morishita, R., Iwatani, Y., Tatsumi, M., et al. (2015). A cell-free enzymatic activity assay for the evaluation of HIV-1 drug resistance to protease inhibitors. *Front. Microbiol.* 6:1220. doi: 10.3389/fmicb.2015.01220

Matsuoka, K., Komori, H., Nose, M., Endo, Y., and Sawasaki, T. (2010). Simple screening method for autoantigen proteins using the N-terminal biotinylated protein library produced by wheat cell-free synthesis. *J. Proteome Res.* 9, 4264–4273. doi: 10.1021/pr9010553

Menendez-Arias, L., and Alvarez, M. (2014). Antiretroviral therapy and drug resistance in human immunodeficiency virus type 2 infection. *Antiviral Res.* 102, 70–86. doi: 10.1016/j.antiviral.2013.12.001

Nandi, J., and Banerjee, K. (1995). Tyrosine phosphorylation as a possible regulatory mechanism in the expression of human immunodeficiency virus genes. *Med. Hypotheses* 45, 476–480. doi: 10.1016/0306-9877(95)90226-0

Nyamweya, S., Hegedus, A., Jaye, A., Rowland-Jones, S., Flanagan, K. L., and Macallan, D. C. (2013). Comparing HIV-1 and HIV-2 infection: lessons for viral immunopathogenesis. *Rev. Med. Virol.* 23, 221–240. doi: 10.1002/rmv.1739

Padua, E., Almeida, C., Nunes, B., Cortes Martins, H., Castela, J., Neves, C., et al. (2009). Assessment of mother-to-child HIV-1 and HIV-2 transmission: an AIDS reference laboratory collaborative study. *HIV Med.* 10, 182–190. doi: 10.1111/j.1468-1293.2008.00669.x

Pavlov, N., Hatzi, E., Bassaglia, Y., Frendo, J. L., Evain Brion, D., and Badet, J. (2003). Angiogenin distribution in human term placenta, and expression by cultured trophoblastic cells. *Angiogenesis* 6, 317–330. doi: 10.1023/B:AGEN.0000029412.95244.81

Ponten, F., Jirstrom, K., and Uhlen, M. (2008). The Human Protein Atlas–a tool for pathology. *J. Pathol.* 216, 387–393. doi: 10.1002/path.2440

Popper, S. J., Sarr, A. D., Travers, K. U., Gueye-Ndiaye, A., Mboup, S., Essex, M. E., et al. (1999). Lower human immunodeficiency virus (HIV) type 2 viral load reflects the difference in pathogenicity of HIV-1 and HIV-2. *J. Infect. Dis.* 180, 1116–1121. doi: 10.1086/315010

Rajendra Kumar, P., Singhal, P. K., Subba Rao, M. R., and Mahalingam, S. (2005). Phosphorylation by MAPK regulates simian immunodeficiency virus Vpx protein nuclear import and virus infectivity. *J. Biol. Chem.* 280, 8553–8563. doi: 10.1074/jbc.M407863200

Roche, D. B., Brackenridge, D. A., and McGuffin, L. J. (2015). Proteins and their interacting partners: an introduction to protein-ligand binding site prediction methods. *Int. J. Mol. Sci.* 16, 29829–29842. doi: 10.3390/ijms161226202

Roy, A., Kucukural, A., and Zhang, Y. (2010). I-TASSER: a unified platform for automated protein structure and function prediction. *Nat. Protoc.* 5, 725–738. doi: 10.1038/nprot.2010.5

Sawasaki, T., Kamura, N., Matsunaga, S., Saeki, M., Tsuchimochi, M., Morishita, R., et al. (2008). *Arabidopsis* HY5 protein functions as a DNA-binding tag for purification and functional immobilization of proteins on agarose/DNA microplate. *FEBS Lett.* 582, 221–228. doi: 10.1016/j.febslet.2007.12.004

Sawasaki, T., Morishita, R., Gouda, M. D., and Endo, Y. (2007). Methods for high-throughput materialization of genetic information based on wheat germ cell-free expression system. *Methods Mol. Biol.* 375, 95–106. doi: 10.1007/978-1-59745-388-2_5

Sawasaki, T., Ogasawara, T., Morishita, R., and Endo, Y. (2002). A cell-free protein synthesis system for high-throughput proteomics. *Proc. Natl. Acad. Sci. U.S.A.* 99, 14652–14657. doi: 10.1073/pnas.232580399

Schwefel, D., Groom, H. C., Boucherit, V. C., Christodoulou, E., Walker, P. A., Stoye, J. P., et al. (2014). Structural basis of lentiviral subversion of a cellular protein degradation pathway. *Nature* 505, 234–238. doi: 10.1038/nature12815

Shemetov, A. A., and Gusev, N. B. (2011). Biochemical characterization of small heat shock protein HspB8 (Hsp22)-Bag3 interaction. *Arch. Biochem. Biophys.* 513, 1–9. doi: 10.1016/j.abb.2011.06.014

Shemetov, A. A., Seit-Nebi, A. S., and Gusev, N. B. (2008). Structure, properties, and functions of the human small heat-shock protein HSP22 (HspB8, H11, E2IG1): a critical review. *J. Neurosci. Res.* 86, 264–269. doi: 10.1002/jnr.21441

Shingai, M., Welbourn, S., Brenchley, J. M., Acharya, P., Miyagi, E., Plishka, R. J., et al. (2015). The expression of functional vpx during pathogenic sivmac infections of rhesus macaques suppresses SAMHD1 in CD4+ memory T cells. *PLoS Pathog.* 11:e1004928. doi: 10.1371/journal.ppat.1004928

Singhal, P. K., Rajendra Kumar, P., Subba Rao, M. R., and Mahalingam, S. (2006). Nuclear export of simian immunodeficiency virus Vpx protein. *J. Virol.* 80, 12271–12282. doi: 10.1128/JVI.00563-06

Smith, C. C., Yu, Y. X., Kulka, M., and Aurelian, L. (2000). A novel human gene similar to the protein kinase (PK) coding domain of the large subunit of herpes simplex virus type 2 ribonucleotide reductase (ICP10) codes for a serine-threonine PK and is expressed in melanoma cells. *J. Biol. Chem.* 275, 25690–25699. doi: 10.1074/jbc.M002140200

Tadokoro, D., Takahama, S., Shimizu, K., Hayashi, S., Endo, Y., and Sawasaki, T. (2010). Characterization of a caspase-3-substrate kinome using an N- and C-terminally tagged protein kinase library produced by a cell-free system. *Cell Death Dis.* 1:e89. doi: 10.1038/cddis.2010.65

Takai, K., Sawasaki, T., and Endo, Y. (2010). Practical cell-free protein synthesis system using purified wheat embryos. *Nat. Protoc.* 5, 227–238. doi: 10.1038/nprot.2009.207

Taouji, S., Dahan, S., Bosse, R., and Chevet, E. (2009). Current screens based on the AlphaScreen technology for deciphering cell signalling pathways. *Curr. Genomics* 10, 93–101. doi: 10.2174/138920209787847041

Uhlen, M., Bjorling, E., Agaton, C., Szigyarto, C. A., Amini, B., Andersen, E., et al. (2005). A human protein atlas for normal and cancer tissues based on antibody proteomics. *Mol. Cell. Proteomics* 4, 1920–1932. doi: 10.1074/mcp.M500279-MCP200

Uhlen, M., Fagerberg, L., Hallstrom, B. M., Lindskog, C., Oksvold, P., Mardinoglu, A., et al. (2015). Proteomics. Tissue-based map of the human proteome. *Science* 347, 1260419. doi: 10.1126/science.1260419

Uhlen, M., Oksvold, P., Fagerberg, L., Lundberg, E., Jonasson, K., Forsberg, M., et al. (2010). Towards a knowledge-based human protein atlas. *Nat. Biotechnol.* 28, 1248–1250. doi: 10.1038/nbt1210-1248

Zawada, J. F., Yin, G., Steiner, A. R., Yang, J., Naresh, A., Roy, S. M., et al. (2011). Microscale to manufacturing scale-up of cell-free cytokine production–a new approach for shortening protein production development timelines. *Biotechnol. Bioeng.* 108, 1570–1578. doi: 10.1002/bit.23103

Conflict of Interest Statement: The authors declare that the research was conducted in the absence of any commercial or financial relationships that could be construed as a potential conflict of interest.

Copyright © 2016 Kudoh, Miyakawa, Matsunaga, Matsushima, Kosugi, Kimura, Hayakawa, Sawasaki and Ryo. This is an open-access article distributed under the terms of the Creative Commons Attribution License (CC BY). The use, distribution or reproduction in other forums is permitted, provided the original author(s) or licensor are credited and that the original publication in this journal is cited, in accordance with accepted academic practice. No use, distribution or reproduction is permitted which does not comply with these terms.

frontiers in Microbiology

ORIGINAL RESEARCH
published: 07 April 2016
doi: 10.3389/fmicb.2016.00468

Binding of Hemagglutinin and Influenza Virus to a Peptide-Conjugated Lipid Membrane

*Teruhiko Matsubara, Rabi Shibata and Toshinori Sato **

Department of Biosciences and Informatics, Faculty of Science and Technology, Keio University, Yokohama, Japan

Hemagglutinin (HA) plays an important role in the first step of influenza virus (IFV) infection because it initiates the binding of the virus to the sialylgalactose linkages of the receptors on the host cells. We herein demonstrate that a HA-binding peptide immobilized on a solid support is available to bind to HA and IFV. We previously obtained a HA-binding pentapeptide (Ala-Arg-Leu-Pro-Arg), which was identified by phage-display selection against HAs from random peptide libraries. This peptide binds to the receptor-binding site of HA by mimicking sialic acid. A peptide-conjugated lipid (pep-PE) was chemically synthesized from the peptide and a saturated phospholipid. A lipid bilayer composed of pep-PE and an unsaturated phospholipid (DOPC) was immobilized on a mica plate; and the interaction between HA and the pep-PE/DOPC membrane was investigated using atomic force microscopy. The binding of IFV to the pep-PE/DOPC membrane was detected by an enzyme-linked immunosorbent assay and real-time reverse transcription PCR. Our results indicate that peptide-conjugated lipids are a useful molecular device for the detection of HA and IFV.

Keywords: influenza, hemagglutinin, sialic acid-mimic peptide, lipid bilayer, atomic force microscopy, peptide-conjugated lipid

OPEN ACCESS

Edited by:
Akio Adachi,
Tokushima University Graduate School, Japan

Reviewed by:
Mineo Hashizume,
Tokyo University of Science, Japan
Hiroshi Tsutsumi,
Tokyo Institute of Technology, Japan
Yasuhito Ebara,
Kobe University, Japan

****Correspondence:***
Toshinori Sato
sato@bio.keio.ac.jp

Specialty section:
This article was submitted to Virology, a section of the journal Frontiers in Microbiology

Received: *25 February 2016*
Accepted: *21 March 2016*
Published: *07 April 2016*

Citation:
Matsubara T, Shibata R and Sato T (2016) Binding of Hemagglutinin and Influenza Virus to a Peptide-Conjugated Lipid Membrane. Front. Microbiol. 7:468. doi: 10.3389/fmicb.2016.00468

INTRODUCTION

Type A influenza virus (IFV) is highly mutagenic, and, thus, often causes epidemics and pandemics. IFV has been classified into subtypes based on the antigenic specificity of the envelope glycoproteins hemagglutinin (HA) and neuraminidase (NA; Gamblin and Skehel, 2010). Although, sixteen HA subtypes (H1-H16) and nine NA subtypes (N1-N9) have been identified to date, only three HA subtypes (H1, H2, and H3) and two NA subtypes (N1 and N2) have so far been identified among human pandemics. In order to prevent the spread of influenza, it needs to be diagnosed influenza quickly and easily in clinical practice by the detection of IFV.

In recent decades, several methods have been developed to detect IFV. Immunochromatography, PCR analyses, enzyme-linked immunoassays, and fluorescence antibody methods are frequency employed for clinical use (Eisfeld et al., 2014) and the surveillance of influenza (Wang and Taubenberger, 2010). On the other hand, a glycan array using oligosaccharides is used for basic research on the carbohydrate recognition of proteins (Feizi et al., 2003; Feizi, 2013). Although all methods have important characteristics, they also have some limitations. Antibodies, which are excellent biological components, are unstable and their production cost is high, PCR methods require expensive equipment and reagents, and the preparation of various kinds of oligosaccharides requires a large amount of work. In order to prevent global pandemics, easy, quick, and inexpensive methods are required to detect influenza.

The first step in the infection of cells by IFV is the binding of HA to sialic acid-containing glycoconjugates (Skehel and Wiley, 2000). Human HA strains preferentially bind to the terminal sialylgalactose structure (Neu5Acα2−6Gal), whereas avian and equine strains bind to the corresponding Neu5Acα2−3Gal (Suzuki, 2005). We previously identified the HA-binding pentapeptide, Ala-Arg-Leu-Pro-Arg, from phage-displayed peptide libraries (Matsubara et al., 2010). This pentapeptide binds to the receptor-binding site of HA by mimicking sialic acid, and exerts the inhibitory effects on IFV infection in cells. Furthermore, dendrimers composed of the peptide exhibit strong high inhibitory activities against IFV infection (Hatano et al., 2014). This peptide has potential in the capture of IFV with high sensitivity and specificity.

In the present study, we developed an artificial raft-like membrane to capture IFV using the HA-binding pentapeptide. IFV receptors such as ganglioside GM3 exist in membrane rafts, lipid domains that are 10–200 nm in diameter and act as a role of platform for protein-lipid interactions (Suzuki et al., 1986; Pike, 2006). In order to immobilize a solid surface, we designed and synthesized a peptide-conjugated lipid (pep-PE) composed of the peptide and dipalmitoylphosphatidylethanolamine (DPPE) using click chemistry (Tornøe et al., 2002). The pep-PE-containing lipid bilayer was immobilized on a mica plate, and influenza HA interacted with the pep-PE membrane. The surface topography of the pep-PE immobilized membrane was investigated using atomic force microscopy (AFM) and the results obtained indicated that HA selectively bound to the membrane. Furthermore, the binding of IFV was detected by ELISA, and the number of virus on the membrane was estimated by real-time reverse transcription PCR (rRT-PCR). These results suggest that the peptide-conjugated lipid designed in this study is useful as a novel device for the detection of IFV.

MATERIALS AND METHODS

Materials

DPPE was purchased from Wako Pure Chemical Industries, Ltd. (Japan). Dioleoylphosphatidylcholine (DOPC) and 1-palmitoyl-2-oleoyl-*sn*-glycelo-3-phosphocholine (POPC) were purchased from Sigma-Aldrich Co., LLC (St. Louis, MO, USA). Ganglioside Neu5Acα2–3Galβ1–4Glcβ1–1′Cer (GM3) from the bovine brain was purchased from Hytest Ltd. (Finland). Influenza hemagglutinins (HAs) derived from A/New Caledonia/20/99 (H1N1) and A/New York/55/2004 (H3N2) viruses were provided by Yujiro Suzuki (The Kitasato Institute, Japan; Matsubara et al., 2010). The human IFV strain A/Puerto Rico/8/34 (H1N1) was provided by Dr. Kyosuke Nagata (University of Tsukuba, Japan; Matsubara et al., 2009).

Synthesis of an Azide-Containing Pentapeptide (1)

A sialic acid-mimic pentapeptide with the ability to bind to the receptor-binding site of HA was previously identified (Matsubara et al., 2010). An azide group-conjugated peptide amide, Ala-Arg-Leu-Pro-Arg-Lys(N_3)-NH_2, was prepared by solid-phase peptide synthesis using standard 9-fluorenylmethoxycarbonyl (Fmoc) chemistry (Matsubara et al., 2009). Briefly, Fmoc-Lys(N_3)-OH was loaded onto Fmoc-NH-SAL Resin (Watanabe Chemical Industries, Ltd., Japan), and the peptide was elongated manually in multiple batches on a 0.1-mmol scale. In order to cleave the peptide from the resin, the resin (0.1 mmol) was treated with 1 mL of a cleavage cocktail (trifluoroacetic acid/water/triisopropylsilane, 95:2.5:2.5 by volume) on ice for 2 h (Schneggenburger et al., 2010). The crude peptide was purified by high-performance liquid chromatography (HPLC), and the fraction of the product was lyophilized. Purity (>98%) and the expected structure were verified by HPLC and matrix-assisted laser desorption ionization/time-of-flight mass spectrometry (MALDI-TOF MS). Ala-Arg-Leu-Pro-Arg-Lys(N_3)-NH_2 **1** (16 mg, 21%): MALDI-TOF MS (*m/z*: calcd exact mass for $C_{32}H_{60}N_{16}O_6$ $[M+H]^+$ 765.5, found 765.8).

Synthesis of Pentynoyl-DPPE (2)

In order to obtain an alkyne-modified lipid, DPPE was conjugated with 4-pentynoic acid using 4-(4,6-dimethoxy-1,3,5-triazin-2-yl)-4-methylmorpholinium chloride (DMT-MM) as a coupling reagent (Watanabe et al., 2004). DPPE (0.01 mmol), 4-pentynoic acid (0.03 mmol), and DMT-MM (0.01 mmol) were stirred at 25°C for 12 h in a mixture of chloroform (3 mL)/methanol (0.2 mL)/triethylamine (0.05 mL). The product was extracted with chloroform/sodium hydrogen carbonate solution, and solvents of the organic layer were evaporated. *N*-(4-pentynoyl)-DPPE **2** (7.2 mg, 90%) was obtained as oil: R_f 0.5 [8:2 (v/v) $CHCl_3$–MeOH]; MALDI-TOF MS (*m/z*: calcd exact mass for $C_{42}H_{78}NO_9P$ $[M+Na]^+$ 794.5, found 794.4).

Synthesis of Peptide-Conjugated DPPE (pep-PE)(3)

Azide-containing peptide **1** (0.2 μmol), pentynoyl-DPPE **2** (0.4 μmol), $CuSO_4$ (1.6 μmol), sodium ascorbate (1.0 μmol), and tris(benzyltriazolylmethyl)amine (TBTA)(0.2 μmol) were stirred at 25°C for 3 h in 1 mL of 50% methanol (Tornøe et al., 2002). The reaction was stopped on ice and the crude product was purified by HPLC on an ODS column with a liner gradient of 20–60% acetonitrile in 0.1% TFA. After lyophilization, purity (>98%) and the expected structure were verified by HPLC and MALDI-TOF MS. Peptide-conjugated DPPE (pep-PE) **3** (0.19 mg, 63%): MALDI-TOF MS (*m/z*: calcd exact mass for $C_{74}H_{138}N_{17}O_{15}P$ $[M+K]^+$ 1575.0, found 1576.2).

AFM Measurements of Lipid Bilayers

In order to investigate the surface topography of the lipid bilayer, lipid bilayers were prepared on mica as described previously (Iijima et al., 2009; Matsubara et al., 2013). Briefly, a POPC lipid monolayer at an air–water interface was prepared on a Langmuir–Blodgett trough at 25°C with a subphase of water, and transferred to freshly cleaved mica (1 × 1 cm) by horizontal deposition at a surface pressure of 35 mN m^{-1} (POPC-coated mica). A second lipid monolayer of pep-PE (or DPPE, DOPC, GM3, or pep-PE/DOPC) was loaded onto POPC-coated mica by horizontal deposition at a surface pressure of 30 mN m^{-1} to give a lipid bilayer.

The lipid bilayer was incubated with HA solution for 1 h at 25°C to observe the binding of H1 HA. After washing three times with phosphate-buffered saline (PBS), the lipid monolayer was subjected to AFM measurements.

AFM measurements of lipid bilayers on mica were carried out using SPM-9600 (Shimadzu Co., Japan) in water at 25°C. A 38-μm-long soft cantilever (BL-AC40TS-C2, Olympus) with integrated pyramidal silicon nitride tips having a spring constant of 0.1 Nm^{-1} was used for all measurements.

A number of topographic images were taken in the dynamic mode at a scanning rate in the range of 1–2 Hz, and the occupied area of target domains was estimated from typical multiple images ($n = 3$, 1×1 μm). In the estimation of domains, AFM images were binarized on the basis of the heights of the membrane, and pixels were counted using image processing software (Adobe Photoshop Elements). For example, the white area of a binarized image by thresholding at 8 nm from the bottom was identified as the area of the HA-bound domain of the pep-PE membrane (**Figure 3**).

Enzyme-Linked Immunosorbent Assay (ELISA)

A lipid monolayer of pep-PE/DOPC (50:50) or DOPC was directly loaded onto a few dozen plastic plates (13.5 mm in diameter; code 174950, Nalge Nunc international) by horizontal deposition at a surface pressure of 30 mN m^{-1}. IFV [800–5600 plaque-forming units (pfu)] in 0.2 mL of PBS was incubated at 25°C for 1 h in pep-PE/DOPC- or DOPC-transferred plastic plates. The plates were washed three times with PBS, and their contents were then transferred into a 24-well plates that were blocked with 5% bovine serum albumin (BSA)/PBS at 4°C overnight.

The IFV-bound plates were incubated with a 1:1000 (v/v) dilution of an anti-hemagglutinin (A/H1N1) antibody (RayBiotech Inc.) for 1 h, and the primary antibody was then labeled with a 1:1000 (v/v) dilution of a peroxidase-conjugated anti-mouse IgG antibody (Merck Millipore) for 1 h. Color was developed using *o*-phenylenediamine, and changes in absorbance (ΔA) at 492 nm were determined by a microplate reader. Each experiment was performed in triplicate.

rRT-PCR

The pep-PE/DOPC (50:50) lipid monolayer was attached horizontally to plastic plates as described above. IFV (H1N1, A/Puerto Rico/8/34; 1600 pfu in 0.14 mL of PBS) was incubated at 25°C for 1 h on the pep-PE/DOPC-transferred plastic plates. After washing with PBS, plates were incubated with AVL viral lysis buffer (QIAamp Viral RNA Mini Kit, QIAGEN) for 10 min. Viral RNA was extracted according to the manufacturer's instructions.

One-step RT-PCR was performed using QuantiTect SYBR Green PCR Kit (QIAGEN) with forward and reverse primers for the sequences of the matrix protein (M) gene for 244 bp (forward M30F2/08: 5′-ATGAGYCTTYTAACCGAGGTCGAAACG-3′; reverse M264R3/08: 5′-TGGACAAANCGTCTACGCTGCAG-3′; Eisfeld et al., 2014). The reaction was performed using a PikoReal Real-Time PCR system (TCR0096, Thermo Scientific). PCR was set up in a 10-μL reaction volume containing 5 μL of 2 × QuantiTect SYBR Green RT-PCR master mix, 0.1 μL of QuantiTect RT Mix, 0.5 μL of RNA template, 1 μL of forward and reverse primers (10 μM each), and 3.4 μL of RNase free water. The optimized cycling conditions were as follows: RT reaction at 50°C for 2 min, 95°C for 15 min, initial denaturation at 95°C for 30 s, followed by 50 cycles of denaturation at 95°C for 5 s, primer annealing at 57°C for 20 s, and extension at 72°C for 10 s. Fluorescence was measured at the end of each cycle. A melt curve analysis was performed following amplification in order to verify the specificities of the amplified products. A melting curve analysis consisted of 60°C for 30 s, and followed by a temperature increase to 95°C for 10 s with the continuous reading of fluorescence. The amplified products were analyzed by agarose gel electrophoresis (2.5% agarose) and detected by staining with ethidium bromide (Supplementary Figure 3A).

A series of two-fold dilutions of the virus solution starting from 400 to 3200 pfu were prepared in order to construct a standard curve. A liner regression relationship was observed between the amount of the virus and threshold cycle (C_t) values with a coefficient of determination (R^2) of 0.954 (Supplementary Figure 3B). The amount of virus that remained on the pep-PE/DOPC (50:50) membrane was estimated from the standard curve.

RESULTS

Synthesis of Peptide-Conjugated DPPE

The sialic acid-mimic pentapeptide (Ala-Arg-Leu-Pro-Arg; Matsubara et al., 2010) was conjugated with DPPE by click chemistry to immobilize the HA-binding peptide on the lipid membrane (**Figure 1A**). Prior to the click reaction, the pentapeptide was modified with an azide group through the side chain of Lys (Ala-Arg-Leu-Pro-Arg-Lys(N_3)-NH_2, **1**; Supplementary Figure 1A). On the other hand, DPPE was modified with 4-pentynoic acid to give *N*-(4-pentynoyl)-DPPE (**2**, Supplementary Figure 1B). The click reaction of **1** and **2** quantitatively gave peptide-conjugated DPPE (pep-PE, **3**), and pep-PE was purified by HPLC and determined by MALDI-TOF MS (Supplementary Figure 1C).

Binding of H1 HA to the pep-PE Membrane

A lipid monolayer of pep-PE was loaded onto POPC-coated mica to give a lipid bilayer that exposed the pep-PE layer (pep-PE membrane, **Figure 1B**; Matsubara et al., 2013). The surface topography of the pep-PE membrane was observed by AFM, and revealed that the height of the lipid domain was ∼5.5 nm (**Figure 2A**). On the other hand, the height of the DPPE domain was ∼3.5 nm (**Figure 2B**); therefore, the height of pep-PE was higher than that of DPPE. The difference in height (2.0 nm) was attributed to the size of the pentapeptide.

HA of the H1N1 strain (A/New Caledonia/20/99) was interacted with the pep-PE membrane at 25°C for 1 h to investigate the binding of influenza HA, and the surface topography was observed by AFM. In order to illuminate the HA-bound area, the original AFM image was binarized on the basis of the height of the membrane (8 nm threshold) because

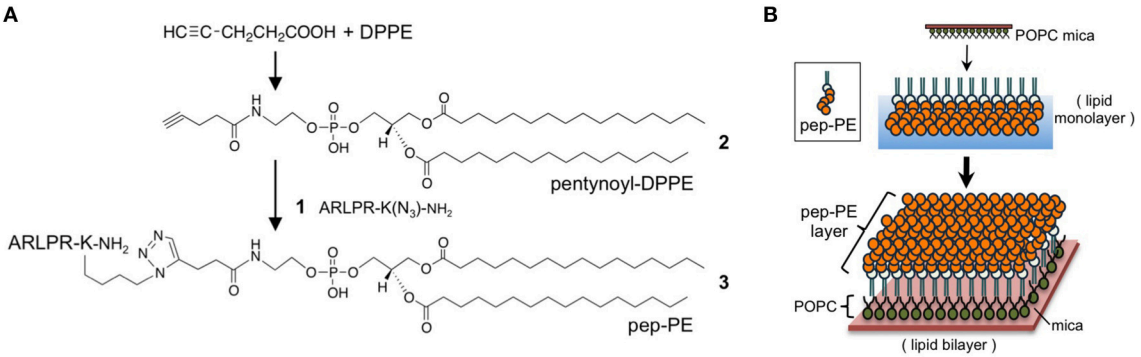

FIGURE 1 | Preparation of peptide-conjugated lipid membrane. (A) Synthesis of a peptide-conjugated lipid. Alkyne-modified dipalmitoylphosphatidylethanolamine (DPPE) was prepared from 4-pentynoic acid and DPPE. The click reaction of the *N*-(4-pentynoyl)-DPPE (pentynoyl-DPPE, (**2**) and an azide-containing pentapeptide (**1**) gave peptide-conjugated DPPE (pep-PE, **3**). ARLPR, Ala-Arg-Leu-Pro-Arg. **(B)** Procedure of construction of pep-PE lipid membrane. A pep-PE monolayer was transferred to the POPC-coated mica to give the pep-PE lipid bilayer.

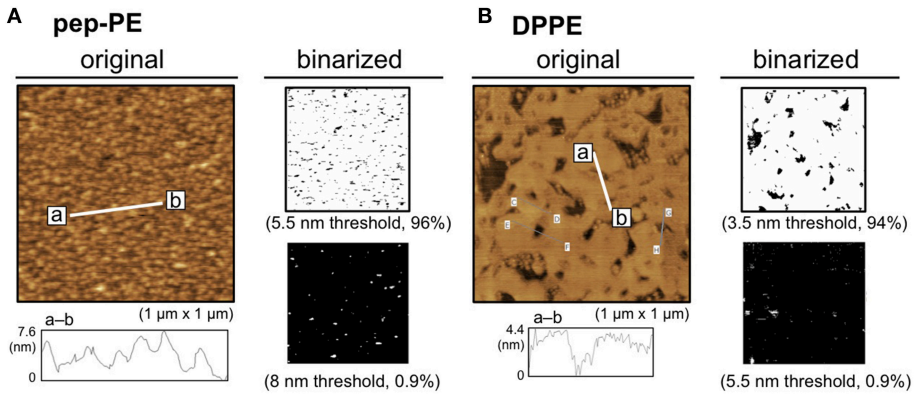

FIGURE 2 | Surface topographic studies of pep-PE and DPPE membranes by AFM. (A) AFM image (original) and binarized AFM images (binarized) of the pep-PE membrane. In order to illuminate the area of higher lipid domains, an original AFM image (*left*) was binarized on the basis of the heights of the membrane (5.5 and 8 nm thresholds; *right*). **(B)** AFM image (original) and binarized AFM images (binarized) of the DPPE membrane. The original AFM image (*left*) was binarized on the basis of the heights of the membrane (3.5 and 5.5 nm thresholds; *right*).

the height of the bare pep-PE membrane was not greater than 8 nm (**Figures 2A**, **3A**). The percentage of white pixels in binarized images was regarded as the HA-bound area. The HA-bound area increased in proportion to HA concentrations, and 65% of the membrane surface was covered at 24 nM of HA (**Figure 3B**). On the other hand, HA showed no significant binding to the DPPE membrane (10% or lower). These results indicated that the binding of HA was responsible for the sialic acid-mimic peptide of pep-PE.

Binding of H1 HA to the GM3 Membrane

The ganglioside GM3 is an IFV receptor because HA binds to GM3 through the sialyllactose structure (Suzuki et al., 1986; Sato et al., 1996). The binding of HA to the GM3 membrane was investigated using AFM as well as pep-PE. The lipid bilayer that exposed the GM3 layer (the GM3 membrane) was prepared, and its surface topography was then observed by AFM. GM3 was similar in height to DPPE, at ∼4 nm (**Figure 4A**). After the H1 HA incubation, the HA-bound area was estimated by the binarization of AFM images (6 nm threshold; **Figure 4B**, *left*). Similar to pep-PE, the HA-bound area increased in proportion to HA concentrations (**Figure 4B**, *right*). These results indicated that pep-PE has potential as an alternative to capture HA instead of GM3.

Construction of the pep-PE/DOPC Membrane

Glycosphingolipids (GSLs) such as gangliosides and neutral GSLs are enriched in the membrane microdomain, e.g., membrane (lipid) raft, of animal cell membranes (Pike, 2006). The membrane microdomain is one of the functional units in the membrane, and is considered to contribute to the many biological activities of lipids and proteins (Simons and Ikonen, 1997). The phase separation of the (glyco) sphingolipid/cholesterol/PC ternary system occurs in the presence of phosphatidylcholine (PC) with unsaturated acyl

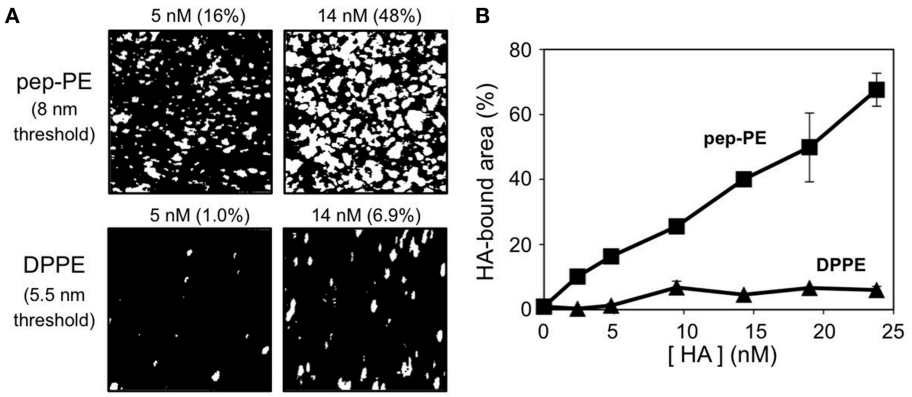

FIGURE 3 | Concentration-dependent binding of H1 HA on the pep-PE membrane. (A) Binarized images of HA-bound pep-PE and DPPE membranes. AFM images were taken after the H1 HA incubation at 25°C for 1 h ([HA] = 2.4–24 nM). In order to illuminate the HA-bound area, original AFM images were binarized on the basis of the heights of the membranes (8 or 5.5 nm threshold). The percentage of white pixels in binarized images was estimated as the HA-bound area. **(B)** The HA-bound area was plotted as a function of HA concentration (H1 HA, $n = 3$).

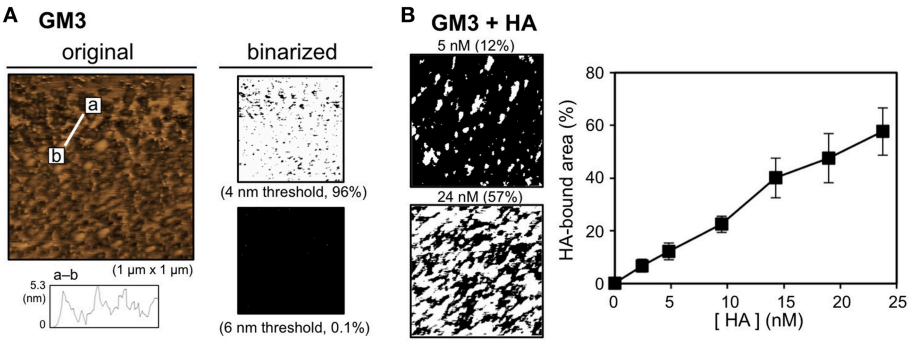

FIGURE 4 | Surface topographic study and the binding of H1 HA on the GM3 membrane. (A) AFM image (original) and binarized AFM images (binarized) of the GM3 membrane. The original AFM image (*left*) was binarized on the basis of the heights of the membranes (4 and 6 nm thresholds; *right*). **(B)** Concentration-dependent binding of H1 HA on the GM3 membrane. AFM images were taken after the H1 HA incubation at 25°C for 1 h ([HA] = 2.4–24 nM). Binarized images of the HA-bound GM3 membrane at [HA] = 5 and 24 nM (6 nm threshold; *left*). The HA-bound area was plotted as a function of HA concentration (H1 HA, $n = 3$; *right*).

chain(s) such as POPC (Simons and Ikonen, 1997; de Almeida et al., 2003). Phase separation is detectable by height differences between the three phases; solid-ordered (s_o), liquid-ordered (L_o), and liquid-disordered (L_d) domains, by AFM imaging (Johnston, 2007). We previously investigated the interaction between wheat germ agglutinin (WGA) and a GM3-containing membrane composed of lipids extracted from mouse B16 melanoma cells (Iijima et al., 2009). Since the results of AFM indicated that WGA binds to the highest domain [L_o and/or s_0 phase(s)], this domain was identified as the GM3-enriched area.

Phase separation is responsible for differences in the phase transition temperatures (T_m) of lipids; therefore, we have the ability to design model membranes composed of a low T_m lipid (e.g., unsaturated PC), high T_m lipid (a saturated PC or a sphingolipid), and cholesterol (de Almeida et al., 2003). In the present study, DOPC was mixed with pep-PE to prepare a membrane raft-like domain, and the binding of HA was investigated. A lipid monolayer of a mixture of pep-PE and DOPC (50:50, molar ratio) was loaded onto POPC-coated mica to give a lipid bilayer that exposed the pep-PE/DOPC layer (pep-PE/DOPC membrane). AFM images of the pep-PE/DOPC (50:50) membrane clearly showed phase separation, and the highest domain was estimated to be an area of 50% from a binarized image (5.5 nm threshold; **Figure 5A**). Since the height of DOPC was ∼3.5 nm (**Figure 5B**), the highest domain in the pep-PE/DOPC (50:50) membrane was considered to be the pep-PE-containing domain.

Binding of H1 HA to the pep-PE/DOPC Membrane

The HAs of H1 and H3 were interacted with the pep-PE/DOPC (50:50) membrane at 25°C for 1 h, and the HA-bound area was estimated from binarized images as described above (8 nm threshold). In the case of H1 HA, the HA-bound area showed a saturation curve against HA concentrations (**Figure 6A**).

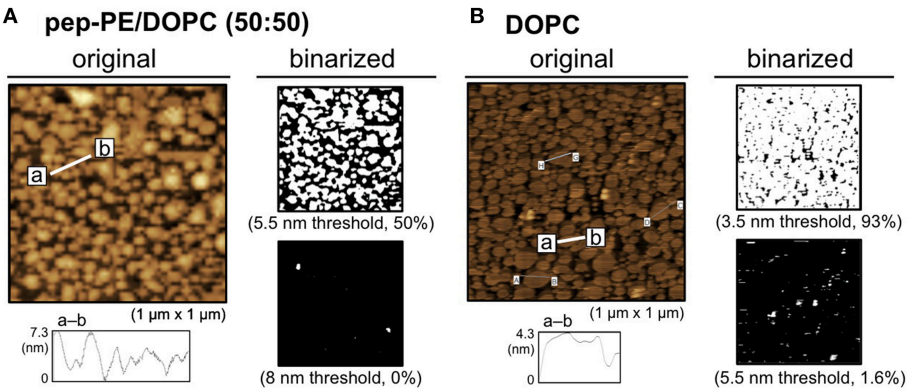

FIGURE 5 | Surface topographic studies of pep-PE/DOPC (50:50) and DOPC membranes by AFM. (A) AFM image (original) and binarized AFM images (binarized) of the pep-PE/DOPC (50:50, molar ratio) membrane. Binarized images were generated by 5.5 and 8 nm thresholds. **(B)** AFM image (original) and binarized AFM images (binarized) of the DOPC membrane. Binarized images were generated by 3.5 and 5.5 nm thresholds.

Although the content of pep-PE was reduced to 50 mol%, the HA-bound area of pep-PE/DOPC (50:50) membrane at around 5–20 nM was comparable to that of pep-PE membrane (**Figure 3**). The HA-bound area (49%) at 24 nM was similar to that of pep-PE domain (50%; **Figure 5A**), indicating that the pep-PE domain was covered with HA. Furthermore, in the case of the GM3/DOPC (50:50) membrane, the HA-bound area was significantly smaller (22%) than that of the GM3 membrane (48%; **Figures 6B**, **4B**), suggesting the superiority of pep-PE over GM3 for HA binding.

On the other hand, the binding of HA to pep-PE/DPPC (50:50) was significantly less than that to pep-PE/DOPC (50:50; **Figure 6A**). A comparison with the AFM image of pep-PE/DOPC (50:50), as shown in **Figure 5A**, revealed the absence of the distinct phase separation of pep-PE/DPPC (50:50; Supplementary Figure 2). This was attributed to the T_m value of pep-PE being markedly different from that of DOPC (−3°C; Koster et al., 1994) and closer to that of DPPE (64°C; Ramezani et al., 2009) and DPPC (41.5°C; Parasassi et al., 1991). Hashizume et al. previously reported that an extensive affinity for lectin was induced by the phase separation of lactosylceramide (LacCer) in a LacCer/DOPC membrane (Hashizume et al., 1998). These findings suggest that the affinity of HA for a pep-PE-containing membrane increases with the formation of a raft-like domain in the presence of DOPC.

In order to investigate the interactions of pep-PE with other proteins, H3 HA, the anti-GM3 antibody, WGA, and two types of serum albumin were incubated with pep-PE/DOPC (50:50; **Figure 6C**). The amount of H3 HA that bound to the pep-PE/DOPC (50:50) membrane was lower than that of H1 HA (**Figure 6A**). An anti-GM3 antibody and WGA showed a lower amount of binding to the pep-PE/DOPC (50:50) membrane than HAs, and no binding was observed by human serum albumin (HSA) or bovine serum albumin (BSA) was observed (**Figure 6C**).

These results indicate that HA specifically interacts with the pep-PE/DOPC (50:50) membrane, and the composition of pep-PE/DOPC (50:50) has the potential to detect HA and IFV effectively.

Capture of IFV by the pep-PE/DOPC Membrane

The binding of IFV of the H1N1 strain (A/Puerto Rico/8/34) to the pep-PE/DOPC membrane and DOPC membrane (as control) was evaluated by ELISA. IFV solutions containing 800, 1600, and 5600 pfu were incubated with membranes at 25°C for 1 h, and IFV that bound to the membranes was then detected. The absorbance of the pep-PE/DOPC (50:50) membrane was significantly increased at more than 1600 pfu (**Figure 7A**).

The amount of IFV that bound to the pep-PE/DOPC (50:50) membrane was quantified by rRT-PCR as described elsewhere (Tsukamoto et al., 2009). The specific amplification of the products (244 bp) from matrix protein (M) gene (Eisfeld et al., 2014) was confirmed by a melting curve analysis and agarose gel electrophoresis (Supplementary Figure 3A). A standard curve was constructed, and a linear regression relationship was observed between the amount of the virus (pfu) and the threshold cycle (C_t) values was observed with a coefficient of determination (R^2) of 0.954 and slope of −0.00199 (Supplementary Figure 3B). After the incubation of virus (1600 pfu) with the membrane for 1 h, 570 pfu of the virus was captured on the pep-PE/DOPC (50:50) membrane, and 100 pfu on the DOPC membrane (**Figure 7B**). These results indicate that IFV selectively binds to pep-PE-containing membranes.

DISCUSSION

Sialyloligosaccharide-containing compounds such as ganglioside GM3 are selected in order to capture HA and IFV on a solid support and are applied for immobilization onto microplates, (Totani et al., 2003) thin-layer chromatography plates, (Suzuki et al., 2000) the gold electrode of quartz-crystal microbalances, (Sato et al., 1996) the sensor chip of surface plasmon resonances,

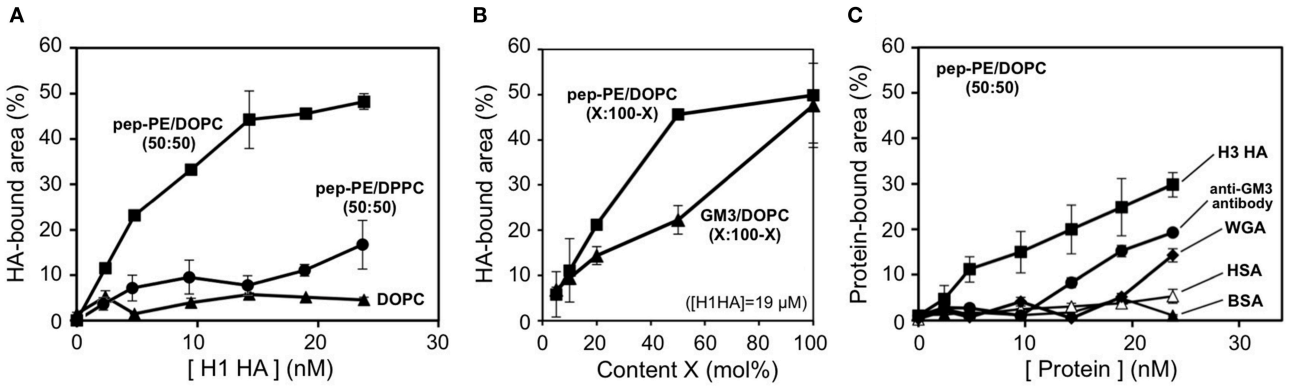

FIGURE 6 | Binding of HAs and proteins to the pep-PE/DOPC membrane. (A) HA-bound areas of the pep-PE/DOPC (50:50), pep-PE/DPPC (50:50), and DOPC membranes were plotted as a function of HA concentration (H1 HA, $n = 3$). The HA-bound area was estimated from binarized AFM images (8 or 5.5 nm threshold, respectively). **(B)** HA-bound areas of the pep-PE/DOPC (X:100-X) and GM3/DOPC (X:100-X) membranes were plotted as a function of pep-PE and GM3 content X ([H1 HA] = 19 μM, $n = 3$). **(C)** Protein-bound areas of the pep-PE/DOPC (50:50) membrane were plotted as a function of protein concentration ($n = 3$). H3 HA, an anti-GM3 antibody, wheat germ agglutinin (WGA), human serum albumin (HSA), and bovine serum albumin (BSA) were incubated with the pep-PE/DOPC (50:50) membrane for at 25°C 1 h. The protein-bound area was estimated from binarized AFM images (8 nm threshold).

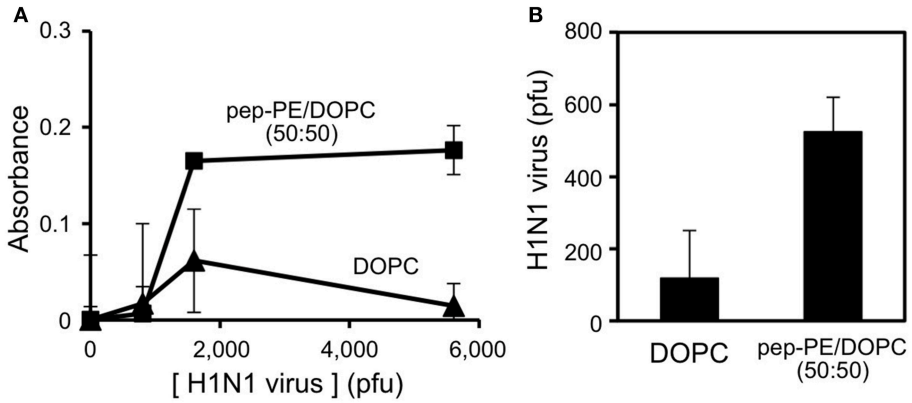

FIGURE 7 | Detection of IFV-binding to the pep-PE/DOPC (50:50) membrane by ELISA (A) and rRT-PCR (B). IFV (H1N1 strain) was interacted with the pep-PE/DOPC (50:50) membrane or DOPC membrane at 25°C for 1 h.

(Hidari et al., 2007) glycan microarrays, (Smith and Cummings, 2014) and nanoparticles, (Jannetto et al., 2010). Various (sialyl) glycoconjugates are needed to conduct these methods. (Koeller and Wong, 2001; Feizi et al., 2003) We have proposed the application of peptides with the ability to bind to lectin instead of glycoconjugates (Matsubara et al., 2010; Matsubara, 2012; Hatano et al., 2014). Such peptides bind to the receptor-binding site by mimicking (sialyl) oligosaccharide structures.

In the present study, we designed a peptide-conjugated lipid with the ability to play the role of gangliosides in the cell membrane. A sialic acid-mimic pentapeptide was conjugated to DPPE by click chemistry (**Figure 1;** Tornøe et al., 2002) and peptide-conjugated DPPE (pep-PE) was used as a constituent of the lipid bilayer (**Figure 2**). Pep-PE-containing lipid bilayers were prepared and immobilized on mica or plastic plates for AFM (**Figures 3**, **5**). When pep-PE co-existed with an unsaturated PC, the pep-PE-containing membrane (pep-PE/DOPC, 50:50) exhibited useful affinity for HA and IFV (**Figures 6**, **7**). AFM images indicated that pep-PE/DOPC membrane forms pep-PE-enriched domains (**Figure 5**), and this excellent affinity for HA and IFV is due to domain formation. This domain is known as a membrane microdomain (membrane raft), and we successfully constructed an artificial lipid bilayer composed of peptide-conjugated lipids without GSLs. Furthermore, ELISA and rRT-PCR indicated that IFV selectively bound to the pep-PE-containing membrane (**Figure 7**).

A comparison with ganglioside GM3 revealed that the ability of pep-PE to capture HA and IFV. The amount of HA that bound to the pep-PE membrane was similar to that of HA to the GM3 membrane (**Figures 3**, **4**). On the other hand, the affinity of HA for the pep-PE-containing membrane was improved by the co-existence of DOPC (pep-PE/DOPC, 50:50; **Figure 6**). These results indicate that pep-PE is superior to GM3 for the binding of HA and IFV to mixed lipid membranes.

Sialylglycoconjugates are valuable compounds, and specific techniques and extensive efforts are required for their organic synthesis and isolation from natural sources (Koeller and Wong, 2001; Feizi et al., 2003). In order to detect proteins and pathogenic materials, glycoconjugates are immobilized on solid supports after biotinylation or another derivatization (Angus et al., 2000; Grün et al., 2006). There are several advantages to using the peptides described in the present study instead of glycoconjugates such as ganglioside GM3: (1) Functional peptides may be obtained by a *de novo* design and affinity selection system including phage-display technology, (Ladner et al., 2004) (2) since peptides are chemically stable, they may be stored for long periods of time, and (3) procedures to produce peptides have already been established (e.g., chemical synthesis) such that peptides are produced cheaply and in large quantities (Bray, 2003). As shown in the present study, the peptide-conjugated lipid was easy to synthesize using a click reaction. Instead of glycoconjugates, artificial peptides that mimic glycoconjugates are considered to be applicable to the capture of glycan-related proteins and pathogenic materials.

CONCLUSION

In the present study, we showed that HA and IFV are detectable using a HA-binding peptide-conjugated lipid. This peptidyl lipid was able to be prepared for a lipid bilayer, and the affinity of HA was improved by domain formation in the presence of unsaturated PC. If a sufficient variety of sugar-mimic peptides is designed, these peptide-conjugated lipids may be used in addition to GSLs. The synthesis of the peptide-conjugated lipid is easier than that of glycolipids. Along with other glycoconjugates, sugar-mimic peptides and peptide-conjugated lipids have the ability to immobilize on nano- and microplates, nanoparticles, and other materials. In addition to IFV, peptide-conjugated lipids have the potential to detect biomolecules, toxins, viruses, and pathogenic materials. Peptide-conjugated lipids may be useful not only for the diagnosis and surveillance of influenza, but also those of other sugar-related diseases.

AUTHOR CONTRIBUTIONS

TS conceived the project and TM and TS designed the research. RS and TM conducted experiments, and all authors discussed the results and implications. TM and TS prepared the manuscript.

ACKNOWLEDGMENTS

This study was supported by JSPS KAKENHI Grant Numbers 23106726 (T.S.).

SUPPLEMENTARY MATERIAL

The Supplementary Material for this article can be found online at: http://journal.frontiersin.org/article/10.3389/fmicb.2016.00468

REFERENCES

Angus, D. I., Kiefel, M. J., and von Itzstein, M. (2000). The synthesis of biotinylated carbohydrates as probes for carbohydrate-recognizing proteins. *Bioorg. Med. Chem.* 8, 2709–2718. doi: 10.1016/S0968-0896(00)00201-7

Bray, B. L. (2003). Large-scale manufacture of peptide therapeutics by chemical synthesis. *Nat. Rev. Drug Discov.* 2, 587–593. doi: 10.1038/nrd1133

de Almeida, R. F., Fedorov, A., and Prieto, M. (2003). Sphingomyelin/phosphatidylcholine/cholesterol phase diagram: boundaries and composition of lipid rafts. *Biophys. J.* 85, 2406–2416. doi: 10.1016/S0006-3495(03)74664-5

Eisfeld, A. J., Neumann, G., and Kawaoka, Y. (2014). Influenza A virus isolation, culture and identification. *Nat. Protoc.* 9, 2663–2681. doi: 10.1038/nprot.2014.180

Feizi, T. (2013). Carbohydrate recognition in the immune system: contributions of neoglycolipid-based microarrays to carbohydrate ligand discovery. *Ann. N. Y. Acad. Sci.* 1292, 33–44. doi: 10.1111/nyas.12210

Feizi, T., Fazio, F., Chai, W., and Wong, C. H. (2003). Carbohydrate microarrays - a new set of technologies at the frontiers of glycomics. *Curr. Opin. Struct. Biol.* 13, 637–645. doi: 10.1016/j.sbi.2003.09.002

Gamblin, S. J., and Skehel, J. J. (2010). Influenza hemagglutinin and neuraminidase membrane glycoproteins. *J. Biol. Chem.* 285, 28403–28409. doi: 10.1074/jbc.R110.129809

Grün, C. H., van Vliet, S. J., Schiphorst, W. E., Bank, C. M., Meyer, S., van Die, I., et al. (2006). One-step biotinylation procedure for carbohydrates to study carbohydrate-protein interactions. *Anal. Biochem.* 354, 54–63. doi: 10.1016/j.ab.2006.03.055

Hashizume, M., Sato, T., and Okahata, Y. (1998). Selective bindings of a lectin for phase-separated glycolipid monolayers. *Chem. Lett.* 27, 399–400. doi: 10.1246/cl.1998.399

Hatano, K., Matsubara, T., Muramatsu, Y., Ezure, M., Koyama, T., Matsuoka, K., et al. (2014). Synthesis and influenza virus inhibitory activities of carbosilane dendrimers peripherally functionalized with hemagglutinin-binding Peptide. *J. Med. Chem.* 57, 8332–8339. doi: 10.1021/jm5007676

Hidari, K. I., Shimada, S., Suzuki, Y., and Suzuki, T. (2007). Binding kinetics of influenza viruses to sialic acid-containing carbohydrates. *Glycoconj. J.* 24, 583–590. doi: 10.1007/s10719-007-9055-y

Iijima, K., Soga, N., Matsubara, T., and Sato, T. (2009). Observations of the distribution of GM3 in membrane microdomains by atomic force microscopy. *J. Colloid Interface Sci.* 337, 369–374. doi: 10.1016/j.jcis.2009.05.032

Jannetto, P. J., Buchan, B. W., Vaughan, K. A., Ledford, J. S., Anderson, D. K., Henley, D. C., et al. (2010). Real-time detection of influenza a, influenza B, and respiratory syncytial virus a and B in respiratory specimens by use of nanoparticle probes. *J. Clin. Microbiol.* 48, 3997–4002. doi: 10.1128/JCM.01118-10

Johnston, L. J. (2007). Nanoscale imaging of domains in supported lipid membranes. *Langmuir* 23, 5886–5895. doi: 10.1021/la070108t

Koeller, K. M., and Wong, C. H. (2001). Enzymes for chemical synthesis. *Nature* 409, 232–240. doi: 10.1038/35051706

Koster, K. L., Webb, M. S., Bryant, G., and Lynch, D. V. (1994). Interactions between soluble sugars and POPC (1-palmitoyl-2-oleoylphosphatidylcholine) during dehydration: vitrification of sugars alters the phase behavior of the phospholipid. *Biochim. Biophys. Acta* 1193, 143–150. doi: 10.1016/0005-2736(94)90343-3

Ladner, R. C., Sato, A. K., Gorzelany, J., and de Souza, M. (2004). Phage display-derived peptides as therapeutic alternatives to antibodies. *Drug Discov. Today* 9, 525–529. doi: 10.1016/S1359-6446(04)03104-6

Matsubara, T. (2012). Potential of peptides as inhibitors and mimotopes: selection of carbohydrate-mimetic peptides from phage display libraries. *J. Nucleic Acids* 2012:740982. doi: 10.1155/2012/740982

Matsubara, T., Iijima, K., Yamamoto, N., Yanagisawa, K., and Sato, T. (2013). Density of GM1 in nanoclusters is a critical factor in the formation of a spherical assembly of amyloid beta-protein on synaptic plasma membranes. *Langmuir* 29, 2258–2264. doi: 10.1021/la3038999

Matsubara, T., Onishi, A., Saito, T., Shimada, A., Inoue, H., Taki, T., et al. (2010). Sialic acid-mimic peptides as hemagglutinin inhibitors for anti-influenza therapy. *J. Med. Chem.* 53, 4441–4449. doi: 10.1021/jm1002183

Matsubara, T., Sumi, M., Kubota, H., Taki, T., Okahata, Y., and Sato, T. (2009). Inhibition of influenza virus infections by sialylgalactose-binding peptides selected from a phage library. *J. Med. Chem.* 52, 4247–4256. doi: 10.1021/jm801570y

Parasassi, T., De Stasio, G., Ravagnan, G., Rusch, R. M., and Gratton, E. (1991). Quantitation of lipid phases in phospholipid vesicles by the generalized polarization of Laurdan fluorescence. *Biophys. J.* 60, 179–189. doi: 10.1016/S0006-3495(91)82041-0

Pike, L. J. (2006). Rafts defined: a report on the keystone symposium on lipid rafts and cell function. *J. Lipid Res.* 47, 1597–1598. doi: 10.1194/jlr.E600002-JLR200

Ramezani, M., Khoshhamdam, M., Dehshahri, A., and Malaekeh-Nikouei, B. (2009). The influence of size, lipid composition and bilayer fluidity of cationic liposomes on the transfection efficiency of nanolipoplexes. *Colloids Surf. B Biointerfaces* 72, 1–5. doi: 10.1016/j.colsurfb.2009.03.018

Sato, T., Serizawa, T., and Okahata, Y. (1996). Binding of influenza A virus to monosialoganglioside (GM3) reconstituted in glucosylceramide and sphingomyelin membranes. *Biochim. Biophys. Acta* 1285, 14–20. doi: 10.1016/S0005-2736(96)00138-1

Schneggenburger, P. E., Worbs, B., and Diederichsen, U. (2010). Azide reduction during peptide cleavage from solid support-the choice of thioscavenger? *J. Pept. Sci.* 16, 10–14. doi: 10.1002/psc.1202

Simons, K., and Ikonen, E. (1997). Functional rafts in cell membranes. *Nature* 387, 569–572. doi: 10.1038/42408

Skehel, J. J., and Wiley, D. C. (2000). Receptor binding and membrane fusion in virus entry: the influenza hemagglutinin. *Annu. Rev. Biochem.* 69, 531–569. doi: 10.1146/annurev.biochem.69.1.531

Smith, D. F., and Cummings, R. D. (2014). Investigating virus-glycan interactions using glycan microarrays. *Curr. Opin. Virol.* 7, 79–87. doi: 10.1016/j.coviro.2014.05.005

Suzuki, Y. (2005). Sialobiology of influenza: molecular mechanism of host range variation of influenza viruses. *Biol. Pharm. Bull.* 28, 399–408. doi: 10.1248/bpb.28.399

Suzuki, Y., Ito, T., Suzuki, T., Holland, R. E. Jr., Chambers, T. M., Kiso, M., et al. (2000). Sialic acid species as a determinant of the host range of influenza A viruses. *J. Virol.* 74, 11825–11831. doi: 10.1128/JVI.74.24.11825-11831.2000

Suzuki, Y., Nagao, Y., Kato, H., Matsumoto, M., Nerome, K., Nakajima, K., et al. (1986). Human influenza A virus hemagglutinin distinguishes sialyloligosaccharides in membrane-associated gangliosides as its receptor which mediates the adsorption and fusion processes of virus infection. Specificity for oligosaccharides and sialic acids and the sequence to which sialic acid is attached. *J. Biol. Chem.* 261, 17057–17061.

Tornøe, C. W., Christensen, C., and Meldal, M. (2002). Peptidotriazoles on solid phase: [1,2,3]-triazoles by regiospecific copper(i)-catalyzed 1,3-dipolar cycloadditions of terminal alkynes to azides. *J. Org. Chem.* 67, 3057–3064. doi: 10.1021/jo011148j

Totani, K., Kubota, T., Kuroda, T., Murata, T., Hidari, K. I., Suzuki, T., et al. (2003). Chemoenzymatic synthesis and application of glycopolymers containing multivalent sialyloligosaccharides with a poly(L-glutamic acid) backbone for inhibition of infection by influenza viruses. *Glycobiology* 13, 315–326. doi: 10.1093/glycob/cwg032

Tsukamoto, K., Ashizawa, T., Nakanishi, K., Kaji, N., Suzuki, K., Shishido, M., et al. (2009). Use of reverse transcriptase PCR to subtype N1 to N9 neuraminidase genes of avian influenza viruses. *J. Clin. Microbiol.* 47, 2301–2303. doi: 10.1128/JCM.02366-08

Wang, R., and Taubenberger, J. K. (2010). Methods for molecular surveillance of influenza. *Expert Rev. Anti Infect. Ther.* 8, 517–527. doi: 10.1586/eri.10.24

Watanabe, Y., Fuji, T., Hioki, K., Tani, S., and Kunishima, M. (2004). Development of a simple system for dehydrocondensation using solid-phase adsorption of a water-soluble dehydrocondensing reagent (DMT-MM). *Chem. Pharm. Bull.* 52, 1223–1226. doi: 10.1248/cpb.52.1223

Conflict of Interest Statement: The authors declare that the research was conducted in the absence of any commercial or financial relationships that could be construed as a potential conflict of interest.

Copyright © 2016 Matsubara, Shibata and Sato. This is an open-access article distributed under the terms of the Creative Commons Attribution License (CC BY). The use, distribution or reproduction in other forums is permitted, provided the original author(s) or licensor are credited and that the original publication in this journal is cited, in accordance with accepted academic practice. No use, distribution or reproduction is permitted which does not comply with these terms.

frontiers in Microbiology

ORIGINAL RESEARCH
published: 21 July 2016
doi: 10.3389/fmicb.2016.01147

Analysis of the Changes in Expression Levels of Sialic Acid on Influenza-Virus-Infected Cells Using Lectin-Tagged Polymeric Nanoparticles

Jaebum Cho[1], *Yukari Miyake*[2], *Ayae Honda*[2], *Keiichiro Kushiro*[1] *and Madoka Takai*[1]*

[1] Department of Bioengineering, The University of Tokyo, Tokyo, Japan, [2] Department of Frontier Bioscience, Hosei University, Tokyo, Japan

Viral infections affect millions around the world, sometimes leading to severe consequences or even epidemics. Understanding the molecular dynamics during viral infections would provide crucial information for preventing or stopping the progress of infections. However, the current methods often involve the disruption of the infected cells or expensive and time-consuming procedures. In this study, fluorescent polymeric nanoparticles were fabricated and used as bioimaging nanoprobes that can monitor the progression of influenza viral infection through the changes in the expression levels of sialic acids expressed on the cell membrane. The nanoparticles were composed of a biocompatible monomer to prevent non-specific interactions, a hydrophobic monomer to form the core, a fluorescent monomer, and a protein-binding monomer to conjugate lectin, which binds sialic acids. It was shown that these lectin-tagged nanoparticles that specifically target sialic acids could track the changes in the expression levels of sialic acids caused by influenza viral infections in human lung epithelial cells. There was a sudden drop in the levels of sialic acid at the initial onset of virus infection ($t = 0 \sim 1$ h) and at approximately 4∼5 h post-infection. The latter drop correlated with the production of viral proteins that was confirmed using traditional techniques. Thus, the accuracy, the rapidity and the efficacy of the nanoprobes were demonstrated. Such molecular bioimaging tools, which allow easy-handling and *in situ* monitoring, would be useful to directly observe and decipher the viral infection mechanisms.

Keywords: nanoparticles, sialic acid, lectin, polymers, infection

OPEN ACCESS

Edited by:
Akio Adachi,
University of Tokushima, Japan

Reviewed by:
Nejat Duzgunes,
University of the Pacific, USA
May Griffith,
Linköping University, Sweden

***Correspondence:**
Madoka Takai
takai@bis.t.u-tokyo.ac.jp

Specialty section:
This article was submitted to Virology, a section of the journal Frontiers in Microbiology

Received: *26 February 2016*
Accepted: *08 July 2016*
Published: *21 July 2016*

Citation:
Cho J, Miyake Y, Honda A, Kushiro K and Takai M (2016) Analysis of the Changes in Expression Levels of Sialic Acid on Influenza-Virus-Infected Cells Using Lectin-Tagged Polymeric Nanoparticles. Front. Microbiol. 7:1147. doi: 10.3389/fmicb.2016.01147

INTRODUCTION

Recently, viral infection has been a major global issue due to the dangers associated with the high death ratio and secondary diseases (Sun et al., 2011; Chen et al., 2012; Sichelstiel et al., 2014), also causing chronic infections in the case of negligence (Landford et al., 2010; Jacobson et al., 2011; Chen et al., 2013). However, the molecular interactions and mechanisms behind these viral infections have not been clarified. Many types of analytical methods have been developed for viral infection such as polymerase chain reaction (PCR) and enzyme-linked immunosorbent assay

(ELISA), but these assays involve disruptive cell lysis processes with expensive reagents due to the complicated nature of these protocols. In order to enable a detailed analysis and develop a deeper understanding of the viral infection process, it is necessary to develop a novel analytical system compatible with living cells.

During viral infection of cells, sialic acids on the cell membrane, which are oligosaccharides with glycoproteins and glycolipids, play essential roles. The influenza viral infection proceeds through the attachment of hemagglutinins (HA) on the viral membrane to sialic acids (de Lima et al., 1995; Fukuzawa et al., 2011; Lai et al., 2012; Zhu et al., 2012). HA is a viral coat glycoprotein, which binds to specific sialic acid receptors in the respiratory tract for penetration into the cell (Connor et al., 1994; Kuiken et al., 2006; Maines et al., 2009). In particular, specific kinds of influenza virus are associated with specific sialic acid binding and modifications for their pathogenic pathway, as well as the types of HA. When the influenza viruses penetrate into the cells for the infection, HA of the virus recognizes and binds to sialic acid on the cell membrane, and so, the expression level of sialic acid on the host cell is affected by viral infection (Ueda et al., 2013). Lectin, a class of carbohydrate-binding proteins, has high specificity for the specific sialic acid bound with other biomolecules. For example, *Sambucus nigra barks* lectin (SNA) can specifically recognize α-2,6-sialic acid and this type of sialic acid is known to be part of a recognizable glycan for binding by HA on viruses. To analyze the receptor-binding preferences, recognition mechanisms and changes in the expression levels of reacted sialic acids, it is necessary to assess the *in situ* changes in the cell membrane structures, such as glycans.

Recently, there have been multiple advances in bioimaging techniques to monitor cells using fluorescent nanoparticles, and they offer multiple advantages such as the capacity for real-time, non-disruptive monitoring of individual cells and ease of handling (Goto et al., 2008; Wolfbeis, 2015). In particular, a polymeric-nanoparticle-based bioimaging platform that can specifically and sensitively measure sialic acid levels have been developed (Cho et al., 2014). More specifically, this biocompatible bioimaging nanoprobe consist of 2-methacryloyloxyethyl phosphorylcholine (MPC), *n*-butyl methacrylate (BMA), *o*-nitrophenyloxycarbonyl polyethleneglycol methacrylate (MEONP), *p*-methacyloxyethyl thiocarbonyl rhodamine B (MTR), and lectin. MPC polymers prevent protein adsorption and thus makes the nanoprobe bioinert to most biomolecules (Moro et al., 2004; Goda et al., 2009). BMA is highly hydrophobic and thus, in conjunction with polylactic acid (PLA) forms the hydrophobic core of the nanoparticle. MEONP contains active ester groups that can conjugate other biomolecules, which in this case is streptavidin that subsequently bind the biotinylated lectin. MTR contains Rhodamine B, which have been safely used for the detection of mitochondria in the living cell in other bioimaging probes (Johnson et al., 1980). In this study, using these lectin-conjugated fluorescent polymeric nanoparticles as nanoprobes, simple and rapid analysis of sialic acid on the cell membrane were performed by tracking the fluorescence of the nanoprobes on the cells. This nanoprobe system was compared to some of the traditional methods to detect sialic acids, and it was suggested that these nanoprobes can be applied as a quick and reliable *in situ* bioimaging technology for the early detection of the changes in sialic acids and to further understand the process of viral infections.

MATERIALS AND METHODS

Reagents

Biotinylated *Sambucus nigra barks* lectin was purchased from Vector Laboratory (Burlingame, U.S.A). Phenylmethylsulfonyl fluoride (PMSF) was purchased from Calbiochem (Darmstadt, Germany). Anti-PB1 antibody was prepared by immunization of rabbit with purified PB1 protein. 4′,6-diamino-2-phenylindole (DAPI), rabbit immunoglobulin G (IgG) antibody and mouse IgG antibody with Alexa Flour 488 were purchased from Invitrogen (Carlsbad, CA, U.S.A). Ethylenediamine-N,N,N′,N′-tetraacetic acid (EDTA), N-cyclohexyl-3-aminopropanesulfonic acid (CAPS) and HEPES buffer solution were purchased from Dojindo (Kumamoto, Japan). Blocking one solution and Tris(hydromethyl) amino methane (Tris-base) were purchased from Nacalai tesque (Kyoto, Japan). Acrylamide, N′,N′-methylene bis(acrylamide) (bis), ammonium persulfate (APS), sodium dodecyl sulfate (SDS), paraformaldehyde (PFA) were purchased from Wako Pure Chemical Industries Co., Ltd. (Osaka, Japan). The details of the other reagents used for the nanoprobe fabrication and the cell probing are described in the previous study (Cho et al., 2014).

Fabrication of Bioimaging Nanoprobes

The details of the fabrication process of the nanoprobes, as well as their chemical and physical characterizations, are described in the previous study (Cho et al., 2014). Briefly, the polymer base of the nanoprobe was synthesized via free radical polymerization by combining MPC, BMA, MEONP, and MTR monomers with α-2,2′-Azobisisobutyronitrile (AIBN), dissolved in degassed ethanol at 0.5 M for the monomers and 10 mM for AIBN. The solution was reacted in the oil bath at 65°C for 15 h then precipitated in the 8:2 (v/v ratio) mixture of diethylether and chloroform, respectively.

For the formation of the nanoparticles, the solvent evaporation technique (Goda et al., 2009) was utilized and lectin was subsequently conjugated. Briefly, 0.1 wt% of PLA in dichloromethane solution was mixed with 0.1 wt% of the aqueous polymer solution, and under the stirring condition at 400 rpm and 0°C, the mixture was sonicated using a probe-type sonicator (VP-5S, TAITEC, Japan) for 5 min. The formed nanoparticles were collected by an ultracentrifuge (XL-A, Beckman Coulter, U.S.A.) ran at 50,000 rpm at 4°C for 2 h, and lastly dispersed in deionized water. For the immobilization of lectins onto the nanoparticle surfaces to complete the nanoprobes, the nanoparticles at 10 mg/mL were first reacted with streptavidin at 10 μg/mL for 3 h, which in turn was conjugated with 10 μg/mL biotinylated SNA lectin for 3 h. In each reaction step, the products were collected by centrifugation at 50,000 rpm at 4°C for 2 h. It should also be noted that the modular design of the nanoprobe enables conjugation of different bioactive molecules to MEONP for various applications.

Cell Culture and Viral Infection

For cell culturing of human lung epithelial cell (H292 from American Type Culture Collection), the E-MEM, and EDTA solution were prepared. 9.8 g of E-MEM was added in 900 mL of deionized water. The solution was autoclaved for sterilization. After cooling of the autoclaved solution at the room temperature, FBS, L-glutamine and 7.5% of $NaHCO_3$ were added in the solution. 7.5% of $NaHCO_3$ was filtered with 0.2 μm of filter. In the serum-free E-MEM, other components except FBS were added. Two types of EDTA solution were prepared: 0.4% in water and 0.04% in DPBS.

To infect influenza virus into the cells, 3×10^4 cells/well of H292 cells were cultured in the glass-bottom 96 well overnight. The cultured cells were washed with serum-free E-MEM medium. The washed cells were pre-incubated in 50 μL of the viral solution (multiplicity of infection of 1) for 1 h at 34°C. The solution included PR8 influenza A virus (H1N1) strain in the serum-free E-MEM. After pre-incubation, 100 μL of E-MEM medium was added in the dish. In the medium, the pre-incubated cells were cultured for infection at 34°C from 1 to 5 h.

Western Blotting and Dot Blot Assay for Detecting the Expression Level of Sialic Acid

For the Western blotting on the PVDF membrane, the cell proteins were extracted by cell lysis. Both the virus-infected and uninfected cells were cultured and sonicated five times for 10 s after addition of 0.1 M phenylmethanesulfonyl fluoride with the extraction buffer. The proteins of the sonicated cells in the solution were separated by centrifugation (15,000 rpm, 4°C, 30 min). The collected cell proteins were heated at 95°C for 3 min, and then the electrophoresis was performed. The samples including cellular proteins were separated on the SDS-PAGE at 30 mA for 1 h and soaked in 10 mM CAPS buffer containing 10% methanol (pH 11) for 20 min. The concentration of CAPS buffer (pH 11) was 0.01 M in deionized water (60-fold diluted from the original solution). After treatment with the membrane in CAPS buffer for 20 min, the sample was blotted by the electrophoresis on PVDF membrane (Nippon Genetics) at 4°C for 1 h. Then, the membrane was treated in the blocking one solution at 37°C for 30 min. On the membrane with cell proteins for various cell concentrations, 10 μg/mL of biotinylated SNA lectin were reacted for 12 h at the room temperature. After washing with DPBS twice in the rotary shaker (NA-301, Nissin, Tokyo, Japan) for 10 min, 10 μg/mL of Alexa-Fluor-488-conjugated streptavidin was reacted on the lectin-immobilized membrane for 12 h at the room temperature. The fluorescence images of the reacted membrane was washed with DPBS twice in the shaker for 10 min, and observed by image analyzer (Typhoon9410, GE Healthcare Life Sciences, Buckinghamshire, U.K.).

For the dot blot assay, attached cells in the dish were removed by treatment with trypsin. Removed cells were harvested by centrifugation at 700 rpm for 5 min at 4°C. The cell pellet was disrupted by adding glass beads in 100 μL Milli-Q water and centrifuged at 6500 rpm using Precelly 24 (Bertin, Provence, France) for 20 s, and placed on ice for 5 s. The disruption of cells was completed after 7 cycles. After the disruption of the cells, the supernatant was harvested by centrifugation at 15000 rpm for 5 min at 4°C and treated with trypsin adjusted to 0.01% for 30 min at 37°C. The supernatant equivalent to 10^5 cells was dotted on the PVDF membrane, reacted with lectin and detected with the chemiluminescence using the luminescent image analyzer.

Bioimaging of the Expression Level of Sialic Acid on the Virus-Infected Cells Using Nanoprobes

Before the cellular experiment, H292 cells infected with influenza virus were incubated from 1 to 5 h at 34°C in the glass bottom 96-well plate with 100 μL of E-MEM medium. On the cells in the well plate, 10 μL of nanoprobe solution were added and reacted with H292 for 15 min at 34°C, respectively. The cells were then washed with PBS three times at room temperature, and then observed at 100x magnification using a fluorescence microscope (Nikon TiE microscope, Japan). The fluorescence intensities were quantified to determine the levels of sialic acid expression levels on the infected cells.

For the fixation of the cells to check HA expression, the influenza virus infected cells were washed twice with PBS at room temperature and fixed with 4% paraformaldehyde (PFA) for 15 min. After fixation, the cells were washed three times with PBS followed by reaction with anti-HA IgG (mouse) solution at 37°C for 1h. The cells were then washed with PBS three times at room temperature, reacted with anti-mouse IgG (rabbit) conjugated with Alexa 488 for 1 h at 37°C, observed at 100x magnification using the fluorescence microscope.

Immunostaining for the Confirmation of Viral Protein Production

To demonstrate viral infection on the cells, immunostaining was performed. The virus-infected cells for various infection times were fixed using 100 μL of 4% paraformaldehyde in DPBS at room temperature for 15 min. Then, 100 μL of 0.1% of Triton X-100, a kind of detergent, in DPBS was reacted to permeabilize virus-infected cells for 5 min. After the reaction, the cells were incubated with 100 μL of 3% bovine serum albumin (BSA) in DPBS at the room temperature for 30 min. Then, the cells were reacted with 50 μL of 3% BSA solution including PB1/HA protein antibody at room temperature for 1 h. To perform fluorescent assay, the washed cells were reacted with Alexa-Fluor-488-conjugated rabbit IgG secondary antibody in 50 μL of 3% BSA solution at room temperature for 1 h. DAPI staining for the cell nucleus was also performed prior to the observation with the microscope. The reacted cells were washed five times with 100 μL of DPBS between each steps. The antibody-conjugated cells were observed using the fluorescence microscope.

Real Time Polymerase Chain Reaction (RT-PCR) for the Confirmation of Transcription of Viral Protein Genes

Total RNA was extracted from 10^5 influenza virus-infected cells at each time point post-influenza virus infection using

Qiagen RNeasy kit (Qiagen, USA). Primer sequences for RT-PCR were designed for the RNA 2 segment, which encodes PB1, a critical subunit of viral RNA polymerase. Forward primer was 5′-ACCGGAGACCCTCCTTACAGCC, reverse primer was 5′- TCGGGTTGAGTTGCGGTGCT. Then RT-PCR assay was performed using primers for RNA 2 segment. The emission from SYBR Green, a nucleic acid stain, was detected using an Applied Biosystems 7500 Real Time PCR System (Applied Biosystems, USA).

RESULTS

Western Blotting to Identify the Detection Levels of α-2,6-Sialic Acid Using Lectin-Fluorescence

Prior to the nanoprobe experiments on living cells, the presence and the relative amount of α-2,6- sialic acids in the H292 cells were examined using the traditional Western blotting approach. The blot was visualized using fluorescently-tagged streptavidin to perform Western blotting (**Figure 1A**). It was shown that the different concentrations of cellular proteins were transferred onto the PVDF membrane, and the signal intensity was confirmed to increase in proportion to the cell number. Below 1×10^4 cells, the fluorescence intensity was sharply decreased, while above 5×10^4 cells, the signal seemed to be saturated. Thus, for the subsequent Western blotting analysis, the optimal range of cell number to investigate the levels of sialic acid of H292 cells using lectin was calibrated to be between these numbers.

Next, the dot blot assay was performed using 2×10^4 cells/dot to determine the relative amounts of sialic acid in the H292 cells at different time points after viral infection (Figure S1). The result showed that the amount of sialic acid in cells decreased in a step-wise fashion over time as the viral infection progressed, ultimately falling below 50% compared to the non-infected cells at 4 h post-infection (hpi) (**Figure 1B**). Also, the decrease in sialic acid level was detected as early as 1 hpi, suggesting that the virus entry into the cells may partially halt the production of sialic acid within an hour. Although the data were normalized to the non-infected control samples resulting in high variance, it was suggested that these differences were significant (Figure S2).

Bioimaging of the Expression Levels of α-2,6-Sialic Acid on the Membrane of the Virus-Infected Cells Using Nanoprobes

Next, the novel approach to detect the expression levels of the sialic acid on the virus-infected cells through bioimaging with the nanoprobes was tested (**Figure 2**). The specificity of these nanoprobes to α-2,6-sialic acid has already been confirmed in the previous study; when cells were pretreated with various sialidases that cleave sialic acids, the nanoprobes did not bind to the cells (Cho et al., 2014; Fujii et al., 2016). Furthermore, it was demonstrated that the lectins tethered to the nanoparticles have enhanced affinity for sialic acid compared to bare, fluorescently-tagged lectins (Figure S3), presumably due to the enhanced avidity of having multiple lectins on the nanoprobe surface. Thus, rapid and efficient analysis of sialic acid on the cell membrane was enabled, and the expression level of α-2,6-sialic acid on the cell membrane was analyzed during the viral infection time from 0 to 5 hpi. These nanoprobes bound the α-2,6-sialic acids and allowed the observations of the changes in the expression levels of the sialic acids by infection time (**Figure 3A**). The expression level of sialic acid was sharply decreased from immediately (0 h) after the infection, and followed a gradual decline thereafter (1∼5 h). Also, HA expression on the cell was observed by immunostaining

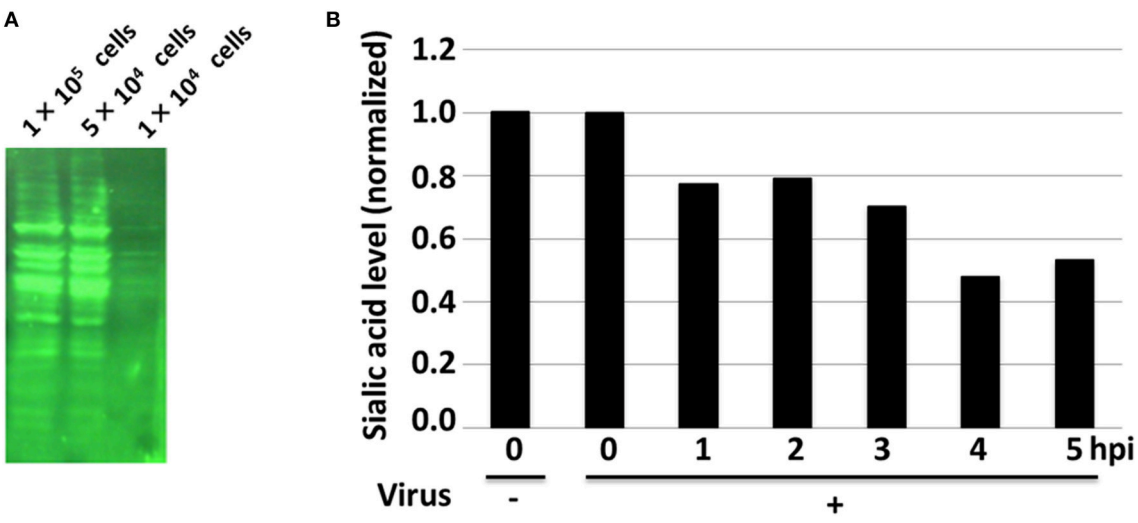

FIGURE 1 | The Western blot analyses of extracted α-2,6-sialic acids visualized using tagged-SNA lectins. (A) Western blotting with different numbers of cells was performed to determine the optimal, non-saturating signals. **(B)** The quantification of the normalized chemiluminescence signals of the sialic acids are shown. Result for the control without viral infection (–) is also shown and the data set was normalized to the control.

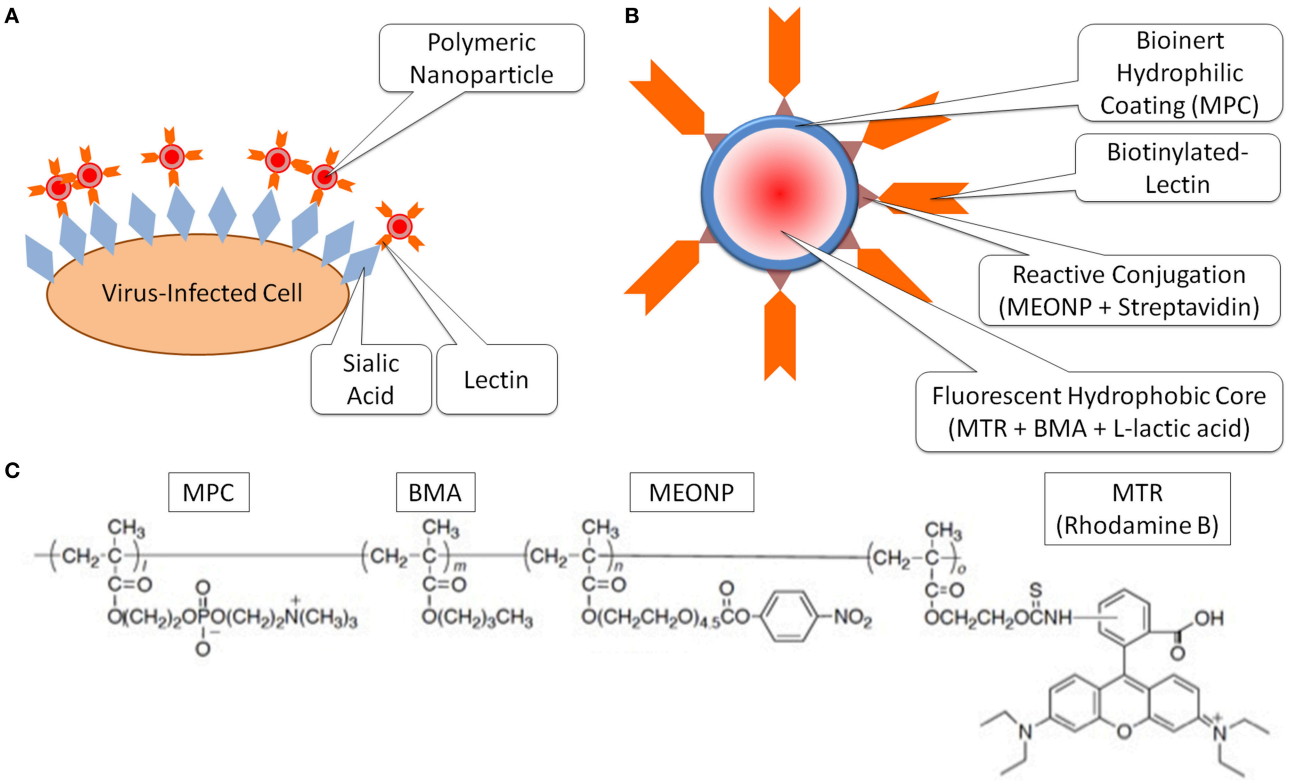

FIGURE 2 | The schematics of the experimental design (A), the design of the nanoprobe to detect sialic acids (B) and the chemical structures of the incorporated functional monomers (C).

using FITC-conjugated anti-HA antibody (**Figure 3A**, 5 hpi), confirming the influenza virus infection.

To quantify the expression level of each sialic acid on the membrane of the virus-infected cells via the nanoprobes, the fluorescence intensities of 50 randomly-picked, representative cells were analyzed. The result showed the quantitative changes of the expression level of sialic acid against viral infection time (**Figure 3B**). For α-2,6-sialic acid, there was indeed a sharp decrease in fluorescence immediately after the infection and also at 5 h post-infection. Although the data were normalized to the non-infected control samples resulting in high variance, it was suggested that these differences were significant (Figure S4).

It is also important to note that nanoprobes are mostly taken up by the cells through endocytosis, as suggested by the fact that the decrease in temperature (to 4°C) causes a sharp decline in the uptake of nanoprobes (Figure S5), presumably due to the loss of fluidity of the membrane. The role of endocytosis was further confirmed using endocytosis inhibitors, such as nystatin and chlorpromazine, which suppressed the nanoprobe intensities to roughly 70 and 50% of the non-treated cells, respectively (data not shown). Thus, the observed nanoprobe fluorescence represent both the surface sialic acids on the outer cell membrane, as well as the endocytosed sialic acids, but not the newly synthesized sialic acids that are not membrane bound.

Confirmation of the Production of Viral Proteins in the Cells through RT-PCR and Immunostaining

To analyze the actual virus activity within the virus-infected cells and correlate it to the expression levels of the sialic acid, the influenza A virus were pre-incubated with cells for 1 h and the subsequent production of the viral proteins within the cells were analyzed. As before, the expression levels of sialic acid on the virus-infected cells were analyzed using lectin-conjugated polymeric nanoparticles. The production of the viral protein PB1, a crucial component of the viral RNA polymerase, was tracked at the level of transcription and translation. Thus, in parallel with the analysis of the expression levels of sialic acid on the incubated cells with viruses using lectin-conjugated polymeric nanoparticles, the analysis of viral protein production were performed by RT-PCR and immunostaining.

First, RT-PCR for mRNA of PB1 was performed to confirm that the observation of sialic acid expression level obtained from the previous time-lapse data was due to the actual viral infection. From the RT-PCR data, the transcription of mRNA coding PB1 was analyzed against viral infection time (**Figure 4**). It was observed that the expression of mRNA of PB1 gene began to rise at past 5 h of viral infection and rapidly increased over time (Table S1). The time-course of PB1 mRNA production as

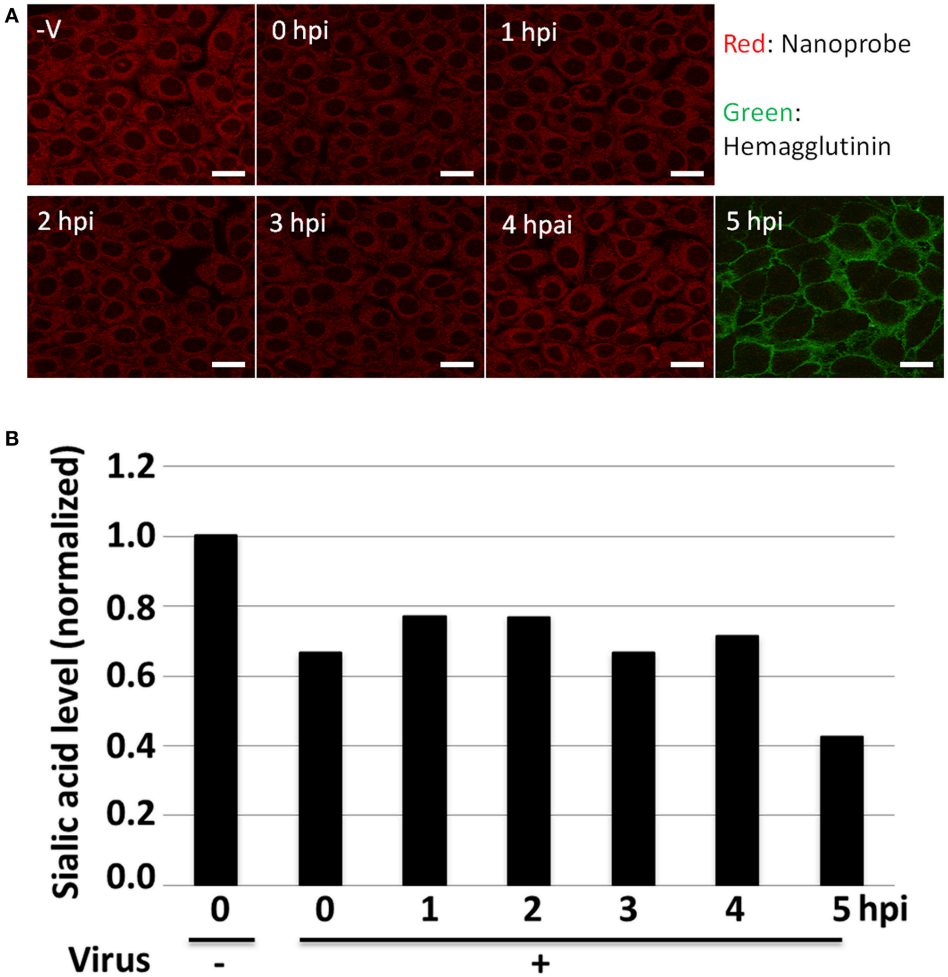

FIGURE 3 | The detection of membrane-bound α-2,6-sialic acids visualized using the nanoprobes. (A) The fluorescence images of virus-infected H292 cells reacted with SNA-conjugated fluorescent polymeric nanoparticles [Red; viral infection time from 0 to 5 h post-infection (hpi)]. Controls without viral infection (–V) and the presence of HA (Green) after the viral infection are also shown. Scale Bar: 20 μm. **(B)** The normalized fluorescence intensities of virus-infected H292 cells reacted with SNA-conjugated fluorescent polymeric nanoparticles [viral infection time from 0 to 5 h post-infection (hpi)]. Result for the control without viral infection (–) is also shown and the data set was normalized to the control.

observed through the RT-PCR experiment was consistent with the decrease in sialic acid expression levels observed in the previous experiments.

Furthermore, immunostaining was performed to monitor the production of PB1 in relations to the sialic acid expression levels of cells. The immunostaining was performed using anti-PB1 antibody and the fluorescent nanoparticles (**Figure 5**). The virus-infected cells were identified by the DAPI stain of the nucleus, while PB1 produced by the virus were tagged with the green fluorescence originating from the secondary antibody. The red signals from the nanoprobes seemed to be significantly reduced by the fixation process. Regardless, it was observed that the production of PB1 started at around 4 h post-infection, and stronger signals were obtained at 5 h post-infection (Figure S6). Again, the time-course of PB1 production as observed through the immunostaining experiment was consistent with the decrease in sialic acid expression levels observed in the previous experiments. Furthermore, the relative intensities of the signals showed a similar trend with the RT-PCR result of PB1 mRNA, where the production levels of PB1 was minute at 4 h and rose rapidly at 5 h.

DISCUSSIONS

All in all, the results demonstrate the accuracy and efficiency of the use of nanoprobes to monitor the changes in sialic acids during viral infections, which may serve as an indicator of viral infection progression. Because the change of expression level of sialic acid on virus-infected cells has not been previously demonstrated, it was confirmed by the detection of viral proteins using immunostaining and Western blotting in this

study. However, it is important to note that the observation of the expression levels of sialic acid using the nanoprobe is much simpler and faster than immunostaining and Western blotting. This bioimaging method, which does not involve cell lysis protocol or electrophoresis, was performed in less than 1 h, and it offers the means to observe the changes in cellular properties *in situ*. Furthermore, it was found that the observation of the changes in the expression level of sialic acid can be observed from 1 h after viral infection, while the detection of PB1 can only be possible from roughly 5 h after a viral infection, suggesting that earlier detection of viral infection can be made possible using the nanoprobe platform.

Some findings in our studies warrant further research and investigation, such as the immediate decrease in the membrane-bound sialic acid levels after viral infection observed using the nanoprobes. To the best of our knowledge, there has not been any report on this immediate decrease in sialic acids during virus infections. However, there are various possibilities for the observed decline in the amount of membrane sialic acid immediately following virus infection. One possibility is that the fluidity of the cell membrane may be affected by virus infection, such that the endocytic process is inhibited, leading to less overall nanoprobe uptake of the cells. Another possibility is that the cell cycle progression is halted at G0/G1 phase during Influenza A virus infection, as shown in previous research (He et al., 2010), which may be hindering the production of sialic acids that generally occur at the end of G2 phase (Rosenberg and Einstein, 1972). Yet another possibility is that the process of virus binding itself may be depleting the available sialic acids on the cell membrane or withholding the endocytosed sialic acids, leading to the apparent decline in the amount of sialic acids on the cell membrane as quantified by the nanoprobe. Any of the above reasons or combinations thereof may be causing the initial decline in sialic acid levels on the cell membrane, but these possibilities still have to be further tested.

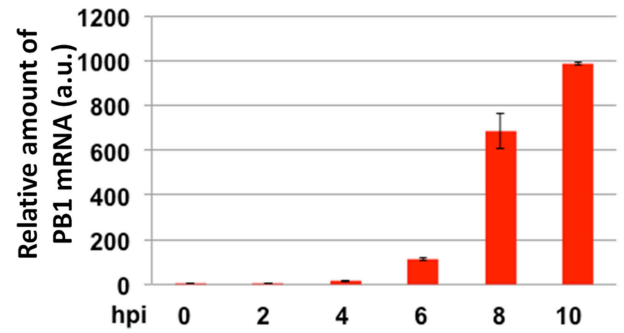

FIGURE 4 | The RT-PCR analysis of the amounts of mRNA coding for PB1 in cells with different hours post-infection (hpi).

Furthermore, differences between the levels of sialic acid on the membrane of the cells (observed through the nanoprobe) and that of the entire cell (observed through the Western Blotting) were found. In particular, the sialic acid levels observed by the nanoprobe dropped immediately after virus infection, while the levels from the Dot Blotting dropped about 1 h post-infection. On the other hand, there was another decline of sialic acid levels at 4 h observed by Dot Blotting, while the nanoprobe detected this decline at 5 h. The former may be explained by some of the explanations listed above regarding endocytosis and receptor obstruction. The latter decline of the sialic acid will need to be further investigated, but it may be related to the diversion of metabolic pathways toward viral proteins instead of the sialic acids, which had a slightly delayed effect on the cell-surface sialic acids.

Lastly, the robustness and the generality of this nanoprobe system for various applications should be discussed. Recently, the mechanisms between different interactions between viruses and sialic acids and their structural correlations have become more apparent (Stencel-Baerenwald et al., 2014). Although the results here are that of one type of sialic acid and lectin combination, other forms of sialic acid, such as α-2,3-sialic acid that specifically interact with *Maackia amurensis II* lectin (MAL), should be tested in order to confirm some of the previous findings and gain further insight into the changes in sialic acid expressions upon viral infections. Furthermore, although the influenza virus infection occurs through the process of sialic acid recognition and the subsequent uptake of virus particles into the cells, other viruses often infect through different mechanisms. The nanoprobes use in this study, comprised of the lectin-tagged polymeric nanoparticles, contains lectins that recognize sialic acids, but they can also be conjugated with other molecules to capture different interactions and properties of the cell membrane surface, which will not only be useful for studying virus

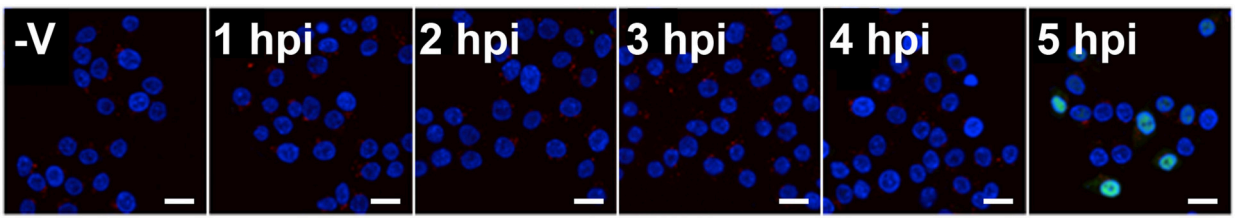

FIGURE 5 | The fluorescence images of the immunostaining of non-infected cells (–V) and virus-infected cells from 1 to 5 h post-infection (hpi) (Blue: nucleus; Red: nanoprobes, Green: PB1 viral protein). Scale Bar: 20 μm.

infections, but also to investigate various cellular functions as well.

CONCLUSION

In this study, the behaviors of sialic acid on the influenza-virus-infected cells for viral infection time were analyzed using various methods. Immediate decline in the sialic acid levels were observed by the nanoprobe and Dot Blot analyses. After 4∼5 h post viral infection, the amounts of sialic acid again decreased sharply, and this was consistent with the initiation of the viral protein production as confirmed by some of the traditional analytical methods. With the nanoprobe system, such analyses and the detection of the sialic acids relevant to virus-infected cells could be performed quickly, requiring only 15 min for the reaction with cells. In conclusion, the polymeric nanoparticle platform offers a rapid and accurate detection of sialic acids on the cell membrane that may find useful applications in the areas of disease control and clinical diagnosis in the future.

AUTHOR CONTRIBUTIONS

JC, YM, AH, KK, and MT designed research; JC and YM performed research; JC and YM analyzed data; JC, YM, AH, KK, and MT wrote the paper.

ACKNOWLEDGMENTS

This work was supported by the grant from CREST (Japan Science and Technology Agency) to AH. This work was also partly supported by the research grant program of the Asahi Glass Foundation.

SUPPLEMENTARY MATERIAL

The Supplementary Material for this article can be found online at: http://journal.frontiersin.org/article/10.3389/fmicb.2016.01147

REFERENCES

Chen, W. H., Toapanta, F. R., Shirey, K. A., Zhang, L., Giannelou, A., Page, C., et al. (2012). Potential role for alternatively activated macrophages in the secondary bacterial infection during recovery from influenza. *Immunol. Lett.* 141, 227–234. doi: 10.1016/j.imlet.2011.10.009

Chen, Y., Liang, W., Yang, S., Wu, N., Gao, H., Sheng, J., et al. (2013). Human infections with the emerging avian influenza A H7N9 virus from wet market poultry: clinical analysis and characterisation of viral genome. *Lancet* 381, 1916–1925. doi: 10.1016/S0140-6736(13)60903-4

Cho, J., Kushiro, K., Teramura, Y., and Takai, M. (2014). Lectin-tagged fluorescent polymeric nanoparticles for targeting of sialic acid on living cells. *Biomacromolecules* 15, 2012–2018. doi: 10.1021/bm500159r

Connor, R. J., Kawaoka, Y., Webster, R. G., and Paulson, J. C. (1994). Receptor specificity in human, avian, and equine H2 and H3 influenza virus isolates. *Virology* 205, 17–23. doi: 10.1006/viro.1994.1615

de Lima, M. C., Ramalho-Santos, J., Flasher, D., Slepushkin, V. A., Nir, S., and Düzgüneş, N. (1995). Target cell membrane sialic acid modulates both binding and fusion activity of influenza virus. *Biochim. Biophys. Acta* 1236, 323–330. doi: 10.1016/0005-2736(95)00067-D

Fujii, T., Watanabe, M., Shimizu, T., Takeshima, H., Kushiro, K., Takai, M., et al. (2016). Positive regulation of the enzymatic activity of gastric H^+,K^+-ATPase by sialylation of its β-subunit. *Biochim. Biophys. Acta* 1858, 1228–1235. doi: 10.1016/j.bbamem.2016.02.029

Fukuzawa, K., Omagari, K., Nakajima, K., Nobusawa, E., and Shigenori, T. (2011). Sialic acid recognition of the pandemic influenza 2009 H1N1 virus: binding mechanism between human Receptor and Influenza Hemagglutinin. *Prot. Pept. Lett.* 18, 530–539. doi: 10.2174/092986611794927893

Goda, T., Matsuno, R., Konno, T., Madoka, T., and Ishihara, K. (2009). Protein adsorption resistance and oxygen permeability of chemically crosslinked phospholipid polymer hydrogel for ophthalmologic biomaterials. *J. Biomed. Mater. Res. B* 89B, 184–190. doi: 10.1002/jbm.b.31204

Goto, Y., Matsuno, R., Konno, T., Takai, M., and Ishihara, K. (2008). Artificial cell membrane-covered nanoparticles embedding quantum dots as stable and highly sensitive fluorescence bioimaging probes. *Biomacromolecules* 9, 3252–3257. doi: 10.1021/bm800819r

He, Y., Xu, K., Keiner, B., Zhou, J., Czudai, V., Li, T., et al. (2010). Influenza A virus replication induces cell cycle arrest in G0/G1 phase. *J. Virol.* 84, 12832–12840. doi: 10.1128/JVI.01216-10

Jacobson, I. M., McHutchison, J. G., Dusheiko, G., Di Bisceglie, A. M., Reddy, K. R., Bzowej, N. H. et al. (2011). Telaprevir for previously untreated chronic hepatitis C virus infection. *New Engl. J. Med.* 364, 2405–2416. doi: 10.1056/NEJMoa1012912

Johnson, L. V., Walsh, M. L., and Chen, L. B. (1980). Localization of mitochondria in living cells with rhodamine 123. *Proc. Natl. Acad. Sci. U.S.A.* 77, 990–994. doi: 10.1073/pnas.77.2.990

Kuiken, T., Holmes, E. C., McCauley, J., Rimmelzwaan, G. F., Williams, C. S., and Grenfell, B. T. (2006). Host species barriers to influenza virus infections. *Science* 312, 394–397. doi: 10.1126/science.1122818

Lai, J. C. C., Garcia, J.-M., Dyason, J. C., Böhm, R., Madge, P. D., Rose, F. J., et al. (2012). A secondary sialic acid binding site on influenza virus neuraminidase: fact or fiction? *Angew. Chem. Int. Ed.* 51, 2221–2224. doi: 10.1002/anie.201108245

Landford, R. E., Hildebrandt-Eriksen, E. S., Petri, A., Persson, R., Lindow, M., Munk, M. E., et al. (2010). Therapeutic silencing of microRNA-122 in primates with chronic hepatitis C virus infection. *Science* 327, 198–201. doi: 10.1126/science.1178178

Maines, T. R., Jayaraman, A., Belser, J. A., Wadford, D. A., Pappas, C., Zeng, H., et al. (2009). Transmission and pathogenesis of swine-origin 2009 A(H1N1) influenza viruses in ferrets and mice. *Science* 325, 484–487. doi: 10.1126/science.1177238

Moro, T., Takatori, Y., Ishihara, K., Konno, T., Takigawa, Y., Matsushita, T., et al. (2004). Surface grafting of artificial joints with a biocompatible polymer for preventing periprosthetic osteolysis. *Nat. Mater.* 3, 829–836. doi: 10.1038/nmat1233

Rosenberg, S. A., and Einstein, A. B. Jr. (1972). Sialic acids on the plasma membrane of cultured human lymphoic cells. Chemical aspects and biosynthesis. *J. Cell Biol.* 53, 466–473. doi: 10.1083/jcb.53.2.466

Sichelstiel, A., Yadava, K., Trompette, A., Salami, O., Iwakura, Y., Nicod, L. P., et al. (2014). Targeting IL-1β and IL-17A driven inflammation during influenza-induced exacerbations of chronic lung inflammation. *PLoS ONE* 9:e98440. doi: 10.1371/journal.pone.0098440

Stencel-Baerenwald, J. E., Reiss, K., Reiter, D. M., Stehle, T., and Dermody, T. S. (2014). The sweet spot: defining virus-sialic acid interactions. *Nat. Rev. Microbiol.* 12, 739–749. doi: 10.1038/nrmicro3346

Sun, K., Ye, J., Perez, D. R., and Metzger, D. W. (2011). Seasonal FluMist vaccination induces cross-reactive T cell immunity against H1N1 (2009) influenza and secondary bacterial infections. *J. Immunol.* 186, 987–993. doi: 10.4049/jimmunol.1002664

Ueda, R., Sugiura, T., Kume, S., Ichikawa, A., Larsen, S., Miyoshi, H., et al. (2013). A novel single virus infection system reveals that influenza virus preferentially infects cells in G1 phase. *PLoS ONE* 8:e67011. doi: 10.1371/journal.pone.0067011

Wolfbeis, O. S. (2015). An overview of nanoparticles commonly used in fluorescent bioimaging. *Chem. Soc. Rev.* 44, 4743–4768. doi: 10.1039/C4CS00392F

Zhu, X., McBride, R., Nycholat, C. M., Yu, W., Paulson, J. C., and Wilson, I. A. (2012). Influenza virus neuraminidases with reduced enzymatic activity that avidly bind sialic Acid receptors. *J. Virol.* 86, 13371–13383. doi: 10.1128/JVI.01426-12

Conflict of Interest Statement: The authors declare that the research was conducted in the absence of any commercial or financial relationships that could be construed as a potential conflict of interest.

Copyright © 2016 Cho, Miyake, Honda, Kushiro and Takai. This is an open-access article distributed under the terms of the Creative Commons Attribution License (CC BY). The use, distribution or reproduction in other forums is permitted, provided the original author(s) or licensor are credited and that the original publication in this journal is cited, in accordance with accepted academic practice. No use, distribution or reproduction is permitted which does not comply with these terms.

frontiers in Microbiology

ORIGINAL RESEARCH
published: 28 June 2016
doi: 10.3389/fmicb.2016.01001

Specific Destruction of HIV Proviral p17 Gene in T Lymphoid Cells Achieved by the Genome Editing Technology

*Tsunao Kishida, Akika Ejima and Osam Mazda**

Department of Immunology, Kyoto Prefectural University of Medicine, Kamikyo, Japan

Recent development in genome editing technologies has enabled site-directed deprivation of a nucleotide sequence in the chromosome in mammalian cells. Human immunodeficiency (HIV) infection causes integration of proviral DNA into the chromosome, which potentially leads to re-emergence of the virus, but conventional treatment cannot delete the proviral DNA sequence from the cells infected with HIV. In the present study, the transcription activator-like effector nucleases (TALENs) specific for the HIV p17 gene were constructed, and their activities to destroy the target sequence were evaluated. SSA assay showed a high activity of a pair of p17-specific TALENs. A human T lymphoid cell line, Jurkat, was infected with a lentivirus vector followed by transfection with the TALEN–HIV by electroporation. The target sequence was destructed in approximately 10–95% of the p17 polymerase chain reaction clones, and the efficiencies depended on the Jurkat–HIV clones. Because p17 plays essential roles for assembly and budding of HIV, and this gene has relatively low nucleotide sequence diversity, genome editing procedures targeting p17 may provide a therapeutic benefit for HIV infection.

Keywords: HIV, genome edition, TALEN, T lymphoid cell line, provirus

OPEN ACCESS

Edited by:
Toshinori Sato,
Keio University, Japan

Reviewed by:
Shinji Fujimoto,
Kyoto University, Japan
Minoru Takeuchi,
Kyoto Sangyo University, Japan

****Correspondence:***
Osam Mazda
mazda@koto.kpu-m.ac.jp

Specialty section:
This article was submitted to Virology, a section of the journal Frontiers in Microbiology

Received: *31 March 2016*
Accepted: *13 June 2016*
Published: *28 June 2016*

Citation:
Kishida T, Ejima A and Mazda O (2016) Specific Destruction of HIV Proviral p17 Gene in T Lymphoid Cells Achieved by the Genome Editing Technology. Front. Microbiol. 7:1001. doi: 10.3389/fmicb.2016.01001

INTRODUCTION

Human immunodeficiency virus type 1 (HIV-1) causes latent infection in $CD4^+$ T cells and macrophages, in which HIV-1 provirus DNA is integrated into the chromosomes. The viral genome is stably maintained in the cells and segregated into their progenies. Anti-HIV medicines such as protease inhibitors and reverse transcriptase inhibitors drastically improved prognosis of HIV-1-infected patients, by interfering with viral amplification (Pierson et al., 2000; Datta et al., 2016). However, perfect cure of HIV infection has not been achieved, because provirus DNA cannot be eliminated from the chromosomes of the infected cells by the present therapies.

Recent genome editing technologies including the zinc finger nuclease, transcription activator-like effector nucleases (TALEN), and clustered regularly interspaced short palindromic repeat (CRISPR)/Cas9 have made it possible to efficiently induce specific alteration or truncation of target nucleotide sequence in the genomic DNA of mammalian cells (Jinwei et al., 2015; Maeder and Gersbach, 2016; Mei et al., 2016). Such technologies may realize novel therapeutic procedures against various genetic diseases by replacing and modifying the genes responsible for the pathogenesis (Jang et al., 2016). Among them, TALEN is an artificial fusion enzyme composed

of the nuclease domain and the DNA binding domain derived from the TALEs of the *Xanthomonas*. Any nucleotide sequence can be targeted by selecting the modules of the DNA-binding domains.

If provirus DNA is destroyed using these technologies, such procedures may provide a novel anti-HIV therapy that may not only eliminate the potential risk of HIV reactivation and AIDS onset but also relieve patients of potential adverse events and economic burden due to lifelong medication. The transactivation response element (TAR) sequence may be a suitable target (Ebina et al., 2015; Strong et al., 2015), while another appropriate target may be a coding sequence for an essential viral structural protein, because truncation of only a small number of nucleotides in the coding sequence may result in deletion of critical amino acid residue(s) or frameshift mutation.

In this context, we constructed TALENs that target the HIV Gag p17 gene, and examined if the p17 coding sequence in the chromosome of HIV-infected cells can be destroyed by transducing the recombinant TALEN vector.

MATERIALS AND METHODS

TALEN Vectors

Two pairs of TALENs, i.e., HIV TALEN 1 (HIV TALEN 1 L and R) and HIV TALEN 2 (HIV TALEN 2 L and R) (**Figure 1A**) were designed to recognize p17 gene sequence (**Figure 1B**), based on the TAL Effector Nuclotide Targeter software.[1] The TALEN vectors were constructed using the Golden Gate reaction as described previously.

Single-Strand Annealing (SSA) Assay

Single-strand annealing assay was performed as described with slight modification (Sakuma et al., 2013). Two pairs of oligonucleotides, HIV p17 TALEN No.1 SSA S and AS, and HIV p17 TALEN No. 2 SSA S and AS (**Figure 2A**), were annealed to form double strand oligonucleotides, which were subsequently inserted into pGL4-SSA reporter plasmid that had been digested by BsaI endonuclease. The resultant plasmids were named pGL4-SSA-HIV_1 and 2. 293TN cells were seeded into 96-well plates at a density of 6×10^4/well. On the next day, cells were co-transfected with 20 ng of TALEN plasmid, 10 ng of pGL4-SSA, and 2 ng of pRL-CMV vector as an internal control by means of X-treme GENE 9 DNA Transfection Reagent (Roche). As a positive control, other aliquot of the cells were co-transfected with HPRT1 TALEN L1, HPRT1 TALEN R1, and pGL4-SSA-HPRT1 (Sakuma et al., 2013). Twenty-four hours later, dual luciferase assay was performed using Dual-Glo luciferase assay system (Promega) and GENios (TECAN Inc.) device.

[1]https://tale-nt.cac.cornell.edu/

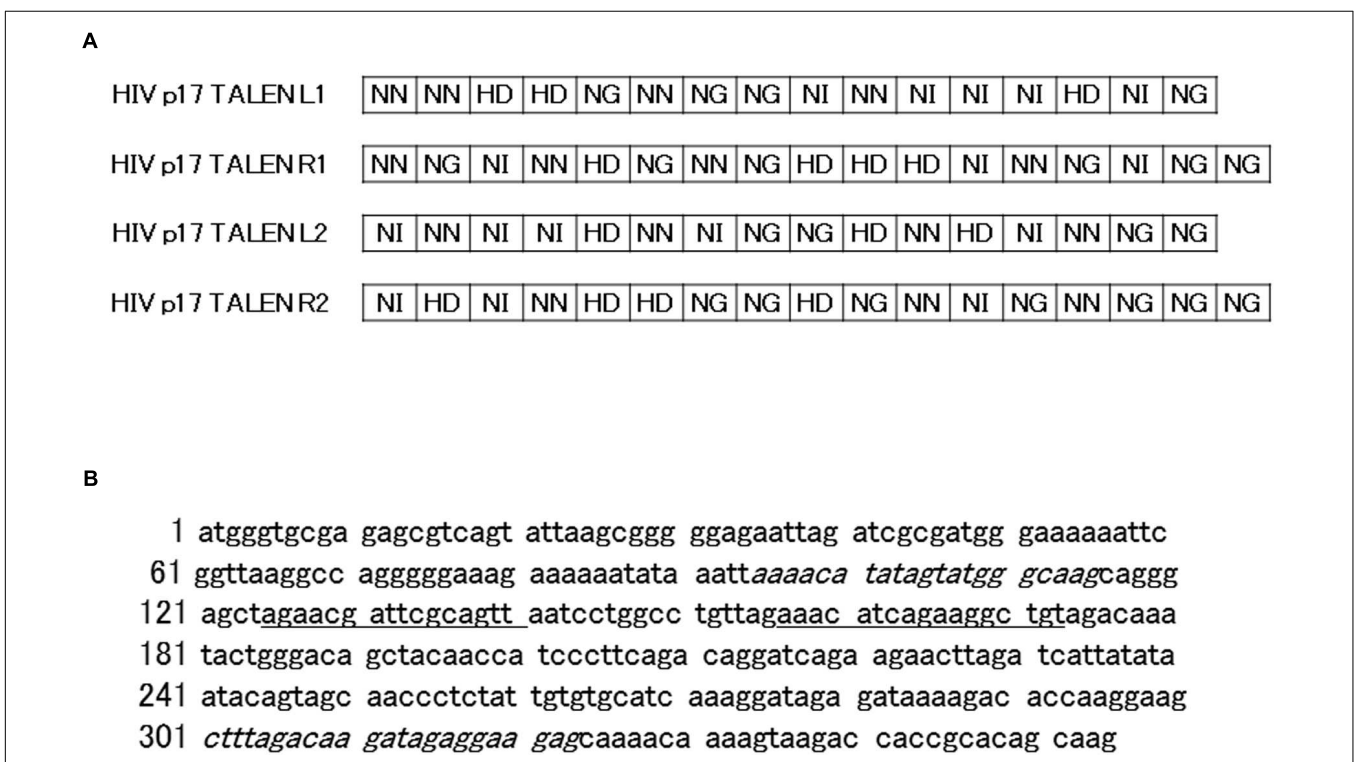

FIGURE 1 | Structure and target sequences of Human immunodeficiency (HIV) transcription activator-like effector nucleases (TALENs). (A) The amino acid sequences of the repeat-variable di-residues (RVDs) of the indicated TALENs are shown with one-letter symbols. **(B)** The p17 gene sequence are shown. Underlined letters (125–140 and 157–173) represent target sites of HIV 1 and 2 TALENs, respectively, while italic letters represent forward and reverse polymerase chain reaction (PCR) primers (95–115, and 301–323, respectively) used for amplification of the p17 gene sequence from chromosomal DNA of Jurkat–HIV cells.

A

Oligomer	Sequence
HIV p17 TALEN No.1 SSA S	5'-gtcggatTAGAACGATTCGCAGTTaatcctggcctgttagAAACATCAGAAGGCTGTAaggt-3'
HIV p17 TALEN No.1 SSA AS	5'-cggtacctTACAGCCTTCTGATGTTTctaacaggccaggattAACTGCGAATCGTTCTAatc-3'
HIV p17 TALEN No.2 SSA S	5'-gtcggatTGGCCTGTTAGAAACATcagaaggctgtagacaAATACTGGGACAGCTACAaggt-3'
HIV p17 TALEN No.2 SSA AS	5'-cggtacctTGTAGCTGTCCCAGTATTtgtctacagccttctgATGTTTCTAACAGGCCAatc-3'

B

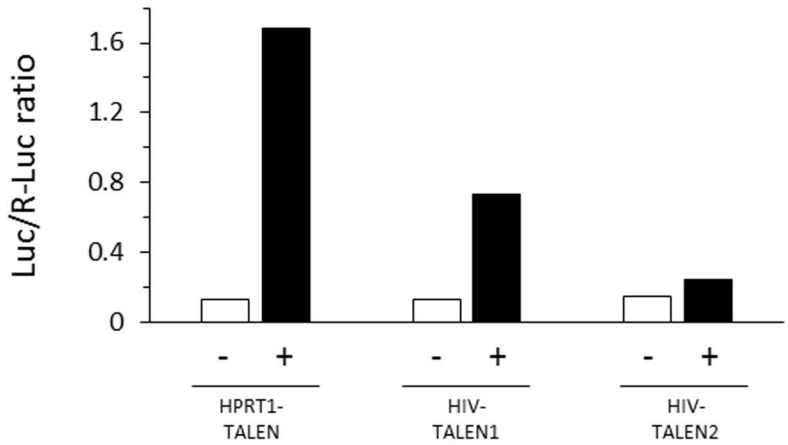

FIGURE 2 | Efficient destruction of p17 sequence by the HIV-1 TALEN. (A) Sequences of the oligomers used in the SSA assay. **(B)** Each target sequence was inserted into pGL4-SSA reporter plasmid. These reporter plasmids (+) or empty pGL4-SSA (−) was co-transfected with the indicated TALEN expression vector and pRL-CMV reference plasmid into the 293TN cells. Twenty-four hours later, dual-Glo luciferase assay was performed to evaluate relative destruction of the target sequence. Luc/R-Luc ratios are shown. In the presence of HPRT1–TALEN, the HPRT target sequence was efficiently destroyed, resulting in high rate of R-Luc activity relative to Luc. HIV–TALEN1 destroyed its target sequence at an intermediate level, whereas HIV–TALEN2 showed very low destruction activity.

Lentivirus Vector

pGreen-puro vectors were purchaced from SBI. 293TN packaging cells (3×10^6) were plated on geratin-coated 100 mm dishes and cultured overnight. They were co-transfected with pGreen-puro, pVSV-G, pPACKH1-REV, and pPACKH1-GAG using the X-treme Gene 9 transfection reagent (Roche Applied Science, Penzberg, Germany) diluted in Opti-MEM. Twenty-four hours later, the culture supernatant was replaced by antibiotic-free culture medium. After culturing for another 24 h, the supernatant was collected and filtered through a 0.45 μm pore-size filter.

Cells, Infection, and Transfection

Jurkat, a human T cell leukemia cell line, was cultured in the RPMI1640 medium supplemented with 100 U/ml penicillin, 100 μg/ml streptomycin, and 10% FBS (Mazda et al., 1997). They were seeded onto culture dishes at a density of 1×10^6 cells/mL. On the next day, cells were transduced with the lentiviral vector in the presence of 4 μg/mL polybrene (day 0). On day 1, cells were reseeded onto 96 well plates at 0.3 cells/well. After culturing with 1 μg/mL puromycin, three drug-resistant cell colonies were randomly chosen and named Jurkat–HIV P1–P3. The colonies were picked up and further cultured in puromycin-free medium. TALEN expression vectors were then transfected into the cells by electroporation (0.25 μg each of HIV TALEN 1 L and R vectors for 10^5 cells).

PCR and DNA Sequencing

Four days after the transfection, DNA was extracted from the cells. Polymerase chain reaction (PCR) was performed to amplify the p17 gene sequence using the primers shown in the **Figure 1B**. The resultant PCR fragments were inserted into a TA cloning vector, MD20, which were subsequently transformed into competent *Escherichia coli*. After seeding onto ampicillin-containing agar plates, twenty colonies were picked up. The sequence of each PCR clone was determined by standard procedure using the SP6 and M13 primers.

RESULTS

The HIV TALENs 1 and 2 were prepared to target HIV gag p17 gene (**Figure 1**) and the activities of the TALENs were assessed

by the SSA assay. The results are shown in **Figure 2B**. The HIV TALENs 1 and 2 exhibited approximately 43 and 15% of activities compared with that of the positive control TALEN that were specific for hypoxanthine–guanine phosphoribosyl transferase (HPRT) sequence (Sakuma et al., 2013). Based on the results, we decided to use the HIV TALEN 1 that digests the HIV gag p17 gene sequence more efficiently than the HIV TALEN 2 in the following experiments.

The T lymphoma cell line, Jurkat, was infected with a lentivirus vector. After selection with puromycin, the resultant clones were expected to possess the lentivirus sequence integrated in their chromosomes. Thus, the lentivirus-infected Jurkat cells were regarded as a model of the T cells latently infected with HIV. Three clones (namely, Jurkat–HIV clone P1–P3) were transfected with the HIV TALEN 1, and nucleotide sequences of the target regions in PCR-amplified clones were determined.

The results are shown in **Tables 1–3**. In the Jurkat–HIV clone P1, 19 out of 20 PCR clones showed truncation of the p17 sequence (**Table 1**). The truncated sites spanned 7–22 nucleotides. Therefore, the HIV TALEN 1 cleaved the HIV sequence that had been integrated in the chromosome of Jurkat–HIV clone P1 at quite high efficiency. In contrast, nucleotide deletion was seen in only two out of twenty PCR clones derived from the Jurkat–HIV clone P2 (**Table 2**). Seven nucleotides were lacking in the p17 gene sequence in the two PCR clones. Meanwhile, a half of PCR clones (10 out of 20) derived from the Jurkat–HIV clone P3 possessed truncated p17 gene sequence (**Table 3**).

TABLE 1 | Specific truncation of chromosomal DNA at p17 gene in Jurkat–HIV clone P1.

Control	agaacgattcgcagttaatcctggcctgttagaaacatcagaaggctgt
1	agaacgattcgca--------ctggcctgttagaaacatcagaaggctgt
2	agaacgattcgca--------ctggcctgttagaaacatcagaaggctgt
3	agaacgattcgca--------ctggcctgttagaaacatcagaaggctgt
4	agaacgattcgca--------ctggcctgttagaaacatcagaaggctgt
5	agaacgattcgca--------ctggcctgttagaaacatcagaaggctgt
6	agaacgattcgca--------ctggcctgttagaaacatcagaaggctgt
7	agaacgattcgca--------ctggcctgttagaaacatcagaaggctgt
8	agaacgattcgca--------ctggcctgttagaaacatcagaaggctgt
9	agaacgattcgca--------ctggcctgttagaaacatcagaaggctgt
10	agaacgattcgca--------ctggcctgttagaaacatcagaaggctgt
11	agaacgatt----------gaaacatcagaaggctgt
12	agaacgatt----------gaaacatcagaaggctgt
13	agaacgatt----------gaaacatcagaaggctgt
14	agaacgatt----------gaaacatcagaaggctgt
15	agaacgatt----------gaaacatcagaaggctgt
16	agaacgatt----- ----------gaaacatcagaaggctgt
17	agaacgattcgcagtt----------agaaacatcagaaggctgt
18	agaacgattcgcagtt----------agaaacatcagaaggctgt
19	agaacgattcgcagtt----------agaaacatcagaaggctgt
20	agaacgattcgcagttaatcctggcctgttagaaacatcagaaggctgt

Nucleotide sequences of 20 clones (No. 1–20) derived from PCR-amplified fragments of p17 gene region in the chromosomal DNA of Jurkat–HIV clone P1 are shown. Control at the top represents wild type p17 sequence.

TABLE 2 | Specific truncation of chromosomal DNA at p17 gene in Jurkat–HIV clone P2.

Control	agaacgattcgcagttaatcctggcctgttagaaacatcagaaggctgt
1	agaacgattcgca--------ctggcctgttagaaacatcagaaggctgt
2	agaacgattcgca--------ctggcctgttagaaacatcagaaggctgt
3	agaacgattcgcagttaatcctggcctgttagaaacatcagaaggctgt
4	agaacgattcgcagttaatcctggcctgttagaaacatcagaaggctgt
5	agaacgattcgcagttaatcctggcctgttagaaacatcagaaggctgt
6	agaacgattcgcagttaatcctggcctgttagaaacatcagaaggctgt
7	agaacgattcgcagttaatcctggcctgttagaaacatcagaaggctgt
8	agaacgattcgcagttaatcctggcctgttagaaacatcagaaggctgt
9	agaacgattcgcagttaatcctggcctgttagaaacatcagaaggctgt
10	agaacgattcgcagttaatcctggcctgttagaaacatcagaaggctgt
11	agaacgattcgcagttaatcctggcctgttagaaacatcagaaggctgt
12	agaacgattcgcagttaatcctggcctgttagaaacatcagaaggctgt
13	agaacgattcgcagttaatcctggcctgttagaaacatcagaaggctgt
14	agaacgattcgcagttaatcctggcctgttagaaacatcagaaggctgt
15	agaacgattcgcagttaatcctggcctgttagaaacatcagaaggctgt
16	agaacgattcgcagttaatcctggcctgttagaaacatcagaaggctgt
17	agaacgattcgcagttaatcctggcctgttagaaacatcagaaggctgt
18	agaacgattcgcagttaatcctggcctgttagaaacatcagaaggctgt
19	agaacgattcgcagttaatcctggcctgttagaaacatcagaaggctgt
20	agaacgattcgcagttaatcctggcctgttagaaacatcagaaggctgt

Nucleotide sequences of 20 clones (No. 1–20) derived from PCR-amplified fragments of p17 gene region in the chromosomal DNA of Jurkat–HIV clone P2 are shown. Control at the top represents wild type p17 sequence.

TABLE 3 | Specific truncation of chromosomal DNA at p17 gene in Jurkat–HIV clone P3.

Control	agaacgattcgcagttaatcctggcctgttagaaacatcagaaggctgt
1	agaacgattcgca--------ctggcctgttagaaacatcagaaggctgt
2	agaacgattcgca--------ctggcctgttagaaacatcagaaggctgt
3	agaacgattcgca--------ctggcctgttagaaacatcagaaggctgt
4	agaacgattcgca--------ctggcctgttagaaacatcagaaggctgt
5	agaacgatt----------gaaacatcagaaggctgt
6	agaacgatt----------gaaacatcagaaggctgt
7	agaacgatt----------gaaacatcagaaggctgt
8	agaacgatt----------gaaacatcagaaggctgt
9	agaacgattcgcagtt----------agaaacatcagaaggctgt
10	agaacgattcgcagtt----------agaaacatcagaaggctgt
11	agaacgattcgcagttaatcctggcctgttagaaacatcagaaggctgt
12	agaacgattcgcagttaatcctggcctgttagaaacatcagaaggctgt
13	agaacgattcgcagttaatcctggcctgttagaaacatcagaaggctgt
14	agaacgattcgcagttaatcctggcctgttagaaacatcagaaggctgt
15	agaacgattcgcagttaatcctggcctgttagaaacatcagaaggctgt
16	agaacgattcgcagttaatcctggcctgttagaaacatcagaaggctgt
17	agaacgattcgcagttaatcctggcctgttagaaacatcagaaggctgt
18	agaacgattcgcagttaatcctggcctgttagaaacatcagaaggctgt
19	agaacgattcgcagttaatcctggcctgttagaaacatcagaaggctgt
20	agaacgattcgcagttaatcctggcctgttagaaacatcagaaggctgt

Nucleotide sequences of 20 clones (No. 1–20) derived from PCR-amplified fragments of p17 gene region in the chromosomal DNA of Jurkat–HIV clone P3 are shown. Control at the top represents wild type p17 sequence.

DISCUSSION

In the present study, the HIV TALEN 1 that we constructed may highly efficiently edit the p17 sequence as suggested by the SSA assay, although the reason why the other TALEN was less efficient remains unknown. The TALEN induced cleavage and truncation of the target sequence in the Jurkat–HIV cells, leading to destruction of the coding sequence of the p17 gene. In HIV-infected cells, the HIV-1 matrix protein p17 is excised by proteolysis from the N-terminus of the Gag polyprotein, and bring the Gag to the host cell membrane via its N-terminal myristoyl group (Freed, 1998). Because the p17 is essential for the assembly and budding of HIV virion, deletion of this gene from the chromosome may bring remarkable therapeutic benefits (Ellenrieder et al., 2004). The p17 gene has less sequence variation among virus subtypes compared with the env genes (Brown and Monaghan, 1988; Markham et al., 1995). Thus, the p17 gene may be suitable as the target of the gene editing therapeutic strategy.

We tested three Jurkat–HIV clones that we established by limiting dilution after the infection with the lentivirus vector. Interestingly, the three clones underwent p17 truncation at different rates ranging from 10 to 95%. The variation among the clones may be due to different integration sites of the provirus sequence in the chromosomes, and/or difference in the copy number of the integrated provirus per cell. Alternatively, efficiency of electro-transfection of the TALEN vector may differ among the Jurkat–HIV cell clones, resulting in different proportion of the cells that sufficiently expressed TALEN among the cell population. In the present study, the TALEN vector was transfected into the cells once by electroporation. If the electroporation is repetitively performed, the efficiency of transfection may be elevated, resulting in a higher rate of p17 gene truncation. Some delivery procedure other than electroporation may also be used to transfer the TALEN vector into the cells to increase the efficiency of the genome edition. A lentivirus vector may be quite suitable for the delivery of a TALEN vector into T cells in patients in whom HIV is latently infected.

AUTHOR CONTRIBUTIONS

TK: Conception and design, Provision of study materials, Data analysis, and interpretation; AE: Data analysis and interpretation, OM: Manuscript writing, Administrative support, and Final approval of manuscript.

ACKNOWLEDGMENT

This work was supported by grants from the Japanese Ministry of Education, Culture, Sports, Science, and Technology (26670485).

REFERENCES

Brown, A. L., and Monaghan, P. (1988). Evolution of the structural proteins of human immunodeficiency virus: selective constraints on nucleotide substitution. *AIDS Res. Hum. Retroviruses* 4, 399–407. doi: 10.1089/aid.1988.4.399

Datta, P. K., Kaminski, R., Hu, W., Pirrone, V., Sullivan, N. T., Nonnemacher, M. R., et al. (2016). HIV-1 Latency and Eradication: past, Present and Future. *Curr. HIV Res.* 14. doi: 10.2174/1570162X14666160324125536 [Epub ahead of print].

Ebina, H., Kanemura, Y., Misawa, N., Sakuma, T., Kobayashi, T., Yamamoto, T., et al. (2015). A high excision potential of TALENs for integrated DNA of HIV-based lentiviral vector. *PLoS ONE* 10:e0120047. doi: 10.1371/journal.pone.0120047

Ellenrieder, A. D., Kremer, W., Kattenbeck, B., Hantschel, O., Horn, G., Kalbitzer, H. R., et al. (2004). The central domain of the matrix protein of HIV-1: influence on protein structure and virus infectivity. *Biol. Chem.* 385, 303–313. doi: 10.1515/bc.2004.026

Freed, E. O. (1998). HIV-1 gag proteins: diverse functions in the virus life cycle. *Virology* 251, 1–15. doi: 10.1006/viro.1998.9398

Jang, Y. Y., Cai, L., and Ye, Z. (2016). Genome editing systems in novel therapies. *Discov. Med.* 21, 57–64.

Jinwei, Z., Qipin, X., Jing, Y., Shumin, Y., and Suizhong, C. (2015). CRISPR/Cas9 genome editing technique and its application in site-directed genome modification of animals. *Yi Chuan* 37, 1011–1020. doi: 10.16288/j.yczz.15-066

Maeder, M. L., and Gersbach, C. A. (2016). Genome-editing technologies for gene and cell therapy. *Mol. Ther.* 24, 430–446. doi: 10.1038/mt.2016.10

Markham, R. B., Yu, X., Farzadegan, H., Ray, S. C., and Vlahov, D. (1995). Human immunodeficiency virus type 1 env and p17gag sequence variation in polymerase chain reaction-positive, seronegative injection drug users. *J. Infect. Dis.* 171, 797–804. doi: 10.1093/infdis/171.4.797

Mazda, O., Satoh, E., Yasutomi, K., and Imanishi, J. (1997). Extremely efficient gene transfection into lympho-hematopoietic cell lines by Epstein–Barr virus-based vectors. *J. Immunol. Methods* 204, 143–151. doi: 10.1016/S0022-1759(97)00036-7

Mei, Y., Wang, Y., Chen, H., Sun, Z. S., and Ju, X. D. (2016). Recent progress in CRISPR/Cas9 Technology. *J. Genet. Genomics* 43, 63–75. doi: 10.1016/j.jgg.2016.01.001

Pierson, T., McArthur, J., and Siliciano, R. F. (2000). Reservoirs for HIV-1: mechanisms for viral persistence in the presence of antiviral immune responses and antiretroviral therapy. *Annu. Rev. Immunol.* 18, 665–708. doi: 10.1146/annurev.immunol.18.1.665

Sakuma, T., Hosoi, S., Woltjen, K., Suzuki, K., Kashiwagi, K., Wada, H., et al. (2013). Efficient TALEN construction and evaluation methods for human cell and animal applications. *Genes Cells* 18, 315–326. doi: 10.1111/gtc.12037

Strong, C. L., Guerra, H. P., Mathew, K. R., Roy, N., Simpson, L. R., and Schiller, M. R. (2015). Damaging the integrated HIV proviral DNA with TALENs. *PLoS ONE* 10:e0125652. doi: 10.1371/journal.pone.0125652

Conflict of Interest Statement: The authors declare that the research was conducted in the absence of any commercial or financial relationships that could be construed as a potential conflict of interest.

Copyright © 2016 Kishida, Ejima and Mazda. This is an open-access article distributed under the terms of the Creative Commons Attribution License (CC BY). The use, distribution or reproduction in other forums is permitted, provided the original author(s) or licensor are credited and that the original publication in this journal is cited, in accordance with accepted academic practice. No use, distribution or reproduction is permitted which does not comply with these terms.

frontiers in Microbiology

ORIGINAL RESEARCH
published: 18 May 2016
doi: 10.3389/fmicb.2016.00745

Proteomic Analysis of a Novel *Bacillus* Jumbo Phage Revealing Glycoside Hydrolase As Structural Component

Yihui Yuan and Meiying Gao *

Key Laboratory of Agricultural and Environmental Microbiology, Wuhan Institute of Virology, Chinese Academy of Sciences, Wuhan, China

Tailed phages with genomes of larger than 200 kbp are classified as Jumbo phages and exhibited extremely high uncharted diversity. The genomic annotation of Jumbo phage is often disappointing because most of the predicted proteins, including structural proteins, failed to make good hits to the sequences in the databases. In this study, 23 proteins of a novel *Bacillus* Jumbo phage, vB_BpuM_BpSp, were identified as phage structural proteins by the structural proteome analysis, including 14 proteins of unknown function, 5 proteins with predicted function as structural proteins, a glycoside hydrolase, a Holliday junction resolvase, a RNA-polymerase β-subunit, and a host-coding portal protein, which might be hijacked from the host strain during phage virion assembly. The glycoside hydrolase (Gp255) was identified as phage virion component and was found to interact with the phage baseplate protein. Gp255 shows specific lytic activity against the phage host strain GR8 and has high temperature tolerance. *In situ* peptidoglycan-hydrolyzing activities analysis revealed that the expressed Gp255 and phage structural proteome exhibited glycoside hydrolysis activity against the tested GR8 cell extracts. This study identified the first functional individual structural glycoside hydrolase in phage virion. The presence of activated glycoside hydrolase in phage virions might facilitate the injection of the phage genome during infection by forming pores on the bacterial cell wall.

Keywords: jumbo bacteriophage, structural proteome, glycoside hydrolase

OPEN ACCESS

Edited by:
Akihide Ryo,
Yokohama City University, Japan

Reviewed by:
Masaaki Murakami,
Hokkaido University, Japan
Halim Maaroufi,
Université Laval, Canada

***Correspondence:**
Meiying Gao
mygao@wh.iov.cn

Specialty section:
This article was submitted to Virology, a section of the journal Frontiers in Microbiology

Received: *24 March 2016*
Accepted: *03 May 2016*
Published: *18 May 2016*

Citation:
Yuan Y and Gao M (2016) Proteomic Analysis of a Novel Bacillus Jumbo Phage Revealing Glycoside Hydrolase As Structural Component. Front. Microbiol. 7:745. doi: 10.3389/fmicb.2016.00745

INTRODUCTION

Bacteriophages are viruses infecting bacteria and exhibit extremely high abundant and diversity (Rohwer, 2003; Mizuno et al., 2013). Tailed phages with genomes larger than 200 kbp are known as "Jumbo phages" or "giant phages" (Hendrix, 2009). Although the Jumbo phage was discovered 47 years ago (*Bacillus* phage G), they have rarely been isolated, and so far, only the genomes of 82 Jumbo phages have been deposited in the GenBank database. The newly isolated Jumbo phages usually exhibit low genome similarity to the previously isolated ones and contain numerous genes of unknown function (Lecoutere et al., 2009; Abbasifar et al., 2014). Hence, genomic annotation of Jumbo phages is often disappointing. Structural proteome analysis of phages has been proved to an effective approach for identifying unknown phage structural proteins and for discovering new phage structural proteins. Proteomic analysis of *Pseudomonas* Jumbo phage 201ϕ2-1 virions revealed that

the RNA polymerase β or β′ subunit is component of phage virions and this phage contains more structural proteins than the smaller phages (Thomas et al., 2008, 2010). In our lab, a novel *Bacillus pumilus* Jumbo phage, vB_BpuM_BpSp, was isolated and sequenced. The phage exhibits extremely low genome similarity to the existing biological entities and its virions contain several unique substructures, including the curly tail fibers (unpublished data). Genomic annotation of phage vB_BpuM_BpSp (GenBank accession number KT895374) identified eight phage structural proteins, including four proteins with no exact function assigned. In this study, we analyzed the structural proteome of the Jumbo phage vB_BpuM_BpSp, and our results show that an individual glycoside hydrolase is component of the phage virion and it was found to interact with the baseplate protein. The existence of a glycoside hydrolase as phage structural component might facilitate the infection of phage vB_BpuM_BpSp to the host strain *B. pumilus*.

Glycoside hydrolases are encoded by microbes and plants to catalyze the hydrolysis of polysaccharides (Bissaro et al., 2015). The function of glycoside hydrolase is similar to that of phage endolysin, which degrades the bacterial cell wall and facilitate the release of mature progeny phages (Hermoso et al., 2007). Several phages employ cell wall hydrolases to facilitate infection. The tail fiber protein of *Escherichia coli* phage T5 acts as a peptidoglycan hydrolase to form pores on the bacterial cell wall to transfer phage genome DNA (Boulanger et al., 2008). The tail spike proteins of *Salmonella* phage P22, *Shigella* phage Sf6, *E. coli* phage HK620 and K5A all exhibit glycoside hydrolase activity (Chen and King, 1991; Bhardwaj et al., 2011). Phage Basilisk contains a chitinase as a virion structural component. However, the function of the chitinase is unknown (Grose et al., 2014). The existence of the glycoside hydrolase domains on phage tail fiber and tail spike proteins could facilitate host recognition and infection of phages, through the binding and degradation of host lipopolysaccharides (Thompson et al., 2010). Genes encoding glycoside hydrolases have been found in several phage genomes (Maaroufi and Levesque, 2015). These discovered glycoside hydrolase domains all are the part of phage structural proteins, and to our knowledge, no individual glycoside hydrolase that might benefit the phage infection has been found. Comparison to phages with small genomes, the Jumbo phages contain large dsDNA genomes. Thus, the injection of Jumbo phage genomes is much more difficult and time consumption. To date, no mechanism that facilitates Jumbo phage genome injection and phage infection has been reported.

MATERIALS AND METHODS

Bacterial Strains and Growth Conditions

Strains and plasmids used in this study are shown in **Table 1**. All strains were cultured in LB broth with moderate shaking.*E. coli* M15 and BL-21 were used for protein expression. *Bacillus anthracis* CMCC63605, *Bacillus thuringiensis* HD-73, *Bacillus cereus* 411A, *Bacillus subtilis* 168, *Pseudomonas aeruginosa* PAO1 (ATCC47085), *Yersinia pseudotuberculosis* NaI were collected by our lab and used for the lytic spectrum test. Antibiotics were used at a concentration of 100 μg/ml for ampicillin and 34 μg/ml for kanamycin.

Structural Proteome Analysis of Phage Virions

Phages purified by sucrose density gradient centrifugation were used for SDS-PAGE (Sodium Dodecyl Sulfate Polyacrylamide Gel Electrophoresis) analysis as described before (Yuan et al., 2015). After separation by 15% SDS-PAGE, the gel was stained b with Coomassie blue and destained with water. The proteins used for HPLC-ESI-MS/MS (High Performance Liquid Chromatography Electrospray Tandem Mass Spectrometry) analysis were separated by 15% SDS-PAGE for 20 min, and the 1.5-cm gel region containing partially separated proteins was excised, followed by in-gel digestion and MS analysis. HPLC-ESI-MS/MS was performed on a linear ion trap mass spectrometer LTQ Orbitrap Velos (Thermo Fisher, Massachusetts, USA). The MS data was analyzed using Mascot version 2.3.0 and Sequest 1.2.0.208 against the local database of all possible phage proteins and host strain proteins, and the online NR (non-redundant protein sequence) database in NCBI.

Bioinformatic Analysis of Protein Gp255

The functional domain composition of protein Gp255 was predicted using Pfam database (Punta et al., 2012), Conseved Domain Database (Marchler-Bauer et al., 2013), PDB database (http://www.rcsb.org/pdb/home/home.do), and HHpred (Soding et al., 2005). The phage proteins belonging to glycoside hydrolase family 25 (GH25) were found by searching the CAZy database (http://www.cazy.org/GH25_viruses.html; Henrissat and Bairoch, 1996). Amino acid sequences of Gp255 and similar proteins were aligned using ClustalW 2.0 (Larkin et al., 2007) and Mega 6.0 (Tamura et al., 2013).

Expression, Purification, and Functional Analysis of *gp*255 and *gp*287

DNA manipulation was carried out as described before (Sambrook et al., 2001). The primers used and plasmids constructed in this study are shown in **Table 1**. Gene *gp*255 and the truncated *gp*255 were amplified from the phage genome and inserted into the *Bam*H I/*Sal* I sites of plasmid pET28a. The recombinant plasmid was transformed into *E. coli* BL21 to generate recombinant *E. coli* strain for protein expression. The proteins was expressed by induction with 0.4 mM IPTG (isopropyl-β-D-thiogalactopyranoside) and purified by Ni-NTA (nickel-nitrilotriacetic acid) columns (Qiagen, Dusseldorf, Germany) and buffer exchanged into 50 mM Tris (pH 8.0), 300 mM NaCl, 10% glycerol, and 1 mM β-mercaptoethanol. The lytic activities of Gp255 against *B. pumilus* GR8 and other strains used for lytic spectrum assay were investigated as described previously (Yuan et al., 2012). The exponential-growth cells were collected and resuspended in the reaction buffer (50 mM Tris [pH8.0], 300 mM NaCl, 10% [vol/vol] glycerol, and 1 mM β-mercaptoethanol) at about 0.8 optical density at 600 nm. Purified protein Gp255 was added into the bacterial suspension to a final concentration

TABLE 1 | Strains and plasmids used in this study.

Bacteria, plasmid, or primer	Relevant characteristics	Reference or resource
BACTERIA		
***B. pumilus* strains**		
GR8	*B. pumilus* strain, pathogen of ginger rhizome rot disease, host strain of phage vB_BpuM_BpSp	Peng et al., 2013
***E. coli* strain**		
BL21(DE3)	F^- *dcm ompT hsdS*($r_B^- m_B^-$)*gal* λ(DE3)	Novagen
M15	*lac gal mtl recA*$^+$ *uvr*$^+$ [pREP4 *lac*I Kan^R]	Qiagen
PLASMIDS		
pET-28a(+)	Expression vector; Kan^r, C/N-terminal His tag/thrombin/T7 tag, T_7 *lac* promoter, T7 transcription start, f1 origin, *lacI*	Novagen
pET/*gp255*	Kan^r, *gp*255 of phage vB_BpuM_BpSp was cloned into pET-28a(+) *Bam*H I/*Sal* I site	This study
pET/*gp255C*	Kan^r, 3′ termini 642 bp of *gp*255 of phage vB_BpuM_BpSp was cloned into pET-28a(+) *Bam*H I/*Sal* I site	This study
pET/*gp255N*	Kan^r, 5′ termini 567 bp of *gp*255 of phage vB_BpuM_BpSp was cloned into pET-28a(+) *Bam*H I/*Sal* I site	This study
pQE30	Expression vector; Amp^r, N-terminal His tag, T_5 *lac* promoter, T5 transcription start, ColE1 origin, *lacI*	Qiagen
pQE/*gp287*	Amp^r, *gp*287 of phage vB_BpuM_BpSp was cloned into pQE30 BamH I/*Sal* I site	This study
PRIMERS		
*gp*255-F/*Bam*H I	GAGGATCCAAAGGTACAGTTGACG, forward primer to amplify *gp255*	This study
*gp*255-R/*Sal* I	GCGTCGACAATACCATTAATTAGAC, reward primer to amplify *gp255*	This study
*gp*255-R567/*Sal* I	GCGTCGACAATACCATTAATTAGAC, reward primer to amplify *gp255N*	This study
*gp*255-F568/*Bam*H I	GAGGATCCAAAGGTACAGTTGACG, forward primer to amplify *gp255C*	This study
*gp*287-F/*Bam*H I	GAGGATCCATGAATGATTTTAAGG, forward primer to amplify *gp287*	This study
*gp*287-F/*Sal* I	CTGTCGACCTATAAATATATTTTTG, reward primer to amplify *gp287*	This study

of 0.05 μM and the absorbance of the bacterial suspension at 600 nm was tested at an interval of 30 s at 37°C. Protein Gp255 used for Far western blotting analysis was labeled with biotin as the manufactures' instruction (Roche, Basel, Switzerland).

The gene *gp*287 was amplified from the phage genome by using primer pairs *gp*287-F/*Bam*H I and *gp*287-R/*Sal* I, and inserted into the *Bam*H I/*Sal* I sites of plasmid pQE30. The recombinant plasmid was transformed into *E. coli* M15 to produce recombinant *E. coli* strain. Protein Gp287 was expressed by inducing the strain with 0.4 mM IPTG and purified by Ni-NTA columns.

Analysis of the Peptidoglycan-Hydrolyzing Activities of the Phage vB_BpuM_BpSp Virion Proteome

The peptidoglycan-hydrolyzing activities of the structural proteomic proteins of phage vB_BpuM_BpSp were analyzed by zymogram analysis as described previously (Buist et al., 1995). The exponential growth bacterial strains were collected by centrifugation and sterilized at 121°C for 20 min before use. The phage proteomic proteins and Gp255 were separated using 12% SDS-PAGE containing 0.4% autoclaved GR8 cells. After separation, the gel was rinsed with 2.5% Triton X-100 for four times (20 min each) at room temperature and was incubated overnight at 37°C in renaturation buffer (50 mM 2-morpholinoethanesulfonic acid, 1% Triton X-100, 1 mM $MgCl_2$, 1 mM $CaCl_2$, pH 6.5). After that, the gel was rinsed with distilled water and stained with 1% methylene blue in 0.01% KOH for 2 h, and subsequently destained with distilled water.

Identification of Proteins That Interact with Gp255

To identify the phage structural proteins that intact with Gp255, purified phage virions were separated by 15% SDS-PAGE and transferred onto PVDF membrane (Millpore, Massachusetts, USA). Far western blotting was carried out as described previously (Javed et al., 2015) by using the biotin-labeled Gp255 at a hybrid concentration of 5 μg/ml. The protein band in the gel corresponding the hybridization band on the PVDF membrane was sliced and in-gel digested, followed by identification with MALDI-TOF-TOF MS (Matrix-assisted Laser Desorption Ionization Tandem Time of Flight Mass Spectrometry) on an Ultraflex MALDI-TOF/-TOF mass spectrometer (Bruker, Karlsruhe, Germany; Lavigne et al., 2006). To verify the interaction of Gp255 with the identified protein Gp287, purified Gp287 was separated by SDS-PAGE, and Far western blotting was carried out as described above. The Western blotting of Gp287 was performed by using the mouse monoclonal antibody anti-His_6 (Roche, Basel, Switzerland), and biotin-labeled Gp255.

RESULTS

Structural Proteome of Jumbo Phage vB_BpuM_BpSp

General Features of Jumbo Phage vB_BpuM_BpSp Structural Proteome

Genomic analysis revealed that eight genes in Jumbo phage vB_BpuM_BpSp genome predictably code phage structural proteins, including virion structural protein (Gp25), major virion structural protein (Gp133), prohead core scaffold protein and protease (Gp191), structural protein precursor (Gp197), tail sheath protein (Gp202), portal vertex protein (Gp204), virion structural protein (Gp269), and baseplate protein (Gp287), whereas the genes encoding the phage capsid protein, tail tube protein, and tail fiber protein, are unknown. To identify the structural proteins in the mature phage virion of vB_BpuM_BpSp, purified phage virions were analyzed using SDS-PAGE followed by HPLC-MS/MS. In total, 23 structural proteins were identified (**Table 2**; **Figure 1**), including 22 phage-coding proteins and one host bacteria-coding protein. Among the 22 phage-coding proteins, 14 of them showed unknown functions, five were annotated as phage structural protein (virion structural protein, major virion structural protein, structural protein precursor, contractile tail sheath protein, and baseplate protein), and the other three proteins are glycoside hydrolase, Holliday junction resolvase, and RNA polymerase (RNAP) β subunit. In addition, by searching the MS data against the genome of the host strain *B. pumilus* GR8, one protein band was identified as phage portal protein (GenBank accession number AKU29927.1). Although three proteins, Gp191, Gp204, and Gp269, were annotated as phage structural proteins by genomic analysis, the corresponding bands were not identified on the SDS-PAGE. This might be due to the low copy numbers of these proteins in phage virion.

According to the bioinformatic analysis of the Jumbo phage vB_BpuM_BpSp genome, the genes encoding these 22 identified phage-coding structural proteins are mainly located at three separate regions in the genome, except for gene *gp*133, which is far from the three gene subclusters. The first gene cluster contains *gp*25, *gp*28, and *gp*31, whose functions are unknown. The second gene cluster contains nine genes from *gp*196 to *gp*223; the functions of most of them (*gp*196, *gp*203, *gp*208, *gp*214, *gp*218, and *gp*223) are unknown, except the following: structural proteins precursor gene (*gp*197), contractile tail sheath protein gene (*gp*202), and RNA polymerase (RNAP) βsubunit gene (*gp*212). The third gene cluster is composed of nine genes from *gp*255 to *gp*316, including the genes for glycoside hydrolase (*gp*255), Holliday junction resolvase (*gp*265), baseplate protein (*gp*287), and other genes with unknown functions (*gp*271, *gp*272, *gp*299, *gp*307, *gp*316, and *gp*2).

TABLE 2 | Characteristic of the vB_BpuM_BpSp virion proteome identified by HPLC-ESI_MS/MS.

Gp	Molecular mass (kDa)	No. of identified peptides	Coverage (%)	Predicted function
Gp2	28.1	2	6.3	Hypothetical protein
Gp25	101.1	8	9.3	Virion structural protein
Gp28	35.3	5	17.4	Hypothetical protein
Gp31	19.3	4	4.2	Hypothetical protein
Gp133	38.5	5	17.7	Major virion structural protein
Gp196	35.2	5	14.2	Hypothetical protein
Gp197	60.8	8	15.2	Structural protein precursor
Gp202	111.9	13	15	Contractile tail sheath protein
Gp203	29.7	6	27.5	Hypothetical protein
Gp208	104.6	8	9.3	Hypothetical protein
Gp212	58.7	6	13.9	RNA polymerase β-subunit
Gp214	15.9	3	19.6	Hypothetical protein
Gp218	11.6	3	29.6	Hypothetical protein
Gp223	38.5	3	11.6	Hypothetical protein
Gp255	43.3	6	14.9	Glycoside hydrolase
Gp265	24.9	2	8.6	Holliday junction resolvase
Gp271	39	6	26.2	Hypothetical protein
Gp272	41	11	31.3	Hypothetical protein
Gp287	16	2	30.9	Baseplate protein
Gp299	15	5	23.5	Hypothetical protein
Gp307	10.8	2	12.2	Hypothetical protein
Gp316	25.2	2	10.3	Hypothetical protein
AKU31945.1[a]	34.2	5	19.2	Phage portal protein

[a] *GenBank accession number of the proteins from host strain GR8.*

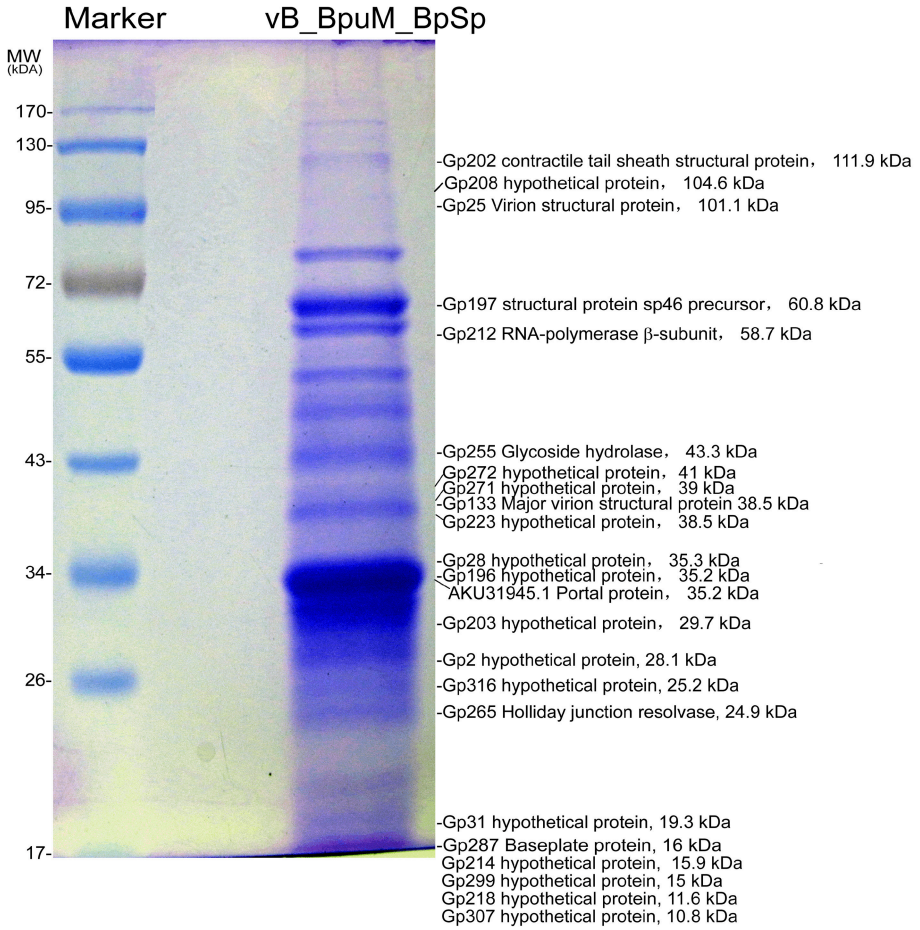

FIGURE 1 | Proteomic analysis of the structural proteins of phage vB_BpuM_BpSp. The phage purified by sucrose density gradient centrifugation was analyzed by SDS-PAGE and the protein bands were further identified by HPLC-MS/MS. The molecular weight standard is indicated on the left. The corresponding CDSs, the predicted functions, and the predicted molecular mass of the proteins identified by mass spectrometry were also indicated.

Candidate Genes for Phage Curly Tail Fibers

A notable feature of the Jumbo phage vB_BpuM_BpSp is their curly tail fibers. The curly tail fibers have also been observed on the virions of *B. thuringiensis* phage 0305ϕ8-36, and the proteins ORF119, ORF129, and ORF131 of phage 0305ϕ8-36 have been speculated to be candidate curly tail fiber proteins (Thomas et al., 2007). However, such candidates for other phages remain unknown. Comparative proteomic analysis of the phages, vB_BpuM_BpSp and 0305ϕ8-36, revealed that two of the identified structural proteins (Gp25 and Gp133) of the phage vB_BpuM_BpSp are similar to the proteins, ORF154 and ORF129, of phage 0305ϕ8-36, respectively. Protein ORF154 was also identified as the associated tail protein in phage 0305ϕ8-36, although its exact function is unknown. Though the phages, vB_BpuM_BpSp and 0305ϕ8-36, exhibit extremely low similarity in genome sequences, they have similar tail fiber structures. The homologous structural protein coding genes, *gp*25 and *gp*133, might be candidate genes for curly tail fiber protein.

Candidate Genes for Phage Capsid Protein

Previous analysis of phage virion proteomes has revealed that the major capsid protein and tail sheath protein are the most abundant proteins in phage virions (Miller et al., 2003; Lecoutere et al., 2009; Chan et al., 2014). Genome annotation of the phage vB_BpuM_BpSp revealed that its capsid proteins are unknown. In this study, the most abundant protein bands on the SDS-PAGE were identified to that of Gp196 and Gp197 (**Figure 1**). By analyzing these two proteins using HHpred, we found that Gp197 contains head vertex protein domain, whereas no functional domain was found in protein Gp196. Among the genes near *gp*196 and *gp*197 in the phage vB_BpuM_BpSp genome, *gp*191, *gp*204, and *gp*198 encode prohead core scaffold protease, portal vertex protein, and terminase large subunit, respectively. Genes with related functions usually form gene clusters in phage genomes (Thomas et al., 2007). Considering the location of these two genes in the phage genome and the results of their bioinformatic, we postulate that *gp*197 might be the major phage capsid protein gene.

Bioinformatic Features of Gp255

Structural proteomic analysis of phage vB_BpuM_BpSp virion revealed that six peptides were mapped to the glycoside hydrolase (Gp255), suggesting Gp255 is the structural component of the phage virion and it is located in the third gene subcluster of the structural protein-associated genes in the phage genome (**Figure 1**). The G+C content of gene *gp*255 is 30.27%, which is a little higher than that of the phage genome (25.9%). Structural analysis of the proteins indicates that protein Gp255 contains a N-terminal glycosyl hydrolase catalytic domain, with four of the six peptides identified by MS mapped to this domain, and three LysM peptidoglycan binding domains, with one peptide identified by MS mapped to the first LysM domain (**Figure 2A**). Though only low similarity was observed, the catalytic domain contain conserved catalytic site residues as the endolysin of *Clostridium perfringens* phage phiSM101 (**Figure 2B**) (Tamai et al., 2014). All three LysM domains have 43 amino acid residues and the first one differs from the second one by only three amino acid residues, whereas the third one shows low similarity to the first and the second ones (**Figure 2C**). Compared to the LysM domains of fungal effector Ecp6, the three LysM domains of Gp255 contain conserved chitin-binding sites for peptidoglycan binding (Sánchez-Vallet et al., 2013). A BlastP search of the protein in the NR database in NCBI revealed that Gp255 exhibits only 23.7% similarity to the endolysin of the *Lactobacillus fermentum* phage ϕPYB5 (Wang et al., 2008), but the protein has higher similarity to bacterial glycoside hydrolases. Based on the similarities of Gp255 to other glycosyl hydrolases, Gp255 belongs to the glycoside hydrolase family 25 (GH25). Among the glycoside hydrolase of GH25 family, 128 proteins encoded by the phage genome were found in the CAZy database and these protein have been annotated largely as phage endolysins. Other than Gp255, there are two more genes that encode polysaccharide hydrolases in the phage vB_BpuM_BpSp genome. These two polysaccharide hydrolases are N-acetylmuramoyl-L-alanine amidase (Gp019) and spore cortex-lytic enzyme (Gp067). The N-acetylmuramoyl-L-alanine amidase could be the phage endolysin that lyse the host cell to release mature progeny phages, while the function of spore cortex-lytic enzyme to phage vB_BpuM_BpSp is unknown.

Functional Characterization of Glycoside Hydrolase Gp255

Glycoside hydrolase protein Gp255 encoded by gene *gp*255 in the phage vB_BpuM_BpSp genome was expressed and its function was analyzed. G255 could lyze the tested cell extracts of strain GR8 and N-termini of protein Gp255 was proved to

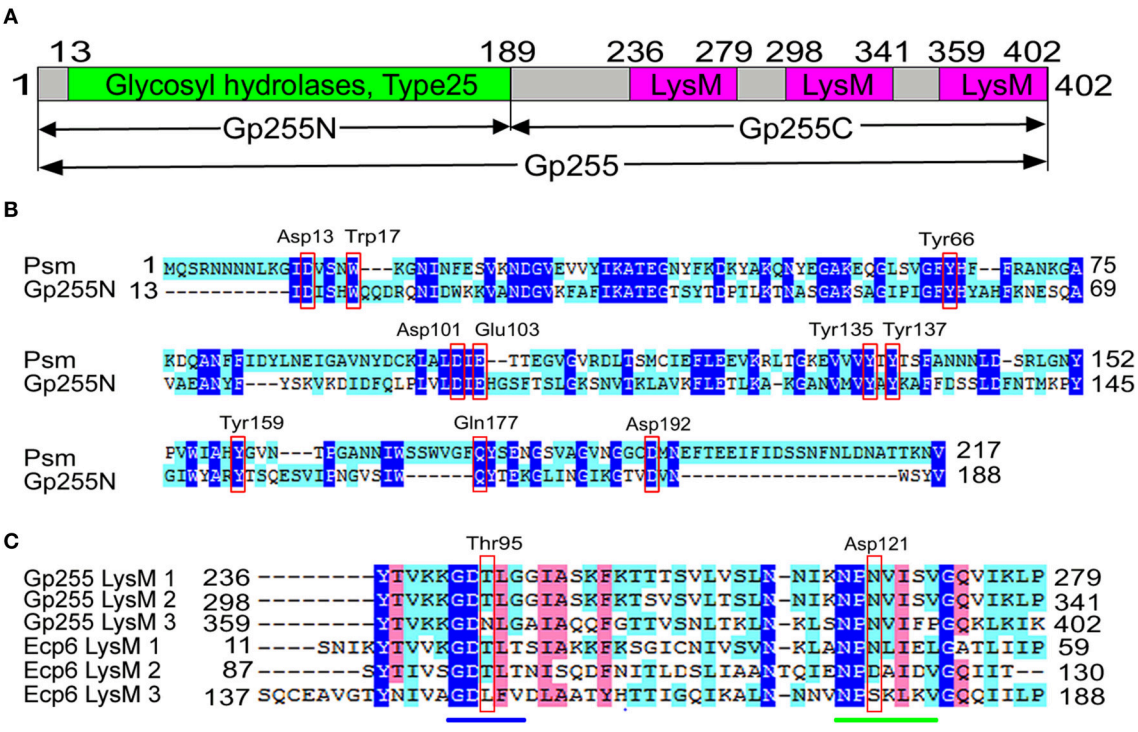

FIGURE 2 | Schematic diagram of Gp255 and amino acid sequence alignment of the LysM domains. (A) The domain composition of Gp255 analyzed by using Pfam and the positions of the amino acid residues at the end of each domain are indicated. The N-terminal catalytic domain and C-terminal cell wall binding domains are shown. **(B)** Alignment of the catalytic domain of Gp255 and endolysin Psm (PDB database accession number 4KRU_A) from phage phiSM101. The catalytic site residues of endolysin Psm are indicated in red box. **(C)** Alignment of the amino acid sequence of the three LysM domains from Gp255 and the three LysM domain from fungal efector Ecp6 (PDB database accession number 4B8V_A). The positions of the three peptides in Gp255 and Ecp6 are indicated. The two chitin-binding sites in LysM1 and LysM3 of Ecp6 are indicated with a blue line and a green line. The chitin-binding sites of LysM2 of Ecp6 are indicated in red box. The sequences were aligned by ClustalW 2.0.

be the catalytic domain of the protein (**Figures 3A,B**). Purified protein Gp255 exhibited high lytic activity against the host strain *B. pumilus* GR8 at a low concentration of 0.0125 μM (**Figure 3C**). Temperature tolerance assay of Gp255 indicated that it has high temperature tolerance and can maintain its lytic activity even after exposure to 100°C for 10 min (**Figure 3D**). Gp255 caused the cell lysis of strain GR8 by a similar catalytic mechanism similar to that of phage endolysin by degrading the cell wall, thus causing further the damage of the bacterial cells (**Figure 3E**). Gp255 showed high lytic specificity to the tested strain GR8 and weak lytic activities to the tested strains of *B. subtilis* and *B. anthracis*, and no lytic activities against the tested strains of *B. thuringiensis*, *B. cereus*, *E. coli*, *Y. pseudotuberculosis*, and *P. aeruginosa* (**Figure 4**).

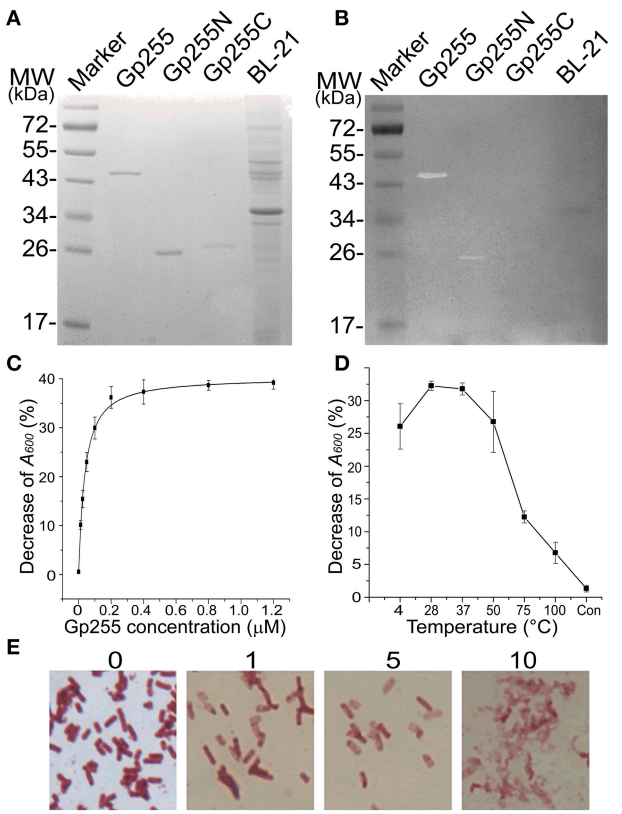

FIGURE 3 | Characterization of protein Gp255. (A) SDS-PAGE analysis of purified Gp255, Gp255N, Gp255C, and *E. coli* strain BL-21. **(B)** In-gel lytic activities of proteins Gp255, Gp255N, Gp255C, and *E. coli* strain BL-21. The purified proteins were mixed with loading buffer for use. **(C)** The influence of protein concentration on the lytic curve of Gp255. Gp255 was used at different concentration and the test was carried out at 37°C. **(D)** Temperature tolerance of Gp255. Gp255 at a concentration of 10 μM was treated at different temperatures for 10 min and the treated proteins were used for lytic activity evaluation at a final concentration of 0.05 μM. The cells treated with PBS solution was used as control (indicated as "Con"). **(E)** Lytic activity of Gp255 against *B. pumilus* strain GR8. The strain GR8 was observed by optical microscope at 0, 1, 2, and 10 min after treatment and the time of observation is indicated. The purified Gp255 was used with a final concentration of 0.05 μM and the tests were carried out at 37°C.

Peptidoglycan-Hydrolyzing Activities of vB_BpuM_BpSp Structural Proteome and Gp255

To analyze the existence and activity of Gp255 in the phage structural proteome, the phage proteome and purified protein Gp255 was separated by SDS-PAGE and the peptidoglycan-hydrolyzing activities were tested *in situ* against the crude cell extract of strain GR8. The results indicate that both the boiled and unboiled protein Gp255 show high lytic activities against the bacterial cell extracts in the gel (**Figure 5**). Though huge reduction of lytic activity after exposure to 100°C was observed in **Figure 3D**, similar activities of Gp255 and boiled Gp255 were observed in the gel, which might be because the lytic activity of the boiled Gp255 was recovered after treatment of renaturation buffer. A degradation zone with almost the same molecular weight as that of Gp255 lane was observed in the lane of phage vB_BpuM_BpSp, indicating that Gp255 is a component of the phage vB_BpuM_BpSp and the protein in phage virion still displays peptidoglycan hydrolase activity.

Interaction of Gp255 and Phage Baseplate Protein Gp287

Purified Gp255 was labeled with biotin and a Far western blotting analysis of Gp255 was carried out. The results indicate that labeled Gp255 possibly interacts with a unique protein with a molecular weight of 16 kDa in the structural proteome of phage vB_BpuM_BpSp, and the protein was identified as the phage baseplate protein (Gp287) by MALDI-TOF-TOF MS (**Figure 6A**). Protein Gp287 was expressed and the interaction between Gp255 and Gp287 was verified by Far western blotting analysis, suggesting Gp255 might indeed interact with Gp287 (**Figure 6B**). According to previous reports, the polysaccharide lytic enzyme domain acts as a part of the phage tail fiber or tail spike proteins, which interacted with the baseplate of the phage (Yap and Rossmann, 2014). Our result showed that Gp255 could also interact with the baseplate substructure. SDS-PAGE analysis of the structural proteome of phage vB_BpuM_BpSp showed that Gp255 is highly abundance (**Figure 1**), suggesting that the baseplate substructure containing Gp255 might be a major substructure of phage vB_BpuM_BpSp.

DISCUSSION

The newly isolated Jumbo phages have often been found to exhibit low similarity to existing biological entities and show numerous uncharted features. The genomic annotation of Jumbo phage genome is often disappointing because most of the predicted proteins, including the structural proteins, fail to make good hits to the sequences in the databases. The genomic annotation of Jumbo phage vB_BpuMP_BpSp only revealed eight predicted phage structural proteins, and the genes encoding other phage structural proteins remain unknown. Structural proteomic analysis combined with bioinformatic analysis of phage vB_BpuM_BpSp identified 22 phage-coding structural proteins, including 14 proteins with unknown function, a glycoside hydrolase, a Holliday junction resolvase, a RNA

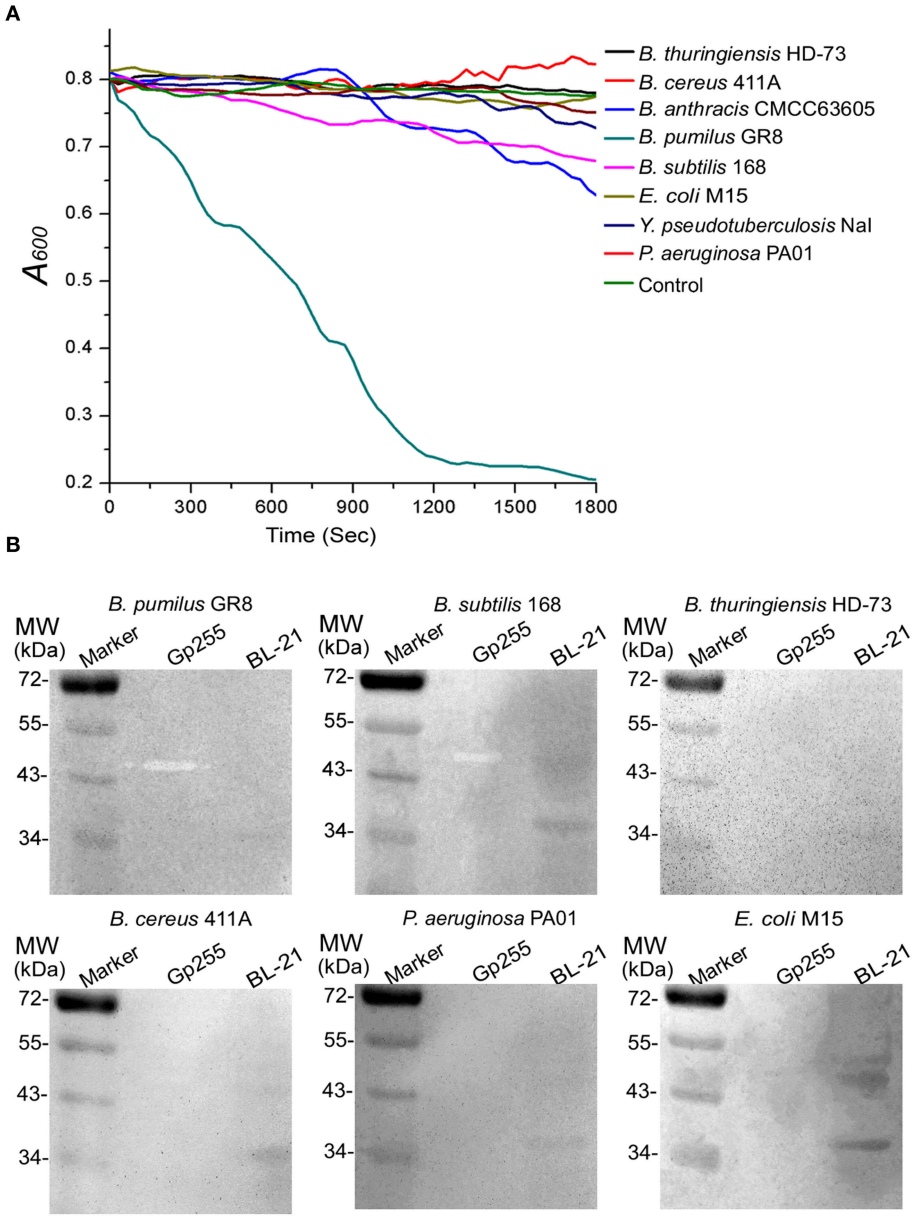

FIGURE 4 | Lytic specificity of Gp255. (A) Lytic activity of Gp255 against eight tested strains. The suspension of exponential-growth GR8 without adding Gp255 was used as control. For the Gram-negative strain, EDTA was added into the reaction buffer at a concentration of 1 mM. **(B)** In-gel lytic activity assay of Gp255. The crude cell extracts of six strains were used.

polymerase (RNAP) β subunit, and five other annotated structural proteins. Among the 14 proteins of unknown function, the candidates for the curly phage tail fiber protein and the major capsid protein were predicted by bioinformatic analysis. To our knowledge, glycoside hydrolase, Holliday junction resolvase, and RNA polymerase (RNAP) β subunit are rarely found in phage virions. Our findings of new structural proteins of phage vB_BpuM_BpSp suggests that structural proteomic analysis of phage virions is a promising approach for the identification of unknown phage structural components.

Besides the identified structural proteins encoded by phage vB_BpuM_BpSp genome, a portal protein encoded by the host strain genome was found. Either the host-coding portal protein, instead the phage-coding portal protein, is hijacked by the phage vB_BpuM_BpSp to assemble progeny phage particle, or the portal protein is packaged into the phage virion by mistake in some non-function way. Besides the identified portal protein, the genome of the host strain GR8 also encode 15 more phage portal protein homologs, which were not identified by proteomic analysis of phage virions, further supporting the speculation that

the identified portal protein might be a functional component hijacked by phage vB_BpuM_BpSp from the host strain.

The RNA polymerase β subunit was identified as one of the phage vB_BpuM_BpSp structural proteins. It was also found in the virion proteome of phage 201ϕ2-1, and possibly in that of *B. subtilis* phage PBS2 as well, and is thought to be phage virion-associated RNAP, which might be injected into the host cell during phage infection to facilitate the synthesis of phage proteins at the early stage after infection, including the genome replication-associated proteins and phage specific proteins, before the expression of other phage RNAPs (Clark et al., 1974; Thomas et al., 2008). Another identified structural protein, the Holliday junction resolvase, binds and cleaves the junction in the phage genome to further facilitate the replication of phage genome, the packaging of circular genome during phage assembly, and the release of condensed genome during phage infection by localizing at portal of the phage head (Golz and Kemper, 1999; Dixit et al., 2011; Green et al., 2013). The Holliday junction resolvase in phage virion might be the remnant of the phage genome package device or the facilitating mechanism for the translocation of large, condensed phage genome to host cell during infection. Phage vB_BpuM_BpSp has a large genome, and the packaging and release of the phage genome is an energy consuming process. The structural RNA polymerase β subunit and Holliday junction resolvase identified in the vB_BpuM_BpSp proteome might be components of an adaption mechanism to overcome these problems. Further confirmation of these findings and functional analysis of these two proteins would shed more light on their roles in phage virions.

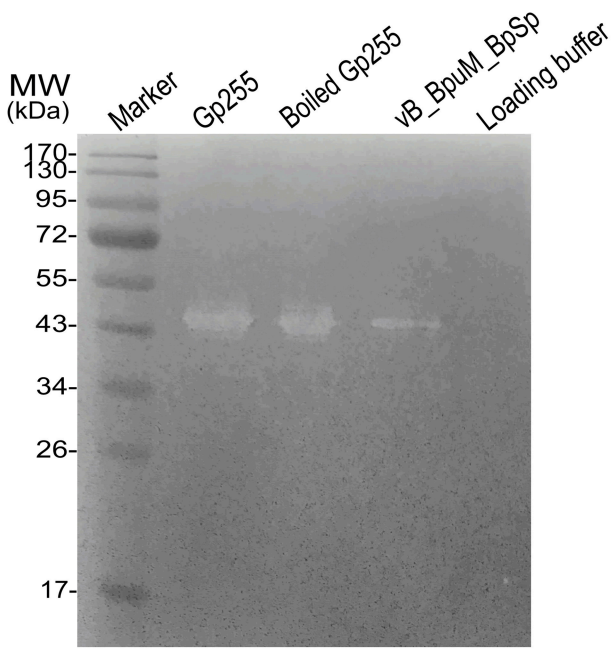

FIGURE 5 | Analysis of peptidoglycan-hydrolyzing activities of phage vB_BpuM_BpSp. The purified phage vB_BpuM_BpSp was mixed with loading buffer and boiled at 100°C for 10 min before separating them by SDS-PAGE. The purified Gp255 was mixed with loading buffer. After that, the unboiled (indicated as "Gp255") and boiled (indicated as "Boiled Gp255") proteins were separated by SDS-PAGE. The sterilized crude cell extracts of GR8 was added into the gel for lytic activity assay. The lane loaded with 1× Loading buffer were used as control.

Phages recognize host cell by the "walk" of the tail fiber on the cell surface (Hu et al., 2015). The reversible binding of phage tail fibers to bacterial cell wall leads the phage to the optimal site for irreversible absorption and subsequent infection. Jumbo phage vB_BpuM_BpSp has a fragile head, and the tail sheath substructure is easily separated. The curly tail fiber of vB_BpSp_BpSp is longer than the tail fiber of myovirus with smaller genome (Hu et al., 2015) and it swing more easily. The long, flexible tail fiber might lead the phage vB_BpuM_BpSp to optimal infection site quickly and reduce the damage of phage

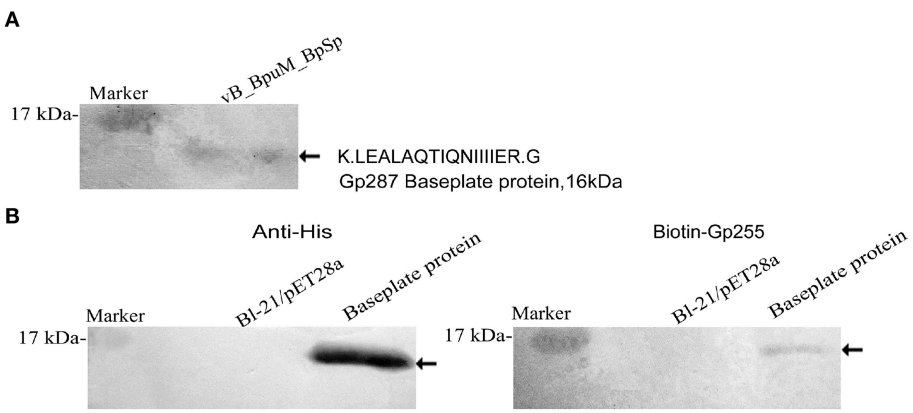

FIGURE 6 | Identification of the phage structural protein that interacted with Gp255. (A) Identification of the interacting protein of Gp255 in phage vB_BpuM_BpSp structural proteome. The virions of phage vB_BpuM_BpSp were separated by SDS-PAGE and biotin-labeled Gp255 was used for Far-western blotting analysis. The detected protein band was identified by MALDI-TOF/-TOF MS. The identified peptide and corresponding protein encoded by phage vB_BpuM_BpSp are indicated. **(B)** Verification of the interaction between Gp255 and Gp287. Purified Gp287 were separated by 15% SDS-PAGE. *E. coli* strain BL-21/pET28a was used as control. Western blotting was carried by using the antibody of 6 × His-tag and the biotin-labeled Gp255, respectively. The detected hybridization bands are indicated.

virion during recognition. Similar helical tail fibers have only been observed in the *B. thuringiensis* phage 0305ϕ8-36 (Serwer et al., 2007), *B. subtilis* phage AR9 (Belyaeva and Azizbeky, 1968), *B. subtilis* phage PBS1 (Eiserlin, 1967), *B. cereus* phage Bace-11 (Ackermann et al., 1995), and *Salmonella* phage c (Schade et al., 1967). Among these six known phages, the hosts of five are strains of *Bacillus* and only phage 0305ϕ8-36 is a Jumbo phage. Proteomic analysis and comparative genomic analysis revealed that Gp133 of phage vB_BpuM_BpSp is a phage structural protein with similarity to the predicted curly tail fiber protein ORF129 of phage 0305ϕ8-36, suggesting that Gp133 might be a component of the curly tail fiber. Further functional analysis of the protein will provide more understanding to the function of curly tail fibers in *Bacillus* phage virion.

The Jumbo phages have huge phage virions and large genomes, which results in high energy consumption during infection. Several genes in the vB_BpuM_BpSp genome exhibit potential functions for facilitating phage infection, such as the genes of glycoside hydrolase and Holliday junction resolvase. The peptidoglycan lytic enzyme domain has been found to be a part of the phage tail fiber and tail spike with function of benefiting infection (Boulanger et al., 2008; Thompson et al., 2010). However, no individual protein with identified glycoside hydrolase activity has been found in phage virion. This study identified the first functional individual phage glycoside hydrolase with a structural function. This glycoside hydrolase, Gp255, was found to interact with the baseplate protein of the phage, but not with the tail spike protein or the tail fiber protein. The infection of myovirus undergoes a series of structural and conformational changes and the changes of baseplate conformation leads to the release of short tail fiber, which interacts with the cell wall (Hu et al., 2015). During this process, the glycoside hydrolase of phage vB_BpuM_BpSp might be released and it may catalyze the pore formation for phage genomic DNA injection. This mechanism might reduce the lytic time of the glycoside hydrolase to the cell wall, and the damage of the glycoside hydrolase to cell wall, and is helpful for maintaining conducive intracellular environment for phage propagation.

AUTHOR CONTRIBUTIONS

MG and YY conceived and designed the work; YY performed the experiment and analyzed the data. YY and MG draft the manuscript; MG revised the manuscript.

FUNDING

This study was supported by the National Natural Science Foundation of China (No. 31500155, 31170123) and the projects of Chinese Academy of Sciences (KSZD-EW-Z-021-2-2). The funders had no role in study design, data collection and interpretation, or the decision to submit the work for publication.

REFERENCES

Abbasifar, R., Griffiths, M. W., Sabour, P. M., Ackermann, H. W., Vandersteegen, K., Lavigne, R., et al. (2014). Supersize me: *Cronobacter sakazakii* phage GAP32. *Virology* 460, 138–146. doi: 10.1016/j.virol.2014.05.003

Ackermann, H. W., Yoshino, S., and Ogata, S. (1995). A *Bacillus* phage that is a living fossil. *Can. J. Microbiol.* 41, 294–297. doi: 10.1139/m95-040

Belyaeva, N. N., and Azizbeky, R. R. (1968). Fine structure of new *Bacillus Subtilis* phage Ar9 with complex morphology. *Virology* 34, 176–179. doi: 10.1016/0042-6822(68)90023-8

Bhardwaj, A., Molineux, I. J., Casjens, S. R., and Cingolani, G. (2011). Atomic structure of bacteriophage Sf6 tail needle knob. *J. Biol. Chem.* 286, 30867–30877. doi: 10.1074/jbc.M111.260877

Bissaro, B., Monsan, P., Faure, R., and O'Donohue, M. J. (2015). Glycosynthesis in a waterworld: new insight into the molecular basis of transglycosylation in retaining glycoside hydrolases. *Biochem. J.* 467, 17–35. doi: 10.1042/BJ20141412

Boulanger, P., Jacquot, P., Plancon, L., Chami, M., Engel, A., Parquet, C., et al. (2008). Phage T5 straight tail fiber is a multifunctional protein acting as a tape measure and carrying fusogenic and muralytic activities. *J. Biol. Chem.* 283, 13556–13564. doi: 10.1074/jbc.M800052200

Buist, G., Kok, J., Leenhouts, K. J., Dabrowska, M., Venema, G., and Haandrikman, A. J. (1995). Molecular cloning and nucleotide sequence of the gene encoding the major peptidoglycan hydrolase of *Lactococcus lactis*, a muramidase needed for cell separation. *J. Bacteriol.* 177, 1554–1563.

Chan, Y. W., Millard, A. D., Wheatley, P. J., Holmes, A. B., Mohr, R., Whitworth, A. L., et al. (2014). Genomic and proteomic characterization of two novel siphovirus infecting the sedentary facultative epibiont cyanobacterium *Acaryochloris marina*. *Environ. Microbiol.* 17, 4239–4252. doi: 10.1111/1462-2920.12735

Chen, B. L., and King, J. (1991). Thermal Unfolding pathway for the thermostable P22 tailspike endorhamnosidase. *Biochemistry* 30, 6260–6269. doi: 10.1021/bi00239a026

Clark, S., Losick, R., and Pero, J. (1974). New RNA-polymerase from *Bacillus-Subtilis* infected with phage Pbs2. *Nature* 252, 21–24. doi: 10.1038/252021a0

Dixit, A., Ray, K., Lakowicz, J. R., and Black, L. W. (2011). Dynamics of the T4 bacteriophage DNA packasome motor endonuclease VII resolvase release of arrested Y-DNA substrates. *J. Biol. Chem.* 286, 18878–18889. doi: 10.1074/jbc.M111.222828

Eiserlin, F. A. (1967). Structure of *Bacillus Subtilis* bacteriophage Pbs 1. *J. Ultrastruct. Res.* 17, 342–347. doi: 10.1016/S0022-5320(67)80053-4

Golz, S., and Kemper, B. (1999). Association of Holliday-structure resolving endonuclease VII with gp20 from the packaging machine of phage T4. *J. Mol. Biol.* 285, 1131–1144. doi: 10.1006/jmbi.1998.2399

Green, V., Curtis, F. A., Sedelnikova, S., Rafferty, J. B., and Sharples, G. J. (2013). Mutants of phage bIL67 RuvC with enhanced Holliday junction binding selectivity and resolution symmetry. *Mol. Microbiol.* 89, 1240–1258. doi: 10.1111/mmi.12343

Grose, J. H., Belnap, D. M., Jensen, J. D., Mathis, A. D., Prince, J. T., Merrill, B. D., et al. (2014). The genomes, proteomes, and structures of three novel phages that infect the *Bacillus cereus* group and carry putative virulence factors. *J. Virol.* 88, 11846–11860. doi: 10.1128/JVI.01364-14

Hendrix, R. W. (2009). Jumbo bacteriophages. *Curr. Top. Microbiol. Immunol.* 328, 229–240. doi: 10.1007/978-3-540-68618-7_7

Henrissat, B., and Bairoch, A. (1996). Updating the sequence-based classification of glycosyl hydrolases. *Biochem. J.* 316, 695–696. doi: 10.1042/bj3160695

Hermoso, J. A., Garcia, J. L., and Garcia, P. (2007). Taking aim on bacterial pathogens: from phage therapy to enzybiotics. *Curr. Opin. Microbiol.* 10, 461–472. doi: 10.1016/j.mib.2007.08.002

Hu, B., Margolin, W., Molineux, I. J., and Liu, J. (2015). Structural remodeling of bacteriophage T4 and host membranes during infection initiation. *Proc. Natl. Acad. Sci. U.S.A.* 112, E4919–E4928. doi: 10.1073/pnas.1501064112

Javed, M. A., van Alphen, L. B., Sacher, J., Ding, W., Kelly, J., Nargang, C., et al. (2015). A receptor-binding protein of Campylobacter jejuni bacteriophage NCTC 12673 recognizes flagellin glycosylated with acetamidino-modified pseudaminic acid. *Mol. Microbiol.* 95, 101–115. doi: 10.1111/mmi.12849

Larkin, M. A., Blackshields, G., Brown, N. P., Chenna, R., McGettigan, P. A., McWilliam, H., et al. (2007). Clustal W and clustal X version 2.0. *Bioinformatics* 23, 2947–2948. doi: 10.1093/bioinformatics/btm404

Lavigne, R., Noben, J. P., Hertveldt, K., Ceyssens, P. J., Briers, Y., Dumont, D., et al. (2006). The structural proteome of *Pseudomonas aeruginosa* bacteriophage phi KMV. *Microbiology* 152, 529–534. doi: 10.1099/mic.0.28431-0

Lecoutere, E., Ceyssens, P. J., Miroshnikov, K. A., Mesyanzhinov, V. V., Krylov, V. N., Noben, J. P., et al. (2009). Identification and comparative analysis of the structural proteomes of phi KZ and EL, two giant *Pseudomonas aeruginosa* bacteriophages. *Proteomics* 9, 3215–3219. doi: 10.1002/pmic.200800727

Maaroufi, H., and Levesque, R. C. (2015). Glycoside hydrolase family 32 is present in *Bacillus subtilis* phages. *Virol. J.* 12:157. doi: 10.1186/s12985-015-0373-6

Marchler-Bauer, A., Zheng, C. J., Chitsaz, F., Derbyshire, M. K., Geer, L. Y., Geer, R. C., et al. (2013). CDD: conserved domains and protein three-dimensional structure. *Nucleic Acids Res.* 41, D348–D352. doi: 10.1093/nar/gks1243

Miller, E. S., Kutter, E., Mosig, G., Arisaka, F., Kunisawa, T., and Ruger, W. (2003). Bacteriophage T4 genome. *Microbiol. Mol. Biol. Rev.* 67, 86–156. doi: 10.1128/MMBR.67.1.86-156.2003

Mizuno, C. M., Rodriguez-Valera, F., Kimes, N. E., and Ghai, R. (2013). Expanding the marine virosphere using metagenomics. *PLoS Genet.* 9:e1003987. doi: 10.1371/journal.pgen.1003987

Peng, Q., Yuan, Y. H., and Gao, M. Y. (2013). *Bacillus pumilus*, a novel ginger rhizome rot pathogen in China. *Plant Dis.* 97, 1308–1315. doi: 10.1094/PDIS-12-12-1178-RE

Punta, M., Coggill, P. C., Eberhardt, R. Y., Mistry, J., Tate, J., Boursnell, C., et al. (2012). The Pfam protein families database. *Nucleic Acids Res.* 40, D290–D301. doi: 10.1093/nar/gkr1065

Rohwer, F. (2003). Global phage diversity. *Cell* 113, 141–141. doi: 10.1016/S0092-8674(03)00276-9

Sambrook, J., Fritsch, F. E., and Maniatis, T. (2001). *Molecular Cloning. A Laboratory Manual. 3rd Edn.* Cold Spring Harbor, NY: Cold Spring Harbor Laboratory Press.

Sánchez-Vallet, A., Saleem-Batcha, R., Kombrink, A., Hansen, G., Valkenburg, D., Thomma, B. P., et al. (2013). Fungal effector Ecp6 outcompetes host immune receptor for chitin binding through intrachain LysM dimerization. *Elife* 2:e00790. doi: 10.7554/eLife.00790

Schade, S. Z., Adler, J., and Ris, H. (1967). How bacteriophage chi attacks motile bacteria. *J. Virol.* 1, 599–609.

Serwer, P., Hayes, S. J., Thomas, J. A., and Hardies, S. C. (2007). Propagating the missing bacteriophages: a large bacteriophage in a new class. *Virol. J.* 4:21. doi: 10.1186/1743-422X-4-21

Soding, J., Biegert, A., and Lupas, A. N. (2005). The HHpred interactive server for protein homology detection and structure prediction. *Nucleic Acids Res.* 33, W244–W248. doi: 10.1093/nar/gki408

Tamai, E., Yoshida, H., Sekya, H., Nariya, H., Miyata, S., Okabe, A., et al. (2014). X-ray structure of a novel endolysin encoded by episomal phage phiSM101 of *Clostridium perfringens*. *Mol. Microbiol.* 92, 326–337. doi: 10.1111/mmi.12559

Tamura, K., Stecher, G., Peterson, D., Filipski, A., and Kumar, S. (2013). MEGA6: molecular evolutionary genetics analysis version 6.0. *Mol. Biol. Evol.* 30, 2725–2729. doi: 10.1093/molbev/mst197

Thomas, J. A., Hardies, S. C., Rolando, M., Hayes, S. J., Lieman, K., Carroll, C. A., et al. (2007). Complete genomic sequence and mass spectrometric analysis of highly diverse, atypical *Bacillus thuringiensis* phage 0305 phi 8-36. *Virology* 368, 405–421. doi: 10.1016/j.virol.2007.06.043

Thomas, J. A., Rolando, M. R., Carroll, C. A., Shen, P. S., Belnap, D. M., Weintraub, S. T., et al. (2008). Characterization of *Pseudomonas chlororaphis* myovirus 201 phi 2-1 via genomic sequencing, mass spectrometry, and electron microscopy. *Virology* 376, 330–338. doi: 10.1016/j.virol.2008.04.004

Thomas, J. A., Weintraub, S. T., Hakala, K., Serwer, P., and Hardies, S. C. (2010). Proteome of the large *Pseudomonas* myovirus 201 phi 2-1: delineation of proteolytically processed virion proteins. *Mol. Cell. Proteomics* 9, 940–951. doi: 10.1074/mcp.M900488-MCP200

Thompson, J. E., Pourhossein, M., Waterhouse, A., Hudson, T., Goldrick, M., Derrick, J. P., et al. (2010). The K5 lyase KflA combines a Viral tail spike structure with a bacterial polysaccharide lyase mechanism. *J. Biol. Chem.* 285, 23963–23969. doi: 10.1074/jbc.M110.127571

Wang, S., Kong, J., and Zhang, X. (2008). Identification and characterization of the two-component cell lysis cassette encoded by temperate bacteriophage phi PYB5 of *Lactobacillus fermentum*. *J. Appl. Microbiol.* 105, 1939–1944. doi: 10.1111/j.1365-2672.2008.03953.x

Yap, M. L., and Rossmann, M. G. (2014). Structure and function of bacteriophage T4. *Future Microbiol.* 9, 1319–1337. doi: 10.2217/fmb.14.91

Yuan, Y. H., Peng, Q., Wu, D. D., Kou, Z., Wu, Y., Liu, P. M., et al. (2015). Effects of actin-like proteins encoded by two *Bacillus pumilus* phages on unstable lysogeny, revealed by genomic analysis. *Appl. Environ. Microbiol.* 81, 339–350. doi: 10.1128/AEM.02889-14

Yuan, Y., Peng, Q., and Gao, M. (2012). Characteristics of a broad lytic spectrum endolysin from phage BtCS33 of *Bacillus thuringiensis*. *BMC Microbiol.* 12:297. doi: 10.1186/1471-2180-12-297

Conflict of Interest Statement: The authors declare that the research was conducted in the absence of any commercial or financial relationships that could be construed as a potential conflict of interest.

Copyright © 2016 Yuan and Gao. This is an open-access article distributed under the terms of the Creative Commons Attribution License (CC BY). The use, distribution or reproduction in other forums is permitted, provided the original author(s) or licensor are credited and that the original publication in this journal is cited, in accordance with accepted academic practice. No use, distribution or reproduction is permitted which does not comply with these terms.

frontiers in Microbiology

ORIGINAL RESEARCH
published: 28 April 2016
doi: 10.3389/fmicb.2016.00587

Characterization of the Deamination Coupled with Sliding along DNA of Anti-HIV Factor APOBEC3G on the Basis of the pH-Dependence of Deamination Revealed by Real-Time NMR Monitoring

Keisuke Kamba[1,2], *Takashi Nagata*[1,2]* *and Masato Katahira*[1,2]*

[1] Institute of Advanced Energy, Kyoto University, Kyoto, Japan, [2] Graduate School of Energy Science, Kyoto University, Kyoto, Japan

OPEN ACCESS

Edited by:
Toshinori Sato,
Keio University, Japan

Reviewed by:
Ryuichi Sugiyama,
Yokohama City University School of Medicine, Japan
Yoshiyuki Tanaka,
Tokushima Bunri University, Japan

***Correspondence:**
Takashi Nagata
nagata.takashi.6w@kyoto-u.ac.jp;
Masato Katahira
katahira@iae.kyoto-u.ac.jp

Specialty section:
This article was submitted to Virology, a section of the journal Frontiers in Microbiology

Received: 20 January 2016
Accepted: 11 April 2016
Published: 28 April 2016

Citation:
Kamba K, Nagata T and Katahira M (2016) Characterization of the Deamination Coupled with Sliding along DNA of Anti-HIV Factor APOBEC3G on the Basis of the pH-Dependence of Deamination Revealed by Real-Time NMR Monitoring. Front. Microbiol. 7:587. doi: 10.3389/fmicb.2016.00587

Human APOBEC3G (A3G) is an antiviral factor that inactivates HIV. The C-terminal domain of A3G (A3G-CTD) deaminates cytosines into uracils within single-stranded DNA (ssDNA), which is reverse-transcribed from the viral RNA genome. The deaminase activity of A3G is highly sequence-specific; the third position (underlined) of a triplet cytosine (CC<u>C</u>) hotspot is converted into CCU. A3G deaminates a CCC that is located close to the 5′ end of ssDNA more effectively than ones that are less close to the 5′ end, so-called 3′ → 5′ polarity. We had developed an NMR method that can be used to analyze the deamination reaction in real-time. Using this method, we previously showed that 3′ → 5′ polarity can be explained rationally by A3G-CTD's nonspecific ssDNA-binding and sliding direction-dependent deamination activities. We then demonstrated that the phosphate backbone is important for A3G-CTD to slide on the ssDNA and to exert the 3′ → 5′ polarity, probably due to an electrostatic intermolecular interaction. In this study, we investigate the pH effects on the structure, deaminase activity, and 3′ → 5′ polarity of A3G-CTD. Firstly, A3G-CTD was shown to retain the native structure in the pH range of 4.0–10.5 by CD spectroscopy. Next, deamination assaying involving real-time NMR spectroscopy for 10-mer ssDNA containing a single CCC revealed that A3G-CTD's deaminase activity decreases as the pH increases in the range of pH 6.5–12.7. This is explained by destabilization of the complex between A3G-CTD and ssDNA due to the weakened electrostatic interaction with the increase in pH. Finally, deamination assaying for 38-mer ssDNA having two CCC hotspots connected by a long poly-adenine linker showed that A3G-CTD retains the same pH deaminase activity preference toward each CCC as that toward the CCC of the 10-mer DNA. Importantly, the 3′ → 5′ polarity turned out to increase as the pH decreases in the range of 6.5–8.0. This suggests that A3G-CTD tends to continue sliding without abortion at lower pH, while A3G-CTD tends to dissociate from ssDNA during sliding at higher pH due to the weakened electrostatic interaction.

Keywords: APOBEC3G, NMR, monitoring, enzyme, HIV-1

INTRODUCTION

Human APOBEC3G (A3G), which belongs to a protein family known as apolipoprotein B mRNA-editing enzyme catalytic polypeptides, exhibits cytidine deaminase activity and converts cytosines (Cs) in single-stranded DNA (ssDNA) into uracils (Us) (Harris and Liddament, 2004; Kitamura et al., 2011; Aydin et al., 2014). A3G targets the newly reverse-transcribed minus ssDNA of human immunodeficiency virus 1 (HIV-1) and converts C to U, which results in introduction of a significant amount of guanine (G) to adenine (A) mutations in the HIV-1 genome (Harris et al., 2003; Zhang et al., 2003; Aydin et al., 2014). Using this activity, A3G inactivates HIV-1 that is deficient of viral infectivity factor (Vif) (Sheehy et al., 2002; Harris et al., 2003; Lecossier et al., 2003; Zhang et al., 2003).

A3G comprises two zinc-coordinating domains: a catalytically inactive N-terminal domain (A3G-NTD) and an active C-terminal domain (A3G-CTD) (Harris and Liddament, 2004; Haché et al., 2005; Navarro et al., 2005; Kitamura et al., 2011; Aydin et al., 2014). A3G-NTD mediates encapsidation and RNA binding (Khan et al., 2005, 2007; Navarro et al., 2005). On the other hand, A3G-CTD is the domain responsible for C to U deamination within ssDNA, and thereby for antiviral capability (Navarro et al., 2005; Browne et al., 2009; Kobayashi et al., 2014). Both A3G-NTD and A3G-CTD possess Zn^{2+}-coordinating motif, His-X-Glu-X_{27-28}-Pro-Cys-X_2-Cys, and this motif is required for A3G-CTD to exert the catalytic activity (Harris and Liddament, 2004). Zn^{2+} is coordinated by histidine, two cysteines, and a water molecule, and glutamate is thought to exchange hydrogens during catalysis (Barnes and Smith, 1993; Betts et al., 1994; Carter, 1995; Xiang et al., 1995). This nucleophilic hydroxyl is responsible for A3G-CTD's deamination activity (Barnes and Smith, 1993; Betts et al., 1994; Carter, 1995). The molecular structure of A3G-CTD in its free form was obtained previously by means of crystallography and NMR (Chen et al., 2008; Holden et al., 2008; Furukawa et al., 2009; Harjes et al., 2009; Shandilya et al., 2010; Lu et al., 2015). A3G-CTD has an αA-β1-β2/β2′-αB-β3-αC-β4-αD-β5-αE-αF fold, which forms a globular domain composed of five β-sheets, flanked by six α-helices. However, how A3G-CTD interacts with ssDNA is still not well understood.

The deaminase activity of A3G is ssDNA-specific and no double-stranded DNA or RNA with any structure can act as a substrate; it is also highly sequence-specific, i.e., a triplet cytosine (CCC) hotspot is converted into CCU, namely the third position of CCC is the most favored (Harris et al., 2003; Langlois et al., 2005; Chelico et al., 2006; Iwatani et al., 2006; Furukawa et al., 2009; Harjes et al., 2013; Kamba et al., 2015). Importantly, A3G exhibits a deamination bias, so-called 3′ → 5′ polarity. *In vitro*, A3G deaminates a CCC hotspot that is located close to the 5′ end more effectively than ones that are less close to the 5′ end (Chelico et al., 2006; Holden et al., 2008; Furukawa et al., 2014) (**Figure 1A**). This phenomena is called 3′ → 5′ polarity (Chelico et al., 2006), because the efficiency of deamination increases in the 3′ → 5′ direction. Just A3G-CTD alone reportedly exhibits this 3′ → 5′ polarity (Holden et al., 2008; Furukawa et al., 2014; Kamba et al., 2015). A3G's 3′ → 5′ polarity has long been observed also *in vivo* as a 5′ → 3′ gradient of G to A hyper-mutations in the HIV genome, which was replicated using minus ssDNA having C to U mutations introduced by A3G (Yu et al., 2004; Suspène et al., 2006; Kobayashi et al., 2014).

The deaminase activity of A3G has long been evaluated *in vitro* by means of various biochemical methods, i.e., uracil-DNA glycosylase-based assaying (Harris et al., 2003; Yu et al., 2004; Navarro et al., 2005; Chelico et al., 2006; Iwatani et al., 2006; Holden et al., 2008). In order to monitor the deamination reaction in real-time, and in a site-specific manner with high temporal and spatial resolution, we developed an NMR-based method (Furukawa et al., 2009, 2014; Kamba et al., 2015). Our real-time NMR monitoring method is increasingly being used to evaluate the deamination reaction of A3G (Harjes et al., 2013; Kouno et al., 2015; Lu et al., 2015), as well as that of other APOBEC family protein (Byeon et al., 2013). We also showed that this method can be applied to monitor the deamination of modified cytosines. We demonstrated that A3G-CTD possesses weak deaminase activity for 5-methyl cytosine (5mC), but none for 5-hydroxymethyl cytosine (5hmC), both of which are known to be epigenetic modifications (Kamba et al., 2015).

We have been using our real-time NMR monitoring method to explore the origin of the 3′ → 5′ polarity. By applying a kinetic model to the data obtained with this method, we showed that deamination is more efficient when A3G-CTD approaches the target cytosine in the 3′ to 5′ direction rather than the opposite one and that this sliding-direction-dependent deaminase activity confers the 3′ → 5′ polarity (Furukawa et al., 2014) (**Figure 1B**). We then used ssDNAs containing a nucleotide analog at a single or multiple positions as substrates for the real-time NMR monitoring method (Kamba et al., 2015). We demonstrated that five consecutive nucleotides, including CCC at the center, are recognized by A3G-CTD for efficient activity. Then, it was shown that the phosphate backbone is important for A3G-CTD to slide on the DNA strand and thereby to exert the 3′ → 5′ polarity (Kamba et al., 2015). Subsequent analysis to investigate the dependence of the 3′ → 5′ polarity on salt concentration suggested that the electrostatic intermolecular interaction tethers A3G-CTD to ssDNA, probably through interaction via the phosphate backbone (Kamba et al., 2015). In the present study, we investigate the pH effects on the structure, deaminase activity, and 3′ → 5′ polarity of A3G-CTD by using our real-time NMR monitoring method.

MATERIALS AND METHODS

Preparation of the Protein and DNA Substrates

Recombinant A3G-CTD (residues 193–384) containing an N-terminal hexahistidine tag (his-tag) was expressed in *Escherichia coli* BL21 (DE3/RIL) cells (Stratagene) and purified as described previously (Furukawa et al., 2009). Following cleavage of the his-tag and column purification, the obtained A3G-CTD was dialyzed against the storage buffer comprising 20 mM Tris-HCl (pH 7.5), 30 mM NaCl, 5 mM DTT, and 10 μM $ZnCl_2$, and then stored until use at 4°C. All substrate ssDNAs (**Table 1**) were purchased from Fasmac Co., Ltd.

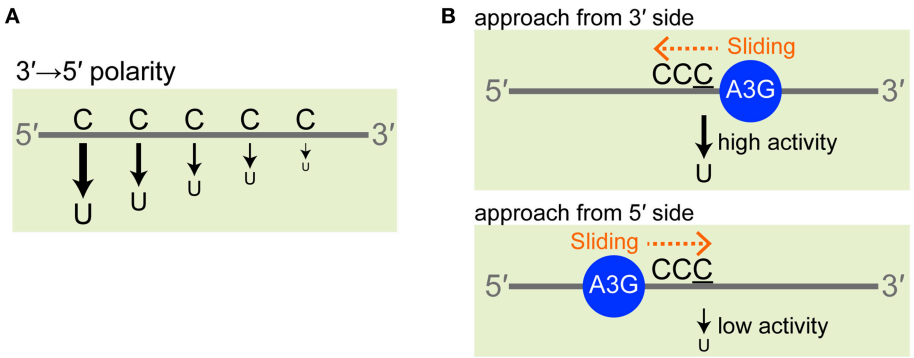

FIGURE 1 | 3′ → 5′ polarity of A3G. (A) A3G deaminates a CCC hotspot that is located close to the 5′ end more effectively than ones that are less close to the 5′ end. For simplicity, the third C of a CCC hotspot is indicated by a single "C" character. **(B)** The analysis of the data obtained by real-time NMR monitoring method revealed that deamination is more efficient when A3G-CTD approaches the target cytosine in the 3′ to 5′ direction rather than the opposite one and that this confers the 3′→5′ polarity.

TABLE 1 | Substrate ssDNAs used in this study.

Substrate name	Sequence[a]	Length	Position of target C
s10-1	ATTCC<u>C</u>GATT	10	6
s10-2	AAACC<u>C</u>GAAA	10	6
s38	AAACC<u>C</u>GA$_{24}$CC<u>C</u>GTAA	38	6 and 34

[a] *The target cytosines deaminated by A3G are underlined.*

Circular Dichroism (CD) and Fluorescence Spectroscopy

Samples were prepared by mixing A3G-CTD in storage buffer with several measurement buffers having different pHs (1:19 ratio). The final concentration of A3G-CTD was adjusted to 6 μM. Different buffer systems were used to obtain different pH solutions: Glycine-HCl (pH 2.5–3.5), Acetic acid-Sodium acetate (pH 4.0–5.5), Bis-Tris-HCl (pH 6.0–7.0), Tris-HCl (pH 7.5–8.5), CHES-NaOH (pH 9.0–9.5), CHAPS-NaOH (pH 10.0–11.0), and Triethylamine-HCl (pH 11.4–12.7). The concentrations of these buffers were adjusted to 20 mM, and 30 mM NaCl, 1 mM DTT and 10 μM $ZnCl_2$ were added to obtain the measurement buffers. Equilibrium denaturation was carried out using different concentrations of guanidine hydrochloride (GdHCl) in the range of 0 to 5.8 M at pH 7.5. All CD and fluorescence measurements were carried out at 25°C.

CD spectra in the far-UV region (200–260 nm) using an optical path cell of 0.1 cm were obtained with a Jasco J-720A spectrometer (Japan Spectroscopic Co.). All spectra were background-corrected, smoothed, and converted to molar ellipticity $[\theta]$ (deg·cm^2·dmol^{-1}) (Kelly et al., 2005).

Fluorescence spectra were collected with a Jasco FP-8500 spectrometer (Japan Spectroscopic Co.) using an optical path cell of 1 cm. The excitation wavelength was 295 nm and the fluorescence intensity at the emission wavelength of 335 nm was monitored. The spectra slit width of 5 nm was used for excitation and emission.

The thermodynamic parameters for guanidine-induced denaturation curves were obtained by least squares fitting using two-state equations (Pace, 1986; Scholtz et al., 2009).

$$s_{obs} = \frac{(a_N + b_N[\mathrm{GdHCl}]) + (a_U + b_U[\mathrm{GdHCl}])\exp\left(\frac{-\Delta G_{app} + m_{app}[\mathrm{GdHCl}]}{RT}\right)}{1 + \exp\left(\frac{-\Delta G_{app} + m_{app}[\mathrm{GdHCl}]}{RT}\right)} \quad (1)$$

The data were fitted using Equation (1), where s_{obs} is the molar ellipticity or fluorescence intensity observed; a_N (a_U) and b_N (b_U) the intercept and slope of the base line at low (N) and high (U) GdHCl concentrations, respectively; R the gas constant; T the absolute temperature in K; [GdHCl] the GdHCl concentration; and ΔG_{app} and m_{app} the free energy and cooperativity of folding calculated with Equation (1), respectively. The errors were estimated using a single-elimination Jack-knife procedure (Harris, 1998).

The fraction of the folded state (f_N) at each pH was calculated using the equation,

$$f_N = (Y - Y_U)/(Y_N - Y_U) \quad (2)$$

where Y is the $[\theta]$ value at 220 nm ($[\theta]_{220}$) at each pH. Y_N and Y_U, corresponding to a_N and a_U indicated above, respectively, are $[\theta]_{220}$ for the folded and unfolded states at pH 7.5 and [GdHCl] = 0, respectively ($Y_N = -5.2\times10^3$, $Y_U = -2.5\times10^3$) (Scholtz et al., 2009).

NMR Spectroscopy

NMR spectra were recorded at 25°C with either a DRX600 or Avance III 600 spectrometer, both being equipped with a cryogenic probe and a Z-gradient (Bruker Biospin).

Samples were prepared by mixing A3G-CTD in storage buffer with several measurement buffers having different pH. The measurement buffers were prepared as in the previous section, except that DTT was adjusted to 5 mM. The concentration of A3G-CTD was set either at 0.8 or 2.0 μM, while that of the ssDNA substrates was adjusted to 200 μM. After mixing A3G-CTD and ssDNA together, a series of two-dimensional TOtal Correlated SpectroscopY (2D TOCSY) with mixing a time of 20 ms were recorded at different reaction time points, by which the deamination reaction of cytosines of ssDNA

could be monitored in real-time. Water signal suppression was achieved with 3-9-19 watergate. Resonance assignments of the substrate ssDNAs were made using 2D TOCSY with an aid of 2D ^{1}H–^{13}C Heteronuclear Single Quantum Coherence (HSQC) spectroscopy and also by comparing the chemical shifts with the assignments for ATTCCCAATT, AAACCCGAAA, and AAACCCGA$_{24}$CCCGTAA, previously studied (Furukawa et al., 2009; Kamba et al., 2015). Spectra were processed with NMRPipe (Delaglio et al., 1995), and analyzed using SPARKY (Goddard and Kneller, 2006).

The intensities of the peaks of either cytosine or uracil were plotted against time and analyzed as previously described (Furukawa et al., 2014; Kamba et al., 2015). The data were fit to a single exponential decaying function, using the following equations, by which apparent deamination rate constants were derived:

$$I(t)_{\mathrm{C}} = I_{\mathrm{s}} \exp(-kt) + I_{\mathrm{b}} \quad (3)$$

$$I(t)_{\mathrm{U}} = I_{\mathrm{s}} (1 - \exp(-kt)) + I_{\mathrm{b}} \quad (4)$$

where I_{b} corresponds to the baseline intensity of the spectrum; $I_{\mathrm{s}} + I_{\mathrm{b}}$ the signal intensity at time point zero for cytosine (3) and ∞ for uracil (4); and k the apparent deamination rate constant, which was always obtained through linear least-squares analysis. The value for the apparent deamination rate constant was used as an index of activity.

We defined the P with the following equation:

$$P = \frac{k_{(\mathrm{C6})}}{k_{(\mathrm{C34})}} \quad (5)$$

where $k_{(\mathrm{C6})}$ and $k_{(\mathrm{C34})}$ are the apparent deamination rate constants at positions C6 and C34 of a 38-mer ssDNA (**Table 1**, s38). "P" can be regarded as a measure of the magnitude of $3' \rightarrow 5'$ polarity. The error was estimated as follows. Firstly, the error of the NMR signal intensity was obtained from the base level noise of each NMR spectrum. Then the error of the rate constant was calculated from data sets constructed by Monte Carlo simulation using the error of the NMR signal intensity. Finally, the errors of the relative activity and the P were obtained by means of error propagation calculation.

RESULTS AND DISCUSSION

Real-Time NMR Monitoring of Cytosine Deamination Catalyzed by A3G-CTD

We have been utilizing our real-time NMR monitoring method to investigate the deamination reaction of A3G and A3G-CTD (Furukawa et al., 2009, 2014; Kamba et al., 2015). The experimental procedure for the method is illustrated in **Figure 2A** (left). We add A3G-CTD to the solution containing ssDNA and mix thoroughly, which is defined as reaction time point zero. The final concentrations of A3G-CTD and s10-1 are 2 and 200 μM, respectively. The mixed solution is immediately transferred to an NMR tube, which is loaded into the magnet. Subsequently, a series of 2D TOCSY spectra are recorded at different reaction time points. The conversion of ATTCCCGATT (s10-1 in **Table 1**) to ATTCCUGATT is monitored as an example in **Figure 2A** (right). The panels in **Figure 2A** (right) shows regions of 2D TOCSY spectra for H5–H6 correlation signals of cytosines and uracils. The three signals in the top-left panel correspond to the C4, C5, and C6 residues of s10-1. With the reaction time, the intensity of the C6 signal gradually decreases and it eventually disappears, which is coupled with the emergence of the U6 signal and a gradual increase of its intensity (**Figure 2A**, panels 1.8, 3.0, and 12 h). We then collect the intensities of these signals and follow the time courses of their changes. In the current case, the signal intensity at each time point is plotted in **Figure 2B**. The plots for C6 and U6 were each fitted to a single exponential function, Equations (3, 4) in the Materials and Methods section, by which the rate constant, k, was found to be 0.28 ± 0.01 and 0.27 ± 0.02 h^{-1}, respectively. This k-value can be used as an index of activity.

The Effects of pH and Denaturant on the Structure of A3G-CTD

Here we assessed the structure of A3G-CTD in buffers having different pHs using CD spectroscopy. Far-UV (200–260 nm) CD spectra were obtained at nine different pH values within the range of 2.5–12.7 (pH 2.5, 3.5, 4.0, 4.5, 7.5, 10.0, 10.5, 11.4, and 12.7; **Figure 3A**). The patterns of the spectra in the range of pH 4.0–10.5 were almost identical to that of the spectrum at pH 7.5, where A3G-CTD reportedly exerts deaminase activity (Holden et al., 2008; Harjes et al., 2013; Furukawa et al., 2014; Kamba et al., 2015), indicating that A3G-CTD is in the native form within this pH range. Indeed, the spectra in the range of pH 4.0–10.5 show strong negative intensity around the wavelength range of 210–230 nm, which is generally known as an indication of the presence of secondary structures (Kelly et al., 2005). In **Figure 3B**, the variation in the molar ellipticity at 220 nm ($[\theta]_{220}$) of A3G-CTD at 20 different pH values in the range of 2.5–12.7 is showed. The average value of $[\theta]_{220}$ was -5.1×10^3 deg·cm^2·dmol^{-1} in the range of pH 4.0–10.5, where A3G-CTD has the native structure, as mentioned above. However, at pH values lower and higher than pH 4.0 and 10.5, respectively, the values of $[\theta]_{220}$ were higher (ca. -4.0×10^3 deg·cm^2·dmol^{-1}), which implies that the content of the secondary structures was somehow lower.

Next, to evaluate whether or not A3G-CTD is in the native form in the region of pH $<$ 4.0 and pH $>$ 10.5 ($[\theta]_{220}$ value of ca. -4.0×10^{-3}), we conducted guanidine-induced denaturation of A3G-CTD at pH 7.5. The $[\theta]_{220}$ value was plotted against the concentration of GdHCl (**Figure 3C**). Then, we fitted the plotted data to Equation (1) in the Materials and Methods section to obtain a guanidine-induced denaturation curve, which describes a two-state transition model, and determined the apparent unfolding free energy (ΔG_{app}) and cooperativity (m_{app}) values to be 3.3 ± 0.3 kcal·mol^{-1} and 1.6 ± 0.1 kcal·mol^{-1}·M^{-1}, respectively (**Table 2**). For reference, we also investigated guanidine-induced denaturation of A3G-CTD at pH 7.5 using fluorescence spectroscopy (**Figure 3D**). The fluorescence spectrum with zero GdHCl showed a maximum at

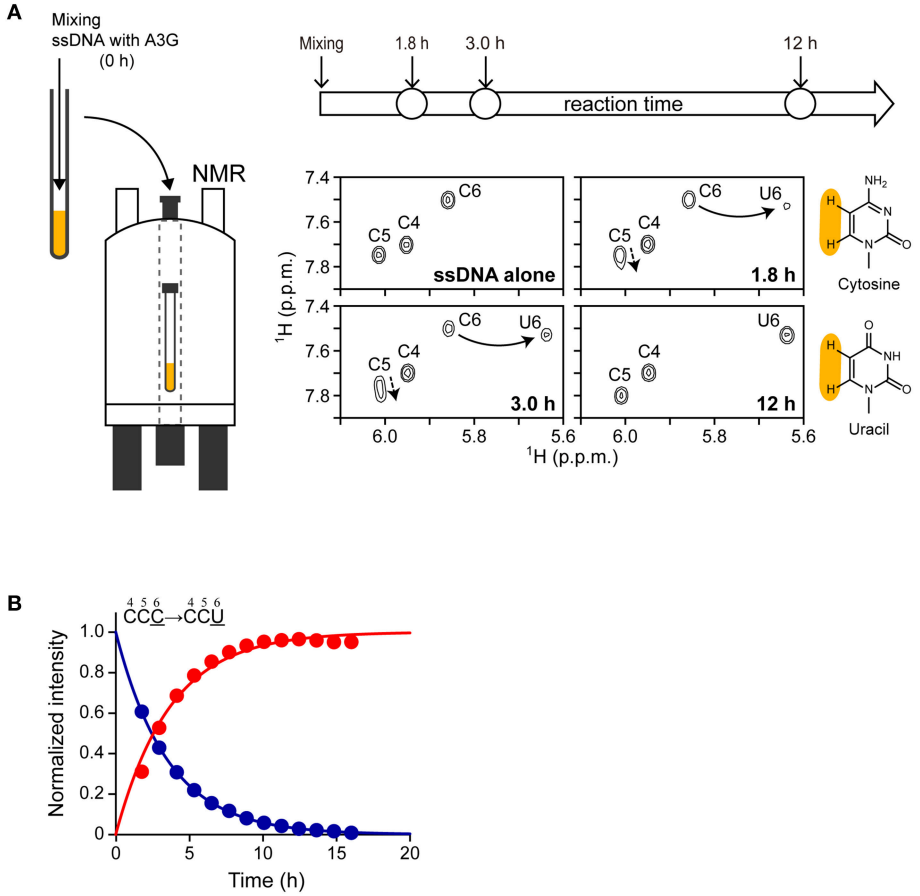

FIGURE 2 | Overview of real-time NMR monitoring. (**A**, left) Illustration of the experimental procedure. The solutions containing A3G-CTD and ssDNA substrate were mixed together (reaction time point 0 h), and the mixture was transferred to an NMR tube. The NMR tube was then loaded into the magnet. A series of 2D TOCSY spectra was recorded at different reaction time points. (**A**, right) Here, a reaction for ATTCCCGATT (s10-1) is monitored as an example. C to U conversion occurred at the underscored cytosine (C6). The panels show the regions of 2D TOCSY spectra for H5–H6 correlation signals of cytosines and uracils at different reaction time points (1.8, 3.0, and 12 h). The spectrum of "ssDNA (s10-1) alone" is shown for comparison. The structural formulas of cytosine and uracil are shown (protons H5 and H6 are highlighted in yellow). Signals for C6 are connected with those for U6 by solid arrows. Signals for C4 and C5 are perturbed (broken arrows) due to the C6 to U6 conversion. **(B)** The intensities of H5–H6 correlation signals for C6 and U6 at different reaction time points are plotted. The data were fitted to a single exponential function, by which the rate constant, *k*, was obtained.

335 nm, while at the highest GdHCl concentration (5.8 M), the maximum was at 348 nm (red-shifted), which strongly suggests that the tertiary structure of A3G-CTD has denatured almost completely (Royer, 2006). Here, fluorescence intensity at 335 nm was plotted against the concentration of GdHCl and fitted to the aforementioned Equation (1), and the ΔG_{app} and m_{app} values were determined to be 3.2 ± 0.4 kcal·mol^{-1} and 2.0 ± 0.2 kcal·mol^{-1}·M^{-1}, respectively (**Table 2**). The $[\theta]_{220}$ value of the CD spectrum and the fluorescence intensity at 335 nm are generally appreciated to be probes to determine the contents of secondary and tertiary structures, respectively (Royer, 2006). Since, the ΔG_{app} values obtained on CD and fluorescence spectroscopies are the same within error, the unfolding of A3G-CTD's secondary and tertiary structures is highly cooperative.

We then estimated the fraction of the folded state for A3G-CTD at different pH values using Equation (2). As a result, in the range of pH 4.0–10.5, the fraction of the folded state was found to be 90%, while it was 58% in the range of pH 11.0–12.7.

TABLE 2 | Thermodynamic parameters for guanidine-induced denaturation of A3G-CTD obtained by CD and fluorescence spectroscopy.

CD		Fluorescence	
ΔG_{app} (kcal·mol^{-1})	m_{app} (kcal·mol^{-1}·M^{-1})	ΔG_{app} (kcal·mol^{-1})	m_{app} (kcal·mol^{-1}·M^{-1})
3.3 ± 0.3	1.6 ± 0.1	3.2 ± 0.4	2.0 ± 0.2

The Effect of pH on the Deaminase Activity of A3G-CTD

Our real-time NMR monitoring method was applied to investigate the deaminase activity of A3G-CTD for a 10-mer

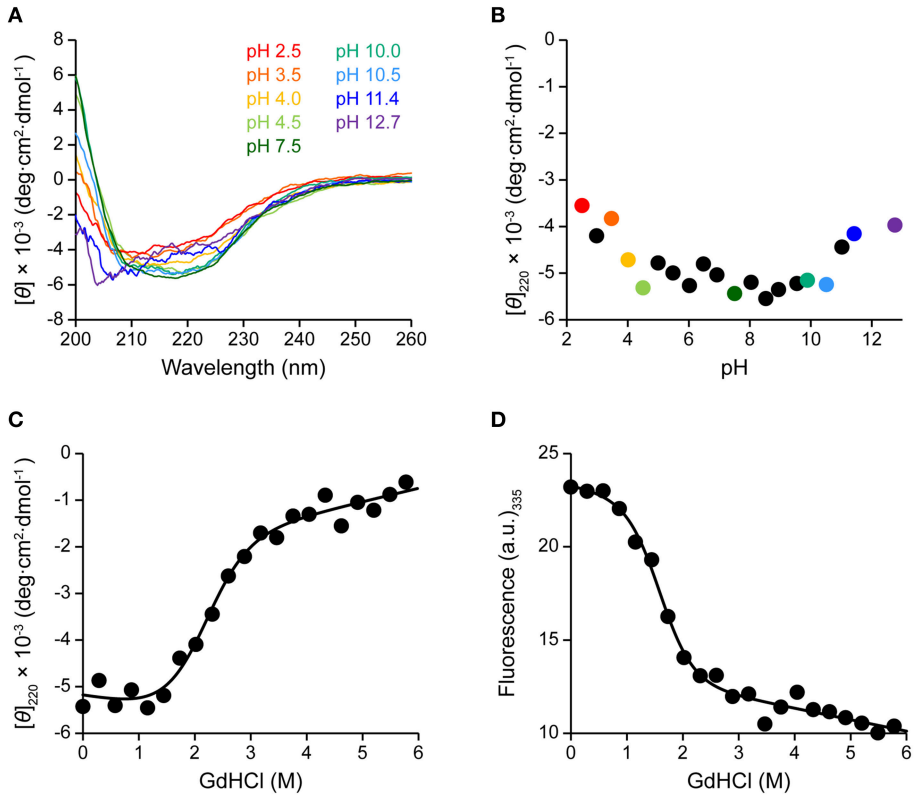

FIGURE 3 | Effects of pH and denaturant on the structure of A3G-CTD as assessed by CD and fluorescence spectroscopy. (A) Far-UV CD spectra of A3G-CTD at pH 2.5, 3.5, 4.0, 4.5, 7.5, 10.0, 10.5, 11.4, and 12.7 are shown. **(B)** Molar ellipticity at 220 nm of A3G-CTD is plotted against pH. The color-coded points corresponds to the corresponding spectra in **(A)**. **(C,D)** Guanidine-induced denaturation of A3G-CTD was investigated at pH 7.5. The molar ellipticity at 220 nm **(C)** and fluorescence intensity at 335 nm **(D)** were each plotted against the concentration of guanidine hydrochloride (GdHCl).

ssDNA (s10-2), AAACCCGAAA (C to U conversion occurs at underscored cytosine, C6), at nine different pH values (pH 6.5, 7.0, 7.5, 8.0, 8.5, 9.5, 10.5, 11.4, and 12.7). In each experiment, the final concentrations of A3G-CTD and s10-2 were adjusted to 0.8 and 200 μM, respectively. A series of 2D TOCSY spectra for s10-2 were obtained at several reaction time points at each pH value. As an example, **Figure 4A** shows the spectra of s10-2 at pH 7.5, at time points 1.6 and 53 h after addition of A3G-CTD to s10-2 (blue and red signals, respectively). In **Figure 4A**, the H5–H6 correlation signals of C4 and U6 overlap, so the assignments were made with the aid of 2D ^{1}H–^{13}C HSQC spectroscopy to discriminate between C and U (data not shown).

We collected the intensities of C6 signals, which were isolated from other signals, and followed their decreases during the reaction time course for each pH value. The time courses of the intensity decrease are plotted in **Figure 4B**. The plot for each pH was fit to aforementioned single exponential decaying function, Equation (3), individually, and the rate constant, *k*, at each pH was obtained (**Table 3**). Since the *k*-value can be considered as an index of activity, we defined the relative activity as the ratio of *k* at a particular pH to that at pH 6.5. In the pH range studied here, the relative activity was highest at pH 6.5 and decreased as the pH increased (**Figure 4C**). It seems physiologically relevant that A3G-CTD exerts the highest activity around at the physiological pH, 6.5.

The deaminase activity of A3G-CTD turned out to be higher at lower pH and decreased as the pH increased within the range of pH 6.5–11.4. ssDNA is negatively charged because it has phosphate moieties, therefore we suppose that this trend is due to a reduction of the stability of the complex between A3G-CTD and ssDNA due to the weakened electrostatic interaction with

TABLE 3 | Relative activities of A3G-CTD for s10-2 at pHs ranging from 6.5 to 12.7.

pH	Relative activity (C6)
6.5	1.00 ± 0.05
7.0	0.64 ± 0.10
7.5	0.25 ± 0.02
8.0	0.091 ± 0.005
8.5	0.089 ± 0.004
9.5	0.015 ± 0.001
10.5	(5.0 ± 0.3) × 10^{-3}
11.4	(6.4 ± 0.5) × 10^{-4}
12.7	n.d.

n.d., not detected.

an increase in pH value. We also noticed that the activity of A3G-CTD was significantly decreased above pH 9.5 and become negligible around pH 12.7. According to the analysis in the previous section, the fraction of the folded state of A3G-CTD in the range of pH 9.5–12.7 was between 92 (pH 9.5) and 50% (pH 12.7). Therefore, we assume that the low deaminase activity in this pH range is due not only to the denaturation of A3G-CTD, but also to decreased stability of the complex between A3G-CTD and ssDNA. The decrease of deaminase activity of A3G-CTD spans in wide range (pH 6.5–11.4). This aspect seems not to be attributable to a single amino acid residue, but rather multiple amino acid residues seem to be involved. It may be possible to find the residues that cause pH dependency if many A3G-CTDs containing different mutations at multiple sites are used for analysis, but this is practically difficult.

We also applied the current analysis to the lower pH rang of pH 2.5–6.0. Within this pH range, the time course of the intensity decrease of C6 signals did not show simple single exponential decay, but rather a sigmoidal-like curve. The reasons for this phenomenon are not apparent, however, the protonation/deprotonation equilibria of histidine and/or cytosine may play roles. Previously, it was shown that the deaminase activity of A3G-CTD becomes maximum at pH 5.5 (Harjes et al., 2013). Since this pH is close to the pKa value of the imidazole of histidine (ca. 6.0 in general), it was suggested that the protonation of histidine 216 is the key to the promotion of the deaminase activity (Harjes et al., 2013). As for cytosine, we observed that the chemical shift values of the H5–H6 correlations were significantly perturbed at different pH values within the range of 2.5–6.0, which is supposed to be related to the protonation of cytosine. Our intention was to investigate the pH dependence of the 3′ → 5′ polarity of the deaminase activity, therefore we decided to carry out the subsequent experiments in the pH range of 6.5–12.7 to make the analysis simple.

The Effect of pH on the 3′ → 5′ Polarity of A3G-CTD

We, next, used a 38-mer ssDNA substrate (s38), AAACCCGA$_{24}$CCCGTAA, to investigate the deamination reaction of A3G-CTD at nine different pH values (pH 6.5, 7.0, 7.5, 8.0, 8.5, 9.5, 10.5, 11.4, and 12.7). This s38 contains two CCC hotspots, whose third positions, C6 and C34 (underlined in the sequence), are converted to uracil by A3G-CTD. In each experiment, the final concentrations of A3G-CTD and s38 were adjusted to 0.8 and 200 μM, respectively. A series of 2D TOCSY spectra for s38 at several reaction time points were obtained at each pH value in the same way as for s10-1 and s10-2 in the previous sections. We collected the intensities of C6 and C34 signals, and plotted them against time (**Figure 5A**). The plots for

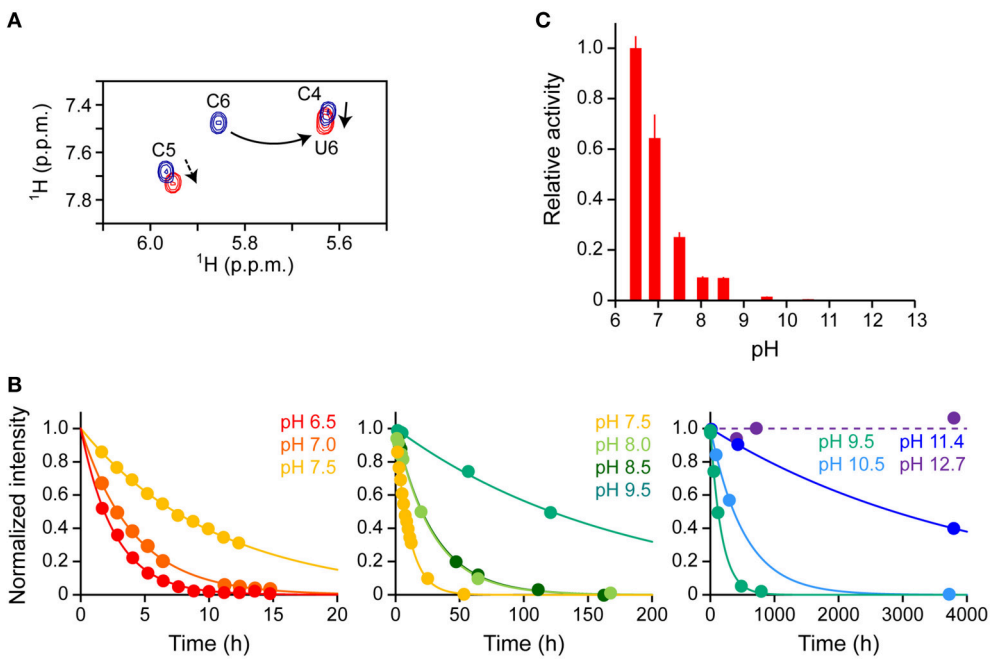

FIGURE 4 | Effect of pH on the deaminase activity of A3G-CTD for a 10-mer ssDNA as assessed by real-time NMR monitoring. (A) Superpositioning of 2D TOCSY spectra of AAACCCGAAA (s10-2 in **Table 1**) at two reaction time points at pH 7.5 is presented as a representative. C to U conversion occurred at the underscored cytosine (C6). The H5–H6 correlation signals of cytosines and uracils are shown: blue and red signals correspond to reaction time points 1.6 and 53 h after addition of A3G-CTD, respectively. The signal of C6 is connected with that of U6 by a solid arrow. The signals of C4 and C5 are perturbed (broken arrows) due to the C6 to U6 conversion. **(B)** The time courses of the intensity changes were plotted for C6 of s10-2 at pH 6.5, 7.0, 7.5, 8.0, 8.5, 9.5, 10.5, 11.4, and 12.7. The data for each pH were fitted to a single exponential function individually, by which the rate constant, *k*, at each pH was obtained. **(C)** Relative activities for C6 are plotted against pH values. The relative activity at each pH was defined as the ratio of *k* at that particular pH to that obtained at pH 6.5.

the C6 and C34 signals at each pH were each fitted to Equation (3) individually, by which the rate constants were obtained. The relative activities at different pHs were then calculated (**Table 4**), and are compared in **Figure 5B**. Here the relative activities for C6 and C34 at each pH were defined as the ratios of their *k*-values to the *k*-value obtained for C6 at pH 6.5. The pH dependence trends of the relative activity for C6 and C34 in s38 were the same in each case as the trend observed for C6 in s10-2; the *k*-values being highest at around pH 6.5–7.0 and decreased as the pH increased (**Figure 5B**). Again, the activity of A3G-CTD decreased significantly above pH 9.5 and became negligible around pH 12.7. At all pH values, the relative activity for C6 was higher than that for C34.

Subsequently, the 3′ → 5′ polarity of A3G-CTD's deaminase activity for s38 at each pH value was quantified as the ratio of the rate constant obtained for C6 to that obtained for C34 (**Figure 5C** and **Table 4**). *P* showed the highest value of ca. 4.8 at pH 6.5 and decreased as the pH increased, and then *P* reached a plateau with a value of ca. 3.5 at pH 8.0 and stayed almost the same to pH 11.4.

Previously, we showed that A3G-CTD does not exert 3′ → 5′ polarity for an ssDNA substrate whose two CCC hotspots are linked by a double-stranded DNA stretch (Furukawa et al., 2014). Additionally, we reported that the single-stranded nucleotide linker does not have to be DNA, but it can be either RNA or abasic DNA for A3G-CTD to exert the 3′ → 5′ polarity (Kamba et al., 2015). Then, we revealed that the electrostatic intermolecular interaction between A3G-CTD and ssDNA is the key for sliding, by demonstrating that the lower the NaCl concentration the higher the 3′ → 5′ polarity (Kamba et al., 2015). These findings indicated that the 3′ → 5′ polarity occurs because A3G-CTD slides along the phosphate backbone of the ssDNA stretch between the two CCC hotspots (Kamba et al., 2015). In the current study, we investigated the pH dependence of the 3′ → 5′ polarity. The results indicated that the lower the pH, the higher the 3′ → 5′ polarity in the range of pH 6.5–8.0. This can be explained by that the electrostatic intermolecular interaction between A3G-CTD and ssDNA is strengthened at lower pH, thereby the abortion of sliding is repressed, resulting in the high 3′ → 5′ polarity. Repression of the abortion of sliding enhances the deamination at the second hot spot after the deamination at the first hot spot. It is physiologically relevant that the repression of the abortion of sliding and thus the 3′ → 5′ polarity are highest around at the physiological pH, 6.5.

TABLE 4 | Relative activity and 3′ → 5′ polarity values (*P*) of A3G-CTD for s38 at pHs ranging from 6.5 to 12.7.

pH	Relative activity (C6)	Relative activity (C34)	3′ → 5′ polarity (*P*)
6.5	1.00 ± 0.14	0.21 ± 0.06	4.8 ± 0.6
7.0	1.03 ± 0.21	0.24 ± 0.06	4.3 ± 0.8
7.5	0.29 ± 0.04	0.073 ± 0.011	3.9 ± 0.4
8.0	0.063 ± 0.011	0.021 ± 0.004	3.0 ± 0.5
8.5	0.076 ± 0.008	0.022 ± 0.002	3.4 ± 0.3
9.5	0.018 ± 0.002	$(5.6 \pm 0.4) \times 10^{-3}$	3.3 ± 0.2
10.5	$(6.6 \pm 0.9) \times 10^{-3}$	$(2.1 \pm 0.2) \times 10^{-3}$	3.2 ± 0.4
11.4	$(1.6 \pm 0.2) \times 10^{-3}$	$(4.7 \pm 1.1) \times 10^{-4}$	3.5 ± 0.3
12.7	n.d.	n.d.	n.a.

n.d., not detected; n.a., not applicable.

Further Improvement of Temporal and Spatial Resolution of Real-Time NMR Monitoring

In the present study, we obtained a series of 2D TOCSY spectra during the deamination reaction. Because it took about 75 min to obtain a single 2D TOCSY spectrum at each reaction time point, the temporal resolution was about 75 min. To achieve higher temporal resolution, one can introduce ^{13}C-labeled cytosines to the substrate ssDNA and obtain a series of 2D ^{1}H–^{13}C HSQC spectra. The deamination can be monitored by means of 2D ^{1}H–^{13}C HSQC spectra through the gradual decrease and eventual disappearance of the H5–C5 correlation peak of a cytosine, which is coupled with the emergence and gradual increase of the H5–C5 correlation peak of a uracil. The measurement of ^{1}H–^{13}C HSQC spectra makes use of much larger one-bond ^{1}H–^{13}C coupling ($^{1}J_{HC} = \sim$200 Hz) than the three-bond ^{1}H–^{1}H coupling ($^{3}J_{HH} = \sim$7 Hz) used for the measurement of TOCSY spectra (Wijmenga and van Buuren, 1998; Fiala et al., 2004). Therefore, it is expected that the signal-to-noise ratio of a ^{1}H–^{13}C HSQC spectrum is much higher than that of a TOCSY spectrum, and that thus a ^{1}H–^{13}C HSQC spectrum can be obtained in a much shorter time period than a TOCSY spectrum. It might even be possible to monitor deamination using a 1D version of a 2D ^{1}H–^{13}C HSQC spectrum. If a 1D version of a ^{1}H–^{13}C HSQC spectrum can be obtained with a reasonable signal-to-noise ratio in one scan, the measurement time would be just 100 ms. Thus, with the proper relaxation delay for the next measurement, the temporal resolution of 300–1000 ms is supposed to be achieved in an ideal case.

The spatial resolution depends on the length of the ssDNA, and the numbers of cytosines and uracils contained in the sequence. So far, we have analyzed non-labeled ssDNA of as long as a 60-mer using 2D TOCSY spectra (Furukawa et al., 2014; Kamba et al., 2015). Residue-specific ^{13}C-labeling of a cytosine of the substrate ssDNA can drastically increase the spatial resolution. It is supposed that ssDNA of a 100- to 300-mer can be analyzed by real-time NMR using 2D ^{1}H–^{13}C HSQC spectra in combination with specific ^{13}C labeling.

Such improvement of the temporal and spatial resolution of real-time NMR monitoring will make this method even more valuable for investigating the characters and behaviors of various biological systems including enzymes.

CONCLUSION

Here we presented methodology for the real-time NMR spectroscopy in detail, and described the ease of its usage, and the applicability to systems exhibiting different temporal and spatial resolution. This real-time NMR monitoring method was used to investigate the effects of pH on the deamination reaction and 3′ → 5′ polarity of A3G-CTD. A3G-CTD was firstly shown

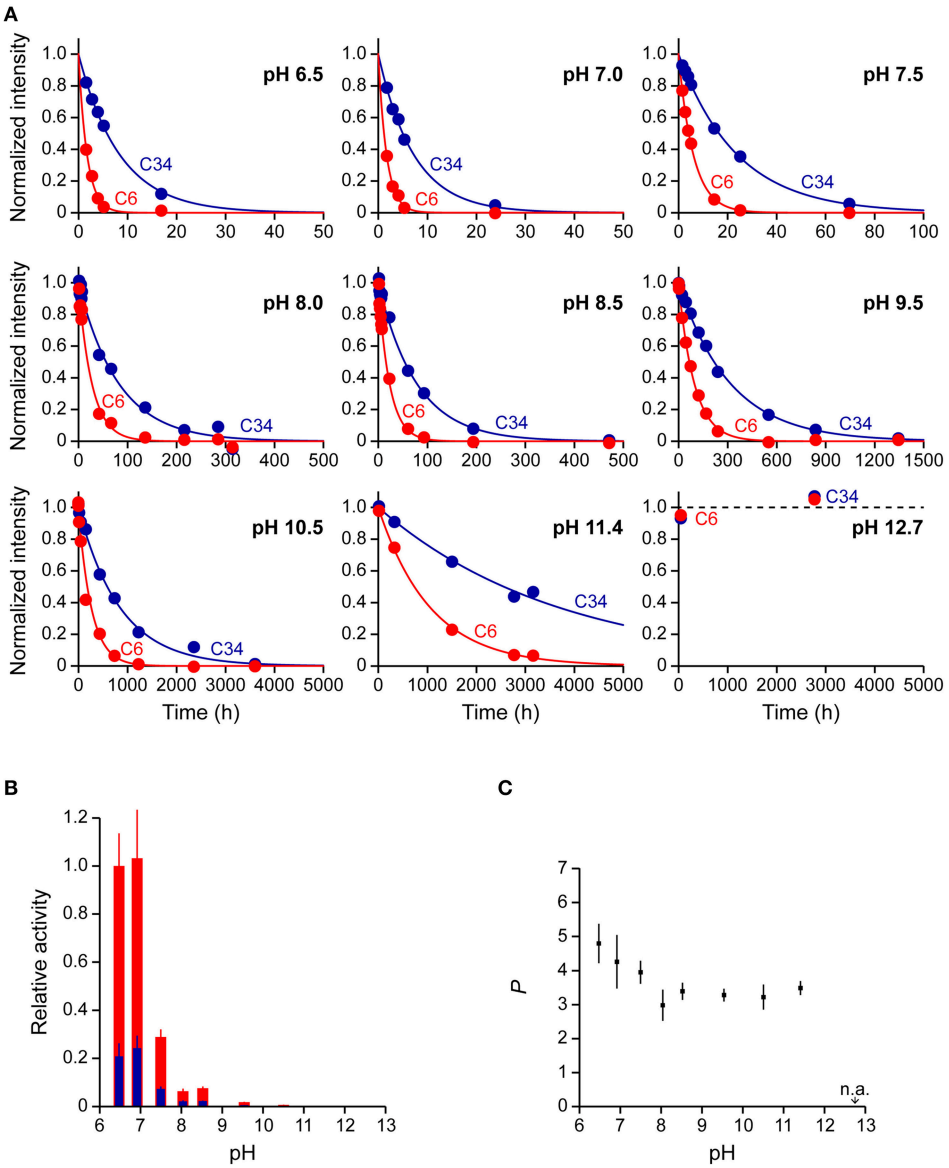

FIGURE 5 | Real-time NMR monitoring of deamination reactions for ssDNA having two CCC hotspots at various pHs. (A) The time courses of the intensity changes were plotted for C6 and C34 of AAACCCGA$_{24}$CCCGTAA (s38 in **Table 1**) at pH 6.5, 7.0, 7.5, 8.0, 8.5, 9.5, 10.5, 11.4, and 12.7. C6 and C34, which are converted to U, are underscored in the sequence. The data of C6 and C34 for each pH were fitted to a single exponential function individually, by which the rate constant, *k*, at each pH was obtained. **(B)** Relative activities for C6 (red) and C34 (blue) are plotted against pH values. The relative activities for C6 and C34 at each pH were defined as the ratio of their *k*s at each pH to that obtained for C6 at pH 6.5. **(C)** 3′ → 5′ polarity values (*P*) are plotted against pH values. The *P* at each pH is defined as the ratio of *k* obtained for C6 to that obtained for C34 (Equation 5).

to retain its native structure fully or to some extent at the pH values studied (pH 4.0–12.7) by CD spectroscopy. Then real-time NMR spectroscopy was applied to a 10-mer ssDNA containing a single CCC, by which it was shown that the deaminase activity of A3G-CTD decreases as the pH increases. This was explained by a reduction in the stability of the complex between A3G-CTD and ssDNA due to the weakened electrostatic interaction with an increase in the pH value. Lastly, a 38-mer ssDNA having two CCC hotspots connected by a long poly-adenine linker was used to show that the 3′ → 5′ polarity of A3G-CTD increases as the pH decreases in the range of 6.5–8.0. This finding can be rationalized that stronger electrostatic intermolecular interaction between A3G-CTD and ssDNA at lower pH represses the abortion of sliding, resulting in high 3′ → 5′ polarity.

AUTHOR CONTRIBUTIONS

Conceived and designed the experiments: KK, TN, MK. Performed the experiments: KK. Analyzed the data: KK, TN, MK. Contributed reagents/materials/analysis tools: TN, MK. Wrote the paper: KK, TN, MK.

ACKNOWLEDGMENTS

This work was supported by the Ministry of Education, Science, Sports and Culture of Japan with Grants-in-Aid for Scientific Research (25291013, 26104520, 26650014, and 15H01256 to MK; and 15H01634 and 26440026 to TN). The funders played no role in the study design, data collection and analysis, decision to publish, or preparation of the manuscript.

REFERENCES

Aydin, H., Taylor, M. W., and Lee, J. E. (2014). Structure-guided analysis of the human APOBEC3-HIV restrictome. *Structure* 22, 668–684. doi: 10.1016/j.str.2014.02.011

Barnes, C., and Smith, H. C. (1993). Apolipoprotein B mRNA editing *in vitro* is a zinc-dependent process. *Biochem. Biophys. Res. Commun.* 197, 1410–1414. doi: 10.1006/bbrc.1993.2634

Betts, L., Xiang, S., Short, S. A., Wolfenden, R., and Carter, C. W. Jr. (1994). Cytidine deaminase. The 2.3 A crystal structure of an enzyme: transition-state analog complex. *J. Mol. Biol.* 235, 635–656. doi: 10.1006/jmbi.1994.1018

Browne, E. P., Allers, C., and Landau, N. R. (2009). Restriction of HIV-1 by APOBEC3G is cytidine deaminase-dependent. *Virology* 387, 313–321. doi: 10.1016/j.virol.2009.02.026

Byeon, I. J., Ahn, J., Mitra, M., Byeon, C. H., Hercík, K., Hritz, J., et al. (2013). NMR structure of human restriction factor APOBEC3A reveals substrate binding and enzyme specificity. *Nat. Commun.* 4:1890. doi: 10.1038/ncomms2883

Carter, C. W. Jr. (1995). The nucleoside deaminases for cytidine and adenosine: structure, transition state stabilization, mechanism, and evolution. *Biochimie* 77, 92–98. doi: 10.1016/0300-9084(96)88110-7

Chelico, L., Pham, P., Calabrese, P., and Goodman, M. F. (2006). APOBEC3G DNA deaminase acts processively 3′ –> 5′ on single-stranded DNA. *Nat. Struct. Mol. Biol.* 13, 392–399. doi: 10.1038/nsmb1086

Chen, K. M., Harjes, E., Gross, P. J., Fahmy, A., Lu, Y., Shindo, K., et al. (2008). Structure of the DNA deaminase domain of the HIV-1 restriction factor APOBEC3G. *Nature* 452, 116–119. doi: 10.1038/nature06638

Delaglio, F., Grzesiek, S., Vuister, G. W., Zhu, G., Pfeifer, J., and Bax, A. (1995). NMRPipe: a multidimensional spectral processing system based on UNIX pipes. *J. Biomol. NMR* 6, 277–293. doi: 10.1007/bf00197809

Fiala, R., Munzarová, M. L., and Sklenár, V. (2004). Experiments for correlating quaternary carbons in RNA bases. *J. Biomol. NMR* 29, 477–490. doi: 10.1023/B:JNMR.0000034358.12599.d1

Furukawa, A., Nagata, T., Matsugami, A., Habu, Y., Sugiyama, R., Hayashi, F., et al. (2009). Structure, interaction and real-time monitoring of the enzymatic reaction of wild-type APOBEC3G. *EMBO J.* 28, 440–451. doi: 10.1038/emboj.2008.290

Furukawa, A., Sugase, K., Morishita, R., Nagata, T., Kodaki, T., Takaori-Kondo, A., et al. (2014). Quantitative analysis of location- and sequence-dependent deamination by APOBEC3G using real-time NMR spectroscopy. *Angew. Chem. Int. Ed Engl.* 53, 2349–2352. doi: 10.1002/anie.201309940

Goddard, T. D., and Kneller, D. G. (2006). *SPARKY 3*. San Francisco, CA: University of California.

Haché, G., Liddament, M. T., and Harris, R. S. (2005). The retroviral hypermutation specificity of APOBEC3F and APOBEC3G is governed by the C-terminal DNA cytosine deaminase domain. *J. Biol. Chem.* 280, 10920–10924. doi: 10.1074/jbc.M500382200

Harjes, E., Gross, P. J., Chen, K. M., Lu, Y., Shindo, K., Nowarski, R., et al. (2009). An extended structure of the APOBEC3G catalytic domain suggests a unique holoenzyme model. *J. Mol. Biol.* 389, 819–832. doi: 10.1016/j.jmb.2009.04.031

Harjes, S., Solomon, W. C., Li, M., Chen, K. M., Harjes, E., Harris, R. S., et al. (2013). Impact of H216 on the DNA binding and catalytic activities of the HIV restriction factor APOBEC3G. *J. Virol.* 87, 7008–7014. doi: 10.1128/JVI.03173-12

Harris, C. D. (1998). Nonlinear least-squares curve fitting with microsoft excel solver. *J. Chem. Educ.* 75, 119–121. doi: 10.1021/ed075p119

Harris, R. S., Bishop, K. N., Sheehy, A. M., Craig, H. M., Petersen-Mahrt, S. K., Watt, I. N., et al. (2003). DNA deamination mediates innate immunity to retroviral infection. *Cell* 113, 803–809. doi: 10.1016/s0092-8674(03)00423-9

Harris, R. S., and Liddament, M. T. (2004). Retroviral restriction by APOBEC proteins. *Nat. Rev. Immunol.* 4, 868–867. doi: 10.1038/nri1489

Holden, L. G., Prochnow, C., Chang, Y. P., Bransteitter, R., Chelico, L., Sen, U., et al. (2008). Crystal structure of the anti-viral APOBEC3G catalytic domain and functional implications. *Nature* 456, 121–124. doi: 10.1038/nature07357

Iwatani, Y., Takeuchi, H., Strebel, K., and Levin, J. G. (2006). Biochemical activities of highly purified, catalytically active human APOBEC3G: correlation with antiviral effect. *J. Virol.* 80, 5992–6002. doi: 10.1128/JVI.02680-05

Kamba, K., Nagata, T., and Katahira, M. (2015). Catalytic analysis of APOBEC3G involving real-time NMR spectroscopy reveals nucleic acid determinants for deamination. *PLoS ONE* 10:e0124142. doi: 10.1371/journal.pone.0124142

Kelly, S. M., Jess, T. J., and Price, C. N. (2005). How to study proteins by circular dichroism. *Biochim. Biophys. Acta* 1751, 119–139. doi: 10.1016/j.bbapap.2005.06.005

Khan, M. A., Goila-Gaur, R., Opi, S., Miyagi, E., Takeuchi, H., Kao, S., et al. (2007). Analysis of the contribution of cellular and viral RNA to the packaging of APOBEC3G into HIV-1 virions. *Retrovirology* 4:48. doi: 10.1186/1742-4690-4-48

Khan, M. A., Kao, S., Miyagi, E., Takeuchi, H., Goila-Gaur, R., Opi, S., et al. (2005). Viral RNA is required for the association of APOBEC3G with human immunodeficiency virus type 1 nucleoprotein complexes. *J. Virol.* 79, 5870–5874. doi: 10.1128/JVI.79.9.5870-5874.2005

Kitamura, S., Ode, H., and Iwatani, Y. (2011). Structural features of antiviral APOBEC3 proteins are linked to their functional activities. *Front. Microbiol.* 2:258. doi: 10.3389/fmicb.2011.00258

Kobayashi, T., Koizumi, Y., Takeuchi, J. S., Misawa, N., Kimura, Y., Morita, S., et al. (2014). Quantification of deaminase activity-dependent and -independent restriction of HIV-1 replication mediated by APOBEC3F and APOBEC3G through experimental-mathematical investigation. *J. Virol.* 88, 5881–5887. doi: 10.1128/JVI.00062-14

Kouno, T., Luengas, E. M., Shigematsu, M., Shandilya, S. M., Zhang, J., Chen, L., et al. (2015). Structure of the Vif-binding domain of the antiviral enzyme APOBEC3G. *Nat. Struct. Mol. Biol.* 22, 485–491. doi: 10.1038/nsmb.3033

Langlois, M. A., Beale, R. C., Conticello, S. G., and Neuberger, M. S. (2005). Mutational comparison of the single-domained APOBEC3C and double-domained APOBEC3F/G anti-retroviral cytidine deaminases provides insight into their DNA target site specificities. *Nucleic Acids Res.* 33, 1913–1923. doi: 10.1093/nar/gki343

Lecossier, D., Bouchonnet, F., Clavel, F., and Hance, A. J. (2003). Hypermutation of HIV-1 DNA in the absence of the Vif protein. *Science* 300:1112. doi: 10.1126/science.1083338

Lu, X., Zhang, T., Xu, Z., Liu, S., Zhao, B., Lan, W., et al. (2015). Crystal structure of DNA cytidine deaminase ABOBEC3G catalytic deamination domain suggests a binding mode of full-length enzyme to single-stranded DNA. *J. Biol. Chem.* 290, 4010–4021. doi: 10.1074/jbc.M114.624262

Navarro, F., Bollman, B., Chen, H., König, R., Yu, Q., Chiles, K., et al. (2005). Complementary function of the two catalytic domains of APOBEC3G. *Virology* 333, 374–386. doi: 10.1016/j.virol.2005.01.011

Pace, C. N. (1986). Determination and analysis of urea and guanidine hydrochloride denaturation curves. *Meth. Enzymol.* 131, 266–280. doi: 10.1016/0076-6879(86)31045-0

Royer, C. A. (2006). Probing protein folding and conformational transitions with fluorescence. *Chem. Rev.* 106, 1769–1784. doi: 10.1002/chin.200631291

Scholtz, J. M., Grimsley, G. R., and Pace, C. N. (2009). Solvent denaturation of proteins and interpretations of the m value. *Meth. Enzymol.* 466, 549–565. doi: 10.1016/S0076-6879(09)66023-7

Shandilya, S. M., Nalam, M. N., Nalivaika, E. A., Gross, P. J., Valesano, J. C., Shindo, K., et al. (2010). Crystal structure of the APOBEC3G catalytic domain reveals potential oligomerization interfaces. *Structure* 18, 28–38. doi: 10.1016/j.str.2009.10.016

Sheehy, A. M., Gaddis, N. C., Choi, J. D., and Malim, M. H. (2002). Isolation of a human gene that inhibits HIV-1 infection and is suppressed by the viral Vif protein. *Nature* 418, 646–650. doi: 10.1038/nature00939

Suspène, R., Rusniok, C., Vartanian, J. P., and Wain-Hobson, S. (2006). Twin gradients in APOBEC3 edited HIV-1 DNA reflect the dynamics of lentiviral replication. *Nucleic Acids Res.* 34, 4677–4684. doi: 10.1093/nar/gkl555

Wijmenga, S. S., and van Buuren, B. N. M. (1998). The use of NMR methods for conformational studies of nucleic acids. *Prog. Nucl. Magn. Reson. Spectros.* 32, 287–387. doi: 10.1016/S0079-6565(97)00023-X

Xiang, S., Short, S. A., Wolfenden, R., and Carter, C. W. Jr. (1995). Transition-state selectivity for a single hydroxyl group during catalysis by cytidine deaminase. *Biochemistry* 34, 4516–4523. doi: 10.1021/bi00014a003

Yu, Q., König, R., Pillai, S., Chiles, K., Kearney, M., Palmer, S., et al. (2004). Single-strand specificity of APOBEC3G accounts for minus-strand deamination of the HIV genome. *Nat. Struct. Mol. Biol.* 11, 435–442. doi: 10.1038/nsmb758c

Zhang, H., Yang, B., Pomerantz, R. J., Zhang, C., Arunachalam, S. C., and Gao, L. (2003). The cytidine deaminase CEM15 induces hypermutation in newly synthesized HIV-1 DNA. *Nature* 424, 94–98. doi: 10.1038/nature 01707

Conflict of Interest Statement: The authors declare that the research was conducted in the absence of any commercial or financial relationships that could be construed as a potential conflict of interest.

Copyright © 2016 Kamba, Nagata and Katahira. This is an open-access article distributed under the terms of the Creative Commons Attribution License (CC BY). The use, distribution or reproduction in other forums is permitted, provided the original author(s) or licensor are credited and that the original publication in this journal is cited, in accordance with accepted academic practice. No use, distribution or reproduction is permitted which does not comply with these terms.

frontiers in Microbiology

ORIGINAL RESEARCH
published: 31 October 2015
doi: 10.3389/fmicb.2015.01220

A cell-free enzymatic activity assay for the evaluation of HIV-1 drug resistance to protease inhibitors

Satoko Matsunaga[1‡], Takashi Masaoka[2‡], Tatsuya Sawasaki[3], Ryo Morishita[1,4], Yasumasa Iwatani[2,5], Masashi Tatsumi[6], Yaeta Endo[3], Naoki Yamamoto[7], Wataru Sugiura[2,5†] and Akihide Ryo[1*]*

[1] Department of Microbiology, School of Medicine, Yokohama City University, Yokohama, Japan, [2] Department of Infection and Immunology, Clinical Research Center, National Hospital Organization Nagoya Medical Center, Nagoya, Japan, [3] Proteo-Science Center, Ehime University, Matsuyama, Japan, [4] CellFree Sciences Co., Ltd., Matsuyama, Japan, [5] Department of AIDS Research, Nagoya University Graduate School of Medicine, Nagoya, Japan, [6] Department of AIDS Research, AIDS Research Center, National Institute of Infectious Diseases, Tokyo, Japan, [7] Department of Microbiology, Yong Loo Lin School of Medicine, National University of Singapore, Singapore, Singapore

OPEN ACCESS

Edited by:
Yasuko Tsunetsugu Yokota, National Institute of Infectious Diseases, Japan

Reviewed by:
Dorian Mcilroy, University of Nantes, France
Wataru Nomura, Tokyo Medical and Dental University, Japan

***Correspondence:**
Akihide Ryo
aryo@yokohama-cu.ac.jp;
Wataru Sugiura
wataru.2.sugiura@gsk.com

†Present address:
Wataru Sugiura, GlaxoSmithKline KK, Tokyo, Japan

‡These authors have contributed equally to this work.

Specialty section:
This article was submitted to Virology, a section of the journal Frontiers in Microbiology

Received: 11 September 2015
Accepted: 19 October 2015
Published: 31 October 2015

Citation:
Matsunaga S, Masaoka T, Sawasaki T, Morishita R, Iwatani Y, Tatsumi M, Endo Y, Yamamoto N, Sugiura W and Ryo A (2015) A cell-free enzymatic activity assay for the evaluation of HIV-1 drug resistance to protease inhibitors. Front. Microbiol. 6:1220. doi: 10.3389/fmicb.2015.01220

Due to their high frequency of genomic mutations, human retroviruses often develop resistance to antiretroviral drugs. The emergence of drug-resistant human immunodeficiency virus type 1 (HIV-1) is a significant obstacle to the effective long-term treatment of HIV infection. The development of a rapid and versatile drug-susceptibility assay would enable acquisition of phenotypic information and facilitate determination of the appropriate choice of antiretroviral agents. In this study, we developed a novel *in vitro* method, termed the Cell-free drug susceptibility assay (CFDSA), for monitoring phenotypic information regarding the drug resistance of HIV-1 protease (PR). The CFDSA utilizes a wheat germ cell-free protein production system to synthesize enzymatically active HIV-1 PRs directly from PCR products amplified from HIV-1 molecular clones or clinical isolates in a rapid one-step procedure. Enzymatic activity of PRs can be readily measured by AlphaScreen (Amplified Luminescent Proximity Homogeneous Assay Screen) in the presence or absence of clinically used protease inhibitors (PIs). CFDSA measurement of drug resistance was based on the fold resistance to the half-maximal inhibitory concentration (IC_{50}) of various PIs. The CFDSA could serve as a non-infectious, rapid, accessible, and reliable alternative to infectious cell-based phenotypic assays for evaluation of PI-resistant HIV-1.

Keywords: HIV-1, protease, cell-free protein synthesis, cell-free drug susceptibility assay, drug resistance

INTRODUCTION

Mortality associated with human immunodeficiency virus (HIV)-related diseases has declined significantly since 1996, when antiretroviral therapy (ART) regimens were introduced as standard interventions for affected patients. However, these regimens increased the risk of emergence of drug-resistant strains of HIV-1 during long-term management of infected patients

Abbreviations: APV, amprenavir; ATV, atazanavir; CFDSA, Cell-free drug susceptibility assay; DHFR, dihydrofolate reductase; DRV, darunavir; GSS, genotypic susceptibility score; GST, glutathione *S*-transferase; HAART, highly active antiretroviral therapy; HIV-1, human immunodeficiency virus type 1; IDV, indinavir; PI, protease inhibitor; PR, protease.

(Gupta et al., 2008). Indeed, the high mutation rates and replication capacity of HIV-1 contribute to the generation of drug-resistant variants (Perelson et al., 1996). The emergence of drug resistance significantly impairs the efficacy of ART (Gupta et al., 2008). Hence, drug resistance testing now provides important information when selecting the most appropriate antiretrovirals for treatment of HIV, leading to improved therapeutic outcomes (Haupts et al., 2003; Bansi et al., 2011).

Currently, genotype- and phenotype-based assays are the two major approaches for evaluating drug resistance of HIV-1. Genotypic assays detect mutations that cause drug resistance, and have the advantages of being less expensive and more rapid than phenotypic methods. However, genotypic approaches have several significant disadvantages: they provide only an indirect measure of drug resistance, and they cannot provide a definitive result, especially in the case of viral strains that have accumulated complex genetic mutations (Hanna and D'Aquila, 2001). In addition, the results of genotyping are sometimes discordant between interpretation algorithms (Ravela et al., 2003), and these strategies can only monitor the majority of quasispecies (Derdelinckx et al., 2003). On the other hand, cell culture–based phenotypic assays provide a direct measurement of drug susceptibility and have the significant advantage of being able to measure the cumulative effects of multiple mutations (Robinson et al., 2000). The main disadvantage of a phenotypic assay is the considerable time needed for completion (∼4 weeks) and the requirement for a Bio-Safety Level 3 (BSL-3) laboratory. Moreover, virus isolation or the use of recombinant virus may select for replication-competent viruses in the cell-culture system at the expense of populations of drug-resistant strains that often exhibit lower replication fitness (Nijhuis et al., 2001). Therefore, there is an urgent demand for a rapid and reliable phenotypic assay that would allow easier acquisition of phenotypic information and facilitate understanding of associated genotyping results without the use of cell-culture.

As a step toward resolving these limitations, we developed a novel CFDSA that combines a wheat germ cell-free protein synthesis system (Ogasawara et al., 1999; Madin et al., 2000; Sawasaki et al., 2002) and the Amplified Luminescent Proximity Homogeneous Assay, AlphaScreen (Eglen et al., 2008; Matsunaga et al., 2012). Our method can readily produce full-length active HIV-1 PR proteins from PCR products and measure their enzymatic activity without intervening protein purification. We show here that CFDSA provides an attractive means for analyzing HIV-1 PR drug resistance.

MATERIALS AND METHODS

Reagents

Wheat germ extracts were obtained from CellFree Sciences, Co. (Yokohama, Japan). Anti-HIV-1 PR monoclonal antibody was purchased from Abcam (clone no. 1696, Cambridge, UK). GST antibodies were purchased from GE Healthcare Biosciences (Pittsburgh, PA, USA). Drug-resistant HIV-1 molecular clones were provided by the AIDS Research Center, National Institute of Infectious Diseases, Japan (Takeuchi et al., 2002).

Construction of *in vitro* Transcription Templates

In vitro transcription templates for each HIV-1 PR gene were constructed by split-primer PCR as described previously. To generate transcription templates, the first round of PCR was performed with 10 ng/μl of each plasmid using 100 nM of a target-specific forward primer containing the S1 sequence at the 5′ end (5′-CCACCCACCACCACCAATGTTTTTTAGGGAA GATCTGGCC-3′; underlined nucleotides indicate the S1 sequence (Takai et al., 2010), and non-underlined nucleotides indicate the 5′-coding region of the target gene) and reverse primer 1 (5′-CCTGATATAGGAAGGCCGGATAAGACGCGAC CGGCGTCGCATCCGGCGCTAGCCGTAAATTCTATACAAA AACTTATTAGCCATCCATTCCTGGCT-3′). The second round of PCR was performed with 1/100th volume of the first PCR product using 100 nM of primer SPu (5′- GCGTAGCATTT AGGTGACACT-3′; Takai et al., 2010), 100 nM of primer sUTR (5′-ACTACCTGATATAGGAAGGCCG-3′), and 1 nM of primer deSP6E01 (5′- GGTGACACTATAGAACTCACCTATCTCCCC AACACCTAATAACATTCAATCACTCTTTCCACTAACCACC TCCACCCACCACCACCAATG-3′). As a substrate corresponding to the p2–p7 junction of HIV-1 Gag, the p2/p7-bls (bls: biotin ligase sequence; GLNDIFEAQKIEWHE) fusion gene was inserted into vector pEU-E01-GST-MCS (CellFree Sciences, Yokohama, Japan), and amplified using primers SPu and AODA2303 (5′-GTCAGACCCCGTAGAAAAGA-3′) with ExTaq (Takara Bio). Gag genes derived from HXB2 were amplified by PCR and cloned into vector pEU-E01. Transcription templates for Gag were constructed by PCR following the method described above, using primers SPu and AODA2303.

In Vitro Transcription and Cell-free Protein Synthesis

In vitro transcription and cell-free protein synthesis were performed using WEPRO7240 wheat germ extract (CellFree Sciences, Yokohama, Japan). Transcription was performed using SP6 RNA polymerase, as described previously (Matsunaga et al., 2014). The translation reaction was performed in bilayer mode with slight modifications. Briefly, translation mixture (forming the bottom layer) consisted of 10 μl of each mRNA (usually 30–35 μg), 10 μl of WEPRO7240 (CellFree Sciences, Yokohama, Japan), and 0.8 μl of 1 μg/μl creatine kinase (Roche Diagnostics K. K., Tokyo, Japan) in 20.8 μl of SUB-AMIX® (CellFree Sciences, Yokohama, Japan). SUB-AMIX (206 μl) was placed on top of the translation mixture, thus forming the top layer. After incubation at 16°C for 16 h, synthesized proteins were confirmed by immunoblotting. For biotinylation of the substrate, 1 μl (50 ng) of crude biotin ligase (BirA) expressed in a wheat germ cell-free system was added to the bottom layer, and 0.5 μM (final concentration) of D-biotin (Nacalai Tesque, Inc., Kyoto, Japan) was added to both the top and bottom layers, as described previously (Matsuoka et al., 2010). As an initial experimental test, radiolabeled protein was produced by cell-free synthesis to confirm the yield and solubility of generated proteins as described previously (Kamura et al., 2005). In actual drug susceptibility testing, quantitations of synthesized

HIV-1 PR proteins were performed by densitometric scanning of Coomassie Brilliant Blue (CBB)-stained bands as compared with purified HIV-1 PR or bovine serum albumin (BSA) (Madin et al., 2000).

Immunoblotting

Five microliters of cell-free synthesized PRs (equivalent to ∼50 ng) was boiled in 2.5 μL of 3X SDS sample buffer [150 mM Tris-HCl (pH 6.8), 6% SDS, 30% glycerol, and 0.6% bromophenol blue]. After separation by 15% SDS-PAGE, the proteins were electrotransferred onto a PVDF membrane (Bio-Rad, Hercules, CA, USA) by application of 100 V for 1 h. The membrane was then blocked in Tris-buffered saline (TBS) containing 5% (w/v) skim milk for 1 h, and then incubated for 1 h with a HIV PR antibody (ab8327; Abcam, Cambridge, MA, USA) in TBS containing 0.1% (v/v) Tween 20 (TBST; 1:1000 dilution) as described previously (Matsunaga et al., 2014). After three washes with TBST, the filter was incubated for 40 min in PBS containing goat-anti mouse IgG-HRP antibody (1:5000; GE Healthcare). After an additional three washes in TBST, HIV PR proteins were detected with SuperSignal West Dura Extended Duration Substrate (Thermo Fisher Scientific, Rockford, IL, USA) on a Lumi-Imager F1 (Roche Diagnostics GmbH, Mannheim, Germany).

Cell-free Enzymatic Assay using a Luminescence Detection System

CFDSA was performed using cell-free–synthesized PR, substrate peptide, and the AlphaScreen® system (PerkinElmer, Boston, MA, USA). Briefly, to bind PR and PI, pre-incubation was performed in a total volume of 10 μl containing 3 μl of cell-free–synthesized PR (∼0.25 μM as a homodimer) and 1X SUB-AMIX® in the presence of serially diluted PI (0.1 to 10^5 nM indinavir, ATV, APV, or DRV). The mixture was incubated at 37°C for 30 min in a 384-well Alphaplate (PerkinElmer). The enzymatic reaction was initiated by the addition of 5 μl of 0.25 μM cell-free–synthesized GST-p2/p7-bls substrate to each well, followed by incubation at 37°C for 2 h. Detection of PR activity was performed essentially as described in the AlphaScreen IgG detection kit instruction manual (PerkinElmer). Briefly, 10 μl of detection mixture containing 20 mM Tris-HCl (pH 7.5), 0.2 mM DTT, 5 mM $MgCl_2$, 5 μg/ml anti-GST antibody, 1 mg/ml BSA, 0.1 μl streptavidin-coated donor beads, and 0.1 μl anti-IgG acceptor beads were added to each well of the 384-well plate, followed by incubation at 23°C for 1 h in the dark. Luminescence signals were analyzed with the AlphaScreen detection program using the EnSpire software (PerkinElmer), and light intensities in the presence of the serially diluted inhibitors were used to calculate their IC_{50} values. PI-resistance levels were determined by comparing the IC_{50} values of drug-resistant PR with those of NL4-3 PR. The results for each PR were normalized based on protein productivity, as determined by liquid scintillation counting. IC_{50} values were calculated using XLfit (ID BUSINESS SOLUTIONS, Guildford, UK). The criteria for CFDSA measurement of resistance were as follows: fold resistance value (FRV) = IC_{50} ratio of test PR/IC_{50} ratio of WT PR.

Clinical Isolates

Serum samples were collected from AIDS patients diagnosed at Nagoya Medical Center. This study was conducted according to the principles expressed in the Declaration of Helsinki, and was approved by the Institutional Review Boards of the National Institute of Infectious Diseases (approval number: 166) and Nagoya Medical Center (approval number: 2010-310). All patients provided written informed consent for collection of samples and subsequent analysis. Some viral clones containing common clusters of drug-resistant mutations were provided by Dr. Robert W. Shafer at Stanford University.

RESULTS

Synthesis of Enzymatically Active HIV-1 Protease using a Wheat Germ Cell-free System

To synthesize catalytically active HIV-1 PR, we initially generated a transcriptional template of this enzyme by PCR, using the HIV-1_{NL4-3} clone as a wild-type (WT) reference sample. We designed a transcription template encoding the open reading frame of HIV-1 PR flanked by 56 N-terminal amino acids (Gag p6 region) and 18 C-terminal amino acids (the reverse-transcriptase region), as shown in **Figure 1A**. The *in vitro* transcription template for the HIV-1 PR gene was constructed by split-primer PCR using primers encoding the SP6 and E01 sites, as described in section "Materials and Methods." To generate a catalysis-incompetent PR, we designed a PR mutant harboring the catalytic active site substitution D25N (D25N; **Figure 1B**). All cDNA templates were subjected to cell-free transcription/translation and then separated by SDS-PAGE. By CBB staining, WT PR migrated at 11 kDa (as the truncated form of PR) due to self-cleavage of the flanking 56 and 18 amino acids at the N- and C-terminal ends, respectively, whereas D25N PR migrated at 19 kDa, corresponding to full-length PR with the flanking sequences (**Figures 1C,D**). Immunoblot analysis with anti-HIV-1 PR antibody recognizing mature form of HIV PR, only detected the cleaved form of WT PR at the expected size (∼11 kDa; **Figure 1D**).

Measurement of HIV-1 Protease Activity using AlphaScreen

For the quantitative and high-throughput measurement of HIV-1 PR activity using AlphaScreen technology, we designed a reporter substrate comprising a partial Gag p2-p7 junction peptide flanked by N-terminal GST and C-terminal biotin binding sequence (GST-p2/p7-biotin) as described in **Figure 2A**. Using the reporter substrate, we attempted to measure the cleavage activity of HIV-1 PR by AlphaScreen (Matsunaga et al., 2012). Cell-free–synthesized HIV-1 PRs were incubated with the reporter substrate, followed by the addition of AlphaScreen streptavidin

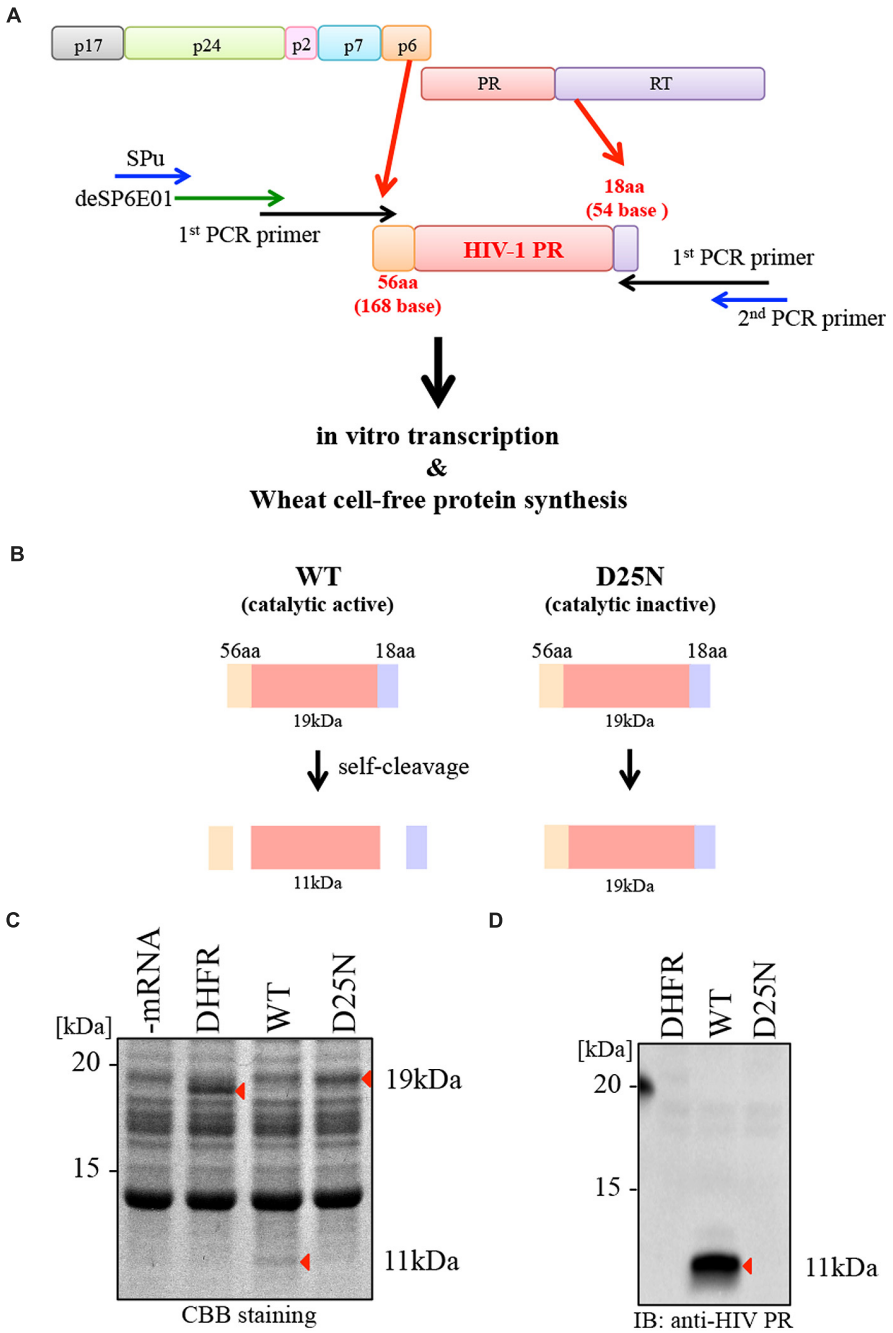

FIGURE 1 | Synthesis of catalytically active HIV-1 PR using the wheat germ cell-free system. (A) Schematic representation of rapid production of HIV-1 PR using a wheat germ cell-free system. A transcriptional template, including the HIV-1 PR open reading frame flanked by N-terminal 168 bases (56 aa) and C-terminal 54 bases (18 aa), produced by split-primer PCR as described in section "Materials and Methods." Cell-free translation was carried out using products of *in vitro* transcription. **(B)** The formation of WT PR (catalytic active) or D25N PR (catalytic inactive) after translation. WT PR generated as a 11 kDa protein by self-cleavage. D25N PR (catalytic inactive) generated as a 19 kDa protein lacking self-cleavage activity. **(C,D)** WT or D25N PRs (-mRNA and DHFR as a negative control) were separated by SDS-PAGE followed by CBB-staining **(C)** and immunoblotting using anti-HIV-1 PR antibody that recognizes only mature HIV protease (PR) but not its precursor **(D)**. Arrows depict protein products.

donor and protein A acceptor beads with anti-GST antibody (**Figure 2A**). In this system, when PR does not cleave the reporter substrate, singlet oxygen energy can be transmitted from the donor beads to the acceptor beads, resulting in emission of light. By contrast, when PR cleaves the substrate, no light is produced.

Consistent with the theory described above, WT HIV-1 PR, but neither D25N PR nor DHFR (used as a negative

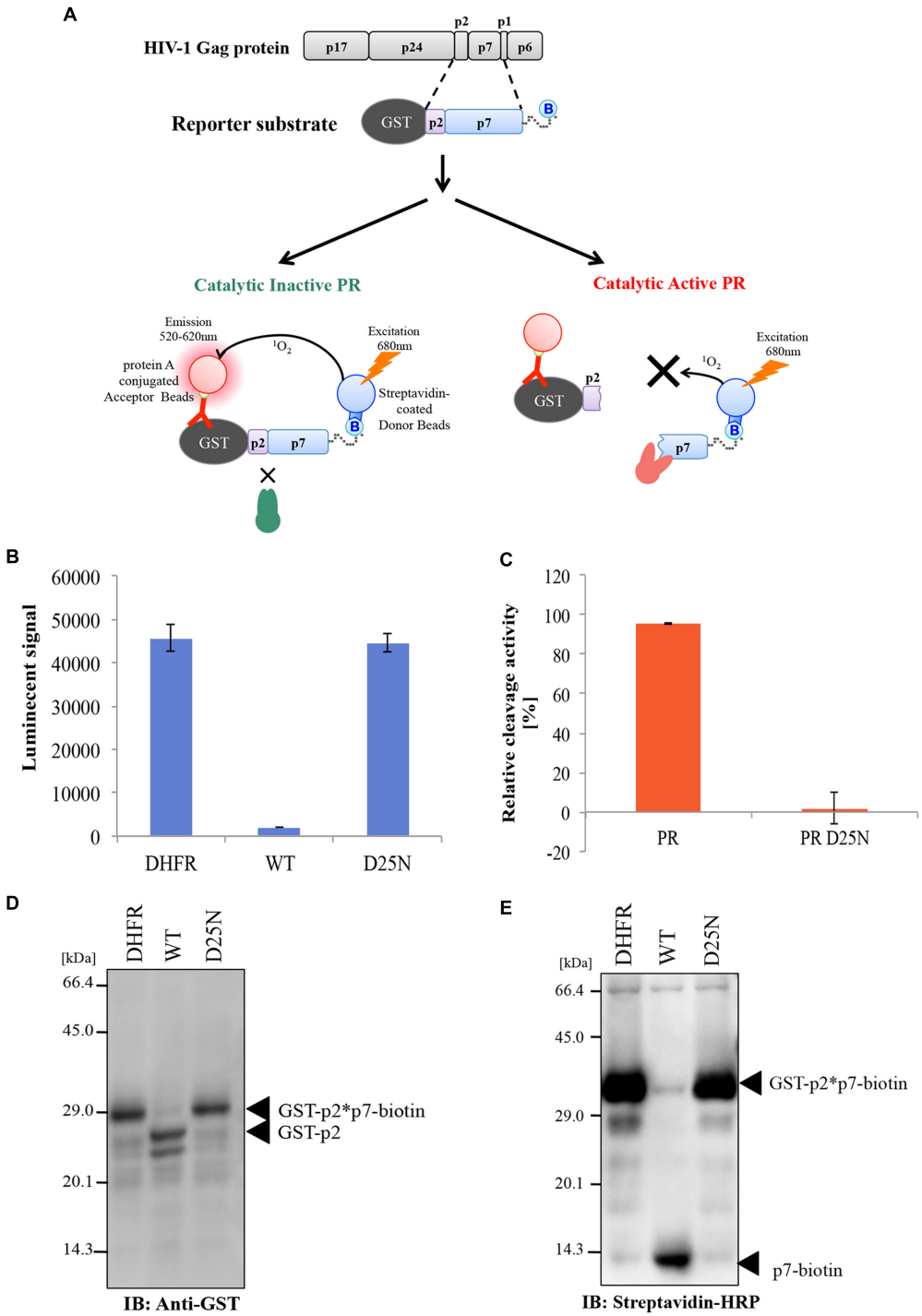

FIGURE 2 | Measurement of HIV-1 PR cleavage activity using AlphaScreen. (A) Design of a reporter substrate (GST-p2/p7-biotin) used in the assay. Schematic representation of the CFDSA used to evaluate drug susceptibility of HIV-1 PR. Cell-free–synthesized PR was incubated with the reporter substrate. Subsequently, protein A–conjugated acceptor beads and streptavidin-coated donor beads were added and bound to the substrate. In this system, when PR does not cleave the test substrate, energy is converted from the donor beads to acceptor beads, resulting in light emission at 520–620 nm (right upper part). By contrast, when PR cleaves the substrate, no light is produced (right lower part). **(B,C)** Cleavage activity of HIV-1 PR was quantitated by AlphaScreen as shown in **(A)**. Luminescent AlphaScreen signal **(B)** and relative enzymatic activity **(C)** are listed. Each bar represents the mean ± SD of four independent experiments. **(D,E)** Conformation of cleavage of the tester polypeptide by immunoblot analysis. The reporter substrate was incubated with HIV-1 PR or D25N mutant, and the reaction mixtures were then separated by SDS-PAGE. Substrate cleavage was analyzed by immunoblotting against a GST antibody (left) or streptavidin conjugated with peroxidase (right). Arrows depict protein products.

control), diminished the AlphaScreen luminescence signal, indicating proteolytic cleavage of the reporter polypeptide (**Figure 2B**). The cleavage activity of PR was normalized against the luminescence activity of DHFR (**Figure 2C**). Parallel immunoblot analysis with an anti-GST antibody or streptavidin-HRP demonstrated that WT PR, but not D25N PR, efficiently digested the reporter substrate into the expected cleavage products (GST -p2 and p7-biotin; **Figures 2D,E**).

Evaluation of Drug-resistant HIV-1 PR by CFDSA

We next investigated whether our assay system is applicable to drug-resistance testing for HIV-1 PR. As an initial approach, we examined the susceptibility of WT HIV-1 PR, or six PRs from clinically drug-resistant clonal isolates (**Figure 3A**), to six different PIs (DRV; APV; ATV; IDV; LPV, lopinavir; and RTV, ritonavir) at a single effective concentration. Although all HIV-1 PIs tested markedly

A

Clones	Major Resistance Mutations	Minor Resistance Mutations	Other Mutations
PR01-A	N88S	L10F, T74S, L89V	I13V, K20T, E35D, M36I, R41K, I62V, L63P, H69K
PR01-B	N88S	L10F, A71T, L89V	I13V, K20T, E35D, M36I, R41K, I62V, L63P, H69K
PR01-C	N88S	L10F, A71T, L89V	I13V, K20T, E35D, M36I, R41K, L63P, H69K
PR01-D	N88S	L10F, A71T, L89V	I13V, K20T, E35D, M36I, R41K, L63P, H69K
PR02-A	G48S, I54V, V82F, L90M	L10I	I13V, G16Q, K20I, E35N, M36I, P39Q, R41K, K45V, I62V, L63P, H69K, L89M
PR02-B	G48A, I54V, V82F, L90M	L10I	I13V, G16E, K20I, E35D, M36I, P39Q, R41K, K45V, I62V, L63P, H69K, L89M

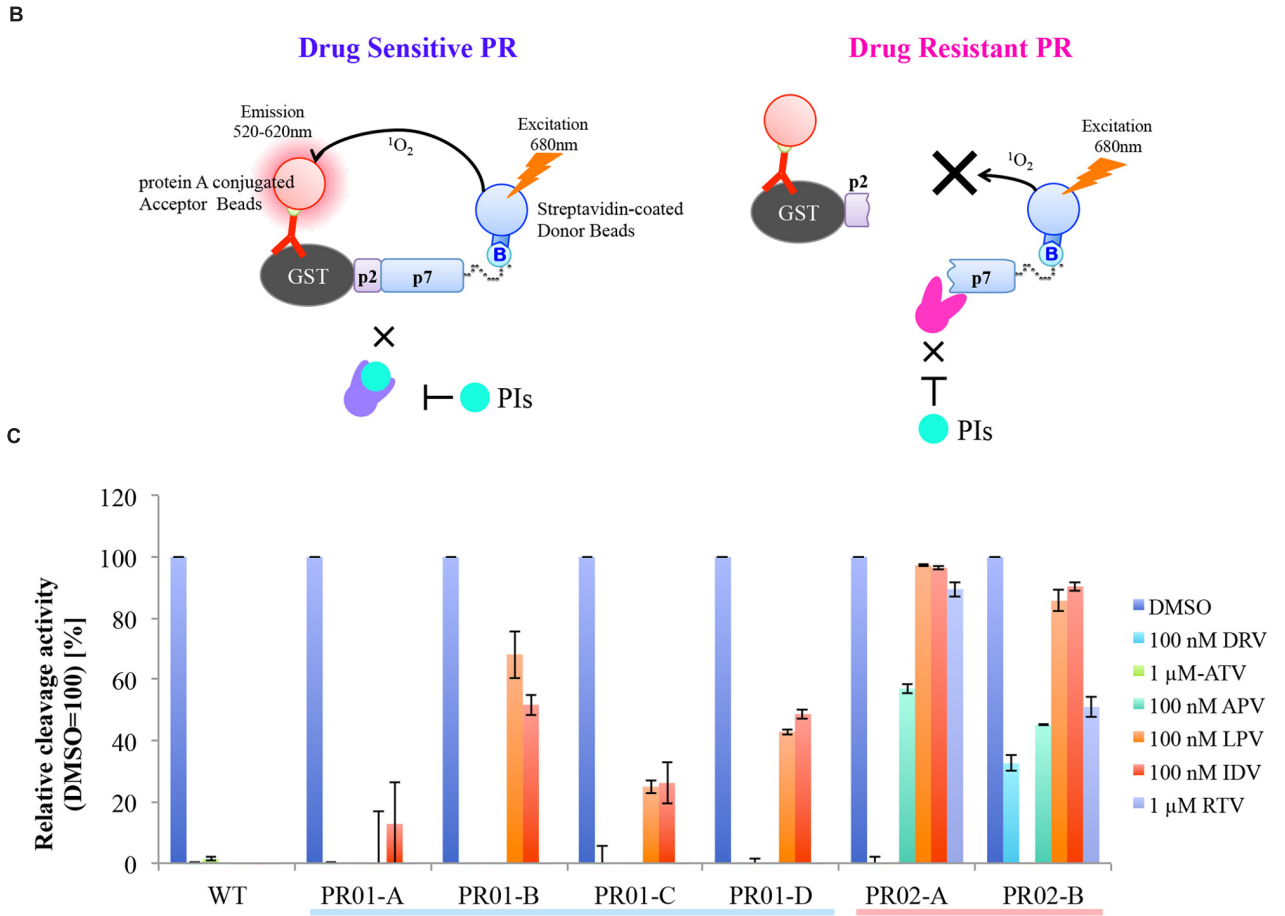

FIGURE 3 | HIV-1 PR drug resistance profiles, as determined by CFDSA in a single-concentration experiment. (A) List of six PRs from clinically drug-resistant clones used in this assay. **(B)** Schematic representation of CFDSA in case of drug sensitive PR or drug resistant PR. Drug sensitive PR does not cleave the reporter substrate with PIs, energy is converted from the donor beads to acceptor beads, resulting in light emission at 520–620 nm. By contrast, when drug resistant PR cleaves the substrate regard less with PIs, no light is produced. **(C)** WT PR and six patient-derived drug-resistant PR mutants were pre-incubated with the indicated protease inhibitors (PI; DRV/darunavir, 100 nM; APV/amprenavir, 100 nM; ATV/atazanavir, 1 mM; IDV/indinavir, 100 nM; LPV/lopinavir, 100 nM; and RTV/ritonavir, 1 mM), and then subjected to CFDSA. Relative cleavage activities were listed. Each bar represents the mean ± SD of two independent experiments.

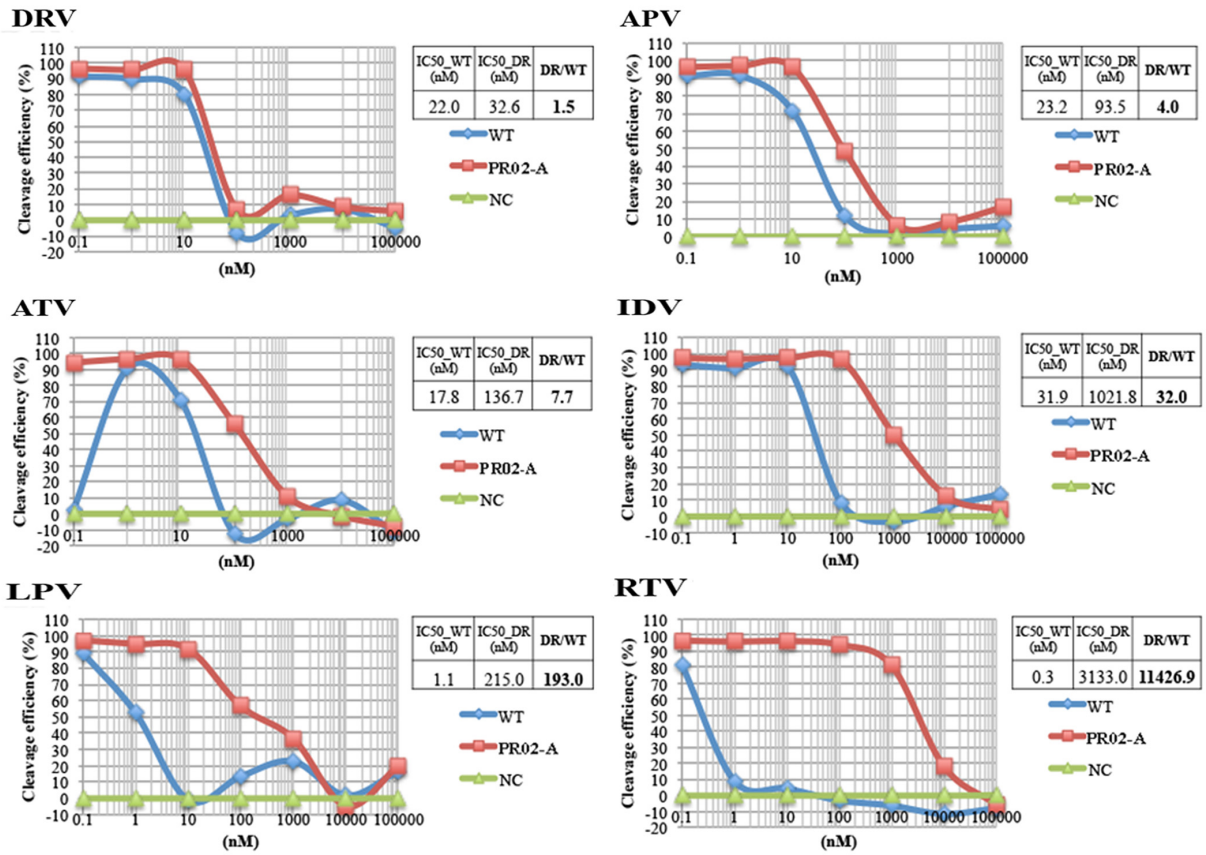

FIGURE 4 | Dose-response curve of HIV-1 PR activity in the presence of PIs, as determined by CFDSA. WT HIV-1 PR or a drug-resistant PR (PR02-A, as shown in **Figure 3**) harboring L10I/G48S/I54V/V82F/L90M mutations was tested in the presence of the indicated concentration of PIs by CFDSA. Luminescent AlphaScreen signals were plotted for each PI, and IC_{50} values were calculated using XLfit for each inhibitor. Fold resistance value (FRV) was calculated using the IC_{50} value of the drug-resistant PR divided by the IC_{50} value of the WT PR. NC, negative control (DHFR).

inhibited WT HIV-1 PR, HIV-1 PRs derived from drug-resistant clones exhibited significantly variable drug resistance at the indicated concentrations (**Figures 3B,C**). Notably, PRs with the comparable "major" or "minor" mutations exhibited distinct drug-resistance profiles, indicating the advantage of CFDSA over the conventional genotyping methods that target only these mutations (**Figures 3B,C**).

We next attempted to determine IC_{50} values by titrating the PIs (**Figure 4**). WT HIV-1 PR and a drug-resistant PR harboring the L10I/G48S/I54V/V82F/L90M mutations were tested. For WT PR, the IC_{50} values for DRV, APV, ATV, IDV, LPV, and RTV were 22.0, 23.2, 17.8, 31.9, 1.1, and 0.3 nM, respectively. For the mutant PR, the IC_{50} values (fold-resistance to WT PR) were 32.6 (1.5-fold higher), 93.5 (4.0-fold higher), 136.7 (7.7-fold higher), 1021.8 (32.0-fold higher), 215.0 (193.0-fold higher), and 3133.0 (11426.9-fold higher) nM, respectively (**Figure 4**). These results indicate that our current assay system can readily determine the susceptibility or resistance of a mutated PR to a particular drug based on the fold change in IC_{50} values relative to those of WT PR.

Comparison of CFDSA with PhenoSense Assay

To evaluate the practical potential of our assay, we compared drug susceptibility profiles obtained via CFDSA with those determined by the phenotypic technique, PhenoSense® . For this purpose, we synthesized 15 patient-derived drug resistant PRs with multiple mutations and measured their IC_{50} values against the same four PIs (DRV, APV, ATV, and IDV). To minimize the effects of cleavage-site mutations, we used molecular clones in which mutant PR genes were inserted into the wild-type pNL4-3 clone. The mutants' sequence profiles are summarized in the lower panel of **Figure 5A**.

Drug-resistance scores determined by CFDSA and PhenoSense® were plotted in scatter plots. The CFDSA results were significantly positively correlated with those of PhenoSense® for ATV, APV, and IDV (**Figure 5B**); for DRV, no correlation was found probably due to its mechanism of action (**Figure 5B**; see discussion). These results indicate that PI-resistance results obtained by CFDSA are almost, but not completely, consistent with those determined by conventional cell-based drug-susceptibility assays.

A

Clones No.	Major Resistance Mutations	Minor Resistance Mutations
1	L24I, V32I, L33F, M46L, I54L, V82A, I84V	L10I, I13V, D60E, L63P, A71V
2	L33F, M46L, G48M, I54M, V82A, I84V	L10I, A71V, I93L
3	M46I, I54V, V82L, L90M	L10I, I13V, K20I, M36I, Q58E, I62V, L63P, A71V, T74P, I93L
4	V32I, M46I, I47V, I84V	L10V, I13V, K20T, M36I, Q58E, L63P
5	M46I, I84V, L90M,	L10I, L63P, A71T, V77I, I85V, I93L
6	L24I, I54V, V82A, I84V	L10I, V11I, M36I, I62V, L63P, A71V
7	L33F, M46L, G48M, I54M, V82A, I84V	L10I, V11I, I13V, L63T, A71V, I93L
8	G48V, I50V, I54V, V82T	L10I, M36I, I62V, A71V
9	M46I, N88S, L90M	L10I, I13V, I62V, L63P, V77I, Q58E, A71T, T74S
10	M46L, I54V, L76V, V82A, L90M	L10I, K20R, M36I, L63P, A71V, I93L
11	M46I, L76V, L90M	L10I, K20I, M36I, I62V, L63P, I64V, A71V, I93L
12	M46L, I54V, L76V, V82A, L90M	L10I, K20R, M36I, L63P, A71V, I93L
13	L24I, M46I, I54V, V82A	L10I
14	L90M	L10I, K20I, I62V, L63P, A71V, G73S, V77I
15	L90M	L10I, I13V, K20T, D60E, L63P, A71V, V77I, I93L

B

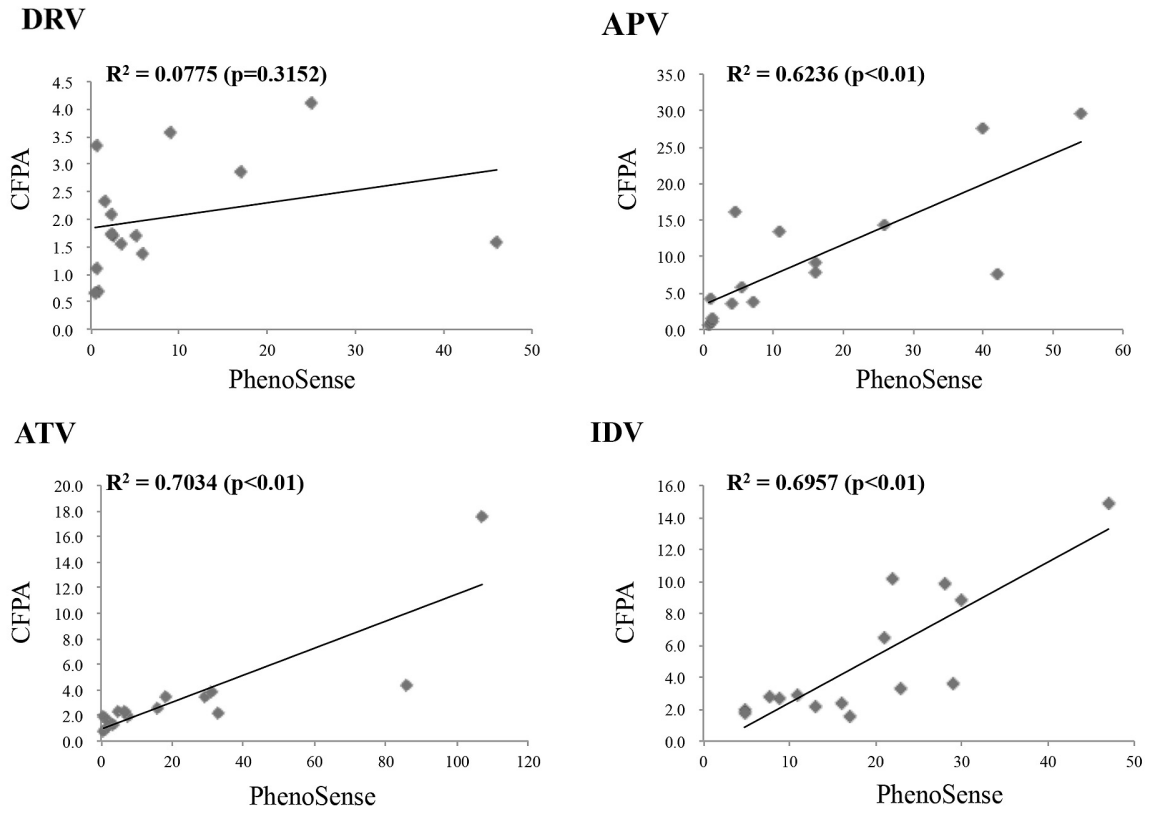

FIGURE 5 | Comparison of CFDSA with the PhenoSense assay. (A) Information about the PR mutants used in this assay. **(B)** Assessment of drug susceptibility and resistance determined by CFDSA, compared to those determined by the PhenoSense® assay. The y-axis indicates CFDSA drug-resistant scores, whereas the x-axis represents PhenoSense® scores.

DISCUSSION

The phenotypic drug-resistance assays in current use are complex, labor-intensive, and expensive. Therefore, there is an urgent need for a simpler, safer, and less expensive method for drug resistance testing (Garcia-Lerma and Heneine, 2002). Here, we describe the development of a novel *in vitro* enzymatic activity assay that provides a rapid and reliable method for evaluating the PI-resistance of clinical HIV samples. Our method is based on the direct measurement of the catalytic activity of HIV-1 PR synthesized using a wheat cell-free system.

The advantages of CFDSA in comparison with conventional cell-based phenotypic assays include (1) a relatively lower cost than alternative *in vitro* and *in vivo* screening technologies (∼50–60 cents/well including protein synthesis); (2) greater rapidity than cell-based phenotypic assays (the entire test procedure is completed in 2 or 3 days vs. several weeks); (3) no requirement for a Bio-Safety Level 3 (BSL3) containment; (4) has the versatility to be used in high-throughput assays with multi-well plates; and (5) is a "mix and measure" assay system which can potentially be automated. Although we demonstrate here that our newly developed CFDSA could be a potentially powerful tool for the measurement of catalytic activity of HIV-1 PR, it is still immature to use for practical and actual HIV-1 PR drug-resistance testing in clinics. Further studies involving a much larger sample size with multiple drug-resistant mutations will be necessary to determine whether CFDSA is truly applicable to clinical testing or use as an effective diagnostic tool in the treatment of HIV-1-infected patients.

Several related biochemical methods have been used to evaluate HIV-1 PI susceptibility (Yu et al., 1995; Gutierrez et al., 2002; Hoffmann et al., 2005; Hu et al., 2005; Matsuda et al., 2007). The basic principle involved in these procedures is to incubate the recombinant PR, substrate peptide, and PI *in vitro*, and then measure the amount of substrate cleaved by PR. The advantage of this approach is that it directly evaluates the drug-resistance phenotype based on the catalytic activity of PR, even in cases when there are cumulative effects of a large number of mutations. However, it is often difficult to produce sufficient quantities of enzymatically active PR in conventional cell-based protein expression systems, such as *Escherichia coli* (*E. coli*). In *E. coli*, HIV PR is usually expressed in the inclusion body fraction due to its insolubility and cytotoxicity (Cheng et al., 2006). In comparison to cell-mediated procedures, the wheat germ cell-free system is advantageous for the efficient preparation of high-quality proteins with natural folding and high enzymatic activity, both of which enable high-throughput functional assays (Endo and Sawasaki, 2006). Moreover, the wheat germ system is suitable for the generation of toxic viral proteins such as HIV-1 PR.

Cell-free drug susceptibility assay was designed to evaluate the drug-resistance properties of PR enzymes that harbor complex and multiple mutations, a key limitation of genotypic assays (Baldanti et al., 2004). Assessment of drug resistance of HIV PRs that harbor highly complex mutations, or PRs derived from non-B subtypes of the virus, is currently the focus of a great deal of attention (Llibre et al., 2010). However, the aforementioned limitations of genotypic assays, which can only indirectly evaluate this characteristic, may result in a lack of information. In this regard, when scoring drug susceptibility, genotypic assays usually consider only predetermined major and minor drug-resistance mutations. On the other hand, our CFDSA method can evaluate PI resistance based on actual enzymatic activity in real time. Thus, CFDSA provides a means for predicting the drug resistance of PRs that have accumulated complex mutations.

Our results demonstrate that the drug-resistance scores of CFDSA were highly concordant with those of PhenoSense®. However, there were some discrepancies, specifically in regard to susceptibility to DRV. DRV is a potent antiretroviral drug that can block the dimerization of HIV-1 PR, and also has high affinity for the mature enzyme, although the mechanism by which it inhibits dimerization has not been well characterized (Huang and Caflisch, 2012). Because CFDSA utilizes mature HIV-1 PR to directly evaluate enzymatic activity, and does not reflect differences in maturation, the results obtained for DRV may not accurately represent the situation *in vivo*. Further biochemical analysis will be necessary to clarify these intriguing findings.

In summary, we show here that our method provides a simple and biologically relevant means for quantitative evaluation of drug-resistant HIV-1 PRs using existing therapeutics.

AUTHOR CONTRIBUTIONS

SM and TM designed and performed the research, analyzed the data, and wrote the manuscript; TS and RM performed the research, developed the screening system and analyzed the data; NY analyzed the data and edited the manuscript; YI, MT, and YE contributed reagents and analyzed the data; WS and AR directed the research, analyzed the data, and wrote the manuscript.

ACKNOWLEDGMENTS

We thank Dr. Hirokazu Kimura for his continuous advice and encouragement throughout the course of this work. We thank M. Nishizawa and H. Miura for technical assistance and Prof. H. Hirano for valuable advices and support. This work was supported in part by the Creation of Innovation Centers for Advanced Interdisciplinary Research Areas Program in the Project for Developing Innovation Systems from the Ministry of Education, Culture, Sports, Science and Technology, grants from Special Coordination Funds for Promoting Science and Technology, Japanese Ministry of Health, Labor, and Welfare, and The Imai Memorial Trust for AIDS Research (to AR). TM was a research fellow of the Japan Foundation for AIDS Prevention.

REFERENCES

Baldanti, F., Paolucci, S., Dossena, L., and Gerna, G. (2004). Assays for determination of HIV resistance to antiviral drugs. *Curr. Drug Metab.* 5, 317–319. doi: 10.2174/1389200043335496

Bansi, L., Smith, C., Phillips, A., Kirk, S., Geretti, A. M., Johnson, M., et al. (2011). The impact of HIV drug resistance testing on changes to treatment. *AIDS* 25, 603–610. doi: 10.1097/QAD.0b013e32834403a0

Cheng, Y. S., Lo, K. H., Hsu, H. H., Shao, Y. M., Yang, W. B., Lin, C. H., et al. (2006). Screening for HIV protease inhibitors by protection against activity-mediated cytotoxicity in *Escherichia coli*. *J. Virol. Methods* 137, 82–87. doi: 10.1016/j.jviromet.2006.06.003

Derdelinckx, I., Van Laethem, K., Maes, B., Schrooten, Y., De Schouwer, K., De Wit, S., et al. (2003). Performance of the VERSANT HIV-1 resistance assays (LiPA) for detecting drug resistance in therapy-naive patients infected with

different HIV-1 subtypes. *FEMS Immunol. Med. Microbiol.* 39, 119–124. doi: 10.1016/S0928-8244(03)00240-2

Eglen, R. M., Reisine, T., Roby, P., Rouleau, N., Illy, C., Bosse, R., et al. (2008). The use of AlphaScreen technology in HTS: current status. *Curr. Chem. Genomics* 1, 2–10. doi: 10.2174/1875397300801010002

Endo, Y., and Sawasaki, T. (2006). Cell-free expression systems for eukaryotic protein production. *Curr. Opin. Biotechnol.* 17, 373–380. doi: 10.1016/j.copbio.2006.06.009

Garcia-Lerma, J. G., and Heneine, W. (2002). Rapid biochemical assays for phenotypic drug resistance testing of HIV-1. *J. Antimicrob. Chemother.* 50, 771–774. doi: 10.1093/jac/dkg005

Gupta, R., Hill, A., Sawyer, A. W., and Pillay, D. (2008). Emergence of drug resistance in HIV type 1-infected patients after receipt of first-line highly active antiretroviral therapy: a systematic review of clinical trials. *Clin. Infect. Dis.* 47, 712–722. doi: 10.1086/590943

Gutierrez, O. A., Salas, E., Hernandez, Y., Lissi, E. A., Castrillo, G., Reyes, O., et al. (2002). An immunoenzymatic solid-phase assay for quantitative determination of HIV-1 protease activity. *Anal. Biochem.* 307, 18–24. doi: 10.1016/S0003-2697(02)00009-X

Hanna, G. J., and D'Aquila, R. T. (2001). Clinical use of genotypic and phenotypic drug resistance testing to monitor antiretroviral chemotherapy. *Clin. Infect. Dis.* 32, 774–782. doi: 10.1086/319231

Haupts, S., Ledergerber, B., Boni, J., Schupbach, J., Kronenberg, A., Opravil, M., et al. (2003). Impact of genotypic resistance testing on selection of salvage regimen in clinical practice. *Antivir. Ther.* 8, 443–454.

Hoffmann, D., Buchberger, B., and Nemetz, C. (2005). In vitro synthesis of enzymatically active HIV-1 protease for rapid phenotypic resistance profiling. *J. Clin. Virol.* 32, 294–299. doi: 10.1016/j.jcv.2004.09.016

Hu, K., Clement, J. F., Abrahamyan, L., Strebel, K., Bouvier, M., Kleiman, L., et al. (2005). A human immunodeficiency virus type 1 protease biosensor assay using bioluminescence resonance energy transfer. *J. Virol. Methods* 128, 93–103. doi: 10.1016/j.jviromet.2005.04.012

Huang, D. Z., and Caflisch, A. (2012). How does darunavir prevent HIV-1 protease dimerization? *J. Chem. Theory Comput.* 8, 1786–1794. doi: 10.1021/ct300032r

Kamura, N., Sawasaki, T., Kasahara, Y., Takai, K., and Endo, Y. (2005). Selection of 5'-untranslated sequences that enhance initiation of translation in a cell-free protein synthesis system from wheat embryos. *Bioorg. Med. Chem. Lett.* 15, 5402–5406. doi: 10.1016/j.bmcl.2005.09.013

Llibre, J. M., Schapiro, J. M., and Clotet, B. (2010). Clinical implications of genotypic resistance to the newer antiretroviral drugs in HIV-1-infected patients with virological failure. *Clin. Infect. Dis.* 50, 872–881. doi: 10.1086/650732

Madin, K., Sawasaki, T., Ogasawara, T., and Endo, Y. (2000). A highly efficient and robust cell-free protein synthesis system prepared from wheat embryos: plants apparently contain a suicide system directed at ribosomes. *Proc. Natl. Acad. Sci. U.S.A.* 97, 559–564. doi: 10.1073/pnas.97.2.559

Matsuda, Z., Iga, M., Miyauchi, K., Komano, J., Morishita, K., Okayama, A., et al. (2007). In vitro translation to study HIV protease activity. *Methods Mol. Biol.* 375, 135–149.

Matsunaga, S., Kawakami, S., Matsuo, I., Okayama, A., Tsukagoshi, H., Kudoh, A., et al. (2014). Wheat germ cell-free system-based production of hemagglutinin-neuraminidase glycoprotein of human parainfluenza virus type 3 for generation and characterization of monoclonal antibody. *Front. Microbiol.* 5:208. doi: 10.3389/fmicb.2014.00208

Matsunaga, S., Sawasaki, T., Ode, H., Morishita, R., Furukawa, A., Sakuma, R., et al. (2012). Molecular and enzymatic characterization of XMRV protease by a cell-free proteolytic analysis. *J. Proteomics* 75, 4863–4873. doi: 10.1016/j.jprot.2012.05.047

Matsuoka, K., Komori, H., Nose, M., Endo, Y., and Sawasaki, T. (2010). Simple screening method for autoantigen proteins using the N-terminal biotinylated protein library produced by wheat cell-free synthesis. *J. Proteome Res.* 9, 4264–4273. doi: 10.1021/pr9010553

Nijhuis, M., Deeks, S., and Boucher, C. (2001). Implications of antiretroviral resistance on viral fitness. *Curr. Opin. Infect. Dis.* 14, 23–28. doi: 10.1097/00001432-200102000-00005

Ogasawara, T., Sawasaki, T., Morishita, R., Ozawa, A., Madin, K., and Endo, Y. (1999). A new class of enzyme acting on damaged ribosomes: ribosomal RNA apurinic site specific lyase found in wheat germ. *EMBO J.* 18, 6522–6531. doi: 10.1093/emboj/18.22.6522

Perelson, A. S., Neumann, A. U., Markowitz, M., Leonard, J. M., and Ho, D. D. (1996). HIV-1 dynamics in vivo: virion clearance rate, infected cell life-span, and viral generation time. *Science* 271, 1582–1586. doi: 10.1126/science.271.5255.1582

Ravela, J., Betts, B. J., Brun-Vezinet, F., Vandamme, A. M., Descamps, D., Van Laethem, K., et al. (2003). HIV-1 protease and reverse transcriptase mutation patterns responsible for discordances between genotypic drug resistance interpretation algorithms. *J. Acquir. Immune. Defic. Syndr.* 33, 8–14. doi: 10.1097/00126334-200305010-00002

Robinson, L. H., Myers, R. E., Snowden, B. W., Tisdale, M., and Blair, E. D. (2000). HIV type 1 protease cleavage site mutations and viral fitness: implications for drug susceptibility phenotyping assays. *AIDS Res. Hum. Retroviruses* 16, 1149–1156. doi: 10.1089/088922200414992

Sawasaki, T., Ogasawara, T., Morishita, R., and Endo, Y. (2002). A cell-free protein synthesis system for high-throughput proteomics. *Proc. Natl. Acad. Sci. U.S.A.* 99, 14652–14657. doi: 10.1073/pnas.232580399

Takai, K., Sawasaki, T., and Endo, Y. (2010). Practical cell-free protein synthesis system using purified wheat embryos. *Nat. Protoc.* 5, 227–238. doi: 10.1038/nprot.2009.207

Takeuchi, H., Suzuki, Y., Tatsumi, M., Hoshino, H., Daar, E. S., and Koyanagi, Y. (2002). Isolation and characterization of an infectious HIV type 1 molecular clone from a patient with primary infection. *AIDS Res. Hum. Retroviruses* 18, 1127–1133. doi: 10.1089/088922202320567860

Yu, S. L., Wang, N., Liou, C. Y., and Syu, W. J. (1995). Assay of HIV-1 protease activity by use of crude preparations of enzyme and biotinylated substrate. *J. Virol. Methods* 53, 63–73. doi: 10.1016/0166-0934(94)00177-I

Conflict of Interest Statement: The authors declare that the research was conducted in the absence of any commercial or financial relationships that could be construed as a potential conflict of interest.

Copyright © 2015 Matsunaga, Masaoka, Sawasaki, Morishita, Iwatani, Tatsumi, Endo, Yamamoto, Sugiura and Ryo. This is an open-access article distributed under the terms of the Creative Commons Attribution License (CC BY). The use, distribution or reproduction in other forums is permitted, provided the original author(s) or licensor are credited and that the original publication in this journal is cited, in accordance with accepted academic practice. No use, distribution or reproduction is permitted which does not comply with these terms.

frontiers in Microbiology

ORIGINAL RESEARCH
published: 09 September 2015
doi: 10.3389/fmicb.2015.00940

Nonlinear electrical impedance spectroscopy of viruses using very high electric fields created by nanogap electrodes

Ryuji Hatsuki[1], *Ayae Honda*[2], *Masayuki Kajitani*[3] *and Takatoki Yamamoto*[1]*

[1] *Department of Mechanical and Control Engineering, Tokyo Institute of Technology, Tokyo, Japan,* [2] *Faculty of Bioscience and Applied Chemistry, Housei University, Tokyo, Japan,* [3] *Department of Bioscience, Teikyo University, Tochigi, Japan*

Our living sphere is constantly exposed to a wide range of pathogenic viruses, which can be either known, or of novel origin. Currently, there is no methodology for continuously monitoring the environment for viruses in general, much less a methodology that allows the rapid and sensitive identification of a wide variety of viruses responsible for communicable diseases. Traditional approaches, based on PCR and immunodetection systems, only detect known or specifically targeted viruses. We here describe a simple device that can potentially detect any virus between nanogap electrodes using nonlinear impedance spectroscopy. Three test viruses, differing in shape and size, were used to demonstrate the general applicability of this approach: baculovirus, tobacco mosaic virus (TMV), and influenza virus. We show that each of the virus types responded differently in the nanogap to changes in the electric field strength, and the impedance of the virus solutions differed depending both on virus type and virus concentration. These preliminary results show that the three virus types can be distinguished and their approximate concentrations determined. Although further studies are required, the proposed nonlinear impedance spectroscopy method may achieve a sensitivity comparable to that of more traditional, but less versatile, virus detection systems.

Keywords: virus, virus sensing, impedance spectroscopy, nanogap, nanofluidics, environmental monitoring

OPEN ACCESS

Edited by:
Slobodan Paessler, University of Texas Medical Branch, USA

Reviewed by:
Kazuya Kabayama, Osaka University, Japan
Hiroshi Kimura, Tokai University, Japan

***Correspondence:**
Takatoki Yamamoto, Department of Mechanical and Control Engineering, Tokyo Institute of Technology, 2-12-1 Ookayama, Meguro-ku, Tokyo 152-8550, Japan
yamamoto@mes.titech.ac.jp

Specialty section:
This article was submitted to Virology, a section of the journal Frontiers in Microbiology

Received: *27 July 2015*
Accepted: *24 August 2015*
Published: *09 September 2015*

Citation:
Hatsuki R, Honda A, Kajitani M and Yamamoto T (2015) Nonlinear electrical impedance spectroscopy of viruses using very high electric fields created by nanogap electrodes. Front. Microbiol. 6:940. doi: 10.3389/fmicb.2015.00940

Introduction

Our environment is posed a constant threat of exposure by pathogenic viruses, whether to humans or pets, domestic animals, or agricultural and marine products (plants, fish, or shellfish). No established methodology exists for inactivating most viruses that could cause widespread communicable viral infection. It is therefore imperative to realize a technology that can monitor the environment for viruses and prevent their spread and disease transmission. The key is to develop a practical sensor that can continuously monitor the environment for viruses. Such virus sensors could be installed at airports, seaports, and other points of entry, and where necessary at farms and ranches, at restaurants, in air conditioning units, in sewage systems, and in other public facilities or utilities. These sensors would continuously monitor for viruses, and if they were detected, measures could be implemented to prevent infection, in contrast to their existing diagnostic application. In cases where detection and countermeasures are too late to prevent an outbreak of a communicable disease, a network of virus sensors could facilitate rapid identification of affected areas,

allowing medical resources to be focused in those areas. This would lead to early-stage detection and treatment, and maximize the efficient use of medical resources.

Currently, there is no technology that can sense viruses in our daily environment. Existing virus detection methods are focused on diagnosing infected individuals, and can be classified into three main categories: (1) those that utilize genomic information and are based on the polymerase chain reaction (PCR) and metagenomic analysis; (2) those that utilize molecular recognition or receptor linking functions of compounds such as antibodies, sugar chains, and peptide aptamers; and (3) those that are based on the electrical or optical properties of viruses (Cheng et al., 2009). In the first category, PCR-based methods provide high detection sensitivity and accuracy but require long analysis times, costly equipment, and specialized techniques, so their range of use is limited in terms of location and qualified personnel (Yang and Rothman, 2004; Espy et al., 2006; Charlton et al., 2009; Hodneland et al., 2011; Cella et al., 2013). In the second category, immunochromatography can provide a relatively fast, simple, and portable means of virus detection in clinical settings such as hospitals, and has therefore become a mainstream technique; however, it suffers from problems such as low sensitivity and accuracy that impede early-stage detection (Lee et al., 1993, 2009; Patolsky et al., 2004; Reichmuth et al., 2008; Heinze et al., 2009; Wang et al., 2009, 2011; Hassen et al., 2011; Lum et al., 2012; Nguyen et al., 2012). Both categories, moreover, basically involve single-use disposable test units, and can only detect known or specifically targeted viruses. In short, neither category is appropriate in principle for application to continuous virus monitoring of the environment, or detecting new or unspecified viruses. Consequently, neither category holds significant promise for the development of a systematic technology for comprehensive environmental virus monitoring.

There have been fewer studies in the third category, which are based on direct measurement of physical properties. The methods in this category are inferior to the other two in terms of sensitivity, and are particularly poor in their ability to selectively distinguish viruses in the presence of numerous contaminants. However, methods in the third category have two key potential advantages: the ability to continuously monitor the environment, and to detect unspecified viruses and mutants, since biological information on genomes or receptors is not required. A high-sensitivity, accurate virus sensor based on direct measurement of physical properties would enable long-term, continuous virus monitoring, which cannot be achieved by the other two categories. This would represent a groundbreaking advance in virus-monitoring technology.

Most virus detection techniques based on physical properties use optical or electrical methods. Typical optical methods use light scattering to achieve high-sensitivity detection to confirm the presence of virus particles. However, optical detection has disadvantages in miniaturization of a complex optical setup and light source (Fan et al., 2008). On hand, electrical method for direct virus detection uses impedance spectroscopy, while another uses dielectric relaxation (Ermolina et al., 2003). Other recent examples include microelectrodes fabricated in microchannels coupled with impedance spectroscopy. This approach is aimed at identifying and quantifying baculovirus and lentivirus in solutions, based on the impedance magnitude at the peak frequency (Poenar et al., 2004). However, the accuracy and sensitivity of these approaches are low compared with PCR-based and immunochromatographic methods, and there have been few publications regarding these techniques.

We investigated the use of impedance spectroscopy for highly sensitive and accurate virus detection based on the nonlinear effect of electrophoretic and dielectrophoretic forces on the virion during measurement to enhance both sensitivity and selectivity. The approach involves applying a sufficiently strong electric field to cause inter-electrode virion movement and allow control of the orientation in the case of non-spherical virions. This active perturbation of the virion allows nonlinear measurement of its properties.

Generally, an electric field of 10^5 V/m or more is required to induce movement of nanometer-sized particles by dielectrophoretic forces, but an applied voltage of several volts or more ordinarily required for this purpose would also induce prominent electrode reactions that would tend to preclude effective for measurement (Turcu and Lucaciu, 1989; Akin et al., 2004; Liu and Bau, 2004; Yang et al., 2008; Pethig, 2010). To obtain an electric field of 10^5 V/m or more using a lower applied voltage, we propose the use of nanogap electrodes. For example, it is possible to generate an electric field of 200 kV/m across a 500 nm gap using an applied voltage of 0.1 V, which is too low for electrolysis to occur. This study reports a high-sensitivity virus detection method by nonlinear impedance spectroscopy with the use of nanogap electrodes to generate strong electric fields under a low applied voltage.

Materials and Methods

Virus Samples

Table 1 shows the shapes and sizes of the three viruses used in this study. The dipole moment induced in a small particle generally depends on its size and shape, and the dipolar effect tends to be particularly strong for long, narrow particles. We therefore used baculovirus, tobacco mosaic virus (TMV), and influenza virus [influenza A (H1N1)] as sample viruses with different sizes and long/short axis ratios. The baculovirus is rod-shaped, with a diameter of 30–60 nm and a length of approximately 260 nm (Burley et al., 1982; Choi et al., 2012). The TMV is approximately 20 nm in diameter and 300 nm in length (Klug, 1999), and the influenza A (H1N1) virus is spherical with a diameter of approximately 100 nm (Tiffany and Blough, 1970; Sai et al., 2011).

TABLE 1 | Dimensions of viruses used in this study.

Virus	Shape	Size
Influenza	Sphere	100 nm
TMV	Rod	20 nm diameter and 300 nm length
Baculo	Rod	30–60 nm diameter and 260 nm length

Quantification of Virus

To date, virus concentrations is generally determined based on the tissue culture infective dose (TCID50) or plaque forming units (PFU) leaving the number of virions is unclear, making it difficult to quantify the sensitivity of the sensing and to compare the results with those of other methods. To prevent this problem, we first visualized and counted the number of virions by fluorescence labeling and observation, then expressed the concentration in terms of virions per unit volume. 1 mM KCl buffer was used, and a fluorescent dye (SYBR-GOLD, Invitrogen Inc.) was added to solution for labeling the viruses. The labeled virions were counted under a fluorescence microscope. **Figure 1** shows a typical result, with each bright spot representing a single baculovirion. The virion concentrations were estimated from the bright spot counts using image analysis software (Image J) (Schneider et al., 2012).

Device Fabrication

Figures 2A,B show top and cross-sectional schematic views of the measurement device. The device is basically fabricated on a quartz substrate patterned with two nanogap electrodes, a polydimethylsiloxane (PDMS) sheet forming the measurement chamber wall, and a glass plate as the chamber lid. The nanogap electrodes were patterned with an Au (250 nm)/Ti (1 nm) layer in strip fabricated by photolithographic lift-off, and the strip was then cut to form opposing electrodes with an intervening nanogap using a focused ion beam (FIB; FB-2200, Hitachi High-Technologies Corp.) (Hatsuki et al., 2013). **Figure 2C** shows a scanning ion micrograph of the fabricated measurement region. The small grooves in the quartz substrate between and on both sides of the nanogap are overrun regions for cutting the parallel flat-plate electrodes in the FIB process. The fabricated gold/metal electrodes were 250 nm in height and 5 μm in width, with an intervening gap width of 510 nm. The depth of the groove was about 530 nm in the middle of the nanogap. A hole with a diameter of 3 mm was opened in the 0.2-mm-thick PDMS sheet to form the wall of the cell chamber (approximately 1.5 μL volume) and the sheet was then bonded in position to form the measurement cell. For the impedance measurements, the chamber was filled with the sample solution and closed with the glass lid.

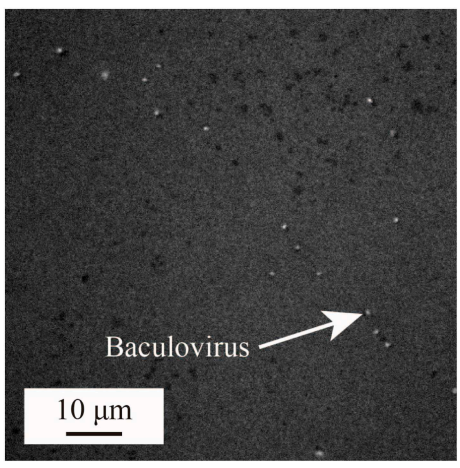

FIGURE 1 | Scanning electron microscopy of baculovirus used for counting the number of virions.

Impedance Measurements

The impedance was measured using a frequency response analyzer (1260, Solartron Analytical) with a dielectric interface (1296, Solartron Analytical), which were controlled with SMART software (Solartron Analytical), and the data were analyzed using Zview software (Solartron Analytical).

The electrical impedance of liquid samples suffer from several problems, including unavoidable electrode decomposition and substantial changes in the conductivity due to the release of ions, and damages to the virus with these ions in high concentrations. These problems were apparently appeared in low frequency region less than 100 kHz in our preliminary measurements, so that the measurements were conducted in the range 100 kHz–6.3 MHz. Prior to each measurement, open/short calibration was performed, and the effects of parasitic capacitance and other parasitic components, wiring induction coupling, and leakage were eliminated. The applied frequency for all of the measurements was 100 kHz or higher, to prevent background effects from the solid-liquid double layer capacitance that tends to form at the interface of the measuring electrode (Poenar et al., 2004); this layer is large at low frequencies but minimal at high frequencies. The virion impedance component was obtained by subtracting the separately measured impedance component for the 1 mM KCl buffer solution from the total solution impedance; corrected measurements were used in all assessments. Because the repeated measurement of the same sample shows no apparent difference in electrical signal, it is assumed that the application of high electric field of 10^5 V/m or more would not be significantly damaging to the virus. It is, however, not confirmed whether the effect of high electric field is how much hazardous to the viruses in their biological activities.

Results and Discussion

Impedance Dependence on Electric Field Strength

We first investigated the presence of a nonlinear impedance effect in a strong electric field by measuring the impedance while increasing the electric field strength incrementally from 10^4 V/m to 2×10^5 V/m, using a baculovirus solution with 10^{14} virions/mL.

As shown in **Figure 3**, at frequencies above 1 MHz, the impedance response is very different for an electric field of 100 kV/m (50 mV) or greater than for an electric field of 20 kV/m (10 mV) or less. This is presumably at least partially attributable to the desired effect of the strong nonlinear electric field and the related dielectrophoretic force that generally arises in strong high-frequency electric fields. Many studies have shown that

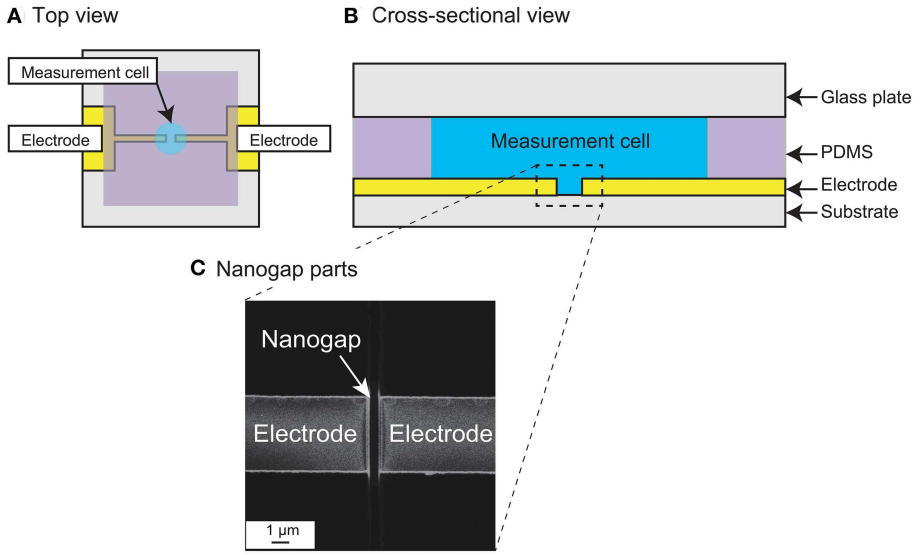

FIGURE 2 | (A) Schematic top view and **(B)** Cross-sectional view of the measurement device with nanogap electrodes. **(C)** Scanning ion microscopy image of the measurement region, showing the nanogap electrodes. The gap width is 510 nm.

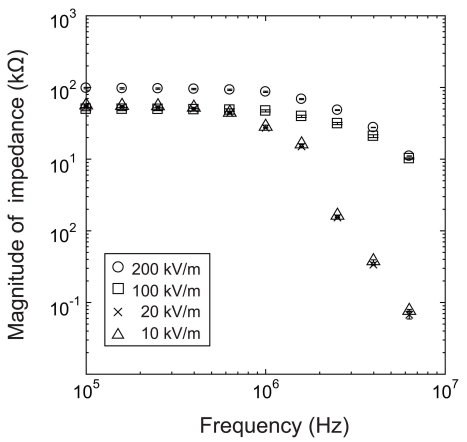

FIGURE 3 | Dependence of impedance response on electric field strength.

positive dielectrophoresis (in which the force is exerted toward higher field strength) occurs in electric fields of several 100 kV/m to several MV/m with frequencies of several 100 kHz or higher (Morgan and Green, 1997; Morgan et al., 1999; Hughes et al., 2001; Park et al., 2007). This suggests that the virions between the electrodes were moved by this force and aligned their long axes with the field direction due to the torque by the electric field. In some cases, the virions adhered to the electrode edges, where the field strength was maximum in the measurement area, resulting in a nonlinear increase in impedance. However, it was not possible to confirm this mechanism because the excitation light required for fluorescence measurements during the impedance measurements would have introduced noise into the system. At present, therefore, this explanation remains speculation.

In summary, the measurements showed changes in impedance that are presumably a nonlinear effect of an applied electric field of 100 kV/m or higher at a frequency above 1 MHz. In light of these results, we used a field strength of 200 kV/m (100 mV) in the subsequent experiments.

The electric field was designed by the finite element method using the commercially available solver COMSOL 4.4 (COMSOL Inc.). Based on simulation, the region between the electrodes for an electric field of 100 kV/m or higher was obtained with a gap length of 510 nm, an electrode width of 5 μm, and a depth of groove approximately 530 nm, corresponding to a volume of about 1.4 fL. This is a rough estimate due to the errors inherent in the measurements; regardless, for a sample concentration of 10^{11} virions/mL, this volume would contain approximately 0.3 virions. Under the assumption that the number of virions measured with a sample concentration of 10^{11} virions/mL would actually be one to several, we set 10^{11} virions/mL concentration as the lower limit for subsequent experiments.

Impedance Dependence on Virus Concentration

Our investigation of the impedance dependence on virus concentration showed that the impedance varies with virus concentration in the range 10^{11}–10^{14} virions/mL for baculovirus, TMV, and influenza virus, as shown in **Figure 4**. In the figure, the solid and dotted lines represent the real and imaginary impedance components, respectively. For the real component, similar behavior is found for the baculovirus and influenza viruses, as shown in **Figure 4A** and **Figure 4C**, respectively. The values decrease moderately with increasing frequency between 100 kHz and 1 MHz, then fall sharply at higher frequency, and also generally increase with increasing sample concentration. In contrast, the imaginary component for both

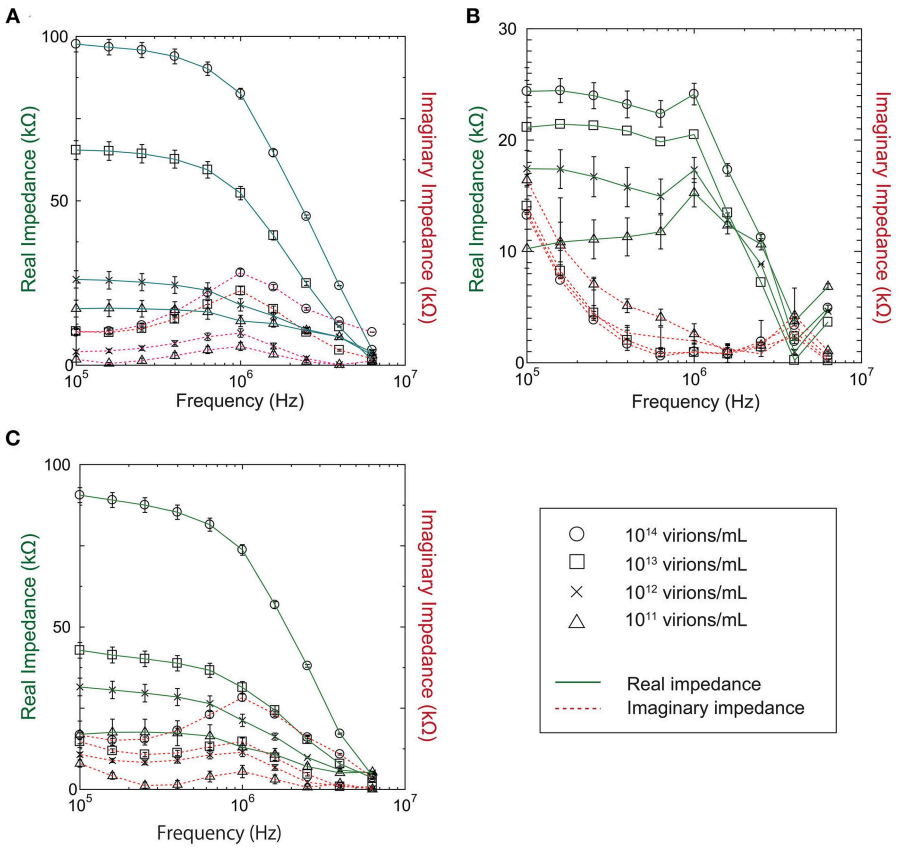

FIGURE 4 | Real and imaginary components of measured impedance for (A) Baculovirus, (B) TMV, and (C) Influenza virus.

viruses shows a peak near 1 MHz that increases in height with increasing sample concentration. As shown in **Figure 4C**, however, the trends exhibited by TMV clearly differ from those for the baculovirus and influenza viruses. The real impedance component for TMV peaks at 1 MHz, then decreases rapidly at higher frequency. The values generally increase with increasing sample concentration as with the other two viruses, whereas the imaginary impedance component for TMV tends to decrease up to a frequency of 1 MHz, and then increase to a maximum near 3.9 MHz.

As shown in **Figure 4**, all three viruses showed an impedance peak and transition point near 1 MHz for both the real component and imaginary components. In **Figure 5**, the vertical and horizontal axes represent the magnitude of the impedance and the virus concentration, respectively. The figure shows the dependence of the impedance magnitude at 1 MHz on the virus concentration for each virus. These results clearly indicate that the impedance values for the three virus types tend to increase with increasing concentration and can therefore be used to quantify the virus concentration.

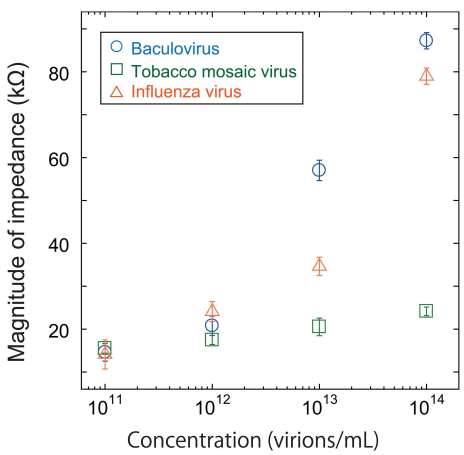

FIGURE 5 | Magnitude of impedance for baculovirus, TMV, and influenza virus solution at 1 MHz. The concentration was varied from 10^{11} to 10^{14} virions/mL.

Distinguish Virus Types

It would be difficult to distinguish quantitatively between the three virus types using only the impedance spectra shown in **Figure 4**. The baculovirus and influenza virus spectra are similar, although they are both distinct from that of TMV.

We therefore compared the three virus types, and particularly the baculovirus and influenza virus, for differences in phase

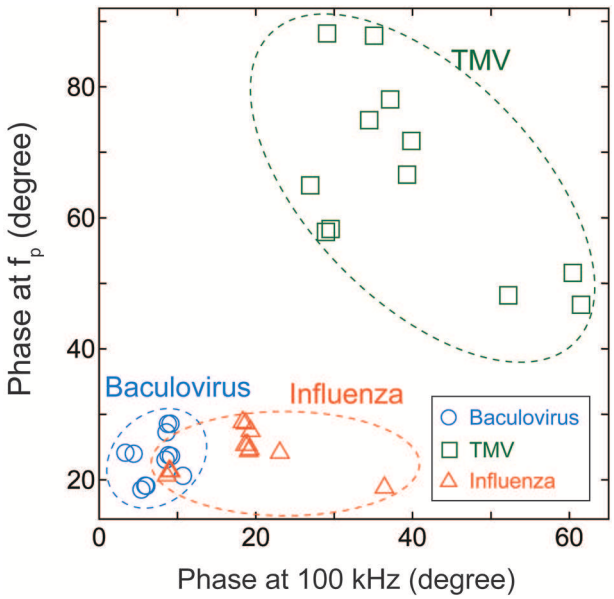

FIGURE 6 | Cluster map of Baculovirus, TMV, and influenza virus. The data were obtained for virus concentrations of 10^{11}–10^{14} virions/mL, and plotted with the phase at 100 kHz along the horizontal axis and the phase at the peak frequency of the imaginary component of impedance along the vertical axis.

effects. **Figure 6** shows the mapped the data obtained for each virus at concentrations of 10^{11}–10^{14} virions/mL. The horizontal and vertical axes represent the phases of the imaginary impedance component somewhat arbitrarily at 100 kHz and the peak frequency, f_p, respectively. Although some overlap is apparent between the three clusters of data points, the graph clearly shows that it is possible to distinguish between virus types on this basis, independent of their concentrations.

It should be noted, however, that this investigation was performed for only these three viruses, and it would be premature to extrapolate the results to other virus types.

Conclusions

Here we proposed a virus detection method by nonlinear impedance spectroscopy under a strong electric field between two nanogap electrodes.

In sweeping frequencies from 100 Hz to 6.3 MHz while varying the electric field strength, we found an apparently marked nonlinear effect on impedance at electric field strengths of 100 kV/m or higher. Further measurements were performed for those electric field strengths and frequency while varying the concentrations of baculovirus, TMV, and influenza A (H1N1) virus solutions. The data clearly showed that the virus concentration can be quantified by the impedance value. Furthermore, the three virus types could be distinguished by plotting the phase at 100 kHz against the phase of the peak value of the imaginary component of the impedance for each virus type.

At the minimum sample concentration of 10^{11} virions/mL used in this study, one to several virions occupied the effective measurement space. This is a rough estimate, and a more detailed study is required for verification. The results nevertheless show that the proposed nonlinear impedance spectroscopy method may achieve a sensitivity comparable to that of PCR and immunodetection systems. The response time to sweep the frequency for each measurement was about a few minutes, which will be enough fast for the continuous monitoring of environment. One of the large remaining issues is to evaluate the detection and identification ability of some specific viruses from the heterogeneous mixture of crude sample. That is the universal challenge for any types of biosensing methods, and also the future work to put this method into practical use.

Acknowledgments

This work was conducted as part of the Four-University Nano-Micro Fabrication Kawasaki Consortium (Fab-4U) and was supported by Kakenhi Grants-in-Aid (No, 25006605, 25289096) from the Japan Society for the Promotion of Science (JSPS), and partly by CREST, JST.

References

Akin, D., Li, H., and Bashir, R. (2004). Real-time virus trapping and fluorescent imaging in microfluidic devices. *Nano Lett.* 4, 257–259. doi: 10.1021/nl034987p

Burley, S. K., Miller, A., Harrap, K. A., and Kelly, D. C. (1982). Structure of the baculovirus nucleocapsid. *Virology* 120, 433–440. doi: 10.1016/0042-6822(82)90043-5

Cella, L. N., Blackstock, D., Yates, M. A., Mulchandani, A., and Chen, W. (2013). Detection of RNA viruses: current technologies and future perspectives. *Crit. Rev. Eukaryot. Gene Expr.* 23, 125–137. doi: 10.1615/CritRevEukaryotGeneExpr.2013006974

Charlton, B., Crossley, B., and Hietala, S. (2009). Conventional and future diagnostics for avian influenza. *Comp. Immunol. Microbiol. Infect. Dis.* 32, 341–350. doi: 10.1016/j.cimid.2008.01.009

Cheng, X., Chen, G., and Rodriguez, W. R. (2009). Micro- and nanotechnology for viral detection. *Anal. Bioanal. Chem.* 393, 487–501. doi: 10.1007/s00216-008-2514-x

Choi, J. Y., Roh, J. Y., Wang, Y., Zhen, Z., Tao, X. Y., Lee, J. H., et al. (2012). Analysis of genes expression of *Spodoptera exigua* larvae upon AcMNPV infection. *PLoS ONE* 7:e42462. doi: 10.1371/journal.pone.0042462

Ermolina, I., Morgan, H., Green, N. G., Milner, J. J., and Feldman, Y. (2003). Dielectric spectroscopy of tobacco mosaic virus. *Biochim. Biophys. Acta* 1622, 57–63. doi: 10.1016/S0304-4165(03)00118-1

Espy, M. J., Uhl, J. R., Sloan, L. M., Buckwalter, S. P., Jones, M. F., Vetter, E. A., et al. (2006). Real-time PCR in clinical microbiology: applications for routine laboratory testing. *Clin. Microbiol. Rev.* 19, 165–256. doi: 10.1128/CMR.19.1.165-256.2006

Fan, X., White, I. M., Shopova, S. I., Zhu, H., Suter, J. D., and Sun, Y. (2008). Sensitive optical biosensors for unlabeled targets: a review. *Anal. Chim. Acta.* 6, 8–26. doi: 10.1016/j.aca.2008.05.022

Hassen, W. M., Duplan, V., Frost, E., and Dubowski, J. J. (2011). Quantitation of influenza A virus in the presence of extraneous protein using electrochemical impedance spectroscopy. *Electrochim. Acta* 56, 8325–8328. doi: 10.1016/j.electacta.2011.07.009

Hatsuki, R., Fuchigami, Y., and Yamamoto, T. (2013). Direct measurement of electric double layer in a nanochannel by electrical impedance spectroscopy. *Microfluid. Nanofluid.* 14, 983–988. doi: 10.1007/s10404-012-1105-5

Heinze, B. C., Song, J. Y., Lee, C. H., Najam, A., and Yoon, J. Y. (2009). Microfluidic immunosensor for rapid and sensitive detection of bovine viral diarrhea virus. *Sens. Actuators B Chem.* 138, 491–496. doi: 10.1016/j.snb.2009.02.058

Hodneland, K., García, R., Balbuena, J. A., Zarza, C., and Fouz, B. (2011). Real-time RT-PCR detection of betanodavirus in naturally and experimentally infected fish from Spain. *J. Fish Dis.* 34, 189–202. doi: 10.1111/j.1365-2761.2010.01227.x

Hughes, M. P., Morgan, H., and Rixon, F. J. (2001). Dielectrophoretic manipulation and characterization of herpes simplex virus-1 capsids. *Eur. Biophys. J.* 30, 268–272. doi: 10.1007/s002490100144

Klug, A. (1999). The tobacco mosaic virus particle: structure and assembly. *Philos. Trans. R. Soc. Lond. B Biol. Sci.* 354, 531–535. doi: 10.1098/rstb.1999.0404

Lee, B. W., Bey, R. F., Baarsch, M. J., and Simonson, R. R. (1993). ELISA method for detection of influenza A infection in swine. *J. Vet. Diagn. Invest.* 5, 510–515. doi: 10.1177/104063879300500402

Lee, Y. F., Lien, K. Y., Lei, H. Y., and Lee, G. B. (2009). An integrated microfluidic system for rapid diagnosis of dengue virus infection. *Biosens. Bioelectron.* 25, 745–752. doi: 10.1016/j.bios.2009.08.020

Liu, H., and Bau, H. H. (2004). The dialectrophoresis of cylindrical and spherical particles submerged in shells and in semi-infinite media. *Phys. Fluids* 16, 1217–1228. doi: 10.1063/1.1649237

Lum, J., Wang, R., Lassiter, K., Srinivasan, B., Abi-Ghanem, D., Berghman, L., et al. (2012). Rapid detection of avian influenza H5N1 virus using impedance measurement of immuno-reaction coupled with RBC amplification. *Biosens. Bioelectron.* 38, 67–73. doi: 10.1016/j.bios.2012.04.047

Morgan, H., and Green, N. G. (1997). Dielectrophoretic manipulation of rod-shaped viral particles. *J. Electrostat.* 40, 279–293. doi: 10.1016/S0304-3886(97)00159-9

Morgan, H., Hughes, M. P., and Green, N. G. (1999). Separation of submicron bioparticles by dielectrophoresis. *Biophys. J.* 77, 516–525. doi: 10.1016/S0006-3495(99)76908-0

Nguyen, B. T., Peh, A. E., Chee, C. Y., Fink, K., Chow, V. T., Ng, M. M., et al. (2012). Electrochemical impedance spectroscopy characterization of nanoporous alumina dengue virus biosensor. *Bioelectrochemistry* 88, 15–21. doi: 10.1016/j.bioelechem.2012.04.006

Park, K., Akin, D., and Bashir, R. (2007). Electrical capture and lysis of vaccinia virus particles using silicon nano-scale probe array. *Biomed. Microdevices* 9, 877–883. doi: 10.1007/s10544-007-9101-3

Patolsky, F., Zheng, G., Hayden, O., Lakadamyali, M., Zhuang, X., and Lieber, C. M. (2004). Electrical detection of single viruses. *Proc. Natl. Acad. Sci. U.S.A.* 101, 14017–14022. doi: 10.1073/pnas.0406159101

Pethig, R. (2010). Dielectrophoresis: status of the theory, technology, and applications. *Biomicrofluidics* 4, 022811. doi: 10.1063/1.3456626

Poenar, D. P., Iliescu, C., Boulaire, J., and Yu, H. (2004). Label-free virus identification and characterization using electrochemical impedance spectroscopy. *Electrophoresis* 35, 433–440. doi: 10.1002/elps.201300368

Reichmuth, D. S., Wang, S. K., Barrett, L. M., Throckmorton, D. J., Einfeld, W., and Singh, A. K. (2008). Rapid microchip-based electrophoretic immunoassays for the detection of swine influenza virus. *Lab Chip* 8, 1319–1324. doi: 10.1039/b801396a

Sai, L., Frederic, E., Christian, S., Andreas, H., Iwan, A. T., and Schaap, I. A. (2011). Bending and puncturing the influenza lipid envelope. *Biophys. J.* 100, 637–645. doi: 10.1016/j.bpj.2010.12.3701

Schneider, C. A., Rasband, W. S., and Eliceiri, K. W. (2012). NIH image to image J: 25 years of image analysis. *Nat. Methods* 9, 671–675. doi: 10.1038/nmeth.2089

Tiffany, J. M., and Blough, H. (1970). Models of structure of the envelope of influenza virus. *Proc. Natl. Acad. Sci. U.S.A.* 65, 1105–1012. doi: 10.1073/pnas.65.4.1105

Turcu, I., and Lucaciu, C. M. (1989). Dielectrophoresis: a spherical shell model. *J. Phys. A Math. Gen.* 22, 985–993. doi: 10.1088/0305-4470/22/8/014

Wang, R., Lin, J., Lassiter, K., Srinivasan, B., Lin, L., Lu, H., et al. (2011). Evaluation study of a portable impedance biosensor for detection of avian influenza virus. *J. Virol. Methods* 178, 52–58. doi: 10.1016/j.jviromet.2011.08.011

Wang, R., Wang, Y., Lassiter, K., Li, Y., Hargis, B., Tung, S., et al. (2009). Interdigitated array microelectrode based impedance immunosensor for detection of avian influenza virus H5N1. *Talanta* 79, 159–164. doi: 10.1016/j.talanta.2009.03.017

Yang, L., Banada, P. P., Bhunia, A. K., and Bashir, R. (2008). Effects of dielectrophoresis on growth, viability and immuno-reactivity of listeria monocytogenes. *J. Biol. Eng.* 2:6. doi: 10.1186/1754-1611-2-6

Yang, S., and Rothman, R. E. (2004). PCR-based diagnostics for infectious diseases: uses, limitations, and future applications in acute-care settings. *Lancet Infect. Dis.* 4, 337–348. doi: 10.1016/S1473-3099(04)01044-8

Conflict of Interest Statement: The authors declare that the research was conducted in the absence of any commercial or financial relationships that could be construed as a potential conflict of interest.

Copyright © 2015 Hatsuki, Honda, Kajitani and Yamamoto. This is an open-access article distributed under the terms of the Creative Commons Attribution License (CC BY). The use, distribution or reproduction in other forums is permitted, provided the original author(s) or licensor are credited and that the original publication in this journal is cited, in accordance with accepted academic practice. No use, distribution or reproduction is permitted which does not comply with these terms.

frontiers in Microbiology

ORIGINAL RESEARCH
published: 20 April 2016
doi: 10.3389/fmicb.2016.00509

Development of Monoclonal Antibody and Diagnostic Test for Middle East Respiratory Syndrome Coronavirus Using Cell-Free Synthesized Nucleocapsid Antigen

*Yutaro Yamaoka[1,2], Shutoku Matsuyama[3], Shuetsu Fukushi[4], Satoko Matsunaga[1], Yuki Matsushima[1,5], Hiroyuki Kuroyama[2], Hirokazu Kimura[6], Makoto Takeda[3], Tomoyuki Chimuro[2] and Akihide Ryo[1]**

[1] Department of Microbiology, School of Medicine, Yokohama City University, Yokohama, Japan, [2] Isehara Research Laboratory, Technology and Development Division, Kanto Chemical Co., Inc., Isehara, Japan, [3] Department of Virology III, National Institute of Infectious Diseases, Musashimurayama, Japan, [4] Department of Virology I, National Institute of Infectious Diseases, Musashimurayama, Japan, [5] Division of Virology, Kawasaki City Institute for Public Health, Kawasaki, Japan, [6] Infectious Disease Surveillance Center, National Institute of Infectious Diseases, Musashimurayama, Japan

OPEN ACCESS

Edited by:
Akio Adachi, Tokushima University Graduate School, Japan

Reviewed by:
Tianlei Ying, Fudan University, China
Masatsugu Obuchi, Toyama Institute of Health, Japan
Kazuya Kabayama, Osaka University, Japan

***Correspondence:**
Akihide Ryo
aryo@yokohama-cu.ac.jp

Specialty section:
This article was submitted to Virology, a section of the journal Frontiers in Microbiology

Received: *09 February 2016*
Accepted: *29 March 2016*
Published: *20 April 2016*

Citation:
Yamaoka Y, Matsuyama S, Fukushi S, Matsunaga S, Matsushima Y, Kuroyama H, Kimura H, Takeda M, Chimuro T and Ryo A (2016) Development of Monoclonal Antibody and Diagnostic Test for Middle East Respiratory Syndrome Coronavirus Using Cell-Free Synthesized Nucleocapsid Antigen. Front. Microbiol. 7:509. doi: 10.3389/fmicb.2016.00509

Protein nativity is one of the most critical factors for the quality of antigens used as immunogens and the reactivities of the resultant antibodies. The preparation and purification of native viral antigens in conventional cell-based protein expression systems are often accompanied by technical hardships. These challenges are attributable mainly to protein aggregation and insolubility during expression and purification, as well as to very low expression levels associated with the toxicity of some viral proteins. Here, we describe a novel approach for the production of monoclonal antibodies (mAbs) against nucleocapsid protein (NP) of the Middle East respiratory syndrome coronavirus (MERS-CoV). Using a wheat germ cell-free protein synthesis system, we successfully prepared large amounts of MERS-CoV NP antigen in a state that was highly soluble and intact for immunization. Following mouse immunization and hybridoma generation, we selected seven hybridoma clones that produced mAbs with exclusive reactivity against MERS-CoV NP. Epitope mapping and subsequent bioinformatic analysis revealed that these mAbs recognized epitopes located within relatively highly conserved regions of the MERS-CoV amino-acid sequence. Consistently, the mAbs exhibited no obvious cross-reactivity with NPs derived from other related viruses, including SARS coronavirus. After determining the optimal combinations of these mAbs, we developed an enzyme-linked immunosorbent assay and a rapid immunochromatographic antigen detection test that can be reliably used for laboratory diagnosis of MERS-CoV. Thus, this study provides strong evidence that the wheat germ cell-free system is useful for the production of diagnostic mAbs against emerging pathogens.

Keywords: MERS-coronavirus, nucleocapsid, antigen, detection, diagnosis, monoclonal antibody, cell-free protein synthesis

INTRODUCTION

Middle East respiratory syndrome coronavirus (MERS-CoV), a novel human coronavirus, was first isolated in 2012 in the Arabian Peninsula (Zaki et al., 2012). MERS-CoV is a positive-sense, enveloped, single-stranded RNA virus of genus *Betacoronavirus* within subfamily *Coronavirinae* (de Groot et al., 2013). MERS-CoV infection often causes fever, cough, and severe pneumonia, occasionally accompanied by renal disease (Banik et al., 2015). More than 1600 laboratory-confirmed cases with high fatality rates (∼36% mortality) have been reported (World Health Organization [WHO], 2016). Because there is currently no specific antiviral drug or vaccine approved for clinical use against MERS-CoV, rapid diagnostic tests are urgently required to manage and control this virus. Indeed, rapid and specific diagnosis is essential for preventing the spread of any kind of infectious disease.

At present, laboratory testing for MERS-CoV is performed by quantitative reverse transcription-PCR assay (qRT-PCR) and RT-loop-mediated isothermal amplification (RT-LAMP) (Corman et al., 2012a,b; Shirato et al., 2014). These tests can detect nucleic acids derived from MERS-CoV in clinical respiratory, serum, and stool specimens. These nucleic acid-based tests require molecular techniques and specialized equipment, and are thus not suitable for point-of-care testing (POCT) or bedside diagnosis. Therefore, it is necessary to develop alternative methods that can be adapted to rapid and reliable clinical detection of MERS-CoV antigen, including enzyme-linked immunosorbent assay (ELISA) and immunochromatographic test (ICT).

Middle East respiratory syndrome coronavirus comprises four structural proteins: spike (S), envelope (E), membrane (M), and nucleocapsid (N) (van Boheemen et al., 2012). S protein is a major component of the viral surface that binds dipeptidyl peptidase 4 (DPP4), enabling the virus to enter and infect cells (Raj et al., 2013). Therefore, S protein is considered to be a prospective therapeutic and diagnostic target (Song et al., 2013; Jiang et al., 2014; Zhang et al., 2014; Li et al., 2015). However, because neutralizing antibodies mainly target this antigen, coronaviruses express several mutant forms of S protein in order to escape the immune response and achieve viral persistence (Tang et al., 2014). On the other hand, amino-acid mutations in N protein are much less common (Wernery et al., 2015). N protein is produced at high levels within infected cells, and is thus a promising candidate target for clinical diagnosis (Lau et al., 2004; He et al., 2005; Kogaki et al., 2005; Liang et al., 2013; Chen et al., 2015).

N protein functions in packaging the viral genomic RNA to form the helical nucleocapsid, as well as in viral transcription and assembly (McBride et al., 2014). It has three distinct and conserved domains: the N-terminal domain (NTD), linker region (LKR), and C-terminal domain (CTD) (McBride et al., 2014). The NTD of human coronavirus N protein contains highly conserved motifs (Yu et al., 2005; Chang et al., 2014). To prevent cross-reactivity with other human coronaviruses and specifically detect MERS-CoV, it is necessary to develop antibodies that target non-conserved regions. However, the viral structural protein is generally unstable and insoluble in its monomeric or oligomeric forms, making it difficult to prepare antigen for immunization. Moreover, refolding of solubilized viral proteins by denaturing agents often results in misfolding and functional loss (Schein, 1991). To overcome these problems, we recently developed a cell-free based viral protein production system using wheat germ extract (Matsunaga et al., 2014). Because wheat is a eukaryote, this system can synthesize properly folded and biologically active viral proteins equivalent to those expressed in mammalian cells (Endo and Sawasaki, 2005, 2006; Goshima et al., 2008).

In this study, we synthesized recombinant MERS-CoV N protein (MERS-NP) and raised monoclonal antibodies (mAbs) that could specifically detect this protein. We also describe the development and evaluation of a rapid test format including ELISA and ICT that can be used in POCT for MERS-CoV infection.

MATERIALS AND METHODS

Expression Plasmid

Complementary DNAs encoding nucleocapsid proteins (NPs) of human coronaviruses (MERS-CoV, GenBank No. NC_019843; SARS-CoV, GenBank No. NC_004718; HCoV-HKU1, GenBank No. NC_006577; HCoV-OC43, GenBank No. NC_005147; HCoV-229E, GenBank No. NC_002645; HCoV-NL63, GenBank No. NC_005831) were synthesized by GENEWIZ (South Plainfield, NJ, USA). Synthetic cDNAs were digested with *Xho*I and *Kpn*I and inserted into pEU-E01-His-TEV-MCS and pcDNA3-HA-MCS. To generate the expression vector for antigen production in the wheat germ cell-free system, the MERS-NP open reading frame encoding amino acids 122–413 was amplified by PCR using the forward primer 5′-GAGAGATATCTGGGTGCATGAGGACGGAG-3′ and the reverse primer 5′-GAGAGATATCTCAGTCTGTG TTCACATCG-3′. The amplified fragment was cloned into the *Eco*RV site of vector pEU-E01-His-TEV-MCS (CellFree Sciences, Yokohama, Japan). Deletion mutants of MERS-NP for epitope mapping were generated using the PrimeSTAR Mutagenesis Basal kit (Takara Bio, Otsu, Japan). The R395H mutation was introduced into MERS-NP using the PrimeSTAR Mutagenesis Basal kit (Takara Bio, Otsu, Japan).

Cell-free Protein Synthesis and Purification

In vitro transcription and cell-free protein synthesis were performed as previously described (Takai and Endo, 2010; Takai et al., 2010; Senchi et al., 2013; Matsunaga et al., 2014, 2015). For cell-free protein synthesis, WEPRO7240H wheat germ extract (CellFree Sciences, Yokohama, Japan) was used in the bilayer translation method as previously described (Matsunaga et al., 2014). Synthesized proteins were confirmed by immunoblotting.

His-MERS-NP (122-413) protein, used for mouse immunization, was synthesized using a Protemist XE robotic protein synthesizer (CellFree Sciences, Yokohama, Japan). The cell-free translation reaction mixture (6 ml) was separated into soluble and insoluble fractions by centrifugation at 15,000 rpm for 15 min. The soluble fraction was mixed with Ni-Sepharose High Performance beads (GE Healthcare, Waukesha, WI, USA)

in the presence of 20 mM imidazole. The beads were washed three times with washing buffer [20 mM Tris-HCl (pH 7.5), 500 mM NaCl] containing 40 mM imidazole. His-MERS-NP (122–413) was then eluted in washing buffer containing 500 mM imidazole. Amicon Ultra centrifugal filters (Millipore, Bedford, MA, USA) were used to concentrate purified His-MERS-NP (122–413) by approximately 10–20-fold. Protein concentration was determined using the Bradford method, with bovine serum albumin (BSA) as a protein standard.

Immunization and Generation of Hybridomas

Immunization of BALB/c mice and generation of hybridomas producing anti-MERS-NP antibody were carried out as previously described (Kimura et al., 1994, 1996; Matsunaga et al., 2014). Primary antibodies in hybridoma culture supernatant were tested by immunoblot analysis with non-tagged recombinant N protein. Animal experiments were performed ethically according to the Guidelines for Animal Experiments at Yokohama City University. All of the procedures were approved by the Committee on Experimental Animals at the Yokohama City University.

Purification of mAbs

Hybridoma cells were grown in CD hybridoma medium AGT medium (Thermo Fisher Scientific, Rockford, IL, USA). Primary antibodies in the culture supernatant of each clone were separated by centrifugation at 8,000 rpm for 15 min and eluted with AcroSep Hyper DF columns (Pall, New York, NY, USA). Samples were then further concentrated 10–20-fold using Amicon Ultra centrifugal filters (Millipore, Bedford, MA, USA). Concentrations of purified IgG were determined by measuring the absorbance at OD_{280}. Immunoglobulin characterization was carried out using the IsoStrip mouse monoclonal antibody isotyping kit (Roche Diagnostics, Basel, Switzerland).

Homology Modeling of MERS-NP and Epitope Localization Analysis

The dimer model of MERS-NP was constructed by homology modeling based on the partial structure of SARS-NP (PDB code. 1SSK, Huang et al., 2004; PDB code. 2CJR, Chen et al., 2007) using the MODELLER9.15 software (Webb and Sali, 2014). Protein structures not registered in PDB were estimated by the I-TASSER and QUARK servers and used as templates for homology modeling (Xu and Zhang, 2012; Yang et al., 2015). Energy minimization of the generated model was carried out using Swiss PDB viewer4.1 (Guex and Peitsch, 1997). Surface localization of each epitope was determined using the UCSF Chimera software (Pettersen et al., 2004).

Immunoprecipitation Analysis

Immunoprecipitation was performed as previously described (Miyakawa et al., 2015). Briefly, HEK293A cells were grown on a 100-mm dish for 24 h, and then transfected with HA-MERS-NP. Cell lysates were immunoprecipitated with EZview Red anti-HA Affinity Gel (Sigma–Aldrich) or 2 μg of each anti-MERS-NP antibody mixed with protein G-Sepharose (GE Healthcare, Little Chalfont, UK). Bound proteins were analyzed by immunoblotting.

Selection of the Optimal Pair of mAbs for Sandwich ELISA

Each mAb was diluted in 50 mM of carbonate buffer (pH 9.6) to a concentration of 10 μg/mL, and then added to an ELISA plate (AGC TECHNO GLASS, Shizuoka, Japan). To immobilize the antibodies, the plate was incubated overnight at 4°C. Wells were blocked with PBS containing 2% (w/v) skim milk for 1 h at room temperature (RT). After three washes with PBS containing 0.05% (v/v) Tween-20 (PBS-T), 100 μL of antigen protein (1 ng/mL) diluted with PBS-T or blank (PBS-T alone) was added and incubated for 60 min at RT. After three washes with PBS-T, 100 μL of each mAb conjugated with horseradish peroxidase (HRP) was added into each well and incubated for 60 min at RT. Antibody labeling was performed using the Peroxidase Labeling Kit -NH_2 (Dojindo Laboratories, Kumamoto, Japan). After three washes with PBS-T, 100 μL of ABTS substrate solution (Kirkegaard & Perry Laboratories, Washington, DC, USA) was added and incubated for 30 min at RT. Absorbance at 415/492 nm was measured on a plate reader, and the signal-to-noise ratio (S/N) was calculated.

Selection of the Optimal Antibody Pair for ICT

For the test line, anti-MERS-NP antibodies #20, #29, and #46 were diluted in 50 mM of phosphate buffer (pH 8.0) to a concentration of 1 mg/mL and immobilized on a nitrocellulose membrane (Millipore, Bedford, MA, USA). To prepare the control line, an anti-mouse IgG antibody was diluted to 0.125 mg/mL and immobilized onto another area of the same membrane. The membrane was dried and blocked at RT, washed with deionized water, and lyophilized.

To produce conjugate pads, anti-MERS-NP mAbs #5, #13, and #20 were diluted in 50 mM of phosphate buffer (pH 8.0) to a concentration of 0.05 mg/mL and labeled with colloidal gold (Tanaka Kikinzoku Kogyo, Tokyo, Japan). The colloidal gold-conjugated mAbs were blocked with 0.5% casein (Kanto Chemical, Tokyo, Japan). After washing three times with phosphate buffer (pH 7.0), labeled mAbs were diluted to an OD_{525} 4.4 and impregnated into glass fibers (Millipore, Bedford, MA, USA). The glass fibers were lyophilized.

Immunochromatographic strips were generated by assembling a glass fiber (sample pad), conjugate pad, nitrocellulose membrane, and liquid absorbent pad. To compare each combination of antibodies, antigen proteins were diluted to 12.5 ng/0.1 mL in 40 mM phosphate buffer containing 150 mM NaCl and applied to the strips. The color intensity of red lines at the test and control position and the background of the membrane were visually observed and evaluated after a 15 min reaction.

Bioinformatic Analysis

Homology of NPs among human coronaviruses (MERS-CoV, GenBank No. NC_019843; SARS-CoV, GenBank No. NC_004718; HCoV-HKU1, GenBank No. NC_006577; HCoV-OC43, GenBank No. NC_005147; HCoV-229E, GenBank No. NC_002645; HCoV-NL63, GenBank No. NC_005831) was analyzed by multiple sequence alignment using the MUSCLE software (Edgar, 2004).

To examine amino-acid variability among NPs of each MERS-CoV strain, 113 MERS-NP sequences from the GenBank were aligned using the MUSCLE software. A Shannon entropy score was calculated for each position in the protein alignment as previously described (Yang, 2009). Phylogenetic trees were generated via the maximum-likelihood method with 1000 bootstrap replicates using MEGA5 after removal of 100% identical sequences (Tamura et al., 2011). The dataset was analyzed using the Jones–Taylor–Thornton (JTT) amino-acid substitution model.

Preparation and Quantitation of MERS-CoV

Prototype strain of MERS-CoV were provided by Drs. Ron A. M. Fouchier and Bart L. Haagmans (Erasmus Medical Center). MERS-CoV were propagated in Vero cells expressing TMPRSS2, as described previously (Shirato et al., 2013). Viral samples were concentrated by centrifugation from culture supernatant of MERS-CoV infected cells. MERS-CoV was inactivated by addition of Nonidet P-40 (NP-40) to a final concentration of 1% (v/v) prior to each immunoassay.

Viral RNA was extracted from the samples using the QIAamp viral RNA mini kit (Qiagen, Valencia, CA, USA). Quantitation of viral copy number was carried out by reverse-transcription droplet digital PCR (RT-ddPCR) using One-Step RT-ddPCR Advanced kit for Probes (Bio-Rad, Hercules, CA, USA). A 20 μL reaction was set up containing 2 μL of RNA (equivalent to 20 ng), 2 μL of a mixture of forward/reverse primers and probe, 1 μL of 300 mM DTT, 2 μL of reverse transcriptase, 8 μL of RNase-free water, and 5 μL of Supermix. Primers and probe sets for *Orf1a* were used as previously reported in qRT-PCR assays (Corman et al., 2012b); final concentrations of primers and probe were 900 and 250 nM, respectively. Droplets were formed in a QX200 droplet generator (Bio-Rad, Hercules, CA, USA). Thermal cycling conditions were as follows: 42°C for 60 min for the RT reaction; 95°C for 10 min; 40 cycles of 95°C for 30 s and 56°C for 1 min; and a final 10 min denaturation step at 95°C. After thermal cycling, plates were transferred to the QX200 droplet reader (Bio-Rad, Hercules, CA, USA). Positive droplets containing amplification products were discriminated from negative droplets by applying a fluorescence amplitude threshold in the QuantaSoft software (Bio-Rad, Hercules, CA, USA).

Immunoblot Analysis

Cell-free synthesized proteins or cell culture supernatants containing inactivated MERS-CoV were mixed with an equal volume of 2X SDS sample buffer [125 mM Tris-HCl (pH 6.8), 4% SDS, 20% glycerol, 10% 2-mercaptoethanol and 0.01% bromophenol blue] and heated at 100°C for 5 min. After separation by 12.5% or 15% SDS-PAGE using Hi-QRAS Gel N (Kanto Chemical, Tokyo, Japan), the proteins were electrotransferred onto an Immobilon-P PVDF Transfer Membrane (Millipore, Bedford, MA, USA) as described previously (Nishi et al., 2014). The membrane was blocked in Tris-buffered saline (TBS) containing 2% (w/v) skim milk for 30 min, and then incubated for 1 h with anti-MERS-NP mAbs or anti-His polyclonal antibody (GTX115045; GeneTex, Irvine, CA, USA) in TBS containing 0.1% (v/v) Tween 20 (TBS-T; 1:1000 dilution) and 0.4% (w/v) skim milk. After three washes with TBS-T, the membrane was incubated for 60 min in PBS containing HRP-conjugated goat-anti mouse or rabbit IgG antibody (1:10000 dilution; GE Healthcare). After an additional three washes in TBS-T, proteins were detected with SuperSignal West Dura Extended Duration Substrate (Thermo Fisher Scientific, Rockford, IL, USA) or Immobilon (Millipore, Bedford, MA, USA) on a Lumi-Imager F1 (Roche Diagnostics, Basel, Switzerland).

Detection Limit of Antigen-Capture ELISA

Sensitivity analysis of antigen-capture ELISA was carried out as described above with some modifications. Briefly, mAb (#46) was immobilized onto a plate at a concentration of 2.5 μg/mL. After the plate was blocked, inactivated MERS-CoV (1.2×10^6 copies/0.1 mL) and recombinant antigen protein (1 ng/0.1 mL) were serially twofold diluted with PBS-T and subjected to analysis. After reaction with HRP-conjugated mAb (#20), a chromogenic reaction was conducted by adding 100 μL of TMB Substrate solution (Kirkegaard & Perry Laboratories, Washington, DC, USA) per well, followed by incubation for 5 min; the reaction was halted by the addition of 100 μL of 1 M H_2SO_4. Absorbance at 450/630 nm was measured on a plate reader.

Detection Limit of ICT

Immunochromatographic detection of MERS-CoV was carried out as described above with some modifications in preparation of the conjugate pad. Conjugation of mAb #20 with colloidal gold was performed at a concentration of 0.2 mg/mL. After blocking and washing, conjugated pads impregnated with labeled antibody solution at an OD_{525} of 8.0.

Sensitivity of ICT was evaluated by adding serially twofold diluted inactivated MERS-CoV (1.2×10^7 copies/0.1 mL) and recombinant antigen protein (2 ng/0.1 mL).

RESULTS

Production of mAbs to Target Nucleocapsid Protein of MERS-CoV

Previous studies described antigenic cross-reactivity among the NTDs of N proteins of human coronaviruses, including SARS-CoV (Yu et al., 2005). To minimize the cross-reactivity when

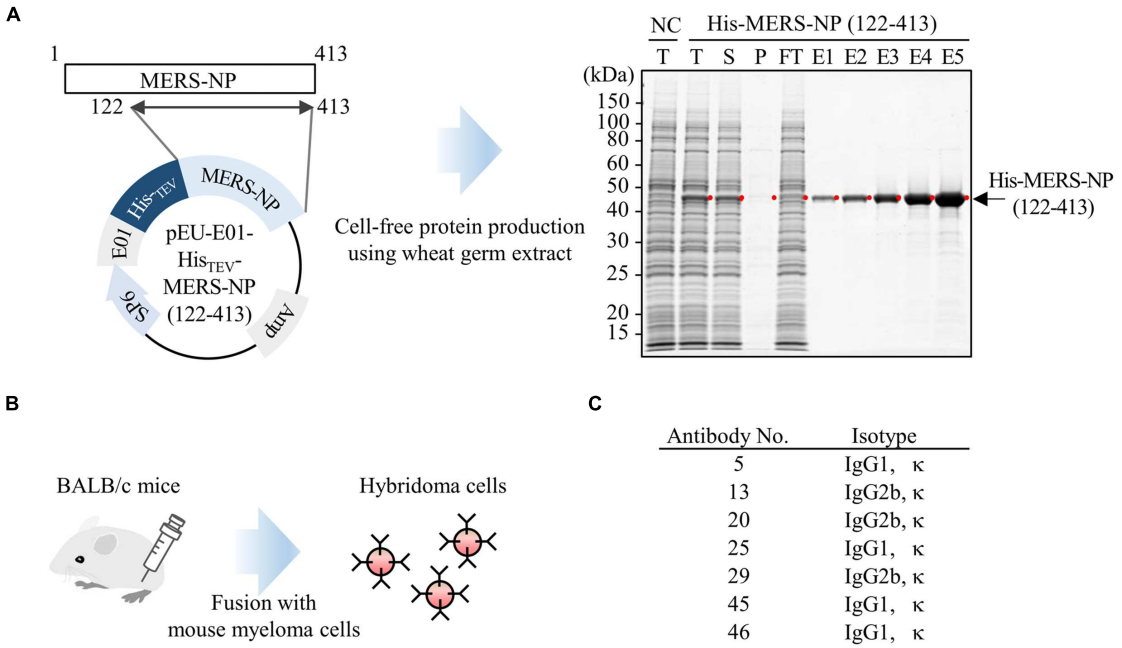

FIGURE 1 | Production of mAb using wheat germ cell-free synthesized nucleocapsid antigen. (A) Schematic representation of antigen protein production. Recombinant Histidine (His)-tagged N-terminally truncated MERS-NP (122–413) was produced in a wheat germ cell-free system, and then purified using nickel-chelated Sepharose beads. Each protein fraction was analyzed by SDS-PAGE and visualized by CBB staining. Red dot and arrow indicate the target protein. NC, negative control; T, total fraction; S, supernatant; P, precipitate; FT, flow-through; E1–5, elution fractions 1–5. **(B)** Schematic diagram of hybridoma cells production generating anti-MERS-NP mAb. Purified His-MERS-NP (122–413) was injected into BALB/c mice. After 4 weeks, immunized mouse splenocytes were fused with myeloma cells, and 48 hybridoma cells were established. Of the 48 clones, seven exhibited relatively high reactivity to antigen proteins, as revealed by immunoblotting analysis, and were selected for further investigation. **(C)** List of selected hybridoma clones producing mAbs.

generating mAbs, we produced N-terminally deleted MERS-NP (amino acids 122–413) as an antigen for antibody production. Complementary DNA encoding MERS-NP (122–413) was subcloned into pEU-His, a vector designed for expression of His-tagged proteins in the wheat germ cell-free system. As predicted, His-tagged MERS-NP (122–413) was expressed (**Figure 1A**). The protein was purified from the soluble fraction of the extracts using Ni-Sepharose beads followed by elution with imidazole.

The purified protein was used to immunize BALB/c mice. After 4 weeks, splenocytes were isolated and hybridomas were generated (**Figure 1B**). Ultimately, 48 stable hybridomas were obtained and designated #1–#48. Among the 48 clones, seven (#5, #13, #20, #25, #29, #45, and #46) were selected for further investigation based on their reactivity to MERS-NP in immunoblot analysis (**Figure 1C**).

Epitope Analysis of Anti-MERS-NP mAb

We next performed epitope mapping to determine the antibody binding sites. Using cell free-synthesized deletion mutants of MERS-NP, we carried out immunoblot analyses with the generated antibodies. In the first screen, we used six deletion mutants (Mut1-6; **Figures 2A,B**); the results revealed that two mAbs (#13 and #46) recognized the middle region corresponding to LKR, whereas the remaining five mAbs (#5, #20, #25, #29, and #45) bound the C-terminal end of the protein (**Figures 2A,B**). More precise epitope mapping was performed using five additional deletion mutants (Mut7-11; **Figures 2A,B**); the results are summarized in **Figure 2C**.

We next investigated whether the antigenic epitopes were located on the surface of MERS-NP. To this end, we used a previously reported solution structure of SARS-NP (PDB ID; 1SSK, 2CJR) for homology modeling of MERS-NP (Huang et al., 2004; Chen et al., 2007). Molecular modeling of MERS-NP using the UCSF Chimera software revealed that all mAb binding regions were located on the surface of N protein (**Figure 3**).

Immunoprecipitation Assay

Next, because an antibody suitable for immunoprecipitation is likely to be conformation-sensitive, we examined whether our selected antibodies could be used in immunoprecipitation analysis (Mancia et al., 2007; Takeda et al., 2015). Cell lysates from HEK293A cells expressing HA-tagged MERS-NP were subjected to immunoprecipitation analysis with each selected antibody (**Figure 4**). The results revealed that all of the generated mAbs could be used for immunoprecipitation analysis.

Screening for Appropriate Combinations of mAbs for Antigen-Capture ELISA and ICT

We next determined the optimal pair of mAbs for antigen-capture ELISA by evaluating all possible combinations of

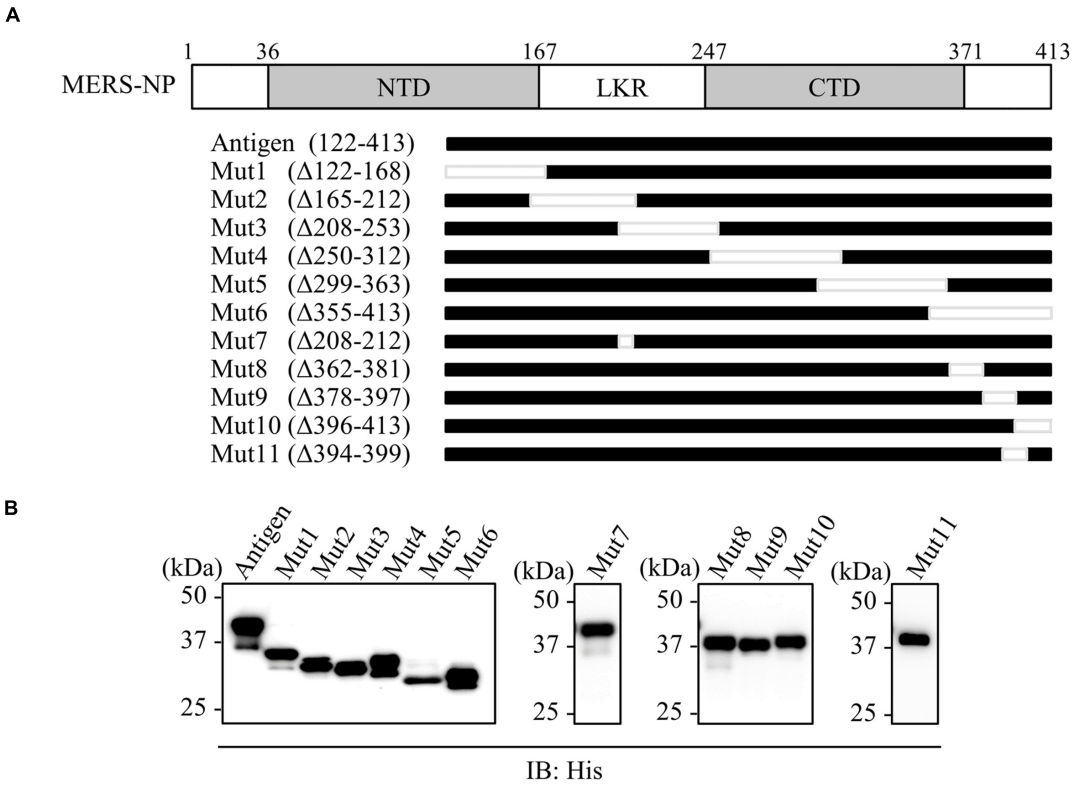

C

Recombinant protein	mAb #5	#13	#20	#25	#29	#45	#46
Mut1	+	+	+	+	+	+	+
Mut2	+	−	+	+	+	+	−
Mut3	+	−	+	+	+	+	−
Mut4	+	+	+	+	+	+	+
Mut5	+	+	+	+	+	+	+
Mut6	−	+	−	−	−	−	+
Mut7	NT	−	NT	NT	NT	NT	−
Mut8	+	NT	+	+	+	+	NT
Mut9	−	NT	−	+	+	−	NT
Mut10	−	NT	−	−	−	+	NT
Mut11	−	NT	−	NT	NT	NT	NT
Determined epitope (amino acid)	394-399	208-212	394-399	396-413	396-413	378-397	208-212

FIGURE 2 | Epitope mapping of mAbs. (A) Schematic diagram of MERS-NP putative domain architecture and deletion mutants. For epitope mapping, 11 deletion mutants were produced as His-tagged proteins in the wheat germ cell-free system. NTD, N-terminal domain; LKR, flexible linker region; CTD, C-terminal domain. **(B)** Confirmation of protein expression. His-tagged NP and deletion mutants were immunoblotted with anti-His-tagged antibody. **(C)** Summary of epitope analysis. Reactivity of each mAb to deletion mutants was evaluated by immunoblotting. + and − indicate positive and negative detection, respectively. NT; not tested. Negative detections are highlighted in gray.

immobilized and labeled mAbs (**Figure 5A**). The combinations of #46/#5, #20/#13, #29/13, #46/#45, and #46/#20 exhibited higher S/N ratios than other pairs (**Figure 5B**). Based on these data, we constructed immunochromatographic strips using five pairs of mAbs (**Figure 6A**). We searched for the combinations yielding the highest color intensity at the positive control at the appropriate position with the lowest overall background on the rest of the membrane. We found that immobilization of mAb #46 and colloidal gold conjugation of #20 was the optimal combination for ICT

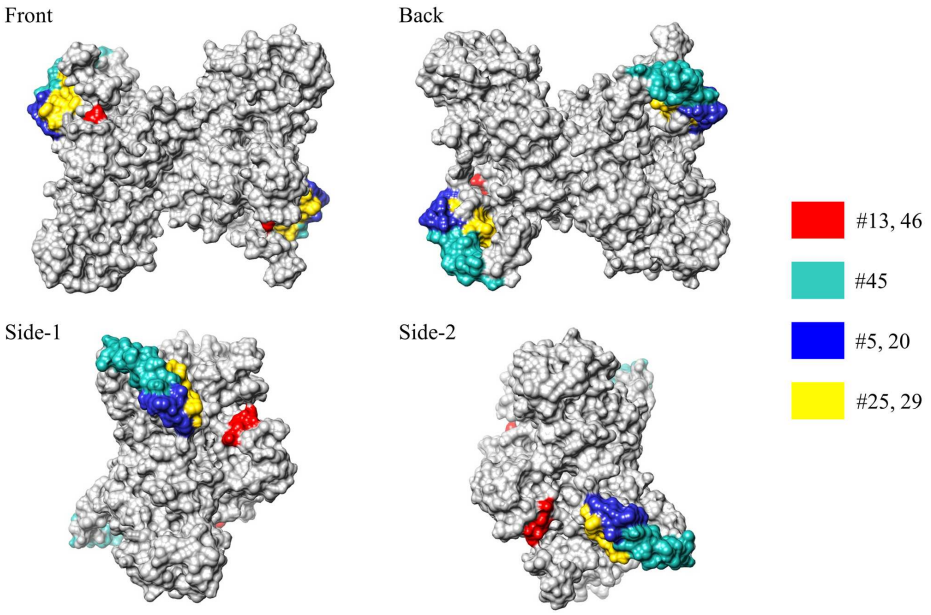

FIGURE 3 | Epitope localization in MERS-CoV-NP structural model. Positions of epitopes in a structural model of dimer-forming MERS-CoV-NP, constructed by homology modeling using the structure of SARS-NP (PDB ID. 1SSK, 2CJR). Epitope localizations of each mAb are highlighted in different colors.

(**Figures 6B,C**). Thus, we selected mAbs #46 and #20 for further investigation.

No Evidence of Cross-Reactivity of Anti-MERS-CoV-NP Antibody to Other Human Coronaviruses

We next investigated the specificity of our newly developed mAbs. Multiple alignment of NPs derived from various human coronaviruses revealed that the amino-acid sequences targeted by the selected antibodies were specific to MERS-CoV (**Figure 7A**). Consistent with these data, immunoblot analysis revealed that our mAbs did not recognize NPs from other coronaviruses (**Figure 7B**).

Reactivity of Antibodies to Divergent Strains of MERS-CoV

To estimate the reactivity of mAbs with different strains of MERS-CoV, we compared the amino-acid sequences of epitopes between 113 isolated strains. Shannon entropy and phylogenetic analysis revealed that the amino-acid sequence of MERS-NP is highly conserved (**Figures 8A,B**). Notably, no obvious amino-acid mutation was observed in the binding region of #46 (**Figures 8A,C**). However, the C-terminal amino acid sequence targeted by #20 was rather variable, containing a specific mutation (R395H) in two strains (**Figures 8A,C**). Therefore, we performed site-directed mutagenesis to introduce the R395H mutation into MERS-NP and examined the effect on the reactivity of #20 antibody by immunoblot analysis. The results showed that mAb #20 could still detect the R395H mutant (**Figure 8D**).

Reactivity of mAbs to Virion Nucleocapsid Protein

We next performed immunoblot analysis with virions released into the cell-culture supernatant of MERS-CoV infected cells. Our mAbs detected a 45 kDa protein band consistent with the molecular mass of the MERS-NP (**Figure 9A**). No other bands were detected by the mAbs, demonstrating their specificity for MERS-NP. Thus, our newly developed antibodies could detect NP antigen derived from MERS-CoV virions as well as recombinant NP.

Sensitivity of Antigen-Capture ELISA

Using the optimal antibody pair (#46 and #20) identified above, we determined the detection threshold for antigen recognition by antigen-capture ELISA. Our results revealed that our system was highly sensitive to recombinant antigen, capable of detecting the protein at a concentration of 0.0625 ng/0.1 mL (**Figure 9B**). In parallel, we investigated the detection limit of ELISA for MERS-CoV virions permeabilized by addition of NP-40. The detection limit of the system was 1.5×10^5 copies/0.1 mL (**Figure 9B**).

Detection Limit of ICT for MERS-CoV

Finally, we evaluated the sensitivity of ICT for MERS-CoV. For this purpose, serial dilutions of purified NPs were subjected to ICT. The results revealed that ICT was highly sensitive, with a detection limit of 0.5 ng/0.1 mL. We next examined the detection limit for virions prepared in phosphate buffer containing 1% NP-40. ICT could detect virions at a concentration of 3.0×10^6 copies/0.1 mL (**Figure 9C**).

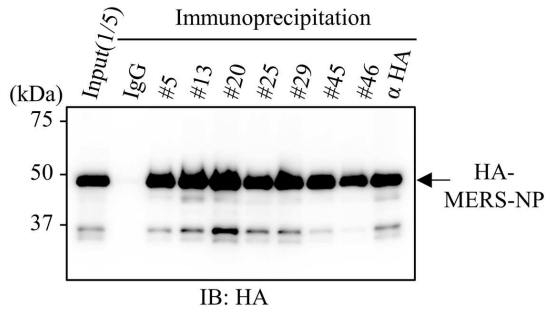

FIGURE 4 | Immunoprecipitation analysis with generated mAbs. Immunoprecipitation analysis. HEK293A cells were transfected with plasmid vector encoding HA-tagged MERS-NP, and cell lysates were collected after 48 h. Samples were subjected to for immunoprecipitation with anti-MERS-NP antibodies followed by immunoblotting analysis with anti-HA antibody.

DISCUSSION

We report the development and prospective evaluation of an ELISA and ICT for the quantitative and qualitative detection of MERS-CoV-NP antigen. Our newly developed assays provide rapid detection of a broad range of NP antigens derived from various isolates of MERS-CoV. Because NP is a principal structural protein that is more abundantly expressed than other MERS-CoV antigens, targeting NP for clinical diagnosis is both reasonable and practical (Chen et al., 2015).

The quality of a mAb is determined mostly by the antigen design, adjuvant selection, and antigen quality (Leenaars and Hendriksen, 2005; Stills, 2005). In particular, preparation of high-quality antigen is essential for creation of a specific mAb. There are several methods for preparing immunizing virus antigen, including synthetic peptide, virus-like particle (VLP), and purified recombinant protein. Synthetic peptides containing predicted immunogenic epitope(s) are the most widely used way to create immunogens derived from virus antigens. However, synthetic peptides are commonly linear and therefore often do not represent the native features of antigens that originate from the actual spatial structures of viral components.

On the other hand, cell-based protein expression systems such as *Escherichia coli* or baculovirus-insect cell systems are also widely used and popular approaches. Although a number of cellular proteins have been successfully generated using a cell-based approach, it is not feasible to use these strategies to generate viral proteins, because many viral antigens including

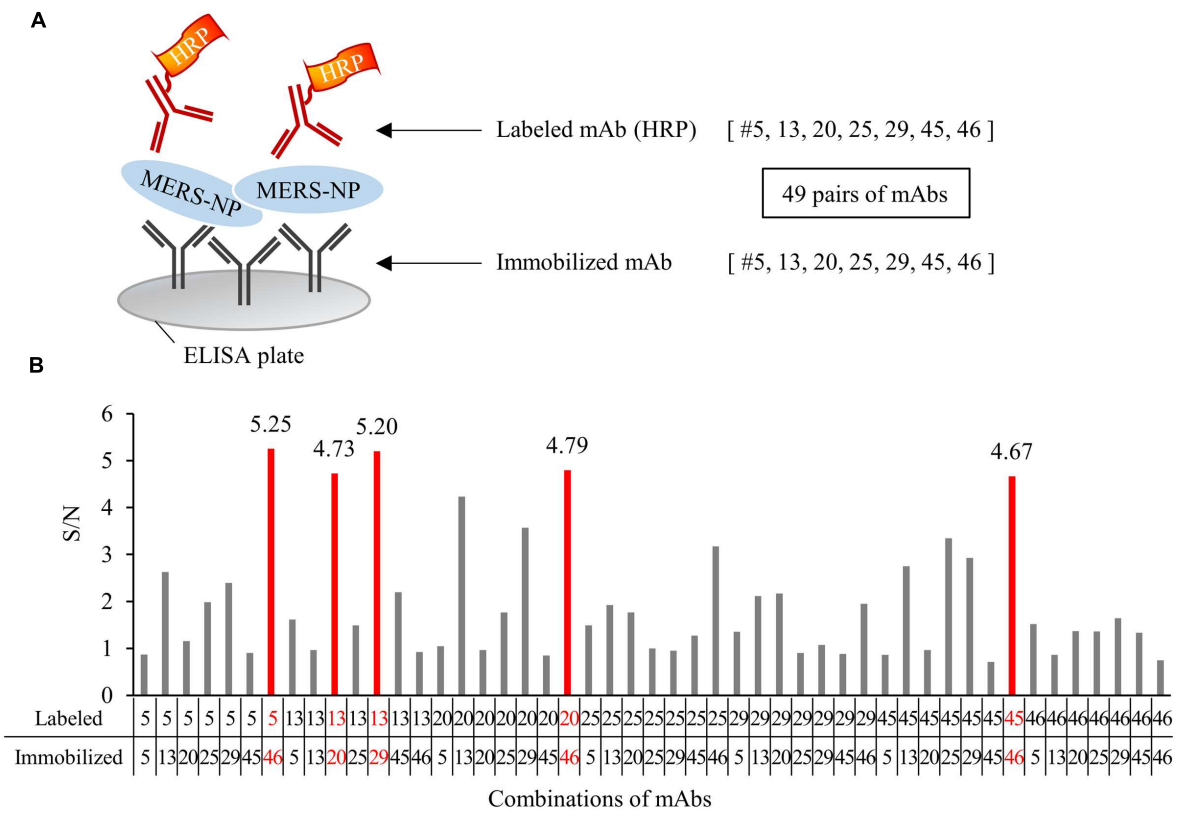

FIGURE 5 | Determination of optimal pairs of mAbs for antigen-capture ELISA. (A) Schematic representation of sandwich ELISA. Each mAb was labeled with horseradish peroxidase (HRP) and subjected to ELISA analysis. 49 pairs of antibodies were tested. **(B)** Determination of the optimal combination of capturing and detection mAbs. S/N ratios for antigen detection by each of the 49 combinations were calculated in the presence of 0.1 ng/0.1 mL antigen V.S. blank. S/N values of selected five pairs were depicted on each bar.

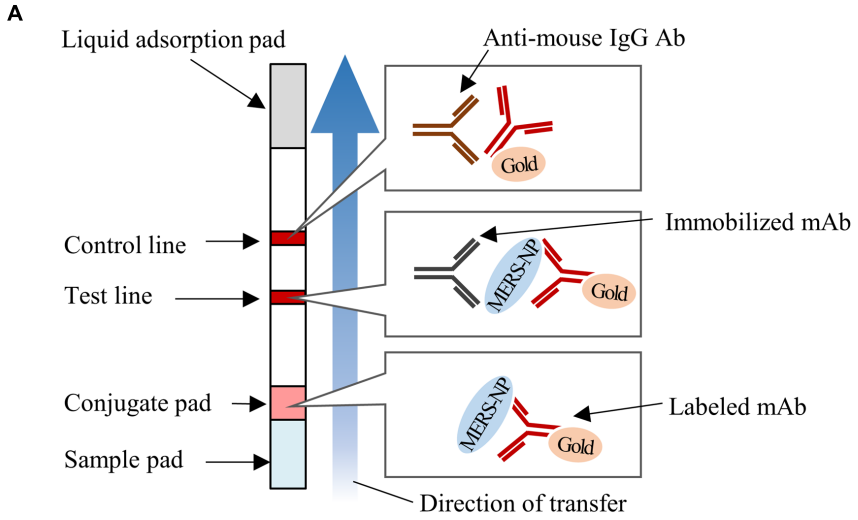

B

Pairs of mAbs		Color intensity	Background
Labeled	Immobilized		
#5	#46	Moderately-high	Low
#13	#20	Low	High
#13	#29	Moderately-high	High
#20	#46	High	Low
#45	#46	Low	Low

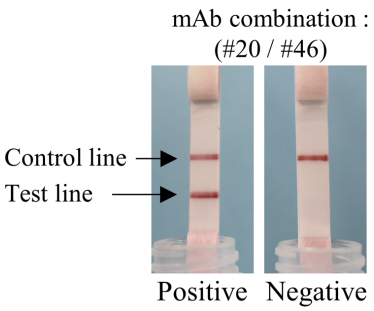

FIGURE 6 | Determination of optimal pairs of mAbs for ICT. (A) Schematic diagram of rapid ICT. **(B)** Selection of appropriate pairs of mAbs for ICT. Color intensity of test line and background level were evaluated with antigen protein at 12.5 ng/0.1 mL. **(C)** Typical positive and negative results of ICT using the optimal antibody pair (#20 and #46).

human coronavirus N proteins are generally insoluble and aggregate in inclusion body fractions (Das and Suresh, 2006). Moreover, viral proteins are often cytotoxic, and expression of these proteins, particularly at high levels, can result in cell death (Cheng et al., 2006). By contrast, the cell-free protein production system permits synthesis of toxic proteins that otherwise cannot be produced in live cells. Wheat germ extract, a commonly used cell-free approach, utilizes a eukaryotic translation system to synthesize properly folded and biologically active proteins similar to those expressed in mammalian cells (Endo and Sawasaki, 2005, 2006; Goshima et al., 2008). These advantages highlight the suitability and availability of the wheat germ cell-free system for the generation of antigenic proteins that can be used to immunize animals and generate mAbs (Matsunaga et al., 2014).

The results of this study clearly demonstrate the advantages of using the wheat germ cell-free system for creating mAbs against MERS-CoV-NP. In general, mAbs can be divided into two groups, conformation-sensitive and -insensitive. Antibodies can be suitable for immunoprecipitation, immunoblotting, or both. A conformation-insensitive (immunoblotting-oriented) mAb can detect denatured linear antigen or peptide immobilized on membrane, whereas a conformation-sensitive (immunoprecipitation-oriented) mAb typically recognizes a native tertiary structure of antigen protein (Mancia et al., 2007; Takeda et al., 2015). In this study, we used the wheat germ system to synthesize MERS-NP antigen as a soluble protein, and consequently we were able to produce antibodies that specifically targeted antigenic epitopes located on the surface of MERS-NP. Accordingly, our newly developed antibodies were suitable for immunoprecipitation, indicating that they are sensitive to protein conformation. Because antibodies binding to protein surface epitopes are suitable for antigen detection assays such as ELISA and ICT, our newly create antibodies can be used in various immunological assays.

Other than MERS-CoV, many types of human coronaviruses are related to respiratory diseases. These include coronaviruses such as HCoV-229E, -OC43, -NL63, and -HKU1, which are responsible for common cold and upper respiratory diseases, as well as SARS-CoV, which causes life-threatening pneumonia. Therefore, it is important to create mAbs with high specificity for MERS-CoV in order to rule out other coronavirus infections. Previous reports indicated that the

A

```
MERS-CoV    --------MASPAAPRAVS---------FADNNDITNTNLSRGRG----RNPKPRAAP-----NNTVSWYTGLTQHGKV- 53
SARS-CoV    -MSDNGPQSNQRSAPR-IT---------FGGPTDSTDNNQNGGRNGARPKQRRPQGLP-----NNTASWFTALTQHGKE- 63
HCoV-HKU1   MSYTPGHYAGSRSSSGNRS--GILKKTSWADQSERNYQTFNRGRK-TQPKFTVSTQPQ--GNTIPHYSWFSGITQFQKGR 75
HCoV-OC43   MSFTPGKQSSSRASSGNRSGNGILK---WADQSDQFRNVQTRGRR-AQPKQTATSQQPSGGNVVPYYSWFSGITQFQKGK 76
HCoV-229E   --------------MATVK---------WADASE--------------PQRGRQGRIP--------YSLYSPLLVDSEQ- 34
HCoV-NL63   --------------MASVN---------WADD----------------RAARKKFPP--------PSFYMPLLVSSDKA 32

MERS-CoV    PLTFPPGQGVPLNANSTPAQNAGYWRRQDRK-INTGNG-IKQLAPRWYFYYTGTGPEAALPFRAVKDGIVWVHEDGATDA 131
SARS-CoV    ELRFPRGQGVPINTNSGPDDQIGYYRRATRR-VRGGDGKMKELSPRWYFYYLGTGPEASLPYGANKEGIVWVATEGALNT 142
HCoV-HKU1   DFKFSDGQGVPIAFGVPPSEAKGYWYRHSRRSFKTADGQQKQLLPRWYFYYLGTGPYANASYGESLEGVFWVANHQADTS 155
HCoV-OC43   EFEFVEGQGVPIAPGVPATEAKGYWYRHNRRSFKTADGNQRQLLPRWYFYYLGTGPHAKDQYGTDIDGVYWVASNQADVN 156
HCoV-229E   PWKVIPRNLVPINKK-DKNKLIGYWNVQKR--FRTRKGKRVDLSPKLHFYYLGTGPHKDAKFRERVEGVVWVAVDGAKTE 111
HCoV-NL63   PYRVIPRNLVPIGKG-NKDEQIGYWNVQER--WRMRRGQRVDLPPKVHFYYLGTGPHKDLKFRQRSDGVVWVAKEGAKTV 109

MERS-CoV    P-STFGTRNPNNDSAIV---TQFAPGTKLPKNFHIEGTGGNSQSSSRASSLSRNSSRSSSQGSRSGNSTRGTSPGPSGIG 207
SARS-CoV    PKDHIGTRNPNNNAATV---LQLPQGTTLPKGFYAEGSRGGSQASSRSS--SR--SRG-NSRNSTPGSSRGNSPARMASG 214
HCoV-HKU1   TPSDVSSRDPTTQEAIP---TRFPPGTILPQGYYVEGS-GRSASNSRPG--SRSQSRGPNNRSLSRSNSNFRHSDSIVKP 229
HCoV-OC43   TPADIVDRDPSSDEAIP---TRFPPGTVLPQGYYIEGS-GRSAPNSRST--SRTSSRASSAGSRSRANSGNRTPTSGVTP 230
HCoV-229E   P-TGYGVRRKNSEPEIPHFNQKLPNGVTVVE---EPDSRAPSRSQSRSQ--SR--GRG-ESKPQSRNPSSDRNHN--SQD 180
HCoV-NL63   N-TSLGNRKRNQKPLEPKFSIALPPELSVVE--FEDRSNNSSRASSRSS--TRNNSRD-SSRSTSRQQSRTRSDSNQSSS 183
                #46 (208-212)
MERS-CoV    AVGGDLLYLDLLNRLQAL------ESGKVKQSQP-------------KVITKKDAAAAK------NKMRHKRTSTKS--F 260
SARS-CoV    G-GETALALLLLDRLNQL---ESKVSGKGQQQQG-------------QTVTKKSAAEAS------KKPRQKRTATKQ--Y 269
HCoV-HKU1   DMADEIANLVLAKLGKD---------------SKP-------------QQVTKQNAKEIRHK--ILTKPRQKRTPNKH--C 278
HCoV-OC43   DMADQIASLVLAKLGKDA------------TKP-------------QQVTKHTAKEVRQK--ILNKPRQKRSPNKQ--C 280
HCoV-229E   DIMKAVA-AALKSLGFDKPQEKDKKSAKTGTPKPSRNQSPASSQTSAKSLARSQSSETKEQKHEMQKPRWKRQPNDDVTS 259
HCoV-NL63   DLVAAVT-LALKNLGFDN---QSKSPSSSGTSTP-------------KKPNKPLSQPRADKPSQLKKPRWKRVPTRE--E 244

MERS-CoV    NMVQAFGLRGPGDLQGNFGDLQLNKLGTEDPRWPQIAELAPTASAFMGMSQFKLTHQNN-----DDHGNPVYFLRYSGAI 335
SARS-CoV    NVTQAFGRRGPEQTQGNFGDQDLIRQGTDYKHWPQIAQFAPSASAFFGMSRIGMEVTPS----------GTWLTYHGAI 338
HCoV-HKU1   NVQQCFGKRGPSQ---NFGNAEMLKLGTNDPQFPILAELAPTPGAFFFGSKLDLVKRDS---EADSPVKDVFELHYSGSI 352
HCoV-OC43   TVQQCFGKRGPNQ---NFGGGEMLKLGTSDPQFPILAELAPTAGAFFFGSRLELAKVQNLSGNPDEPQKDVYELRYNGAI 357
HCoV-229E   NVTQCFGPRDLDH---NFGSAGVVANGVKAKGYPQFAELVPSTAAMLFDSHIVSKESGN----------TVVLTFTTRV 325
HCoV-NL63   NVIQCFGPRDFNH---NMGDSDLVQNGVDAKGFPQLAELIPNQAALFFDSEVSTDEVGD----------NVQITYTYKM 310
                                                                                #20 (394-399)
MERS-CoV    KLDPKNPNYNKWLELLEQNIDAY---------KTFPKKEKKQKAPK--EESTDQMSEPPKEQRVQ----GSITQRTRTRP 400
SARS-CoV    KLDDKDPQFKDNVILLNKHIDAY---------KTFPPTEPKKDKKKKTDEAQPLPQRQKKQPTVTLLPAADMDDFSRQLQ 409
HCoV-HKU1   RFDSTLPGFETIMKVLEENLNAYVNSNQNTDSDSLSSKPQRKRGVKQLPEQFDSLNLSAGTQHIS----NDFTPEDHSLL 428
HCoV-OC43   RFDSTLSGFETIMKVLNENLNAY---QQQDGMMNMSPKPQRQRGHKNGQGENDNISVAVPKSRVQQNKSRELTAEDISLL 434
HCoV-229E   TVPKDHPHLGKFL----EELNAF---------------TREMQQHPLLNPSALEFNPSQTSPATA----EPVRDEVSIET 382
HCoV-NL63   LVAKDNKNLPKFI----EQISAF----------TKPSSIKEMQSQSSHVAQNTVLNASIPES-------KPLADDDSAII 369

MERS-CoV    SVQPGPMIDVNTD- 413
SARS-CoV    NSMSGASADSTQA- 422
HCoV-HKU1   ATLDDPYVEDSVA- 441
HCoV-OC43   KKMDEPYTEDTSEI 448
HCoV-229E   DIIDEVN------- 389
HCoV-NL63   EIVNEVLH------ 377
```

B

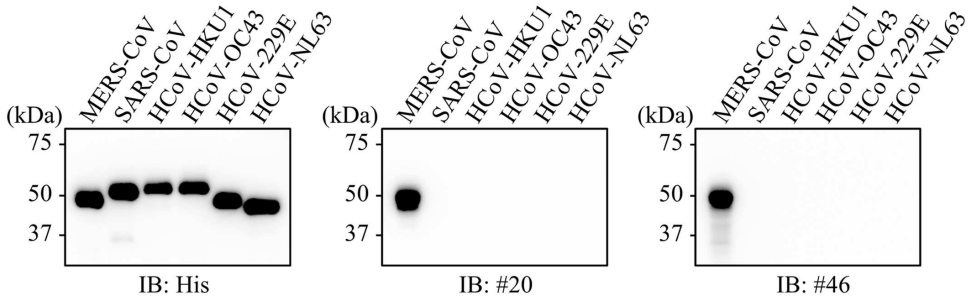

FIGURE 7 | No evidence of cross-reactivity with mAbs of other human coronaviruses. (A) Multiple sequence alignments of human coronavirus N proteins. Shaded positions represent conserved residues among the sequences. Dashes indicate gaps in the aligned sequences. **(B)** Specificity of selected mAbs. His-tagged NPs derived from several human coronaviruses were produced in the wheat germ extract system. Reactivity of generated mAbs was validated by immunoblot analysis using either anti-His or the indicated antibodies.

NTD of NP of many human coronaviruses share common sequences (Yu et al., 2005; Chang et al., 2014). Therefore, we used a recombinant MERS-CoV-NP devoid of conserved regions as an immunogen to produce mAbs. Consequently, our newly developed mAbs can recognize species-specific amino-acid sequences in MERS-CoV. Consistent with this, the mAbs did not cross-react with NPs derived from other human coronaviruses. Viral species can be determined by structural characterization of the capsid/nucleocapsid (Gelderblom, 1996). Therefore, we suspect that highly species-specific mAbs were obtained due to the appropriate design and native properties of the antigen.

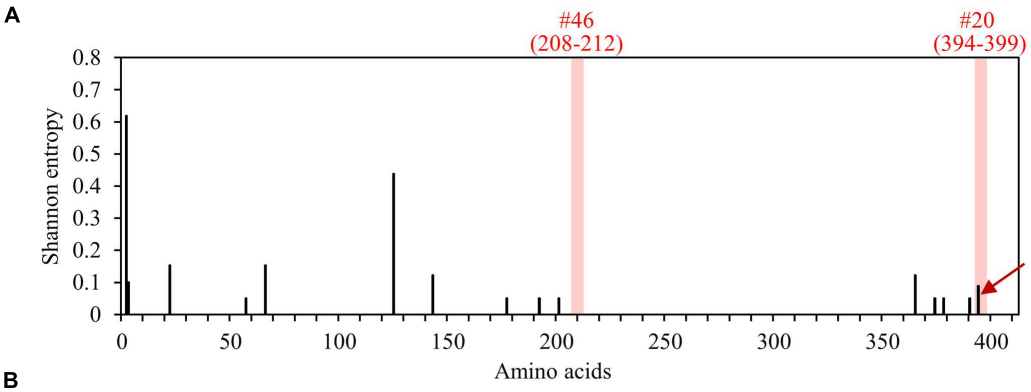

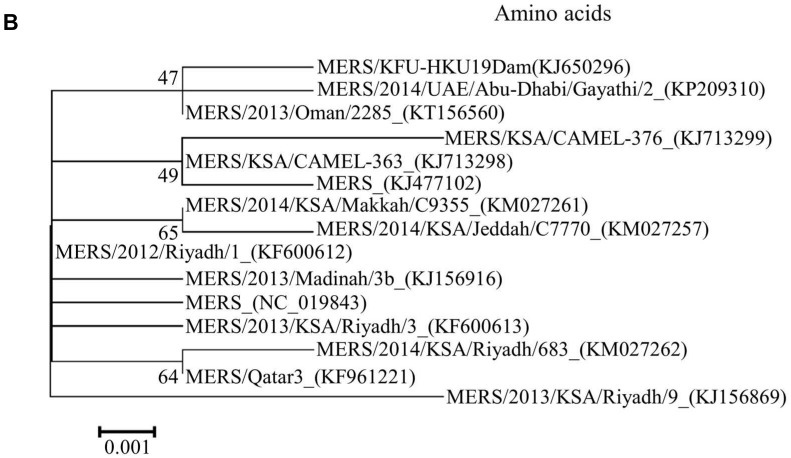

C

Name of strains	Number of strains (100 % identical)	Amino acid number 208-212	394-399
MERS_(NC_019843)	1	A V G G D	Q R T R T R
MERS_(KJ477102)	1	. . . . .	. . . . .
MERS/KFU-HKU19Dam_(KJ650296)	4	. . . . .	. . . . .
MERS/KSA/CAMEL-363_(KJ713298)	1	. . . . .	. . . . .
MERS/KSA/CAMEL-376_(KJ713299)	1	. . . . .	. . . . .
MERS/Qatar3_(KF961221)	1	. . . . .	. . . . .
MERS/2012/Riyadh/1_(KF600612)	47	. . . . .	. . . . .
MERS/2013/Oman/2285_(KT156560)	30	. . . . .	. . . . .
MERS/2013/Madinah/3b_(KJ156916)	4	. . . . .	. . . . .
MERS/2013/KSA/Riyadh/3_(KF600613)	1	. . . . .	. . . . .
MERS/2013/KSA/Riyadh/9_(KJ156869)	1	. . . . .	. . . . .
MERS/2014/KSA/Makkah/C9355_(KM027261)	17	. . . . .	. . . . .
MERS/2014/KSA/Jeddah/C7770_(KM027257)	1	. . . . .	. . . . .
MERS/2014/UAE/AbuDhabi/Gayathi/2_(KP209310)	1	. . . . .	. . . . .
MERS/2014/KSA/Riyadh/683_(KM027262)	2	. . . . .	. H . . .

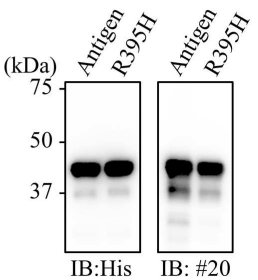

FIGURE 8 | Comprehensive detection of MERS-CoV isolates by the generated mAbs. (A) Distribution of amino-acid variation of NP in 113 MERS-CoV strains. Shannon entropy, as a quantitative measure of variation, was calculated for each amino-acid residue of MERS-NP. Arrow indicates amino-acid mutation in the epitope of mAb (#20) from two MERS-CoV strains. **(B)** Phylogenetic analysis of MERS-CoV based on multiple sequence alignment of NP. The unrooted phylogeny is generated from amino-acid sequence alignments of nucleocapsid proteins based on the maximum-likelihood method. Sequences with identity of 100% are removed from the dataset. Bootstrap values (1,000 replicates) are indicated around the branches. The scale bar represents amino-acid substitutions per site. **(C)** Identification of amino-acid substitution in the antigenic epitope in 15 identical strains. Dots indicate sequence identity relative to the prototype strain. The R395H substitution was noted in two strains. **(D)** Reactivity of mAb (#20) to MERS-NP (122–413) derived from the prototype and a mutant strain harboring R395H. Reactivity was determined by immunoblot analysis.

Development of international trade and worldwide travel brings about significant risk of the spread of emerging infectious diseases, including MERS-CoV. Needless to say, there is no obvious boundary between virus-free countries and those facing endemics. Thus, the establishment of rapid and reliable laboratory diagnostic tests for these pathogens is an urgent matter in all countries. The most widely used current diagnostics for MERS-CoV involve detection of virus nucleic acids by qRT-PCR in the laboratory (Corman et al., 2012a,b). Although qRT-PCR is a sensitive and powerful tool for obtaining evidence

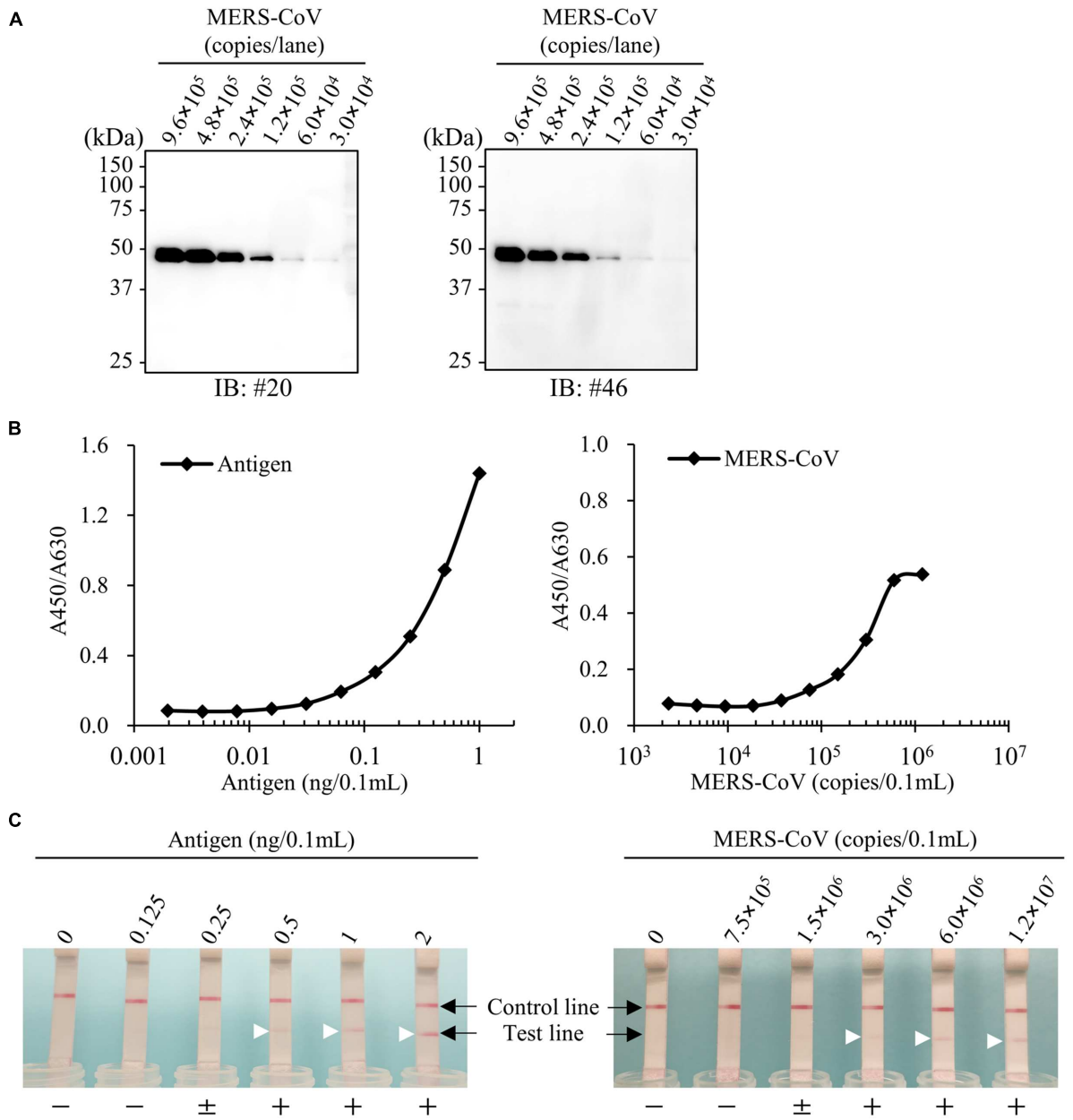

FIGURE 9 | Establishment of antigen detection assays for MERS-CoV. (A) Immunoblot analysis for virus particles of MERS-CoV. Cell culture medium of MERS-CoV-infected Vero-TMPRSS2 cells were collected and analyzed by immunoblotting with the newly developed anti-MERS-NP mAbs. **(B,C)** Detection limit of ELISA and ICT. Recombinant antigen protein and MERS-CoV were subjected to either ELISA or ICT analysis. + and − indicate positive and negative detection, respectively; ± means moderately positive. Arrowheads show positive test line.

of virus infection, it requires specialized lab equipment and expertise with molecular technology; moreover, due to the time required for the enzymatic reaction, it is rather time-consuming. These disadvantages prevent qRT-PCR from being used in POCT. Therefore, case-oriented comprehensive tests should be conducted using multiple diagnostic assays.

Enzyme-linked immunosorbent assay and ICT are two major clinical tests used to detect viral antigens. Both methods employ pairs of mAbs used as capture and detection antibodies. The optimal combination of capture and detection antibodies should be thoroughly investigated before the test kits are assembled. In this study, the utilization of natively folded antigen protein to evaluate each test allowed us to identify the optimal pair of antibodies for the detection of MERS-CoV-NP. Our antibody set is suitable for detecting MERS-CoV-NP by either ELISA or ICT.

At the early stage of illness, high titers of infectious virions and virus antigens are present in the lower respiratory tract (LRT) and sputum of patients. The viral loads in LRT and expectorated

sputum of patients during acute infection are more than 10^6 copies/mL (Drosten et al., 2013; Kapoor et al., 2013; Corman et al., 2015), making it feasible to detect viral antigens of MERS-CoV for clinical diagnosis at an early stage of infection. The current version of our assay can detect 0.0625 (ELISA) or 0.5 ng (ICT) of recombinant N protein and 1.5×10^5 (ELISA) or 3.0×10^6 viral copies (ICT), ensuring its feasibility in practical clinical tests.

Other groups have also developed antigen-capture ELISA and ICT for detection of MERS-NP antigen (Chen et al., 2015; Song et al., 2015). Song et al. used synthetic peptides as immunogens to raise an NP-specific mAb. The other group used recombinant N proteins as antigens, but did not perform precise epitope mapping (Chen et al., 2015). On the other hand, we developed structure-sensitive mAbs against MERS-NP and thoroughly investigated their targeting epitopes. Bioinformatic analysis based on a phylogenetic approach further revealed that our newly developed mAbs can detect NP antigens derived from existing isolates of MERS-CoV.

In summary, we developed a novel antigen-detection assay using newly created mAbs for the rapid and reliable assessment of NP antigen of MERS-CoV. Further evaluations using actual patient samples warrants the usability and benefit of this assay for the clinical diagnosis of MERS-CoV infection.

AUTHOR CONTRIBUTIONS

YY designed and performed the research, analyzed the data, and wrote the manuscript. SM and SF performed the research, contributed the virus preparation, analyzed the data. SM performed the research, analyzed the data. YM performed the bioinformatics analysis. HK, HK, MT, and TC edited the manuscript. AR directed the research, analyzed the data, and wrote the manuscript.

ACKNOWLEDGMENTS

We thank Drs. Ron A. M. Fouchier and Bart L. Haagmans for providing MERS-CoV, and Dr. Naohito Nozaki for technical assistance. This work was supported in part by the Creation of Innovation Centers for Advanced Interdisciplinary Research Areas Program and grant-in-aid from the Ministry of Education, Culture, Sports, Science and Technology of Japan, and by Research Program on Emerging and Re-emerging Infectious Diseases from Japan Agency for Medical Research and Development, AMED.

REFERENCES

Banik, G. R., Khandaker, G., and Rashid, H. (2015). Middle East respiratory syndrome coronavirus "MERS-CoV": current knowledge gaps. *Paediatr. Respir. Rev.* 16, 197–202. doi: 10.1016/j.prrv.2015.04.002

Chang, C., Hou, M.-H., Chang, C.-F., Hsiao, C.-D., and Huang, T. (2014). The SARS coronavirus nucleocapsid protein–forms and functions. *Antiviral Res.* 103, 39–50. doi: 10.1016/j.antiviral.2013.12.009

Chen, C.-Y., Chang, C.-K., Chang, Y.-W., Sue, S.-C., Bai, H.-I., Riang, L., et al. (2007). Structure of the SARS coronavirus nucleocapsid protein RNA-binding dimerization domain suggests a mechanism for helical packaging of viral RNA. *J. Mol. Biol.* 368, 1075–1086. doi: 10.1016/j.jmb.2007.02.069

Chen, Y., Chan, K.-H., Kang, Y., Chen, H., Luk, H. K., Poon, R. W., et al. (2015). A sensitive and specific antigen detection assay for middle east respiratory syndrome coronavirus. *Emerg. Microbes Infect.* 4:e26. doi: 10.1038/emi.2015.26

Cheng, Y.-S. E., Lo, K.-H., Hsu, H.-H., Shao, Y.-M., Yang, W.-B., Lin, C.-H., et al. (2006). Screening for HIV protease inhibitors by protection against activity-mediated cytotoxicity in *Escherichia coli*. *J. Virol. Methods* 137, 82–87. doi: 10.1016/j.jviromet.2006.06.003

Corman, V. M., Albarrak, A. M., Omrani, A. S., Albarrak, M. M., Farah, M. E., Almasri, M., et al. (2015). Viral shedding and antibody response in 37 patients with middle east respiratory syndrome coronavirus infection. *Clin. Infect. Dis.* 62, 477–483. doi: 10.1093/cid/civ951

Corman, V. M., Eckerle, I., Bleicker, T., Zaki, A., Landt, O., Eschbach-Bludau, M., et al. (2012a). Detection of a novel human coronavirus by real-time reverse-transcription polymerase chain reaction. *Euro. Surveill.* 17:20285.

Corman, V. M., Müller, M. A., Costabel, U., Timm, J., Binger, T., Meyer, B., et al. (2012b). Assays for laboratory confirmation of novel human coronavirus (hCoV-EMC) infections. *Euro. Surveill.* 17:20334.

Das, D., and Suresh, M. R. (2006). Copious production of SARS-CoV nucleocapsid protein employing codon optimized synthetic gene. *J. Virol. Methods* 137, 343–346. doi: 10.1016/j.jviromet.2006.06.029

de Groot, R. J., Baker, S. C., Baric, R. S., Brown, C. S., Drosten, C., Enjuanes, L., et al. (2013). Middle East respiratory syndrome coronavirus (MERS-CoV): announcement of the Coronavirus study group. *J. Virol.* 87, 7790–7792. doi: 10.1128/JVI.01244-13

Drosten, C., Seilmaier, M., Corman, V. M., Hartmann, W., Scheible, G., Sack, S., et al. (2013). Clinical features and virological analysis of a case of middle east respiratory syndrome coronavirus infection. *Lancet Infect. Dis.* 13, 745–751. doi: 10.1016/S1473-3099(13)70154-3

Edgar, R. C. (2004). MUSCLE: multiple sequence alignment with high accuracy and high throughput. *Nucleic Acids Res.* 32, 1792–1797. doi: 10.1093/nar/gkh340

Endo, Y., and Sawasaki, T. (2005). Advances in genome-wide protein expression using the wheat germ cell-free system. *Methods Mol. Biol.* 310, 145–167. doi: 10.1007/978-1-59259-948-6_11

Endo, Y., and Sawasaki, T. (2006). Cell-free expression systems for eukaryotic protein production. *Curr. Opin. Biotechnol.* 17, 373–380. doi: 10.1016/j.copbio.2006.06.009

Gelderblom, H. R. (1996). "Chapter 41: Structure and classification of viruses," in *Medical Microbiology*, 4th Edn, ed. S. Baron (Galveston, TX: University of Texas Medical Branch).

Goshima, N., Kawamura, Y., Fukumoto, A., Miura, A., Honma, R., Satoh, R., et al. (2008). Human protein factory for converting the transcriptome into an in vitro-expressed proteome. *Nat. Methods* 5, 1011–1017. doi: 10.1038/nmeth.1273

Guex, N., and Peitsch, M. C. (1997). SWISS-MODEL and the Swiss-PdbViewer: an environment for comparative protein modeling. *Electrophoresis* 18, 2714–2723. doi: 10.1002/elps.1150181505

He, Q., Du, Q., Lau, S., Manopo, I., Lu, L., Chan, S.-W., et al. (2005). Characterization of monoclonal antibody against SARS coronavirus nucleocapsid antigen and development of an antigen capture ELISA. *J. Virol. Methods* 127, 46–53. doi: 10.1016/j.jviromet.2005.03.004

Huang, Q., Yu, L., Petros, A. M., Gunasekera, A., Liu, Z., Xu, N., et al. (2004). Structure of the N-terminal RNA-binding domain of the SARS CoV nucleocapsid protein. *Biochemistry* 43, 6059–6063. doi: 10.1021/bi036155b

Jiang, L., Wang, N., Zuo, T., Shi, X., Poon, K.-M. V., Wu, Y., et al. (2014). Potent neutralization of MERS-CoV by human neutralizing monoclonal antibodies to the viral spike glycoprotein. *Sci. Transl. Med.* 6, 234ra59. doi: 10.1126/scitranslmed.3008140

Kapoor, M., Pringle, K., Kumar, A., Dearth, S., Liu, L., Lovchik, J., et al. (2013). Clinical and laboratory findings of the first imported case of middle east respiratory syndrome coronavirus (MERS-CoV) into the United States. *Clin. Infect. Dis.* 59, 1511–1518. doi: 10.1093/cid/ciu635

Kimura, K., Nozaki, N., Enomoto, T., Tanaka, M., and Kikuchi, A. (1996). Analysis of M phase-specific phosphorylation of DNA topoisomerase II. *J. Biol. Chem.* 271, 21439–21445. doi: 10.1074/jbc.271.35.21439

Kimura, K., Nozaki, N., Saijo, M., Kikuchi, A., Ui, M., and Enomoto, T. (1994). Identification of the nature of modification that causes the shift of DNA topoisomerase II beta to apparent higher molecular weight forms in the M phase. *J. Biol. Chem.* 269, 24523–24526.

Kogaki, H., Uchida, Y., Fujii, N., Kurano, Y., Miyake, K., Kido, Y., et al. (2005). Novel rapid immunochromatographic test based on an enzyme immunoassay for detecting nucleocapsid antigen in SARS-associated coronavirus. *J. Clin. Lab. Anal.* 19, 150–159. doi: 10.1002/jcla.20070

Lau, S. K. P., Woo, P. C. Y., Wong, B. H. L., Tsoi, H.-W., Woo, G. K. S., Poon, R. W. S., et al. (2004). Detection of severe acute respiratory syndrome (SARS) coronavirus nucleocapsid protein in sars patients by enzyme-linked immunosorbent assay. *J. Clin. Microbiol.* 42, 2884–2889. doi: 10.1128/JCM.42.7.2884-2889.2004

Leenaars, M., and Hendriksen, C. F. M. (2005). Critical steps in the production of polyclonal and monoclonal antibodies: evaluation and recommendations. *ILAR J.* 46, 269–279. doi: 10.1093/ilar.46.3.269

Li, Y., Wan, Y., Liu, P., Zhao, J., Lu, G., Qi, J., et al. (2015). A humanized neutralizing antibody against MERS-CoV targeting the receptor-binding domain of the spike protein. *Cell Res.* 25, 1237–1249. doi: 10.1038/cr.2015.113

Liang, F.-Y., Lin, L.-C., Ying, T.-H., Yao, C.-W., Tang, T.-K., Chen, Y.-W., et al. (2013). Immunoreactivity characterisation of the three structural regions of the human coronavirus OC43 nucleocapsid protein by Western blot: implications for the diagnosis of coronavirus infection. *J. Virol. Methods* 187, 413–420. doi: 10.1016/j.jviromet.2012.11.009

Mancia, F., Brenner-Morton, S., Siegel, R., Assur, Z., Sun, Y., Schieren, I., et al. (2007). Production and characterization of monoclonal antibodies sensitive to conformation in the 5HT2c serotonin receptor. *Proc. Natl. Acad. Sci. U.S.A.* 104, 4303–4308. doi: 10.1073/pnas.0700301104

Matsunaga, S., Kawakami, S., Matsuo, I., Okayama, A., Tsukagoshi, H., Kudoh, A., et al. (2014). Wheat germ cell-free system-based production of hemagglutinin-neuraminidase glycoprotein of human parainfluenza virus type 3 for generation and characterization of monoclonal antibody. *Front. Microbiol.* 5:208. doi: 10.3389/fmicb.2014.00208

Matsunaga, S., Masaoka, T., Sawasaki, T., Morishita, R., Iwatani, Y., Tatsumi, M., et al. (2015). A cell-free enzymatic activity assay for the evaluation of HIV-1 drug resistance to protease inhibitors. *Front. Microbiol.* 6:1220. doi: 10.3389/fmicb.2015.01220

McBride, R., van Zyl, M., and Fielding, B. C. (2014). The coronavirus nucleocapsid is a multifunctional protein. *Viruses* 6, 2991–3018. doi: 10.3390/v6082991

Miyakawa, K., Matsunaga, S., Watashi, K., Sugiyama, M., Kimura, H., Yamamoto, N., et al. (2015). Molecular dissection of HBV evasion from restriction factor tetherin: a new perspective for antiviral cell therapy. *Oncotarget* 6, 21840–21852. doi: 10.18632/oncotarget.4808

Nishi, M., Akutsu, H., Kudoh, A., Kimura, H., Yamamoto, N., Umezawa, A., et al. (2014). Induced cancer stem-like cells as a model for biological screening and discovery of agents targeting phenotypic traits of cancer stem cell. *Oncotarget* 5, 8665–8680. doi: 10.18632/oncotarget.2356

Pettersen, E. F., Goddard, T. D., Huang, C. C., Couch, G. S., Greenblatt, D. M., Meng, E. C., et al. (2004). UCSF Chimera–a visualization system for exploratory research and analysis. *J. Comput. Chem.* 25, 1605–1612. doi: 10.1002/jcc.20084

Raj, V. S., Mou, H., Smits, S. L., Dekkers, D. H. W., Müller, M. A., Dijkman, R., et al. (2013). Dipeptidyl peptidase 4 is a functional receptor for the emerging human coronavirus-EMC. *Nature* 495, 251–254. doi: 10.1038/nature12005

Schein, C. H. (1991). Optimizing protein folding to the native state in bacteria. *Curr. Opin. Biotechnol.* 2, 746–750. doi: 10.1016/0958-1669(91)90046-8

Senchi, K., Matsunaga, S., Hasegawa, H., Kimura, H., and Ryo, A. (2013). Development of oligomannose-coated liposome-based nasal vaccine against human parainfluenza virus type 3. *Front. Microbiol.* 4:346. doi: 10.3389/fmicb.2013.00346

Shirato, K., Kawase, M., and Matsuyama, S. (2013). Middle East respiratory syndrome coronavirus infection mediated by the transmembrane serine protease TMPRSS2. *J. Virol.* 87, 12552–12561. doi: 10.1128/JVI.01890-13

Shirato, K., Yano, T., Senba, S., Akachi, S., Kobayashi, T., Nishinaka, T., et al. (2014). Detection of middle east respiratory syndrome coronavirus using reverse transcription loop-mediated isothermal amplification (RT-LAMP). *Virol. J.* 11, 139. doi: 10.1186/1743-422X-11-139

Song, D., Ha, G., Serhan, W., Eltahir, Y., Yusof, M., Hashem, F., et al. (2015). Development and validation of a rapid immunochromatographic assay for detection of Middle East respiratory syndrome coronavirus antigen in dromedary camels. *J. Clin. Microbiol.* 53, 1178–1182. doi: 10.1128/JCM.03096-14

Song, F., Fux, R., Provacia, L. B., Volz, A., Eickmann, M., Becker, S., et al. (2013). Middle East respiratory syndrome coronavirus spike protein delivered by modified vaccinia virus Ankara efficiently induces virus-neutralizing antibodies. *J. Virol.* 87, 11950–11954. doi: 10.1128/JVI.01672-13

Stills, H. F. (2005). Adjuvants and antibody production: dispelling the myths associated with Freund's complete and other adjuvants. *ILAR J.* 46, 280–293. doi: 10.1093/ilar.46.3.280

Takai, K., and Endo, Y. (2010). The cell-free protein synthesis system from wheat germ. *Methods Mol. Biol.* 607, 23–30. doi: 10.1007/978-1-60327-331-2_3

Takai, K., Sawasaki, T., and Endo, Y. (2010). The wheat-germ cell-free expression system. *Curr. Pharm. Biotechnol.* 11, 272–278. doi: 10.2174/138920110791111933

Takeda, H., Ogasawara, T., Ozawa, T., Muraguchi, A., Jih, P.-J., Morishita, R., et al. (2015). Production of monoclonal antibodies against GPCR using cell-free synthesized GPCR antigen and biotinylated liposome-based interaction assay. *Sci. Rep.* 5:11333. doi: 10.1038/srep11333

Tamura, K., Peterson, D., Peterson, N., Stecher, G., Nei, M., and Kumar, S. (2011). MEGA5: molecular evolutionary genetics analysis using maximum likelihood, evolutionary distance, and maximum parsimony methods. *Mol. Biol. Evol.* 28, 2731–2739. doi: 10.1093/molbev/msr121

Tang, X.-C., Agnihothram, S. S., Jiao, Y., Stanhope, J., Graham, R. L., Peterson, E. C., et al. (2014). Identification of human neutralizing antibodies against MERS-CoV and their role in virus adaptive evolution. *Proc. Natl. Acad. Sci. U.S.A.* 111, E2018–E2026. doi: 10.1073/pnas.1402074111

van Boheemen, S., de Graaf, M., Lauber, C., Bestebroer, T. M., Raj, V. S., Zaki, A. M., et al. (2012). Genomic characterization of a newly discovered coronavirus associated with acute respiratory distress syndrome in humans. *MBio* 3:e00473-12. doi: 10.1128/mBio.00473-12

Webb, B., and Sali, A. (2014). Protein structure modeling with MODELLER. *Methods Mol. Biol.* 1137, 1–15. doi: 10.1007/978-1-4939-0366-5_1

Wernery, U., Ei Rasoul, I. H., Wong, E. Y., Joseph, M., Chen, Y., Jose, S., et al. (2015). A phylogenetically distinct Middle East respiratory syndrome coronavirus detected in a dromedary calf from a closed dairy herd in Dubai with rising seroprevalence with age. *Emerg. Microbes Infect.* 4:e74. doi: 10.1038/emi.2015.74

World Health Organization [WHO] (2016). Middle East respiratory syndrome coronavirus (MERS-CoV). Available at: http://www.who.int/emergencies/mers-cov/en/ [accessed January 28, 2016].

Xu, D., and Zhang, Y. (2012). Ab initio protein structure assembly using continuous structure fragments and optimized knowledge-based force field. *Proteins* 80, 1715–1735. doi: 10.1002/prot.24065

Yang, J., Yan, R., Roy, A., Xu, D., Poisson, J., and Zhang, Y. (2015). The I-TASSER Suite: protein structure and function prediction. *Nat. Methods* 12, 7–8. doi: 10.1038/nmeth.3213

Yang, O. O. (2009). Candidate vaccine sequences to represent intra- and inter-clade HIV-1 variation. *PLoS ONE* 4:e7388. doi: 10.1371/journal.pone.0007388

Yu, F., Le, M. Q., Inoue, S., Thai, H. T. C., Hasebe, F., Del Carmen, P. M. et al. (2005). Evaluation of inapparent nosocomial severe acute respiratory syndrome coronavirus infection in Vietnam by use of highly specific recombinant

truncated nucleocapsid protein-based enzyme-linked immunosorbent assay. *Clin. Diagn. Lab. Immunol.* 12, 848–854. doi: 10.1128/CDLI.12.7.848-854.2005

Zaki, A. M., van Boheemen, S., Bestebroer, T. M., Osterhaus, A. D. M. E., and Fouchier, R. A. M. (2012). Isolation of a Novel Coronavirus from a Man with Pneumonia in Saudi Arabia. *N. Engl. J. Med.* 367, 1814–1820. doi: 10.1056/NEJMoa1211721

Zhang, N., Jiang, S., and Du, L. (2014). Current advancements and potential strategies in the development of MERS-CoV vaccines. *Expert Rev. Vaccines* 13, 761–774. doi: 10.1586/14760584.2014.912134

Conflict of Interest Statement: The authors declare that the research was conducted in the absence of any commercial or financial relationships that could be construed as a potential conflict of interest.

Copyright © 2016 Yamaoka, Matsuyama, Fukushi, Matsunaga, Matsushima, Kuroyama, Kimura, Takeda, Chimuro and Ryo. This is an open-access article distributed under the terms of the Creative Commons Attribution License (CC BY). The use, distribution or reproduction in other forums is permitted, provided the original author(s) or licensor are credited and that the original publication in this journal is cited, in accordance with accepted academic practice. No use, distribution or reproduction is permitted which does not comply with these terms.

frontiers in Microbiology

ORIGINAL RESEARCH
published: 20 April 2016
doi: 10.3389/fmicb.2016.00554

Visual Detection of West Nile Virus Using Reverse Transcription Loop-Mediated Isothermal Amplification Combined with a Vertical Flow Visualization Strip

Zengguo Cao[1], Hualei Wang[1,2], Lina Wang[1,3], Ling Li[1,4], Hongli Jin[1,5], Changping Xu[1,6], Na Feng[1,2], Jianzhong Wang[1], Qian Li[1], Yongkun Zhao[1], Tiecheng Wang[1], Yuwei Gao[1,2], Yiyu Lu[1,6], Songtao Yang[1,2]* and Xianzhu Xia[1,2]**

[1] Key Laboratory of Jilin Province for Zoonosis Prevention and Control, Institute of Military Veterinary, Academy of Military Medical Sciences, Changchun, China, [2] Jiangsu Co-innovation Center for Prevention and Control of Important Animal Infectious Disease and Zoonoses, Yangzhou, China, [3] Animal Science and Technology College, Jilin Agricultural University, Changchun, China, [4] College of Veterinary Medicine, Jilin University, Changchun, China, [5] Changchun SR Biological Technology Co., Ltd., Changchun, China, [6] Key Laboratory of Emergency Detection for Public Health of Zhejiang Province, Zhejiang Provincial Center for Disease Control and Prevention, Hangzhou, China

OPEN ACCESS

Edited by:
Toshinori Sato,
Keio University, Japan

Reviewed by:
Ryosuke Suzuki,
National Institute of Infectious Diseases, Japan
Sonja Best,
National Institute of Allergy and Infectious Diseases, USA

***Correspondence:**
Xianzhu Xia
xiaxzh@cae.cn;
Songtao Yang
yst62041@163.com;
Hualei Wang
whl831125@163.com

Specialty section:
This article was submitted to Virology, a section of the journal Frontiers in Microbiology

Received: 02 February 2016
Accepted: 04 April 2016
Published: 20 April 2016

Citation:
Cao Z, Wang H, Wang L, Li L, Jin H, Xu C, Feng N, Wang J, Li Q, Zhao Y, Wang T, Gao Y, Lu Y, Yang S and Xia X (2016) Visual Detection of West Nile Virus Using Reverse Transcription Loop-Mediated Isothermal Amplification Combined with a Vertical Flow Visualization Strip. Front. Microbiol. 7:554. doi: 10.3389/fmicb.2016.00554

West Nile virus (WNV) causes a severe zoonosis, which can lead to a large number of casualties and considerable economic losses. A rapid and accurate identification method for WNV for use in field laboratories is urgently needed. Here, a method utilizing reverse transcription loop-mediated isothermal amplification combined with a vertical flow visualization strip (RT-LAMP-VF) was developed to detect the envelope (E) gene of WNV. The RT-LAMP-VF assay could detect 10^2 copies/μl of an WNV RNA standard using a 40 min amplification reaction followed by a 2 min incubation of the amplification product on the visualization strip, and no cross-reaction with other closely related members of the *Flavivirus* genus was observed. The assay was further evaluated using cells and mouse brain tissues infected with a recombinant rabies virus expressing the E protein of WNV. The assay produced sensitivities of $10^{1.5}$ $TCID_{50}$/ml and $10^{1.33}$ $TCID_{50}$/ml for detection of the recombinant virus in the cells and brain tissues, respectively. Overall, the RT-LAMP-VF assay developed in this study is rapid, simple and effective, and it is therefore suitable for clinical application in the field.

Keywords: West Nile virus, visual detection, reverse transcription loop-mediated isothermal amplification, visualization strip, RT-LAMP-VF

INTRODUCTION

West Nile virus (WNV) infection leads to an acute febrile zoonosis, which can cause disease in birds, humans and horses[1] (Gubler, 2001). The manifestations of WNV infection include West Nile fever and West Nile encephalitis, which together comprise symptoms ranging from a benign or often symptomless infection to fever and neuroinvasive disease (Gubler, 2001; Sejvar et al., 2003; Hayes and O'Leary, 2004; Hayes and Gubler, 2006). WNV infection gained worldwide attention in

[1]http://www.oie.int/en/for-the-media/animal-diseases/animal-disease-information-summaries/

1999, when it was first detected in America during an outbreak in New York City (Nash et al., 2001; Hayes and Gubler, 2006). In America, as of January 12, 2016, a total of 48 states have reported WNV infection in humans, birds, or mosquitoes[2].

WNV is an arthropod-borne, neurotropic, enveloped *Flavivirus* with a single-stranded, positive-sense RNA genome and is a member of the Japanese encephalitis virus (JEV) serogroup, which includes JEV, Murray Valley encephalitis virus (MVEV) and St. Louis encephalitis virus (Mukhopadhyay et al., 2003; Solomon et al., 2003; Lim et al., 2011). The RNA genome of WNV is approximately 11,000 nucleotides in length and encodes three structural [capsid (C), premembrane (prM) or membrane (M), and envelope (E)] proteins and seven non-structural (NS1, NS2a, NS2b, NS3, NS4a, NS4b, and NS5) proteins (Deubel et al., 2001; Brinton, 2002; Parida et al., 2004). Phylogenetic analysis of the WNV E protein sequence has indicated that WNV can be separated into two main lineages (lineages 1 and 2) as well as several additional minor lineages (lineage 3, lineage 4, lineage 5 and the putative lineage 6; Lanciotti et al., 2002; Vazquez et al., 2010; Del Amo et al., 2013; Faggioni et al., 2014).

There are many laboratory methods for diagnosing WNV, including virus isolation, immunohistochemistry, immunofluorescence, plaque reduction neutralization test (PRNT), enzyme-linked immunosorbent assay (ELISA), reverse transcription PCR (RT-PCR), real-time RT-PCR, and nested RT-PCR, among others (Dauphin and Zientara, 2007; De Filette et al., 2012). Some of these methods have been approved by the American Centers for Disease Control and Prevention (American CDC). However, the ELISA has cross-reactivity with other flaviviruses when used for serodiagnosis. Additionally, the above nucleic acid amplification methods are disadvantageous because they require expensive equipment and are time-consuming to perform. Furthermore, both virus isolation and PRNT are tedious and technically complex and require over a week to perform. Thus, there is an urgent need to develop a rapid and simple diagnostic method for WNV to improve detection efficiency.

Loop-mediated isothermal amplification (LAMP) is a novel technique that can amplify DNA with high efficiency, specificity and rapidity under isothermal conditions (Notomi et al., 2000). Because this amplification technique requires isothermal conditions, LAMP can be performed using only a simple water bath. Moreover, LAMP can detect RNA templates by using reverse transcriptase together with DNA polymerase for amplification (Whiting and Champoux, 1998; Notomi et al., 2000; Ge et al., 2013). Several RNA viruses have been successfully detected using RT-LAMP assays (Kurosaki et al., 2007; Ge et al., 2013). The gold immunochromatographic assay is another technique that has been widely applied for the detection of various viruses (Mikawa et al., 2009; Wang et al., 2010). Amplicon detection using a vertical flow (VF) visualization strip has been previously applied to accelerate and simplify the process of interpreting LAMP assay results (Cui et al., 2012). In the current study, we developed a RT-LAMP assay coupled with a VF visualization strip for rapid, simple, and accurate visual detection of WNV. Because of these characteristics, this RT-LAMP-VF assay is useful for field laboratory diagnosis of WNV infection.

MATERIALS AND METHODS

Viruses and Extraction of Viral RNA

The recombinant rabies virus SRV9 strain was modified to express the E protein (EP) of WNV (GenBank Accession: DQ211652; rRABV-WNVE) and stored in our laboratory. The recombinant virus was propagated in BSR cells, a clone of the BHK-21 cell line (baby hamster kidney cells), which were grown in Dulbecco's modified Eagle's medium (DMEM, Gibco, Grand Island, NY, USA) supplemented with 5% fetal bovine serum (FBS, Gibco, Grand Island, NY, USA) at 37°C in an incubator. rRABV was titrated in Neuroblastoma (NA) cell as described previously (Wang et al., 2011). Viral RNA was extracted using a commercial RNA extraction kit (RNeasy Mini Kit, Qiagen, Hilden, Germany). All operations were performed according to the manufacturer's instructions.

Preparation of WNV RNA Standards

Artificial viral RNA encoding a partial WNV E gene sequence (GenBank Accession: DQ211652) was synthesized; this construct was modified via PCR to include the T7 promoter sequence at its 5′ terminus. The PCR products were transcribed *in vitro* using T7 RNA polymerase (TaKaRa Biotechnology Co., Ltd., Dalian, China) according to the manufacturer's instructions. The RNA transcripts were then purified and quantified, and 10-fold serial dilutions of the RNA ranging from 10^7 to 10^0 copies per μl were prepared.

Primer Design

The complete genome sequences of 30 strains of WNV isolated over various years from different regions and disparate species were analyzed, and the E gene of WNV was selected as the target region for the RT-LAMP-VF assay (the alignment of WNV E gene sequences was shown in **Figure 1**). Six primers, targeting eight distinct regions of the gene, were designed for the assay using the PrimerExplorer V4 program[3]. To detect reaction products by VF, the LF and LB primers were 5′-labeled with biotin and FITC. The details are shown in **Figure 2** and **Table 1**. All primers were synthesized by Sangon Biotech Biotechnology Co., Ltd., (Shanghai, China).

RT-LAMP-VF Reaction and Product Detection

The RT-LAMP-VF assay was performed using a 25-μl total reaction volume containing a mixture of 0.4 μM of the inner primers FIP and BIP, 0.2 μM of the loop primers LF and LB, 0.1 μM of the outer primers F3 and B3, 1.4 mM of each deoxynucleoside triphosphate (dNTP), 8 mM $MgSO_4$, 0.2 M betaine, 5 U of avian myeloblastosis virus reverse transcriptase (Bioer Technology Co., Ltd., Hangzhou, China), 8 U of Bst DNA

[2]http://www.cdc.gov/westnile/index.html

[3]http://primerexplorer.jp/elamp4.0.0/index.html

FIGURE 1 | Alignment of West Nile virus (WNV) E gene sequences and positions of the primers used for RT-LAMP. The E gene of WNV was retrieved from GenBank and analyzed using MegAlign software. Primers were designed based on a conserved region (nucleotides 2065–2277 of the genome). The GenBank accession numbers of the aligned strains (from top to bottom) are HQ596519.1, AF260968.1, AF196520, KJ131504.1, AF196835.1, HQ705675.1, JN183897.1, DQ164195.1, JF357960.1, JF899530.1, JF899531.1, JN817352.1, JN891.1, JN183890.1,HQ671797.1, JF920759.1, EU391640.1, JX442282.1, AF260969.1, AJ 965628.1, KM488117.1, HM756678.1, FJ265702.1, FJ265703.1, HM756661.1, JX015519.1, JN183893.1, KC493970.1, AF394221.1, and AF196520.1.

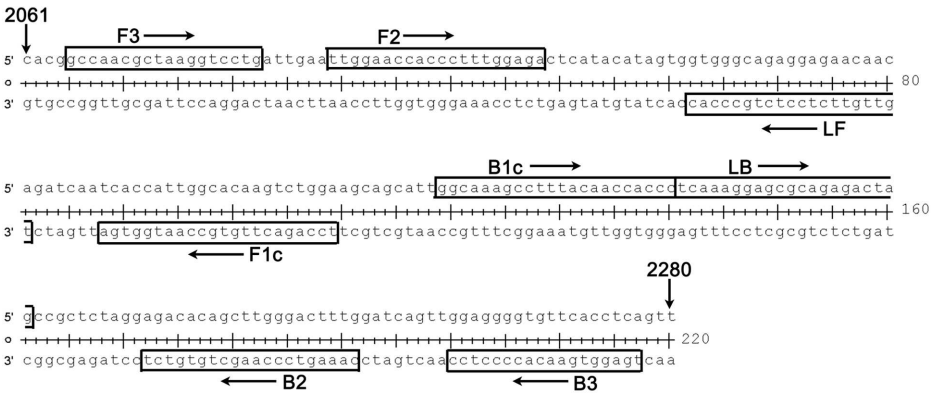

FIGURE 2 | Details (location and sequence) for each primer used in our RT-LAMP-VF assay. The target region spanned nucleotides 2065–2277 of the complete genome of WNV strain NY99 (GenBank Accession: DQ211652); this region is located in the E gene of WNV.

TABLE 1 | Primer sequences used for the RT-LAMP-VF assay.

Primer name	Sequences (5′ to 3′)	Genome position
LAMP-F3	GCCAACGCTAAGGTCCTG	2065–2082
LAMP-B3	TGAGGTGAACACCCCTCC	2260–2277
LAMP-FIP (F1C + F2)	TCCAGACTTGTGCCAATGGTGA TTGGAACCACCCTTTGGAGA	F1C:2148–2169 F2:2089–2108
LAMP-BIP (B1C + B2)	GGCAAAGCCTTTACAACCACCC CAAAGTCCCAAGCTGTGTCT	B1C:2179–2200 B2:2232–2251
LAMP-LF[a]	Biotin-TGTTGTTCTCCTCTGCCCAC	2122–2141
LAMP-LB[b]	FITC-TCAAAGGAGCGCAGAGACTAG	2201–2221

[a]*The 5′ ends of the LAMP-LF was labeled with biotin.* [b]*The 5′ ends of the LAMP-LB was labeled with FITC.*

polymerase large fragment (New England BioLabs), and 5 μl of target RNA. The mixture was incubated at varying temperatures (58, 60, 62, 64, or 66°C) for 60 min, followed by heating at 80°C for 2 min to terminate the reaction. The mixture was incubated for different lengths of time (30, 40, 50 or 60 min) at the optimal temperature. In parallel with the optimization of the reaction time, two different concentrations were used: one group of the six primers was used at the concentration described above, and the other group was used at half this concentration. The RT-LAMP products were detected using a VF visualization strip (Ustar Biotech Co., Ltd., Hangzhou, China) as previously described (Cui et al., 2012).

Specificity and Sensitivity of the RT-LAMP-VF Assay

RNAs of rRABV-WNVE (10^5 $TCID_{50}$/ml), JEV (10^5 PFU/ml), dengue virus (DENV, 10^5 PFU/ml), and classical swine fever virus (CSFV, 10^5 $TCID_{50}$/ml) were extracted using a commercial RNA extraction kit (RNeasy Mini Kit, Qiagen, Hilden, Germany). All operations were performed according to the manufacturer's instructions, and the level of extracted RNAs was determined as 80–120 ng/μl. To evaluate the specificity of the RT-LAMP-VF assay, 5 μl of RNAs extracted from above viruses and synthesized RNA transcripts (10^7 copies/μl) were added into the optimal reaction system.

The synthesized WNV RNA transcripts (1092 ng/μl) were purified, quantified, and prepared as standard samples with a concentration of 10^9 copies/μl. Then, 10-fold serial dilutions of the standard samples (ranging from 10^7 to 10^0 copies/μl) were used to assess the detection limits of the RT-LAMP-VF assay.

Evaluation of the RT-LAMP-VF Assay Using Live Virus RNA

Viral RNA extracted from rRABV-WNVE was used to further evaluate the performance ability of the RT-LAMP-VF assay. rRABV-WNVE at a titer of $10^{6.5}$ $TCID_{50}$/ml was 10-fold serial diluted in DMEM. RNA was extracted from the dilutions, and the RNA samples were detected using the RT-LAMP-VF assay.

Evaluation of the RT-LAMP-VF Assay Using Clinical Specimens

The feasibility of using the RT-LAMP-VF assay to detect WNV in clinical specimens was evaluated using 5-day-old and 3-week-old ICR mice. The mice were randomly divided into seven groups and intracerebrally infected with 10-fold dilutions of rRABV-WNVE ranging from 10^6 to 10^1 $TCID_{50}$ per mouse. DMEM was used as a placebo. At 7 days post-infection, the mice were submitted to humane euthanasia by cervical dislocation under ketamine-xylazine anesthesia at a dose of 0.1 mL/10 g body weight, after which their brains were collected. The brain samples were then homogenized in phosphate-buffered saline (PBS, 10 mM, pH 7.2–7.4). The homogenates were centrifuged to remove debris, and the supernatants were collected for RNA extraction and virus titration.

Total RNA was extracted from the brain homogenate using an RNAeasy Mini Kit (Qiagen, Hilden, Germany). The extracted RNA was then assessed using the RT-LAMP-VF assay and real-time PCR as described previously (Yang et al., 2012). After viral titration, the brain homogenate with a high titer of 7.03 Log ($TCID_{50}$/g tissue) was selected to evaluate the sensitivity of the assay. To accomplish this, RNA was extracted from a 10-fold serial dilution of the brain homogenate and measured using the

RT-LAMP-VF assay; brain homogenate from healthy mice was used as a control.

Ethics Statement

All animal studies performed in this work were approved by the Animal Care and Use Committee of the Chinese People's Liberation Army (No. SYXK2009-045). All volunteers involved in this study provided written informed consent for the use of blood samples. All efforts were made to minimize animal suffering.

RESULTS

Product Detection Using the RT-LAMP-VF Assay

When using the VF visualization strip, a clearly visible red-purple band at the control line was necessary for the test to be considered valid. The appearance of two red-purple bands at both the test and control lines was regarded as a positive result. If only the band at the control line appeared, then the result was considered negative (**Figure 3**).

Optimization of RT-LAMP-VF Reaction Conditions

To determine the optimal conditions for the RT-LAMP-VF assay, synthesized RNA transcripts were used as a template to optimize both assay temperature and assay time. To determine the optimal temperature for the assay, 60-min reactions were performed at five different temperatures (58, 60, 62, 64, and 66°C). The results indicated that running the assay at 64°C produced the strongest amplification signal (**Table 2**); therefore, 64°C was considered the optimal temperature for the assay.

To determine the optimal duration of time required for the RT-LAMP-VF assay, four different reaction times (30, 40, 50, or 60 min) were compared at 64°C. The best sensitivity and specificity were found when the reaction lasted for 40 min at 64°C (**Table 3**). Therefore, an amplification time of 40 min was selected as the optimal time for the assay.

As shown in **Table 3**, primer concentration was also optimized when optimizing the reaction time. The following primer concentrations were considered optimal: 0.4 μM for the inner primers FIP and BIP, 0.2 μM for the loop primers LF and LB, and 0.1 μM for the outer primers F3 and B3.

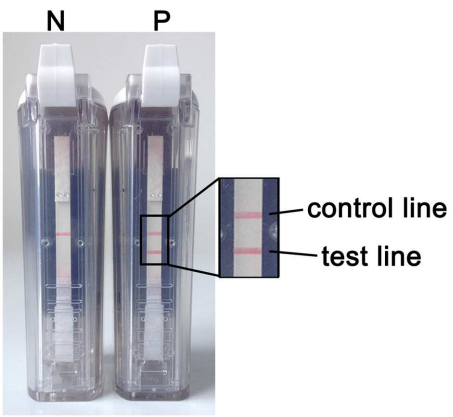

FIGURE 3 | RT-LAMP-VF assay results. *N* denotes a negative result. In this case, only one red-purple band appears at the control line. *P* denotes a positive result. In this case, two red-purple bands appear: one at the test line and one at the control line.

TABLE 2 | Reaction temperature optimization for RT-LAMP[a].

Temperature/°C	RNA dilution (Copies/μl)							
	10^7	10^6	10^5	10^4	10^3	10^2	10^1	10^0
58	+	+	+	+	−	−	−	−
60	+	+	+	+	−	−	−	−
62	+	+	+	+	+[b]	−	−	−
64	+	+	+	+	+	−	−	−
66	+	+	+	+	−	−	−	−

[a]*Three replications were performed for each trial.* [b]*The result was weakly positive.*

Specificity of the RT-LAMP-VF Assay

The analytical specificity of the RT-LAMP-VF assay was determined using synthesized RNA transcripts and RNA extracted from control viruses, including JEV, DENV, and CSFV. As shown in **Figure 4**, all of the tested control samples appeared identical to the blank control and produced only one red–purple band at the location of the control line; therefore, all of these samples produced negative test results. A positive test line was observed when using synthetic WNV RNA transcripts and RNA extracted from rRABV-WNVE as templates. Thus, because the RT-LAMP-VF assay had no cross-reactivity with other viruses related to WNV, the assay was considered to have high specificity.

Sensitivity of the RT-LAMP-VF Assay

Synthetic WNV RNA transcripts were 10-fold serially diluted to create samples ranging in concentration from 10^7 to 10^0 copies

TABLE 3 | Reaction time optimization for RT-LAMP[a].

Time/min	Primers group	RNA dilution (Copies/μl)							
		10^7	10^6	10^5	10^4	10^3	10^2	10^1	10^0
30	1[b]	+	+	+[d]	+[d]	−	−	−	−
	2[c]	+	+	+	+	−	−	−	−
40	1	+	+	+	+	+	+	−	−
	2	+	+	+	+	−	−	−	−
50	1	+	+	+	+	+	−	−	−
	2	+	+	+	+	−	−	−	−
60	1	+	+	+	+[d]	−	−	−	−
	2	+	+	+	+	+	−	−	−

[a]*Three replications were performed for each trial.* [b]*The six primers was used as described as bellow: 0.4 μM each of inner primers FIP and BIP, 0.2 μM loop primers LF and LB, 0.1 μM outer primers F3 and B3.* [c]*The six primers was used as described as bellow: 0.2 μM each of inner primers FIP and BIP, 0.1 μM loop primers LF and LB, 0.05 μM outer primers F3 and B3.* [d]*The result was weakly positive.*

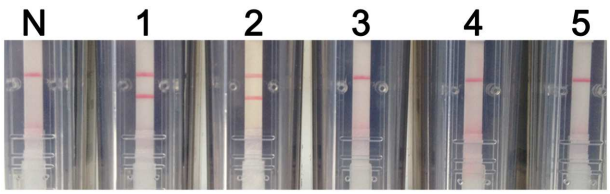

FIGURE 4 | RT-LAMP-VF assay specificity. The specificity of the RT-LAMP-VF assay was determined by analyzing synthesized RNA transcripts and RNA extracted from rRABV-WNVE, JEV, DENV, and CSFV. N: blank control; 1: synthesized RNA transcripts; 2: rRABV-WNVE RNA; 3: JEV RNA; 4: DENV RNA; 5: CSFV RNA.

per μl. These samples were then used to assess the sensitivity of the RT-LAMP-VF assay. After a 40-min amplification reaction, negative results were produced at concentrations lower than 10^2 copies/μl. Thus, the RT-LAMP-VF assay had a detection limit of 10^2 copies/μl of synthetic RNA (**Figure 5**).

Evaluation of the RT-LAMP-VF Assay Using Live Virus RNA

Total RNA was extracted from serial dilutions of rRABV-WNVE and then assessed using the RT-LAMP-VF assay. As shown in **Figure 6**, RNA extracted from a 10^5-fold dilution of virus ($10^{1.5}$ $TCID_{50}$/ml) produced positive results when assayed; thus, the detection limit of the assay for rRABV-WNVE in cell culture is $10^{1.5}$ $TCID_{50}$/ml. To confirm the absence of non-specific reactions, total RNA extracted from DMEM and NA cells was also evaluated; no amplification was found in either case.

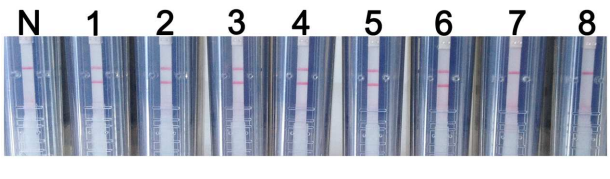

FIGURE 5 | RT-LAMP-VF assay sensitivity. The sensitivity of the RT-LAMP-VF assay was analyzed by using tenfold serial dilutions of synthesized RNA transcripts. N: blank control; 1: 10^7 copies/μl; 2: 10^6 copies/μl; 3: 10^5 copies/μl; 4: 10^4 copies/μl; 5: 10^3 copies/μl; 6: 10^2 copies/μl; 7: 10^1 copies/μl; 8: 10^0 copies/μl.

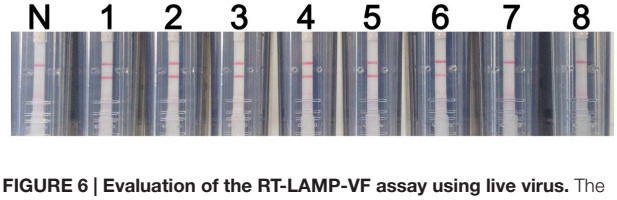

FIGURE 6 | Evaluation of the RT-LAMP-VF assay using live virus. The sensitivity of the RT-LAMP-VF assay was analyzed by using 10-fold serial dilutions of recombinant virus (rRABV-WNVE). N: blank control; 1: $10^{6.5}$ $TCID_{50}$/ml; 2: $10^{5.5}$ $TCID_{50}$/ml; 3: $10^{4.5}$ $TCID_{50}$/ml; 4: $10^{3.5}$ $TCID_{50}$/ml; 5: $10^{2.5}$ $TCID_{50}$/ml; 6: $10^{1.5}$ $TCID_{50}$/ml; 7: $10^{0.5}$ $TCID_{50}$/ml; 8: $10^{-0.5}$ $TCID_{50}$/ml.

Evaluation of the RT-LAMP-VF Assay Using Clinical Specimens

Brain tissues collected from mice infected with rRABV-WNVE were used as clinical specimens to further evaluate the RT-LAMP-VF assay. As shown in **Table 4**, rRABV-WNVE mRNA in the range of 6.14–10.02 Log(copy number/g tissue) was extracted from the brains of rRABV-WNVE-infected suckling mice, corresponding to viral titers in the range of 4.31–7.35 Log($TCID_{50}$/g tissue); the RT-LAMP-VF results were positive across this entire range. Unlike the suckling mice, substantially less rRABV-WNVE mRNA was extracted from the brains of 3-week-old mice brain: from 2.16 to 5.56 Log(copy number/g tissue) mRNA was extracted, and two of the samples from the 10^2 group were not detected. Thus, viral titers could not be determined for the 3-week-old mice; however, all of the RT-LAMP-VF results were positive, except for three samples in the 10^1 and 10^2 groups (**Table 5**).

The sensitivity of the RT-LAMP-VF assay was further evaluated using brain homogenates collected from rRABV-WNVE-infected mice; brain homogenates from uninfected mice were used as a control. After diluting the rRABV-WNVE-infected

TABLE 4 | Assay detection results from suckling mouse brain tissue samples.

Samples[a]		mRNA [Log (copy number/g tissue)]	Virus titers [Log ($TCID_{50}$/g tissue)]	RT-LAMP
Blank		Not detected	Not detected	–
Negative 1		Not detected	Not detected	–
Negative 2		Not detected	Not detected	–
10^1	1	8.05	5.32	+
	2	7.21	6.67	+
	3	9.59	5.67	+
	4	6.14	6.66	+
10^2	1	9.29	6.15	+
	2	10.02	7.03	+
	3	9.28	7.27	+
	4	7.30	6.18	+
10^3	1	8.93	5.46	+
	2	8.46	6.24	+
	3	8.14	6.33	+
	4	7.65	5.68	+
10^4	1	7.58	6.18	+
	2	9.45	5.09	+
	3	7.35	7.21	+
	4	6.51	6.16	+
10^5	1	8.96	6.62	+
	2	8.79	4.31	+
	3	7.48	7.35	+
	4	7.17	7.34	+
10^6	1	8.38	5.22	+
	2	8.28	6.65	+
	3	9.27	4.35	+
	4	8.82	6.23	+

[a] *10^1, 10^2, 10^3, 10^4, 10^5, 10^6 are the virus dose which was infected in mice ($TCID_{50}$/mouse); 1, 2, 3 are different numbers of mouse in each group.*

TABLE 5 | Assay detection results from 3-week-old mouse brain tissue samples.

Samples[a]		mRNA [Log (copy number/g tissue)]	Virus titers [Log ($TCID_{50}$/g tissue)]	RT-LAMP
Blank		Not detected	Not detected	−
Negative 1		Not detected	Not detected	−
Negative 2		Not detected	Not detected	−
10^1	1	2.36	Not detected	+
	2	4.11	Not detected	+
	3	2.16	Not detected	−
10^2	1	Not detected	Not detected	−
	2	Not detected	Not detected	−
	3	2.49	Not detected	+
10^3	1	4.73	Not detected	+
	2	3.02	Not detected	+
	3	5.11	Not detected	+
10^4	1	3.23	Not detected	+
	2	5.76	Not detected	+
	3	3.52	Not detected	+
10^5	1	3.53	Not detected	+
	2	4.00	Not detected	+
	3	4.13	Not detected	+
10^6	1	4.68	Not detected	+
	2	4.97	Not detected	+
	3	5.56	Not detected	+

[a] *10^1, 10^2, 10^3, 10^4, 10^5, 10^6 are the virus dose which was infected in mice ($TCID_{50}$/mouse); 1, 2, 3, 4 are different numbers of mouse in each group.*

brain homogenates by 10^5-fold, the RT-LAMP-VF assay still produced positive results. Therefore, the sensitivity of the assay for rRABV-WNV-infected mouse brain tissue is $10^{1.33}$ $TCID_{50}$/ml.

DISCUSSION

With the unexpected appearance of WNV in many countries, it is becoming increasingly important to develop adequate surveillance methods for WNV. Such methods are needed not only in countries where WNV infections are epidemic but also in countries threatened by WNV infection and even in countries where WNV infection has not yet spread. In addition, the development of a rapid and reliable method for diagnosing WNV is critically important for the prevention of infection, the implementation of appropriate countermeasures, and the optimization of healthcare resources. In the current study, we described the development of a RT-LAMP-VF assay that provides a simple and rapid method to detect WNV infection.

To accomplish the above, we analyzed the complete genome sequences of 30 strains of WNV isolated over various years from different regions and disparate species, including representative strains from WNV lineages 1, 2, and 3. Bases on this analysis, we selected two target regions for RT-LAMP-VF, a region located in the E gene and a region located in the 5′-UTR and spanning part of the C gene. However, when using the RT-LAMP-VF assay to detect the latter region, the assay produced low sensitivity (data not shown). Several previously reported molecular biology methods have used the E gene as a target sequence with excellent results, consistent with our previous study (Parida et al., 2004; Zink et al., 2013; Kumar et al., 2014). Therefore, we chose a relatively conserved region of the genome spanning nucleotide positions 2065–2277 as a target sequence.

We designed a set of six primers (including two loop primers) targeting eight regions located in the conserved region of the WNV E gene to ensure high specificity for nucleic acid amplification. The use of loop primers accelerated the reaction time, enabling the reaction to be completed in less than half the time required for our original LAMP assay (Nagamine et al., 2002). Indeed, amplification could be completed within 40 min, which is faster than other molecular biology methods.

Compared to other molecular biology detection technologies, the RT-LAMP-VF assay is economical, technically simple, and rapid. For this assay, reverse transcription and cDNA amplification are performed in a single step, and no additional procedures are needed. Moreover, some conventional molecular biology methods, such as RT-PCR, nested RT-PCR and real-time PCR, have inherent flaws; in particular, specialized PCR instruments are needed, and temperature must be precisely controlled for a lengthy period of time. This inhibits the application of these methods in rural and remote areas (Deng et al., 2015). As the reaction conditions for RT-LAMP-VF are isothermal, only a water bath is needed to complete the assay, offering a measure of practicality for field laboratories in economically impoverished areas.

Parida et al. (2004) developed a RT-LAMP method for the rapid detection of WNV. In this method, the results were analyzed using agarose gel electrophoresis or real-time turbidity analysis (Parida et al., 2004). Generally, the use of gel electrophoresis to detect amplification products increases the risk of product contamination and degradation, while real-time turbidity analysis suffers from background interference (Iwamoto et al., 2003; Ge et al., 2013). In the current study, we modified the RT-LAMP technique by using two loop primers labeled with FITC and biotin. This allowed labeled amplification products to be analyzed using a VF visualization strip housed inside of an enclosed, plastic, leak-proof device, without the need for an electrophoresis apparatus or a turbidimeter. Within the strip, the FITC-labeled amplification products can bind to the anti-FITC antibody located on the test line, and the biotin-labeled amplification products are captured by colloidal gold particles conjugated to the anti-biotin antibodies (Chow et al., 2008; Cui et al., 2012). Using this strategy, we reduced not only the reaction time but also the chances of product contamination. Moreover, the results of the assay can be directly visualized within 2 min, and the plastic device was designed to prevent leakage of the amplification products.

As encephalitis is the main clinical symptom of WNV infection, we used brain samples from *Charadrius alexandrinus* and *Recurvirostra avosetta* to evaluate the specificity of the RT-LAMP-VF assay. All of the samples were negative (data not shown). Clinical specimens infected with WNV (e.g., blood and brain tissue) are difficult to obtain in non-endemic countries such as China; however, we hypothesized that using

a recombinant virus expressing the E gene of WNV would produce similar assay results. Therefore, we assessed brain tissues collected from rRABV-WNVE-infected mice as clinical specimens in this study. Our results indicated that the assay could successfully detect clinical samples infected with the recombinant virus. Additionally, the assay thresholds for detecting cell culture samples infected with the recombinant virus (sensitivity: $10^{1.5}$ $TCID_{50}$/ml) and mouse brain tissues infected with the recombinant virus (sensitivity: $10^{1.33}$ $TCID_{50}$/ml) were nearly identical, which indicated that the presence of tissue-specific RNA did not influence the performance of the RT-LAMP-VF assay. Furthermore, three of the samples collected from the 3-week-old ICR mice had very little rRABV-WNVE mRNA, and the RT-LAMP-VF results were negative for these samples. This result indicates that the assay's results may be ambiguous in cases of very small viral loads. Under such conditions, sample detection should be performed in duplicate or combined with other methods. To simulate brief viremia, blood samples from healthy volunteers were mixed with rRABV-WNVE and evaluated using the RT-LAMP-VF assay. In this case, similar results were produced as those generated by the rRABV-WNVE-infected mouse brain tissues (data not shown). The broad capacity to accurately identify the presence of WNVE in clinical specimens validated the RT-LAMP-VF assay for the detection of WNV infection.

In summary, we developed a method to diagnose WNV using isothermal amplification combined with a VF visualization strip. This method was shown to have high specificity and high sensitivity for the detection of WNV. To simulate clinical samples, brain tissue infected with a recombinant virus expressing the E gene of WNV was evaluated. The results showed that the assay could accurately detect the virus with no interference from tissue-specific RNA. Furthermore, in the clinic, viral RNA loads reach higher levels than the detection limit of our assay (Ramos et al., 2012; Caraballo et al., 2015). Collectively, the above results demonstrate that our RT-LAMP-VF assay offers rapid, simple and effective diagnostic identification of WNV infection.

AUTHOR CONTRIBUTIONS

HW, SY, and XX designed the experiments. ZC, LW, LL, HJ, CX, FY, JW, QL, YZ, and TW performed the experiment. ZC, HW, LL, YG, YL, SY, and XX analyzed the data. ZC and HW wrote the manuscript. All authors reviewed the manuscript.

ACKNOWLEDGMENT

This work was supported in part by the military medical health project grant (NO. 13CXZ024) and National Key Technologies R&D Program (No. 2013BAD12B04).

REFERENCES

Brinton, M. A. (2002). The molecular biology of West Nile Virus: a new invader of the western hemisphere. *Annu. Rev. Microbiol.* 56, 371–402. doi: 10.1146/annurev.micro.56.012302.160654

Caraballo, E. V., Hunsperger, E., and Martinez, I. (2015). Characterization of puerto rican west nile virus isolates in mice. *Virol. J.* 12:137. doi: 10.1186/s12985-015-0363-8

Chow, W. H., McCloskey, C., Tong, Y., Hu, L., You, Q., Kelly, C. P., et al. (2008). Application of isothermal helicase-dependent amplification with a disposable detection device in a simple sensitive stool test for toxigenic *Clostridium difficile*. *J. Mol. Diagn.* 10, 452–458. doi: 10.2353/jmoldx.2008.080008

Cui, L., Ge, Y., Qi, X., Xu, G., Li, H., Zhao, K., et al. (2012). Detection of severe fever with thrombocytopenia syndrome virus by reverse transcription-cross-priming amplification coupled with vertical flow visualization. *J. Clin. Microbiol.* 50, 3881–3885. doi: 10.1128/JCM.01931-12

Dauphin, G., and Zientara, S. (2007). West Nile virus: recent trends in diagnosis and vaccine development. *Vaccine* 25, 5563–5576. doi: 10.1016/j.vaccine.2006.12.005

De Filette, M., Ulbert, S., Diamond, M., and Sanders, N. N. (2012). Recent progress in West Nile virus diagnosis and vaccination. *Vet. Res.* 43:16. doi: 10.1186/1297-9716-43-16

Del Amo, J., Sotelo, E., Fernandez-Pinero, J., Gallardo, C., Llorente, F., Aguero, M., et al. (2013). A novel quantitative multiplex real-time RT-PCR for the simultaneous detection and differentiation of West Nile virus lineages 1 and 2, and of Usutu virus. *J. Virol. Methods* 189, 321–327. doi: 10.1016/j.jviromet.2013.02.019

Deng, J., Pei, J., Gou, H., Ye, Z., Liu, C., and Chen, J. (2015). Rapid and simple detection of Japanese encephalitis virus by reverse transcription loop-mediated isothermal amplification combined with a lateral flow dipstick. *J. Virol. Methods* 213, 98–105. doi: 10.1016/j.jviromet.2014.12.006

Deubel, V., Fiette, L., Gounon, P., Drouet, M. T., Khun, H., Huerre, M., et al. (2001). Variations in biological features of West Nile viruses. *Ann. N. Y. Acad. Sci.* 951, 195–206. doi: 10.1111/j.1749-6632.2001.tb02697.x

Faggioni, G., De Santis, R., Pomponi, A., Fantini, M., Savini, G., Monaco, F., et al. (2014). Rapid molecular detection and genotyping of West Nile Virus lineages 1 and 2 by real time PCR and melting curve analysis. *J. Virol. Methods* 207, 54–59. doi: 10.1016/j.jviromet.2014.06.020

Ge, Y., Wu, B., Qi, X., Zhao, K., Guo, X., Zhu, Y., et al. (2013). Rapid and sensitive detection of novel avian-origin influenza A (H7N9) virus by reverse transcription loop-mediated isothermal amplification combined with a lateral-flow device. *PLoS ONE* 8:e69941. doi: 10.1371/journal.pone.0069941

Gubler, D. J. (2001). Human arbovirus infections worldwide. *Ann. N. Y. Acad. Sci.* 951, 13–24. doi: 10.1111/j.1749-6632.2001.tb02681.x

Hayes, E. B., and Gubler, D. J. (2006). West Nile virus: epidemiology and clinical features of an emerging epidemic in the United States. *Annu. Rev. Med.* 57, 181–194. doi: 10.1146/annurev.med.57.121304.131418

Hayes, E. B., and O'Leary, D. R. (2004). West Nile virus infection: a pediatric perspective. *Pediatrics* 113, 1375–1381. doi: 10.1542/peds.113.5.1375

Iwamoto, T., Sonobe, T., and Hayashi, K. (2003). Loop-mediated isothermal amplification for direct detection of *Mycobacterium tuberculosis* complex, *M. avium*, and *M. intracellulare* in sputum samples. *J. Clin. Microbiol.* 41, 2616–2622. doi: 10.1128/JCM.41.6.2616-2622.2003

Kumar, J. S., Saxena, D., and Parida, M. (2014). Development and comparative evaluation of SYBR Green I-based one-step real-time RT-PCR assay for detection and quantification of West Nile virus in human patients. *Mol. Cell. Probes* 28, 221–227. doi: 10.1016/j.mcp.2014.03.005

Kurosaki, Y., Takada, A., Ebihara, H., Grolla, A., Kamo, N., Feldmann, H., et al. (2007). Rapid and simple detection of Ebola virus by reverse transcription-loop-mediated isothermal amplification. *J. Virol. Methods* 141, 78–83. doi: 10.1016/j.jviromet.2006.11.031

Lanciotti, R. S., Ebel, G. D., Deubel, V., Kerst, A. J., Murri, S., Meyer, R., et al. (2002). Complete genome sequences and phylogenetic analysis of West Nile virus strains isolated from the United States, Europe, and the Middle East. *Virology* 298, 96–105. doi: 10.1006/viro.2002.1449

Lim, S. M., Koraka, P., Osterhaus, A. D., and Martina, B. E. (2011). West Nile virus: immunity and pathogenesis. *Viruses* 3, 811–828. doi: 10.3390/v3060811

Mikawa, A. Y., Santos, S. A., Kenfe, F. R., da Silva, F. H., and da Costa, P. I. (2009). Development of a rapid one-step immunochromatographic

assay for HCV core antigen detection. *J. Virol. Methods* 158, 160–164. doi: 10.1016/j.jviromet.2009.02.013

Mukhopadhyay, S., Kim, B. S., Chipman, P. R., Rossmann, M. G., and Kuhn, R. J. (2003). Structure of West Nile virus. *Science* 302, 248. doi: 10.1126/science.1089316

Nagamine, K., Hase, T., and Notomi, T. (2002). Accelerated reaction by loop-mediated isothermal amplification using loop primers. *Mol. Cell. Probes* 16, 223–229. doi: 10.1006/mcpr.2002.0415

Nash, D., Mostashari, F., Fine, A., Miller, J., O'Leary, D., Murray, K., et al. (2001). The outbreak of West Nile virus infection in the New York City area in 1999. *N. Engl. J. Med.* 344, 1807–1814. doi: 10.1056/NEJM200106143442401

Notomi, T., Okayama, H., Masubuchi, H., Yonekawa, T., Watanabe, K., Amino, N., et al. (2000). Loop-mediated isothermal amplification of DNA. *Nucleic Acids Res.* 28:E63. doi: 10.1093/nar/28.12.e63

Parida, M., Posadas, G., Inoue, S., Hasebe, F., and Morita, K. (2004). Real-time reverse transcription loop-mediated isothermal amplification for rapid detection of West Nile virus. *J. Clin. Microbiol.* 42, 257–263. doi: 10.1128/JCM.42.1.257-263.2004

Ramos, H. J., Lanteri, M. C., Blahnik, G., Negash, A., Suthar, M. S., Brassil, M. M., et al. (2012). IL-1beta signaling promotes CNS-intrinsic immune control of West Nile virus infection. *PLoS Pathog.* 8:e1003039. doi: 10.1371/journal.ppat.1003039

Sejvar, J. J., Haddad, M. B., Tierney, B. C., Campbell, G. L., Marfin, A. A., Van Gerpen, J. A., et al. (2003). Neurologic manifestations and outcome of West Nile virus infection. *JAMA* 290, 511–515. doi: 10.1001/jama.290.4.511

Solomon, T., Ooi, M. H., Beasley, D. W., and Mallewa, M. (2003). West Nile encephalitis. *BMJ* 326, 865–869. doi: 10.1136/bmj.326.7394.865

Vazquez, A., Sanchez-Seco, M. P., Ruiz, S., Molero, F., Hernandez, L., Moreno, J., et al. (2010). Putative new lineage of west nile virus. *Spain. Emerg. Infect. Dis.* 16, 549–552. doi: 10.3201/eid1603.091033

Wang, H., Feng, N., Yang, S., Wang, C., Wang, T., Gao, Y., et al. (2010). A rapid immunochromatographic test strip for detecting rabies virus antibody. *J. Virol. Methods* 170, 80–85. doi: 10.1016/j.jviromet.2010.09.002

Wang, H., Zhang, G., Wen, Y., Yang, S., Xia, X., and Fu, Z. F. (2011). Intracerebral administration of recombinant rabies virus expressing GM-CSF prevents the development of rabies after infection with street virus. *PLoS ONE* 6:e25414. doi: 10.1371/journal.pone.0025414

Whiting, S. H., and Champoux, J. J. (1998). Properties of strand displacement synthesis by *Moloney murine* leukemia virus reverse transcriptase: mechanistic implications. *J. Mol. Biol.* 278, 559–577. doi: 10.1006/jmbi.1998.1720

Yang, Y. J., Zhao, P. S., Zhang, T., Wang, H. L., Liang, H. R., Zhao, L. L., et al. (2012). Small interfering RNAs targeting the rabies virus nucleoprotein gene. *Virus Res.* 169, 169–174. doi: 10.1016/j.virusres.2012.07.024

Zink, S. D., Jones, S. A., Maffei, J. G., and Kramer, L. D. (2013). Quadraplex qRT-PCR assay for the simultaneous detection of Eastern equine encephalitis virus and West Nile virus. *Diagn. Microbiol. Infect. Dis.* 77, 129–132. doi: 10.1016/j.diagmicrobio.2013.06.019

Conflict of Interest Statement: The authors declare that the research was conducted in the absence of any commercial or financial relationships that could be construed as a potential conflict of interest.

Copyright © 2016 Cao, Wang, Wang, Li, Jin, Xu, Feng, Wang, Li, Zhao, Wang, Gao, Lu, Yang and Xia. This is an open-access article distributed under the terms of the Creative Commons Attribution License (CC BY). The use, distribution or reproduction in other forums is permitted, provided the original author(s) or licensor are credited and that the original publication in this journal is cited, in accordance with accepted academic practice. No use, distribution or reproduction is permitted which does not comply with these terms.

frontiers in Microbiology

ORIGINAL RESEARCH
published: 14 April 2016
doi: 10.3389/fmicb.2016.00488

Finite Element Analysis on Nanomechanical Detection of Small Particles: Toward Virus Detection

Gaku Imamura[1]*, *Kota Shiba*[1,2] *and Genki Yoshikawa*[1]

[1] World Premier International Research Center Initiative, International Center for Materials Nanoarchitectonics, National Institute for Materials Science, Tsukuba, Japan, [2] International Center for Young Scientists, National Institute for Materials Science, Tsukuba, Japan

Detection of small particles, including viruses and particulate matter (PM), has been attracting much attention in light of increasing need for environmental monitoring. Owing to their high versatility, a nanomechanical sensor is one of the most promising sensors which can be adapted to various monitoring systems. In this study, we present an optimization strategy to efficiently detect small particles with nanomechanical sensors. Adsorption of particles on the receptor layer of nanomechanical sensors and the resultant signal are analyzed using finite element analysis (FEA). We investigate the effect of structural parameters (e.g., adsorption position and embedded depth of a particle and thickness of the receptor layer) and elastic properties of the receptor layer (e.g., Young's modulus and Poisson's ratio) on the sensitivity. It is found that a membrane-type surface stress sensors (MSS) has the potential for robust detection of small particles.

Keywords: nanomechanical sensors, cantilever sensors, membrane-type surface stress sensors (MSS), finite element analysis (FEA), virus detection

OPEN ACCESS

Edited by:
Akihide Ryo,
Yokohama City University, Japan

Reviewed by:
Takatoki Yamamoto,
Tokyo Institute of Technology, Japan
Keiichiro Kushiro,
The University of Tokyo, Japan
Ryuichi Sugiyama,
Yokohama City University School of Medicine, Japan

***Correspondence:**
Gaku Imamura
imamura.gaku@nims.go.jp

Specialty section:
This article was submitted to Virology, a section of the journal Frontiers in Microbiology

Received: *22 January 2016*
Accepted: *24 March 2016*
Published: *14 April 2016*

Citation:
Imamura G, Shiba K and Yoshikawa G (2016) Finite Element Analysis on Nanomechanical Detection of Small Particles: Toward Virus Detection. Front. Microbiol. 7:488. doi: 10.3389/fmicb.2016.00488

INTRODUCTION

Nanomechanical sensors have been attracting great attention because of their versatility. For example, they can detect diverse chemical species ranging from gaseous to biological molecules, including volatile organic compounds (VOCs), DNA, and proteins (Barnes et al., 1994; Gimzewski et al., 1994; Thundat et al., 1994; Buchapudi et al., 2011). Detection of bioorganisms such as viruses and bacteria has also been reported (Buchapudi et al., 2011). Since the first demonstration of nanomechanical sensing in 1994 (Gimzewski et al., 1994), cantilever-type sensors with optical read-outs have been widely used. In 2011, a membrane-type surface stress sensor (MSS) was developed and achieved both high sensitivity and small size by means of structural optimization with chip-integrated piezoresistive read-out (Yoshikawa et al., 2011). This MSS platform also demonstrated the detection of proteins using a simple dipping system that is compatible with a standard 96-well plate for practical assays (Hosokawa et al., 2014).

Owing to these advantages, nanomechanical sensors are expected to be a key technology to environmental monitoring systems. In addition to toxic chemical species in air, there is a great need for detection of airborne particles including dust, particulate matter (PM), and viruses (Aliabadi et al., 2011; Després et al., 2012; Nemmar et al., 2013; Kim et al., 2015). As nanomechanical sensors can recognize such particles by detecting mechanical properties, it is important to understand the mechanics of the nanomechanical sensing system: Adsorption of particles on the receptor layer and the stress and deformation caused by adsorbed particles.

In the present study, we investigate the nanomechanical detection of particles using finite element analysis (FEA). We focus on the two types of nanomechanical sensors; cantilever-type sensors and MSS, and explore an optimized structure for the efficient detection of particles through the mechanical stress induced in the receptor layer. We also discuss the perspective on virus detection using these nanomechanical sensors.

MATERIALS AND METHODS

Analytical solutions of nanomechanical sensing are available for a simple cantilever model. For example, the deflection of the free-end of a cantilever (Δz) induced by isotropic internal strain in a receptor layer (ε_f) is given by the following equation (Yoshikawa, 2011):

$$\Delta z = \frac{3l^2\left(t_f + t_c\right)}{(A+4)\,t_f^2 + \left(A^{-1}+4\right)t_c^2 + 6t_f t_c}\varepsilon_f, \tag{1}$$

$$A = \frac{E_f w_f t_f\,(1-\nu_c)}{E_c w_c t_c\left(1-\nu_f\right)}, \tag{2}$$

where l is the length of a cantilever, and E_f (E_c), ν_f (ν_c), and t_f (t_c) are the Young's modulus, the Poisson's ratio, and the thickness of a receptor layer (a cantilever), and w_c and w_f are the width of a cantilever and a receptor layer, respectively. If a cantilever is covered with a very thin receptor layer ($t_c \gg t_f$ and $w_c = w_f$), Equation (1) reduces to the following equation, which is known as the Stoney's equation (Stoney, 1909):

$$\Delta z = \frac{3\,(1-\nu_c)\,l^2}{E_c t_c^2}\sigma_{\text{surf}}, \tag{3}$$

where σ_{surf} is the surface stress defined as $\sigma_{\text{surf}} = \sigma_f \cdot t_f$, and $\sigma_f = \varepsilon_f \cdot E_f/\left(1-\nu_f\right)$. However, the application of these models is limited to analytically simple problems. To investigate more complex systems, FEA is an effective option, providing numerical solutions. Since the adsorption of particles on a solid receptor layer with three dimensional stress distribution is too complicated to be analytically modeled, we employed FEA in the present study.

FEA simulations were performed in COMSOL Multiphysics 5.1® with the Structural Mechanics module. Each structure was meshed with 20,000∼60,000 elements, which give sufficient resolution for the present simulations. We investigated the deflection of a silicon cantilever with dimensions 500 × 100 × 1 μm as shown in **Figure 1A**. A fixed constraint was applied on one end (fixed-end). The receptor layer with a thickness of t μm is coated on the cantilever. A particle with a radius of 0.1 μm is embedded in the receptor layer with a depth of h μm, applying a constant pressure p Pa at the interface (**Figure 1B**). To simulate such a situation, we set a dent on the receptor layer with a boundary load of p Pa at the surface. The dent is located

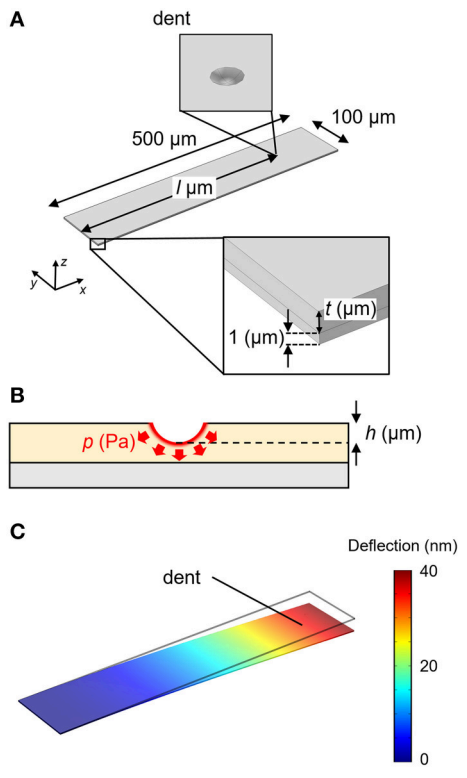

FIGURE 1 | (A) Structure of the cantilever-type sensor. **(B)** Cross sectional image of the cantilever at the dent. **(C)** Result of the FEA simulation for the cantilever-type sensor. The distribution of displacement is plotted as a color gradient.

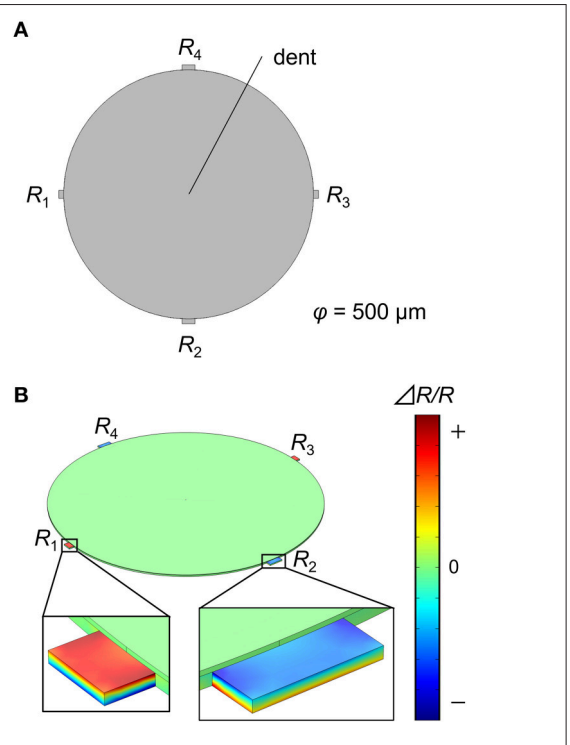

FIGURE 2 | (A) Structure of the MSS. **(B)** Result of the FEA simulation for the MSS. The distribution of relative resistance change is plotted as a color gradient.

at l μm from the fixed-end. We investigated the deflection; the displacement of the free-end of the cantilever (**Figure 1C**). In the case of MSS, the diameter and the thickness of the membrane are set at 500 and 2.5 μm, respectively, with a t-μm-thick receptor layer on it (**Figure 2A**). The dent is also placed on the receptor layer (default position is set at the center) to simulate the adsorption of a particle. We investigated the change in the relative resistance ($\Delta R_{tot}/R_{tot}$) of a full Wheatstone bridge in an MSS composed of four resistors embedded in the sensing beams, R_1–R_4 (**Figure 2B**). The sensing signal, V_{out} is approximately described as:

$$V_{out} = \frac{V_B}{4}\left(\frac{\Delta R_1}{R_1} - \frac{\Delta R_2}{R_2} + \frac{\Delta R_3}{R_3} - \frac{\Delta R_4}{R_4}\right) = \frac{V_B}{4}\left(\frac{\Delta R_{tot}}{R_{tot}}\right), \quad (4)$$

where V_B is the bridge voltage, andΔR_i is the change in the resistance of R_i (Yoshikawa et al., 2011). A fixed constraint was applied on the end of each beam.

RESULTS

Cantilever-Type Sensor

The dependence on the applied pressure, p, is investigated. It is clear that the deflection of the cantilever is exactly proportional to p over a wide range (**Figure 3A**). This result suggests that the dependence of the deflection on the other parameters is not affected by p. We confirmed this condition by investigating the dependence on the other parameters while varying p. **Figures 3B,C** show the dependence on l, showing a natural consequence of simple mechanics: a particle adsorbed near the end of the cantilever leads to a larger deflection. The depth of the dent which corresponds to the embedded depth of a particle strongly affects the deflection. **Figure 3D** shows the deflection as a function of dent depth h with a nonlinear relationship. Since the data in **Figure 3D** can be fitted well with the quadratic function, the deflection is found to be related with the projected area of the dent s [$s = \pi\ (2rh–h^2)$, where r is a radius of a particle], rather than the surface area of the dent S ($S = 2\pi rh$).

Figures 4A,B show the effects of Young's modulus E and Poisson's ratio ν, respectively. It has been found that the deflection is independent of ν, while E significantly affects the deflection. The deflection exhibits little dependence on E below 10^8 Pa. However, a higher Young's modulus yields a lower deflection when E is larger than 10^9 Pa. The thickness dependence is summarized in **Figure 4C**. It clearly shows that the thickness dependence is significantly affected by Young's modulus. The deflection decreases with increasing thickness, and it becomes drastic with $E > 10^7$ Pa.

MSS

The effects of applied pressure p, position, and dent depth h on $\Delta R_{tot}/R_{tot}$ were investigated for MSS. **Figure 5A** depicts

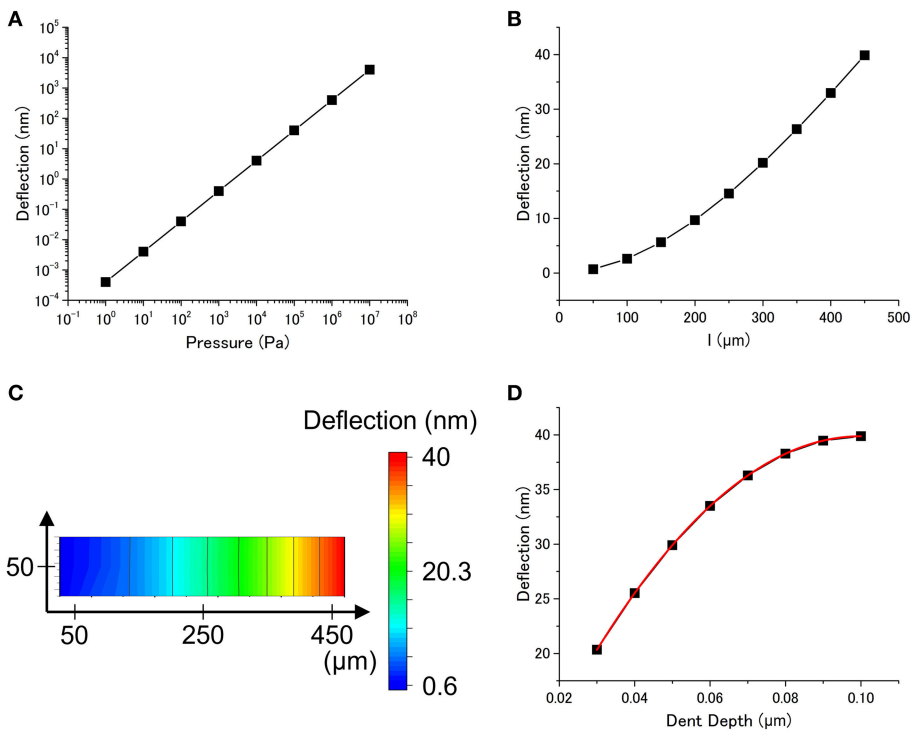

FIGURE 3 | (A) Dependence of the deflection on the applied pressure (l = 450 μm, h = 0.1 μm, t = 1 μm, E = 1 × 10^9 Pa, ν = 0.4). **(B)** Dependence of the deflection on the position of the dent (distance from the fixed end). **(C)** Dependence of the deflection on the position of the dent. The resultant cantilever deflection is plotted as a color gradient (p = 1 × 10^5 Pa, h = 0.1 μm, t = 1 μm, E = 1 × 10^9 Pa, ν = 0.4). **(D)** Dependence of the deflection on the dent depth (p = 1 × 10^5 Pa, l = 450 μm, t = 1 μm, E = 1 ×10^9 Pa, ν = 0.4). The plot is fitted with a quadratic function (red curve).

$\Delta R_{tot}/R_{tot}$ as a function of p, showing a linear relationship over a wide range. Same as a cantilever-type sensor, variation in p is found not to affect the dependence on other parameters in the case of MSS as well. **Figure 5B** shows the dependence on the position of the dent. It has been found that a higher signal can be obtained when a particle adsorbs near the center of the membrane. An interesting feature of MSS is that it is more robust in position of the dent compared to cantilever-type sensors. In the case of cantilever-type sensors, a dent at $l = 450$ μm causes ~60 times larger deflection than a dent at $l = 50$ μm. On the other hand, the signal caused by a dent at the center of MSS is not 10 times larger than the signal caused by a dent at 50 μm from the edge. This result indicates that MSS is more robust in the adsorption position of a particle compared to cantilever-type sensors. The dependence of $\Delta R_{tot}/R_{tot}$ on a dent depth h is quite similar to the case of cantilever-type sensors; a higher sensing signal can be obtained for a deeper dent (**Figure 5C**).

$\Delta R_{tot}/R_{tot}$ for various E and ν are plotted in **Figure 6**. **Figure 6A** shows $\Delta R_{tot}/R_{tot}$ has little dependence on E below 10^9 Pa, while $\Delta R_{tot}/R_{tot}$ decreases with E over 10^9 Pa. As shown in **Figure 6B**, Poisson's ratio does not significantly affect $\Delta R_{tot}/R_{tot}$ when E is below 10^9 Pa. However, a higher Poisson's ratio results in a lower $\Delta R_{tot}/R_{tot}$ in the case of $E > 10^9$ Pa. The simulated $\Delta R_{tot}/R_{tot}$ as a function of thickness is plotted in **Figure 6C**. The behavior is similar to the case of cantilever-type sensors (**Figure 4C**). The receptor layer with a soft material ($E < 10^8$ Pa) exhibits little dependence on thickness, while the signal drastically decreases with thickness for a hard material ($E > 10^8$ Pa).

DISCUSSION

The presented results indicate that a thinner and softer receptor layer will lead to a larger signal for the purpose of the detection of particles. It is known that there is an optimum thickness which yields maximum deflection in the cases of two typical nanomechanical sensing systems: the 2D stress applied homogeneously on the surface of a receptor layer, and the isotropic internal strain induced in a receptor layer (Yoshikawa, 2011; Yoshikawa et al., 2014). In contrast to such systems, an optimum thickness has not been found for any Young's moduli in the present simulation. This difference can be ascribed to the lack of the lateral stress enhancement effect in the case of particle adsorption. The effective stress induced on a sensing body is enhanced with increasing thickness of a receptor layer for the 2D stress or the isotropic internal strain because the lateral component of the force is applied further away from the neutral axis of the system. However, such effect for the present simulation is marginal because an effective force in the lateral direction is minute, hardly contributing to the deflection. Thus, the stiffening effect caused by the increase in thickness and/or Young's modulus becomes dominant, resulting in a smaller signal for thicker and stiffer receptor layer. The dependence on the position is found to be consistent with simple mechanics; a larger distance from a fixed-end provides a larger deflection in the cases of both cantilever-type and MSS.

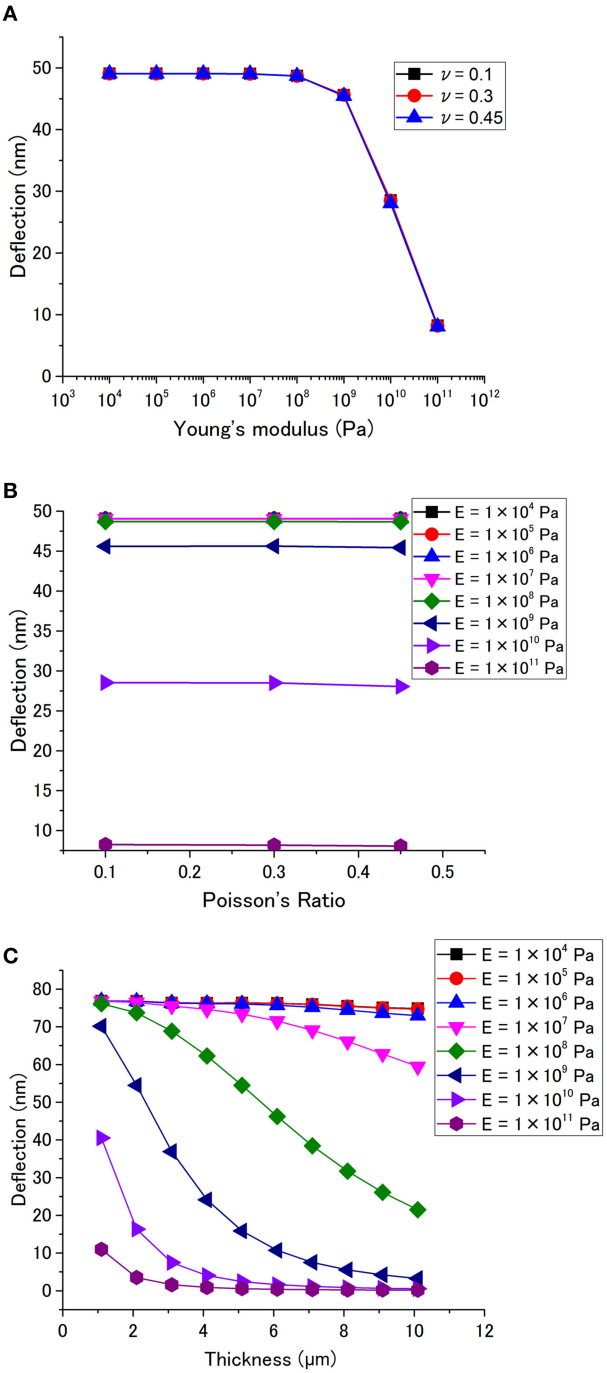

FIGURE 4 | Cantilever deflection as a function of (A) Young's modulus, and (B) Poisson's ratio. ($p = 1 \times 10^5$ Pa, $l = 450$ μm, $h = 0.1$ μm, $t = 1$ μm) **(C)** Dependence of the deflection on the thickness for different Young's modulus ($p = 1 \times 10^5$ Pa, $l = 450$ μm, $h = 0.1$ μm).

Toward Virus Detection

Based on these results, here we discuss a strategy to efficiently detect viruses with nanomechanical sensors. Several studies reported virus detection using nanomechanical sensors. These studies fall into two categories in terms of the operation

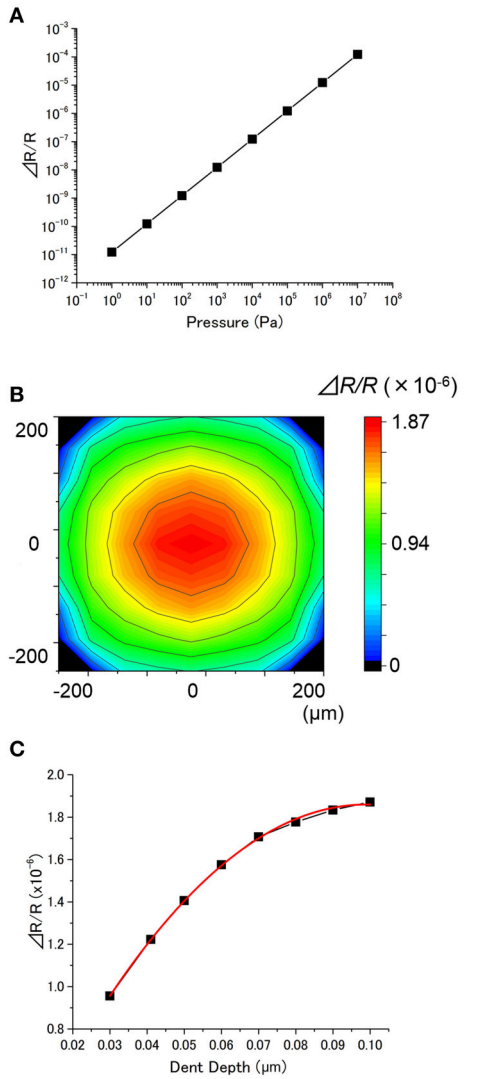

FIGURE 5 | (A) Dependence of $\Delta R/R$ on the applied pressure (the dent is at the center, $h = 0.1\,\mu m$, $t = 1\,\mu m$, $E = 1 \times 10^9$ Pa, $\nu = 0.4$). **(B)** Dependence of $\Delta R/R$ on the position of the dent. The resultant relative resistance change is plotted as a color gradient ($p = 1 \times 10^5$ Pa, $h = 0.1\,\mu m$, $t = 1\,\mu m$, $E = 1 \times 10^9$ Pa, $\nu = 0.4$). **(C)** Dependence of $\Delta R/R$ on the dent depth ($p = 1 \times 10^5$ Pa, the dent is at the center, $t = 1\,\mu m$, $E = 1 \times 10^9$ Pa, $\nu = 0.4$). The plot is fitted with a quadratic function (red curve).

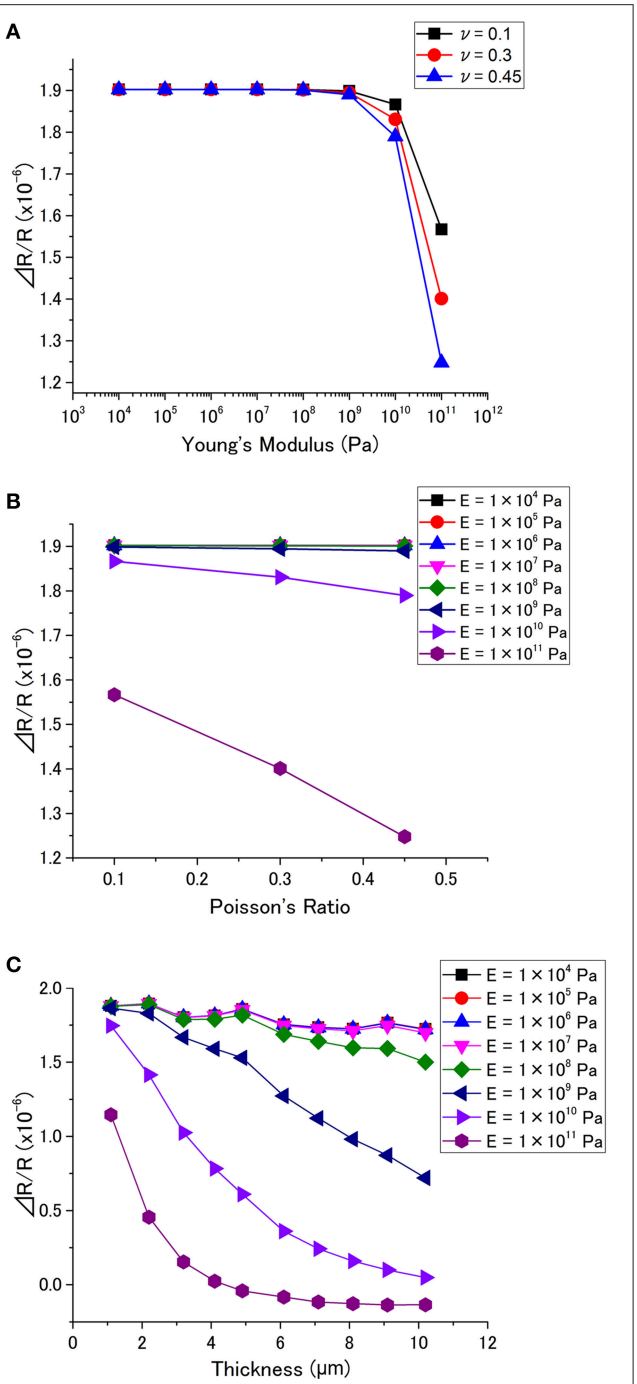

FIGURE 6 | ΔR/R as a function of (A) Young's modulus, and (B) Poisson's ratio ($p = 1 \times 10^5$ Pa, the dent is at the center, $h = 0.1\,\mu m$, $t = 1\,\mu m$). (C) Dependence of $\Delta R/R$ on the thickness for different Young's modulus ($p = 1 \times 10^5$ Pa, the dent is at the center, $h = 0.1\,\mu m$).

mode: dynamic mode and static mode. Nanomechanical sensors operated in dynamic mode detect viruses by their mass (more specifically, shifts in the resonant frequency; Johnson et al., 2006; Braun et al., 2009; Cha et al., 2009; Capobianco et al., 2010) while static mode operates based on the stress or strain (Gunter et al., 2003; Sreepriya and Hai-Feng, 2006; Alodhayb et al., 2013; Xu et al., 2014; Gorelkin et al., 2015; Kim et al., 2015). Thus, the FEA simulation in the present study can be adapted to the detection of viruses in static mode.

Previous studies revealed that the force caused by a virus attached to a cell is on the order of 10 pN (Lee et al., 2006; Sieben et al., 2012; Tsai et al., 2015). Assuming that a virus of 0.1 μm in radius is embedded 0.1 μm deep into a cell, the pressure applied to the interface is estimated to be $\sim 10^3$ Pa. In the present simulations, the applied pressure p is set at 1×10^5 Pa (**Figures 3B–D**, **4**, **5B,C**, **6**), which is two orders of magnitude higher than the pressure caused by a virus. As the deflection

and relative resistance changes of a cantilever-type sensor and MSS, respectively, are proportional to the applied pressure p, it is expected that the deflection/relative resistance change increases linearly with the number of adsorbed viruses on the receptor layer if the adsorbed positions of viruses are effectively regarded as constant. Accordingly, the presented simulations, in which p is set at 1×10^5 Pa, are comparable to a system where a hundred of viruses are attached to a specific position on the receptor layer. Considering that the typical detection limits for cantilever-type sensors and MSS are estimated as $\sim$1 nm and $\sim 10^{-6}$, respectively (Yoshikawa et al., 2011, 2012), a detectable signal can be obtained when $\sim 10^2$ of viruses adsorb near the free-end of a cantilever or the center of MSS with a receptor layer having optimal properties ($t = 1\ \mu$m, $h = 0.1\ \mu$m, $E < 10^8$ Pa). To compare with typical nanomechanical sensing based on isotropic internal strain or surface stress, we also evaluated the corresponding detectable sensing signals. We performed FEA simulations on both a cantilever and an MSS which are coated with poly (methyl methacrylate; PMMA); a commonly used polymer as a receptor material, which has the Young's modulus and the Poisson's ratio of 3×10^9 Pa and 0.4, respectively. The thickness was set at their optimum values: 2.5 and 8.0 μm for the cantilever and the MSS, respectively (Yoshikawa, 2011; Yoshikawa et al., 2014). The minimum isotropic internal strain or surface stress which induces detectable signals (e.g., 1 nm deflection for the cantilever and 10^{-6} relative resistance change for the MSS) has been estimated as $10^{-9} \sim 10^{-8}$ or $10^{-5} \sim 10^{-4}$ N/m, respectively.

In terms of the receptor material, it has been confirmed that higher sensing signals can be obtained by using a material with low Young's modulus ($<10^9$ Pa). This is a favorable condition for practical applications because most biological materials which can interact with viruses have a low Young's modulus. For example, the Young's moduli of proteins and cells which are typically used for viral cultures are $10^4 \sim 10^9$ Pa and $\sim 10^4$ Pa, respectively. Another advantage of using soft materials is that signals are less affected by thickness, leading to higher reproducibility for virus detection. It should be noted that the force caused by the viruses may not be fully transmitted to the cantilever or MSS membrane in an actual measurement system if the receptor layer is thick and soft. Since viscoelastic properties are not taken into account in the present simulations, signals can be reduced as a result of stress relaxation within a receptor layer.

As living cells are the only media where viruses can be cultivated, there is a possibility that living cells are used as receptor materials. It is expected that selectivity will be enhanced depending on the cell types only if cells are stably maintained on nanomechanical sensors. However, the noise caused by cell migration is one of the biggest experimental issues. Bischofs et al. measured the surface stress induced by an endothelial cell and estimated it to be $\sim$2 mN/m (Bischofs et al., 2009). Our FEA simulations showed that a surface stress of 2 mN/m leads to a sensing signal comparable to adsorption of $\sim 10^2$ viruses on a receptor layer. Thus, the cellular force should give rise to a non-negligible background noise. It is estimated that at least $10^2 \sim 10^3$ of viruses are needed to obtain a detectable sensing signal when living cells are used as receptor materials.

Finally, let us compare the practical aspects between a cantilever and MSS. While the sensitivity of a cantilever sensor with an optical read-out is comparable to that of an MSS, a cantilever sensor requires a bulky instrumentation. In contrast, a compact measurement system can be realized with an MSS because of the chip-integrated piezoresistive electric sensing. Furthermore, MSS exhibits higher robustness to the adsorption position and in homogeneous coating (Loizeau et al., 2015). Thus, MSS seems to be a more favorable option for practical applications such as mobile environmental monitoring systems, point-of-care-testing (POCT) and primary screening for infectious diseases, etc. Although the sensitivity of MSS is not as high as that of enzyme-linked immunosorbent assay (ELISA), which can detect $\sim 10^1$ of viruses (Pineda et al., 2009), MSS is a promising candidate for a portable real-time virus detection device based on its simple detection mechanism and the easier experimental protocols.

AUTHOR CONTRIBUTIONS

GI, KS, and GY designed the simulation models. GI conducted the finite element analysis, and wrote the main paper. All authors discussed the results and implications, and commented on the manuscript at all stages.

ACKNOWLEDGMENTS

We express our appreciation to Mr. Masaki Anraku, graduate school of medicine, Yokohama City University, for his advice on the sensitivity of ELISA. We acknowledge Mr. Max Hamilton and Ms. Manasa Kaniselvan, University of Waterloo, for a valuable discussion. This research was supported by the World Premier International Research Center Initiative (WPI) on Materials Nanoarchitectonics (MANA).

REFERENCES

Aliabadi, A. A., Rogak, S. N., Bartlett, K. H., and Green, S. I. (2011). Preventing airborne disease transmission: review of methods for ventilation design in health care facilities. *Adv. Prev. Med.* 2011, 21. doi: 10.4061/2011/124064

Alodhayb, A., Brown, N., Saydur Rahman, S. M., Harrigan, R., and Beaulieu, L. Y. (2013). Towards detecting the human immunodeficiency virus using microcantilever sensors. *Appl. Phys. Lett.* 102, 173106. doi: 10.1063/1.4803771

Barnes, J. R., Stephenson, R. J., Welland, M. E., Gerber, C., and Gimzewski, J. K. (1994). Photothermal spectroscopy with femtojoule sensitivity using a micromechanical device. *Nature* 372, 79–81. doi: 10.1038/372079a0

Bischofs, I. B., Schmidt, S. S., and Schwarz, U. S. (2009). Effect of adhesion geometry and rigidity on cellular force distributions. *Phys. Rev. Lett.* 103, 048101. doi: 10.1103/PhysRevLett.103.048101

Braun, T., (2009). Quantitative time-resolved measurement of membrane protein-ligand interactions using microcantilever array sensors. *Nat. Nano* 4, 179–185. doi: 10.1038/nnano.2008.398

Buchapudi, K. R., Huang, X., Yang, X., Ji, H.-F., and Thundat, T. (2011). Microcantilever biosensors for chemicals and bioorganisms. *Analyst* 136, 1539–1556. doi: 10.1039/c0an01007c

Capobianco, J. A., Shih, W.-H., Leu, J.-H., Lo, G. C.-F., and Shih, W. Y. (2010). Label free detection of white spot syndrome virus using lead magnesium niobate–lead titanate piezoelectric microcantilever sensors. *Biosens. Bioelectron.* 26, 964–969. doi: 10.1016/j.bios.2010.08.004

Cha, B. H., (2009). Detection of Hepatitis B Virus (HBV) DNA at femtomolar concentrations using a silica nanoparticle-enhanced microcantilever sensor. *Biosens. Bioelectron.* 25, 130–135. doi: 10.1016/j.bios.2009.06.015

Després, V. R., Huffman, J. A., Burrows, S. M., Hoose, C., Safatov, A. S., Buryak, G., et al. (2012). Primary biological aerosol particles in the atmosphere: a review. *Tellus B* 64:15598. doi: 10.3402/tellusb.v64i0.15598

Gimzewski, J. K., Gerber, C., Meyer, E., and Schlittler, R. R. (1994). Observation of a chemical reaction using a micromechanical sensor. *Chem. Phys. Lett.* 217, 589–594. doi: 10.1016/0009-2614(93)E1419-H

Gorelkin, P. V., (2015). Synthetic sialylglycopolymer receptor for virus detection using cantilever-based sensors. *Analyst* 140, 6131–6137. doi: 10.1039/C5AN01102G

Gunter, R. L., Delinger, W. G., Manygoats, K., Kooser, A., and Porter, T. L. (2003). Viral detection using an embedded piezoresistive microcantilever sensor. *Sens. Actuators A Phys.* 107, 219–224. doi: 10.1016/S0924-4247(03)00379-0

Hosokawa, N., Nakamichi, M., Honda, N., Shiba, K., and Yoshikawa, G. (2014). "Antibody-based protein detection using nanomechanical Membrane-type Surface Stress Sensor (MSS)," in *11th International Workshop on Nanomechanical Sensing Workshop (NMC2014)* (Madrid).

Johnson, L., Gupta, A. K., Ghafoor, A., Akin, D., and Bashir, R. (2006). Characterization of vaccinia virus particles using microscale silicon cantilever resonators and atomic force microscopy. *Sens. Actuators B Chem.* 115, 189–197. doi: 10.1016/j.snb.2005.08.047

Kim, H. H., (2015). Highly sensitive microcantilever biosensors with enhanced sensitivity for detection of human papilloma virus infection. *Sens. Actuators B Chem.* 221, 1372–1383. doi: 10.1016/j.snb.2015.08.014

Kim, K.-H., Kabir, E., and Kabir, S. (2015). A review on the human health impact of airborne particulate matter. *Environ. Int.* 74, 136–143. doi: 10.1016/j.envint.2014.10.005

Lee, J. W. M., Chu, J. J. H., and Ng, M. L. (2006). Quantifying the specific binding between West Nile virus envelope domain III protein and the cellular receptor alpha V beta 3 integrin. *J. Biol. Chem.* 281, 1352–1360. doi: 10.1074/jbc.M506614200

Loizeau, F., (2015). Comparing membrane- and cantilever-based surface stress sensors for reproducibility. *Sens. Actuators A Phys.* 228, 9–15. doi: 10.1016/j.sna.2015.02.039

Nemmar, A., Holme, J. A., Rosas, I., Schwarze, P. E., and Alfaro-Moreno, E. (2013). Recent advances in particulate matter and nanoparticle toxicology: a review of the *in vivo* and *in vitro* studies. *Biomed Res. Int.* 2013:279371. doi: 10.1155/2013/279371

Pineda, M. F., (2009). Rapid specific and label-free detection of porcine rotavirus using photonic crystal biosensors. *IEEE Sens. J.* 9, 470–477. doi: 10.1109/JSEN.2009.2014427

Sieben, C., (2012). Influenza virus binds its host cell using multiple dynamic interactions. *Proc. Natl. Acad. Sci. U.S.A.* 109, 13626–13631. doi: 10.1073/pnas.1120265109

Sreepriya, V., and Hai-Feng, J. (2006). Detection of feline coronavirus using microcantilever sensors. *Meas. Sci. Technol.* 17, 2964. doi: 10.1088/0957-0233/17/11/015

Stoney, G. G. (1909). The tension of metallic films deposited by electrolysis. *Proc. R. Soc. Lond. A Math. Phys. Eng. Sci.* 82, 172–175. doi: 10.1088/0957-0233/17/11/015

Thundat, T., Warmack, R. J., Chen, G. Y., and Allison, D. P. (1994). Thermal and ambient−induced deflections of scanning force microscope cantilevers. *Appl. Phys. Lett.* 64, 2894–2896. doi: 10.1063/1.111407

Tsai, B.-Y., Chen, J.-Y., Chiou, A., and Ping, Y.-H. (2015). Using optical tweezers to quantify the interaction force of dengue virus with host cellular receptors. *Microsc. Microanal.* 21, 219–220. doi: 10.1017/S1431927615001890

Xu, D., Liu, L., Guan, J., Xu, J., Wang, T., Qin, A., et al. (2014). Label-free microcantilever-based immunosensors for highly sensitive determination of avian influenza virus H9. *Microchim. Acta* 181, 403–410. doi: 10.1007/s00604-013-1129-x

Yoshikawa, G. (2011). Mechanical analysis and optimization of a microcantilever sensor coated with a solid receptor film. *Appl. Phys. Lett.* 98, 173502. doi: 10.1063/1.3583451

Yoshikawa, G., Akiyama, T., Gautsch, S., Vettiger, P., and Rohrer, H. (2011). Nanomechanical membrane-type surface stress sensor. *Nano Lett.* 11, 1044–1048. doi: 10.1021/nl103901a

Yoshikawa, G., Lee, C. J. Y., and Shiba, K. (2014). Effects of coating materials on two dimensional stress-induced deflection of nanomechanical sensors. *J. Nanosci. Nanotechnol.* 14, 2908–2912. doi: 10.1166/jnn.2014.8604

Yoshikawa, G., Akiyama, T., Loizeau, F., Shiba, K., Gautsch, S., Nakayama, T., et al. (2012). Two dimensional array of piezoresistive nanomechanical Membrane-Type Surface Stress Sensor (MSS) with improved sensitivity. *Sensors* 12, 15873–15887. doi: 10.3390/s121115873

Conflict of Interest Statement: The authors declare that the research was conducted in the absence of any commercial or financial relationships that could be construed as a potential conflict of interest.

The reviewer TY and handling Editor declared a current collaboration and the handling Editor states that the process nevertheless met the standards of a fair and objective review.

Copyright © 2016 Imamura, Shiba and Yoshikawa. This is an open-access article distributed under the terms of the Creative Commons Attribution License (CC BY). The use, distribution or reproduction in other forums is permitted, provided the original author(s) or licensor are credited and that the original publication in this journal is cited, in accordance with accepted academic practice. No use, distribution or reproduction is permitted which does not comply with these terms.

frontiers in Microbiology

MINI REVIEW
published: 22 September 2016
doi: 10.3389/fmicb.2016.01500

Quantification of Virus Particles Using Nanopore-Based Resistive-Pulse Sensing Techniques

Lu Yang and Takatoki Yamamoto *

Department of Mechanical Engineering, School of Engineering, Tokyo Institute of Technology, Tokyo, Japan

Viruses have drawn much attention in recent years due to increased recognition of their important roles in virology, immunology, clinical diagnosis, and therapy. Because the biological and physical properties of viruses significantly impact their applications, quantitative detection of individual virus particles has become a critical issue. However, due to various inherent limitations of conventional enumeration techniques such as infectious titer assays, immunological assays, and electron microscopic observation, this issue remains challenging. Thanks to significant advances in nanotechnology, nanostructure-based electrical sensors have emerged as promising platforms for real-time, sensitive detection of numerous bioanalytes. In this paper, we review recent progress in nanopore-based electrical sensing, with particular emphasis on the application of this technique to the quantification of virus particles. Our aim is to provide insights into this novel nanosensor technology, and highlight its ability to enhance current understanding of a variety of viruses.

Keywords: virus particle, quantification, resistive-pulse sensing, out-of-plane nanopore, in-plane nanopore

OPEN ACCESS

Edited by:
Akio Adachi,
University of Tokushima, Japan

Reviewed by:
Hiroshi Kimura,
Tokai University, Japan
Osam Mazda,
Kyoto Prefectural University of Medicine, Japan

***Correspondence:**
Takatoki Yamamoto
yamamoto.t.ba@m.titech.ac.jp

Specialty section:
This article was submitted to Virology, a section of the journal Frontiers in Microbiology

Received: *17 July 2016*
Accepted: *08 September 2016*
Published: *22 September 2016*

Citation:
Yang L and Yamamoto T (2016) Quantification of Virus Particles Using Nanopore-Based Resistive-Pulse Sensing Techniques. Front. Microbiol. 7:1500. doi: 10.3389/fmicb.2016.01500

INTRODUCTION

Viruses are a major cause of infectious diseases. As such, they hold great significance in virological and immunological research and have extensive applications in clinical diagnosis and therapy. Determining both the dimensions and number of viruses is extremely important in many applications, such as the production of virus-based vaccines and therapeutic agents; hence, quantitative detection of viruses is becoming increasingly important. From a microbiological perspective, viruses are infectious agents that replicate only inside host cells. Single virus particles, also known as virions, generally consist of either double-stranded or single-stranded genetic molecules (DNA or RNA) surrounded by a protein shell called a capsid. In some cases, the capsid is enclosed within an outer lipid envelope. Several techniques are available for virus quantification (Heider and Metzner, 2014), including (1) determination of infectivity levels via plaque-forming and 50% tissue culture infectious-dose assays; (2) detection of virus proteins via antibody-antigen binding (e.g., enzyme-linked immunosorbent assays); (3) quantification of the viral genome using polymerase chain reaction (PCR), quantitative reverse-transcription (qRT)-PCR, and a range of metagenomic techniques; and (4) simultaneous determination of the presence of both stained proteins and nucleic acids using flow cytometry. Although these methods offer high specificity, drawbacks such as time-consuming and complicated procedures still limit their widespread utilization; thus, the development of new sensing technologies is highly desired.

The typical physical dimensions of individual virus particles range from several tens to hundreds of nanometers. Viruses are thus a type of functional nanoparticle. Current widely used

nanoparticle-sensing technologies should therefore be suitable for the characterization of virus particles, since to some extent, virus particles can be treated as soft nanoparticles. Theoretically, these technologies should detect all virus and virus-like particles, regardless of their infectivity, providing important complementary information (e.g., the ratio of total to infective virus particles). Nanoparticle-sensing technologies can be broadly classified into two categories: visualization-based and non-visualization-based techniques. Visualization-based techniques include transmission electron microscope (TEM) (Schatten, 2011; Harris, 2014) and atomic force microscope (Kasas and Thomson, 1997; Ohnesorge et al., 1997; Allison et al., 2010; Mateu, 2012), in which the size, shape, and concentrations of viruses are determined visually. However, these techniques are somewhat low-throughput, labor-intensive, and require high-level technical expertise to operate the costly associated equipment. Additionally, special treatment of samples is required, which sometimes results in inaccurate measurements due to aggregation and deformation of virus particles. Non-visualization-based techniques are based on light scattering analysis, including dynamic light scattering (DLS) (Driskell et al., 2011) and nanoparticle tracking analysis (NTA) (Kramberger et al., 2012; Nikolai et al., 2015). DLS measures the hydrodynamic Stokes-Einstein radius of particles undergoing Brownian motion by light scattering generated by an incident laser light source. The main problems associated with this technique are low sensitivity and resolution caused by detection of the ensemble average of particles and unsuitability for polydispersed samples. In contrast to DLS, NTA is suitable for identifying and tracking individual particles. However, the refractive index of the sample must be distinctive from that of the surrounding medium, and NTA often overestimates the size of particles compared with TEM.

Development of a rapid, high-throughput, real-time, label-free, sensitive, accurate, and (hopefully) miniaturized system to detect single virus particles must address the problems and limitations associated with the aforementioned technologies. One promising approach is the use of electrical detection techniques based on probing changes in resistance and/or capacitance using a nanoscale constriction. Over the last two decades, these techniques have demonstrated great capabilities of sensing a wide range of biomolecules (Yurt et al., 2012; Harms et al., 2015a), driven by significant advances in nanofabrication and electronics technologies. Electrical detectors utilizing a variety of sensing principles are available; nevertheless, we focus here primarily on the popular resistive-pulse sensing (RPS) detector, which is based on resistance measurement. We review recent progress and discuss future perspectives for this emerging electrical sensing technique, with the goal of providing insights into the key issues of reliable and effective quantification of individual viruses.

BASIC THEORY OF NANOPORE-BASED RPS

The origin of RPS dates back to Coulter counting technique, patented in 1953. The basic apparatus comprises two separate electrolyte solution-containing chambers connected by a small pore with dimensions comparable to the analyte of interest. As shown in **Figure 1A**, an electrical current is generated when a constant electric potential is applied between two electrodes placed on each side of the pore. As electrolyte buffer carrying insulated or poorly conductive particles passes through the chambers, translocation of particles across the pore causes a transient increase in pore resistance and a corresponding drop in current, recorded as a series of pulses. In the simplest case, where a spherical particle passes through a cylindrical pore, the relative change in resistance is described by:

$$\frac{\triangle R}{R} = \frac{d^3}{D^2 L}$$

where d and D are the particle and pore diameters, respectively. L is the pore length. The particle translocation process is driven predominantly by convection flow and electrokinetic flow, including electrophoretic and electroosmotic flow. According to the Nernst-Planck equation, the translocating particle flux, J,

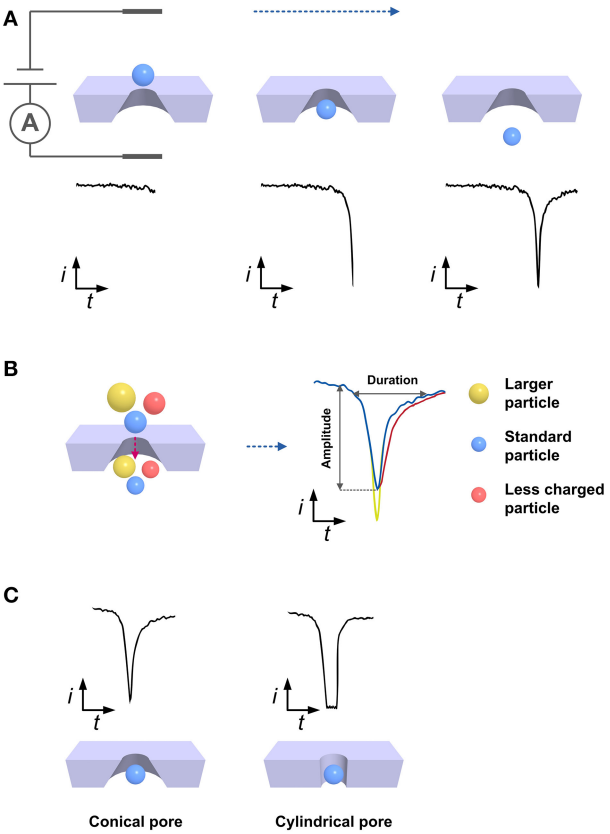

FIGURE 1 | Schematic illustrating basic principles of nanopore-based RPS technique. (A) Current changes during particle translocation across the nanopore. **(B)** Differences in pulses resulting from the translocation of particles with different sizes or surface charges. The yellow sphere is larger than the blue one and they carry the same amount of surface charge. The red sphere is less charged compared to the blue one and they have the same size. **(C)** Effect of pore's geometry on pulse shape. Conical and cylindrical pores commonly give rise to the asymmetric and symmetric pulses.

referring to the number of particles passing through a unit area of the pore per unit time, is expressed as:

$$J \approx J_{eph} + J_{eo} + J_{pd},$$

where J_{eph}, J_{eo}, and J_{pd} represent the electrophoretic, electroosmotic, and pressure-driven fluxes, respectively (Willmott and Smith, 2014). The sum of electrokinetic fluxes is given by:

$$J_{eph} + J_{eo} \approx \frac{C\varepsilon}{\eta}\left(\zeta_{particle} - \zeta_{pore}\right)E,$$

where C represents the particle concentration, ε and η represent the permittivity and viscosity of the electrolyte, respectively, ζ represents the Zeta potential of the subscripted surface, and E represents the electric field strength. **Figure 1B** shows that the amplitude of the pulse is directly proportional to the particle volume. The pulse duration and frequency can also be used to infer information regarding the particle concentration and Zeta potential, which is related to the surface charge of the particle and serves as an indicator of colloidal system stability (Kozak et al., 2011).

This particle-by-particle readout technique provides a wealth of information while requiring a lower sample concentration ($\sim 10^7$ particles/mL), smaller sample volume ($\sim$40 μL), and less operating time ($\sim$10 min) than traditional sensing techniques. Consequently, PRS has been employed for detection of DNA, proteins, viruses, bacteria, particles for drug delivery system (e.g., emulsions and liposomes), extracellular vesicles, and inorganic and polymeric nanoparticles (Venkatesan and Bashir, 2001; Howorka and Siwy, 2009; Oukhaled et al., 2012; Platt et al., 2012; Colby et al., 2013; Somerville et al., 2013; Stoloff and Wanunu, 2013; Willmott et al., 2013). The application of RPS for virus particle analysis is introduced in the following section.

APPLICATIONS OF RPS FOR VIRUS DETECTION

PRS detectors are generally composed of sensing electronics and nanopores that enable every single nanoparticle in a sample to pass through them one by one. The sensing electronics commonly include Ag/AgCl electrodes, a current amplifier, filter, and data acquisition unit, whereas the nanopores can vary distinctly in dimension, material, geometry, and structure. Although some biological pores made of natural proteins embedded in lipid bilayer membranes exist, the lack of robustness and extremely small pores (<5 nm) make them unsuitable for virus detection (Haque et al., 2013; Ying et al., 2014). Hence, we focus mainly on synthetic nanopores. As shown in **Figure 1C**, some pores are cylindrical and generate a symmetric pulse, although the overwhelming majority of pores are conical in shape and produce an asymmetric pulse that indicates the translocation direction (Davenport et al., 2013). Nanopores generally fall into one of two prototype categories according to the pore orientation relative to the substrate: out-of-plane or in-plane. Out-of-plane nanopores are perpendicular to the substrate surface and independent of the fluid chamber, which is commonly fabricated on a thin membrane supported by an insulating substrate. In contrast, in-plane nanopores are parallel to the substrate surface, which is embedded into a micro/nanofluidic channel as a built-in unit.

Out-of-Plane Nanopore Sensors

Solid-State Nanopores

Nanopores were utilized to analyze virus particles as early as 1977 (DeBlois and Wesley, 1977). Using submicron-diameter polycarbonate pores, DeBlois and Wesley measured the size of several type C oncornaviruses (Rauscher murine leukemia [122.3 ± 2 nm], simian sarcoma [109.7 ± 3 nm], Mason-Pfizer monkey [140.0 ± 2.5 nm], RD-114 [115 ± 5 nm], and feline leukemia [127.4 ± 2 nm]) and T2 bacteriophage (5.10 ± 0.15 × 10^{-16} cm^3) by comparing their pulse height to that of standard polystyrene latex beads. In addition, viruses were counted not only by comparing viruses and latex beads, but also by measuring the flow rates, which is related to the concentration. They reported achieving a lower practical count limit of 5 × 10^7 particles/mL. The same group subsequently compared measurements of other viruses (including Tipula iridescent virus, nuclear polyhedrosis viruses of the gypsy moth and European pine sawfly, Sindbis virus, and vesicular stomatitis virus) using light-scattering and electron microscopy to RPS measurements (DeBlois et al., 1978; Feuer et al., 1978). The results obtained using the different techniques were in general agreement.

Recently, Uram and coworkers investigated the interactions between *Paramecium bursaria* chlorella virus (diameter ~190 nm) and specific antibody using RPS as shown in **Figure 2A** (Uram et al., 2006). A conical pore with a 650-nm diameter was fabricated on a glass cover slide using a femtosecond-pulsed laser. They estimated the maximum number of antibodies binding to *Paramecium bursaria* chlorella virus and attempted to elucidate the kinetics of the antibody-virus interaction by simply detecting changes in the pulse amplitude after adding antibodies to the virus samples. Zhou and coworkers (Zhou et al., 2011) succeeded in discriminating between hepatitis B virus (HBV) capsids assembled from different numbers of dimers. They fabricated a 40-nm track-etched conical pore in a poly(ethylene terephthalate) membrane. Notably, the surface of this nanopore was covalently modified with triethylene glycol to minimize capsid adsorption and suppress electroosmotic flow within the pore. Arjmandi and coworkers constructed pyramidal-shaped pores as shown in **Figure 2B** to detect human immunodeficiency virus and Epstein-Barr virus (Arjmandi et al., 2012, 2014). They fabricated pores of 20–500 nm in size on a silicon membrane using electron beam lithography followed by anisotropic wet etching using potassium hydroxide. Their major contribution was that they established a Zeta potential measurement method based on the translocation velocity of particles. Their work revealed that the results of Zeta potential measurements agreed well with DLS measurements.

In addition to a great number of studies focusing on sphere viruses, due to their well-defined shapes, the translocation

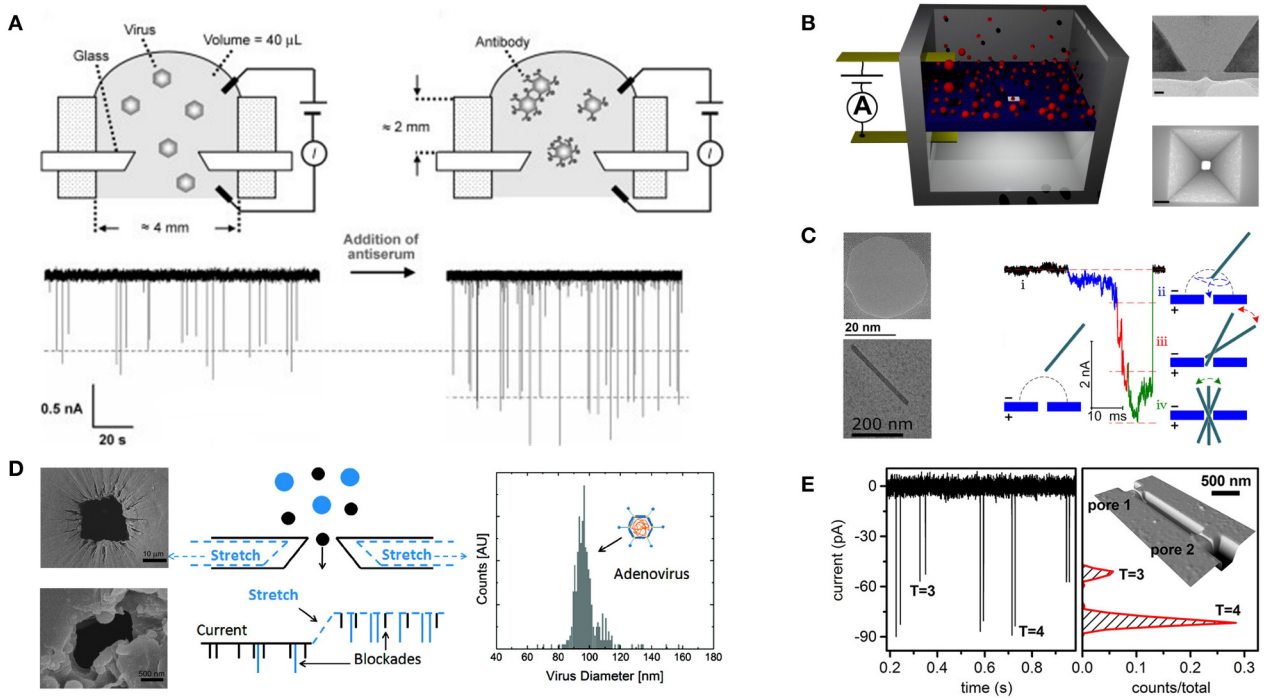

FIGURE 2 | Examples of RPS being applied to virus detection. (A) Characterization of the binding of antibodies to virus particles by detecting virions passing through a sub-micrometer glass pore. The binding of antibodies to the virus leads to an increase in the pulse amplitude. Reprinted with permission from Uram et al. (2006). Copyright Wiley-VCH Verlag GmbH & Co. KGaA, Weinheim. **(B)** Pyramidal-shaped solid-state nanopores. Images on the right side are TEM cross section image of a 40 nm nanopore and SEM top-view image of a 120 × 120 nm nanopore. Adapted with permission from Arjmandi et al. (2014). Copyright 2014 American Chemical Society. **(C)** Translocation dynamics of the rod-shaped virus. TEM images on the left side show a typical 30 nm solid-state nanopore and a single TMV particle. Adapted with permission from Wu et al. (2016). Copyright 2016 American Chemical Society. **(D)** Particle size distribution of adenovirus detected by TRPS. SEM images represent the large and small pore openings of a thermoplastic polyurethane membrane. Adapted with permission from Vogel et al. (2011). Copyright 2011 American Chemical Society. **(E)** Detection of HBV capsids ($T = 3$ and $T = 4$ refer to capsids with outer diameter of 32 and 35 nm, respectively) passing through in-series nanopores. Reprinted with permission from Harms et al. (2015b). Copyright 2014 American Chemical Society.

of rod-shaped virus particles across a nanopore has also been investigated. McMullen and coworkers examined the basic physics of translocation of the stiff filamentous virus fd (6.6 × 880 nm) (McMullen et al., 2014). TEM-drilled nanopores of 12–50 nm in diameter were formed in silicon nitride membranes. Using these pores, the authors could distinguish translocation of viruses through the nanopore from side-on collisions of the viruses with the sidewall of the nanopore by comparing the amplitude and duration of the corresponding pulses. Wu and colleagues (Wu et al., 2016) used similar nanopores to observe and simulate the translocation of tobacco mosaic virus (18 × 300 nm). They found that tobacco mosaic virus has to rotate to pass through the nanopore after interacting with the pore surface. **Figure 2C** shows that this rotation significantly influences the current signal.

Overall, solid-state nanopores with fixed pore sizes ranging from several nanometers to sub-micrometer have been fabricated in a broad range of materials (e.g., glass, silicon, silicon nitride, polymers) using a variety of state-of-the-art nanofabrication techniques (e.g., electron beam and focused ion beam milling) (Miles et al., 2013). A tremendous number of advantages are recognized, such as the ease of manufacturing and introducing surface modifications, nanopore size comparable to virus size range, exceptional robustness, and increased signal-to-noise ratios. Currently, these nanopore sensors play a dominant role in virus sensing, suggesting that their use will only increase in the future.

Tunable Elastomeric Nanopores

The aforementioned nanopores with fixed pore sizes are not suitable for polydispersed sample measurements, resulting in a slightly limited detectable size range. To overcome this limitation, size-tunable nanopores that enable *in situ* adjustment of nanopore size to match that of the analyte were introduced in 2011, leading to improved measurement sensitivity (Blundell et al., 2015; Weatherall, 2015). This technology, which is designated tunable resistive-pulse sensing (TRPS), was developed almost exclusively by Izon Science Ltd. (Christchurch, New Zealand). The nanopores are fabricated on thermoplastic polyurethane membranes using tungsten needles. The pore size can be finely tuned by stretching and relaxing the membrane in a biaxial and reversible manner. These physically and chemically stable nanopores with tunable pore

sizes both extend the analysis range and make it possible to recover clogged pores by simply stretching them. Izon Science has released several commercially available products ("qNano" and "qViro-X") containing compactly integrated nanopores with actuation and electronic components. In addition, qNano is equipped with a variable pressure module that can generate external positive or negative pressure to facilitate or hinder particle passage to optimize the translocation rate. The qNano system is also equipped with data collection and analysis software. Measurement protocols have been established to simultaneously elucidate the particle size, concentration, and Zeta potential (Kozak et al., 2012; Vogel et al., 2012; Eldridge et al., 2014). The results of TPRS studies have been comparable to measurements using other techniques, such as TEM, DLS, and NTA (Anderson et al., 2013).

In analyses of both synthetic and biological particles, TRPS has demonstrated substantial benefits, including portability, simplicity, and versatility (Roberts et al., 2012; Adela Booth et al., 2013; Yu et al., 2014; Anderson et al., 2015; Lane et al., 2015). With respect to virus analysis, Vogel and colleagues demonstrated the feasibility of sizing adenovirus (70–90 nm) using qNano as shown in **Figure 2D** (Vogel et al., 2011). They determined the size distribution of purified adenoviruses and calculated their modal diameter (96.5 ± 15 nm). Farkas and coworkers counted rotavirus (75 nm) using both qRT-PCR and qNano to evaluate the purification of the viruses by size-exclusion chromatography (Farkas et al., 2013). Akpinar and Yin counted vesicular stomatitis virus (70 × 200 nm) using both TRPS and a plaque assay (Akpinar and Yin, 2015). The average total to infectious particle ratio was calculated as 2.91 ± 1.42. In addition, the mean equivalent particle diameter of this bullet-shaped virus, which reflects the diameter of a sphere with an equal volume, was measured as 107.8 and 111.8 nm by TRPS and TEM, respectively.

Despite these applications, to date only a few studies have reported using TRPS for quantification of virus particles, perhaps due to insufficient familiarity with TRPS, which was invented only a few years ago and remains in an early stage of development. Another reason is that the lowest detection limit of TRPS is reportedly only 70 nm when the smallest nanopore (NP100; 100 nm pore diameter) is used. This is insufficient for detecting the majority of viruses with a size in the 10 s of nm or viruses with strongly anisotropic dimensions (e.g., bacteriophages and rod-shaped viruses). There is thus a demand for further decreases in pore size to improve detection limits.

In-plane Nanopore Sensors

In-plane naopores are compactly integrated into micro/nanofluidic devices, leading to enhanced portability and fluid control, lower sample consumption, ease of observing particle translocation optically, and improved mass transfer of analytes to the nanopore. Moreover, incorporating multiple pores in series or in parallel can increase the throughput and the device functionality (Fraikin et al., 2011; Haywood et al., 2015). However, the number of relevant studies is low. A systematic method for quantitative measurements of particle size, concentration, as well as surface charge using in-plane nanopores is needed.

Harms and coworkers fabricated a nanochannel with two nanopores in series to detect HBV capsids as shown in **Figure 2E** (Harms et al., 2011). The nanochannel and nanopores were made on a silicon wafer using electron beam lithography and a two-step thermal oxidation process. The nanochannel and nanopore dimensions were 1000 × 50 × 1000 nm and 50 × 50 × 40 nm (width × depth × length), respectively. A pulse pair representing a single capsid passing through two pores successively exhibited almost identical amplitudes. The migration time needed for a capsid traveling from the first pore to the second pore was calculated from pairs of adjacent pulses, which were used to estimate the electrophoretic mobility of HBV capsids. The authors also used focused ion beams to make nanochannels and nanopores on a glass substrate to determine the electrophoretic mobility of HBV capsids with different molecular weights and to monitor the assembly process (Harms et al., 2015b,c).

CONCLUSIONS AND OUTLOOK

In conclusion, nanopore-based electrical sensing techniques have experienced significant growth as emerging yet promising platforms for nanoparticle detection, driven by dramatic advances in nanotechnology. Nanopore-based electrical sensing provides excellent capabilities of quantifying virus particles in a real-time, label-free, high-throughput, and particle-by-particle manner.

However, current trends suggest that some challenges still remain and need to be overcome if the range of practical applications is to widen. First, improvements in pore fabrication and signal readout are needed. Reproducible fabrication and improved readout capabilities will enhance measurement reproducibility, increase sensitivity, and lower the detection limits. Introducing surface modifications or coatings within nanopores is necessary as well, as this can minimize non-specific adsorption and pore clogging. Second, even though research indicates that the accuracy of electrical sensing is comparable to that of DLS and TEM technologies, the combination with other non-electrical sensing techniques during measurements will be an interesting trend. For example, it was reported that simultaneous electrical and optical analysis can provide "double-checked" results (Liu et al., 2014; Hauer et al., 2015). Finally, a greater diversity of viruses should be analyzed in terms of viron size, concentration, and surface charge. Determination of the total to infectious particle ratio and the kinetics of virus-antibody binding would be of particular interest. For diagnostic applications, strict steps should be taken to avoid false-positive and false-negative results. If advances enable nanopore-based methods to provide better performance than conventional biochemical assays, they could be adapted for routine clinical use.

The most obvious advantage of nanopore-based electrical methods is the possibility of detecting unknown and new species of viruses. Unknown viruses are intrinsically difficult to detect using traditional methods because information regarding the genome or membrane proteins is necessary prior to the design of PCR primers or antibodies, respectively. Furthermore, host cells must be found for isolating and obtaining the source

DNA/RNA or protein from the viruses. Nanopore-based assays can detect unknown viruses in the absence of such biochemical information, however, based simply on virus electrical properties. Further developments in in-plane sensor technology could lead to mobile and wearable devices for monitoring infectious viruses ubiquitously, which could enhance public safety and health. From a long-term prospective, we can believe that nanopore-based virus-sensing techniques will assume a more central role in the quantification of viruses.

AUTHOR CONTRIBUTIONS

LY wrote the draft and TY revised the manuscript.

ACKNOWLEDGMENTS

This work was supported by grants from the Japan Society for the Promotion of Science (JSPS) KAKENHI (Nos. 15H06205 and 25289096) and by CREST, JST.

REFERENCES

Adela Booth, M., Vogel, R., Curran, J. M., Harbison, S., and Travas-Sejdic, J. (2013). Detection of target-probe oligonucleotide hybridization using synthetic nanopore resistive pulse sensing. *Biosens. Bioelectron.* 45, 136–140. doi: 10.1016/j.bios.2013.01.044

Akpinar, F., and Yin, J. (2015). Characterization of vesicular stomatitis virus populations by tunable resistive pulse sensing. *J. Virol. Methods* 218, 71–76. doi: 10.1016/j.jviromet.2015.02.006

Allison, D. P., Mortensen, N. P., Sullivan, C. J., and Doktycz, M. J. (2010). Atomic force microscopy of biological samples. *Wiley Interdiscip. Rev. Nanomed. Nanobiotechnol.* 2, 618–634. doi: 10.1002/wnan.104

Anderson, W., Kozak, D., Coleman, V. A., Jämting, K. A., and Trau, M. (2013). A comparative study of submicron particle sizing platforms: accuracy, precision and resolution analysis of polydisperse particle size distributions. *J. Colloid Interface Sci.* 405, 322–330. doi: 10.1016/j.jcis.2013.02.030

Anderson, W., Lane, R., Korbie, D., and Trau, M. (2015). Observations of tunable resistive pulse sensing for exosome analysis: improving system sensitivity and stability. *Langmuir* 31, 6577–6587. doi: 10.1021/acs.langmuir.5b01402

Arjmandi, N., Van Roy, W., and Lagae, L. (2014). Measuring mass of nanoparticles and viruses in liquids with nanometer-scale pores. *Anal. Chem.* 86, 4637–4641. doi: 10.1021/ac500396t

Arjmandi, N., Van Roy, W., Lagae, L., and Borghs, G. (2012). Measuring the electric charge and zeta potential of nanometer-sized objects using pyramidal-shaped nanopores. *Anal. Chem.* 84, 8490–8496. doi: 10.1021/ac300705z

Blundell, E. L. C. J., Mayne, L. J., Billinge, E. R., and Platt, M. (2015). Emergence of tunable resistive pulse sensing as a biosensor. *Anal. Methods* 7, 7055–7066. doi: 10.1039/C4AY03023K

Colby, A. H., Colson, Y. L., and Grinstaff, M. W. (2013). Microscopy and tunable resistive pulse sensing characterization of the swelling of pH-responsive, polymeric expansile nanoparticles. *Nanoscale* 5, 3496–3504. doi: 10.1039/c3nr00114h

Davenport, M. W., Healy, K., Pevarnik, M., Teslich, N., Cabrini, S., Morrison, A., et al. (2013). The role of pore geometry in single particle detection. *Biophys. J.* 104, 521a. doi: 10.1016/j.bpj.2012.11.2881

DeBlois, R. W., Uzgiris, E. E., Cluxton, D. H., and Mazzone, H. M. (1978). Comparative measurements of size and polydispersity of several insect viruses. *Anal. Biochem.* 90, 273–288. doi: 10.1016/0003-2697(78)90032-5

DeBlois, R. W., and Wesley, R. K. (1977). Sizes and concentrations of several type C oncornaviruses and bacteriophage T2 by the resistive-pulse technique. *J. Virol.* 23, 227–233.

Driskell, J. D., Jones, C. A., Tompkins, S. M., and Tripp, R. A. (2011). One-step assay for detecting influenza virus using dynamic light scattering and gold nanoparticles. *Analyst* 136, 3083. doi: 10.1039/c1an15303j

Eldridge, J. A., Willmott, G. R., Anderson, W., and Vogel, R. (2014). Nanoparticle ζ-potential measurements using tunable resistive pulse sensing with variable pressure. *J. Colloid Interface Sci.* 429, 45–52. doi: 10.1016/j.jcis.2014.05.013

Farkas, K., Pang, L., Lin, S., Williamson, W., Easingwood, R., Fredericks, R., et al. (2013). A gel filtration-based method for the purification of infectious rotavirus particles for environmental research applications. *Food Environ. Virol.* 5, 231–235. doi: 10.1007/s12560-013-9122-4

Feuer, B. I., Uzgiris, E. E., Deblois, R. W., Cluxton, D. H., and Lenard, J. (1978). Length of glycoprotein spikes of vesicular stomatitis virus and sindbis virus, measured in Situ using quasi elastic light scattering and a resistive-pulse technique. *Virology* 90, 156–161. doi: 10.1016/0042-6822(78)90344-6

Fraikin, J., Teesalu, T., McKenney, C. M., Ruoslahti, E., and Cleland, A. N. (2011). A high-throughput label-free nanoparticle analyser. *Nat. Nanotechnol.* 6, 308–313. doi: 10.1038/nnano.2011.24

Haque, F., Li, J., Wu, H. C., Liang, X. J., and Guo, P. (2013). Solid-state and biological nanopore for real-time sensing of single chemical and sequencing of DNA. *Nano Today* 8, 56–74. doi: 10.1016/j.nantod.2012.12.008

Harms, Z. D., Haywood, D. G., Kneller, A. R., and Jacobson, S. C. (2015a). Conductivity-based detection techniques in nanofluidic devices. *Analyst* 140, 4779–4791. doi: 10.1039/C5AN00075K

Harms, Z. D., Haywood, D. G., Kneller, A. R., Selzer, L., Zlotnick, A., and Jacobson, S. C. (2015b). Single-particle electrophoresis in nanochannels. *Anal. Chem.* 87, 699–705. doi: 10.1021/ac503527d

Harms, Z. D., Mogensen, K. B., Nunes, P. S., Zhou, K., Hildenbrand, B. W., Mitra, I., et al. (2011). Nanofluidic devices with two pores in series for resistive-pulse sensing of single virus capsids. *Anal. Chem.* 83, 9573–9578. doi: 10.1021/ac202358t

Harms, Z. D., Selzer, L., Zlotnick, A., and Jacobson, S. C. (2015c). Monitoring assembly of virus capsids with nanofluidic devices. *ACS Nano* 9, 9087–9096. doi: 10.1021/acsnano.5b03231

Harris, J. R. (2014). Transmission electron microscopy in molecular structural biology: a historical survey. *Arch. Biochem. Biophys.* 581, 3–18. doi: 10.1016/j.abb.2014.11.011

Hauer, P., Le Ru, E. C., and Willmott, G. R. (2015). Co-ordinated detection of microparticles using tunable resistive pulse sensing and fluorescence spectroscopy. *Biomicrofluidics* 9:014110. doi: 10.1063/1.4905874

Haywood, D. G., Saha-Shah, A., Baker, L. A., and Jacobson, S. C. (2015). Fundamental studies of nanofluidics: nanopores, nanochannels, and nanopipets. *Anal. Chem.* 87, 172–187. doi: 10.1021/ac504180h

Heider, S., and Metzner, C. (2014). Quantitative real-time single particle analysis of virions. *Virology* 462–463, 199–206. doi: 10.1016/j.virol.2014.06.005

Howorka, S., and Siwy, Z. (2009). Nanopore analytics: sensing of single molecules. *Chem. Soc. Rev.* 38, 2360–2384. doi: 10.1039/b813796j

Kasas, S., and Thomson, N. (1997). Biological applications of the AFM: from single molecules to organs. *J. Imaging* 8, 151–161.

Kozak, D., Anderson, W., Vogel, R., Chen, S., Antaw, F., and Trau, M. (2012). Simultaneous size and ζ-potential measurements of individual nanoparticles in dispersion using size-tunable pore sensors. *ACS Nano* 6, 6990–6997. doi: 10.1021/nn3020322

Kozak, D., Anderson, W., Vogel, R., and Trau, M. (2011). Advances in resistive pulse sensors: devices bridging the void between molecular and microscopic detection. *Nano Today* 6, 531–545. doi: 10.1016/j.nantod.2011.08.012

Kramberger, P., Ciringer, M., Štrancar, A., and Peterka, M. (2012). Evaluation of nanoparticle tracking analysis for total virus particle determination. *Virol. J.* 9, 265. doi: 10.1186/1743-422X-9-265

Lane, R. E., Korbie, D., Anderson, W., Vaidyanathan, R., and Trau, M. (2015). Analysis of exosome purification methods using a model liposome system and tunable-resistive pulse sensing. *Sci. Rep.* 5:7639. doi: 10.1038/srep07639

Liu, S., Zhao, Y., Parks, J. W., Deamer, D. W., Hawkins, A. R., and Schmidt, H. (2014). Correlated electrical and optical analysis of single nanoparticles and biomolecules on a nanopore-gated optofluidic chip. *Nano Lett.* 14, 4816–4820. doi: 10.1021/nl502400x

Mateu, M. G. (2012). Mechanical properties of viruses analyzed by atomic force microscopy: a virological perspective. *Virus Res.* 168, 1–22. doi: 10.1016/j.virusres.2012.06.008

McMullen, A., de Haan, H. W., Tang, J. X., and Stein, D. (2014). Stiff filamentous virus translocations through solid-state nanopores. *Nat. Commun.* 5, 4171. doi: 10.1038/ncomms5171

Miles, B. N., Ivanov, A. P., Wilson, K. A., Dogan, F., Japrung, D., and Edel, J. B. (2013). Single molecule sensing with solid-state nanopores: novel materials, methods, and applications. *Chem. Soc. Rev.* 42, 15–28. doi: 10.1039/C2CS35286A

Nikolai, N., Ekaterina, T., Evgeniy, E., Mikhail, K., Joseph, A., and Olga, K. (2015). Comparative study of non-enveloped icosahedral viruses size. *PLoS ONE* 10:e0142415. doi: 10.1371/journal.pone.0142415

Ohnesorge, F. M., Hörber, J. K., Häberle, W., Czerny, C. P., Smith, D. P., and Binnig, G. (1997). AFM review study on pox viruses and living cells. *Biophys. J.* 73, 2183–2194. doi: 10.1016/S0006-3495(97)78250-X

Oukhaled, A., Bacri, L., Pastoriza-Gallego, M., Betton, J. M., and Pelta, J. (2012). Sensing proteins through nanopores: fundamental to applications. *ACS Chem. Biol.* 7, 1935–1949. doi: 10.1021/cb300449t

Platt, M., Willmott, G. R., and Lee, G. U. (2012). Resistive pulse sensing of analyte-induced multicomponent rod aggregation using tunable pores. *Small* 8, 2436–2444. doi: 10.1002/smll.201200058

Roberts, G. S., Yu, S., Zeng, Q., Chan, L. C. L., Anderson, W., Colby, A. H., et al. (2012). Tunable pores for measuring concentrations of synthetic and biological nanoparticle dispersions. *Biosens. Bioelectron.* 31, 17–25. doi: 10.1016/j.bios.2011.09.040

Schatten, H. (2011). Low voltage high-resolution SEM (LVHRSEM) for biological structural and molecular analysis. *Micron* 42, 175–185. doi: 10.1016/j.micron.2010.08.008

Somerville, J. A., Willmott, G. R., Eldridge, J., Griffiths, M., and McGrath, K. M. (2013). Size and charge characterisation of a submicrometre oil-in-water emulsion using resistive pulse sensing with tunable pores. *J. Colloid Interface Sci.* 394, 243–251. doi: 10.1016/j.jcis.2012.11.071

Stoloff, D. H., and Wanunu, M. (2013). Recent trends in nanopores for biotechnology. *Curr. Opin. Biotechnol.* 24, 699–704. doi: 10.1016/j.copbio.2012.11.008

Uram, J. D., Ke, K., Hunt, A. J., and Mayer, M. (2006). Submicrometer pore-based characterization and quantification of antibody-virus interactions. *Small* 2, 967–972. doi: 10.1002/smll.200600006

Venkatesan, B. M., and Bashir, R. (2001). Nanopore sensors for nucleic acid analysis. *Nat. Nanotechnol.* 6, 615–624. doi: 10.1038/nnano.2011.129

Vogel, R., Anderson, W., Eldridge, J., Glossop, B., and Willmott, G. (2012). A variable pressure method for characterizing nanoparticle surface charge using pore sensors. *Anal. Chem.* 84, 3125–3131. doi: 10.1021/ac2030915

Vogel, R., Willmott, G., Kozak, D., Roberts, G. S., Anderson, W., Groenewegen, L., et al. (2011). Quantitative sizing of nano/microparticles with a tunable elastomeric pore sensor. *Anal. Chem.* 83, 3499–3506. doi: 10.1021/ac200195n

Weatherall, E. (2015). Applications of tunable resistive pulse sensing. *Analyst* 140, 3318. doi: 10.1039/c4an02270j

Willmott, G. R., Fisk, M. G., and Eldridge, J. (2013). Magnetic microbead transport during resistive pulse sensing. *Biomicrofluidics* 7:064106. doi: 10.1063/1.4833075

Willmott, G. R., and Smith, B. G. (2014). Modelling of resistive pulse sensing: flexible methods for submicron particles. *ANZIAM J.* 55, 197–213. doi: 10.21914/anziamj.v55i0.5376

Wu, H., Chen, Y., Zhou, Q., Wang, R., Xia, B., Ma, D., et al. (2016). Translocation of rigid rod-shaped virus through various solid-state nanopores. *Anal. Chem.* 88, 2502–2510. doi: 10.1021/acs.analchem.5b04905

Ying, Y.-L., Cao, C., and Long, Y.-T. (2014). Single molecule analysis by biological nanopore sensors. *Analyst* 139, 3826–3835. doi: 10.1039/C4AN00706A

Yu, A. C. S., Loo, J. F. C., Yu, S., Kong, S. K., and Chan, T. F. (2014). Monitoring bacterial growth using tunable resistive pulse sensing with a pore-based technique. *Appl. Microbiol. Biotechnol.* 98, 855–862. doi: 10.1007/s00253-013-5377-9

Yurt, A., Daaboul, G. G., Connor, J. H., Goldberg, B. B., and Selim Ünlü, M. (2012). Single nanoparticle detectors for biological applications. *Nanoscale* 4, 715. doi: 10.1039/c2nr11562j

Zhou, K., Li, L., Tan, Z., Zlotnick, A., and Jacobson, S. C. (2011). Characterization of hepatitis B virus capsids by resistive-pulse sensing. *J. Am. Chem. Soc.* 133, 1618–1621. doi: 10.1021/ja108228x

Conflict of Interest Statement: The authors declare that the research was conducted in the absence of any commercial or financial relationships that could be construed as a potential conflict of interest.

Copyright © 2016 Yang and Yamamoto. This is an open-access article distributed under the terms of the Creative Commons Attribution License (CC BY). The use, distribution or reproduction in other forums is permitted, provided the original author(s) or licensor are credited and that the original publication in this journal is cited, in accordance with accepted academic practice. No use, distribution or reproduction is permitted which does not comply with these terms.

frontiers in Microbiology

ORIGINAL RESEARCH
published: 07 June 2016
doi: 10.3389/fmicb.2016.00875

DGV: Dengue Genographic Viewer

*Akifumi Yamashita[1], Tetsuya Sakamoto[1,2], Tsuyoshi Sekizuka[1], Kengo Kato[1], Tomohiko Takasaki[3] and Makoto Kuroda[1]**

[1] Pathogen Genomics Center, National Institute of Infectious Diseases, Tokyo, Japan, [2] Remote Operations Services Department, CTC System Management Corporation, Tokyo, Japan, [3] Department of Virology I, National Institute of Infectious Diseases, Tokyo, Japan

Dengue viruses (DENVs) and their vectors are widely distributed throughout the tropical and subtropical regions of the world. An autochthonous case of DENV was reported in Tokyo, Japan, in 2014, for the first time in 70 years. A comprehensive database of DENV sequences containing both serotype and genotype data and epidemiological data is crucial to trace DENV outbreak isolates and promptly respond to outbreaks. We constructed a DENV database containing the serotype, genotype, year and country/region of collection by collecting all publically available DENV sequence information from the National Center for Biotechnology Information (NCBI) and assigning genotype information. We also implemented the web service Dengue Genographic Viewer (DGV), which shows the geographical distribution of each DENV genotype in a user-specified time span. DGV also assigns the serotype and genotype to a user-specified sequence by performing a homology search against the curated DENV database, and shows its homologous sequences with the geographical position and year of collection. DGV also shows the distribution of DENV-infected entrants to Japan by plotting epidemiological data from the Infectious Agents Surveillance Report (IASR), Japan. This overview of the DENV genotype distribution may aid in planning for the control of DENV infections. DGV is freely available online at: (https://gph.niid.go.jp/geograph/dengue/content/genomemap).

Keywords: NGS, dengue virus, genotyping, genograph, web service

OPEN ACCESS

Edited by:
Akihide Ryo,
Yokohama City University, Japan

Reviewed by:
Takayuki Hishiki,
Tokyo Metropolitan Institute of Medical Science, Japan
Hwa-Jen Teng,
Centers for Disease Control, Taiwan

****Correspondence:***
Makoto Kuroda
makokuro@niid.go.jp

Specialty section:
This article was submitted to Virology, a section of the journal Frontiers in Microbiology

Received: *22 April 2016*
Accepted: *24 May 2016*
Published: *07 June 2016*

Citation:
Yamashita A, Sakamoto T, Sekizuka T, Kato K, Takasaki T and Kuroda M (2016) DGV: Dengue Genographic Viewer. Front. Microbiol. 7:875. doi: 10.3389/fmicb.2016.00875

INTRODUCTION

Dengue viruses (DENVs) are members of the genus *Flavivirus* in the family *Flaviviridae* and consist of four serotypes (DENV-1 to -4) (Lanciotti et al., 1992; Kuhn et al., 2002). Each serotype can be divided into five to six genotypes. However, there is no standard genotyping classification [DENV-1, (Goncalvez et al., 2002); DENV-2, (Anez et al., 2011; Khan et al., 2013); DENV-3, (Lanciotti et al., 1994; Wittke et al., 2002; Klungthong et al., 2008); DENV-4, (Abubakar et al., 2002)]. DENV has a positive-sense, single-stranded RNA genome that is ∼11 kb in length and encodes a capsid protein (C), premembrane protein (prM), and envelope glycoprotein (E) in addition to seven non-structural proteins (NSs, NS1, NS2A, NS2B, NS3, NS4A, NS4B, and NS5). DENV infection causes dengue illness, which may range from dengue fever (a mild illness) to dengue hemorrhagic fever and dengue shock syndrome (the severe forms of the illness) in addition to asymptomatic cases

Abbreviations: DENV, Dengue virus; C, capsid protein; prM, premembrane protein; E, envelope glycoprotein; NS, non-structural protein; NCBI, national center for biotechnology information; IASR, Infectious Agents Surveillance Report.

(Centers for Disease Control and Prevention; http://www.cdc.gov/dengue/clinicalLab/clinical.html). Infection results in lifetime immunity against the same serotype, but successive exposure to different DENVs increases the likelihood of contracting a severe form of dengue illness, such as dengue hemorrhagic fever or dengue shock syndrome (Chiappelli et al., 2014).

DENV and its vectors have become widely distributed throughout the tropical and subtropical regions of the world (Murray et al., 2013). An autochthonous case of DENV infection was reported in Tokyo, Japan, in 2014 for the first time in 70 years (Kutsuna et al., 2015). To ensure prompt action in response to a DENV outbreak, a comprehensive DENV database based on the genotypes would be essential for tracing the outbreak source. To date, only two DENV databases provide genotype information. The web service ViPR[1] (Pickett et al., 2012) supports genetic analysis based on the viral genome for a tested input sequence, including DENV sequences. The second database is the Dengue virus genotyping database[2] (Yamashita et al., 2013), which provides a summary table containing the DENV serotype/genotype, year and country of collection and accession number. There are many other DENV databases; however, no other sites provide summarized genotype information. The Dengue Virus Resource[3] facilitates the retrieval of DENV sequences deposited in GenBank according to serotype, disease symptom, host, region/country, genome region, and collection and/or release data (Resch et al., 2009). DENVirDB[4] provides sequence information and computationally curated information of dengue viral proteins (Asnet et al., 2014). DENVDB focuses on the dengue virus sequence database for keyword searches (no publication: http://proline.bic.nus.edu.sg/denvdb/). Finally, the Dengue Virus Portal is a sequence collection with metadata (no publication: https://www.broadinstitute.org/annotation/viral/Dengue/Home.html).

Here, we constructed the website Dengue Genographic Viewer (DGV), which presents DENV information based on the genotype and epidemiological data by using the geographic tool Google Maps© to update the recent dissemination of DENV genotypes from a global perspective.

TABLE 1 | Number of DENV records (March 4, 2016).

Serotype	Genotype	Records on public database	Total sequences of each serotype
DENV-1			
	I	2508	
	Ib	13	
	II	7	
	III	6	
	IV	407	
	V	879	
	Recombinant	49	
	Lab strain	3	3872
DENV-2			
	American	101	
	Asian-American	1245	
	Asian I	858	
	Asian II	105	
	Cosmopolitan	1042	
	Sylvatic	26	
	Recombinant	35	
	Unknown	2	3414
DENV-3			
	I	326	
	II	742	
	III	1192	
	IV	5	
	V	34	
	Recombinant	9	
	Unknown	1	2309
DENV-4			
	I	295	
	IIA	223	
	IIB	385	
	III	7	
	Sylvatic	6	
	Recombinant	3	919

MATERIALS AND METHODS

Construction of the DENV Database

The DENV genotype database was constructed as follows: (1) all accessible DENV nucleotide sequences were collected; (2) the complete sequences of each protein region (C, prM, E, NS1, NS2A, NS2B, NS3, NS4A, NS4B, and NS5) were extracted from the sequences; (3) a blastn homology search was performed against the genotype database and the genotype of the most homologous sequence was assigned; (4) and the genotype data were stored in a database using SQLite (https://www.sqlite.org/).

1. The DENV nucleotide sequences were downloaded from the NCBI database using key words ("Dengue virus"[porgn:__txid12637]).
2. A blastx homology search was performed to detect nucleotide regions that corresponded to each mature DENV protein; nucleotide regions that exhibited more than 85% sequence coverage to the protein were used for the subsequent analysis.
3. To reduce the time required to obtain the most homologous sequences in the genotype database, we reduced the number of sequences used in the blast search by clustering highly homologous sequences. We performed a uclust search (Edgar, 2010) against the nucleotide sequences of each protein region and selected one representative sequence for each homologous sequence group with a clustering threshold of 99% identity;

[1]ViPR (Virus Pathogen Database and Analysis Resource): http://www.viprbrc.org/brc/home.spg?decorator=flavi_dengue

[2]Dengue virus genotyping database: http://www.gen-info.osaka-u.ac.jp/~uhmin/genotyping/index.html

[3]Dengue Virus Resource: https://www.ncbi.nlm.nih.gov/genome/viruses/variation/dengue/

[4]DEnvirDB: http://www.ladydoakcollege.edu.in/denvirdb/index.php

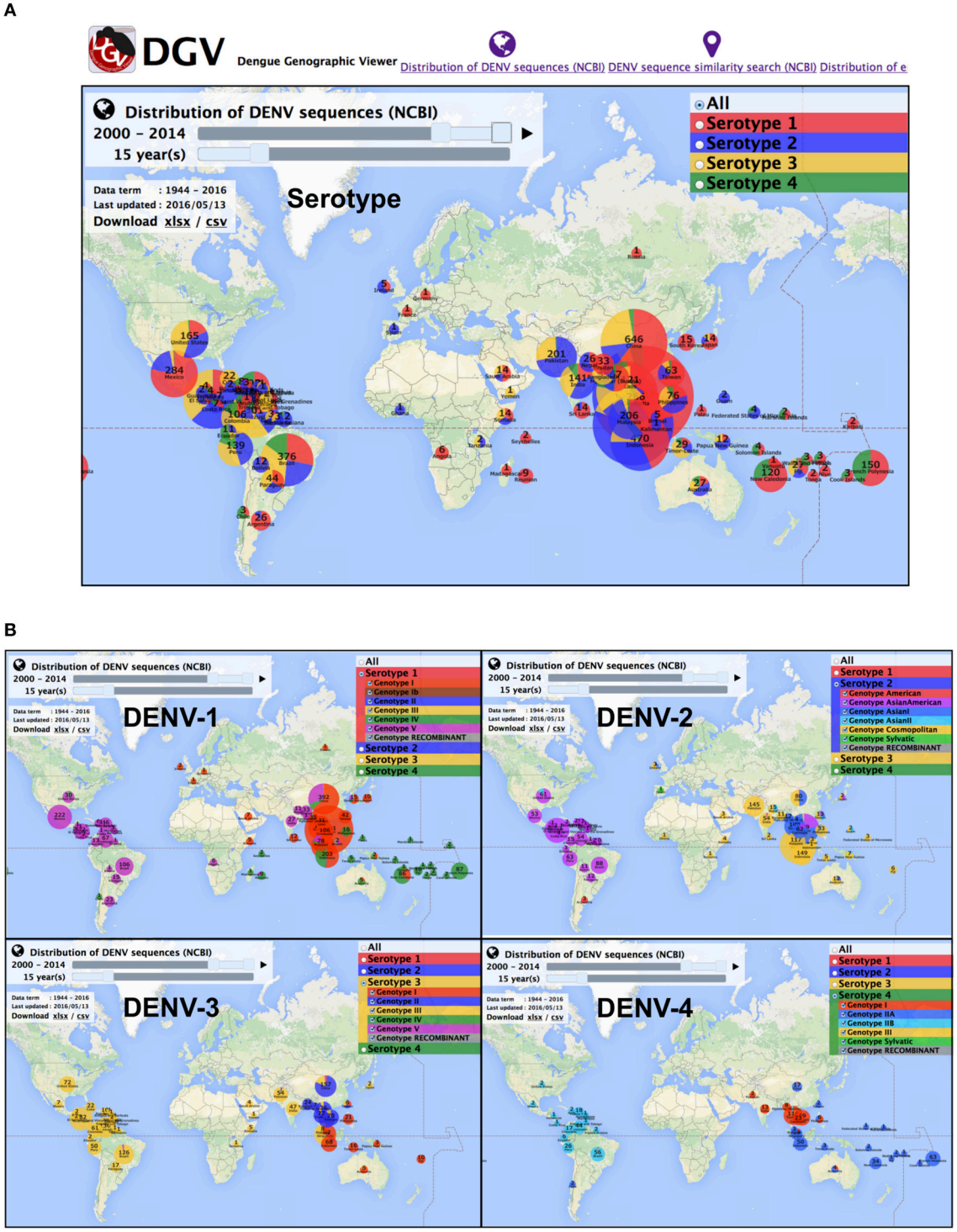

FIGURE 1 | Overview of DGV for serotype distribution for all DENV (A) and genotype distribution for each serotype (B) in 2000–2014.

then, the representative sequences were subjected to a homology search against the genotype database. The original genotype database was constructed according to the method proposed by previous report (Yamashita et al., 2013). Briefly, the representative sequences were aligned by using the mafft (Katoh and Standley, 2014) program and Neighbor joining (NJ) phylogenetic trees were constructed using the MEGA5 program (Tamura et al., 2011). The genotype of each gene

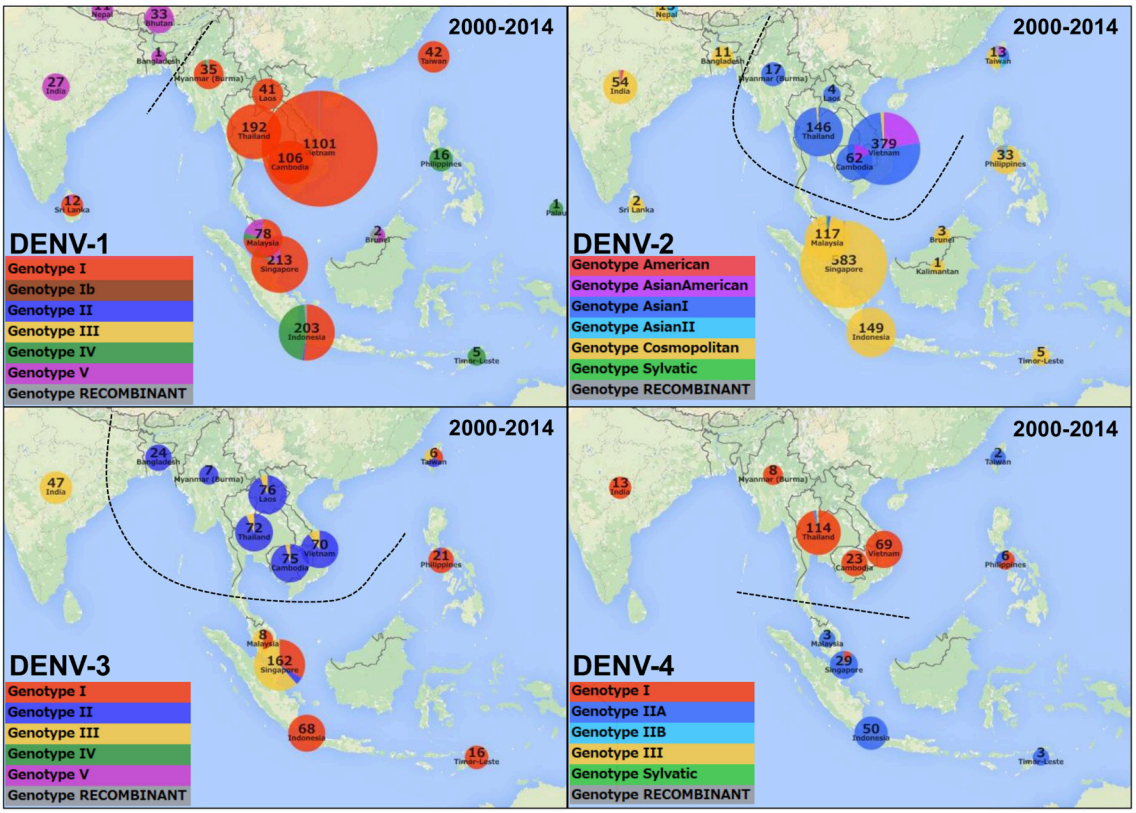

FIGURE 2 | Genotype distribution for each DENV serotype in Asia in 2000–2014. Possible borderline of genotype distribution in each serotype is shown as dash line.

was assigned manually according to the previous genotype database (Yamashita et al., 2013).

4. Sequence ID, country/region and year of collection were extracted from the deposited GenBank data and integrated into the SQL database by using an in house Perl script.

The above processes except for the original database construction are performed automatically every night to update the recent DENV database.

Interactive Viewer Using Web Interface

We implemented a set of viewer applications on DGV by using Google Maps©, which shows the data in a temporal and spatial manner. One application presents the geographical distribution of each DENV genotype on the map in a user-specified time span. Another option is a homology search program that searches for the most homologous DENV sequence in the DGV database and show the geographical positions of closely related sequences on the map. The other interface shows the sources of imported dengue cases on the map, according to the Infectious Agents Surveillance Report (IASR), Japan (http://www.nih.go.jp/niid/en/iasr-e.html). This set of applications is available at the DGV web site (https://gph.niid.go.jp/geograph/dengue/content/genomemap).

RESULTS AND DISCUSSION

Distribution of DENV Genotypes

On March 4, 2016, DGV included a total of 10,514 DENV sequences, which consisted of 3872, 3414, 2309, and 919 DENV serotype-1, -2, -3, and -4 sequences, respectively (**Table 1**). Some genotypes have been abundantly sequenced and deposited in the public database, whereas other genotypes have rarely been sequenced (i.e., DENV-1 genotype II was reported in only seven records from 1960 to 2012, DENV-4 genotype III was also reported in only seven records from 1997 to 2001, and DENV-3 genotype IV has not been reported since 1977). These rare genotypes may have become minor populations or may be undergoing a silent transmission cycle (Lanciotti et al., 1994; Chen and Vasilakis, 2011; Santiago et al., 2012).

Fifteen years' worth of data from 2000 to 2014 for all serotypes showed that DENV sequences were primarily reported from South to Southeast Asia, Central to South America, and the countries of Oceania (**Figure 1A**). Some biases in DENV serotype compositions were observed in several countries. For instance, the dominant serotypes were DENV-1 and -2 in Mexico, DENV-1 and -4 in Polynesian countries with the exception of Fiji, and DENV-2 and -3 in Pakistan. In contrast, all serotypes were sampled in Brazil and Thailand.

Intriguingly, when focusing on the genotype instead of the serotype, the data from 2000 to 2014 showed at least three

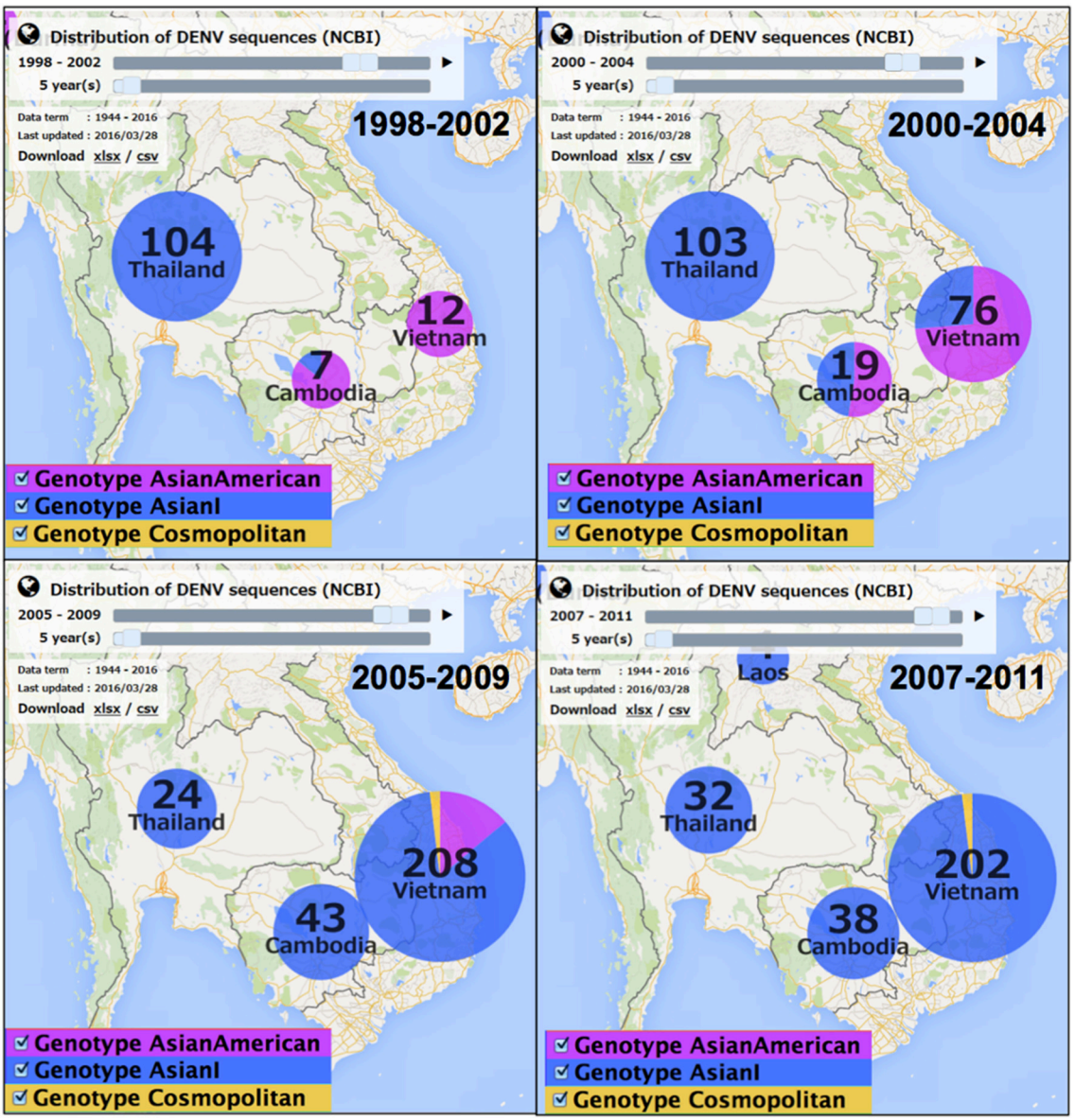

FIGURE 3 | Genotype distribution of DENV-2 in Indochina from 1998 to 2011. The movie of the genotype distribution in 1986–2014 can be downloaded as **Movie S1**.

potential geographical genotype distribution border lines in Asia (**Figures 1B,2**). The first border is between the American continents and other regions (**Figure 1B**), the second is located between Bangladesh and Myanmar for the genotype distributions of DENV-1 and -2 and India and Myanmar for DENV-3, and the third is located between Indochina and the Malay Peninsula (**Figure 2**). There seem to be differences in the DENV-1 and -3 distributions between Malaysia, Singapore and Indonesia; however, the border line is not clear because Malaysia and Indonesia consist of many islands and share Kalimantan Island and the deposited sequence data do not specify the original island isolation site. Although, some boundaries are not clear, these boundaries are roughly conserved among all serotypes except for the Bangladesh-Myanmar border line for DENV-4, suggesting potential barriers against the vector mosquitos' movements or human activities between the countries.

We also found a timeline change in the predominant genotypes. From 1998 to 2007, the dominant genotype in Asia was Cosmopolitan, although India-Pakistan-Sri Lanka and Southeast-Oceania belonged to different lineages (Khan et al., 2013). The major genotypes in the Indochina countries were different from those of the other Asian countries; genotype

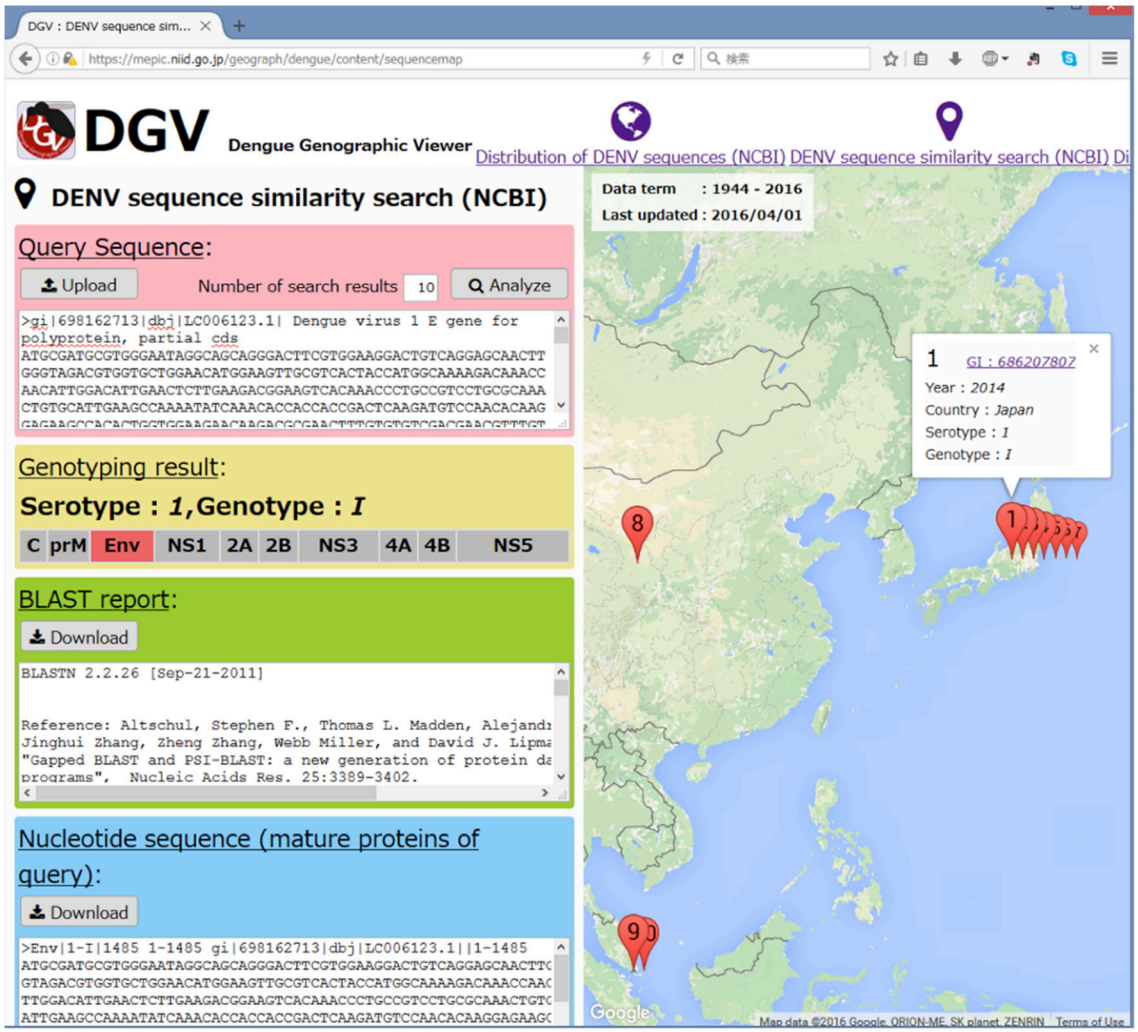

FIGURE 4 | A screenshot of the DENV sequence similarity search. An Env sequence derived from an autochthonous case in Japan (LC006123 or gi: 698162713) was used as a sample query. The query was assigned as the Env region of DENV-1 genotype I.

Asian I was predominant in Thailand, whereas genotype Asian American was predominant in Cambodia and Vietnam (**Figure 3** and **Movie S1**). From 2001, Asian I increased in Cambodia and Vietnam until finally in 2007 Asian I became the predominant genotype in Indochina. The genotype Asian I viruses in Thailand seemed to be widely disseminated into Vietnam via Cambodia but did not reach Malaysia and Bangladesh (**Figure 2**). Thus, the Asian American genotype was replaced by Asian I in Cambodia and Vietnam between 1998 and 2011. This example also suggests the idea of genotype transition, which probably reflects the mosquito vector habitat and human activities in the Indochinese Peninsula.

DGV currently does not support the prediction of Dengue epidemics, because number of deposited sequence data does not always reflect the actual number of events, in addition, it takes long time to be a public sequence through isolation, sequencing, and publication.

DENV Sequence Similarity Search

DGV provides a search engine for the assignment of the DENV serotype, genotype, and origin country according to the most homologous sequence on the basis of a blastn search against the DENV database. The search results are shown as text and are also plotted through Google Maps©. Subsequently, the query sequence is divided into mature protein regions and displayed with a serotype/genotype assignment. The homology search results and the divided nucleotide sequences in fasta format can be downloaded.

Here, we present an example similarity search for an Env sequence derived from an autochthonous case in Japan (LC006123 or gi: 698162713). DGV assigned the sequence as the Env region of the DENV-1 genotype I and identified homologous sequences from Japan, China, Singapore and Indonesia. These results are consistent with those from a previous study (**Figure 4**; Kutsuna et al., 2015).

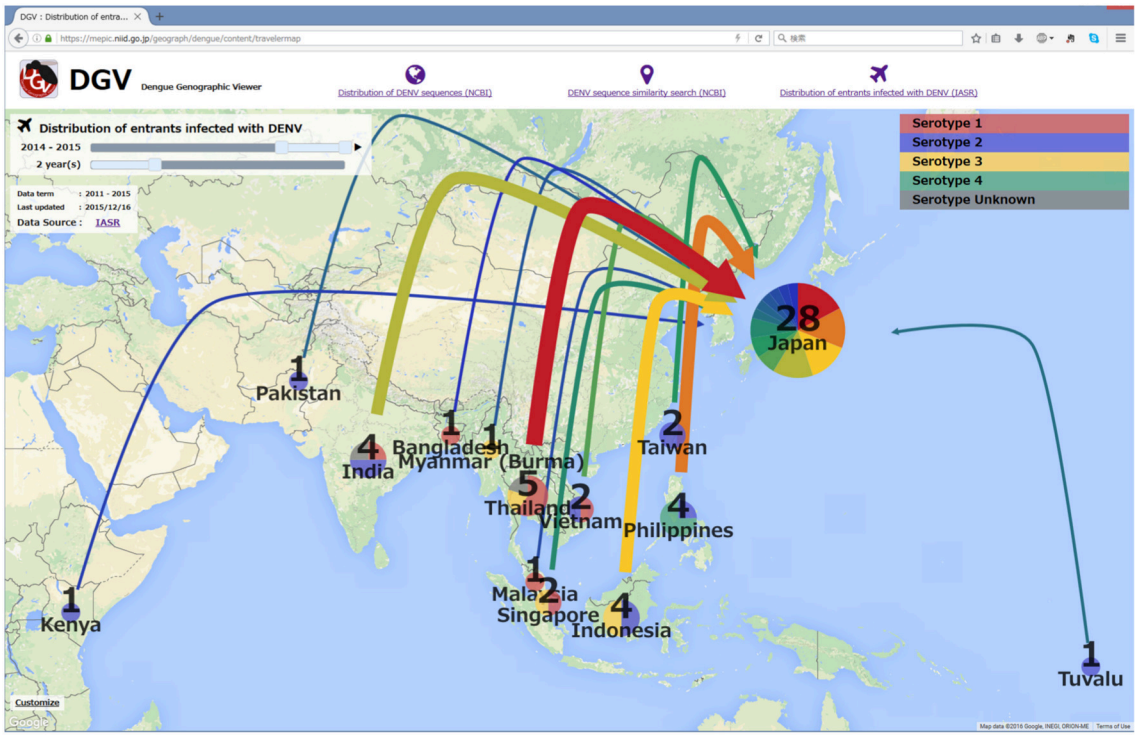

FIGURE 5 | A screenshot of the distribution of entrants infected with DENV, which shows the cumulative number of infected entrants from 2014 to 2015 based on the IASR.

Distribution of Entrants Infected with DENV

To aid in visualizing the source countries of dengue infection cases imported to Japan, the number of annual imported cases was also mapped on Google Maps©. The serotype (but not genotype), year, and visiting country/area are also indicated based on the Infectious Agents Surveillance Report (IASR), which releases monthly data and information obtained from prefectural and municipal public health institutes and quarantine stations to the public (**Figure 5**).

AUTHOR CONTRIBUTIONS

AY performed the experimental design, participated in the analysis and drafted the manuscript. TS1 implemented the application, performed the data collection, constructed the original genotype database, and participated in the analysis. TS2, KK, and TT reviewed the application and participated in the discussion. MK contributed to the experimental design, performed the analysis and drafted the manuscript. All authors read and approved the final manuscript.

FUNDING

This work was supported by a grant for Research on Emerging and Re-emerging Infectious Diseases (H25 Shinko-Ippan-015/H26 Shinko-Gyosei-Shitei-002) from the Ministry of Health, Labor and Welfare, Japan, and was also supported by the Research Program on Emerging and Re-emerging Infectious Diseases (15fk0108011h0003 and 15fm0108022h0001) from the Japan Agency for Medical Research and Development, AMED. This work was also partially supported by JSPS KAKENHI Grant Number 15K08488.The funders had no role in the study design, data collection and analysis, decision to publish, or preparation of the manuscript.

ACKNOWLEDGMENTS

We are grateful to Ms. Inamine from NIID for drawing the DGV icon. We thank Prof. Ikuta and Prof. Yasunaga from BIKEN for allowing us to use the original dataset "dengue virus genotyping database."

SUPPLEMENTARY MATERIAL

The Supplementary Material for this article can be found online at: http://journal.frontiersin.org/article/10.3389/fmicb.2016.00875

Movie S1 | Genotype transition of DENV-2 in Asia from 1986–1990 to 2010–2014.

REFERENCES

Abubakar, S., Wong, P. F., and Chan, Y. F. (2002). Emergence of dengue virus type 4 genotype IIA in Malaysia. *J. Gen. Virol.* 83, 2437–2442. doi: 10.1099/0022-1317-83-10-2437

Anez, G., Morales-Betoulle, M. E., and Rios, M. (2011). Circulation of different lineages of dengue virus type 2 in Central America, their evolutionary time-scale and selection pressure analysis. *PLoS ONE* 6:e27459. doi: 10.1371/journal.pone.0027459

Asnet, M. J., Rubia, A. G., Ramya, G., Nagalakshmi, R. N., and Shenbagarathai, R. (2014). DENVirDB: a web portal of dengue virus sequence information on Asian isolates. *J. Vector Borne Dis.* 51, 82–85.

Chen, R., and Vasilakis, N. (2011). Dengue–quo tu et quo vadis? *Viruses* 3, 1562–1608. doi: 10.3390/v3091562

Chiappelli, F., Santos, S. M., Caldeira Brant, X. M., Bakhordarian, A., Thames, A. D., Maida, C. A., et al. (2014). Viral immune evasion in dengue: toward evidence-based revisions of clinical practice guidelines. *Bioinformation* 10, 726–733. doi: 10.6026/97320630010726

Edgar, R. C. (2010). Search and clustering orders of magnitude faster than BLAST. *Bioinformatics* 26, 2460–2461. doi: 10.1093/bioinformatics/btq461

Goncalvez, A. P., Escalante, A. A., Pujol, F. H., Ludert, J. E., Tovar, D., Salas, R. A., et al. (2002). Diversity and evolution of the envelope gene of dengue virus type 1. *Virology* 303, 110–119. doi: 10.1006/viro.2002.1686

Katoh, K., and Standley, D. M. (2014). MAFFT: iterative refinement and additional methods. *Methods Mol. Biol.* 1079, 131–146. doi: 10.1007/978-1-62703-646-7_8

Khan, M. A., Ellis, E. M., Tissera, H. A., Alvi, M. Y., Rahman, F. F., Masud, F., et al. (2013). Emergence and diversification of dengue 2 cosmopolitan genotype in Pakistan, 2011. *PLoS ONE* 8:e56391. doi: 10.1371/journal.pone.0056391

Klungthong, C., Putnak, R., Mammen, M. P., Li, T., and Zhang, C. (2008). Molecular genotyping of dengue viruses by phylogenetic analysis of the sequences of individual genes. *J. Virol. Methods* 154, 175–181. doi: 10.1016/j.jviromet.2008.07.021

Kuhn, R. J., Zhang, W., Rossmann, M. G., Pletnev, S. V., Corver, J., Lenches, E., et al. (2002). Structure of dengue virus: implications for flavivirus organization, maturation, and fusion. *Cell* 108, 717–725. doi: 10.1016/S0092-8674(02)00660-8

Kutsuna, S., Kato, Y., Moi, M. L., Kotaki, A., Ota, M., Shinohara, K., et al. (2015). Autochthonous dengue fever, Tokyo, Japan, 2014. *Emerg. Infect. Dis.* 21, 517–520. doi: 10.3201/eid2103.141662

Lanciotti, R. S., Calisher, C. H., Gubler, D. J., Chang, G. J., and Vorndam, A. V. (1992). Rapid detection and typing of dengue viruses from clinical samples by using reverse transcriptase-polymerase chain reaction. *J. Clin. Microbiol.* 30, 545–551.

Lanciotti, R. S., Lewis, J. G., Gubler, D. J., and Trent, D. W. (1994). Molecular evolution and epidemiology of dengue-3 viruses. *J. Gen. Virol.* 75(Pt 1), 65–75. doi: 10.1099/0022-1317-75-1-65

Murray, N. E., Quam, M. B., and Wilder-Smith, A. (2013). Epidemiology of dengue: past, present and future prospects. *Clin. Epidemiol.* 5, 299–309. doi: 10.2147/CLEP.S34440

Pickett, B. E., Greer, D. S., Zhang, Y., Stewart, L., Zhou, L., Sun, G., et al. (2012). Virus pathogen database and analysis resource (ViPR): a comprehensive bioinformatics database and analysis resource for the coronavirus research community. *Viruses* 4, 3209–3226. doi: 10.3390/v4113209

Resch, W., Zaslavsky, L., Kiryutin, B., Rozanov, M., Bao, Y., and Tatusova, T. A. (2009). Virus variation resources at the National Center for Biotechnology Information: dengue virus. *BMC Microbiol* 9:65. doi: 10.1186/1471-2180-9-65

Santiago, G. A., Mcelroy-Horne, K., Lennon, N. J., Santiago, L. M., Birren, B. W., Henn, M. R., et al. (2012). Reemergence and decline of dengue virus serotype 3 in Puerto Rico. *J. Infect. Dis.* 206, 893–901. doi: 10.1093/infdis/jis426

Tamura, K., Peterson, D., Peterson, N., Stecher, G., Nei, M., and Kumar, S. (2011). MEGA5: molecular evolutionary genetics analysis using maximum likelihood, evolutionary distance, and maximum parsimony methods. *Mol. Biol. Evol.* 28, 2731–2739. doi: 10.1093/molbev/msr121

Wittke, V., Robb, T. E., Thu, H. M., Nisalak, A., Nimmannitya, S., Kalayanrooj, S., et al. (2002). Extinction and rapid emergence of strains of dengue 3 virus during an interepidemic period. *Virology* 301, 148–156. doi: 10.1006/viro.2002.1549

Yamashita, A., Sasaki, T., Kurosu, T., Yasunaga, T., and Ikuta, K. (2013). Origin and distribution of divergent dengue virus: novel database construction and phylogenetic analyses. *Future Virol.* 8, 1061–1083. doi: 10.2217/fvl.13.99

Conflict of Interest Statement: The authors declare that the research was conducted in the absence of any commercial or financial relationships that could be construed as a potential conflict of interest.

Copyright © 2016 Yamashita, Sakamoto, Sekizuka, Kato, Takasaki and Kuroda. This is an open-access article distributed under the terms of the Creative Commons Attribution License (CC BY). The use, distribution or reproduction in other forums is permitted, provided the original author(s) or licensor are credited and that the original publication in this journal is cited, in accordance with accepted academic practice. No use, distribution or reproduction is permitted which does not comply with these terms.

frontiers in Microbiology

REVIEW
published: 13 May 2016
doi: 10.3389/fmicb.2016.00676

Strategies for Human Tumor Virus Discoveries: From Microscopic Observation to Digital Transcriptome Subtraction

Ezra D. Mirvish[1] *and Masahiro Shuda*[2]*

[1] Department of Dermatology, University of Pittsburgh Medical Center, Pittsburgh, PA, USA, [2] Cancer Virology Program, University of Pittsburgh Cancer Institute, University of Pittsburgh, Pittsburgh, PA, USA

Over 20% of human cancers worldwide are associated with infectious agents, including viruses, bacteria, and parasites. Various methods have been used to identify human tumor viruses, including electron microscopic observations of viral particles, immunologic screening, cDNA library screening, nucleic acid hybridization, consensus PCR, viral DNA array chip, and representational difference analysis. With the Human Genome Project, a large amount of genetic information from humans and other organisms has accumulated over the last decade. Utilizing the available genetic databases, Feng et al. (2007) developed digital transcriptome subtraction (DTS), an *in silico* method to sequentially subtract human sequences from tissue or cellular transcriptome, and discovered Merkel cell polyomavirus (MCV) from Merkel cell carcinoma. Here, we review the background and methods underlying the human tumor virus discoveries and explain how DTS was developed and used for the discovery of MCV.

Keywords: tumor virus discoveries, methods, history, digital transcriptome subtraction, Merkel cell polyomavirus

OPEN ACCESS

Edited by:
Akihide Ryo,
Yokohama City University, Japan

Reviewed by:
Iwao Kukimoto,
National Institute of Infectious Diseases, Japan
David Wang,
Washington University, USA
Massimo Tommasino,
International Agency for Research on Cancer, France

****Correspondence:***
Masahiro Shuda
mas253@pitt.edu

Specialty section:
This article was submitted to Virology, a section of the journal Frontiers in Microbiology

Received: *01 March 2016*
Accepted: *26 April 2016*
Published: *13 May 2016*

Citation:
Mirvish ED and Shuda M (2016) Strategies for Human Tumor Virus Discoveries: From Microscopic Observation to Digital Transcriptome Subtraction. Front. Microbiol. 7:676. doi: 10.3389/fmicb.2016.00676

INTRODUCTION

Approximately 20% of human cancers worldwide are associated with infectious agents, including parasites, bacteria, and viruses (Parkin, 2006). In 12% of cancers, seven different viruses have been causally linked to human oncogenesis (**Table 1**): Epstein–Barr virus (EBV), hepatitis B virus (HBV), human T-lymphotropic retrovirus type 1 (HTLV-1), high-risk human papillomaviruses (HPV), hepatitis C virus (HCV), Kaposi's sarcoma herpesvirus (KSHV), and Merkel cell polyomavirus (MCV). The epidemiological and clinical information provides clues that indicate whether an infectious agent is involved in the development of cancer. Cancers that are related to immunosuppression, for example, are candidates for being caused by tumor viruses (Grulich et al., 2007). During the 20th century, various methods, ranging from the classical electron microscopic observation to the advanced molecular biology techniques, were used to identify cancer-causing viruses. Here, we will review the background and methods underlying the tumor virus discoveries during the past century as well as the newest virus discovery strategy, digital transcriptome subtraction (DTS) that we used to discover MCV.

TABLE 1 | Discovery methods of human tumor viruses.

Virus	Initial discovery method	Year	Associated human cancers	Reference
Epstein–Barr virus	Electron microscopic observation	1964	Burkitt's lymphoma, Hodgkin's lymphoma, post-transplantation lymphoproliferative disorder, and nasopharyngeal carcinoma, gastric carcinoma	Epstein et al., 1964
Hepatitis B	Immunology	1967	Hepatocellular carcinoma (HCC)	Blumberg et al., 1967
HTLV-1	Cell culture	1980	Adult T cell leukemia	Poiesz et al., 1980
Papillomavirus (high risk 16 and 18)	Nucleotide acid hybridization	1983–1984	Cervical carcinoma, head and neck carcinoma, anogenital cancer	Durst et al., 1983; Boshart et al., 1984
Hepatitis C	cDNA cloning	1989	HCC	Choo et al., 1989
Kaposi's sarcoma associated herpesvirus	Representational difference analysis	1994	Kaposi's sarcoma, primary effusion lymphoma, Castleman's disease	Chang et al., 1994
Merkel cell polyomavirus	Digital transcriptome subtraction	2008	Merkel cell carcinoma	Feng et al., 2008

METHODS USED FOR THE HUMAN TUMOR VIRUS DISCOVERIES

Cell Culture and Electron Microscopy

By the early 1960s, many viruses were known to cause tumors in animals (Javier and Butel, 2008), but none had been identified in human cancers. Burkitt (1958) first described his eponymous lymphoma in 1958 as a sarcoma involving the jaws of African children and hypothesized that the cancer's geographic distribution might implicate some infectious agent as an etiologic factor in disease development. When the first Burkitt's lymphoma-derived cell line was established *in vitro* and examined by electron microscopy, obvious herpesvirus morphology was readily observed (Epstein et al., 1964). Biological examinations demonstrated that this was a new human herpesvirus, which became known as the EBV after the cell line in which it was discovered (Epstein et al., 1965).

The human T-lymphotropic virus type 1 (HTLV-1), the first known human retrovirus, was also identified in cell culture (Poiesz et al., 1980). Retrovirus particles with type C morphology were observed in thin-section electron micrographs of fixed, pelleted cellular materials from two T-cell lymphoblastoid cell lines (HUT102 and CTCL-3) and peripheral blood lymphocytes from a patient with a cutaneous T-cell lymphoma. Mature particles were 100–110 nm in diameter, and consisted of an electron-dense core separated by an electron-lucent region from an outer membrane. Similar type C particles were identified in MT-1 cells derived from Japanese patients with adult T cell leukemia (ATL), which is now known to be caused by HTLV-1 (Hinuma et al., 1981). Indirect immunofluorescence staining was also used in the studies of ATL. A unique antigen was identified in MT-1 cells derived from ATL that was not found in other human lymphoid cell lines. All 44 examined ATL patients had positive serological reactions for this antigen.

In general, it is very rare that human cancer arises directly from the acute consequences of viral infection. Tumorigenesis usually occurs after a latency period of 15–40 years. However, a special exception is the X-chromosome-linked lymphoproliferative disorder (XLP) found in some EBV-infected patients. Mutated immune response genes leave susceptible males unable to respond to interferon (IFN) signaling, which can in turn lead to the development of an acute lymphoproliferative disease as a consequence of EBV replication (Kutok and Wang, 2006). Most viruses do not replicate efficiently in common laboratory cell lines due to the innate immune system, which controls IFN signaling. By targeting molecules in the IFN signaling pathway through knockout technology or RNA interference, it is possible to produce cells that are permissive for viral replication. Cell culture models with a defective IFN signaling pathway are useful for novel virus identification and characterization, especially in monitoring for cytopathic effects (CPE). The robust replication of a virus often gives rise to CPE, which involves morphological changes in the host cell, such as cell rounding, disorientation, swelling or shrinking, detachment from the culture surface, and cell death, and may indicate that the cells being studied are a good model in which to amplify the genome of the putative virus. This strategy was successfully used in acute infection with African green monkey kidney cells (Vero, a IFN-deficient cell) to identify previously uncharacterized human coronavirus (HCoV-NL63; van der Hoek et al., 2004). Humanized mice have also been developed to study viral infection in a systemic setting (Lassnig et al., 2005). In this study, viral replication was markedly enhanced in the offspring of mice with human viral receptor genes that were crossed with IFN unresponsive Stat1$^{-/-}$ mice. Such cell and animal models, which take advantage of advanced techniques in molecular biology and genetic engineering, have the potential to provide novel insights into the biology of otherwise unculturable infectious agents and to identify the tumorigenic potential of a virus.

Immunologic Methods to Detect Viral Antigen

Tissue culture, animal inoculation, and other virological methods were all applied unsuccessfully in early attempts to identify HBV (Blumberg, 1977). Blumberg et al. (1965) performed a systematic study of the sera collected from leukemia and hemophilia patients who had experienced frequent blood transfusions in order to detect precipitating iso-antibodies against unknown

antigens found in donor serum. The 'Australia antigen' was identified in the serum of an Australian Aborigine as being a target of precipitating antibodies generated in the serum of transfusion patients (Blumberg et al., 1965). It was found to be rare in normal Americans, but was common in normal people from Africa, Asia, and Oceania. These data led some to hypothesize a relationship between leukemia, the unknown agent, and genetic polymorphism(s) in Australia. Subsequently, the Australian antigen was revealed to be an antigen shared by multiple hepatitis patients (Blumberg et al., 1967; Prince, 1968). Virus-like particles containing 'Australian antigen' on their surface were eventually found by electronic microscopy in the blood of three patients with 'serum hepatitis' (Dane et al., 1970; Jokelainen et al., 1970). These findings were the first indication that the disease now known as hepatitis B is caused by a virus (HBV).

The discovery of HCV was an extraordinary achievement, because isolation of the viral genome did not rely on previously visualized viral particles, growth of the virus *in vitro*, or development of an immunological assay. Patients who had transfusion-associated hepatitis were described, despite being negative for hepatitis A and B antigens, which suggested the existence of another, unidentified infectious agent (Feinstone et al., 1975). Although several immunologic and serologic assays were developed, none was a specific, reliable serologic marker for this unknown hepatitis antigen. However, administration of the putative infectious reagent induced non-A, non-B hepatitis in chimpanzees, which confirmed that an infectious agent was likely responsible for the disease (Tabor et al., 1978). A decade after the development of the chimpanzee disease model, Alter and Houghton (2000), utilizing novel methodologies in molecular biology, conducted a blind immunoscreen using a recombinant phage expression library. In searching for an unknown virus in these non-A, non-B hepatitis patients, a randomly primed cDNA library was constructed from the plasma of chimpanzees that had been injected with serum from non-A, non-B hepatitis patients. cDNA was inserted into the bacteriophage λgt11 and expressed in *Escherichia coli*. The expressed proteins were then screened against serum from an infected non-A, non-B hepatitis patient. Among millions of the clones screened, one clone encoded an antigen that showed specific seroreactivity in non-A, non-B hepatitis patients. The putative virus was shown to contain a positive-strand RNA molecule of about 10,000 nucleotides that belongs to the *Flaviviridae* family (Choo et al., 1989). Novel virus discovery by screening recombinant expression libraries from infected tissues against patient sera represented a significant breakthrough. However, library screenings are also laborious, as hundreds of millions of bacterial cDNA clones had to be screened (Alter and Houghton, 2000).

Cross-hybridization to Identify Related Viruses

The *Papillomaviridae* comprise a super-family with several 100 members, most of which were identified in birds and mammals (de Villiers et al., 2004). Papillomaviruses are highly host-tropic and tissue-specific, causing small benign tumors known as papillomas or warts. HPV particles were observed by electron microscopy in cervical dysplasia (Della Torre et al., 1978; Meisels et al., 1981), whereas in cervical intraepithelial lesions and cervical cancer specimens, virus particles are not generally observed due to the viral integration into host genome. High-risk HPV 16 was isolated from an invasive cervical cancer by cross-hybridization with HPV type 11 DNA under non-stringent conditions (Durst et al., 1983). Using virus-specific probes, HPV 16 presence was confirmed in precursor lesion of malignant tumors (Ikenberg et al., 1983). High-risk HPV18 was subsequently identified by low stringency hybridization with HPV 8, 9, 10, and 11-related sequences (Boshart et al., 1984). zur Hausen's (1999) research group identified both HPV16 and 18, which together are responsible for approximately 70% of invasive cervical cancers (de Sanjose et al., 2010). His group further demonstrated that HPV DNA is integrated into the host genome in cervical cancer cell lines and that viral E6 and E7 genes are expressed in cervical cancer tumors (Schwarz et al., 1985).

Nucleic acid hybridization with a single or few probes is restricted by its ability to detect only a limited number of candidate viruses. To obviate this problem, Virochip was invented to detect a broad spectrum of viruses in a single analysis (Wang et al., 2002). The Virochip was successfully used to identify a previously uncharacterized coronavirus isolated from a SARS patient during the outbreak of the severe acute respiratory syndrome (SARS; Rota et al., 2003). For the tumor virus identification, the Virochip was used to screen RNA samples from prostate tumors. A novel gammaretrovirus, Xenotropic murine leukemia virus-related virus (XMRV), which is closely related to the xenotropic murine leukemia viruses (MuLVs), was found in patients with prostate cancers (Urisman et al., 2006), and chronic fatigue syndrome (Lombardi et al., 2009). XMRV is detected in malignant prostate epithelium by using quantitative PCR assay and immunohistochemistry with an anti-XMRV specific antiserum, raising the possibility of the virus may indirectly support tumorigenesis (Schlaberg et al., 2009). However, subsequent reports disprove the etiologic connection between XMRV infection and these two diseases (Fischer et al., 2008; Hohn et al., 2009; Lee et al., 2012). XMRV was found to have arisen during the passage of a human prostate cancer in mice, as a result of recombination between two endogenous MuLVs from the mouse cells. The resulting XMRV infected human prostate cancer cells due to its xenotropic host range (Paprotka et al., 2011).

With the widespread usage of PCR and availability of extensive viral sequences, it is possible to combine short-primer hybridization and the power of PCR to amplify potential viral sequences. This method is commonly known as consensus sequence-base PCR or degenerate PCR. Primer sequences are designed based on a conserved region of a viral genome. Human hepatitis G virus was identified by amplifying a segment of a putative helicase gene with consensus primers from hepatitis A, B, and C virus (Simons et al., 1995a). As with genomic nucleotide acid hybridization, consensus PCR/degenerate PCR relies on known viral sequences, and as such has limitations in identifying novel viruses. Moreover, false-positives due to non-specific

amplification and PCR contamination may introduce costly and fruitless downstream analyses. Thus, careful optimization of reaction and primer annealing temperatures and the use of nested or semi-nested strategies, as well as the use of known viruses as positive controls, are necessary.

Differential Display Strategy in Viral Pathogen Discovery

The recent molecular techniques for virus discovery are solely based on nucleic acids—rather than conventional viral particle morphology, *in vitro* cell culture, or serological assays—but must be used in conjunction with strong epidemiologic evidence (Gao and Moore, 1996). These methods identify discrepancies in nucleotide sequence between disease-associated tissue and normal tissue by subtractive strategies. Representational difference analysis (RDA) combines physical subtractive hybridization with gene amplification to detect differences between tumor genomic DNA and that of normal cells (Lisitsyn et al., 1993). Epidemiologic evidence indicated that Kaposi's sarcoma may be caused by a pathogen other than human immunodeficiency virus (HIV; Beral et al., 1990, 1992). By using RDA, novel viral fragments were identified in AIDS patients and further characterized as human Kaposi's sarcoma associated herpesvirus (KSHV; Chang et al., 1994; Moore et al., 1996). RDA has also been used to successfully identify hepatitis G virus (Simons et al., 1995b) and Torque Teno virus (TTV) in non-A–E hepatitis patients (Nishizawa et al., 1997). While RDA was used to successfully identify these viruses, this technique relies heavily on the non-diseased tissue controls and is not quantitative.

In Silico Subtraction Approach Using Nucleic Acid Database

With initiation of the Human Genome Project, the nucleic acid databases for humans and many other organisms rapidly expanded. Taking advantage of this new wealth of data, Weber et al. (2002) developed an *in silico* subtraction approach capable of identifying non-human sequences in 'human' expressed-sequence tag (EST) libraries. In this computational subtraction technique, sequences with high similarity to the human genome are subtracted from cDNA libraries, such that the remaining data are enriched for sequences of non-human origin. Weber et al. (2002) directly identified multiple human tumor viruses erroneously deposited as human ESTs in GenBank, including EBV, HBV, HPV type 16 and 18, HCV, and KSHV. Viral sequences were also found in data deposited from hepatocellular carcinoma (HCC) and cervical carcinoma cell lines: HBV sequences represented 0.1% of deposited HCC data, while HPV18 sequences accounted for 0.03% of the cervical carcinoma library. The same group also generated a cDNA library from a patient with post-transplant lymphoproliferative disorder (PTLD; Xu et al., 2003). A total of 27,840 cDNA sequences were generated and filtered by computational subtraction against known human sequences, leaving 32 non-matching sequences. Among these sequences, 10 (accounting for 0.03% of total sequences analyzed) were from EBV viruses. Taken together, these results suggest that it is possible to identify viral sequences by sampling fewer than 10,000 sequences.

DEVELOPMENT OF DIGITAL TRANSCRIPTOME SUBTRACTION

Feng et al. (2007) developed DTS as a quantitative means to search for viral infection in human cancers (**Figure 1**) (Feng et al., 2007). High quality sequences are extracted with a high stringency score (Phred $> = 20$) to avoid sequencing errors, and all sequences artificially used in the cDNA library preparation, such as sequencing primers, are removed. All sequences matching human databases are computationally subtracted to leave 'non-human' candidates. There are approximately 200,000 mRNA transcripts in a cell (Bishop et al., 1974; Velculescu et al., 1999), which correspond to five transcripts per million (TPM) for a single transcript per cell. In theory, one can analyze the whole transcriptome to search for viral etiology in human cancers. Thus, if no viral transcript is found, the possibility of a virus expressing transcript in a given tumor can be excluded above a certain threshold level.

Long serial analysis of gene expression (L-SAGE) was used to sample the cellular transcriptome for the presence of viral transcripts. L-SAGE quantitatively concatenates ∼21 bp cDNA tags from the 3′ end of mRNA transcripts, allowing for the measurement of gene expression via high-throughput sequencing (**Figure 1**) (Saha et al., 2002). When they performed a pilot analysis of DTS on 9,026 SAGE tags from an expression library of BCBL-1 cells infected with KSHV, only three candidate sequences were identified as being of non-human origin: two of these sequences belonged to KSHV transcripts and the third belonged to an unannotated human expression sequence tag, as confirmed by additional experiments. Overall, 0.24% of transcripts from this cell line were of viral origin. DTS was then applied to 258,302 SAGE tags from squamous cell conjunctival carcinoma (SCCC), a cancer strongly associated with immunosuppression (**Figure 1**). Only 21 of these sequences did not align to human databases, excluding one KSHV tag as an internal control. All 21 candidates were ruled out as viral sequences by further experimental examination (Feng et al., 2007). This analysis shows that it is unlikely that distinguishable viral transcripts are present in SCCC at 20 TPM or higher, which is the equivalent of approximately four transcripts per cell.

MERKEL CELL POLYOMAVIRUS DISCOVERY BY DTS

We further performed high-throughput sequencing on cDNA libraries constructed from Merkel cell carcinoma (MCC), a malignant skin tumor frequently found among immunosuppressed, transplant, and AIDS patients (Feng et al., 2008). A total of 395,734 sequences were subtracted through DTS analysis, leaving 2,395 'non-human' sequences (**Figure 1**). One transcript was similar to but distinct from African green monkey lymphotropic polyomavirus (LPV) and human BK

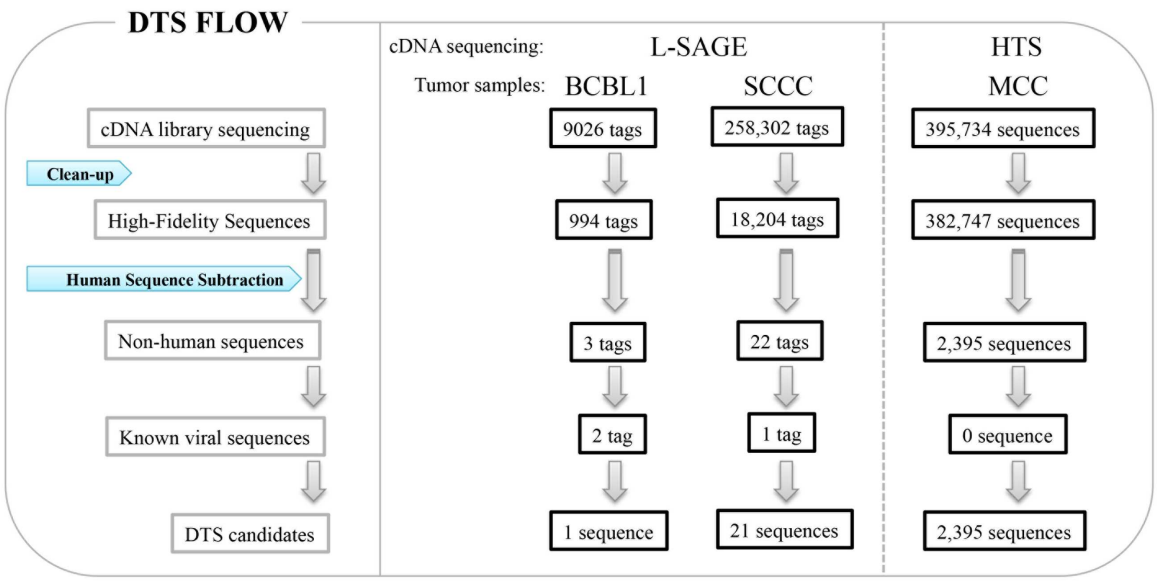

FIGURE 1 | Digital transcriptome subtraction (DTS). L-SAGE libraries were constructed from BCBL1, a KSHV positive cell line and squamous cell conjunctival carcinoma (SCCC), and short cDNA tags were sequenced for whole transcriptome analysis. High throughput sequencing (HTS) was performed on cDNA libraries from human Merkel cell carcinoma (MCC).

polyomavirus T antigen sequences, defining a new polyomavirus, MCV. Subsequently, we sequenced the complete closed circular genome of MCV (5,387 bp), which encodes a T antigen locus, late gene cassette for viral capsids, and replication origin sequences. MCV is the first human member of the murine polyomavirus subgroup, and shares highest homology with LPV and a new polyomavirus recently isolated from orangutans (Groenewoud et al., 2010). Overall, DTS is a simple screening method to discover novel viral nucleic acids in a quantitative manner with high throughput sequencing. We found MCV transcripts in MCC at a level of 10 TPM or approximately five transcripts per cell and can exclude distinguishable viral transcripts in SCCC at 20 TPM or higher, which is the equivalent of approximately four transcripts per cell. This provides, for the first time, quantitative evidence against some classes of viral etiology when no viral transcripts are found, thereby reducing the uncertainty involved in new pathogen discovery.

MCV IS THE FIRST HUMAN POLYOMAVIRUS CAUSING MCC

Virus discovery is only the first step to determining the etiology behind a disease. The detection of nucleic acid is not sufficient to prove causality. Our initial discovery of MCV demonstrated that the MCV genome is clonally integrated in ∼80% of MCC tumor cell DNA (Feng et al., 2008). Similar to other polyomaviruses, the MCV T antigen locus encodes for three major overlapping transcripts: large T (LT), small T (sT), and 57 kT antigens (Shuda et al., 2008). With respect to other well-studied polyomavirus T antigens, MCV LT has conserved N-terminus DnaJ and Rb binding domains, as well as C-terminus origin binding (OBD) and helicase domains, which are required for viral replication. MCV sT has a conserved PP2A binding domain (Shuda et al., 2008). Our viral sequence analysis in MCC tumors revealed that integrated MCV LT antigens are C-terminally truncated by tumor-specific mutations, which results in the loss of helicase function, whereas MCV sT remains intact (Shuda et al., 2008). This indicates that MCV is replication-defective in tumors and not a passenger virus that secondarily infects MCC tumors. We developed monoclonal antibodies, which specifically recognize MCV LT or MCV sT and carried out immunohistochemistry using these antibodies in MCC tissue microarrays. We identified that approximately ∼70% of MCC tumors express the truncated LT and sT proteins consistent with their role as directly transforming oncoproteins in MCC cancers (Shuda et al., 2009, 2011).

We identified three MCC cell lines harboring clonally integrated MCV, expressing both truncated LT and sT proteins (Houben et al., 2010; Guastafierro et al., 2013). If MCV is a direct viral carcinogen that causes most cases of MCC, we anticipate that its viral oncogene expression is necessary for the growth of MCC cells. The panT antigen knockdown (both LT and sT) by shRNA results in G0/G1 cell cycle arrest in MCV-positive MCC tumor cells and non-apoptotic cell death as measured by caspase cleavage (Houben et al., 2010). To further assess the importance of individual T antigens in MCC, we exploited an shRNA that knocks down sT antigen alone. Knockdown of MCV sT expression abolished tumor cell growth capacity (Shuda et al., 2011). On the other hand, Houben et al. (2015) demonstrated that shRNA knockdown of MCV LT alone also inhibits MCV-positive MCC cell proliferation. These results indicate that both MCV sT and LT play critical roles in the maintenance of a tumorigenic phenotype in MCC cells.

Our *in vitro* transformation studies demonstrated that MCV sT expression alone is sufficient to transform immortalized rodent fibroblast cell lines in a soft agar assay, while MCV LT expression was not (Shuda et al., 2011). MCV LT expression, however, promoted cell proliferation in human fibroblasts through its Rb binding domain (Cheng et al., 2013; Richards et al., 2015). Further, multiple groups demonstrated the oncogenic activities of MCV T antigen in transgenic mouse models. The MCC-derived MCV T antigen expression in mice, driven by the keratin 14 promoter induces papillomatosis (Spurgeon et al., 2015). MCV sT expression using a keratin 5 promoter also induces hyperproliferative lesions (Verhaegen et al., 2015). We have also demonstrated that MCV sT expression by the ubiquitin promoter in p53 null mice induces high-grade tumors in spleen and liver tissues (Shuda et al., 2015). These results are consistent with MCV being a human tumor virus encoding T antigen viral oncoproteins.

Among 13 known human polyomaviruses, eleven have been identified over the past 9 years by molecular technologies and next generation DNA sequencing (DeCaprio and Garcea, 2013; Rinaldo and Hirsch, 2013; Mishra et al., 2014). While JC virus and SV40 are suspected to play a role in human cancers, the viral copy numbers in the associated tumors are very low (less than one copy per cell; Gordon et al., 2002; Rollison et al., 2005). Recently, to survey for the presence of human polyomaviruses in cancer, Toptan et al. (2016) developed the immunohistochemistry-based pan-human polyomavirus screening that can detect T antigen protein expression of all known human polyomaviruses including SV40. However, the study did not find any evidence of the polyomavirus T antigen expression in the 1,184 various tumor cases except the MCV T antigen expression in MCC tumors (Toptan et al., 2016). Thus MCV is the only polyomavirus strongly linked to a human cancer at present.

CONCLUDING REMARKS

Identification of 'non-human' sequences from a whole transcriptome does not necessarily indicate the presence of other genomes in human disease, as contamination from sample preparation may introduce some 'non-human' sequences. The existence of such sequences is only meaningful in the context of a strong association with human disease. Koch's postulates and their revisions provide a valid standard for judging disease causation (Fredricks and Relman, 1996). In spite of acute infection, tumorigenesis usually occurs after a long latency period. To move from association to causation for putatively carcinogenic viral agents, zur Hausen (1999) has also proposed new criteria for defining a causal role of an infection in human cancers: (1) strong epidemiological plausibility and evidence that a viral infection represents a risk factor for the development of a specific tumor; (2) the consistent presence and persistence of the 'non-human' sequences in cells of the tumor; (3) the stimulation of cell proliferation by the 'non-human' genome (or part of it) in corresponding cell culture systems; (4) the demonstration that the 'non-human' genome induces proliferation and the malignant phenotype of the tumor. To address whether MCV is causally relevant to MCC, additional evidence is needed to elucidate tumorigenic potential of the MCV T antigen.

In addition to the cancers known to be caused by human viruses, there are many tumors in which a viral etiology is suspected, including some hematopoietic malignancies, breast cancer, colorectal cancer, basal cell carcinoma of the skin, and lung cancers in non-smokers (Zur Hausen, 2009). Undoubtedly, DTS analysis on whole transcriptomes of human tumors, in conjunction with other approaches of the sort described above, will help us to identify new clues or eliminate potential viral etiologies. Despite the power of DTS in searching for viral etiologies, there are some caveats that should be kept in mind: (1) DTS relies on high database quality and unique features of non-human sequences. Viral sequences that have been accidentally deposited into human databases or viral sequences that are indistinguishable from human transcripts will cause analyses to fail. A specific subgroup of human endogenous retrovirus (HERV-K) is suspected to be associated with multiple cancers (Moyes et al., 2007). DTS against the human genome would subtract out endogenous retroviral sequences as human and thus fail to detect pathogenic sequences. (2) Viral transcripts that lack polyadenylation sites, such as found in *Flaviviridae* and *Reoviridae,* cannot be detected. (3) Viruses causing tumors without gene expression, such by insertional mutagenesis, will be missed. Thus, extra efforts should be made to overcome the caveats of DTS analysis by combining with other methods for virus discovery.

The invention of high throughput sequencing technology developed massive transcriptome database generated from various human cancers in the Cancer Genome Atlas (TCGA), which could be a direct resource for DTS. Several studies interrogated transcriptome sequencing data from nearly 4,000 different tumors generated within the TCGA consortium for the presence of viral sequences by using the strategy similar to DTS (Khoury et al., 2013; Tang et al., 2013). One of these studies revealed a rare bladder cancer with BK polyomavirus integration that expresses full length LT antigen (Tang et al., 2013) and also identified a novel enterovirus in colon adenocarcinoma which is unlikely to be oncogenic. The use of DTS to the expanding transcriptome database in the TCGA may allow us to discover the eighth human tumor virus in the near future.

AUTHOR CONTRIBUTIONS

All authors listed, have made substantial, direct and intellectual contribution to the work, and approved it for publication.

ACKNOWLEDGMENTS

We would like to thank Drs. Huichen Feng, Patrick S. Moore, and Yuan Chang for their helpful comments on earlier versions of this manuscript. The authors also wish to thank Celestino Velásquez and Justin Wendzicki who assisted in the proofreading of this manuscript.

REFERENCES

Alter, H. J., and Houghton, M. (2000). Clinical medical research award. Hepatitis C virus and eliminating post-transfusion hepatitis. *Nat. Med.* 6, 1082–1086. doi: 10.1038/80394

Beral, V., Bull, D., Darby, S., Weller, I., Carne, C., Beecham, M., et al. (1992). Risk of Kaposi's sarcoma and sexual practices associated with faecal contact in homosexual or bisexual men with AIDS. *Lancet* 339, 632–635. doi: 10.1016/0140-6736(92)90793-3

Beral, V., Peterman, T. A., Berkelman, R. L., and Jaffe, H. W. (1990). Kaposi's sarcoma among persons with AIDS: a sexually transmitted infection? *Lancet* 335, 123–128. doi: 10.1016/0140-6736(90)90001-L

Bishop, J. O., Morton, J. G., Rosbash, M., and Richardson, M. (1974). Three abundance classes in HeLa cell messenger RNA. *Nature* 250, 199–204. doi: 10.1038/250199a0

Blumberg, B. S. (1977). Australia antigen and the biology of hepatitis B. *Science* 197, 17–25. doi: 10.1126/science.325649

Blumberg, B. S., Alter, H. J., and Visnich, S. (1965). A "New" antigen in leukemia sera. *JAMA* 191, 541–546. doi: 10.1001/jama.1965.03080070025007

Blumberg, B. S., Gerstley, B. J., Hungerford, D. A., London, W. T., and Sutnick, A. I. (1967). A serum antigen (Australia antigen) in Down's syndrome, leukemia, and hepatitis. *Ann. Int. Med.* 66, 924–931. doi: 10.7326/0003-4819-66-5-924

Boshart, M., Gissmann, L., Ikenberg, H., Kleinheinz, A., Scheurlen, W., and Zur Hausen, H. (1984). A new type of papillomavirus DNA, its presence in genital cancer biopsies and in cell lines derived from cervical cancer. *EMBO J.* 3, 1151–1157.

Burkitt, D. (1958). A sarcoma involving the jaws in African children. *Br. J. Surg.* 46, 218–223. doi: 10.1002/bjs.18004619704

Chang, Y., Cesarman, E., Pessin, M. S., Lee, F., Culpepper, J., Knowles, D. M., et al. (1994). Identification of herpesvirus-like DNA sequences in AIDS-associated Kaposi's sarcoma. *Science* 266, 1865–1869. doi: 10.1126/science.7997879

Cheng, J., Rozenblatt-Rosen, O., Paulson, K. G., Nghiem, P., and Decaprio, J. A. (2013). Merkel cell polyomavirus large T antigen has growth-promoting and inhibitory activities. *J. Virol.* 87, 6118–6126. doi: 10.1128/JVI.00385-13

Choo, Q. L., Kuo, G., Weiner, A. J., Overby, L. R., Bradley, D. W., and Houghton, M. (1989). Isolation of a cDNA clone derived from a blood-borne non-A, non-B viral hepatitis genome. *Science* 244, 359–362. doi: 10.1126/science.2523562

Dane, D. S., Cameron, C. H., and Briggs, M. (1970). Virus-like particles in serum of patients with Australia-antigen-associated hepatitis. *Lancet* 1, 695–698. doi: 10.1016/S0140-6736(70)90926-8

de Sanjose, S., Quint, W. G., Alemany, L., Geraets, D. T., Klaustermeier, J. E., Lloveras, B., et al. (2010). Human papillomavirus genotype attribution in invasive cervical cancer: a retrospective cross-sectional worldwide study. *Lancet Oncol.* 11, 1048–1056. doi: 10.1016/S1470-2045(10)70230-8

de Villiers, E. M., Fauquet, C., Broker, T. R., Bernard, H. U., and Zur Hausen, H. (2004). Classification of papillomaviruses. *Virology* 324, 17–27. doi: 10.1016/j.virol.2004.03.033

DeCaprio, J. A., and Garcea, R. L. (2013). A cornucopia of human polyomaviruses. *Nat. Rev. Microbiol.* 11, 264–276. doi: 10.1038/nrmicro2992

Della Torre, G., Pilotti, S., De Palo, G., and Rilke, F. (1978). Viral particles in cervical condylomatous lesions. *Tumori* 64, 549–553.

Durst, M., Gissmann, L., Ikenberg, H., and Zur Hausen, H. (1983). A papillomavirus DNA from a cervical carcinoma and its prevalence in cancer biopsy samples from different geographic regions. *Proc. Natl. Acad. Sci. U.S.A.* 80, 3812–3815. doi: 10.1073/pnas.80.12.3812

Epstein, M. A., Achong, B. G., and Barr, Y. M. (1964). Virus particles in cultured lymphoblasts from Burkitt's lymphoma. *Lancet* 1, 702–703. doi: 10.1016/S0140-6736(64)91524-7

Epstein, M. A., Henle, G., Achong, B. G., and Barr, Y. M. (1965). morphological and biological studies on a virus in cultured lymphoblasts from Burkitt's lymphoma. *J. Exp. Med.* 121, 761–770. doi: 10.1084/jem.121.5.761

Feinstone, S. M., Kapikian, A. Z., Purcell, R. H., Alter, H. J., and Holland, P. V. (1975). Transfusion-associated hepatitis not due to viral hepatitis type A or B. *N. Engl. J. Med.* 292, 767–770. doi: 10.1056/NEJM197504102921502

Feng, H., Shuda, M., Chang, Y., and Moore, P. S. (2008). Clonal integration of a polyomavirus in human Merkel cell carcinoma. *Science* 319, 1096–1100. doi: 10.1126/science.1152586

Feng, H., Taylor, J. L., Benos, P. V., Newton, R., Waddell, K., Lucas, S. B., et al. (2007). Human transcriptome subtraction by using short sequence tags to search for tumor viruses in conjunctival carcinoma. *J. Virol.* 81, 11332–11340. doi: 10.1128/JVI.00875-07

Fischer, N., Hellwinkel, O., Schulz, C., Chun, F. K., Huland, H., Aepfelbacher, M., et al. (2008). Prevalence of human gammaretrovirus XMRV in sporadic prostate cancer. *J. Clin. Virol.* 43, 277–283. doi: 10.1016/j.jcv.2008.04.016

Fredricks, D. N., and Relman, D. A. (1996). Sequence-based identification of microbial pathogens: a reconsideration of Koch's postulates. *Clin. Microbiol. Rev.* 9, 18–33.

Gao, S. J., and Moore, P. S. (1996). Molecular approaches to the identification of unculturable infectious agents. *Emerg. Infect. Dis.* 2, 159–167. doi: 10.3201/eid0203.960301

Gordon, G. J., Chen, C. J., Jaklitsch, M. T., Richards, W. G., Sugarbaker, D. J., and Bueno, R. (2002). Detection and quantification of SV40 large T-antigen DNA in mesothelioma tissues and cell lines. *Oncol. Rep.* 9, 631–634.

Groenewoud, M. J., Fagrouch, Z., Van Gessel, S., Niphuis, H., Bulavaite, A., Warren, K. S., et al. (2010). Characterization of novel polyomaviruses from Bornean and Sumatran orang-utans. *J. Gen. Virol.* 91, 653–658. doi: 10.1099/vir.0.017673-0

Grulich, A. E., Van Leeuwen, M. T., Falster, M. O., and Vajdic, C. M. (2007). Incidence of cancers in people with HIV/AIDS compared with immunosuppressed transplant recipients: a meta-analysis. *Lancet* 370, 59–67. doi: 10.1016/S0140-6736(07)61050-2

Guastafierro, A., Feng, H., Thant, M., Kirkwood, J. M., Chang, Y., Moore, P. S., et al. (2013). Characterization of an early passage merkel cell polyomavirus-positive merkel cell carcinoma cell line, MS-1, and its growth in NOD scid gamma mice. *J. Virol. Methods* 187, 6–14. doi: 10.1016/j.jviromet.2012.10.001

Hinuma, Y., Nagata, K., Hanaoka, M., Nakai, M., Matsumoto, T., Kinoshita, K. I., et al. (1981). Adult T-cell leukemia: antigen in an ATL cell line and detection of antibodies to the antigen in human sera. *Proc. Natl. Acad. Sci. U.S.A.* 78, 6476–6480. doi: 10.1073/pnas.78.10.6476

Hohn, O., Krause, H., Barbarotto, P., Niederstadt, L., Beimforde, N., Denner, J., et al. (2009). Lack of evidence for xenotropic murine leukemia virus-related virus(XMRV) in German prostate cancer patients. *Retrovirology* 6:92. doi: 10.1186/1742-4690-6-92

Houben, R., Angermeyer, S., Haferkamp, S., Aue, A., Goebeler, M., Schrama, D., et al. (2015). Characterization of functional domains in the Merkel cell polyoma virus Large T antigen. *Int. J. Cancer* 136, E290–E300. doi: 10.1002/ijc.29200

Houben, R., Shuda, M., Weinkam, R., Schrama, D., Feng, H., Chang, Y., et al. (2010). Merkel cell polyomavirus-infected Merkel cell carcinoma cells require expression of viral T antigens. *J. Virol.* 84, 7064–7072. doi: 10.1128/JVI.02400-09

Ikenberg, H., Gissmann, L., Gross, G., Grussendorf-Conen, E. I., and Zur Hausen, H. (1983). Human papillomavirus type-16-related DNA in genital Bowen's disease and in Bowenoid papulosis. *Int. J. Cancer* 32, 563–565. doi: 10.1002/ijc.2910320507

Javier, R. T., and Butel, J. S. (2008). The history of tumor virology. *Cancer Res.* 68, 7693–7706. doi: 10.1158/0008-5472.CAN-08-3301

Jokelainen, P. T., Krohn, K., Prince, A. M., and Finlayson, N. D. (1970). Electrn microscopic observations on virus-like particles associated with SH antigen. *J. Virol.* 6, 685–689.

Khoury, J. D., Tannir, N. M., Williams, M. D., Chen, Y., Yao, H., Zhang, J., et al. (2013). Landscape of DNA virus associations across human malignant cancers: analysis of 3,775 cases using RNA-Seq. *J. Virol.* 87, 8916–8926. doi: 10.1128/JVI.00340-13

Kutok, J. L., and Wang, F. (2006). Spectrum of Epstein-Barr virus-associated diseases. *Annu. Rev. Pathol.* 1, 375–404. doi: 10.1146/annurev.pathol.1.110304.100209

Lassnig, C., Kolb, A., Strobl, B., Enjuanes, L., and Muller, M. (2005). Studying human pathogens in animal models: fine tuning the humanized mouse. *Transgenic Res.* 14, 803–806. doi: 10.1007/s11248-005-1676-y

Lee, D., Das Gupta, J., Gaughan, C., Steffen, I., Tang, N., Luk, K. C., et al. (2012). In-depth investigation of archival and prospectively collected samples reveals no evidence for XMRV infection in prostate cancer. *PLoS ONE* 7:e44954. doi: 10.1371/journal.pone.0044954

Lisitsyn, N., Lisitsyn, N., and Wigler, M. (1993). Cloning the differences between two complex genomes. *Science* 259, 946–951. doi: 10.1126/science.8438152

Lombardi, V. C., Ruscetti, F. W., Das Gupta, J., Pfost, M. A., Hagen, K. S., Peterson, D. L., et al. (2009). Detection of an infectious retrovirus, XMRV, in blood cells of patients with chronic fatigue syndrome. *Science* 326, 585–589. doi: 10.1126/science.1179052

Meisels, A., Roy, M., Fortier, M., Morin, C., Casas-Cordero, M., Shah, K. V., et al. (1981). Human papillomavirus infection of the cervix: the atypical condyloma. *Acta Cytol.* 25, 7–16.

Mishra, N., Pereira, M., Rhodes, R. H., An, P., Pipas, J. M., Jain, K., et al. (2014). Identification of a novel polyomavirus in a pancreatic transplant recipient with retinal blindness and vasculitic myopathy. *J. Infect. Dis.* 210, 1595–1599. doi: 10.1093/infdis/jiu250

Moore, P. S., Gao, S. J., Dominguez, G., Cesarman, E., Lungu, O., Knowles, D. M., et al. (1996). Primary characterization of a herpesvirus agent associated with Kaposi's sarcomae. *J. Virol.* 70, 549–558.

Moyes, D., Griffiths, D. J., and Venables, P. J. (2007). Insertional polymorphisms: a new lease of life for endogenous retroviruses in human disease. *Trends Genet.* 23, 326–333. doi: 10.1016/j.tig.2007.05.004

Nishizawa, T., Okamoto, H., Konishi, K., Yoshizawa, H., Miyakawa, Y., and Mayumi, M. (1997). A novel DNA virus (TTV) associated with elevated transaminase levels in posttransfusion hepatitis of unknown etiology. *Biochem. Biophys. Res. Commun.* 241, 92–97. doi: 10.1006/bbrc.1997.7765

Paprotka, T., Delviks-Frankenberry, K. A., Cingoz, O., Martinez, A., Kung, H. J., Tepper, C. G., et al. (2011). Recombinant origin of the retrovirus XMRV. *Science* 333, 97–101. doi: 10.1126/science.1205292

Parkin, D. M. (2006). The global health burden of infection-associated cancers in the year 2002. *Int. J. Cancer* 118, 3030–3044. doi: 10.1002/ijc.21731

Poiesz, B. J., Ruscetti, F. W., Gazdar, A. F., Bunn, P. A., Minna, J. D., and Gallo, R. C. (1980). Detection and isolation of type C retrovirus particles from fresh and cultured lymphocytes of a patient with cutaneous T-cell lymphoma. *Proc. Natl. Acad. Sci. U.S.A.* 77, 7415–7419. doi: 10.1073/pnas.77.12.7415

Prince, A. M. (1968). Relation of Australia and SH antigens. *Lancet* 2, 462–463. doi: 10.1016/S0140-6736(68)90512-6

Richards, K. F., Guastafierro, A., Shuda, M., Toptan, T., Moore, P. S., and Chang, Y. (2015). Merkel cell polyomavirus T antigens promote cell proliferation and inflammatory cytokine gene expression. *J. Gen. Virol.* doi: 10.1099/jgv.0.000287 [Epub ahead of print].

Rinaldo, C. H., and Hirsch, H. H. (2013). The human polyomaviruses: from orphans and mutants to patchwork family. *APMIS* 121, 681–684. doi: 10.1111/apm.12125

Rollison, D. E., Utaipat, U., Ryschkewitsch, C., Hou, J., Goldthwaite, P., Daniel, R., et al. (2005). Investigation of human brain tumors for the presence of polyomavirus genome sequences by two independent laboratories. *Int. J. Cancer* 113, 769–774. doi: 10.1002/ijc.20641

Rota, P. A., Oberste, M. S., Monroe, S. S., Nix, W. A., Campagnoli, R., Icenogle, J. P., et al. (2003). Characterization of a novel coronavirus associated with severe acute respiratory syndrome. *Science* 300, 1394–1399. doi: 10.1126/science.1085952

Saha, S., Sparks, A. B., Rago, C., Akmaev, V., Wang, C. J., Vogelstein, B., et al. (2002). Using the transcriptome to annotate the genome. *Nat. Biotechnol.* 20, 508–512. doi: 10.1038/nbt0502-508

Schlaberg, R., Choe, D. J., Brown, K. R., Thaker, H. M., and Singh, I. R. (2009). XMRV is present in malignant prostatic epithelium and is associated with prostate cancer, especially high-grade tumors. *Proc. Natl. Acad. Sci. U.S.A.* 106, 16351–16356. doi: 10.1073/pnas.0906922106

Schwarz, E., Freese, U. K., Gissmann, L., Mayer, W., Roggenbuck, B., Stremlau, A., et al. (1985). Structure and transcription of human papillomavirus sequences in cervical carcinoma cells. *Nature* 314, 111–114. doi: 10.1038/314111a0

Shuda, M., Arora, R., Kwun, H. J., Feng, H., Sarid, R., Fernandez-Figueras, M. T., et al. (2009). Human merkel cell polyomavirus infection I. MCV T antigen expression in merkel cell carcinoma, lymphoid tissues and lymphoid tumors. *Int. J. Cancer* 125, 1243–1249. doi: 10.1002/ijc.24510

Shuda, M., Feng, H., Kwun, H. J., Rosen, S. T., Gjoerup, O., Moore, P. S., et al. (2008). T antigen mutations are a human tumor-specific signature for Merkel cell polyomavirus. *Proc. Natl. Acad. Sci. U.S.A.* 105, 16272–16277. doi: 10.1073/pnas.0806526105

Shuda, M., Guastafierro, A., Geng, X., Shuda, Y., Ostrowski, S. M., Lukianov, S., et al. (2015). Merkel cell polyomavirus small T antigen induces cancer and embryonic merkel cell proliferation in a transgenic mouse model. *PLoS ONE* 10:e0142329. doi: 10.1371/journal.pone.0142329

Shuda, M., Kwun, H. J., Feng, H., Chang, Y., and Moore, P. S. (2011). Human Merkel cell polyomavirus small T antigen is an oncoprotein targeting the 4E-BP1 translation regulator. *J. Clin. Invest.* 121, 3623–3634. doi: 10.1172/JCI46323

Simons, J. N., Leary, T. P., Dawson, G. J., Pilot-Matias, T. J., Muerhoff, A. S., Schlauder, G. G., et al. (1995a). Isolation of novel virus-like sequences associated with human hepatitis. *Nat. Med.* 1, 564–569. doi: 10.1038/nm0695-564

Simons, J. N., Pilot-Matias, T. J., Leary, T. P., Dawson, G. J., Desai, S. M., Schlauder, G. G., et al. (1995b). Identification of two flavivirus-like genomes in the GB hepatitis agent. *Proc. Natl. Acad. Sci. U.S.A.* 92, 3401–3405. doi: 10.1073/pnas.92.8.3401

Spurgeon, M. E., Cheng, J., Bronson, R. T., Lambert, P. F., and Decaprio, J. A. (2015). Tumorigenic activity of merkel cell polyomavirus T antigens expressed in the stratified epithelium of mice. *Cancer Res.* 75, 1068–1079. doi: 10.1158/0008-5472.CAN-14-2425

Tabor, E., Gerety, R. J., Drucker, J. A., Seeff, L. B., Hoofnagle, J. H., Jackson, D. R., et al. (1978). Transmission of non-A, non-B hepatitis from man to chimpanzee. *Lancet* 1, 463–466. doi: 10.1016/S0140-6736(78)90132-0

Tang, K. W., Alaei-Mahabadi, B., Samuelsson, T., Lindh, M., and Larsson, E. (2013). The landscape of viral expression and host gene fusion and adaptation in human cancer. *Nat. Commun.* 4:2513. doi: 10.1038/ncomms3513

Toptan, T., Yousem, S. A., Ho, J., Matsushima, Y., Stabile, L. P., Fernandez-Figueras, M. T., et al. (2016). Survey for human polyomaviruses in cancer. *JCI Insight* 1:e85562. doi: 10.1172/jci.insight.85562

Urisman, A., Molinaro, R. J., Fischer, N., Plummer, S. J., Casey, G., Klein, E. A., et al. (2006). Identification of a novel Gammaretrovirus in prostate tumors of patients homozygous for R462Q RNASEL variant. *PLoS Pathog.* 2:e25. doi: 10.1371/journal.ppat.0020025

van der Hoek, L., Pyrc, K., Jebbink, M. F., Vermeulen-Oost, W., Berkhout, R. J., Wolthers, K. C., et al. (2004). Identification of a new human coronavirus. *Nat. Med.* 10, 368–373. doi: 10.1038/nm1024

Velculescu, V. E., Madden, S. L., Zhang, L., Lash, A. E., Yu, J., Rago, C., et al. (1999). Analysis of human transcriptomes. *Nat. Genet.* 23, 387–388. doi: 10.1038/70487

Verhaegen, M. E., Mangelberger, D., Harms, P. W., Vozheiko, T. D., Weick, J. W., Wilbert, D. M., et al. (2015). Merkel cell polyomavirus small T antigen is oncogenic in transgenic mice. *J. Invest. Dermatol.* 135, 1415–1424. doi: 10.1038/jid.2014.446

Wang, D., Coscoy, L., Zylberberg, M., Avila, P. C., Boushey, H. A., Ganem, D., et al. (2002). Microarray-based detection and genotyping of viral pathogens. *Proc. Natl. Acad. Sci. U.S.A.* 99, 15687–15692. doi: 10.1073/pnas.242579699

Weber, G., Shendure, J., Tanenbaum, D. M., Church, G. M., and Meyerson, M. (2002). Identification of foreign gene sequences by transcript filtering against the human genome. *Nat. Genet.* 30, 141–142. doi: 10.1038/ng818

Xu, Y., Stange-Thomann, N., Weber, G., Bo, R., Dodge, S., David, R. G., et al. (2003). Pathogen discovery from human tissue by sequence-based computational subtraction. *Genomics* 81, 329–335. doi: 10.1016/S0888-7543(02)00043-5

zur Hausen, H. (1999). Viruses in human cancers. *Eur. J. Cancer* 35, 1878–1885. doi: 10.1016/S0959-8049(99)00113-6

Zur Hausen, H. (2009). The search for infectious causes of human cancers: where and why. *Virology* 392, 1–10. doi: 10.1016/j.virol.2009.06.001

Conflict of Interest Statement: The authors declare that the research was conducted in the absence of any commercial or financial relationships that could be construed as a potential conflict of interest.

Copyright © 2016 Mirvish and Shuda. This is an open-access article distributed under the terms of the Creative Commons Attribution License (CC BY). The use, distribution or reproduction in other forums is permitted, provided the original author(s) or licensor are credited and that the original publication in this journal is cited, in accordance with accepted academic practice. No use, distribution or reproduction is permitted which does not comply with these terms.

frontiers in Microbiology

REVIEW
published: 10 March 2016
doi: 10.3389/fmicb.2016.00300

Filopodia and Viruses: An Analysis of Membrane Processes in Entry Mechanisms

*Kenneth Chang[1], John Baginski[1], Samer F. Hassan[2], Michael Volin[1], Deepak Shukla[2] and Vaibhav Tiwari[1]**

[1] Department of Microbiology and Immunology, Chicago College of Osteopathic Medicine, Midwestern University, Downers Grove, IL, USA, [2] Department of Ophthalmology and Visual Sciences, University of Illinois at Chicago, Chicago, IL, USA

Filopodia are thin, actin rich bundles protruding from cell plasma membranes, serving physiological purposes, such as probing the environment and facilitating cell-to-cell adhesion. Recent studies have highlighted that actively polymerized filopodial-protrusions are exploited during virus entry, trafficking, spread, and the development of clinical pathology of viral diseases. These observations have caused a surge in investigation of the key determinants of filopodial induction and their influence on cell topography including receptor expression for viral entry. It is now very clear that filopodia can provide unique opportunities for many viruses to invade host cells vertically during primary infection, or horizontally during virus spread from cell-to-cell. These emerging concepts can explain the unprecedented ability of viruses to invade both nearby and long-distant host cells, a feature that may directly contribute to viral tropism. In this review, we summarize the significance of filopodia in viral diseases and discuss future therapeutic possibilities to precisely target filopodial-flyovers to prevent or control infectious diseases.

Keywords: filopodia, heparan sulfate, virus-cell interaction, virus entry

OPEN ACCESS

Edited by:
Ayae Honda,
Hosei University, Japan

Reviewed by:
Tatsuo Shioda,
Osaka University, Japan
Masato Tsurudome,
Mie University, Japan

****Correspondence:***
Vaibhav Tiwari
vtiwar@midwestern.edu

Specialty section:
This article was submitted to Virology, a section of the journal Frontiers in Microbiology

Received: *07 January 2016*
Accepted: *23 February 2016*
Published: *10 March 2016*

Citation:
Chang K, Baginski J, Hassan SF, Volin M, Shukla D and Tiwari V (2016) Filopodia and Viruses: An Analysis of Membrane Processes in Entry Mechanisms. Front. Microbiol. 7:300. doi: 10.3389/fmicb.2016.00300

INTRODUCTION: FILOPODIA- A MASTER EXPLORER

Filopodia are actin-rich plasma-membrane processes that allow cells to probe their environment (Mattila and Lappalainen, 2008). The functions of filopodia are broad in nature; they contribute to wound healing processes, adhesion to the extracellular matrix (ECM), guidance toward chemoattractants, neuronal growth-cone path finding and embryonic development. Their size can range from 10 μm in length (nerve growth-cone filopodia) to 40 μm in length (sea-urchin embryo filopodia) (Welch and Mullins, 2002). Filopodia, or microspikes, may also be present in the cell cortex or leading edge. Despite the vital role of filopodia in cell functions, the biological mechanisms that govern filopodial functions are not completely understood. Current studies have only scratched the surface of the numerous roles of filopodia, whether beneficial or pathogenic. An emerging example of filopodia functions in infectious diseases is the recent discovery of the role of filopodia in viral surfing during entry and trafficking (Lehmann et al., 2005; Dixit et al., 2008; Oh et al., 2010; Bienkowska-Haba and Sapp, 2011; Schudt et al., 2013; Xu et al., 2015). Similarly, virus activated filopodia in dendritic cells have been proposed to transfer the virus with higher efficiency compared to the cell free route (Nikolic et al., 2011; Shrivastava et al., 2015).

One long-standing function of filopodia is to probe the environment and promote cell motility. It has receptors for signaling molecules and ECM molecules, which allows it to sense the

surroundings and interact with other cells. Along the tip and shaft of filopodia exist two classes of cell adhesion molecules known as integrins and cadherins (Mattila and Lappalainen, 2008). During cell spreading, integrin-containing filopodia form the initial adhesion sites. Then, other components, such as talin and paxillin, are recruited to form the mature focal adhesions (Mattila and Lappalainen, 2008). Filopodia also play a role in cell-to-cell adhesion (Mattila and Lappalainen, 2008). An example of this interaction can be seen during embryonic development and wound healing (Mattila and Lappalainen, 2008). During these processes, there is a fusion of sheets of epithelial cells. Dynamic filopodia are present at the edges of epithelial cells and project to adjacent cells to aid in these processes. Interdigitated filopodia, which protrude from opposing cells, also help the sheets of cells align and adhere together (Mattila and Lappalainen, 2008). Embryonic epithelial fusion must occur in a precise fashion such as for dorsal closure in *Drosophila*. Filopodia facilitate cell-to-cell matching by allowing a cell to search for its match, and then pull misaligned sheets into alignment (Mattila and Lappalainen, 2008).

Membrane protrusions from neurons have been the most extensively studied (Bornschlogl, 2013). Filopodia are active in the neuronal growth cones of neurons, which guide axons and dendrites to their proper targets (Dent et al., 2011). Growth cones contain many filopodia. In this instance, filopodia sense the various gradients of chemoattractants and guide the neurite in the appropriate direction (Mattila and Lappalainen, 2008). However, filopodia are not essential for all types of neurite guidance. Retinal ganglion cells that are depleted of filopodia can still migrate along the optic tract, but they fail to establish axon terminal branching inside the tectum. The tectum is the midbrain "roof" and receives information from the retina (Mattila and Lappalainen, 2008).

STRUCTURAL ELEMENTS OF FILOPODIA

High-resolution electron microscopy has shown that the core of filopodia consists of 15-30 tightly packed actin filaments, with a dense protein complex at the tip (Bornschlogl, 2013). The actin filaments in filopodia are cross-linked by fascin into a stiff structure (Leijnse et al., 2015a). There are proteins, which maintain the shape of the membrane, such as I-BAR proteins, which are actin-cytoskeleton adaptors that have been shown to contribute to formation of filopodia (Chen et al., 2015). Integrins are the transmembrane proteins, which link the actin to extracellular substrates to transfer force onto the substrate (Takada et al., 2007). Myosin-X, which provides a link between integrins and the cytoskeleton, transports membrane components like integrins to the filopodial tip (Zhang et al., 2004; Leijnse et al., 2015a). Other proteins include Enabled/vasodilator-stimulated phosphoprotein (Ena/VASP) and cofilin. There are high concentrations of fascin within the actin bundle (Leijnse et al., 2015a). Fascin are important because they are present in metastatic cancer cells as a notable hallmark. The role of filopodia in cancer is described at the end of this review article. In addition, protruding and retracting filopodia differ in actin composition. Protruding filopodia have a continuous actin filament, while retracting filopodia contain more disorganized and discontinuous actin filaments (Leijnse et al., 2015a).

Actin fibers present in filopodia have two forms: monomeric globular actin, also known as G-actin and polymeric filamentous actin, or F-actin (Cooper, 2000). F-actin is composed of two parallel strands of actin monomers. During viral infection, cellular actin is reconfigured and reorganized to affect the different stages of the viral life cycle. Polymerization of actin monomers begins with stabilization by an initiation complex. An example of this is the actin-related protein-2/3 (ARP2/3) complex. ARP2/3 is an initiation complex that is known to interact with viruses and multiple other pathogens (Cossart, 2000; Komano et al., 2004; Taylor et al., 2011). Taken togther, cells use a large repertoire of proteins to remodel the actin cytoskeleton including many events of simultaneous breakdown and assembly asprofilin can stimulate F-actin assembly, while cofilin promotes disassembly (Taylor et al., 2011).

F-actin is a part of the cytoskeleton composed of two parallel strands of ATP-bound globular actin monomers, which can assemble into finger-like protrusions (Xiang et al., 2012). The assembly of actin is involved in neuronal morphogenesis and migration. Errors in actin assembly within the neuron can lead to neurological diseases, such as non-syndromic X-linked mental retardation and William's syndrome (Xiang et al., 2012).

Actin molecule binds to small proteins that help control its polymerization (Alberts et al., 1994). For example, the actin-depolymerizing factor (ADF)/cofilin family remodels the actin cytoskeleton. Cofilin is a family of actin-binding proteins, which disassemble F-actin by binding to older ADP-actin filaments and promoting phosphate disassociation from actin subunits (Xiang et al., 2012).

Polymerization of actin is critical to filopodial mechanics. To increase the length of the filopodia, the filopodial actin core grows inside the plasma membrane tube and then pushes out. Force is required because the plasma membrane is constantly under tension. It is the polymerization of actin that can produce the necessary protrusion force, often against 10 pN (piconewton) (Bornschlogl, 2013). Within the cell, actin is also arranged in sheet-like extensions, such as lamellipodia, microvilli, podosomes, and large membrane ruffles (Taylor et al., 2011). The length of filopodia ranges from 1 to 100 μm. Short filopodia are often called microspikes, while longer ones are called cytonemes or tunneling nanotubes (TNTs). Cytonemes can form long distance intercellular bridges. (Leijnse et al., 2015a). In addition, greater TNT production has been observed in the presence of HIV-1 (Hashimoto et al., 2016). Another type of cellular protrusion is known as lamellipodia, which are thin and sheet-like with a branched network of actin. Filopodia often protrude from the lamellipodial actin network as thin finger-like structures filled with tight parallel bundles of filamentous F-actin. In order for the cell to migrate, actin filaments push the leading edge (front of the cell) forward. (Mattila and Lappalainen, 2008).

Another role of filopodia is the initial neurite formation of cortical neurons. Dendritic spines are the postsynaptic regions of most excitatory neuronal synapses. These spines have been shown to play a role in higher brain functions, such as learning

and memory. Dendritic spines require filopodia-like precursors. (Mattila and Lappalainen, 2008). Neurites can provide unique sites for virus adhesion and eventual spread to nearby cells and other neurons.

VIRAL UTILIZATION OF FILOPODIA

Enveloped viruses can spread by two different routes: the cell-free aqueous environment or by cell-to-cell contact (Sherer et al., 2007; Mothes et al., 2010). Cell-free spreading requires a large number of viral particles to be released and to reach distant areas by diffusion. If these criteria are not met, cell-free spreading is impaired. Furthermore, cell-free virus is advantageous because it is not restricted to cell-to-cell interaction and can spread from person to person (Mothes et al., 2010). In contrast, cell-to-cell contact has unique advantages. The speed of transfer is greater because the replication cycle of release, transmission, and entry can proceed in a faster manner. Another advantage of cell-to-cell contact is immune evasion because the limited exposure in extracellular space avoids interaction with neutralizing antibodies. Lastly, by exploiting cell-to-cell communication, the physical and immunological barriers can be overcome to spread the infection (Mothes et al., 2010).

Viruses can hijack the filopodia system for their own use during the life cycle (**Figure 1**) (Tiwari et al., 2015). Viral infection, a battle between pathogen and host, can occur because the virus travels along the filopodia from the infected cell toward the target cell. The ensuing result is "cell death, elimination of the virus, or latent infection, keeping both cells and pathogens alive" (Greber, 2002). It should be noted that pathogens and immune cells both could utilize filopodia in the different ways. For example, invasive bacteria use the protrusions of epithelial cells to approach the host cell before infection occurs, and macrophages use them as precursors for phagocytosis and their filopodia can capture both latex beads and beads covered with bacterial surface proteins (Bornschlogl, 2013). Viruses can travel along filopodia to enter the target cell. In addition to providing entry to an uninfected (target) cell, the filopodia can be used as an exit from an infected cell. In addition, host enzymes can induce filopodia formation upon sensing viral invasion. It was shown that zebrafish encoded heparan sulfate (HS) modifying enzyme 3-O sulfotransferase-3 (3-OST-3), which also generates a HSV-1 entry receptor, enhances filopodial protrusion formation and promotes viral entry (Choudhary et al., 2013). Given that viruses take advantage of filopodia during their life cycle, therapeutics can target filopodial formation to inhibit infection.

G-PROTEIN STIMULATION IN FILOPODIA FORMATION

Small GTPases of the Rho superfamily regulate cell morphology, particularly the actin cytoskeleton. Members of this family regulate many cellular processes, including F-actin polymerization, assembly of intercellular junctions, cell polarity, and membrane trafficking. Pathogens, such as viruses, possess gene products that engage and disrupt the actin cytoskeleton and Rho-family GTPase signaling system (**Figure 1**). Ultimately, F-actin is remodeled for the main stages of the viral life cycle - entry, assembly, and egress (Taylor et al., 2011). The best-studied mammalian Rho GTPases are RhoA, Cdc42, and Rac1. RhoA stimulates the formation of stress fibers while Rac1 induces membrane ruffles or lamellipodia. Cdc42 regulates the formation of filopodia (Taylor et al., 2011). It operates through distinct signaling pathways, such as the induction of the ARP2/3 complex-dependent actin filament nucleation through activation of Wiskott–Aldrich syndrome protein (WASP) (Mattila and Lappalainen, 2008). ARP2/3 complex initiates polymerization of actin monomers; it is the complex most often described as interacting with viruses. Although ARP2/3 has little polymerization-stimulating activity, interaction with induction factors such as the WASP will enhance polymerization ability (Taylor et al., 2011).

Although Cdc42 is important, filopodia formation can occur in cells depleted of Cdc42. A small GTPase, called Rho in filopodia (RIF) can stimulate filopodia formation following overexpression. In contrast to the filopodia induced by Cdc42, the filopodia induced by RIF are longer and project from the apical surface of the cell. Overall, multiple Rho GTPases can induce cellular protrusion when over-expressed, but their roles under physiological conditions remain to be explained (Mattila and Lappalainen, 2008).

Cdc-42 – A Model Rho GTPase Supporting Viral Invasion

Cdc42 is a RhoA GTPase that has been associated with cell mediated processes involving actin modifications. Rho-GTPases are associated with events such as modulation of cytoskeletal components, cell migration, cell trafficking and cell polarity (Nikolic et al., 2011). Numerous pathogens, both bacterial and viral, have been shown to interact with Cdc42 within the host cell to facilitate the remodeling of actin within the host cells. In the cases of viruses such as herpes simplex virus-1 (HSV-1) and human immunodeficiency virus (HIV), viral activation of Cdc42 leads to the production of filopodia and filopodia-like structures. Studies performed with HSV-1 have demonstrated that a down-regulation of Cdc42 not only results in a decline in filopodia but also infection in general (Oh et al., 2010). Similar studies performed with HIV demonstrated similar results when Cdc42 was inhibited with secramine A, indicating the potential role of Cdc42 in viral infections (Nikolic et al., 2011). Guillou et al. (2008) performed an experiment wherein fibroblasts spread on micropatterned surfaces. Filopodia, which contains adhesion structures, converted to lamellipodia-like protrusions. Expression of a dominant-negative form of the small GTPase Cdc42 stopped filopodia formation, which impaired cell spreading (Mattila and Lappalainen, 2008).

It has been postulated that viral activation of Cdc42 is mediated by Src kinases. Src kinase is a non-receptor tyrosine kinase protein (Wheeler et al., 2009). In a study performed by Nikolic et al. (2011) incubation of dendritic cells with wild

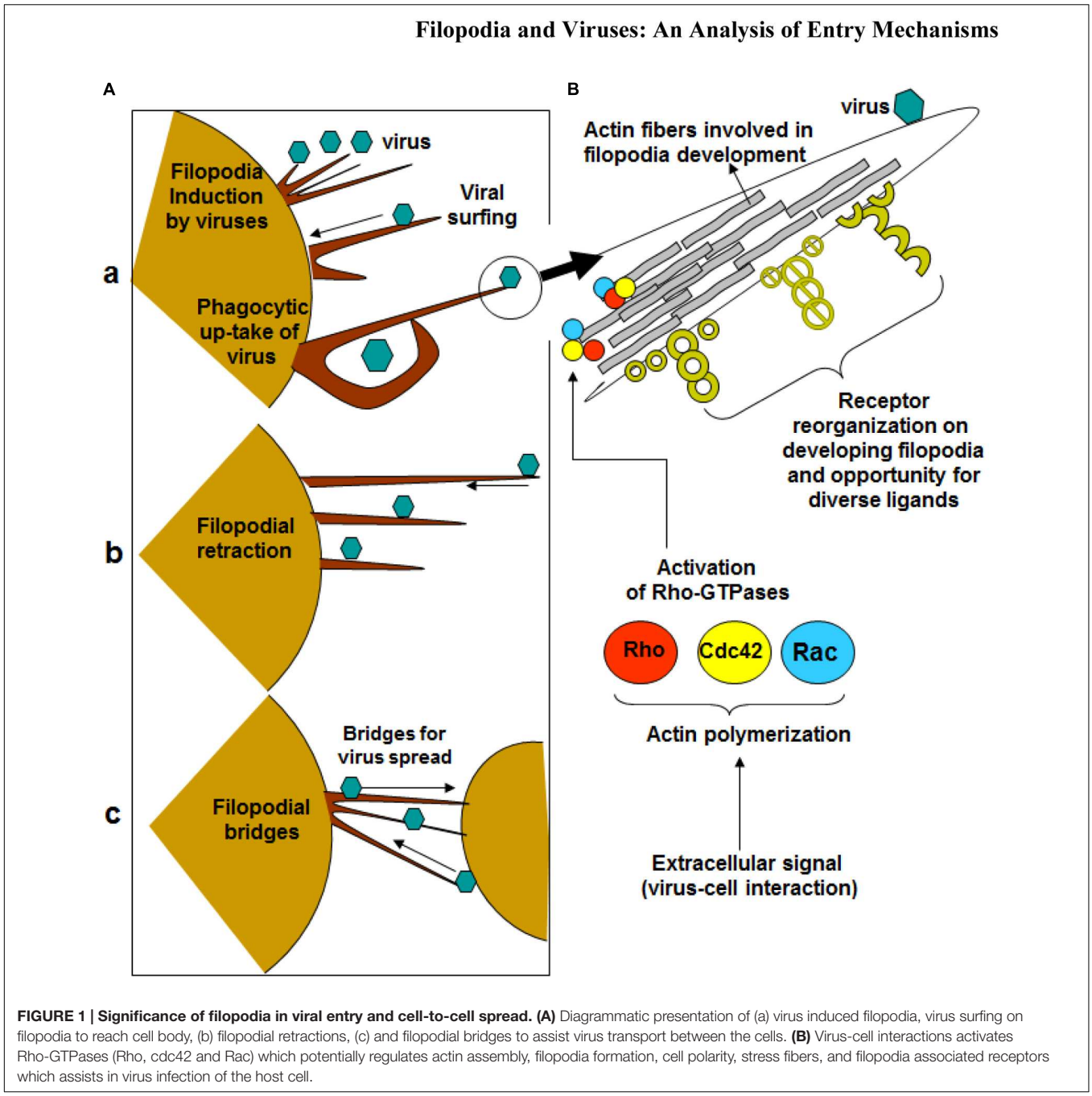

FIGURE 1 | Significance of filopodia in viral entry and cell-to-cell spread. (A) Diagrammatic presentation of (a) virus induced filopodia, virus surfing on filopodia to reach cell body, (b) filopodial retractions, (c) and filopodial bridges to assist virus transport between the cells. **(B)** Virus-cell interactions activates Rho-GTPases (Rho, cdc42 and Rac) which potentially regulates actin assembly, filopodia formation, cell polarity, stress fibers, and filopodia associated receptors which assists in virus infection of the host cell.

type HIV, demonstrated activation of Src kinase, Pak1, and WASP. Inhibition of Cdc42 or the Src kinases suggested that the initial Src activation occurs upstream of Cdc42, Pak1 and WASP. Nikolic suggests Src kinases serve as a link between HIV interaction on the surface of the cell with the subsequent activation of Cdc42, Pak1, and WASP, leading to the eventual increase in cell surface extensions (Nikolic et al., 2011). Levels of Src kinase are linked to cancer progression by promoting other signals (Wheeler et al., 2009). Therefore, since Cdc42 pathway is mediated by Src kinase, there is a link between cancer and filopodia formation (Cancer – Src kinase – Cdc42 – Filopodia). This linkage is another evidence of how filopodia promotes cancer formation as described at the end of this review article.

Rho Proteins Involvement in HSV-1 Infection

It has been speculated that RhoA, a member of the Rho GTPase family, may play a role in HSV-1 infection. Studies have suggested that RhoA may facilitate entry of HSV-1 via endocytosis into human corneal fibroblasts (Salameh et al., 2012). Other members of the Rho GTPase family have been

implicated in the development of filopodia (Salameh et al., 2012). Specifically, Rac-1 and CDC42 are activated in epithelial cells and fibroblasts during HSV-1 infection (Quetglas et al., 2012). To complicate matters, signaling pathways change for different cells. In nectin-1-CHO and corneal fibroblasts, RhoA is induced, but not Cdc42 or Rac1 (Clement et al., 2006). The different mechanisms of communication may explain why the HSV-1 mode of entry is cell type-specific. For example, filopodia play a role in HSV-1 entry for nectin-1-CHO cells. However, in cells from human trabecular meshwork tissues, relatively few protrusions are seen and intracellular vesicles containing virions were absent (Clement et al., 2006).

OVERVIEW OF VIRAL ENTRY MECHANISMS

Filopodia provide a way for cells to physically interact with each other and transmit materials such as ligands or other substances. Retroviruses exploit the transport mechanism, thereby facilitating infection by movement of viruses and viral proteins (Sherer et al., 2007). Inhibiting the surfing mechanism results in a modest reduction in infection of cultured fibroblast cells where viruses have relatively easy access to the cell body. However, interference with surfing leads to a significant reduction in infection of polarized epithelial cells that are covered in dense microvilli. Lehmann et al. (2005) hypothesize that virus cell surfing enables the penetration of the microvilli-rich mucosal surfaces to efficiently infect the host. An example of mucosal transmission is HIV infection, through which mucosal transmission occurs for 80% of infections (Lehmann et al., 2005).

Specialized movements occur among different viruses. For example, animal viruses typically display a period of lateral movement along filopodia before internalizing into the cell. A highly directional movement exists for murine leukemia virus (MLV), enveloped RNA viruses, and human papilloma virus-16 (HPV-16). HPV-16 is linked to the development of cervical cancer (Schelhaas et al., 2008). In addition, filopodia can be a marker for viral infection. The number of these actin-rich protrusions increases during infection with either HSV-1, cytomegalovirus (CMV), or human herpesvirus-8 (HHV-8). Experiments were performed on three different cell types for each virus. The number of filopodia increased in varying degrees, from 2-fold increase to 6-fold increase (Tiwari and Shukla, 2012).

Lastly, filopodia provide an alternative mechanism for viral entry. In vaccinia virus (VACV), the two strains – International Health Department-J (IHD-J) and Western Reserve (WR) – enter host cells by different mechanisms. IHD-J mature virions (MVs) induce filopodia formation, such that exposure to IHD-J increases the number and length of filopodia dramatically. Filopodia remain a permanent feature of the infected cells for many hours. In contrast, WR MVs alter actin dynamics, which leads to transient membrane blebbing followed by macropinocytic internalization of virus particles. Unlike the filopodia of IHD-J, the blebs induced by WR MVs are transient (Mercer et al., 2010a).

Viral Binding

Glycoproteins play an important role in viral attachment to cells. Their positively charged moieties often recognize negatively charged domains of cell surface receptors such as HS. As number of human viruses including HSV-1, HHV-8, HPV-16, HIV, avian sarcoma leukosis virus (ALV), and vesicular stomatitis virus (VSV) bind HS (Tiwari et al., 2012), and the latter is shown to be highly expressed on filopodia (Oh et al., 2010), it is likely that filopodia contribute directly to virus binding. In fact, it has been clearly shown with HSV-1 that its preferred binding location on the cell surface is filopodia (Oh et al., 2010). The HSV glycoprotein that participates in filopodial binding is gB, which is a known HS binding protein. Although remains to be shown, it is likely that for other viruses their HS binding proteins are responsible for viral interactions with filopodia.

Viral Surfing

Binding of virus to filopodia induced a rapid lateral movement toward the cell body, a process called surfing (Lehmann et al., 2005). Viral Surfing is a mechanism through which high affinity interactions with receptor on the target cell engage the F-actin flow to move toward the cell body of the target cell (Mothes et al., 2010) (**Figure 1**). Filopodia have been proven to be involved in the surfing process, as well as in the process of inhibition of surfing. Since virus cell surfing is a pathway of viral infection, the visual block to surfing by blebbistatin and cytochalasin D theoretically should result in reduced infectivity. Studies looking at the earlier stages of infection found that the inhibitory effects of blebbistatin on MLV and VSV were significant only when cells were cultured at low confluencies. Under these conditions, cells exhibit abundant filopodia. At higher confluencies, when cells contacted each other, blebbistatin had reduced effects. This suggests that blebbistatin affects the earliest steps of MLV entry when cells exhibit abundant filopodia (Lehmann et al., 2005). Similarly, cytochalasin D had greater inhibitory effects on virus entry when cells contained abundant filopodia.

Mucosal epithelia are also relevant to viral infection. Polarized epithelial cells covered with dense microvilli (MDCK cells) have been tested to see if surfing was required for efficient infection. The data obtained indicated that infection of polarized MDCK cells by MLV or VSVG-containing viruses was reduced by at least fivefold in the presence blebbistatin and cytochalasin D when virus was added to the microvilli-rich apical side but not to the basolateral side. Blebbistatin and cytochalasin D were added in separate treatments (Lehmann et al., 2005). In comparing infection of cultured fibroblast cells to infection of polarized epithelial cells, only a modest reduction in infection of cultured fibroblast cells was observed. It has been shown that viruses have relatively easy access to the fibroblast cell body (Lehmann et al., 2005). However, a blockade to surfing leads to a reduction in infection of polarized epithelial cells. Lehmann et al. (2005) hypothesized that *in vivo*, virus cell surfing enables

the penetration of microvilli-rich mucosal surfaces to efficiently infect the host.

Filopodial Retraction

The filopodia on virally infected cells pull the virus inward (**Figure 1**). A similar action is seen when macrophages bind to bacteria and pull them toward the cell body, where phagocytosis occurs. Macrophages utilize numerous filopodia per cell to explore the environment. When a pathogen is found, the filopodia bind to it and retract toward the macrophage cell body (Mattila and Lappalainen, 2008). The pulling mechanism is conserved because cells retract filopodia for entry of certain virus, such as HPV (Smith et al., 2008).

A hypothesized model for how the filopodia pulls is through an action known as "frictional coupling" (Bornschlogl, 2013). Since filopodia and lamellipodial structures are connected, friction could drive retrograde flow (Bornschlogl, 2013). The cytoskeleton is generating friction on the substrate environment. Filopodia act along with lamellipodial actin network to drive retrograde flow. The cytoskeleton was shown to promote retraction force rather than just membrane tension by the finding that the force was measured at 1-2 nN (Bornschlogl, 2013).

The retraction force was examined through an experimental set-up consisting of a bead attached to filopodia and observation through confocal fluorescence microscopy (Bornschlogl, 2013). The extension and retraction of filopodia was determined by the difference between the actin polymerization rate at the tip and the retrograde flow at the base of the filopodium. Actin polymerization was shown to reduce locally at the tip and then the protrusion retracted. Within this model, the bead is analogous to the virus. The results obtained allow for easy data collection regarding the actual retraction forces. (Bornsclogl et al., 2013).

Originally, the pulling force of filopodia was attributed to retrograde flow of actin, but recently, experiments show that rotational dynamics also make a contribution. Force measurements indicate a step-like behavior for the retraction force, but no direct evidence links the behavior to the myosin motor protein. Thus, the mechanical and biochemical mechanism for filopodial retraction requires further examination (Leijnse et al., 2015a).

Endocytosis of Virus

Conversely, after viruses flow along filopodia, they can undergo endocytosis to enter the uninfected cell. Most animal viruses depend on endocytic uptake, vesicular transport through the cytoplasm, and delivery to endosomes and other intracellular organelles. The internalization may involve clathrin-mediated endocytosis (CME), macropinocytosis, caveolar/lipid raft-mediated endocytosis, or a variety of other still poorly characterized mechanisms (Mercer et al., 2010b). It should be noted that viruses could skip the filopodia transport (**Figure 1**). In this instance, they would simply bind to receptors on the cell surface and induce endocytosis. Receptors promote entry "by binding, by initiating conformational changes in the virus, by activating cellular signaling, and by inducing fusion at the plasma membrane or by promoting endocytosis" (Schelhaas, 2010). Both fusion and endocytosis can be utilized, but the latter is advantageous for three reasons. First, there will be a delay in immune response because there is no trace of virus on the plasma membrane. Second, the built-in transport mechanism across the plasma membrane is utilized. Third, vesicular trafficking provides access to intracellular organelles, allowing virus to sense their environment to changing conditions of pH, redox, and proteases (Schelhaas, 2010). Most RNA viruses replicate in the cytosol, while DNA viruses must gain access to the nucleus to facilitate this process (Schelhaas, 2010). Endocytosis is important for eukaryotic cells to internalize extracellular particles, fluid and ligands. The process begins with the formation of primary endocytic vesicles, which pinch-off from the plasma membrane. It has been long thought that receptor-mediated endocytosis consists mainly of clathrine-mediated endocytosis (Schelhaas, 2010). Now, recent research shows additional pathways: macropinocytosis, caveolar/raft-dependent endocytosis, among others (Schelhaas, 2010). Taken together, different viruses use different endocytic pathways.

Viral Budding

Filopodia have been discussed above as a structural component for viral entry. However, filopodia can also be used to facilitate "budding"- a common exit mechanism for viruses. For example, Marburg virus (MARV) and Ebola virus virogenesis begins with formation of perinuclear inclusions which are sites of viral replication and assembly of new nucleocapsids (NCs). NCs are detected in the cytosol, at the plasma membrane, and in filopodia, the preferred sites of MARV budding (Schudt et al., 2013). In case of Varicella-Zoster virus and Sindbis virus, the imaging studies have demonstrated the presence of virions on filopodia during viral egress (Carpenter et al., 2008; Jose et al., 2015).

The actin cortex can facilitate or hinder the movement of virus that bud at the plasma membrane. For VACV, actin polymerization helps propel the virus away. For equine infectious anemia virus, actin cortex hindered the release of viral particles (Kolesnikova et al., 2007). Therefore, budding involves a rearrangement of the actin cortex. Once the virus buds, the presence of actin in purified virus particles is a sign that the process has occurred (Kolesnikova et al., 2007). Filopodial budding is advantageous because filopodia make connections to neighboring cells, thus facilitating access to the next target cell. On the other hand, the release of budding virions directly to target cells minimizes the appearance of virions in the extracellular space, which avoids recognition by the hostile environment (immune system) (Schudt et al., 2013).

Observations of mouse mammary tumor virus (MMTV), a retrovirus, revealed the first connection between the virion exit and the actin cytoskeleton (Taylor et al., 2011). Mammary tumor epithelial cells released viral particles from the ends of microvilli (Taylor et al., 2011). Since HIV is also a retrovirus, it was important to determine whether viral proteins interact with the actin cytoskeleton for the final steps of assembly and release. Studies in which actin filaments were disrupted by cytochalasin D lead to an impairment of virus budding and reduced virus yield by 80% (Taylor et al., 2011).

CYTOSKELETAL REARRANGEMENT

Virus-induced cytoskeletal rearrangements are commonly initiated via cellular signaling to prepare and facilitate infection. Rearrangement of cortical actin filaments is observed in virus infected cells and has been shown contribute to infection efficiency. Once internalized, the virus can use microtubule cytoskeleton and motor protein machinery to reach the nucleus (Smith et al., 2008).

Different findings have been reported about the mechanisms of actin assembly in filopodia. The convergent elongation model argues that "filopodia arise from the lamellipodial F-actin network and a continuous actin bundle extends from the root to the tip of filopodia" (Mattila and Lappalainen, 2008). The *de novo* filament nucleation model states that actin filaments of filopodia "do not derive from the underlying lamellipodial network, but are nucleated at filopodial tips by formins" (Mattila and Lappalainen, 2008).

EXAMPLES OF VIRAL INTERACTION WITH FILOPODIA

HSV-1

(HSV-1) and herpes simplex virus-2 (HSV-2) are some of the first viruses to have demonstrated a dependency upon filopodia during infection. They are part of the herpesviridae family, which consists of over 70 viral species: including varicella-zoster virus, CMV, human herpesvirus-6 (HHV-6) and Epstein-Barr virus. Herpesviruses have linear, double-stranded DNA enclosed in icosahedral capsids. They enter latency after primary infection, establishing infection for the lifetime of their hosts (Salameh et al., 2012). During stressful conditions, HSV-1 reactivates and proceeds with viral replication, leading to perioral lesions of the skin, mucosa, or lesions on the cornea. On the other hand, HSV-2 is primarily associated with genital and newborn infections (Xiang et al., 2012). HSV-1 has been shown to travel down filopodia-like membrane protrusions to reach the cell body for internalization. This action appears to be regulated by activation of Cdc42 (Oh et al., 2010). Exposure to HSV-1 can induce the formation of actin-rich, filopodia-like structures by the cell. Filopodial formation is facilitated through members of the Rho GTPase family, which serve as a link between surface receptors and the actin cytoskeleton underneath. Glycoprotein gB seems to regulate viral surfing. This notion is reinforced by the fact that gB binds to HS (Oh et al., 2010). HS receptors serve as attachment sites for HSV-1 which is also present on filopodia (**Figure 2**). Once the virus binds, it can travel to the cell surface, where gD proceeds to bind with one of its four receptors. The process of virus penetration and membrane fusion follows (Salameh et al., 2012).

Entry Mechanisms

Heparan sulfate glycosaminoglycans are hybrid molecules with unbranched polysaccharide polymers covalently attached to the protein core. HS can be sulfated to produce 3-*O*-sulfated HS which can independently make cells susceptible to HSV infection. Glycoprotein B and C are bound first to unmodified HS; next, gD binds to 3-*OS* HS to facilitate fusion pore formation during viral entry. Again presence of 3-*OS* HS on filopodia may allow virus-cell fusion (**Figure 2**). Virus trafficking via virus-cell fusion at the cell surface results in the release of viral genome into the nucleus. Deconvolution microscopy using capsid-tagged green fluorescent virus showed that HSV-1 can infect the corneal stroma through HS associated trafficking (Tiwari et al., 2015).

Endocytosis

HSV-1 can induce primary human corneal fibroblasts to engulf it in a form of an atypical endocytosis (Clement et al., 2006). The uptake of HSV resembles phagocytosis because it is not pH dependent and does not involve the use of clathrin-coated vesicles or caveolae (Salameh et al., 2012). Furthermore, there is rearrangement of actin cytoskeleton and trafficking of the virions in large phagosome-like vesicles. HSV-1 can induce endocytosis of *E. coli* bioparticles and virions cointernalized with phagocytic tracers (Clement et al., 2006). Endocytosis would be the second method through which HSV-1 can enter cells, with the first being surfing. Transport is initially along filopodia and virion fusion occurs at the vesicular membrane.

Cytoskeletal Rearrangements

HSV interacts with the host cytoskeleton, specifically with the F-actin components. A role for cofilin was discovered in HSV-1 infection. HSV-1 infection increases F-actin assembly at the early stage of infection to facilitate viral transport. In the later stages of infection, F-actin decreases to facilitate viral reproduction. Therefore, HSV-1 infection induces biphasic dynamics of F-actin in neuroblastoma cells (Xiang et al., 2012). Cofilin-1 regulation may mediate HSV-1-induced F-actin remodeling in assembly and disassembly. Specifically, Cofilin-1 may promote F-actin assembly during the HSV-1 infection of neuronal cells. Regulation of Cofilin-1 decreased the formation of F-actin-based structures, such as lamellipodia (Xiang et al., 2012).

F-actin is important for HSV-1 infection. In the past, the major capsid protein of HSV-1 has been immunostained and utilized as a marker to indicate localization of HSV-1 particles. Cells infected by HSV-1 have been shown to grow long dendrites and filopodia. The filopodia formed during this infection have been found to have viral particles "docked" on them (Xiang et al., 2012). This suggests that HSV-1 may interact with F-actin for transport to the soma. The viral particles were randomly distributed around the cell and approached the soma and nucleus from many directions. With cytoskeletal rearrangement involving F-actin, HSV-1 can infect the cell by interacting with F-actin (Xiang et al., 2012).

HPV – The Ultimate Filopodial Utilization

In a study performed by Smith et al. (2008), filopodial structures facilitate viral uptake because induction of filopodia occurred at 30 min after binding. Over several hours, the virions began to disappear from the ECM. Viral diffusion was ruled out by fluorescence recovery after photobleaching (FRAP). The results from FRAP indicated that the virions were immobile. It was later revealed that filopodia can act to increase virion acquisition from the ECM to cells over many hours. The HPV31 virions have a

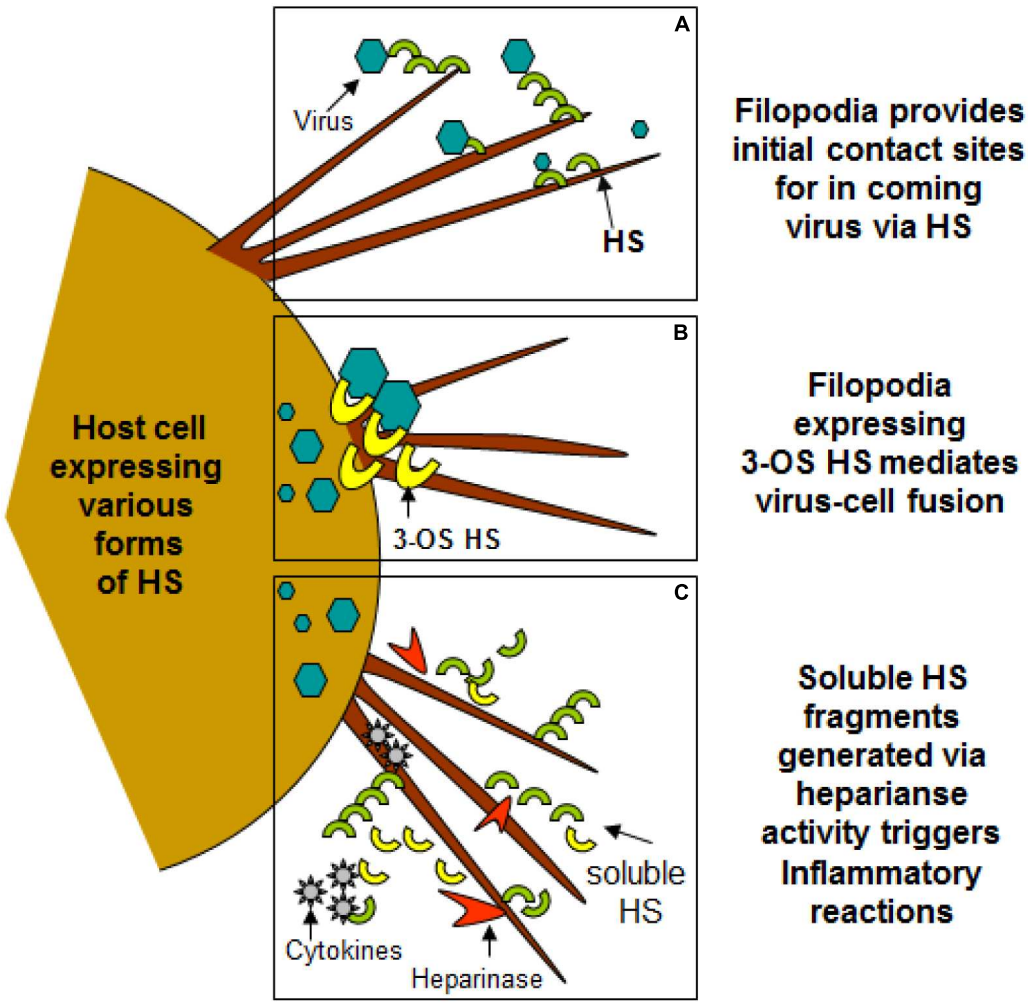

FIGURE 2 | Filopodia expresses diverse form of heparan sulfate (HS) and 3-*O* sulfated heparan sulfate (3-*OS* HS) assisting in viral entry of HSV-1. **(A,B)** Shows HS and 3-OS HS in assisting virus attachment and fusion events using filopodia. **(C)** Indicates the upregulation of heparinase activity during infection results shedding of HS/3-OS HS which potentially are involved in recruitment of inflammatory cells which may utilize filopodia.

long internalization half time (14 h) because of the active and protracted virion uptake from the ECM by filopodia (Smith et al., 2008).

Other direct evidence showed that HPV surfs along filopodia. Electron microscopy and acid wash of FITC-labeled virions also showed the association between virions and the outer surface of filopodia. Using fluorescence video microscopy, the human papilloma virus-16 (HPV-16) virion demonstrated a transport speed equal to the speed of F-actin retrograde flow. Inhibitors of actin polymerization and depolymerization affected HPV-16 directed flow, which again suggests transport via actin. (Bienkowska-Haba and Sapp, 2011). It was notable that transport along actin protrusions significantly enhanced HPV-16 infection in sparse tissue culture cells, but not in dense cultures (Schelhaas et al., 2008).

Studies using human papilloma virus-31 (HPV-31) have been the first to report filopodial translocation by a non-enveloped virus (Smith et al., 2008). The retrograde filopodial movement and entry of HPV-31 are comparable to those seen for MLV and VSV infections. It is interesting to note that a few HPV-31 virions bind directly to the plasma membrane where they enter prior to filopodia activation in human keratinocytes (Hks). This argues against a strict requirement for filopodia in HPV31 infection of HKs. Rather, filopodial transport serves to increase cell exposure to virions and particle uptake (Smith et al., 2008).

Retraction and Lateral Curling

Aside from surfing, two other modes of distal particle transfer to the cell body via filopodia occur: filopodial retraction and lateral curling. Lateral curling is when the filopodial tip with attached virion bends back toward the cell body. (Smith et al., 2008). The lateral curling mechanism is significant because it indicates that another pulling mechanism exists to retract filopodia. Another name for lateral curling is buckling, which has been observed by confocal microscopy and atomic force spectroscopy. The

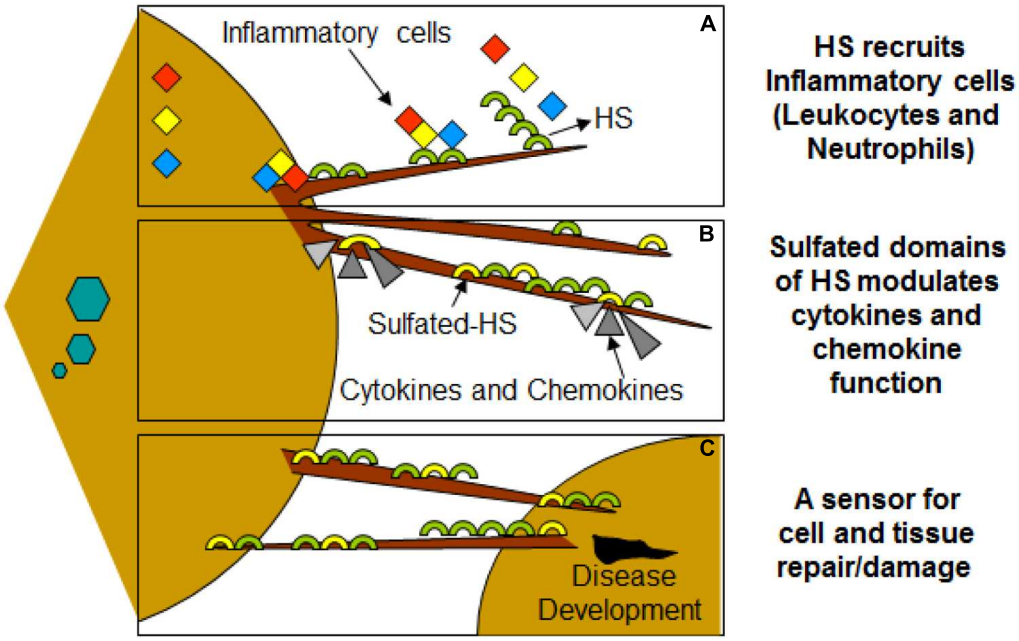

FIGURE 3 | Filopodia may play additional role in disease development during viral infection of HSV-1. (A) Molecular diversity of HS present on filopodia results recruitments of leucocytes and neutrophils. **(B)** HS also assist in binding and bringing conformational changes in bound chemokines, establishing chemokine gradients. **(C)** HSV infected cells shed HS on the filopodia which may serve as a potent inducers of inflammatory response.

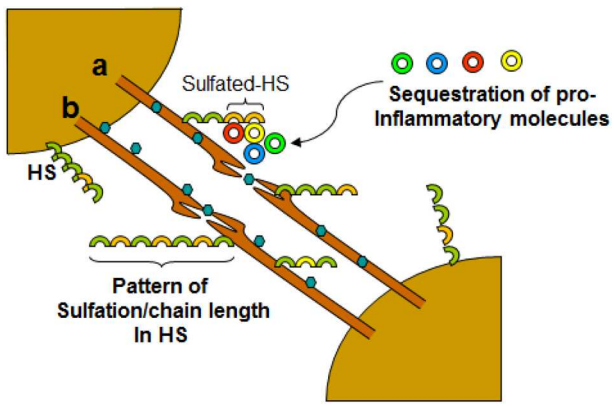

FIGURE 4 | Dynamic role of filopodia connecting neurons influencing HSV-1 infections and associated inflammation. Virus travel either intracellular **(a)** or extracellular **(b)** between the cells. The diversity of HS chain in terms of sulfation pattern and chain length play a crucial role in interactions with cell surface molecules including leucocytes and soluble inflammatory cytokines.

rotation of the actin shaft accumulates torsional energy in the actin that can be released by helical bending. Studies examining the filopodia of human embryonic kidney-293 (HEK-293) cells revealed rotation, bending, and shortening of the actin within filopodia (Leijnse et al., 2015a). Buckling can be thought of as the "pulling and bending that arises when twisting a rubber band at one end and keeping the other end fixed" (Leijnse et al., 2015b).

Endocytosis

On the other hand, internalization of HPV is unusually slow and asynchronous, with half-times ranging from 4 and 14 h. HPV-16 is a lab strain and pseudovirion which carried a marker plasmid coding for a dimeric green fluorescent protein (GFP). HPV-16 internalizes via clathrin-, caveolin-, and dynamin-independent novel pathways. Studies using siRNAs and inhibitors of endocytosis excluded macropinocytosis and phagocytosis as possible mechanisms for internalization. (Bienkowska-Haba and Sapp, 2011). During observation of HPV-31, another lab strain, virion motion transitioned from active transport to rapid diffusion once the particles reached the cell body. This shift is indicative of one of two mechanisms: internalization at the base of the filopodia or transfer to the adherent (basolateral) cell surface (Smith et al., 2008). The mechanism for HPV-31 endocytosis is different from that of HPV-16. The reason for this difference is under debate. While HPV-31 endocytosis seems to occur via caveolae, one study showed that entry occurs through a clathrin-mediated pathway (Bienkowska-Haba and Sapp, 2011).

Murine Leukemia Virus

For MLV, a group of retroviruses known to cause cancer in mice, the filopodia originates from the target cell and extends to the infected cell. The infected cell can exert a pull force to increase the length of viral cytonemes. Filopodial length can therefore increase toward the center of an infected cell. Extension is accompanied by a net flow of membrane toward the infected cell (Sherer et al.,

2007). Specific effects of filopodia extension are discussed below.

Viral Invasion

For cells infected by MLV, the infected cell grabs filopodia using contacts between viral envelope glycoprotein (Env) and its receptor in the target cell. "The infected cell tears off and takes in chunks of filopodial membrane by endocytosis" (LeBrasseur, 2007). The tips of cytonemes colocalized at the infected cell surface with endocytic markers: dynamin 2, caveolin-1, cholera toxin B-subunit (Sherer et al., 2007). This allows invasion of the neighboring cell via viral transport on cytonemes.

Surfing Mechanism

Confocal time-lapse microscopy of HEK-293 cells showed that MLV viral particles attach to filopodia, but also underwent directed reverse movement, surfing toward the cell body. MLV labeled with a fusion-competent envelope-YFP protein (Env-YFP) was added to HEK 293 cells expressing the receptor mCAT-1 fused to CFP (mCAT-1-CFP). This assay demonstrated that when viral particles come in contact with the cell body of the mCAT-1-CFP expressing cells, the viral particles lose their envelope, as demonstrated by a loss of label. This result is consistent with the idea of fusion-mediated diffusion into the surface of the plasma membrane (Lehmann et al., 2005). The previously mentioned assay also demonstrated that surfing occurs prior viral fusion. This was indicated by the lack of complete diffusion of the Env-YFP label until reaching the base of the filopodia. Previous studies with an MLV carrying a fusion defective envelope demonstrated surfing characteristics. Fusion intermediates or intracellular capsids were detected only at the widening base of the filopodia or at the cell body. This suggests that the viral envelope is not required for surfing actions (Lehmann et al., 2005).

Vaccinia Virus

The filopodia of HeLa cells infected with VACV have been shown to retract in two different ways. One is a ruffling retraction, where viruses bound to cell edges or active ruffling areas are transported to the cell body. The second way is 'grabbing' by the waving actin protrusions, which brings the virus back to the cell body (Huang et al., 2008).

Viral Entry

After binding to filopodia of HeLa cells, VACV enters cells through an endocytic route that requires a dynamin-mediated pathway, but not a clathrin- or caveola- mediated pathway. Virus entry involves a novel cellular protein, vaccinia virus penetration factor (VPEF) (Huang et al., 2008). VPEF was detected on lipid rafts in the plasma membrane and on vesicle-like structures in the cytoplasm (Huang et al., 2008). VPEF likely mediates VACV entry through a fluid uptake endocytosis process in HeLa cells. Huang et al. (2008) hypothesized that vaccinia intracellular MV recruited a cellular vesicle protein for its own benefit. Therefore, HeLa cells were incubated with fluorescence labeled ligands – dextran or transferrin. Dextran normally undergoes fluid phase endocytosis. In Huang's experiment, dextran showed colocalization with VPEF. When VPEF expression was knocked down, vaccinia penetration and intracellular transport of dextran were both blocked. Due to these findings, VPEF plays a role in regulating the fluid phase of the endocytic pathway in HeLa cells (Huang et al., 2008).

Routes of Infection

In order to determine some of the differences and similarities between the various strains of VACV, some studies have focused on IHD-J and WR strains and their influences (Mercer et al., 2010a). As indicated previously, WR induces transient blebs on the surface of cells, while IHD-J induces permanent and lengthening filopodia. Aside from having two different strains, VACV is also notable for using two different routes of infection for HeLa cells and CHO cells (Mercer et al., 2010a). In HeLa cells, activation of epidermal growth factor receptor (EGFR) is a necessary step in infection. Blocking EGFR with antibodies and other agents inhibits VACV infection in L cells of the intestinal enteroendocrine cells. With CHO cells, VACV can infect the cell even though it does not express EGFR. Based on these results, it can be inferred VACV is part of a group of viruses that use alternative strategies to enter cells (Mercer et al., 2010b).

TABLE 1 | Summary of cell mechanisms of filopodial entry by different viruses.

Virus entry Mechanisms	HSV-1[1]	HPV[2]	MLV[3]	ALV[4]	HIV-1[5]	vsv[6]	HHV-8[7]	MARV[8]	VACV[9]
Receptor/Co-receptor interaction	*	*	*				*		*
Cytoskeletal rearrangements	*	*							*
Surfing	*	*	*	*	*	*		*	*
Filopodia retraction		*	*						*
Endocytosis	*	*	*				*		*
Budding	*		*		*			*	*
Alteration of entry mechanism	*				*				*

[1]*HSV, herpes simplex virus:* Clement et al., 2006; Taylor et al., 2011; Salameh et al., 2012; Xiang et al., 2012; Tiwari et al., 2015. [2]*HPV, human papilloma virus:* Hindmarsh and Laimins, 2007; Schelhaas et al., 2008; Smith et al., 2008; Bienkowska-Haba and Sapp, 2011; Leijnse et al., 2015a,b). [3]*MLV, murine leukemia virus:* Lehmann et al., 2005; Sherer et al., 2007; Mercer et al., 2010a. [4]*ALV, avian leukosis virus:* Lehmann et al., 2005. [5]*HIV, human immunodeficiency virus:* Lehmann et al., 2005; Do et al., 2014. [6]*VSV, vesicular stomatitis virus:* Lehmann et al., 2005. [7]*HHV-8, human herpesvirus-8:* Akula et al., 2003. [8]*MARV, Marburg virus:* Schudt et al., 2013. [9]*VACV, vaccinia virus:* Huang et al., 2008; Mercer et al., 2010b; Taylor et al., 2011.

CLINICAL SIGNIFICANCE

Virus infection is also related to cancer because an oncovirus is a virus that can cause cancer (Butt and Miggin, 2012). For example, HPV can increase the risk of cervical cancer (American Cancer Society, 2015). HHV-8 is associated with Kaposi's sarcoma, a type of skin cancer (Chang et al., 1994). Lastly, human cytamegalovirus is associated with mucoepidermoid carcinoma (Melnick et al., 2012). Therefore, a quick understanding of the use of filopodia by cancer cells shows the clinical importance of filopodia. The invasive motility in cancer cells is partly due to the formation of filopodia. Much attention has focused on the actin bundling protein, fascin, which localizes to filopodia, microspikes, and other actin-based protrusions underneath the plasma membrane (Machesky and Li, 2010). Fascin localizes to the leading edge of crawling cells and is important for assembly of filopodia. Inhibiting fascin results in reduced migration of the cell (Machesky and Li, 2010). Therefore, fascin provides normal and cancerous cells with increased motility. In aggressive and metastatic epithelial cancers, high fascin expression is an independent prognostic indicator of poor outcome (Machesky and Li, 2010). Cancers include: liver, ovary, lung, pancreas, colorectal, head and neck squamous cell carcinoma and brain (Machesky and Li, 2010). However, fascin expression is not applicable to many cancers, such as breast and prostate (Machesky and Li, 2010). For cancers such as biliary tract (gallbladder cancer), although fascin is not an independent prognostic indicator, it is marginally significant in correlating with poor prognosis (Machesky and Li, 2010). Further, filopodia or filopodial bridges may be able to trap the soluble fragments of diverse HS generated as results of high heparanase activity during HSV infection, which may facilitate influx of inflammatory cells (**Figure 2C**) (Hadigal et al., 2015). Similarly, specific forms of sulfated-HS on filopodia or on filopodial bridges may orchestrate wide variety of inflammatory reactions by regulating various inflammatory processes (**Figure 3**) (Simon Davis and Parish, 2013). Finally, HSV being a neurotropic virus widely utilizes neuronal axons to move across the cells. The later system expressing HS mimics filopodial model to influence virus infection and associated inflammation in the brain (**Figure 4**) (Zhang et al., 2014).

CONCLUDING REMARKS

Filopodia were first identified for their roles in cell migration and chemoattractant sensory mechanisms through utilization of their neuronal growth cones. Recently, filopodia have gained increasing attention because they have been found to facilitate viral infection including viral spread (**Table 1**). Cell-to-cell spreading has advantages including increased speed, immune evasion, overcoming physiological barriers, and greater infectivity of cells. The process of viral entry using filopodia consists of multiple steps. Receptor and co-receptor binding leads to cellular signaling, which rearranges the cytoskeleton of the cell. Viruses are seen to 'surf' along filopodia, almost like beads on a conveyor belt. Filopodia further enable viral entry by filopodial retraction and endocytosis at the base of the filopodia. There are notable similarities among the viruses that utilize filopodia for viral entry. For example, HPV and HSV-1 surf along filopodia and internalize at the base of filopodia through endocytosis. Still, filopodia are so diverse in function that they can facilitate budding. Two prime examples are the related viruses, MARV and Ebola Virus. However, viral infection is not the only factor stimulating formation of these actin protrusions – inflammation also enhances filopodia. Inflammatory cytokines such as TNFα, IL-1β, INFγ and LPS produced filopodia in as early as 1 h. Second, chemokines, such as CXCL8, also facilitate filopodia formation. The filopodia were found to associate with leukocytes and facilitate increased neutrophil migration. Overall, filopodia are clinically significant not only because of its role in viral entry, exit, and inflammatory response, but also because filopodia promote cancer metastasis.

AUTHOR CONTRIBUTIONS

KC, JB, SH, and VT wrote the article. MV, DS, and VT did the editing work. VT develop the images.

ACKNOWLEDGMENTS

We would like to thank the reviewers for their insightful comments on the manuscript, as their remarks led to an improvement of the work. The Kenneth A. Suarez Summer Research Program by Midwestern University supported KC and JB. VT was supported by NIH research funding.

REFERENCES

Akula, S. M., Naranatt, P. P., Walia, N.-S., Wang, F.-Z., Fegley, B., and Chandran, B. (2003). Kaposi's sarcoma-associated herpesvirus (Human herpesvirus 8) infection of human fibroblast cells occurs through endocytosis. *J. Virol.* 77, 7978–7990. doi: 10.1128/JVI.77.14.7978-7990.2003

Alberts, B., Bray, D., Lewis, J., Raff, M., ROberts, K., and Watson, J. (1994). *Molecular Biology of the Cell*, 3 Edn. New York, NY: Garland Publishing Inc.

American Cancer Society (2015). *Viruses that Can Lead to Cancer*. Available at: http://www.cancer.org/cancer/cancercauses/othercarcinogens/infectiousagents/infectiousagentsandcancer/infectious-agents-and-cancer-viruses

Bienkowska-Haba, M., and Sapp, M. (2011). March 10. The cytoskeleton in papillomavirus infection. *Viruses* 3, 260–271. doi: 10.3390/v3030260

Bornschlogl, T. (2013). How filopodia pull: what we know about the mechanics and dynamics of filopodia. *Cytoskeleton* 70, 590–603. doi: 10.1002/cm.21130

Bornsclogl, T., Romero, S., Vestergaard, C. L., Joanny, J.-F., Nhieu, G. T., and Bassereau, P. (2013). Filopodial retraction force is generated by cortical actin dynamics and controlled by reversible tethering at the tip. *Proc. Natl. Acad. Sci. U.S.A.* 110, 18928–18933. doi: 10.1073/pnas.1316572110

Butt, A. Q., and Miggin, S. M. (2012). Cancer and viruses: a double-edged sword. *Proteomics* 12, 2127–2138. doi: 10.1002/pmic.201100526

Carpenter, J. E., Hutchinson, J. A., Jackson, W., and Grose, C. (2008). Egress of light particles among filopodia on the surface of Varicella-Zoster virus-infected cells. *J. Virol.* 82, 2821–2835. doi: 10.1128/JVI.01821-07

Chang, Y., Cesarman, E., Pessin, M., Lee, F., Culpepper, J., Knowles, D., et al. (1994). Identification of herpesvirus-like DNA sequences in AIDS-associated Kaposi's sarcoma. *Science* 266, 1865–1869. doi: 10.1126/science.7997879

Chen, Z., Shi, Z., and Baumgart, T. (2015). Regulation of membrane-shape transitions induced by I-BAR domains. *Biophys. J.* 109, 298–307. doi: 10.1016/j.bpj.2015.06.010

Choudhary, S., Burnham, L., Thompson, J. M., Shukla, D., and Tiwari, V. (2013). Role of filopodia in HSV-1 entry into zebrafish 3-O-sulfotransferase-3-expressing cells. *Open. Virol. J.* 7, 41–48. doi: 10.2174/18743579013070 10041

Clement, C., Tiwari, V., Scanlan, P. M., Valyi-Nagy, T., Yue, B. Y., and Shukla, D. (2006). A novel role for phagocytosis-like uptake in herpes simplex virus entry. *J. Cell. Biol.* 174, 1009–1021. doi: 10.1083/jcb.200509155

Cooper, G. M. (2000). "The cell: a molecular approach," in *Structure and Organization of Actin Filaments*, 2nd Edn, ed. G. M. Cooper (Sunderland, MA: Sinauer Associates). Available at: http://www.ncbi.nlm.nih.gov/books/NBK9908

Cossart, P. (2000). Actin-based motility of pathogens: the Arp2/3 complex is a central player. *Cell. Microbiol.* 2, 195–205. doi: 10.1046/j.1462-5822.2000.00053.x

Dent, E. W., Gupton, S. L., and Gertler, F. B. (2011). The growth cone cytoskeleton in axon outgrowth and guidance. *Cold Spring Harb. Perspect. Biol.* 3:a001800. doi: 10.1101/cshperspect.a001800

Dixit, R., Tiwari, V., and Shukla, D. (2008). Herpes simplex virus type 1 induces filopodia in differentiated P19 neural cells to facilitate viral spread. *Neurosci. Lett.* 440, 113–118. doi: 10.1016/j.neulet.2008.05.031

Do, T., Murphy, G., Earl, L. A., Del Prete, G. Q., Grandinetti, G., Li, G.-H., et al. (2014). Three-dimensional imaging of HIV-1 virological synapses reveals membrane architectures involved in virus transmission. *J. Virol.* 88, 10327–10339. doi: 10.1128/JVI.00788-14

Greber, U. (2002). Signalling in viral entry. *Cell. Mol. Life Sci.* 59, 608–626. doi: 10.1007/s00018-002-8453-3

Guillou, H., Depraz-Depland, A., Planus, E., Vianaya, B., Chaussy, J., Grichine, A., et al. (2008). Lamellipodia nucleation by filopodia depends on integrin occupancy and downstream Rac1 signaling. *Exp. Cell Res.* 314, 478–488. doi: 10.1016/j.yexcr.2007.10.026

Hadigal, S. R., Agelidis, A. M., Karasneh, G. A., Antoine, T. E., Yakoub, A. M., and Ramani, V. C. (2015). Heparanase is a host enzyme required for herpes simplex virus-1 release from cells. *Nat. Commun.* 6:6985. doi: 10.1038/ncomms7985

Hashimoto, M., Bhuyan, F., Hiyoshi, M., Noyori, O., Nasser, H., Miyazaki, M., et al. (2016). Potential role of the formation of tunneling nanotubes in HIV-1 spread in macrophages. *J. Immunol.* 196, 1832–1841. doi: 10.4049/jimmunol.1500845

Hindmarsh, P. L., and Laimins, L. A. (2007). Mechanisms regulating expression of the HPV 31 L1 and L2 capsid proteins and pseudovirion entry. *J. Virol.* 4:19. doi: 10.1186/1743-422X-4-19

Huang, C.-Y., Lu, T.-Y., Bair, C.-H., Chang, Y.-S., Jwo, J.-K., and Chang, W. (2008). A novel cellular protein, VPEF, facilitates vaccinia virus penetration into HeLa cells through fluid phase endocytosis. *J. Virol.* 82, 7988–7999. doi: 10.1128/JVI.00894-08

Jose, J., Tang, J., Taylor, A. B., Baker, T. S., and Kuhn, R. J. (2015). Fluorescent protein-tagged sindbis virus E2 glycoprotein allows single particle analysis of virus budding from live cells. *Viruses* 7, 6182–6199. doi: 10.3390/v7122926

Kolesnikova, L., Bohil, A., Cheney, R., and Becker, S. (2007). Budding of Marburgvirus is associated with filopodia. *Cell. Microbiol.* 9, 939–951. doi: 10.1111/j.1462-5822.2006.00842.x

Komano, J., Miyauchi, K., Matsuda, Z., and Yamamoto, N. (2004). Inhibiting the Arp2/3 complex limits infection of both intracellular mature vaccinia virus and primate lentiviruses. *Mol. Biol. Cell.* 15, 5197–5207. doi: 10.1091/mbc.E04-04-0279

LeBrasseur, N. (2007). Viruses infect filopodia. *J. Cell. Biol.* 176:733. doi: 10.1083/jcb.1766rr1

Lehmann, M. J., Sherer, N. M., Marks, C. B., Pypaert, M., and Mothes, W. (2005). Actin- and myosin-driven movement of viruses along filopodia precedes their entry into cells. *J. Cell. Biol.* 170, 317–325. doi: 10.1083/jcb.200 503059

Leijnse, N., Oddershede, L. B., and Bendix, P. M. (2015a). An updated look at actin dynamics in filopodia. *Cytoskeleton* 72, 71–79. doi: 10.1002/cm.21216

Leijnse, N., Oddershede, L. B., and Bendix, P. M. (2015b). Helical buckling of actin inside filopodia generates traction. *Proc. Natl. Acad. Sci. U.S.A.* 112, 136–141. doi: 10.1073/pnas.1411761112

Machesky, L. M., and Li, A. (2010). Fascin: invasive filopodia promoting metastasis. *Commun. Integr. Biol.* 3, 263–270. doi: 10.4161/cib.3.3.11556

Mattila, P. K., and Lappalainen, P. (2008). Filopodia: molecular architecture and cellular functions. *Nat. Rev. Mol. Cell. Biol.* 9, 446–454. doi: 10.1038/nrm2406

Melnick, M., Sedghizadeh, P. P., Allen, C. M., and Jaskoll, T. (2012). Human cytomegalovirus and mucoepidermoid carcinoma of salivary glands: cell-specific localization of active viral and oncogenic signaling proteins is confirmatory of a causal relationship. *Exp. Mol. Pathol.* 92, 118–125. doi: 10.1016/j.yexmp.2011.10.011

Mercer, J., Knebel, S., Schmidt, F. L., and Helenius, A. (2010a). Vaccinia virus strains use distinct forms of macropinocytosis for host-cell entry. *Proc. Natl. Acad. Sci. U.S.A.* 107, 9346–9351. doi: 10.1073/pnas.1004618107atl.

Mercer, J., Schelhaas, M., and Helenius, A. (2010b). Virus entry by endocytosis. *Annu. Rev. Biochem.* 79, 803–833. doi: 10.1146/annurev-biochem-060208-104626

Mothes, W., Sherer, N. M., Jin, J., and Zhong, P. (2010). Virus Cell-to-cell transmission. *J. Virol.* 84, 8360–8368. doi: 10.1128/JVI.00443-10

Nikolic, D., Lehmann, M., Felts, R., Garcia, E., Blanchet, F., Subramaniam, S., et al. (2011). HIV-1 activates Cdc42 and induces membrane extensions in immature dendritic cells to facilitate cell-to-cell virus propagation. *Blood* 118, 4841–4852. doi: 10.1182/blood-2010-09-305417

Oh, M., Akhtar, J., Desai, P., and Shukla, D. (2010). A role for heparan sulfate in viral surfing. *Biochem. Biophs. Res. Commun.* 391, 176–181. doi: 10.1016/j.bbrc.2009.11.027

Quetglas, J. I., Hernáez, B., Galindo, I., Muñoz-Moreno, R., Cuesta-Geijo, M. A., and Alonso, C. (2012). Small Rho GTPases and cholesterol biosynthetic pathway intermediates in african swine fever virus infection. *J. Virol.* 86, 1758–1767. doi: 10.1128/JVI.05666-11

Salameh, S., Sheth, U., and Shukla, D. (2012). Early events in herpes simplex virus lifecycle with implications for an infection of lifetime. *Open. Virol. J.* 6, 1–6. doi: 10.2174/1874357901206010001

Schelhaas, M. (2010). Come in and take your coat off – how host cells provide endocytosis for virus entry. *Cell Microbiol.* 12, 1375–1388. doi: 10.1111/j.1462-5822.2010.01510.x

Schelhaas, M., Ewers, H., Rajamäki, M.-L., Day, P. M., Schiller, J. T., and Helenius, A. (2008). Human papillomavirus type 16 entry: retrograde cell surface transport along actin-rich protrusions. *PLoS Pathog.* 4:148. doi: 10.1371/journal.ppat.1000148

Schudt, G., Kolesnikova, L., Dolnik, O., Sodeik, B., and Becker, S. (2013). Live-cell imaging of Marburg virus-infected cells uncovers actin-dependent transport of nucleocapsids over long distances. *Proc. Natl. Acad. Sci. U.S.A.* 110, 14402–14407. doi: 10.1073/pnas.1307681110

Sherer, N. M., Lehmann, M. J., and Jimenez-Soto, L. F. (2007). Retroviruses can establish filopodial bridges for efficient cell-to-cell transmission. *Nat. Cell. Biol.* 9, 310–315. doi: 10.1038/ncb1544

Shrivastava, A., Prasad, A., Kuzontkoski, P. M., Yu, J., and Groopman, J. E. (2015). Slit2N inhibits transmission of HIV-1 from dendritic cells to T-cells by modulating novel cytoskeletal elements. *Sci. Rep.* 19:16833. doi: 10.1038/srep16833

Simon Davis, D. A., and Parish, C. R. (2013). Heparan Sulfate: a ubiquitous glycosaminoglycan with multiple roles in immunity. *Front. Immunol.* 4:470. doi: 10.3389/fimmu.2013.00470

Smith, J. L., Lidke, D. S., and Ozbun, M. A. (2008). Virus activated filopodia promote human papillomavirus type 31 uptake from the extracellular matrix. *Virology* 381, 16–21. doi: 10.1016/j.virol.2008.08.040

Takada, Y., Isono, K., Shinga, J., Turner, J. M., Kitamura, H., Ohara, O., et al. (2007). Mammalian polycomb Scmh1 mediates exclusion of polycomb complexes from the XY body in the pachytene spermatocytes. *Development* 134, 579–590. doi: 10.1242/dev.02747

Taylor, M. P., Koyuncu, O. O., and Enquist, L. W. (2011). Subversion of the actin cytoskeleton during viral infection. *Nat. Rev. Microbiol.* 9, 427–439. doi: 10.1038/nrmicro2574

Tiwari, V., Maus, E., Sigar, I. M., Ramsey, K. H., and Shukla, D. (2012). Role of heparan sulfate in sexually transmitted infections. *Glycobiology* 22, 1402–1412. doi: 10.1093/glycob/cws106

Tiwari, V., and Shukla, D. (2012). Nonprofessional phagocytosis can facilitate herpesvirus entry into ocular cells. *Clin. Dev. Immunol.* 8, 651–691. doi: 10.1155/2012/651691

Tiwari, V., Tarbutton, M. S., and Shukla, D. (2015). Diversity of heparan sulfate and hsv entry: basic understanding and treatment strategies. *Molecules* 20, 2707–2727. doi: 10.3390/molecules20022707

Welch, M., and Mullins, R. (2002). Cellular control of actin nucleation. *Annu. Rev. Cell Dev. Biol.* 18, 247–288. doi: 10.1146/annurev.cellbio.18.040202.112133

Wheeler, D. L., Iida, M., and Dunn, E. F. (2009). The role of Src in solid tumors. *Oncologist* 14, 667–678. doi: 10.1634/theoncologist.2009-0009

Xiang, Y., Zheng, K., Ju, H., Wang, S., Pei, Y., Wang, Y., et al. (2012). Cofilin 1-mediated biphasic F-actin dynamics of neuronal cells affect herpes simplex virus 1 infection and replication. *J. Virol.* 86, 8440–8451. doi: 10.1128/JVI.00609-12

Xu, H., Hao, X., Wang, S., Wang, Z., Cai, M., Jiang, J., et al. (2015). Real-time imaging of rabies virus entry into living vero cells. *Sci. Rep.* 5:11753. doi: 10.1038/srep11753

Zhang, H., Berg, J. S., Li, Z., Wang, Y., Lång, P., Sousa, A. D., et al. (2004). Myosin-X provides a motor-based link between integrins and the cytoskeleton. *Nat. Cell Biol.* 6, 523–531. doi: 10.1038/ncb1136

Zhang, X., Wang, B., and Li, J. P. (2014). Implications of heparan sulfate and heparanase in neuroinflammation. *Matrix Biol.* 35, 174–181. doi: 10.1016/j.matbio.2013.12.009

Conflict of Interest Statement: The authors declare that the research was conducted in the absence of any commercial or financial relationships that could be construed as a potential conflict of interest.

Copyright © 2016 Chang, Baginski, Hassan, Volin, Shukla and Tiwari. This is an open-access article distributed under the terms of the Creative Commons Attribution License (CC BY). The use, distribution or reproduction in other forums is permitted, provided the original author(s) or licensor are credited and that the original publication in this journal is cited, in accordance with accepted academic practice. No use, distribution or reproduction is permitted which does not comply with these terms.

frontiers in Microbiology

REVIEW
published: 09 November 2015
doi: 10.3389/fmicb.2015.01237

Biogenesis, Function, and Applications of Virus-Derived Small RNAs in Plants

*Chao Zhang[1], Zujian Wu[1], Yi Li[2] and Jianguo Wu[1,2]**

[1] *Key Laboratory of Plant Virology of Fujian Province, Institute of Plant Virology, Fujian Agriculture and Forestry University, Fuzhou, China,* [2] *Peking-Yale Joint Center for Plant Molecular Genetics and Agrobiotechnology, The National Laboratory of Protein Engineering and Plant Genetic Engineering, College of Life Sciences, Peking University, Beijing, China*

RNA silencing, an evolutionarily conserved and sequence-specific gene-inactivation system, has a pivotal role in antiviral defense in most eukaryotic organisms. In plants, a class of exogenous small RNAs (sRNAs) originating from the infecting virus called virus-derived small interfering RNAs (vsiRNAs) are predominantly responsible for RNA silencing-mediated antiviral immunity. Nowadays, the process of vsiRNA formation and the role of vsiRNAs in plant viral defense have been revealed through deep sequencing of sRNAs and diverse genetic analysis. The biogenesis of vsiRNAs is analogous to that of endogenous sRNAs, which require diverse essential components including dicer-like (DCL), argonaute (AGO), and RNA-dependent RNA polymerase (RDR) proteins. vsiRNAs trigger antiviral defense through post-transcriptional gene silencing (PTGS) or transcriptional gene silencing (TGS) of viral RNA, and they hijack the host RNA silencing system to target complementary host transcripts. Additionally, several applications that take advantage of the current knowledge of vsiRNAs research are being used, such as breeding antiviral plants through genetic engineering technology, reconstructing of viral genomes, and surveying viral ecology and populations. Here, we will provide an overview of vsiRNA pathways, with a primary focus on the advances in vsiRNA biogenesis and function, and discuss their potential applications as well as the future challenges in vsiRNAs research.

Keywords: RNA silencing, small RNAs, virus-derived small RNAs, DCLs, RDRs, AGOs, plant antiviral defense

OPEN ACCESS

Edited by:
Toshinori Sato,
Keio University, Japan

Reviewed by:
Akio Kanai,
Keio University, Japan
Alberto Carbonell,
Instituto de Biología Molecular y Celular de Plantas, Spain

****Correspondence:***
Jianguo Wu
wujianguo81@126.com

Specialty section:
This article was submitted to Virology, a section of the journal Frontiers in Microbiology

Received: *30 July 2015*
Accepted: *26 October 2015*
Published: *09 November 2015*

Citation:
Zhang C, Wu Z, Li Y and Wu J (2015) Biogenesis, Function, and Applications of Virus-Derived Small RNAs in Plants. Front. Microbiol. 6:1237. doi: 10.3389/fmicb.2015.01237

INTRODUCTION

In plants and other eukaryotic organisms, small RNAs (sRNAs) have emerged as key players of RNA silencing in the regulation of various biological processes, including plant growth and development, host immunity and pathogen virulence. To date, a series of pathways beginning with different precursors and resulting in sRNAs of various sizes with dedicated functions has been elucidated in the model plant *Arabidopsis* through both forward and reverse genetic screens.

Small RNAs are grouped into two major classes: microRNAs (miRNAs) and small interfering RNAs (siRNAs). MiRNAs are generated from a primary transcript (pri-miRNA) containing a stem–loop structure and processed into 20–25 nucleotide (nt) sRNAs by RNase III endonuclease DICER-LIKE 1 (DCL1), with the exception of the DCL4-dependent miRNAs such as miR822, miR839, and miR859 (Rajagopalan et al., 2006; Ben Amor et al., 2009). Many other cellular proteins are also required for miRNAs metabolism from processing to degradation, such as Methyltransferase

HUA ENHANCER1 (HEN1), zinc finger protein SERRATE (SE), dsRNA-binding protein HYPONASTIC LEAVES 1 (HYL1), G-patch domain-containing protein TOUGH (TGH), HEN1 SUPPRESSOR1 (HESO1) and a family of SMALL-RNA DEGRADING NUCLEASES (SDNs) reviewed in Xie et al. (2015). siRNAs are divided into four subgroups: *trans*-acting siRNAs (ta-siRNAs), heterochromatic-associated siRNAs (hc-siRNAs), natural antisense transcript siRNAs (nat-siRNAs), and virus-activated siRNAs (vasiRNAs), which are primarily generated from diverse perfectly double-stranded RNA precursors and excised by DCL1 and its homologs (DCL2, DCL3, and DCL4) either cooperatively or redundantly (Bouche et al., 2006; Axtell, 2013; Cao et al., 2014). sRNAs are recruited by an ARGONAUTE (AGO) ribonucleoprotein complex, referred to as the RNA-induced silencing complex (RISC; Poulsen et al., 2013; Carbonell and Carrington, 2015). The programmed sRNA/RISC targets and silences RNA or DNA through post-transcriptional gene silencing (PTGS) or transcriptional gene silencing (TGS), respectively, in a sequence-specific manner (Martinez de Alba et al., 2013). Several updated reviews regarding the functions of miRNAs and siRNAs in controlling a plenty of biological processes are available (Harfouche et al., 2015; Weiberg and Jin, 2015; Zhang, 2015).

In regard to virus-derived small RNAs (vsiRNAs), many studies have shown in various organisms that the production of vsiRNAs is linked to antiviral immunity via silencing the viral genomic RNA. Two lines of evidences, including the biogenesis of vsiRNAs and the viral suppressors of RNA silencing (VSRs)-regulated counter-defense help us to understand the vsiRNAs-mediated antiviral RNA silencing pathway. In this review, we mainly summarize the current knowledge of the biogenesis and function of vsiRNAs in plants and discuss their potential applications as well as their future challenges in crop breeding systems.

BIOGENESIS OF VIRUS-DERIVED SMALL RNAs IN PLANTS

Virus-derived siRNAs, a class of exogenous sRNAs, are one of the earliest discovered sRNAs (Hamilton and Baulcombe, 1999). The biogenesis of vsiRNAs, however, has not been clearly elucidated over the past decade. What is known has been deduced based on the insights from genetic analysis in *Arabidopsis* and vsiRNAs profiling from various plant species. It indicates that the biogenesis of vsiRNAs is analogous to that of endogenous sRNAs, which requires the actions of various DCLs, RDRs, and AGOs. **Table 1** lists the specific plant DCLs, RDRs, and AGOs known to contribute to the biogenesis of vsiRNAs.

Origin of Viral siRNAs

Early models of the origin of vsiRNAs hypothesized that the double-stranded replication intermediates (RIs) of positive-strand RNA viruses trigger the activation of the production of vsiRNAs (Ahlquist, 2002). If this was the case, the read counts of vsiRNAs derived from both the positive and negative strand in the virus-infected host plant cells should be similar. However, profiling of vsiRNAs derived from *Cymbidium ringspot virus* (CymRSV)-infected plants led to several interesting observations: (i) vsiRNAs derived from the genomic or positive strand far outnumbered those derived from the negative strand; (ii) most vsiRNAs were concentrated in a limited number of hotspots in the CymRSV genome; and (iii) double-stranded vsiRNAs bound to VSR protein p19 appeared to contain mismatches, as they were more sensitive to RNase A digestion than fully double-stranded controls (Ahlquist, 2002). These observations and others suggest that vsiRNAs are derived from the processing of highly structured regions of genomic RNA rather than from the perfectly paired dsRNAs-like RIs (Molnar et al., 2005; Koukiekolo et al., 2009). Several recent vsiRNA profiling studies in diverse eukaryotes have revealed that there are hotspots for vsiRNAs generation and there is a clear preference for a polarity, which have similar vsiRNA distribution to CymRSV (Xu et al., 2012; Vives et al., 2013; Visser et al., 2014). These results show, at least for some viruses, that RIs do not contribute significantly to the biogenesis of vsiRNAs. Rather, dsRNA-like secondary structures of single-stranded (ss) viral RNAs are most likely the dominant source of vsiRNAs (Donaire et al., 2009; Szittya et al., 2010; Wang et al., 2010). There is limited research on the origin of vsiRNAs derived from DNA viruses. This was characterized in *geminiviruses*, a family of plant DNA viruses with one or two circular ssDNA genomes that are replicated via dsDNA intermediates by a rolling circle mechanism. The dsRNA-like structures of DNA viruses are dominantly formed by the annealing of converging sense/antisense transcripts (Chellappan et al., 2004; Aregger et al., 2012).

Roles of DCLs in the Biogenesis of Viral siRNAs

Members of the plant Dicer-like (DCL) protein family are the critical components of the RNA-silencing pathway that produce vsiRNAs of different lengths (DCL4: 21-nt, DCL2: 22-nt, DCL3: 24-nt; Deleris et al., 2006). In *Arabidopsis*, the production of siRNAs from plant RNA viruses is mainly catalyzed under hierarchical action of the enzyme activities of DCL4 and DCL2 (Deleris et al., 2006; **Figure 1**). These results were first verified with *Tobacco rattle virus* (TRV) infected *dcl* combination mutants. Specifically, TRV-specific siRNAs accumulated as discrete 21- and 24-nt species in wild-type (WT) *Arabidopsis*, similar to that in *dcl2* mutants, while in *dcl3*, and *dcl2*/*dcl3* double mutants, only 21-nt siRNAs accumulated, suggesting that DCL4 is mainly responsible for the processing of 21-nt vsiRNAs from RNA viruses (Fusaro et al., 2006; Garcia-Ruiz et al., 2010). In the case when DCL4 is absent or its activity is reduced or inhibited by virus, DCL2 produces 22-nt vsiRNAs. Although the abundance is lower, they are sufficient to trigger protective immunity, thus rescuing antiviral silencing. In the *dcl2*/*dcl4* double mutant, DCL3 can produce 24-nt vsiRNAs, which play a minor role in antiviral defense. Additionally, Bouche et al. (2006) reported the DCLs functions in the production of *Cucumber mosaic virus* (CMV)-specific siRNA. Their results indicate that CMV siRNAs are produced by DCL4 in WT plants, or DCL2 and DCL3 in

TABLE 1 | Plant DCLs, RDRs, and AGOs involve in the vsiRNA biogenesis and function.

Virus	Genus	Host	DCLs	RDRs	AGOs	Reference
TRV	*Tobravirus*	*Arabidopsis thaliana*	DCL2/3/4	RDR1/2/6	AGO2/4	Fusaro et al., 2006; Donaire et al., 2008; Ma et al., 2015
TuMV	*Potyvirus*	*Arabidopsis thaliana*	DCL2/4	RDR1/2/6	AGO1/2/5/7/10	Garcia-Ruiz et al., 2010, 2015; Carbonell et al., 2012
TMV	*Tobamovirus*	*Arabidopsis thaliana*	Unknown	RDR1/6	Unknown	Qi et al., 2009
ToRSV	*Nepovirus*	*Nicotiana benthamiana*	Unknown	Unknown	AGO1	Ghoshal and Sanfaçon, 2014
CMV	*Cucumovirus*	*Arabidopsis thaliana*	DCL1/2/3/4	RDR1/6	AGO1/2/4/5	Bouche et al., 2006; Diaz-Pendon et al., 2007; Wang et al., 2010, 2011
BMV	*Bromovirus*	*Arabidopsis thaliana*	DCL2/4	RDR6	AGO1	Dzianott et al., 2012
TCV	*Carmovirus*	*Arabidopsis thaliana*	DCL2/4	Unknown	AGO1/2/7	Qu et al., 2008; Harvey et al., 2011; Zhang et al., 2012
TBSV	*Tombusvirus*	*Nicotiana benthamiana*	Unknown	Unknown	AGO2	Scholthof et al., 2011; Schuck et al., 2013
PVX	*Potexvirus*	*Arabidopsis thaliana, Nicotiana benthamiana*	DCL2/4	RDR6	AGO2/5	Schwach et al., 2005; Bouche et al., 2006; Andika et al., 2015; Brosseau and Moffett, 2015
TYLCV	*Begomovirus*	*Nicotiana benthamiana, cassava*	DCL2/3	Unknown	Unknown	Akbergenov et al., 2006
CaMV	*Caulimovirus*	*Arabidopsis thaliana*	DCL1/2/3/4	Unknown	AGO4	Blevins et al., 2006; Raja et al., 2014
BCTV	*Curtovirus*	*Arabidopsis thaliana*	DCL3	Unknown	AGO4	Raja et al., 2008
CaLCuV	*Begomovirus*	*Arabidopsis thaliana*	DCL1/2/3/4	RDR1/2/6-independent	AGO4	Blevins et al., 2006; Aregger et al., 2012; Raja et al., 2014
RSV	*Tenuivirus*	*Oryza sativa*	Unknown	RDR6	AGO1/18	Jiang et al., 2012; Wu et al., 2015
RDV	*Phytoreovirus*	*Oryza sativa*	Unknown	RDR6	AGO1/18	Hong et al., 2015; Wu et al., 2015
OsEV	*Endornavirus*	*Oryza sativa*	DCL2	Unknown	Unknown	Urayama et al., 2010

Specific plant DCLs, RDRs, and AGOs known to contribute to the biogenesis of vsiRNAs. TRV, Tobacco rattle virus; TuMV, Turnip mosaic virus; TMV, Tobacco mosaic virus; ToRSV, Tomato ring spot nepovirus; CMV, Cucumber mosaic virus; BMV, Brome mosaic virus; TCV, Turnip crinkle virus; PVX, Potato virus X; TYLCV, Tomato yellow leaf curl virus; CaMV, Cauliflower mosaic virus; BCTV, Beet curly top virus; CaLCuV, Cabbage leaf curl virus; RSV, Rice stripe virus; RDV, Rice dwarf virus; OsEV, Oryza sativa endornavirus.

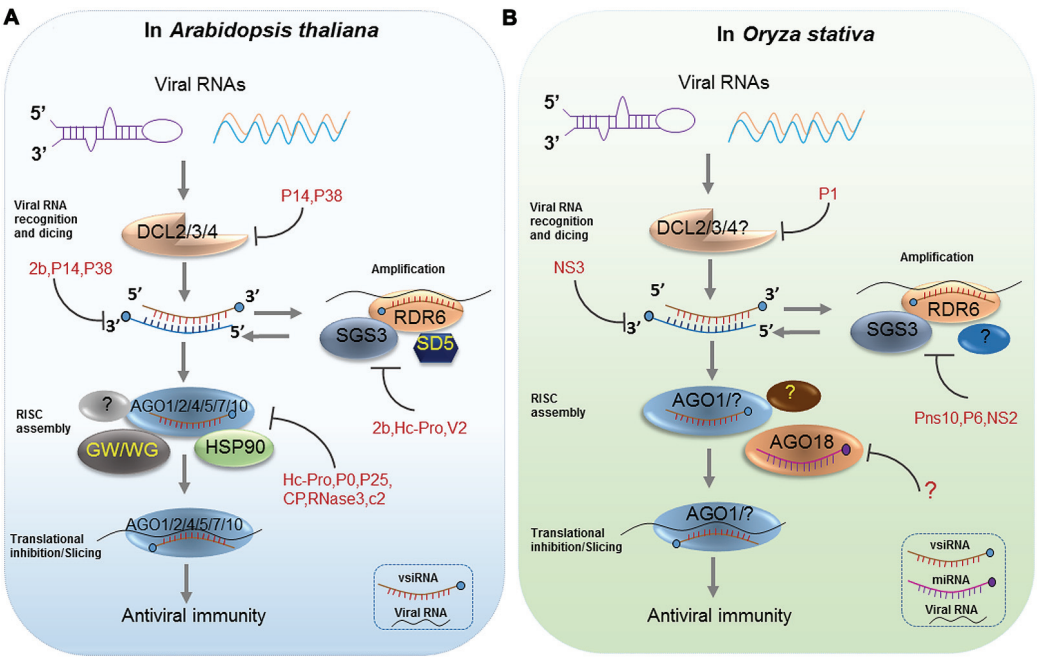

FIGURE 1 | Antiviral RNA Silencing in *Arabidopsis* and *Oryza stativa*. RNA silencing is initiated by the recognition of viral dsRNAs or partially double-stranded hairpin RNAs, which are processed into viral siRNAs (vsiRNAs) by Dicer-like proteins (DCL2/3/4) in *Arabidopsis* **(A)** and *Oryza stativa* **(B)**. Next, HSP90-activated AGO1/2/4/5/7/10 is loaded with a vsiRNA, thereby forming a large RNA-induced silencing complex (RISC), which has likely incorporated other proteins such as the GW motif-containing AGO interactors in *Arabidopsis* **(A)**. In rice, AGO18 positively regulates AGO1 binding to vsiRNAs by sequestering miR168 **(B)**. Afterward, the vsiRNA-loaded RISC targets viral RNAs by slicing or translational inhibition. Secondary vsiRNAs are produced in an amplification loop through the actions of RNA-dependent RNA polymerases (RDRs) and cofactors (SGS3 and SDE5). Diverse viral silencing suppressors (VSRs) target various steps of antiviral silencing in plants **(A)** and **(B)**.

dcl4 mutants, which behave similar to ta-siRNAs. They also detected very low levels of 21-nt CMV-siRNAs in *dcl2/dcl3/dcl4* triple mutant plants, suggesting that DCL1 could produce 21-nt CMV-siRNAs in the absence of DCL2, DCL3 and DCL4, although much less efficiently than ta-siRNAs (Bouche et al., 2006). Likewise, this group reported an opposite situation of DCLs activities in the production of Turnip crinkle virus (TCV)-specific siRNAs in *Arabidopsis*. They found that DCL2 was the major contributor of TCV siRNAs, but DCL4 could also produce TCV siRNAs in the absence of DCL2 (Bouche et al., 2006). They later gave an interpretation for the discrepancy of DCL-dependent vsiRNAs processing between TCV and CMV. They thought DCL2 produced TCV siRNAs dominantly because DCL4 was inhibited by TCV but not because DCL2 had a stronger affinity than DCL4 for TCV dsRNA. In the *Brome mosaic virus* (BMV)-inoculated *Arabidopsis* Columbia-0 (Col-0) plants, BMV RNA accumulated higher level than that in *dcl2*/*dcl4* double mutant plants but similar to that in *dcl2* or *dcl4* single mutant plants (Dzianott et al., 2012). As for the silencing suppressor (HC-Pro)-deficient *Turnip mosaic virus* (TuMV)-infected *Arabidopsis*, blot assays showed that the 21-nt vsiRNA from the 5′ UTR region were sensitive to loss-of-function in DCL4, but in the absence of DCL4, this region yielded siRNAs that were 22-nt in length and dependent on DCL2 (Garcia-Ruiz et al., 2010). Recently, the differential requirement for DCL4 and DCL2 proteins in the inhibition of intracellular and systemic infection by *Potato virus X* (PVX) in *Arabidopsis* was also reported (Andika et al., 2015). In rice, there are six putative DCL proteins (OsDCL1, OsDCL2a, OsDCL2b, OsDCL3a, OsDCL3b, and OsDCL4). Liu et al. (2007) found that OsDCL4 is the major Dicer responsible for the generation of 21-nt siRNAs that are associated with inverted repeat transgenes and ta-siRNAs derived from the endogenous TAS3 gene and OsDCL1, but not OsDCL4, is important for miRNA accumulation. However, of the six rice DCLs, their function in vsiRNA biogenesis remain poorly understood. Interestingly, rice DCL2 negatively affected maintenance of *Oryza sativa endornavirus* (OsEV), an endogenous dsRNA virus by increasing the accumulation of vsiRNAs, and indicated that rice DCL2 plays a major role in processing vsiRNA from OsEV (Urayama et al., 2010). Functions of rice DCLs in vsiRNAs biogenesis are always deduced from their homology to *Arabidopsis* DCLs. However, Xu et al. (2012) found that the distribution of vsiRNAs derived from *Rice stripe virus* (RSV), a negative-strand RNA virus, is very different in rice, *Nicotiana benthamiana*, and *Laodelphax striatellus* (insect vector). This suggests that the origins of vsiRNAs derived from different hosts are likely distinct.

Although the biogenesis of vsiRNAs by DCLs has been extensively documented in plant RNA viruses, little is known regarding viruses with DNA genomes. Indeed, the vsiRNAs biogenesis pathway of plant DNA viruses, which have a dsDNA intermediate stage, differs from that of RNA viruses (Chellappan et al., 2004; Akbergenov et al., 2006; Blevins et al., 2006). For instance, *Geminiviruses* trigger accumulation of various vsiRNA classes. Specifically, in *begomovirus*-infected *N. benthamiana* and *cassava*, three major size-classes of vsiRNAs, 21-, 22-, and 24-nt, are generated, and more than one DCL is involved in their biogenesis (Akbergenov et al., 2006). DCL3 is required to produce 24-nt siRNAs, while the production of the 22-nt siRNAs depends on DCL2, as well as other as yet unidentified DCL activities. From the studies of another *geminivirus*, *Cabbage leaf curl virus* (CaLCuV), DCL1 also processes some CaLCuV long dsRNAs into residual 21-nt vsiRNAs in the absence of DCL2, DCL3, and DCL4 (Blevins et al., 2006). In the case of plant viruses with a dsDNA genome, such as *Cauliflower mosaic virus* (CaMV), 21-, 22-, and 24-nt siRNAs from both sense and antisense polarities, coding and non-coding regions accumulated in CaMV-infected *Arabidopsis* (Blevins et al., 2006). DCL3 and DCL2 are required for the biogenesis of 24- and 22-nt CaMV siRNAs, respectively. Furthermore, the key role of DCL1 in the biogenesis 21-nt siRNAs from CaMV leader region was confirmed by the finding that high levels of 21-nt CaMV siRNAs accumulated in *dcl2/dcl3/dcl4*. Taken together, unlike siRNA derived from RNA viruses, current knowledge suggests the accumulation of vsiRNAs from DNA viruses requires the action of all four DCL enzymes in a coordinated and hierarchical manner.

Roles of RDRs and AGOs in the Biogenesis of Viral siRNAs

Mechanistically, the biogenesis of viral siRNAs consists of two phases: DCL-dependent initiation phase and RDR-dependent amplification phase. RDRs play important roles in a second round of vsiRNA formation following viral RNA replication- or high-structural dsRNA-triggered biogenesis of primary siRNAs. The process of secondary siRNA-generation is thought to be similar to the RDR6-dependent tasi-RNA pathway. Specifically, primary vsiRNAs initiate the PTGS process involving diverse functional AGOs with RNase H-type activity (discussed latter) in plants. PTGS pathways recruit suppressor of gene silencing 3 (SGS3, a protein that blocks RNAs degradation), a putative RNA trafficking protein SDE5, and the RDR6 to transform cleaved ssRNA fragments into long, perfect dsRNA precursors. Then, these are subsequently processed into 21-nt siRNAs by DCL4 and its dsRNA binding partner DRB4 or 22-nt siRNAs by DCL2 (Dalmay et al., 2000; Mourrain et al., 2000; Gasciolli et al., 2005; Bouche et al., 2006; Martinez de Alba et al., 2015). Thus, it is assumed that an amplification loop is established whereby siRNA-guided AGO1 cleavage of viral transcripts leads to the RDR6/SGS3/SDE5-dependent production of dsRNAs, which serves as a substrate for the DCL-dependent formation of secondary vsiRNAs (Voinnet, 2008; Mallory and Vaucheret, 2009, 2010; **Figure 1**). In the beginning, there was some indirect evidence to support the role of host RDRs in vsiRNAs biogenesis and antiviral defense. First, host RDRs' activity is induced after virus infection. For instance, in tobacco mosaic virus (TMV)-infected tobacco leaves, a host polymerase RDR activity was stimulated by TMV (Romaine and Zaitlin, 1978). Moreover, loss-of-function mutations in host RDRs lead to hyper-susceptibility to virus infection (Dorssers et al., 1982; Xie et al., 2001; Schwach et al., 2005). Later, profiles of vsiRNAs in RDR mutants by deep sequencing directly revealed that host RDRs play a role in vsiRNAs biogenesis (Donaire et al., 2008;

Wang et al., 2010). Among the six RDR genes that are encoded by the *Arabidopsis* genome, the functions of RDR1, RDR2, and RDR6 have been well demonstrated. The production of CMV-derived siRNAs in the absence of the CMV VSR protein 2b is largely dependent on RDR1 originally (Diaz-Pendon et al., 2007). Wang et al. (2010) found that there is a twofold decrease in the relative abundance of viral siRNAs in CMV-infected *rdr1*/*rdr6* double and *rdr1*/*rdr2*/*rdr6* triple mutants plants compared to *rdr1* and WT plants, suggesting RDR1 and RDR6 are all required for amplification of CMV-derived siRNAs. They also suggested that RDR1 preferentially amplifies the 5′-terminal end of the three genomic RNAs of CMV, whereas RDR6 amplifies the remaining regions (Wang et al., 2010, 2011). Consistent with these studies, another group found that both RDR1 and RDR6 play important roles in biogenesis of TMV-Cg siRNAs in virus-infected cells (Qi et al., 2009). The biogenesis of TRV- and TuMV-derived siRNAs involves the combined activity of RDR1, RDR2, and RDR6 (Donaire et al., 2008; Garcia-Ruiz et al., 2010). In rice, there are five RDR genes that have been annotated (Zong et al., 2009) but no insights to their roles in the biogenesis of vsiRNAs was provided to date except for the findings given by Jiang et al. (2012). They were the first to report that rice RDR6 plays a role in the accumulation of siRNAs derived from RSV genomic RNA. Through deep sequencing, they found that compared to the WT, the abundance of the RSV-derived siRNAs showed a 53% reduction in OsRDR6 knockdown transgenic plants in which transcription levels were extremely reduced (Jiang et al., 2012). Recently, the same group confirmed the function of RDR6 in *Rice dwarf virus* (RDV) vsiRNA biogenesis. They found that the accumulation of RDV vsiRNAs was reduced in the OsRDR6 knockdown transgenic plants (Hong et al., 2015).

The biogenesis of RDR-dependent secondary vsiRNAs requires activity of AGOs, which serve as the effector proteins functioning in the antiviral RNA silencing. In *Arabidopsis,* there are 10 AGOs, categorized into three clades, while rice has 19 AGOs classified into four clades (Morel et al., 2002; Nonomura et al., 2007; Vaucheret, 2008). Many reports have shown that *Arabidopsis* AGO1, AGO2, AGO5, and AGO10 act in PTGS targeting RNA viruses (Qu et al., 2008; Harvey et al., 2011; Scholthof et al., 2011; Carbonell et al., 2012; Ghoshal and Sanfaçon, 2014; Brosseau and Moffett, 2015; Carbonell and Carrington, 2015; Garcia-Ruiz et al., 2015; Ma et al., 2015). For rice, little is known regarding how the various AGOs regulate antiviral RNA silencing except for AGO1 and AGO18, which synergistically play a role in antiviral defense (**Figure 1**; Du et al., 2011a; Wu et al., 2015). Actually, the role of AGOs in vsiRNAs biogenesis is almost restricted to their effector activity in the PTGS pathway. Specifically, AGOs associate with vsiRNAs to target complementary viral RNAs, and the cleaved ssRNAs are source of production of RDR-dependent secondary vsiRNAs.

Suppression of Viral siRNAs Biogenesis by Various VSRs

In the arms race between hosts and viruses, viruses developed potent VSRs that can target multiple steps of RNA silencing pathway to counter host antiviral strategies (Csorba et al., 2015; Wieczorek and Obrepalska-Steplowska, 2015). Apparently, the hallmark of the antiviral silencing response is the DCL-dependent production of vsiRNAs, thus the biogenesis of vsiRNAs is one important target of various VSRs. VSRs have ability to block the vsiRNA biogenesis by inhibiting DCL proteins and/or co-factors activity, sequestrating dsRNA/siRNA or AGO protein destabilization prior of RISC assembly. For instance, in the presence of TCV P38, siRNAs are undetectable, suggesting P38 acts to suppress DCL's activity (Qu et al., 2003). Deleris et al. (2006) later demonstrated using genetic analysis that P38 inhibits DCL4 but not DCL2. Moreover, P1 of RYMV also has ability to inhibit DCLs activities including both DCL4 and DCL3 (Lacombe et al., 2010; Weinheimer et al., 2010; Gillet et al., 2013). Some VSRs, such as *Pothos latent aureusvirus* (PolV) P14, TCV p38, CMV 2b, and RSV NS3 have been described to bind dsRNAs in a size-independent manner and therefore to block vsiRNA maturation (Merai et al., 2005; Deleris et al., 2006; Goto et al., 2007; Xiong et al., 2009). Furthermore, other VSRs such as RDV Pns10, CMV 2b, and *Rice yellow stunt virus* (RYSV) P6 block secondary siRNA biogenesis by downregulating RDR6 expression or suppressing the activity of RDR1, which are critical for secondary siRNAs synthesis (Diaz-Pendon et al., 2007; Ren et al., 2010; Guo et al., 2013). RSV NS2 as well as V2 protein of *Tomato yellow leaf curl virus* (TYLCV) directly interact with SGS3, the cofactor of RDR6, and compete with SGS3 for dsRNA binding (Glick et al., 2008; Fukunaga and Doudna, 2009; Kumakura et al., 2009; Du et al., 2011b; **Figure 1**). *Potyvirus* HC-Pro, one of the best characterized viral silencing suppressors, plays multiple roles in the suppression of vsiRNAs biogenesis, such as ds-siRNA binding, blocking HEN1 methyltransferase, HEN1 binding, blocking primary siRNA biogenesis by RAV2 interaction, RDR6 downregulation. A comprehensive review on the current knowledge of the diverse VSRs and their strategies to suppress vsiRNAs biogenes is available (Csorba et al., 2015).

Taken together, these findings support a model for vsiRNA biogenesis in plants in which DCL4 processes various viral dsRNA transcripts into primary vsiRNAs; RDRs and AGOs produce secondary vsiRNA through amplification. However, VSRs can inhibit the production of vsiRNAs by countering multiple steps of the antiviral silencing pathway. Notably, questions such as how, when, and where in the cell vsiRNAs are initially accessed by the RNA silencing machinery remain elusive.

ROLES OF VIRUS-DERIVED SMALL RNAs IN ANTIVIRAL DEFENSE

Besides the cellular components involved in vsiRNA biogenesis, there is accumulating evidence that the vsiRNA themselves are directly playing roles in antiviral immunity in plants. Considering the general function of sRNAs in directing RISC to target transcripts for PTGS or TGS, it is easy to assume that the main role of vsiRNAs is to target viral mRNA molecules. This may be a more effective method to inhibit viral replication than the production of primary vsiRNAs by DCL-dependent action

on the RIs or highly structural dsRNA derived from the viral genome.

VsiRNAs Function to Downregulate Viral RNAs

Virus-derived small interfering RNAs are recruited by diverse AGOs to form RISC and direct the degradation of viral RNA molecules through PTGS in a sequence-specific manner (Simon-Mateo and Garcia, 2006). AsatsiR-12, an artificial siRNA derived from the satellite RNA (satRNA) of SD-CMV (a severe field Shan-Dong strain), which targets the 3′ UTR of CMV RNA and triggers the RDR6-dependent antiviral silencing pathway, has a positive effect on antiviral defense. The accumulation of CMV RNAs was reduced in the CMV-Δ2b-infected transgenic plants expressing asatsiR-12 but this reduction was inhibited by the 2b suppressor (Zhu et al., 2011). Their findings provided the first demonstration that viral satRNAs could mediate silencing against their helper virus. However, whether any AGO protein is involved in the silencing process as part of an active vsiRNA-RISC was not demonstrated at that time. Later, plenty of *in vitro* experiments involving different combinations of cell-free systems and viruses were conducted and results have shown the existence of endonucleolytic of antiviral RISCs but not directly AGOs (Szittya and Burgyan, 2013). The slicer activity of AGOs was verified by using *in vitro* assays involving cytoplasmic extracts of evacuolated tobacco protoplasts (Iki et al., 2010; Schuck et al., 2013). For instance, 'RISC formation/cleavage assay' and 'replication inhibition assay' showed that AGO1, AGO2, AGO3, AGO5, AGO7 and AGO10 had slicer activity with 21- and 22-nt siRNAs and thus inhibited RNA replication of TBSV *in vitro* (Schuck et al., 2013). Actually, *in vivo* experiments have indicated that *N. benthamiana* AGO with similarity to *Arabidopsis* AGO2 is involved in antiviral defense against TBSV (Scholthof et al., 2011; Odokonyero et al., 2015). A recent study on the antiviral role of AGO2 has shown that AGO2, AGO10, and to a lesser extent AGO1 associate with vsiRNAs derived from HC-Pro-deficient TuMV-AS9 (Garcia-Ruiz et al., 2015). Until now, *Arabidopsis* AGO1, AGO2, AGO5, AGO7, AGO10, and rice AGO1 and AGO18 are all the AGOs reported that associate with vsiRNAs upon virus infection, reviewed in Carbonell and Carrington (2015; **Figure 1**). Notably, previous studies on miRNA-mediated antiviral RNA silencing have revealed that many molecular chaperones, such as HSP90 and GW/WG motif-containing proteins, assist in or promote the antiviral defense response (Mayor et al., 2007; Iki et al., 2010, 2012; Earley and Poethig, 2011; Yang et al., 2012). Here, we hypothesized that the vsiRNA-mediated antiviral RNA silencing is likely to require various molecular chaperones (**Figure 1**). However, to date, no evidence verifies this. Additionally, there is still much that remains missing from our knowledge of vsiRNA-mediated antiviral defense due to several obstacles: (i) It remains unknown whether the majority of, if not all, vsiRNAs can load into specific AGO proteins; (ii) Even though some AGO proteins play a role in virus infection and are able to bind vsiRNAs, the RISC complex alone may not be able to access target the viral genome due to their complex secondary structures or VSR activity; (iii) At present, evidence that specific vsiRNAs can target the viral genome for inhibition of virus infection *in vivo* is limited. Therefore, the efficiency of antiviral RNA silencing may be determined by the accessibility of target sites (Simon-Mateo and Garcia, 2006). More research should be done on these aspects to make more advancement, which would give us more insight into vsiRNA-mediated antiviral defense through PTGS.

VsiRNAs Function to Downregulate Viral DNAs

Virus-derived small interfering RNAs can also be recruited by AGO proteins to form antiviral RISC that target viral DNA. It has been reported in plants that DNA methylation not only stabilizes transposons in the genome but is also involved in defense against invasive viral DNA genomes guided by abundant vsiRNAs (Chellappan et al., 2004; Vanitharani et al., 2005; Moissiard and Voinnet, 2006). DNA methylation at gene promoters can be triggered by dsRNAs through the RNA-directed DNA methylation (RdDM) pathway and induces TGS. The RdDM pathway requires 24-nt siRNAs for *de novo* DNA methylation of cytosines in all sequence contexts and AGO4 to target transcripts (Chan et al., 2004; Xie et al., 2004; Henderson et al., 2006). However, there is little molecular evidence of a vsiRNA-mediated RdDM pathway in plant antiviral defense. Studies on vsiRNA-mediated RdDM pathway have been conducted based on ssDNA plant *geminivirus* (Brough et al., 1992; Ermak et al., 1993; Wang et al., 2003, 2005; Raja et al., 2008). A group has shown that *Arabidopsis* plants defective in methyltrasferase or related cofactor activity are hypersensitive to geminivirus infection, suggesting that the viral genome is targeted by RdDM. They also demonstrated that Beet curly top virus L2-mutant DNA present in tissues that have recovered from infection is hypermethylated and that host recovery requires AGO4, a component of RdDM pathway (Raja et al., 2008). Recently, the same group reported that *Arabidopsis* Double-stranded RNA Binding 3 (DRB3) functions with DCL3 and AGO4 to induce repressive viral genome methylation against *geminiviruses* (Raja et al., 2014). This work demonstrates that the vsiRNA-mediated RdDM pathway is likely the predominant defense approach for hosts to counter plant DNA viruses during infection. Furthermore, we hypothesized that the vsiRNA-mediated RdDM pathway also requires various host factors such as reiterated GW/WG repeats, a conserved effector motif on the plant-specific DNA-directed RNA polymerase IVb (PolIVb), also called the AGO hook. As previous studies described, they are binding platforms for AGO4 and are essential for the biogenesis of 24-nt siRNAs (**Figure 1**; El-Shami et al., 2007).

VsiRNAs Function to Downregulate Host Transcripts

Some have hypothesized that viruses might use sRNAs to silence specific host genes when there is near perfect complementarity (Addo-Quaye et al., 2008). However, the potential role of viral

siRNAs in regulating host gene expression has rarely been reported. This idea can be first exemplified by the disease symptoms induced by the CMV Y-satellite RNA (Y-Sat), which relies entirely upon its helper virus (CMV) for replication and movement. In one instance, viral siRNA derived from the CMV-Y satellite RNA (Y-Sat) can specifically target the 22-nt sequence in *CHLI* mRNA, encoding a magnesium chelatase subunit. Down-regulation *CHLI* leads to impairment in the chlorophyll biosynthesis pathway and the resulting yellowing symptom in the leaves (Shimura et al., 2011). In another case, two *Peach latent mosaic viroid* (PLMVd)-derived siRNAs specifically target host *CHLOROPLASTIC HEAT-SHOCK PROTEIN 90* transcripts, resulting in the albino phenotype characteristic of peach leaves infected with PLMVd (Navarro et al., 2012). Recently, by performing artificial microRNA experiments in a transient expression system and by using RNA ligase-mediated rapid amplification of cDNA ends, a single small RNA derived from the virulence modulating region of two *Potato spindle tuber viroid* (PSTVd) variants was characterized. It targets several callose synthase genes of tomato plants (*CalS11*-like and *CalS12*-like), which are essential for callose formation during pathogen infection (Adkar-Purushothama et al., 2015). Intriguingly, we also identified a sRNA derived from a rice virus with the potential to target rice endogenous transcripts and induce abnormal phenotypes in rice (unpublished). These observations indicate vsiRNAs possess an ability to silence specific host genes with nearly perfect complementary. Nonetheless, according to results from degradome sequencing datasets from virus-infected plants and/or 5′ Rapid Amplification of cDNA Ends analysis of putative transcripts show that only rare endogenous genes were targeted by characterized siRNAs (Li et al., 2013; Miozzi et al., 2013), suggesting that vsiRNAs only occasionally regulate the host gene expression through PTGS.

Suppression of vsiRNA Function by Various VSRs

Current research has verified the functions of vsiRNAs in targeting viral RNAs or DNAs and, occasionally, host transcripts. In turn, many plant viruses evolved VSRs counteract the antiviral silencing process mostly through arresting the functional vsiRNAs-RISC assembly (Csorba et al., 2015). Co-immunoprecipitation and small RNA profiling revealed that *Potyvirus* HC-Pro can associate with vsiRNAs during TuMV infection, suggesting that HC-Pro may interfere with vsiRNAs function in antiviral defense by binding vsiRNAs and blocking vsiRNA-RISC assembly (Garcia-Ruiz et al., 2015). P25 can inhibit the antiviral RNA silencing pathway by precluding AGO proteins from accessing viral RNA, as well as by directly inhibiting the formation of RNA silencing machinery (Brosseau and Moffett, 2015). *Polerovirus* P0 interacts with E3-ligase S-phase kinase regulated protein 1 (SKP1) through its F-box motif to enhance the degradation of multiple AGOs (AGO1, 2, 4–6, 9) before holo-RISC assembly. ToRSV suppressor coat protein (CP) binds to AGO1 to suppress its translational inhibitory activity and to enhance AGO1 degradation through autophagy (Karran and Sanfacon, 2014). RNase 3, a VSR encoded by *Sweet potato chlorotic stunt crinivirus* (SPCSV), affects vsiRNA function by using a completely different strategy, in which RNase3 cleaves 21–24-nt vsiRNAs into 14 bp products and renders them inactive, thus effectively preventing the formation of antiviral RISC (Kreuze et al., 2005; Cuellar et al., 2009). C2 protein, encoded by DNA virus *Beet severe curly top virus*, is an effector that counteracts antiviral defense by interfering with gene silencing and metabolic defense responses. C2 mediates a decrease in DNA methylation, which is linked with reduced accumulation of siRNAs derived from the methylated promoters, to result in upregulation of the corresponding coding genes (Yang et al., 2013; **Figure 1**). Regrettably, the activity of VSRs encoded by rice viruses in suppression of vsiRNAs function is completely unknown.

Though many evidences indicate that vsiRNAs play a key role in plant antiviral RNA silencing, the molecular mechanisms are elusive. Much work on the studies of biological roles of specific vsiRNAs and function mechanism of VSRs should be done in the future to further extend our understanding on the vsiRNAs function.

THE APPLICATION OF VIRUS-DERIVED SMALL RNAs

Use of vsiRNAs to Induce Antiviral Resistance

Current knowledge suggest RNA silencing make a great contribution to the resistance against pathogens on their respective crops (Nicaise, 2014). Whereas, naturally occurred vsiRNAs or miRNAs induced virus resistance is not enough for protecting the host plants from viral infection. By using hairpin constructs, dsRNA can be expressed in plants relatively easily, and RNA silencing is activated to silence the expression of genes of invading pathogens (Mansoor et al., 2006; Prins et al., 2008; Collinge et al., 2010). For viruses, this strategy is increasingly being used. Some cases directly characterize the application of vsiRNA in inducing antiviral resistance such as AsatsiR-12 (Zhu et al., 2011). However, many evidences indicating the application of vsiRNAs to induce antiviral resistance are indirect. In transgenic tobacco expressing hairpin RNA derived from TMV movement protein (MP) or CMV replication protein, two T4 transgenic lines with single copy were completely resistant to the corresponding virus (Hu et al., 2011). In rice, strong resistance is induced in transgenic rice plants expressing hairpin RNA of the viral genes, such as *RDV* viroplasm matrix protein Pns12 (Shimizu et al., 2009), *RSV* CP (Park et al., 2012), *Rice gall dwarf virus* Pns9 (Shimizu et al., 2012), *Rice grassy stunt virus* CP or MP (Shimizu et al., 2013). In transgenic maize, expressing the hairpin structure transcribed from the *CP* gene of *Sugarcane mosaic virus* (SCMV) led to inhibition of SCMV infection, although to varying degrees (Gan et al., 2014). Thus, in a variety of crops, based on the knowledge of vsiRNAs-mediated antiviral RNA silencing, expressing hairpin constructs strategy has been a potential approach with high efficiency to combat the virus.

Use of vsiRNAs to Assemble Virus and Viroid Genomes

Additionally, the complete genome of a certain virus can be reconstructed based on vsiRNAs derived from the virus by combining small RNA deep sequencing with *de novo* assembly of viral siRNAs using bioinformatics tools. For instance, Ruiz-Ruiz et al. (2011) used vsiRNAs sequencing to reconstruct the full genome of the T318A Spanish *Citrus tristeza virus* (CTV) isolate that infects sweet (*Citrus sinensis* Osbeck) and sour orange (*C. aurantium* L.) and Mexican lime (*C. aurantifolia* Christ.) seedlings. Seguin et al. (2014) reconstructed DNA viruses from *Caulimoviridae* and *Geminiviridae* families by utilizing this approach, subsequently, they also reconstructed an emerging DNA virus and two viroids associated with economically important red blotch disease of grapevine to verify that vsiRNA-based deep sequencing allows for *de novo* reconstruction of any DNA or RNA virus genome and its microvariants (Seguin et al., 2014). A new virus, Citrus vein enation virus (CVEV), was identified as the causal agent of citrus vein enation disease by deep sequencing sRNAs from infected and healthy Etrog citron plants (Vives et al., 2013). Another research group reported the presence of a *Tobamovirus* on *Cicer arietinum* in Europe for the first time and a viroid referring to Hop stunt viroid (NC_001351.1) was reported in chickpea based on short RNAs sequencing (Pirovano et al., 2014).

Use of vsiRNAs to Study Viral Population Genetics

Virus-derived small interfering RNAs-based deep sequencing was also used to survey the *in planta* virus population for the first time. Viral RNAs and vsiRNAs both congruently portrayed the mutational landscape of the virus within the plant host (Kutnjak et al., 2015). Next generation sequencing (NGS) technology has previously been shown to be a powerful tool for studying viral ecology (Stobbe and Roossinck, 2014) and viral populations (Beerenwinkel and Zagordi, 2011; Palmer et al., 2014; Chateigner et al., 2015; Skums et al., 2015). Nowadays, many population genetics experts prefer to study plant virus ecology or populations by sequencing the vsiRNAs. For instance, SG29 (aggressive) and Bau282 (mild), two representative isolates of a CTV population in Sicily, were sequenced from vsiRNAs of budlings of sweet orange grafted on sour orange trees. The phylogenetic relationships with Mediterranean and exotic isolates revealed that SG29 clustered within the "VT-Asian" subtype, whereas Bau282 belonged to cluster T30 (Licciardello et al., 2015). Notably, although vsiRNAs-based NGS technology is a more effective way to study virus ecology and populations, there is relatively high error rate. Thus, several computational pipelines such as ViVan (Isakov et al., 2015), ViVaMBC (Verbist et al., 2015), and LayerCake (Correll et al., 2015), tools with different applications for analyzing viral deep sequencing data, have been developed.

In summary, much of what we know already and what we will uncover in the future regarding plant viruses is possible by the study of vsiRNAs. Previous studies have proven that it is not only a feasible tool to control virus in crop plants by artificially expressing vsiRNAs, but also a high-throughput and cost-effective approach for reconstructing viral genomes, discovering novel virus, and studying viral ecology and populations by vsiRNAs deep sequencing experiments.

FUTURE CHALLENGES

With the advance of NGS technologies, it is predicted that more studies using RNA profiling of plants infected with various pathogens will help identify more vsiRNAs. However, understanding the mechanism of action of vsiRNA-mediated antiviral silencing is a big challenge for researchers. Additionally, the interactions between host plants, viruses, and the abundant various vsiRNAs are extremely complex. The question of how to determine and classify the roles of a large number of vsiRNAs in the co-evolutionary battle between hosts and viruses also remains largely unanswered. Furthermore, it is unknown whether it is a general phenomenon that the vsiRNAs are able to induce disease by targeting host endogenous genes. Until now it is unknown whether vsiRNA-mediated endogenous gene silencing is a common mechanism in virus-infected plants. Albeit great advances have been made in our knowledge of sRNA-mediated plant immunity against viruses, studies on effective antiviral drugs against plant viruses and/or approaches on improving host resistance to virus disease are still deficient. Lastly, evidence suggests a potential method for controlling viral diseases is the expression of artificial sRNAs targeting the viral genome. However, any potential risks or safety issues of using this tool in crops must be evaluated.

ACKNOWLEDGMENTS

We thank Dr. Yifan Lii, Dr. Liang Wu, and Dr. Zhenguo Du for their critical reading of the manuscript. This work was supported by grants from the National Basic Research Program 973 (2014CB138403 and 2013CBA01402), Natural Science Foundation of China (31272018, 31201491 and 31171821), Natural Science Foundation of Fujian Province of China and Outstanding Young Scientific Research Plan in Higher Education of Fujian Province (2013J01089 and JA3091). We apologize for not citing some publications owing to space limitations.

REFERENCES

Addo-Quaye, C., Eshoo, T. W., Bartel, D. P., and Axtell, M. J. (2008). Endogenous siRNA and miRNA targets identified by sequencing of the *Arabidopsis* degradome. *Curr. Biol.* 18, 758–762. doi: 10.1016/j.cub.2008.04.042

Adkar-Purushothama, C. R., Brosseau, C., Giguere, T., Sano, T., Moffett, P., and Perreault, J. P. (2015). Small RNA derived from the virulence modulating region of the potato spindle tuber viroid silences callose synthase genes of tomato plants. *Plant Cell* 27, 2178–2194. doi: 10.1105/tpc.15.00523

Ahlquist, P. (2002). RNA-dependent RNA polymerases, viruses, and RNA silencing. *Science* 296, 1270–1273. doi: 10.1126/science.1069132

Akbergenov, R., Si-Ammour, A., Blevins, T., Amin, I., Kutter, C., Vanderschuren, H., et al. (2006). Molecular characterization of geminivirus-derived small RNAs in different plant species. *Nucleic Acids Res.* 34, 462–471. doi: 10.1093/nar/gkj447

Andika, I. B., Maruyama, K., Sun, L., Kondo, H., Tamada, T., and Suzuki, N. (2015). Different Dicer-like protein components required for intracellular and systemic antiviral silencing in *Arabidopsis thaliana*. *Plant Signal. Behav.* 10:e1039214. doi: 10.1080/15592324.2015.1039214

Aregger, M., Borah, B. K., Seguin, J., Rajeswaran, R., Gubaeva, E. G., Zvereva, A. S., et al. (2012). Primary and secondary siRNAs in geminivirus-induced gene silencing. *PLoS Pathog* 8:e1002941. doi: 10.1371/journal.ppat.1002941

Axtell, M. J. (2013). Classification and comparison of small RNAs from plants. *Annu. Rev. Plant Biol.* 64, 137–159. doi: 10.1146/annurev-arplant-050312-120043

Beerenwinkel, N., and Zagordi, O. (2011). Ultra-deep sequencing for the analysis of viral populations. *Curr. Opin. Virol.* 1, 413–418. doi: 10.1016/j.coviro.2011.07.008

Ben Amor, B., Wirth, S., Merchan, F., Laporte, P., d'Aubenton-Carafa, Y., Hirsch, J., et al. (2009). Novel long non-protein coding RNAs involved in *Arabidopsis* differentiation and stress responses. *Genome Res.* 19, 57–69. doi: 10.1101/gr.080275.108

Blevins, T., Rajeswaran, R., Shivaprasad, P. V., Beknazariants, D., Si-Ammour, A., Park, H. S., et al. (2006). Four plant Dicers mediate viral small RNA biogenesis and DNA virus induced silencing. *Nucleic Acids Res.* 34, 6233–6246. doi: 10.1093/nar/gkl886

Bouche, N., Lauressergues, D., Gasciolli, V., and Vaucheret, H. (2006). An antagonistic function for *Arabidopsis* DCL2 in development and a new function for DCL4 in generating viral siRNAs. *EMBO J.* 25, 3347–3356. doi: 10.1038/sj.emboj.7601217

Brosseau, C., and Moffett, P. (2015). Functional and genetic analysis identify a role for *Arabidopsis* ARGONAUTE5 in antiviral RNA silencing. *Plant Cell* 27, 1742–1754. doi: 10.1105/tpc.15.00264

Brough, C. L., Gardiner, W. E., Inamdar, N. M., Zhang, X. Y., Ehrlich, M., and Bisaro, D. M. (1992). DNA methylation inhibits propagation of tomato golden mosaic virus DNA in transfected protoplasts. *Plant Mol. Biol.* 18, 703–712. doi: 10.1007/BF00020012

Cao, M., Du, P., Wang, X., Yu, Y. Q., Qiu, Y. H., Li, W., et al. (2014). Virus infection triggers widespread silencing of host genes by a distinct class of endogenous siRNAs in *Arabidopsis*. *Proc. Natl. Acad. Sci. U.S.A.* 111, 14613–14618. doi: 10.1073/pnas.1407131111

Carbonell, A., and Carrington, J. C. (2015). Antiviral roles of plant ARGONAUTES. *Curr. Opin. Plant Biol.* 27, 111–117. doi: 10.1016/j.pbi.2015.06.013

Carbonell, A., Fahlgren, N., Garcia-Ruiz, H., Gilbert, K. B., Montgomery, T. A., Nguyen, T., et al. (2012). Functional analysis of three *Arabidopsis* ARGONAUTES using slicer-defective mutants. *Plant Cell* 24, 3613–3629. doi: 10.1105/tpc.112.099945

Chan, S. W., Zilberman, D., Xie, Z., Johansen, L. K., Carrington, J. C., and Jacobsen, S. E. (2004). RNA silencing genes control de novo DNA methylation. *Science* 303:1336. doi: 10.1126/science.1095989

Chateigner, A., Bezier, A., Labrousse, C., Jiolle, D., Barbe, V., and Herniou, E. A. (2015). Ultra deep sequencing of a baculovirus population reveals widespread genomic variations. *Viruses* 7, 3625–3646. doi: 10.3390/v7072788

Chellappan, P., Vanitharani, R., Pita, J., and Fauquet, C. M. (2004). Short interfering RNA accumulation correlates with host recovery in DNA virus-infected hosts, and gene silencing targets specific viral sequences. *J. Virol.* 78, 7465–7477. doi: 10.1128/JVI.78.14.7465-7477.2004

Collinge, D. B., Jorgensen, H. J., Lund, O. S., and Lyngkjaer, M. F. (2010). Engineering pathogen resistance in crop plants: current trends and future prospects. *Annu. Rev. Phytopathol.* 48, 269–291. doi: 10.1146/annurev-phyto-073009-114430

Correll, M., Bailey, A. L., Sarikaya, A., O'Connor, D. H., and Gleicher, M. (2015). LayerCake: a tool for the visual comparison of viral deep sequencing data. *Bioinformatics* 31, 3522–3528. doi: 10.1093/bioinformatics/btv407

Csorba, T., Kontra, L., and Burgyan, J. (2015). Viral silencing suppressors: tools forged to fine-tune host-pathogen coexistence. *Virology* 479–480, 85–103. doi: 10.1016/j.virol.2015.02.028

Cuellar, W. J., Kreuze, J. F., Rajamaki, M. L., Cruzado, K. R., Untiveros, M., and Valkonen, J. P. (2009). Elimination of antiviral defense by viral RNase III. *Proc. Natl. Acad. Sci. U.S.A.* 106, 10354–10358. doi: 10.1073/pnas.0806042106

Dalmay, T., Hamilton, A., Rudd, S., Angell, S., and Baulcombe, D. C. (2000). An RNA-dependent RNA polymerase gene in *Arabidopsis* is required for posttranscriptional gene silencing mediated by a transgene but not by a virus. *Cell* 101, 543–553. doi: 10.1016/S0092-8674(00)80864-8

Deleris, A., Gallego-Bartolome, J., Bao, J., Kasschau, K. D., Carrington, J. C., and Voinnet, O. (2006). Hierarchical action and inhibition of plant Dicer-like proteins in antiviral defense. *Science* 313, 68–71. doi: 10.1126/science.1128214

Diaz-Pendon, J. A., Li, F., Li, W. X., and Ding, S. W. (2007). Suppression of antiviral silencing by cucumber mosaic virus 2b protein in *Arabidopsis* is associated with drastically reduced accumulation of three classes of viral small interfering RNAs. *Plant Cell* 19, 2053–2063. doi: 10.1105/tpc.106.047449

Donaire, L., Barajas, D., Martinez-Garcia, B., Martinez-Priego, L., Pagan, I., and Llave, C. (2008). Structural and genetic requirements for the biogenesis of tobacco rattle virus-derived small interfering RNAs. *J. Virol.* 82, 5167–5177. doi: 10.1128/JVI.00272-08

Donaire, L., Wang, Y., Gonzalez-Ibeas, D., Mayer, K. F., Aranda, M. A., and Llave, C. (2009). Deep-sequencing of plant viral small RNAs reveals effective and widespread targeting of viral genomes. *Virology* 392, 203–214. doi: 10.1016/j.virol.2009.07.005

Dorssers, L., Zabel, P., van der Meer, J., and van Kammen, A. (1982). Purification of a host-encoded RNA-dependent RNA polymerase from cowpea mosaic virus-infected cowpea leaves. *Virology* 116, 236–249. doi: 10.1016/0042-6822(82)90416-0

Du, P., Wu, J., Zhang, J., Zhao, S., Zheng, H., Gao, G., et al. (2011a). Viral infection induces expression of novel phased microRNAs from conserved cellular microRNA precursors. *PLoS Pathog* 7:e1002176. doi: 10.1371/journal.ppat.1002176

Du, Z., Xiao, D., Wu, J., Jia, D., Yuan, Z., Liu, Y., et al. (2011b). p2 of rice stripe virus (RSV) interacts with OsSGS3 and is a silencing suppressor. *Mol. Plant Pathol.* 12, 808–814. doi: 10.1111/j.1364-3703.2011.00716.x

Dzianott, A., Sztuba-Solinska, J., and Bujarski, J. J. (2012). Mutations in the antiviral RNAi defense pathway modify Brome mosaic virus RNA recombinant profiles. *Mol. Plant-Microbe Interact.* 25, 97–106. doi: 10.1094/MPMI-05-11-0137

Earley, K. W., and Poethig, R. S. (2011). Binding of the cyclophilin 40 ortholog SQUINT to Hsp90 protein is required for SQUINT function in *Arabidopsis*. *J. Biol. Chem.* 286, 38184–38189. doi: 10.1074/jbc.M111.290130

El-Shami, M., Pontier, D., Lahmy, S., Braun, L., Picart, C., Vega, D., et al. (2007). Reiterated WG/GW motifs form functionally and evolutionarily conserved ARGONAUTE-binding platforms in RNAi-related components. *Genes Dev.* 21, 2539–2544. doi: 10.1101/gad.451207

Ermak, G., Paszkowski, U., Wohlmuth, M., Mittelsten Scheid, O., and Paszkowski, J. (1993). Cytosine methylation inhibits replication of African cassava mosaic virus by two distinct mechanisms. *Nucleic Acids Res.* 21, 3445–3450. doi: 10.1093/nar/21.15.3445

Fukunaga, R., and Doudna, J. A. (2009). dsRNA with 5' overhangs contributes to endogenous and antiviral RNA silencing pathways in plants. *EMBO J.* 28, 545–555. doi: 10.1038/emboj.2009.2

Fusaro, A. F., Matthew, L., Smith, N. A., Curtin, S. J., Dedic-Hagan, J., Ellacott, G. A., et al. (2006). RNA interference-inducing hairpin RNAs in plants act through the viral defence pathway. *EMBO Rep.* 7, 1168–1175. doi: 10.1038/sj.embor.7400837

Gan, D., Ding, F., Zhuang, D., Jiang, H., Jiang, T., Zhu, S., et al. (2014). Application of RNA interference methodology to investigate and develop SCMV resistance in maize. *J. Genet.* 93, 305–311. doi: 10.1007/s12041-014-0364-1

Garcia-Ruiz, H., Carbonell, A., Hoyer, J. S., Fahlgren, N., Gilbert, K. B., Takeda, A., et al. (2015). Roles and programming of *Arabidopsis* ARGONAUTE proteins during turnip mosaic virus infection. *PLoS Pathog* 11:e1004755. doi: 10.1371/journal.ppat.1004755

Garcia-Ruiz, H., Takeda, A., Chapman, E. J., Sullivan, C. M., Fahlgren, N., Brempelis, K. J., et al. (2010). *Arabidopsis* RNA-dependent RNA polymerases and dicer-like proteins in antiviral defense and small interfering RNA biogenesis during Turnip Mosaic Virus infection. *Plant Cell* 22, 481–496. doi: 10.1105/tpc.109.073056

Gasciolli, V., Mallory, A. C., Bartel, D. P., and Vaucheret, H. (2005). Partially redundant functions of *Arabidopsis* DICER-like enzymes and a role for

DCL4 in producing trans-acting siRNAs. *Curr. Biol.* 15, 1494–1500. doi: 10.1016/j.cub.2005.07.024

Ghoshal, B., and Sanfaçon, H. (2014). Temperature-dependent symptom recovery in *Nicotiana benthamiana* plants infected with tomato ringspot virus is associated with reduced translation of viral RNA2 and requires ARGONAUTE 1. *Virology* 456–457, 188–197. doi: 10.1016/j.virol.2014.03.026

Gillet, F. X., Cattoni, D. I., Petiot-Becard, S., Delalande, F., Poignavent, V., Brizard, J. P., et al. (2013). The RYMV-encoded viral suppressor of RNA silencing P1 is a zinc-binding protein with redox-dependent flexibility. *J. Mol. Biol.* 425, 2423–2435. doi: 10.1016/j.jmb.2013.03.028

Glick, E., Zrachya, A., Levy, Y., Mett, A., Gidoni, D., Belausov, E., et al. (2008). Interaction with host SGS3 is required for suppression of RNA silencing by tomato yellow leaf curl virus V2 protein. *Proc. Natl. Acad. Sci. U.S.A.* 105, 157–161. doi: 10.1073/pnas.0709036105

Goto, K., Kobori, T., Kosaka, Y., Natsuaki, T., and Masuta, C. (2007). Characterization of silencing suppressor 2b of cucumber mosaic virus based on examination of its small RNA-binding abilities. *Plant Cell Physiol.* 48, 1050–1060. doi: 10.1093/pcp/pcm074

Guo, H., Song, X., Xie, C., Huo, Y., Zhang, F., Chen, X., et al. (2013). Rice yellow stunt rhabdovirus protein 6 suppresses systemic RNA silencing by blocking RDR6-mediated secondary siRNA synthesis. *Mol. Plant-Microbe Interact.* 26, 927–936. doi: 10.1094/MPMI-02-13-0040-R

Hamilton, A. J., and Baulcombe, D. C. (1999). A species of small antisense RNA in posttranscriptional gene silencing in plants. *Science* 286, 950–952. doi: 10.1126/science.286.5441.950

Harfouche, L., Haichar Fel, Z., and Achouak, W. (2015). Small regulatory RNAs and the fine-tuning of plant-bacteria interactions. *New Phytol.* 206, 98–106. doi: 10.1111/nph.13195

Harvey, J. J., Lewsey, M. G., Patel, K., Westwood, J., Heimstadt, S., Carr, J. P., et al. (2011). An antiviral defense role of AGO2 in plants. *PLoS ONE* 6:e14639. doi: 10.1371/journal.pone.0014639

Henderson, I. R., Zhang, X., Lu, C., Johnson, L., Meyers, B. C., Green, P. J., et al. (2006). Dissecting *Arabidopsis thaliana* DICER function in small RNA processing, gene silencing and DNA methylation patterning. *Nat. Genet.* 38, 721–725. doi: 10.1038/ng1804

Hong, W., Qian, D., Sun, R., Jiang, L., Wang, Y., Wei, C., et al. (2015). OsRDR6 plays role in host defense against double-stranded RNA virus, Rice Dwarf Phytoreovirus. *Sci. Rep.* 5:11324. doi: 10.1038/srep11324

Hu, Q., Niu, Y., Zhang, K., Liu, Y., and Zhou, X. (2011). Virus-derived transgenes expressing hairpin RNA give immunity to Tobacco mosaic virus and Cucumber mosaic virus. *Virol. J.* 8:41. doi: 10.1186/1743-422X-8-41

Iki, T., Yoshikawa, M., Meshi, T., and Ishikawa, M. (2012). Cyclophilin 40 facilitates HSP90-mediated RISC assembly in plants. *EMBO J.* 31, 267–278. doi: 10.1038/emboj.2011.395

Iki, T., Yoshikawa, M., Nishikiori, M., Jaudal, M. C., Matsumoto-Yokoyama, E., Mitsuhara, I., et al. (2010). In vitro assembly of plant RNA-induced silencing complexes facilitated by molecular chaperone HSP90. *Mol. cell* 39, 282–291. doi: 10.1016/j.molcel.2010.05.014

Isakov, O., Borderia, A. V., Golan, D., Hamenahem, A., Celniker, G., Yoffe, L., et al. (2015). Deep sequencing analysis of viral infection and evolution allows rapid and detailed characterization of viral mutant spectrum. *Bioinformatics* 31, 2141–2150. doi: 10.1093/bioinformatics/btv101

Jiang, L., Qian, D., Zheng, H., Meng, L. Y., Chen, J., Le, W. J., et al. (2012). RNA-dependent RNA polymerase 6 of rice (*Oryza sativa*) plays role in host defense against negative-strand RNA virus, Rice stripe virus. *Virus Res.* 163, 512–519. doi: 10.1016/j.virusres.2011.11.016

Karran, R. A., and Sanfacon, H. (2014). Tomato ringspot virus coat protein binds to ARGONAUTE 1 and suppresses the translation repression of a reporter gene. *Mol. Plant-Microbe Interact.* 27, 933–943. doi: 10.1094/MPMI-04-14-0099-R

Koukiekolo, R., Jakubek, Z. J., Cheng, J., Sagan, S. M., and Pezacki, J. P. (2009). Studies of a viral suppressor of RNA silencing p19-CFP fusion protein: a FRET-based probe for sensing double-stranded fluorophore tagged small RNAs. *Biophys. Chem.* 143, 166–169. doi: 10.1016/j.bpc.2009.05.001

Kreuze, J. F., Savenkov, E. I., Cuellar, W., Li, X., and Valkonen, J. P. (2005). Viral class 1 RNase III involved in suppression of RNA silencing. *J. Virol.* 79, 7227–7238. doi: 10.1128/JVI.79.11.7227-7238.2005

Kumakura, N., Takeda, A., Fujioka, Y., Motose, H., Takano, R., and Watanabe, Y. (2009). SGS3 and RDR6 interact and colocalize in cytoplasmic SGS3/RDR6-bodies. *FEBS Lett.* 583, 1261–1266. doi: 10.1016/j.febslet.2009.03.055

Kutnjak, D., Rupar, M., Gutierrez-Aguirre, I., Curk, T., Kreuze, J. F., and Ravnikar, M. (2015). Deep sequencing of virus-derived small interfering RNAs and RNA from viral particles shows highly similar mutational landscapes of a plant virus population. *J. Virol.* 89, 4760–4769. doi: 10.1128/JVI.03685-14

Lacombe, S., Bangratz, M., Vignols, F., and Brugidou, C. (2010). The rice yellow mottle virus P1 protein exhibits dual functions to suppress and activate gene silencing. *Plant J.* 61, 371–382. doi: 10.1111/j.1365-313X.2009.04062.x

Li, Y. F., Zheng, Y., Jagadeeswaran, G., and Sunkar, R. (2013). Characterization of small RNAs and their target genes in wheat seedlings using sequencing-based approaches. *Plant Sci.* 203–204, 17–24. doi: 10.1016/j.plantsci.2012.12.014

Licciardello, G., Scuderi, G., Ferraro, R., Giampetruzzi, A., Russo, M., Lombardo, A., et al. (2015). Deep sequencing and analysis of small RNAs in sweet orange grafted on sour orange infected with two *Citrus tristeza* virus isolates prevalent in Sicily. *Arch. Virol.* 160, 2583–2589. doi: 10.1007/s00705-015-2516-x

Liu, B., Chen, Z., Song, X., Liu, C., Cui, X., Zhao, X., et al. (2007). *Oryza sativa* dicer-like4 reveals a key role for small interfering RNA silencing in plant development. *Plant Cell* 19, 2705–2718. doi: 10.1105/tpc.107.052209

Ma, X., Nicole, M. C., Meteignier, L. V., Hong, N., Wang, G., and Moffett, P. (2015). Different roles for RNA silencing and RNA processing components in virus recovery and virus-induced gene silencing in plants. *J. Exp. Bot.* 66, 919–932. doi: 10.1093/jxb/eru447

Mallory, A. C., and Vaucheret, H. (2009). ARGONAUTE 1 homeostasis invokes the coordinate action of the microRNA and siRNA pathways. *EMBO Rep.* 10, 521–526. doi: 10.1038/embor.2009.32

Mallory, A., and Vaucheret, H. (2010). Form, function, and regulation of ARGONAUTE proteins. *Plant Cell* 22, 3879–3889. doi: 10.1105/tpc.110.080671

Mansoor, S., Amin, I., Hussain, M., Zafar, Y., and Briddon, R. W. (2006). Engineering novel traits in plants through RNA interference. *Trends Plant Sci.* 11, 559–565. doi: 10.1016/j.tplants.2006.09.010

Martinez de Alba, A. E., Elvira-Matelot, E., and Vaucheret, H. (2013). Gene silencing in plants: a diversity of pathways. *Biochim. Biophys. Acta* 1829, 1300–1308. doi: 10.1016/j.bbagrm.2013.10.005

Martinez de Alba, A. E., Moreno, A. B., Gabriel, M., Mallory, A. C., Christ, A., Bounon, R., et al. (2015). In plants, decapping prevents RDR6-dependent production of small interfering RNAs from endogenous mRNAs. *Nucleic Acids Res.* 43, 2902–2913. doi: 10.1093/nar/gkv119

Mayor, A., Martinon, F., De Smedt, T., Petrilli, V., and Tschopp, J. (2007). A crucial function of SGT1 and HSP90 in inflammasome activity links mammalian and plant innate immune responses. *Nat. Immunol.* 8, 497–503. doi: 10.1038/ni1459

Merai, Z., Kerenyi, Z., Molnar, A., Barta, E., Valoczi, A., Bisztray, G., et al. (2005). Aureusvirus P14 is an efficient RNA silencing suppressor that binds double-stranded RNAs without size specificity. *J. Virol.* 79, 7217–7226. doi: 10.1128/JVI.79.11.7217-7226.2005

Miozzi, L., Gambino, G., Burgyan, J., and Pantaleo, V. (2013). Genome-wide identification of viral and host transcripts targeted by viral siRNAs in Vitis vinifera. *Mol. Plant Pathol.* 14, 30–43. doi: 10.1111/j.1364-3703.2012.00828.x

Moissiard, G., and Voinnet, O. (2006). RNA silencing of host transcripts by cauliflower mosaic virus requires coordinated action of the four *Arabidopsis* Dicer-like proteins. *Proc. Natl. Acad. Sci. U.S.A.* 103, 19593–19598. doi: 10.1073/pnas.0604627103

Molnar, A., Csorba, T., Lakatos, L., Varallyay, E., Lacomme, C., and Burgyan, J. (2005). Plant virus-derived small interfering RNAs originate predominantly from highly structured single-stranded viral RNAs. *J. Virol.* 79, 7812–7818. doi: 10.1128/JVI.79.12.7812-7818.2005

Morel, J. B., Godon, C., Mourrain, P., Beclin, C., Boutet, S., Feuerbach, F., et al. (2002). Fertile hypomorphic ARGONAUTE (ago1) mutants impaired in post-transcriptional gene silencing and virus resistance. *Plant Cell* 14, 629–639. doi: 10.1105/tpc.010358

Mourrain, P., Beclin, C., Elmayan, T., Feuerbach, F., Godon, C., Morel, J. B., et al. (2000). *Arabidopsis* SGS2 and SGS3 genes are required for posttranscriptional gene silencing and natural virus resistance. *Cell* 101, 533–542. doi: 10.1016/S0092-8674(00)80863-6

Navarro, B., Gisel, A., Rodio, M. E., Delgado, S., Flores, R., and Di Serio, F. (2012). Small RNAs containing the pathogenic determinant of a chloroplast-replicating

viroid guide the degradation of a host mRNA as predicted by RNA silencing. *Plant J.* 70, 991–1003. doi: 10.1111/j.1365-313X.2012.04940.x

Nicaise, V. (2014). Crop immunity against viruses: outcomes and future challenges. *Front. Plant Sci.* 5:660. doi: 10.3389/fpls.2014.00660

Nonomura, K., Morohoshi, A., Nakano, M., Eiguchi, M., Miyao, A., Hirochika, H., et al. (2007). A germ cell specific gene of the ARGONAUTE family is essential for the progression of premeiotic mitosis and meiosis during sporogenesis in rice. *Plant Cell* 19, 2583–2594. doi: 10.1105/tpc.107.053199

Odokonyero, D., Mendoza, M. R., Alvarado, V. Y., Zhang, J., Wang, X., and Scholthof, H. B. (2015). Transgenic down-regulation of ARGONAUTE2 expression in *Nicotiana benthamiana* interferes with several layers of antiviral defenses. *Virology* 486, 209–218. doi: 10.1016/j.virol.2015.09.008

Palmer, B. A., Dimitrova, Z., Skums, P., Crosbie, O., Kenny-Walsh, E., and Fanning, L. J. (2014). Analysis of the evolution and structure of a complex intrahost viral population in chronic hepatitis C virus mapped by ultradeep pyrosequencing. *J. Virol.* 88, 13709–13721. doi: 10.1128/JVI.01732-14

Park, H. M., Choi, M. S., Kwak, D. Y., Lee, B. C., Lee, J. H., Kim, M. K., et al. (2012). Suppression of NS3 and MP is important for the stable inheritance of RNAi-mediated rice stripe virus (RSV) resistance obtained by targeting the fully complementary RSV-CP gene. *Mol. Cells* 33, 43–51. doi: 10.1007/s10059-012-2185-5

Pirovano, W., Miozzi, L., Boetzer, M., and Pantaleo, V. (2014). Bioinformatics approaches for viral metagenomics in plants using short RNAs: model case of study and application to a *Cicer arietinum* population. *Front. Microbiol.* 5:790. doi: 10.3389/fmicb.2014.00790

Poulsen, C., Vaucheret, H., and Brodersen, P. (2013). Lessons on RNA silencing mechanisms in plants from eukaryotic argonaute structures. *Plant Cell* 25, 22–37. doi: 10.1105/tpc.112.105643

Prins, M., Laimer, M., Noris, E., Schubert, J., Wassenegger, M., and Tepfer, M. (2008). Strategies for antiviral resistance in transgenic plants. *Mol. Plant Pathol.* 9, 73–83. doi: 10.1111/j.1364-3703.2007.00447.x

Qi, X., Bao, F. S., and Xie, Z. (2009). Small RNA deep sequencing reveals role for *Arabidopsis thaliana* RNA-dependent RNA polymerases in viral siRNA biogenesis. *PLoS ONE* 4:e4971. doi: 10.1371/journal.pone.0004971

Qu, F., Ren, T., and Morris, T. J. (2003). The coat protein of turnip crinkle virus suppresses posttranscriptional gene silencing at an early initiation step. *J. Virol.* 77, 511–522. doi: 10.1128/JVI.77.1.511-522.2003

Qu, F., Ye, X., and Morris, T. J. (2008). *Arabidopsis* DRB4, AGO1, AGO7, and RDR6 participate in a DCL4-initiated antiviral RNA silencing pathway negatively regulated by DCL1. *Proc. Natl. Acad. Sci. U.S.A.* 105, 14732–14737. doi: 10.1073/pnas.0805760105

Raja, P., Jackel, J. N., Li, S., Heard, I. M., and Bisaro, D. M. (2014). *Arabidopsis* double-stranded RNA binding protein DRB3 participates in methylation-mediated defense against geminiviruses. *J. Virol.* 88, 2611–2622. doi: 10.1128/JVI.02305-13

Raja, P., Sanville, B. C., Buchmann, R. C., and Bisaro, D. M. (2008). Viral genome methylation as an epigenetic defense against geminiviruses. *J. Virol.* 82, 8997–9007. doi: 10.1128/JVI.00719-08

Rajagopalan, R., Vaucheret, H., Trejo, J., and Bartel, D. P. (2006). A diverse and evolutionarily fluid set of microRNAs in *Arabidopsis thaliana*. *Genes Dev.* 20, 3407–3425. doi: 10.1101/gad.1476406

Ren, B., Guo, Y., Gao, F., Zhou, P., Wu, F., Meng, Z., et al. (2010). Multiple functions of Rice dwarf phytoreovirus Pns10 in suppressing systemic RNA silencing. *J. Virol.* 84, 12914–12923. doi: 10.1128/JVI.00864-10

Romaine, C. P., and Zaitlin, M. (1978). RNA-dependent RNA polymerases in uninfected and tobacco mosaic virus-infected tabacco leaves: viral induced stimulation of a host polymerase activity. *Virology* 86, 241–253. doi: 10.1016/0042-6822(78)90024-7

Ruiz-Ruiz, S., Navarro, B., Gisel, A., Pena, L., Navarro, L., Moreno, P., et al. (2011). *Citrus tristeza* virus infection induces the accumulation of viral small RNAs (21-24-nt) mapping preferentially at the 3'-terminal region of the genomic RNA and affects the host small RNA profile. *Plant Mol. Biol.* 75, 607–619. doi: 10.1007/s11103-011-9754-4

Scholthof, H. B., Alvarado, V. Y., Vega-Arreguin, J. C., Ciomperlik, J., Odokonyero, D., Brosseau, C., et al. (2011). Identification of an ARGONAUTE for antiviral RNA silencing in *Nicotiana benthamiana*. *Plant Physiol.* 156, 1548–1555. doi: 10.1104/pp.111.178764

Schuck, J., Gursinsky, T., Pantaleo, V., Burgyan, J., and Behrens, S. E. (2013). AGO/RISC-mediated antiviral RNA silencing in a plant in vitro system. *Nucleic Acids Res.* 41, 5090–5103. doi: 10.1093/nar/gkt193

Schwach, F., Vaistij, F. E., Jones, L., and Baulcombe, D. C. (2005). An RNA-dependent RNA polymerase prevents meristem invasion by potato virus X and is required for the activity but not the production of a systemic silencing signal. *Plant Physiol.* 138, 1842–1852. doi: 10.1104/pp.105.063537

Seguin, J., Rajeswaran, R., Malpica-Lopez, N., Martin, R. R., Kasschau, K., Dolja, V. V., et al. (2014). De novo reconstruction of consensus master genomes of plant RNA and DNA viruses from siRNAs. *PLoS ONE* 9:e88513. doi: 10.1371/journal.pone.0088513

Shimizu, T., Nakazono-Nagaoka, E., Akita, F., Wei, T., Sasaya, T., Omura, T., et al. (2012). Hairpin RNA derived from the gene for Pns9, a viroplasm matrix protein of Rice gall dwarf virus, confers strong resistance to virus infection in transgenic rice plants. *J. Biotechnol.* 157, 421–427. doi: 10.1016/j.jbiotec.2011.12.015

Shimizu, T., Ogamino, T., Hiraguri, A., Nakazono-Nagaoka, E., Uehara-Ichiki, T., Nakajima, M., et al. (2013). Strong resistance against Rice grassy stunt virus is induced in transgenic rice plants expressing double-stranded RNA of the viral genes for nucleocapsid or movement proteins as targets for RNA interference. *Phytopathology* 103, 513–519. doi: 10.1094/PHYTO-07-12-0165-R

Shimizu, T., Yoshii, M., Wei, T., Hirochika, H., and Omura, T. (2009). Silencing by RNAi of the gene for Pns12, a viroplasm matrix protein of Rice dwarf virus, results in strong resistance of transgenic rice plants to the virus. *Plant Biotechnol. J.* 7, 24–32. doi: 10.1111/j.1467-7652.2008.00366.x

Shimura, H., Pantaleo, V., Ishihara, T., Myojo, N., Inaba, J., Sueda, K., et al. (2011). A viral satellite RNA induces yellow symptoms on tobacco by targeting a gene involved in chlorophyll biosynthesis using the RNA silencing machinery. *PLoS Pathog* 7:e1002021. doi: 10.1371/journal.ppat.1002021

Simon-Mateo, C., and Garcia, J. A. (2006). MicroRNA-guided processing impairs *Plum pox* virus replication, but the virus readily evolves to escape this silencing mechanism. *J. Virol.* 80, 2429–2436. doi: 10.1128/JVI.80.5.2429-2436.2006

Skums, P., Artyomenko, A., Glebova, O., Ramachandran, S., Mandoiu, I., Campo, D. S., et al. (2015). Computational framework for next-generation sequencing of heterogeneous viral populations using combinatorial pooling. *Bioinformatics* 31, 682–690. doi: 10.1093/bioinformatics/btu726

Stobbe, A. H., and Roossinck, M. J. (2014). Plant virus metagenomics: what we know and why we need to know more. *Front. Plant Sci.* 5:150. doi: 10.3389/fpls.2014.00150

Szittya, G., and Burgyan, J. (2013). RNA interference-mediated intrinsic antiviral immunity in plants. *Curr. Top. Microbiol. Immunol.* 371, 153–181. doi: 10.1007/978-3-642-37765-5_6

Szittya, G., Moxon, S., Pantaleo, V., Toth, G., Rusholme Pilcher, R. L., Moulton, V., et al. (2010). Structural and functional analysis of viral siRNAs. *PLoS Pathog* 6:e1000838. doi: 10.1371/journal.ppat.1000838

Urayama, S., Moriyama, H., Aoki, N., Nakazawa, Y., Okada, R., Kiyota, E., et al. (2010). Knock-down of OsDCL2 in rice negatively affects maintenance of the endogenous dsRNA virus, *Oryza sativa* endornavirus. *Plant Cell Physiol.* 51, 58–67. doi: 10.1093/pcp/pcp167

Vanitharani, R., Chellappan, P., and Fauquet, C. M. (2005). Geminiviruses and RNA silencing. *Trends Plant Sci.* 10, 144–151. doi: 10.1016/j.tplants.2005.01.005

Vaucheret, H. (2008). Plant ARGONAUTES. *Trends Plant Sci.* 13, 350–358. doi: 10.1016/j.tplants.2008.04.007

Verbist, B., Clement, L., Reumers, J., Thys, K., Vapirev, A., Talloen, W., et al. (2015). ViVaMBC: estimating viral sequence variation in complex populations from illumina deep-sequencing data using model-based clustering. *BMC Bioinformatics* 16:59. doi: 10.1186/s12859-015-0458-7

Visser, M., Maree, H. J., Rees, D. J., and Burger, J. T. (2014). High-throughput sequencing reveals small RNAs involved in ASGV infection. *BMC Genomics* 15:568. doi: 10.1186/1471-2164-15-568

Vives, M. C., Velazquez, K., Pina, J. A., Moreno, P., Guerri, J., and Navarro, L. (2013). Identification of a new enamovirus associated with citrus vein enation disease by deep sequencing of small RNAs. *Phytopathology* 103, 1077–1086. doi: 10.1094/PHYTO-03-13-0068-R

Voinnet, O. (2008). Use, tolerance and avoidance of amplified RNA silencing by plants. *Trends Plant Sci.* 13, 317–328. doi: 10.1016/j.tplants.2008.05.004

Wang, H., Buckley, K. J., Yang, X., Buchmann, R. C., and Bisaro, D. M. (2005). Adenosine kinase inhibition and suppression of RNA silencing by geminivirus AL2 and L2 proteins. *J. Virol.* 79, 7410–7418. doi: 10.1128/JVI.79.12.7410-7418.2005

Wang, H., Hao, L., Shung, C. Y., Sunter, G., and Bisaro, D. M. (2003). Adenosine kinase is inactivated by geminivirus AL2 and L2 proteins. *Plant Cell* 15, 3020–3032. doi: 10.1105/tpc.015180

Wang, X. B., Jovel, J., Udomporn, P., Wang, Y., Wu, Q., Li, W. X., et al. (2011). The 21-nucleotide, but not 22-nucleotide, viral secondary small interfering RNAs direct potent antiviral defense by two cooperative argonautes in *Arabidopsis thaliana*. *Plant Cell* 23, 1625–1638. doi: 10.1105/tpc.110.082305

Wang, X. B., Wu, Q., Ito, T., Cillo, F., Li, W. X., Chen, X., et al. (2010). RNAi-mediated viral immunity requires amplification of virus-derived siRNAs in *Arabidopsis thaliana*. *Proc. Natl. Acad. Sci. U.S.A.* 107, 484–489. doi: 10.1073/pnas.0904086107

Weiberg, A., and Jin, H. (2015). Small RNAs-the secret agents in the plant-pathogen interactions. *Curr. Opin. Plant Biol.* 26, 87–94. doi: 10.1016/j.pbi.2015.05.033

Weinheimer, I., Boonrod, K., Moser, M., Zwiebel, M., Fullgrabe, M., Krczal, G., et al. (2010). Analysis of an autoproteolytic activity of rice yellow mottle virus silencing suppressor P1. *Biol. Chem.* 391, 271–281. doi: 10.1515/BC.2010.022

Wieczorek, P., and Obrepalska-Steplowska, A. (2015). Suppress to survive-implication of plant viruses in PTGS. *Plant Mol. Biol. Rep.* 33, 335–346. doi: 10.1007/s11105-014-0755-8

Wu, J., Yang, Z., Wang, Y., Zheng, L., Ye, R., Ji, Y., et al. (2015). Viral-inducible argonaute18 confers broad-spectrum virus resistance in rice by sequestering a host microRNA. *Elife* 17:4. doi: 10.7554/eLife.05733

Xie, M., Zhang, S., and Yu, B. (2015). microRNA biogenesis, degradation and activity in plants. *Cell. Mol. Life Sci.* 72, 87–99. doi: 10.1007/s00018-014-1728-7

Xie, Z., Fan, B., Chen, C., and Chen, Z. (2001). An important role of an inducible RNA-dependent RNA polymerase in plant antiviral defense. *Proc. Natl. Acad. Sci. U.S.A.* 98, 6516–6521. doi: 10.1073/pnas.111440998

Xie, Z., Johansen, L. K., Gustafson, A. M., Kasschau, K. D., Lellis, A. D., Zilberman, D., et al. (2004). Genetic and functional diversification of small RNA pathways in plants. *PLoS Biol.* 2:E104. doi: 10.1371/journal.pbio.0020104

Xiong, R., Wu, J., Zhou, Y., and Zhou, X. (2009). Characterization and subcellular localization of an RNA silencing suppressor encoded by Rice stripe tenuivirus. *Virology* 387, 29–40. doi: 10.1016/j.virol.2009.01.045

Xu, Y., Huang, L., Fu, S., Wu, J., and Zhou, X. (2012). Population diversity of rice stripe virus-derived siRNAs in three different hosts and RNAi-based antiviral immunity in Laodelphgax striatellus. *PLoS ONE* 7:e46238. doi: 10.1371/journal.pone.0046238

Yang, L. P., Fang, Y. Y., An, C. P., Dong, L., Zhang, Z. H., Chen, H., et al. (2013). C2-mediated decrease in DNA methylation, accumulation of siRNAs, and increase in expression for genes involved in defense pathways in plants infected with beet severe curly top virus. *Plant J.* 73, 910–917. doi: 10.1111/tpj.12081

Yang, L., Wu, G., and Poethig, R. S. (2012). Mutations in the GW-repeat protein SUO reveal a developmental function for microRNA-mediated translational repression in *Arabidopsis*. *Proc. Natl. Acad. Sci. U.S.A.* 109, 315–320. doi: 10.1073/pnas.1114673109

Zhang, B. (2015). MicroRNA: a new target for improving plant tolerance to abiotic stress. *J. Exp. Bot.* 66, 1749–1761. doi: 10.1093/jxb/erv013

Zhang, X., Zhang, X., Singh, J., Li, D., and Qu, F. (2012). Temperature-dependent survival of *Turnip crinkle* virus-infected *arabidopsis* plants relies on an RNA silencing-based defense that requires dcl2, AGO2, and HEN1. *J. Virol.* 86, 6847–6854. doi: 10.1128/JVI.00497-12

Zhu, H., Duan, C. G., Hou, W. N., Du, Q. S., Lv, D. Q., Fang, R. X., et al. (2011). Satellite RNA-derived small interfering RNA satsiR-12 targeting the 3' untranslated region of Cucumber mosaic virus triggers viral RNAs for degradation. *J. Virol.* 85, 13384–13397. doi: 10.1128/JVI.05806-11

Zong, J., Yao, X., Yin, J., Zhang, D., and Ma, H. (2009). Evolution of the RNA-dependent RNA polymerase (RdRP) genes: duplications and possible losses before and after the divergence of major eukaryotic groups. *Gene* 447, 29–39. doi: 10.1016/j.gene.2009.07.004

Conflict of Interest Statement: The authors declare that the research was conducted in the absence of any commercial or financial relationships that could be construed as a potential conflict of interest.

Copyright © 2015 Zhang, Wu, Li and Wu. This is an open-access article distributed under the terms of the Creative Commons Attribution License (CC BY). The use, distribution or reproduction in other forums is permitted, provided the original author(s) or licensor are credited and that the original publication in this journal is cited, in accordance with accepted academic practice. No use, distribution or reproduction is permitted which does not comply with these terms.

frontiers in Microbiology

DATA REPORT
published: 15 June 2016
doi: 10.3389/fmicb.2016.00926

Genome Sequence of *Dengue virus 3* from the *Pythium insidiosum* Transcriptomes

Yeonhwa Jo[1], *Hoseong Choi*[1] *and Won K. Cho*[1,2]*

[1] Department of Agricultural Biotechnology, College of Agriculture and Life Sciences, Seoul National University, Seoul, Republic of Korea, [2] The Taejin Genome Institute, Hoengseong, Republic of Korea

Keywords: genome, *Dengue virus 3*, *Pythium insidiosum*, *de novo* assembly, single nucleotide polymorphism

BACKGROUND

Pythium species are a kind of the fungus-like oomycetes presenting in soil and aquatic environments (Latijnhouwers et al., 2003). They are regarded as serious plant pathogens, resulting in economic losses of many crops. Of known *Pythium* species, *P. insidiosum* is the only oomycete that can infect both humans and animals (Gaastra et al., 2010). *P. insidiosum* causes a life-threatening infectious diseases known as pythiosis (Mendoza et al., 1993; Gaastra et al., 2010). So far, infection of *P. insidiosum* has been reported in horses, dogs, and humans in tropical and subtropical regions. *P. insidiosum* inhabits swampy areas and produces motile zoospores colonizing surfaces of water plants (Mendoza et al., 1993; Gaastra et al., 2010). Contact of zoospores with tissues of human and animal causes serious infection (Mendoza et al., 1993).

Dengue virus (DENV) causes severe visceral and central nervous system disease in humans (Martina et al., 2009). DENV belongs to the genus *Flavivirus* and consists of single-stranded positive-sense RNA (Chambers et al., 1990; Bai et al., 2013). Infection of DENV is mediated by two major mosquito vectors: *Aedes albopictus* and *Aedes aegypti* (Martina et al., 2009). So far, four different serotypes of DENV have been identified in tropical and subtropical regions (Bai et al., 2013). The genome of DENV is composed of a single-stranded positive-sense RNA about 10,700 nucleotides (nt) in length. The DENV genome consists of a single open reading frame (ORF) encoding three structural (C, prM, and E) and seven nonstructural (NS1, NS2A, NS2B, NS3, NS4A, NS4B, and NS5) proteins (Chambers et al., 1990).

Next generation sequencing (NGS) facilitates the identification of known viruses in various organisms (Radford et al., 2012). NGS can be applied not only in detection or diagnosis of viruses but also in metagenome-based approaches to detect unexpected disease-associated viruses and novel viruses (Adams et al., 2009; Radford et al., 2012). In addition, complete or draft viral genomes can be assembled from NGS data (Jo et al., 2015).

In this study, we identified DENV3 from *P. insidiosum* transcriptome data and assembled a nearly complete genome of DENV3. In addition, we examined single nucleotide variations (SNVs) in the *P. insidiosum* transcriptome, demonstrating quasispecies of DENV3.

METHODS

Oomycete Material, Growth Condition, and Library Preparation for 454 Sequencing

The *P. insidiosum* transcriptome data was obtained from the previous study (Krajaejun et al., 2014). In brief, *P. insidiosum* strain Pi-S was isolated from a Thai patient showing vascular pythiosis. The obtained *P. insidiosum* was cultured in Sabouraud dextrose broth and incubated at 28°C and 37°C for 1 week. Mycelia from each condition was harvested and washed with sterile water. Again, the

OPEN ACCESS

Edited by:
Ayae Honda,
Hosei University, Japan

Reviewed by:
Takeshi Kurosu,
National Institute of Infectious Diseases, Japan
Shigeo Sugita,
Equine Research Institute, Japan Racing Association, Japan

***Correspondence:**
Won K. Cho
wonkyong@gmail.com

Specialty section:
This article was submitted to Virology, a section of the journal Frontiers in Microbiology

Received: *24 January 2016*
Accepted: *31 May 2016*
Published: *15 June 2016*

Citation:
Jo Y, Choi H and Cho WK (2016) Genome Sequence of Dengue virus 3 from the Pythium insidiosum Transcriptomes. Front. Microbiol. 7:926. doi: 10.3389/fmicb.2016.00926

mycelia samples were transferred to 2 ml of microcentrifuge tube and incubated at 28°C and 37°C, respectively, for 24 h. Harvested mycelia was immediately frozen in liquid nitrogen for further study. Poly-A tailed mRNAs were isolated from total RNAs and used for cDNA library preparation. Sequencing was performed using the Genome Sequencer (GS) FLX Titanium platform (Roche Applied Sciences, Penzberg, Germany).

De novo Transcriptome Assembly

We downloaded two raw data with following accession numbers, DRR004443 and DRR004444, from DDBJ (DNA Data Bank of Japan) (https://trace.ddbj.nig.ac.jp/index_e.html). We used a workstation (two six-core CPUs and 256-GB RAM) operated using the Ubuntu 12.04.5 LTS operation system for all bioinformatics analyses in this study. Each individual FASTQ file for each library was first subjected to *de novo* transcriptome assembly using the Trinity program (version 2.0.2, released 22nd January 2015) with default parameters (Grabherr et al., 2011). We obtained two independent transcriptomes from the two samples (**Table 1**). For *de novo* genome assembly of DENV3, we combined two raw data sets and performed transcriptome assembly again using Trinity, Velvet programs (Zerbino and Birney, 2008), and iAssembler program (Zheng et al., 2011). After that, contigs associated with DENV3 were selected by blast search against known DENV3 reference sequences. Genome of DENV3 was manually assembled.

Identification of Viruses in the *P. insidiosum* Transcriptomes

To identify viruses in the *P. insidiosum* transcriptomes, two different approaches were used. For the first, *de novo* assembled contigs were blasted against complete viral reference sequences (http://www.ncbi.nlm.nih.gov/genome/viruses/). For the BLAST search, the MEGABLAST algorithm with a cut-off *e*-value of 1e-5 was applied. MEGABLAST is much faster than other sequence similarity programs and provides very reliable sequence similarities for the identification of viruses. For the second approach, all the FASTQ files were converted into FASTA files using the FASTX-Toolkit (http://hannonlab.cshl.edu/fastx_toolkit/) and FASTA files from each library were directly blasted against complete viral reference sequences.

TABLE 1 | Summary of *de novo* transcriptome assembly and the number of identified DENV3 associated reads and contigs.

Index	28°C	37°C
SRA accession No.	DRR004443	DRR004444
Total genes	14,327	17,761
Total transcripts	14537	18049
Percent GC	59.23	60.29
Contig N50	794	827
Median contig length	697	726
Average contig	751.7	797.18
Total assembled bases	10927464	14388240
Total No. of reads	177947	204241
No. of DENV3 reads	638	229
No. of DENV3 contigs	116	20

Examination of Single Nucleotide Variations

To identify SNVs, all the raw data (FASTQ files) were aligned on the obtained DENV3 genome sequence using the Burrows–Wheeler Aligner (BWA) with default parameters (Li and Durbin, 2009). The obtained SAM files were converted to BAM files for sorting using SAMtools (Li et al., 2009). The BAM files were sorted for SNV calling using SAMtools. Afterward, mpileup was conducted to generate the VCF format. The SNVs were then called using BCFtools implemented in SAMtools, and finally, SNVs were filtered using BCFtools. For the visualization of mapped reads on the genome, aligned SAM files were imported to the Tablet program (Milne et al., 2010).

RESULTS

Identification of DENV3 in the *P. insidiosum* transcriptomes

In a search of viruses infecting fungi in the publicly available transcriptome data, we found DENV3-associated sequences from *P. insidiosum* transcriptomes. The transcriptomes were composed of two different libraries, which were generated from two different growth conditions, 28°C and 37°C. BLAST search revealed that 0.36% (638 reads) and 0.11% (229 reads) at 28°C and 37°C, respectively, were sequences associated with DENV3 (**Figure 1A**). The portion of DENV3 associated reads at 28°C was more than three times that at 37°C. This result indicates that replication of DENV3 was reduced two-fold when the temperature was increased.

De novo Viral Genome Assembly for DENV3

Many sequenced reads were associated DENV3. Therefore, we *de novo* assembled transcriptome of *P. insidiosum* to identify contigs associated with the DENV3 genome. BLAST search identified 116 (28°C) and 20 (37°C) contigs associated with DENV3 (**Figure 1B**; **Supplementary Table S1**). The longest contig was 2332 bp, while the shortest contig was 177 bp. We assembled the genome of DENV3. The genome of DENV3, referred to as isolate Pythium, was 10,671 nucleotides (nt) in length (accession number: KT424097). By BLASTN search against the NCBI nucleotide database, the DENV3 isolate Pythium was found to be highly matched to the known DENV3 isolate HN/2013/20 (KJ622192.1) with 98% sequence identity. The DENV3 isolate HN/2013/20 was isolated from Henan, China, in 2013, indicating the possible origin of DENV3 isolate Pythium.

We mapped raw data on the genome of the obtained DENV3 isolate Pythium. As shown in **Figure 1C**, the number of reads mapped on the genome was much higher in the transcriptome from 28°C as compared to that of 37°C (**Figure 1C**).

Analysis of Single Nucleotide Variations

We examined SNVs for DENV3 in two different transcriptomes (**Supplementary Table S2**). From the transcriptome at 28°C, we identified 73 SNVs including 11 InDels (Insertion and Deletions), while 23 SNVs harboring nine InDels were detected from the

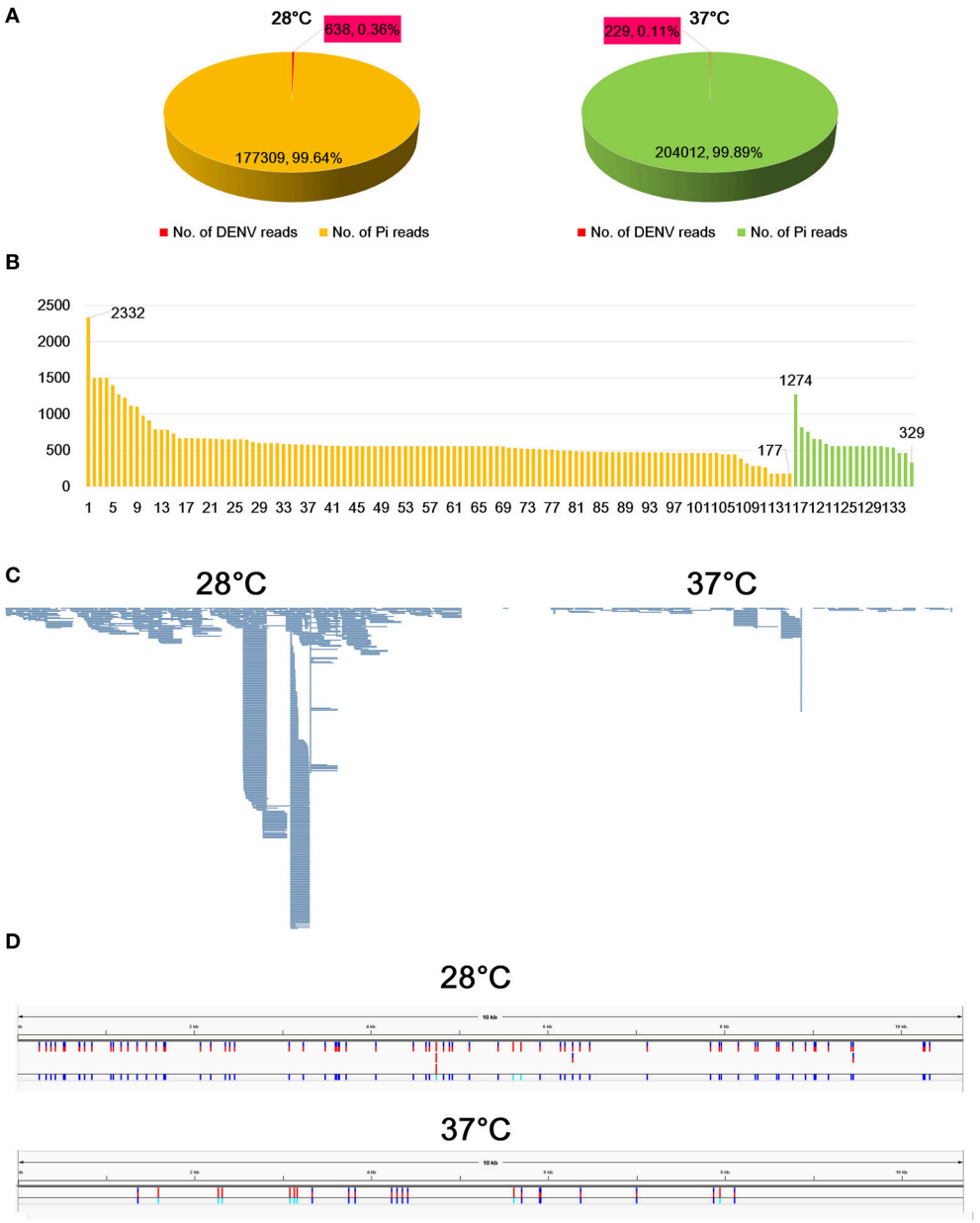

FIGURE 1 | Identification of sequences associated with DENV3 from *P. insidiosum* transcriptome data. (A) The number of reads associated with DENV3 in samples grown at 28°C and 37°C indicated by red colored box. **(B)** The length distribution of identified contigs associated with DENV3. Orange and green colored bars indicate samples grown at 28°C and 37°C, respectively. The number indicates the length of contigs (bp) **(C)** Mapped DENV3 associated with reads on the assembled DENV3 genome, which was visualized by the Tablet program. **(D)** The locations of identified SNVs along the DENV3 genome in two samples grown at 28°C and 37°C, respectively.

transcriptome at 37°C (**Figure 1D**). This data strongly supports the quasispecies nature of DENV3 within the *P. insidiosum* host (Kurosu, 2011).

DISCUSSION

The host ranges of viruses were numerous, from single cellular organisms to multicellular organisms. Previously, several viruses have been identified in many oomycetes, including *Phytophthora* and *Pythium* species (Gillings et al., 1993; Cai and Hillman, 2013). In addition, double-stranded RNA virus has been identified in the human pathogenic fungus *Blastomyces dermatitidis* (Kohno et al., 1994). A recent study using electron microscopy demonstrated that several human pathogenic fungi were infected by virus-like particles (Sharma et al., 2011). However, to our knowledge, no study has

clearly identified a virus in the human pathogenic fungus so far.

To clearly demonstrate the presence of DENV3 in *P. insidiosum* transcriptomes, we assembled the genome of DENV3 isolate *Pythium* and examined its SNVs using *Pythium* transcriptome data. However, we are not sure whether the *P. insidiosum* was really infected by DENV3. It seems that the contamination rate of DENV3 in *P. insidiosum* culture should be very high. For example, a patient was infected with dengue virus and had viremia. Total RNAs from the viremia were transferred into *P. insidiosum* culture medium and slowly degraded during culture. Libraries were prepared from the culture medium containing dengue virus and sequenced by a next-generation sequencer. Moreover, the low amount of DENV3 at 37°C as compared to that at 28°C indicates the instability of the DENV3 RNA genome at higher temperatures. If DENV3 can replicate in *P. insidiosum*, we can get a high level of DENV3 RNA genome at 37°C, because flavivirus polymerase usually works better at higher temperatures (Simon et al., 2015).

Many previous studies have also reported microbial contamination in clinical samples by NGS. For example, substantial bacterial contamination has routinely been identified in RNA-Seq data (Strong et al., 2014) as well as DNA data (Laurence et al., 2014). Due to the high level of sensitivity of the NGS technique, NGS is currently used to discover new viruses associated with diseases in clinical virology (Datta et al., 2015; Perlejewski et al., 2015). Taken together, this study provides the complete genome of DENV3 from *P. insidiosum* transcriptomes that might have been contaminated during sample preparation.

DATA ACCESS

The two raw data in this study can be available from DDBJ (DNA Data Bank of Japan) (https://trace.ddbj.nig.ac.jp/index_e.html) with following accession numbers, DRR004443 and DRR004444. Genome sequence of DENV3 isolate Pythium was deposited in GenBank with accession number KT424097.

AUTHOR CONTRIBUTIONS

WC designed the research; YJ, HC, and WC performed the research; YJ, HC, and WC analyzed the data; and YJ, HC, and WC wrote the paper.

ACKNOWLEDGMENTS

This work was carried out with the support of the "Cooperative Research Program for Agriculture, Science and Technology Development (Project No. PJ01186102)" conducted by the Rural Development Administration, Republic of Korea. This work is dedicated to the memory of my father, Tae Jin Cho (1946–2015).

SUPPLEMENTARY MATERIAL

The Supplementary Material for this article can be found online at: http://journal.frontiersin.org/article/10.3389/fmicb.2016.00926

Supplementary Table S1 | Detailed information of megablast results to identify contigs associated with DENV3.

Supplementary Table S2 | Information of identified single nucleotide variations for DENV3 in two samples grown at 28°C and 37°C, respectively.

REFERENCES

Adams, I. P., Glover, R. H., Monger, W. A., Mumford, R., Jackeviciene, E., Navalinskiene, M., et al. (2009). Next-generation sequencing and metagenomic analysis: a universal diagnostic tool in plant virology. *Mol. Plant Pathol.* 10, 537–545. doi: 10.1111/j.1364-3703.2009.00545.x

Bai, Z., Liu, L.-C., Jiang, L.-Y., Liu, Q., Cao, Y.-M., Xu, Y., et al. (2013). Complete genome sequence of dengue virus serotype 3 from Guangzhou, China. *Genome Announc.* 1:e0020812. doi: 10.1128/genomeA.00208-12

Cai, G., and Hillman, B. I. (2013). Phytophthora viruses. *Adv. Virus Res.* 86, 327–350. doi: 10.1016/B978-0-12-394315-6.00012-X

Chambers, T. J., Hahn, C. S., Galler, R., and Rice, C. M. (1990). Flavivirus genome organization, expression, and replication. *Annu. Rev. Microbiol.* 44, 649–688. doi: 10.1146/annurev.mi.44.100190.003245

Datta, S., Budhauliya, R., Das, B., and Chatterjee, S. (2015). Next-generation sequencing in clinical virology: discovery of new viruses. *World J. Virol.* 4:265. doi: 10.5501/wjv.v4.i3.265

Gaastra, W., Lipman, L. J., De Cock, A. W., Exel, T. K., Pegge, R. B., Scheurwater, J., et al. (2010). Pythium insidiosum: an overview. *Vet. Microbiol.* 146, 1–16. doi: 10.1016/j.vetmic.2010.07.019

Gillings, M., Tesoriero, L., and Gunn, L. (1993). Detection of double-stranded RNA and virus-like particles in Australian isolates of Pythium irregulare. *Plant Pathol.* 42, 6–15. doi: 10.1111/j.1365-3059.1993.tb01466.x

Grabherr, M. G., Haas, B. J., Yassour, M., Levin, J. Z., Thompson, D. A., Amit, I., et al. (2011). Full-length transcriptome assembly from RNA-Seq data without a reference genome. *Nat. Biotechnol.* 29, 644–652. doi: 10.1038/nbt.1883

Jo, Y., Choi, H., and Cho, W. K. (2015). De novo assembly of a bell pepper endornavirus genome sequence using RNA sequencing data. *Genome Announc.* 3, e00061–e00015. doi: 10.1128/genomeA.00061-15

Kohno, S., Fujimura, T., Rulong, S., and Kwon-Chung, K. (1994). Double-stranded RNA virus in the human pathogenic fungus *Blastomyces dermatitidis*. *J. Virol.* 68, 7554–7558.

Krajaejun, T., Lerksuthirat, T., Garg, G., Lowhnoo, T., Yingyong, W., Khositnithikul, R., et al. (2014). Transcriptome analysis reveals pathogenicity and evolutionary history of the pathogenic oomycete Pythium insidiosum. *Fungal Biol.* 118, 640–653. doi: 10.1016/j.funbio.2014.01.009

Kurosu, T. (2011). Quasispecies of dengue virus. *Trop. Med. Health* 39, 29. doi: 10.2149/tmh.2011-S02

Latijnhouwers, M., De Wit, P. J., and Govers, F. (2003). Oomycetes and fungi: similar weaponry to attack plants. *Trends Microbiol.* 11, 462–469. doi: 10.1016/j.tim.2003.08.002

Laurence, M., Hatzis, C., and Brash, D. E. (2014). Common contaminants in next-generation sequencing that hinder discovery of low-abundance microbes. *PLoS ONE* 9:e97876. doi: 10.1371/journal.pone.0097876

Li, H., and Durbin, R. (2009). Fast and accurate short read alignment with Burrows–Wheeler transform. *Bioinformatics* 25, 1754–1760. doi: 10.1093/bioinformatics/btp324

Li, H., Handsaker, B., Wysoker, A., Fennell, T., Ruan, J., Homer, N., et al. (2009). The sequence alignment/map format and SAMtools. *Bioinformatics* 25, 2078–2079. doi: 10.1093/bioinformatics/btp352

Martina, B. E., Koraka, P., and Osterhaus, A. D. (2009). Dengue virus pathogenesis: an integrated view. *Clin. Microbiol. Rev.* 22, 564–581. doi: 10.1128/CMR.00035-09

Mendoza, L., Hernandez, F., and Ajello, L. (1993). Life cycle of the human and animal oomycete pathogen Pythium insidiosum. *J. Clin. Microbiol.* 31, 2967–2973.

Milne, I., Bayer, M., Cardle, L., Shaw, P., Stephen, G., Wright, F., et al. (2010). Tablet—next generation sequence assembly visualization. *Bioinformatics* 26, 401–402. doi: 10.1093/bioinformatics/btp666

Perlejewski, K., Popiel, M., Laskus, T., Nakamura, S., Motooka, D., Stokowy, T., et al. (2015). Next-generation sequencing (NGS) in the identification of encephalitis-causing viruses: unexpected detection of human herpesvirus 1 while searching for RNA pathogens. *J. Virol. Methods* 226, 1–6. doi: 10.1016/j.jviromet.2015.09.010

Radford, A. D., Chapman, D., Dixon, L., Chantrey, J., Darby, A. C., and Hall, N. (2012). Application of next-generation sequencing technologies in virology. *J. Gen. Virol.* 93, 1853–1868. doi: 10.1099/vir.0.043182-0

Sharma, S., Gupta, S., and Shrivastava, J. (2011). Presence of virus like particles in human pathogenic fungi: chrysosporium sps and *Candida albicans*. *Indian J. Virol.* 22, 104–110. doi: 10.1007/s13337-011-0048-x

Simon, A. Y., Sutherland, M. R., and Pryzdial, E. L. (2015). Dengue virus binding and replication by platelets. *Blood* 126, 378–385. doi: 10.1182/blood-2014-09-598029

Strong, M. J., Xu, G., Morici, L., Bon-Durant, S. S., Baddoo, M., Lin, Z., et al. (2014). Microbial contamination in next generation sequencing: implications for sequence-based analysis of clinical samples. *PLoS Pathog.* 10:e1004437. doi: 10.1371/journal.ppat.1004437

Zerbino, D. R., and Birney, E. (2008). Velvet: algorithms for de novo short read assembly using de Bruijn graphs. *Genome Res.* 18, 821–829. doi: 10.1101/gr.074492.107

Zheng, Y., Zhao, L., Gao, J., and Fei, Z. (2011). iAssembler: a package for de novo assembly of Roche-454/Sanger transcriptome sequences. *BMC Bioinformatics* 12:453. doi: 10.1186/1471-2105-12-453

Conflict of Interest Statement: The authors declare that the research was conducted in the absence of any commercial or financial relationships that could be construed as a potential conflict of interest.

Copyright © 2016 Jo, Choi and Cho. This is an open-access article distributed under the terms of the Creative Commons Attribution License (CC BY). The use, distribution or reproduction in other forums is permitted, provided the original author(s) or licensor are credited and that the original publication in this journal is cited, in accordance with accepted academic practice. No use, distribution or reproduction is permitted which does not comply with these terms.

Advantages of publishing in Frontiers

OPEN ACCESS
Articles are free to read, for greatest visibility

COLLABORATIVE PEER-REVIEW
Designed to be rigorous – yet also collaborative, fair and constructive

FAST PUBLICATION
Average 85 days from submission to publication (across all journals)

COPYRIGHT TO AUTHORS
No limit to article distribution and re-use

TRANSPARENT
Editors and reviewers acknowledged by name on published articles

SUPPORT
By our Swiss-based editorial team

IMPACT METRICS
Advanced metrics track your article's impact

GLOBAL SPREAD
5'100'000+ monthly article views and downloads

LOOP RESEARCH NETWORK
Our network increases readership for your article

Frontiers
EPFL Innovation Park, Building I • 1015 Lausanne • Switzerland
Tel +41 21 510 17 00 • Fax +41 21 510 17 01 • info@frontiersin.org
www.frontiersin.org

Find us on